
THE UNIVERSITY
*of* EDINBURGH

# Impact of rock properties on landscape form and detrital studies


THE UNIVERSITY
*of* EDINBURGH

Chrystiann Lavarini Ferreira

Thesis submitted in fulfilment of the requirements for the degree of Doctor of Philosophy to the University of Edinburgh –2018

## Declaration

I hereby declare that this thesis has been done only by myself and has not been published elsewhere, individually or as a whole, as part of any previous degree. The work contained in this thesis is entirely own my own, excepting in cases clearly stated.

Chrystiann Lavarini Ferreira

*Edinburgh, October 2018.*

## Abstract

The nature of the rocks exposed at the surface of the Earth influence both geomorphology and the release of sediment from hillslopes to rivers. Whereas this has been known for centuries, very few studies have quantitatively linked landscape form to rock type. Even fewer studies have linked rock type, abrasion and the selective release of minerals from gravel to sand, and their impact on the information contained in a river sediment sample. This thesis aims to address these two key issues in geomorphology. Detrital studies use properties of river sediment to infer processes and rates across the catchment from which it has been sourced; they have been crucial in addressing issues such as linkage between tectonics and erosion and the recycling of materials though cycles of mountain building and destruction. However, these studies rely on the assumption that a sand sample integrates catchment–wide information without bias. In a first chapter, I perform a series of experiments with an abrasion model to test if abrasion, which controls the release of minerals from gravel to sand, influences detrital age signatures and the erosion rates retrieved from them. In the study case (Marsyandi watershed, Himalaya), I use an extensive zircon age population dataset published by Amidon et al. (2005). The results demonstrate that pebble abrasion can change the zircon mixing proportions of upstream source units as well as the age distribution of mixed fluvial sands. This change is particularly significant when there is strong contrast in rock resistance within the watershed (e.g., when pebbles of sandstone have 31 % of mass loss/km, and pebbles of quartzite have 0.15 % of mass loss/km). Pebble abrasion is one of many factors that can change the mixing proportion of sands, including hillslope gravel supply, erosion rates, and mineral fertility. In our study, the abrasion model predicts age distributions that are statistically indistinguishable from those predicted by a no–abrasion model. However, the relative erosion rates estimated by the model largely differ from the results of a no–abrasion model (e.g., in one of the samples, relative erosion rates were 29% for Tethyan Series (TTS) and 71% for Formation II-III (FII-III) from the abrasion model against 42% and 58%, respectively, from the no-abrasion model), and are closer to those from other studies that suggest a strong correlation between modern erosion rates, tectonics and precipitation intensity in the Marsyandi watershed (e.g., one study found 22.5% for TTS and 77.5% for FII-III).

These findings suggest that pebble abrasion must be accounted to avoid uncorrected erosion rates estimated from detrital studies. In the following chapter, I analyse the influence of rock types on the development of mountain topography on the young island of Corsica (Mediterranean Sea). I investigate the topographic state of both drainage network and regional drainage divide in response to post–Miocene tectonics combined with variations in sea–level. The results suggest that the northern section of the drainage divide is currently moving to the east, while the southern section is moving to the opposite direction (i.e., westward). These patterns reinforce that Corsica is currently in a transient topographic state. The analysis of the drainage network highlights both rock type and structural units as major controls on the modern river profiles. I found that knickpoints are preferentially located at a similar distance from the sea level (20 to 25 km), which could suggest a common base level drop. However, given the existence of a strong structural control on the island, caution must be taken when interpreting spatial patterns of knickpoints in terms of external trigger. I have not found any correlation between the knickpoint metrics (slope, length, magnitude and relief) and the thermochonometric age domains compiled from other workers. These findings suggest that the current topographic state of the drainage network and divide of Corsica is controlled by both rock strength and structural boundaries rather than by long–term (and long–scale) exhumation patterns. Finally, I combine the techniques developed in the two previous chapters to assess what can be reliably retrieved from detrital studies, using the Tavignano watershed in Corsica (Mediterranean Sea) as a template. There, I find that the majority of the sampled zircon types are linked to the upstream sub–alkaline granites (e.g., S, J, P and G zircon types). The U–Pb ages of mixed samples show relatively similar peaks in the uppermost and lowermost sampling sites, while the intermediate site has several missing peaks. The main explanation for these results is the very small amount of grains collected for typology and U–Pb dating (from 6 to 59 zircon grains). The absence of zircon constraints in many of the contributing sources is also a major biasing factor. Through mineral mixing modelling, I demonstrate how analytical issues such as too few dated grains and age peak overlapping affect source–to–sink analysis. I also demonstrate how mineral mixing proportion in poorly constrained settings can be equally explained by different natural bias (e.g., zircon fertility or erosion) without being able to disentangle them. These results reinforce the importance of choosing the proper mineral tracer and recognising the factors acting on it to assess what controls the stratigraphic record.

## Lay summary

The type of the rocks exposed at the surface of the Earth influence both the landscape and the sediments transported by rivers. Few scientists have assessed the connection between rock type, landforms and sediments. This thesis aims to address these issues. Detrital studies use properties of river sediment to infer processes and rates across catchments. They have been crucial in addressing issues such as linkage between tectonics and erosion and the recycling of materials though mountain building and destruction. However, these studies rely on the assumption that a sand sample integrates catchment–wide information without bias. In a first chapter, I perform a series of experiments with a mathematical model to test if abrasion, which controls the release of minerals from gravel to sand, influences detrital ages and the erosion rates retrieved from them. In the study case (Marsyandi watershed, Himalaya), I use an extensive zircon age population dataset published by Amidon et al. (2005). The results demonstrate that pebble abrasion can change the amount of zircon grains in fluvial sands. This change is particularly significant when there is strong contrast in rock resistance within the watershed. Pebble abrasion is one of many factors that can change the mixing proportion of sands, including hillslope gravel supply, erosion rates, and mineral concentration. These findings suggest that pebble abrasion must be accounted to avoid uncorrected erosion rates estimated from detrital studies. In the following chapter, I analyse the influence of rock types on the development of mountain topography on the young island of Corsica (Mediterranean Sea). I investigate thetopographic state of both drainage network and regional drainage divide in response to post–Miocene tectonics combined with variations in sea–level. The results suggest that the northern section of the drainage divide is currently moving to the east, while the southern section is moving to the opposite direction (i.e., westward). These patterns reinforce that Corsica is currently adapting by changing elevation. The analysis of the drainage network highlights both rock type and structural units (e.g., faults) as major controls on the modern river profiles. Finally, I combine the techniques developed in the two previous chapters to assess what can be reliably retrieved from detrital studies, using the Tavignano watershed in Corsica (Mediterranean Sea) as a template. There, I find that the majority of the sampled zircon types are linked to upstream granites. The ages of the samples show relatively similar peaks in the uppermost and lowermost sampling sites, while the

intermediate site has several missing peaks. The main explanation for these results is the very small amount of grains collected for typologyand U–Pb dating. The absence of zircon constraints in many of the contributing sources is also a major biasing factor. Through mineral mixing modelling, I demonstrate how analytical issues such as too few dated grains and age peak overlapping affect source–to–sink analysis. I also demonstrate how mineral mixing proportion in poorly constrained settings can be equally explained by different natural bias (e.g., zircon fertility or erosion) without being able to disentangle them. These results reinforce the importance of choosing the proper mineral tracer and recognising the factors acting on it to assess what controls the stratigraphic record.

## Acknowledgements

This thesis is a collective construction that relied on my hands, and, when I say collective, I mean not only those who instructed or worked with me. I mean more than two hundred million women and men who supported me as taxpayers through the CAPES Brazilian foundation ("Coordenação de Aperfeiçoamento de Pessoal de Nível Superior"). I am immensely grateful for the PhD scholarship that you have provided to me (grant BEX 13193–13–9).

Firstly, I would like to thank Mikael Attal and Linda Kirstein, my supervisors, for accepting me as their PhD candidate. It has been an incredible journey and intellectually challenging to have feedbacks about my work from you both. I feel that I am in debit for the detailed review, patience and motivation about my writings and experiments (I will never forget the first time I saw Corsica from the sea and Mikael's first version of the Python code!).

Secondly, I am very thankful to Boris Gailleton, Carlos Alberto da Costa Filho, and Simon Mudd for assistance with code analysis and debugging. I am thankful to Guohui Shen and Nicola Rigonat for helping during zircon preparation.

Thirdly, I would like to thank Carlos A. da Costa Filho and Pedro L. S. de Miranda for making me enjoying Edinburgh more than I thought I could. I am also grateful to my friends of the "Jülich team", particularly, Aayush Srivastava, Daniel Sperl, Juliane Krenz, and Thomas. Equally, I am thankful to my friends of the "CCCP team" and our thought provoking debates.

Fourthly, I would like to thank David Whipp and two anonymous reviewers for their useful comments. I thank the Associate Editor Jon Warrick and the Editor Giovanni Coco for their additional comments. I am extremely grateful to William Amidon for providing the U–Pb Marsyandi's river dataset.

Finally, I am very grateful to my mom (Scheila), my dad (Jefferson), my brother (Alexandre) and my partner (Cristina) for creating over these years the best environment to make me happy. I am glad to have you here, in my heart, even in the other side of the Atlantic Ocean.

**Contents**

# List of figures

## Chapter 1

**Chapter 2**

**Chapter 3**

**Chapter 4**

**Supporting Information**

**Chapter 2**

## List of tables

## Chapter 2



## Chapter 3



## Chapter 4

**Supporting Information**

**Chapter 2**

**Chapter 3**



**Chapter 4**

# Chapter 1–Introduction

## 1.1. Motivation

Bedrock is one of the fundamental elements that make landscapes on Earth and other planets so diverse. The influence of rock properties on landforms and on the characteristics of materials transported from their disintegration, i.e., sediments, has a crucial role in landscape evolution. In the long–term ($10^4$ –$10^6$ years [Myr]), landscapes made of lithologies with different resistances to erosion have varying responses to perturbations: harder rocks are destroyed and removed slower so that their landforms remain longer, while softer rocks are altered and vanished faster. This diverse outcome explains why many outstanding hard rock landforms can be observed today after millions of years, while some landforms can be reconstructed only by analysing the detrital products of their disintegration in the sedimentary record (Liu, 2014; Mandal et al., 2015; Forte et al., 2016).

Two of the most successful ways to investigate past landscape changes in geosciences is through the study of the detrital products of erosion, i.e. sediments, and the morphology of the landscape, i.e. topography.

The sediments produced from bedrock disintegration contain minerals that work as an archive for geoscientists to reconstruct processes over a range of timescales (of centuries to billions of years). Therefore, retrieving information about source rocks from detrital minerals has been a key tool to answer several questions in geosciences. These answers include reconstructing palaeogeography (e.g., Sharman et al., 2015; Fernández–Suárez et al., 2014; Shaw et al., 2014), sedimentary basin genesis (e.g., Priyatkina et al., 2016; Zhong et al., 2015), long–term environmental/climate changes (e.g., Litty et al., 2017; Mason et al., 2017), mountain growth/decay (e.g., Lease et al., 2016; Bush et a., 2016), including the estimation of the Earth's age (e.g., Wilde et al., 2001) and subglacial erosion (e.g., Tochilin et al., 2012; Thomson et al., 2013).

In the last decades, detrital grain analysis has been boosted with new dating techniques such as cosmogenic nuclides (e.g., $^{10}$Be, $^{26}$Al, $^{36}$Cl in quartz) and geo–thermochronometric dating systems (e.g., U–Pb, $^{40}$Ar–$^{39}$Ar, (U–Th)/He, fission–track analysis in zircon and apatite). Cosmogenic nuclides have enabled dating of the exposure time of rocks to cosmic radiation as well as estimating both *in situ* and catchment–wide erosion rates over millennial timescales (see Goose and Phillips, 2001). Geochronological dating systems have allowed the understanding of crystallisation ages of minerals and their host bedrocks in a timescale of billions of years (see Jackson et al., 2004). Similarly, thermochronometric dating systems have permitted the understanding of landscape exhumation histories (i.e., crustal uplift with erosion accounted) and to constraining sedimentary records over millions of years (e.g., estimating the lag time between a grain crossed a certain depth in the crust, their later erosion and deposition in a sedimentary basin) (see Hurford, 2019).

However, to reconstruct accurately the history of detrital grains is essential to understand the factors operating from their initial formation (source) until their final deposition (sink) (Helland–Hansen et al., 2016). It is known that after exposure at the surface, rocks are disintegrated by physical and chemical processes known as weathering (Dosseto et al., 2014). Weathering converts rocks into unconsolidated materials that compose the regolith available for erosion on hillslopes (e.g., Murphy et al., 2016; Oh and Richter, 2005). Then, a combined action of hillslope processes (e.g., mass movements) and river dynamics are able to carry this unconsolidated material to their depositional sites (i.e., floodplains, sedimentary basins, etc.). During fluvial transport, sediments are fractionated by their size–density and by physical breaking (abrasion) (see Malusà et al., 2016; Attal and Lavé, 2006). Eventually, grain information retrieved from sediments such as mineralogy, age, size and morphology are determined by their source characteristics and by processes occurring during transport and deposition (see Nesbitt et al., 1996). After sampling, statistical limitations such as the number of analysed grains, overlapping source age distributions and laboratory processing can also introduce new distortions that create a biased history retrieved from the samples (see Sircombe and Stern, 2002).

Despite many advances regarding the determination of natural and analytical biases that happen from source to sink and their influence on detrital grains, many are still poorly known, or have been assumed to not interfere with age distributions without being empirically tested. From

these unexplored biases, physical breaking by pebble abrasion in detrital grains used in geo–thermochronology (e.g., detrital zircon and apatite) has never been investigated, while some other biases have started to received attention by the scientific community just recently (e.g., analytical biases when finding source rocks from detrital grain ages in mixed river samples) (e.g., Sláma and Košler, 2012; Naylor et al., 2015; Garzanti, 2016; Garzanti et al., 2015; Yang et al., 2012).

Similarly, with the advent of new topographic data (e.g., high–resolution digital elevation models), scientists have been able to remotely assess past landscape changes. For instance, until recently, recognition of landscapes undergoing a varying elevation over time (i.e., in topographic transience) or uniform elevations in time (i.e., in topographic steady state) could be done only by field–based investigations, such as by estimating erosion rates in opposing watersheds (e.g., Stokes et al., 2002; Mather, 2000) or by checking regolith thickness along hillslopes (see Heimsath et al., 1997). Today, topographic parameters can be readily extracted from digital elevation models and serve as a proxy for erosion. These techniques have enabled the identification of elements of transience and steady–state conditions by predicting drainage divide stability (e.g., Willett et al., 2014), identifying topographic signatures of discrete river capture (i.e., when a river takes the drainage of another) (e.g., Forte and Whipple, 2018; Whipple et al., 2017), and distinguishing deviations on the slope of river profiles (i.e., knickpoints) caused by changes in rock resistance, uplift and base level (e.g., Perron and Royden, 2013; Mudd et al., 2018). Such novel techniques can provide a quick assessment of poorly constrained areas and bring relevant insights about the response timescales of the surface processes to perturbations (e.g., Hurst et al., 2012; Forte et al., 2015).

Corsica, a small island in the Mediterranean is an ideal setting to investigate geomorphological responses to perturbations. Several studies have provided erosional constrains of catchment (e.g., Molliex et al., 2017; Sømme et al., 2011) and drainage divides (e.g., Kuhlemann et al., 2008, 2009), a temporally constrained sea level (e.g., Lambeck et al., 2004), climatic data sets (e.g., Kuhlemann et al., 2008; Lambert et al., 2011) and a relatively detailed geological mapping, among other parameters, that increase the robustness of a landscape evolution analysis based primarily on topography. Moreover, the recognition of the current topographic state of Corsica a relevant topic to understand the response time between tectonics and surface processes, particularly in the context of Alpine and Apennine events (i.e., the main

subduction zones in the region) (e.g., Malusà et al., 2015; Molli, 2008; Molli et al., 2006). In addition, a recent debate about Corsica has also emerged with some scientists claiming that it is currently approaching a topographic steady state (e.g., Molliex et al., 2017), while others claim that it is still in transience (e.g., Fellin et al., 2005). New techniques to interrogate the topography could therefore shed light to this debate.

Similarly, the Himalaya is a setting with a rare suite of well–constrained parameters and an extensive data set required to investigate biases produced in the sedimentary record. Many studies have provided independently data about erosion rates (e.g., Scherler et al., 2014; Abrahami et al., 2016; Sinclair et al., 2017), tectonic uplift (e.g., Godard et al., 2014; van der Beek et al., 2016), sediment transport dynamics and mineral characteristics of the bedrocks and sedimentary archives (e.g., Dingle et al., 2017; Garzanti et al., 2007; Gehrels et al., 2011; Guo et al., 2017).

I use two settings as natural laboratories in this thesis: the Marsyandi watershed (Himalaya) and the island of Corsica (Mediterranean Sea). In the following sections of this introduction, I provide a justification for the choice of these settings (1.2), state the thesis objectives more clearly (1.3), provide a theoretical background on how rock properties modulate topographic and sedimentary characteristics (1.4) and, lastly, I provide a thesis outline (1.5).

The analyses performed in this thesis are intended to contribute on two different cutting–edge debates of modern surface processes research. The first aim is to test how different factors occurring from source to sink can change detrital grain information retrieved in sedimentary archives. More particularly, I test how U–Pb detrital zircon ages, zircon source contribution and zircon typology are affected by natural processes prior to deposition and potential biases introduced by analytical processes after sampling. The second aim of this thesis is a study, where I test if a Mediterranean island (Corsica) is currently at topographic steady or transient–state by using primarily topographic metrics. More precisely, I investigate what factors (e.g., rock resistance, uplift or base level drop) can explain drainage divide stability and the river channel profiles of the island.

## 1.2. Justifying the choice of the study areas

The Marsyandi watershed in the Himalaya is an exceptionally well–constrained setting with the main parameters required to simulate numerically our original hypothesis, which is how different factors occurring from source to sink can change detrital grain information retained in sedimentary archives. These constrains include empirically derived data on hillslope grain size supply, pebble abrasion rates (Attal and Lavé, 2006), erosion rates, zircon fertility, zircon source ages and zircon ages of river sediments (Amidon et al., 2005). For this reason, I focus particularly on the influence of these variables on characteristics of zircon grains along the Marsyandi watershed. The objectives of this investigation are explored in the following section (1.3) and their analyses are performed in the Chapter 2.

After choosing to work with a well–constrained setting, I chose Corsica Island as a second study area for two main reasons.

Firstly, in spite of many studies focusing on erosion rates, exhumation history and landscape evolution, no scientific investigation has tested if the island is approaching a condition of topographic steadiness over time (i.e., topographic steady state) or it is still adapting morphologically (i.e., transient). Similarly, although some works have investigated the river profiles of Corsica, none has explored the relationship between their knickpoints and several factors that can have caused them (e.g., sea level drop, structural boundaries and changes in rock resistance). By combining these techniques, I am able to unravel the current topographic state of Corsican river channels and drainage for the first time, which can bring new insights about the timing of geodynamic processes in the context of the Mediterranean, including changes in tectonics, climate and sea level. The objectives of this investigation are explored in the following section (1.3) and their analyses are performed in the Chapter 3.

Secondly, I use the Tavignano watershed in Corsica as a template to test what factors can explain not only the measured U–Pb ages, source proportion and typology of detrital zircons, but, equally, the difficulties found by scientists to disentangle causal factors of detrital grain populations in poorly constrained sites. In many detrital studies, two main limitations usually arise to scientists: (i) the number of analysed grains after sampling and laboratory processing is

far below the minimum suggested for a statistically significant investigation (see Vermeesch, 2004) and (ii) a poor understanding of the upstream controlling factors of the detrital information is available. The objectives of this investigation are explored in the following section (1.3) and their analyses are performed in the Chapter 4.

## 1.3. Approach

The explanations presented in this thesis are derived from field, laboratory, modelling and literature analyses, which were collected to answer three broad questions:

1. Does pebble abrasion influence detrital age population statistics?
2. Is the landscape of Corsica Island (Mediterranean Sea) in topographic steady or transient–state?
3. What can be reliably retrieved from detrital grains in poorly constrained settings?

Further explanation about specific objectives of those three broad questions (hypotheses) is given in the thesis outline (1.6) and in the Chapters 2, 3 and 4. In the next section (1.4), I introduce the basic background required to understand the nature of these questions and the study areas used in this thesis.

## 1.4. Theoretical background

In this section, I provide two main subjects as theoretical background. In the first subsection (1.4.1), I discuss the theory and application of detrital grains, and the linkage between detrital information in stratigraphic record and source areas is explored. In the second subsection (1.4.2), I describe the influence of rock properties and environmental controls on landscape dynamics in tectonically active landscapes. More specifically, numerical models to predict past, current and future changes in topographic elements (e.g., rivers and drainage divide) are highlighted.

### *1.4.1. Biases in detrital studies*

From crystallisation to their final deposition, mineral grains are exposed to environmental conditions that change them chemically, physically and numerically (Lukens et al., 2016). As previously argued (1.1), these natural factors are able to cause important transformations in the population of grains retrieved from a sedimentary record. Disentangling these factors is therefore a crucial step to unravel the characteristics of source areas, especially in cases where post–sampling analytical processes produce disturbance.

The use of detrital grains to explore source to sink relationships has evolved over time. One of the tools available for sediment provenance analysis is using crystallography of detrital grains to estimate magmatic activity (e.g., magmatic zoning), metamorphism (e.g., recrystallised domains, reabsorption) and recycling (e.g., rounding and opaque internal structure) (see Corfu et al., 2003). By linking detrital grain to source area information, scientists were able to estimate semi–quantitatively source to sink relationships when many advanced techniques were unavailable (e.g., Morton, 1985). These crystallographic analyses are still relevant, including the application of the Pupin (1980) zircon typology to classifying detrital zircons and their petrographic origin. The zircon typology of Pupin (1980) is a combination of their most common crystalline faces (pyramids {101}, {211} and prisms {100}, {110}) (Fig. 1.1).

Main types and subtypes are reported according to two variables: A (IA) and T indexes (IT). This classification scheme is based on the development of prismatic and pyramidal crystal faces of zircons. The A index (IA) has been associated to the Al/(Na + K) ratio and pyramidal faces. The pyramids {211}, {101} and {301} are known to correlate well with aluminous, alkaline and peralkaline mediums, respectively. The T index (IT) is associated with the temperature of zircon crystallisation, which regulates the development of prismatic faces.

This classification scheme allows grouping zircon types into different environment of crystallisation. While, low A and T indices are typical of crustal origin (i.e., which crystallised in the crust) such as leucogranites and aluminous monzogranites. Larger ranges of A and varying T

indexes are associated to granitoids in between crustal and mantle origin (i.e., a hybrid–group) such as calc–alkaline and sub–alkaline monzogranites/granodiorites. The highest values of A and T indexes are typical of mantle origin, with prevalence of alkaline granitoids (Pupin, 1980). Given the very small size of detrital zircons (63 –125 µm), morphological analysis are usually performed in optical microscopy and cathodoluminescence detector (CL).

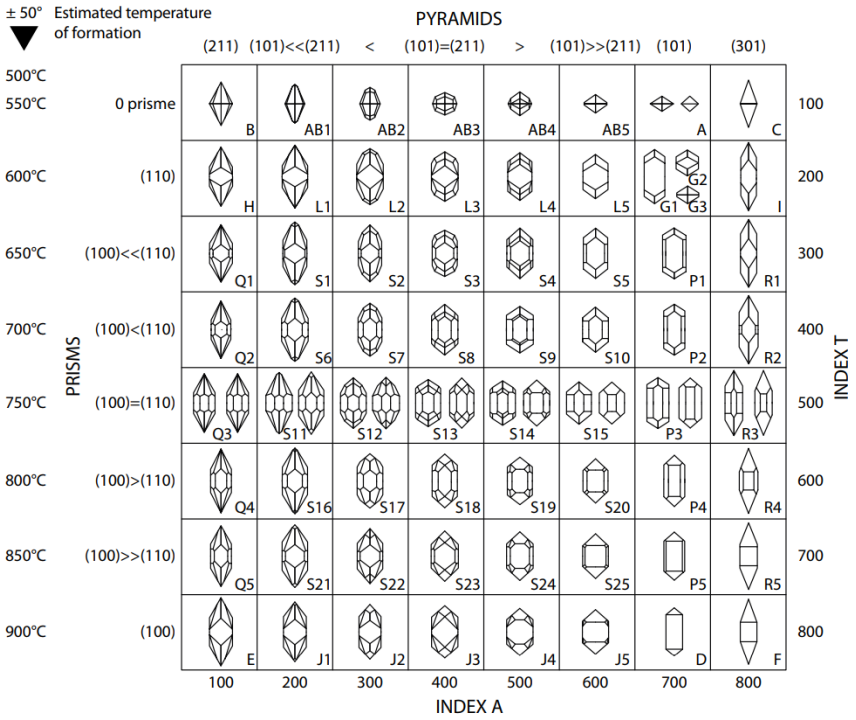


Figure 1.1: Zircon typological classification proposed by Pupin (1980). Index A defines the Al/alkali ratio, controlling the development of pyramids {101} and {211} in the crystals. Index T defines the temperature effect on the development of prisms {100} and {110}.

More recently, with the advent of analytical techniques that allow estimating detrital grain ages very quickly (e.g., laser–ablation inductively coupled mass spectrometry (LA–ICPMS) and Secondary Ionisation Mass Spectrometry (SIMS)), a boom in the number of published detrital studies has occurred (Ireland and Williams, 2003). Similarly, new techniques to investigate the thermochronmetric history of minerals (e.g., fission–track and (U–Th)/He in zircon and apatite) have expanded the utility of detrital grains (Chew and Donelick, 2012). At the same time, scientists have revealed analytical biases that occur in detrital analysis and proposed solutions that minimise them. Among the solutions proposed, I emphasise the minimum number of grains

per sample for a statistically significant analysis (117), proposed by Vermeesch (2004), the recognition of biases during sample preparation (e.g., in magnetic and density separation in laboratory) (e.g., Sláma and Košler, 2012; Garzanti et al., 2015; Yang et al., 2012), and the identification of biases during dating procedures (e.g., while using SIMS and fission–tracks) (e.g., Farley, 2000). Further effort has enhanced the understanding of natural biases in detrital geo–thermochronology. Among these new understandings, scientists found evidence that different relative erosion rates (e.g., Amidon et al., 2005), mineral concentration and exposure areas of contributing sources (e.g., Dickinson, 2008), together with hydraulic sorting processes during transport (e.g., Malusà et al., 2013), are able to change the composition of detrital grain populations.

One of the most effective ways to disentangle natural processes that bias the sedimentary record is through a combination of inverse and forward mixing modelling of grain ages (Sundell and Saylor, 2017). In cases where the scientist wants to discover only the proportion of zircon sources in a mixed sample, an inverse mixing modelling technique can be used to find the best–fit of several source age inputs (e.g., Saylor et al., 2013; Kimbrough et al., 2015; Licht et al., 2016). Conversely, in cases where the scientist wants to test a number of upstream controlling factors in a mixed sample, a forward modelling can be used to find the best–fit of source ages by testing those factors (e.g., Amidon et al., 2005; Garzanti et al., 2012). Through years of natural and laboratory investigations, the main natural factors recognised to acting on grain age populations from source to sink have been: (1) mineral concentration (see Moecher and Samson, 2006; Spencer et al., 2018), (2) exposure area (e.g., Lease et al., 2007: Saylor et al., 2013), and (3) relative erosion rates of the source rocks (e.g., Amidon et al., 2005). In mixing models, these variables can be incorporated from field–based estimations to predict the characteristics of source areas and sediments (in modern rivers and ancient sedimentary records). Mixing models have been used to unravel the evolution of several detrital minerals, particularly, about biases on both cosmogenic nuclides ($^{10}$Be) in detrital quartz (e.g., Lukens et al., 2016) and U–Pb ages in detrital zircon grains (e.g., Sharman and Johnstone, 2017).

To find the best–fit mixing proportion of different sources from a downstream mixed sediment sample (i.e., an inverse modelling approach), several statistical analyses have been suggested (see Saylor and Sundell, 2016). To date, the most common are Kolmogorov–Smirnov

(K–S) test, Kuiper test, Cross–Correlation coefficient, Similarity coefficient, and more recently, Monte Carlo simulation (Sundell and Saylor, 2017; see Fig. 1.2).

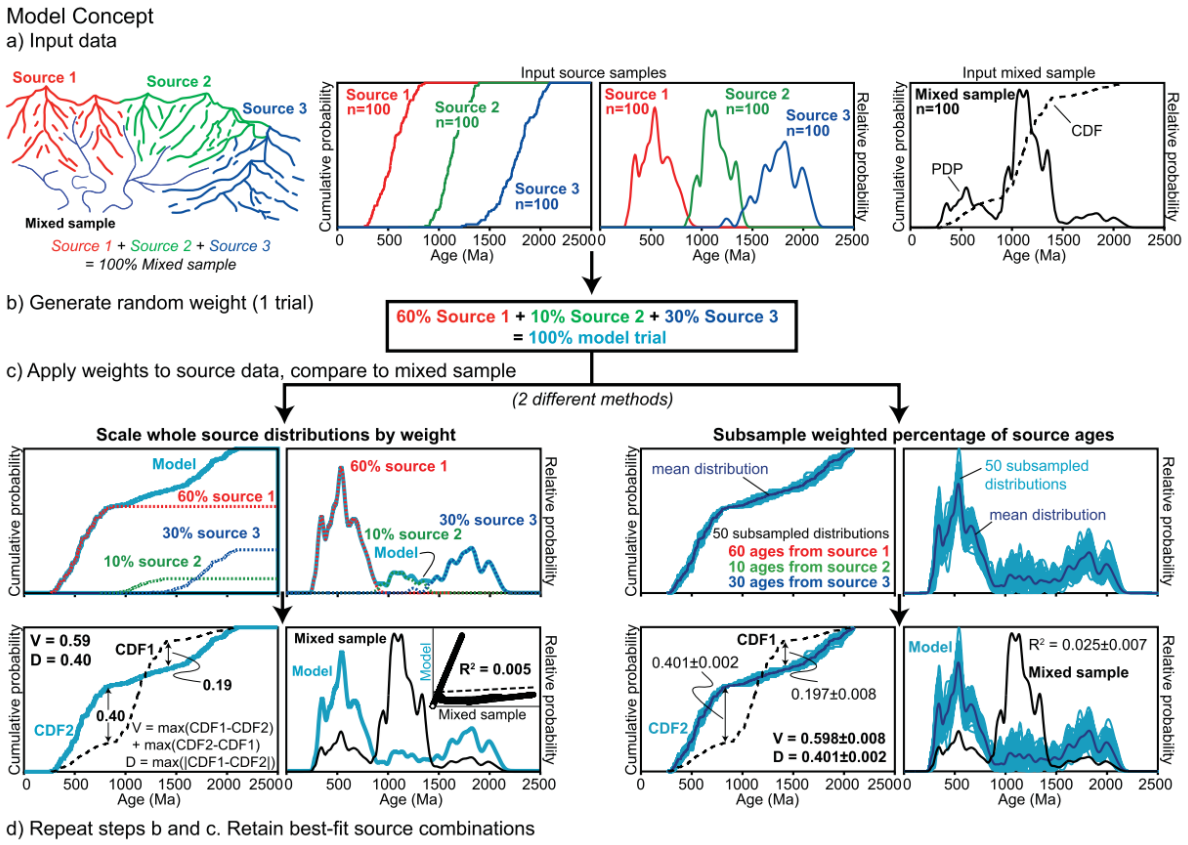


Figure 1.2: An illustration showing how to (un)mix detrital age distribution through inverse Monte Carlo simulation.(a) Detrital age distributions representing three different sources are shown as cumulative distribution plots (CDFs, in the left) and probability density plots (PDPs, in the centre). In the right, a downstream mixed river sample with 20% of source 1, 70% of source 2, and 10% of source 3 is shown. (b) A random distribution of weight is used in each source (1–3). (c) The initial randomly generated weights from b are applied to every source age distribution in both CDFs (in the left) and PDPs (in the right). A statistical analysis is performed to minimise the misfit between model trials (in blue) and downstream real mixed sample (in black) using the K–S test, Kuiper test, and cross-correlation coefficient. The best–fit between mode trial and mixed sample yields a single distribution when random weighting is applied to CDFs or PDPs (in the left), and gives a range (with mean and standard deviation) when based on the subsampled source ages (in the right). (d) The steps previously performed (b and c) are repeated a number of times and a percent of best model fits are retained according to a user–specified criteria. Adapted from Sundell and Saylor (2017).

To test for controlling factors that can influence detrital age populations, forward mixing models can be applied to estimate the relative contribution of each of them (see Sharman and

Johnstone, 2017). For example, (1) mineral concentration, (2) exposure area, and (3) relative erosion rates of the sources can be used as weights to test how well they match the measured downstream mixed sample. By using forward mixing modelling, Amidon et al. (2005) was able to estimate (3) relative erosion rates by minimising the mismatch between the predicted age distributions of a mixed sample using a combination of controlling factors 1 and 2.

Although many natural and analytical biases have been investigated over the years, some common empirical information of sediment transport dynamics has never been included in detrital grain analysis. Among these untested dynamics, I highlight: (1) pebble abrasion rates and (2) the influence of hillslope grain size supply. Numerical, empirical and laboratory results demonstrate that size reduction and mineral liberation by (1) abrasion is an active process in pebble size (Krumbein, 1941; Kuenen, 1956; Schumm and Stevens, 1973; Mills, 1979; Parker, 1991; Attal and Lavé, 2006, 2009; Le Bouteiller et al., 2011; Domokos and Gibbons, 2012; Miller et al., 2014), while no evidence has been found in grains finer than sand (Malusà et al., 2013, 2016). This ambiguous fact has been incorrectly assumed in (un)mixing sediment models as if pebble abrasion were not able to bias detrital information. Similarly, (2) hillslope grain size supply has been shown to be important in steep terrains by biasing the concentration of cosmogenic nuclides in detrital quartz from river sediments (Lukens et al., 2016). These evidences highlight that the common practice of collecting a narrow range of sizes for detrital analysis (e.g., zircon and apatite between 63 μm and 125 μm) may not yield a representative result when the grain size supply is spatially variable. A detailed discussion about biases caused by untested river dynamics processes and how sediment mixing modelling works is given in the Chapter 2 of this thesis.

In the following subsection, I introduce a quantitative approach on how topography can be used to infer past, current and future changes in erosion due to rock properties and other environmental factors.

### *1.4.2. Development of topography and the influence of rocks*

River channels are one of the most sensitive elements of the landscape to changes in rock properties and in environmental conditions (Whipple and Tucker, 1999). As a result, they are key–objects in surface processes research. Mathematically, a river profile evolution can be described by advection and diffusion equations (Pelletier, 2008). In fluvial geomorphology, diffusion equations describe a flux of sediment (i.e., transport of mass) that is proportional to a sediment gradient, where any change in flux results in a change of mass (i.e., conversation of mass):

$$q = -pk\frac{\partial h}{\partial x}, \quad (1)$$

where $q$ is sediment flux per unit length (M/L/T), $p$ is bulk sediment density (M/L$^3$), $k$ is sediment diffusivity (L$^2$/T), $h$ is elevation (L) and $x$ is distance (L) (Willgoose et al., 1991). Assuming that any change in flux ($q$) results in change in elevation ($h$), the rate of change in elevation on time ($\partial h/\partial t$) is equal to the change in flux per unit length ($\partial q/\partial x$) divided by the bulk density ($p$):

$$\frac{\partial h}{\partial t} = -\frac{1}{p}\frac{\partial q}{\partial x}. \quad (2)$$

Substituting equation 1 into equation 2 gives us the classical diffusion equation (3):

$$\frac{\partial h}{\partial t} = k\frac{\partial^2 h}{\partial x^2}, \quad (3)$$

where the change in elevation with time is proportional to curvature $\frac{\partial^2 h}{\partial x^2}$ (i.e., change in gradient $\frac{\partial h}{\partial x}$) along a river profile (Hanks, 2000).

In summary, diffusion describes the transfer of mass/energy from higher to lower regions at a rate proportional to the curvature between these regions. Over time, the elevation difference between regions is smoothed, characterising a diffusional behaviour (Fig. 1.3).

Conversely, advection involves a lateral change of mass/energy with time that is directly proportional to the gradient from higher to lower regions. These mechanisms (i.e., diffusion and advection) operate together and can happen in both bedrock and alluvial river profiles (e.g., Cowie et al., 2008) but often occur differently according to the river type.

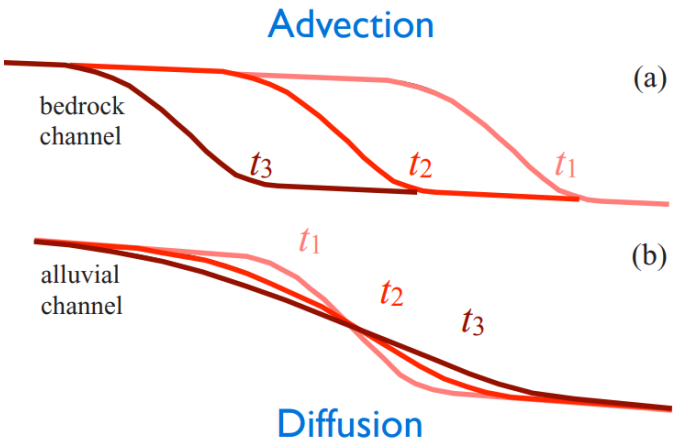


Figure 1.3: Advection and diffusion behaviours operating at 1D river profile evolution at different time steps ($t_1$ to $t_3$). a) Shows how lateral propagation (advection) of a wave of incision is driven by the river slope. b) Shows how elevation dissipation (diffusion) is driven by river curvature. Note that the first describes the behaviour of bedrock channels and the second alluvial ones but both diffusion and advection can also happen in bedrock channels. Adapted from Pelletier (2008) .

Bedrock rivers are generally advection-controlled and erode their bed by sediment abrasion, and by modulating erosion rates according to hydraulic conditions, sediment volume, and rock strength. These bedrock rivers are "detachment-limited" systems where sediment must be detached from their bed and are assumed to be always transportable (Shobe et al., 2017). Alluvial rivers due to the unconsolidated material where they overlie are generally diffusionally-controlled and erosion rates are modulated by hydraulic conditions, grain size and river morphology. These alluvial rivers are "transport-limited" systems where sediment is always available but may (or may not) be transportable (Willgoose et al., 1991).

Advection in river profiles can be mathematically defined as:

$$\frac{\partial h}{\partial t} = -vx^m \left(\frac{\partial h}{\partial x}\right)^n, \qquad (4)$$

where $n$ and $m$ are empirical constants that control the river profile concavity, $x^m$ is a proxy for discharge, and $x$ is the distance along a river (Hack, 1957; Roberts and White, 2010; Weissel and Seidl, 1998). If $n = 1$ and $m = 0$, then $v$ is an advective velocity term that controls upstream river slope break (i.e., knickpoint) propagation. If $n \neq 1$ and $m > 0$, the advective velocity term ($v$) is a nonlinear function of (local) slope and distance (along the river). Together, $n$, $m$, and $v$ are parameters that set the advective velocity term, which dictates the shape of the river profile and

its knickpoint propagation. This transient behaviour is mathematically described by a detachment–limited model (Whipple and Tucker, 2002).

Finally, the governing equations of diffusion and advective behaviour of river profiles when combined provide an erosional term $E$ ($x$, $t$):

$$E(x,t) = -vx^m \left(\frac{\partial h}{\partial x}\right)^n + k\frac{\partial^2 h}{\partial x^2}, \quad (5)$$

that when incorporated with uplift $U$ ($x$, $t$), becomes the largely known stream power river incision model, where:

$$\frac{\partial h}{\partial t} = U(x,t) - E(x,t). \quad (6)$$

The stream power river incision model is widely used to simulate landscape and river profile response to perturbations in climate, sediment supply and tectonics (Lague, 2014). In response to base level changing, rivers incise (or aggrade), while propagate an upstream wave of incision (or aggradation) captured by advection–diffusion equations. The majority of studies in bedrock river evolution ignore the diffusion term, so that the erosion is described as in the equation (4), i.e., as an advective term only (Bressan et al., 2014).

In fluvially dominated landscapes, river incision regulates the base level for all surface processes. Therefore, to investigate landscape evolution, it is crucial to understand spatial erosion in rivers (e.g., DiBiase et al., 2010; Kirby and Whipple, 2012). Since the pioneering work of Gilbert (1877), scientists have reasoned that steeper channel slopes should result in faster erosion, if everything else is equal. In addition, many authors claim that erosion rates correlate with river discharge (e.g., Howard and Kerby, 1983), so a normalisation is needed in order to compare gradients for rivers of varying discharge (or drainage area, which works a proxy for discharge) (Wobus et al., 2006). Flint (1974) proposes a law where properties of channels, such as gradient ($S$) and drainage area ($A$), are related via power laws. It can be written as:

$$S = k_s A^{-\theta} \quad (7)$$

where $k_s$ and $\theta$ are two empirical coefficients, called steepness index and concavity index respectively. The steepness index ($k_s$) defines how steep the slope ($S$) of a river is for a given drainage area ($A$). The concavity index ($\theta$) defines how concave a river profile is by controlling

how quickly slope increases when drainage area decreases. Spatial variations in the steepness index have been interpreted as a spatial variation in erosion or uplift rates (e.g., Cyr et al., 2010: Kirby and Whipple, 2012). However, the gradient *S* needed to calculate $k_s$ suffers from noise when derived (by differentiation) from topographic data (e.g., Wobus et al., 2006). To avoid this problem, some workers (e.g., Perron and Royden, 2013; Royden and Perron, 2013) suggested integrating drainage area along flow distance to create normalised river profiles as a function of elevation. Given that the slope term (*S*) in equation (7) is the same as the derivative of elevation over distance, equation (7) may be integrated from a base level ($x_b$) to any point ($x$) along the channel (e.g., Whipple et al., 2017):

$$z(x) = \mathrm{z}(x_b) + \left(\frac{k_s}{{A_0}^{-\theta}}\right) \int_{x_b}^{x} \left(\frac{A_0}{\mathrm{A(x)}}\right)^{\theta} dx \qquad (8),$$

where $A_0$ is a reference drainage area, introduced to non–dimensionalise the integrand in equation (8). Then, it is possible to generate a longitudinal transformation, $\chi$, with dimensions of distance (Perron and Royden, 2013):

$$\chi = \int_{x_b}^{x} \left(\frac{A_0}{\mathrm{A(x)}}\right)^{\theta} dx. \qquad (9)$$

The longitudinal transformation ($\chi$) is thus defined as:

$$z(x) = \mathrm{z}(x_b) + \left(\frac{k_s}{{A_0}^{-\theta}}\right) \chi. \qquad (10)$$

The longitudinal transformation, $\chi$, can be calculated from several watersheds from topographic data for a fixed 'reference' value of $\theta$ (called $\theta_{ref}$). If the reference drainage areais set to unit (i.e., $A_0 = 1\ m^2$), then from equation (10) the 'normalised' steepness index ($k_{sn}$) is the local slope of the elevation profile in $\chi$–space. By using $\chi$–transformation of river profiles, it is finally possible to estimate the normalised steepness index ($k_{sn}$) and have a proxy of erosion in river profiles (Mudd, 2017).

In cases of drainage networks sharing a common base level elevation, map visualization of the longitudinal $\chi$ coordinate across drainage divides can reveal disequilibrium (or equilibrium) between competing watersheds (e.g., Willett et al., 2014; Giachetta et al., 2014: Robl et al., 2017). Contrasts in $\chi$ across a drainage divide may indicate that the watershed with lower $\chi$ values is

currently gaining area due to river capture/divide migration at the expenses of the neighbouring watershed with higher $\chi$ values (Fig. 1.4, see Willett et al., 2014).

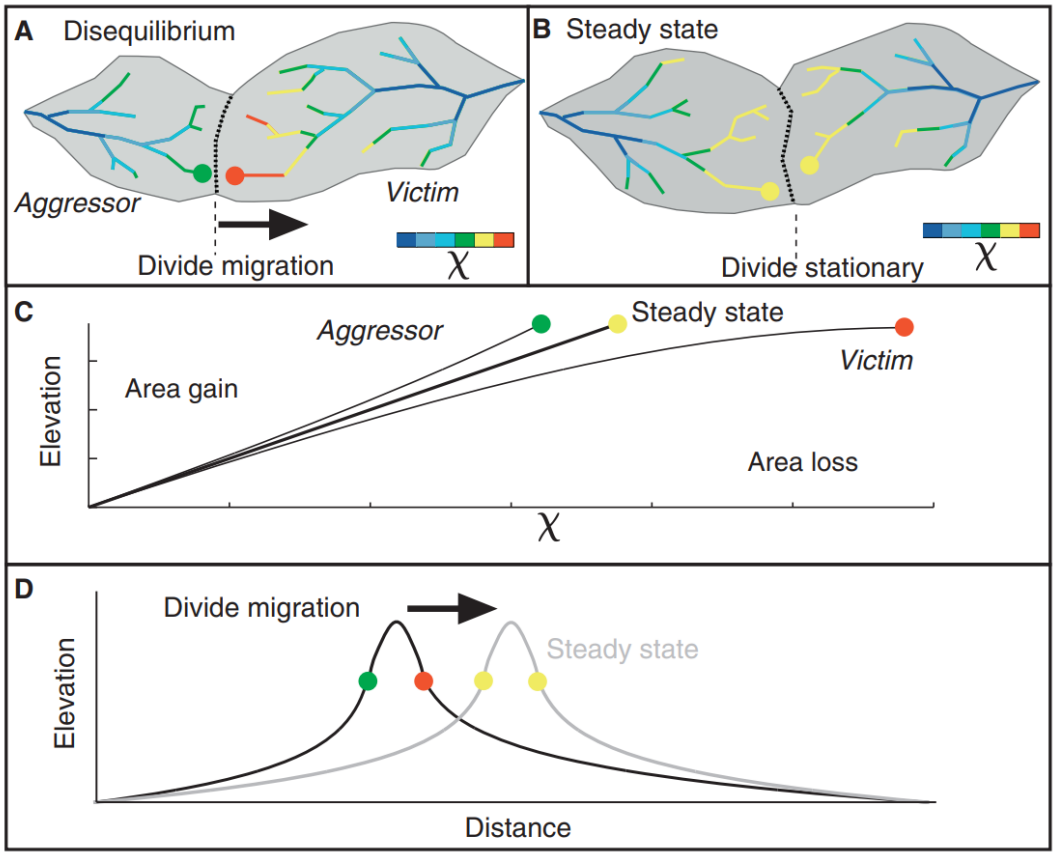


Figure 1.4: Watersheds and river profiles in transient–state (A) and steady–state (B). Panel C shows changes in the river lengths of two opposing watersheds sharing a common divide evolving from a state of transience (A) to a steady–state (B). According to their work, Willett et al. (2014) claims that an aggressor watershed (i.e., capturing other river) has lower steady–state elevation at channel heads and therefore drives the drainage divide toward the victim watershed (i.e., the one losing drainage). Panel D shows the changes in elevation of two rivers sharing a common drainage divide. Adapted from Willett et al. (2014).

Recent work has criticised this method to assess drainage divide stability, as local conditions (e.g., uplift rate or rock type) can influence the $\chi$ –transformation (Whipple et al., 2017; Forte and Whipple, 2018). More precisely, local conditions can counterbalance a predicted migration trend of the divides based on $\chi$–anomalies, for example, by promoting higher erosion in the channel heads of the watershed that had the potential of shrinking, so the divide remains steady. To avoid mistakenly predicting drainage divide migration, Forte and Whipple (2018)

have suggested morphometric parameters that empirically vary with erosion rates, such as those proposed by Gilbert in his 'Law of Unequal Declivities'. Named after him as 'Gilbert' metrics, they are based on upstream gradient, upstream relief and elevation at channel heads of opposing drainage divides. These parameters serve as a proxy for erosion rates and, by extension, to unravel trends of drainage divide migration. All metrics are founded on the idea that the horizontal steady–state condition is achieved when nearly equal quantities of gradient, relief and elevation at channel heads on either side of the divide occurs. These directions of motion are recorded differently according to the metrics used. For $\chi$ and elevation metrics, the drainage divide moves towards the side with higher values, whereas for relief and gradient, the drainage divide moves towards the side with lower values (Fig. 1.5).

The drainage network reorganisation can occur through continuous expansion/retraction of river profiles and/or discrete river captures. While the former does not often leave geological records available for interpreting the landscape, the latter generally causes changes in the topology of drainage network (e.g., elbows of capture), wind gaps and abrupt changes in $\chi$ values (Fig. 1.6). Identifying topographies of potential discrete river captures from continuous area–gain signatures in $\chi$–normalised profiles is an essential observation due to the extremely short time–scale of preservation for such signatures within topography (Forte et al., 2015; Whipple et al., 2017).

Given the short–lived signatures of topographic disequilibrium, an alternative approach is to extract detrital information from the sedimentary record, where preservation potential can be much longer (Lewin and Macklin, 2003). As the mechanisms occurring from source to sink (section 1.4.1), river captures can change the characteristics of the sedimentary record due to new added rock type properties. These changes involve varying mineralogical composition, grain size, detrital grain ages, detrital morphology, and sediment volume, among several other characteristics (Bracciali et al., 2015; Clift et al., 2006; Maher et al., 2007). As a result, recognizing natural factors controlled by rock properties can help to distinguish between changes in the stratigraphic record caused by area gain/discrete river capture from other naturally varying processes that are lithologically–controlled (e.g., erosion, abrasion, mineral fertility, etc.). Thus, this work also contribute indirectly to river capture studies.

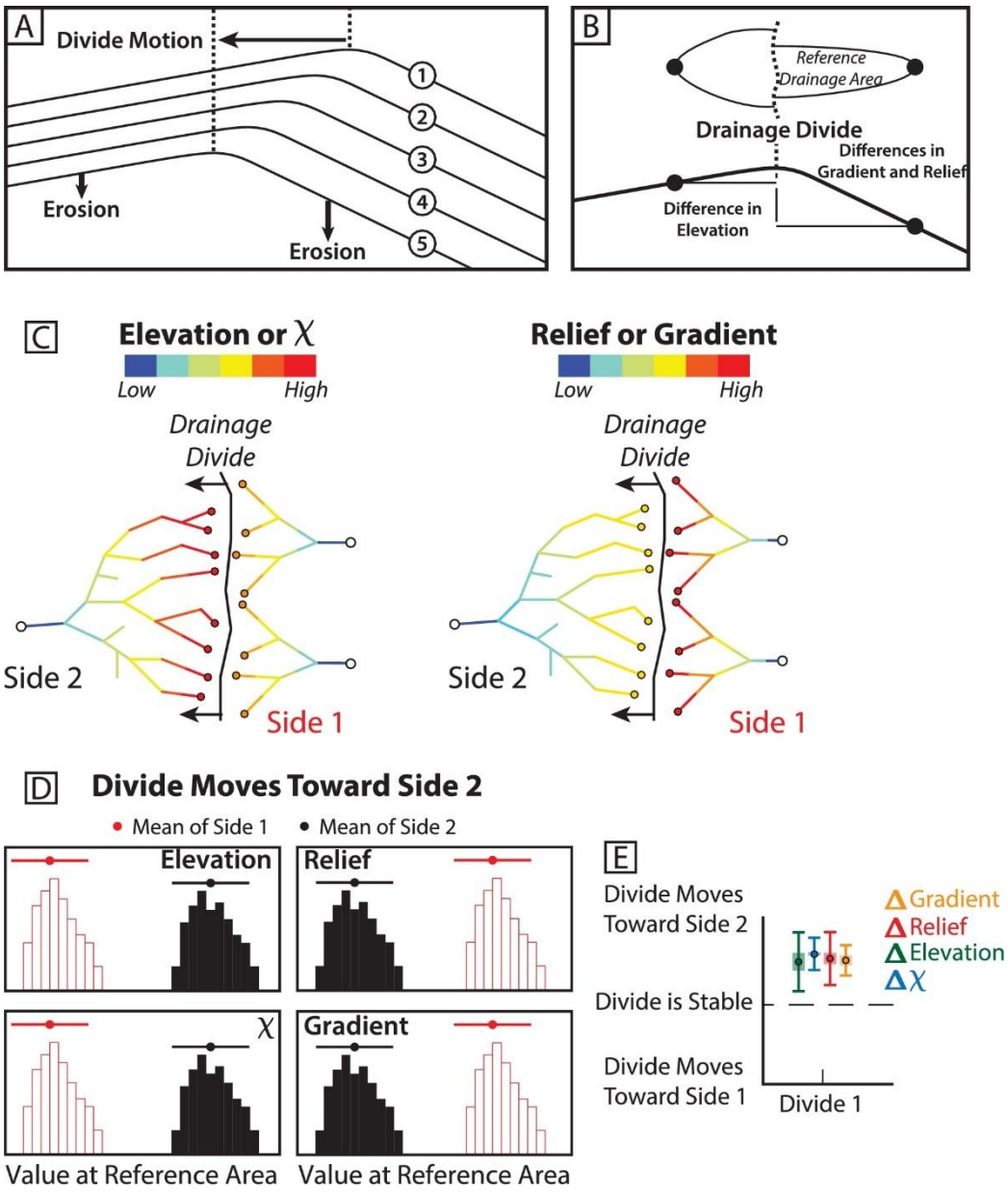


Figure 1.5: A) An illustration showing what Gilbert's (1877) meant in his 'Law of Unequal Declivities'. In summary, the drainage divides (represented by dots) move when erosion rates are not equal on both sides of the divide. According to this theory, unequal declivities will produce differences in erosion rates and cause divide migration. B) Reference drainage area used in all metrics for calculating across divide differences. C) An illustration showing how different is the prediction according to the used metrics of divide stability. Basically, the divide moves from low to high χ values, while the opposite happens with 'Gilbert' metrics. D) Histograms provided by the algorithm written by Forte and Whipple (2018) to compare metrics of opposite sides of drainage divide. E) Box–plots comparing the 'Gilbert' and χ metrics shown in panel C. Adapted from Forte and Whipple (2018).

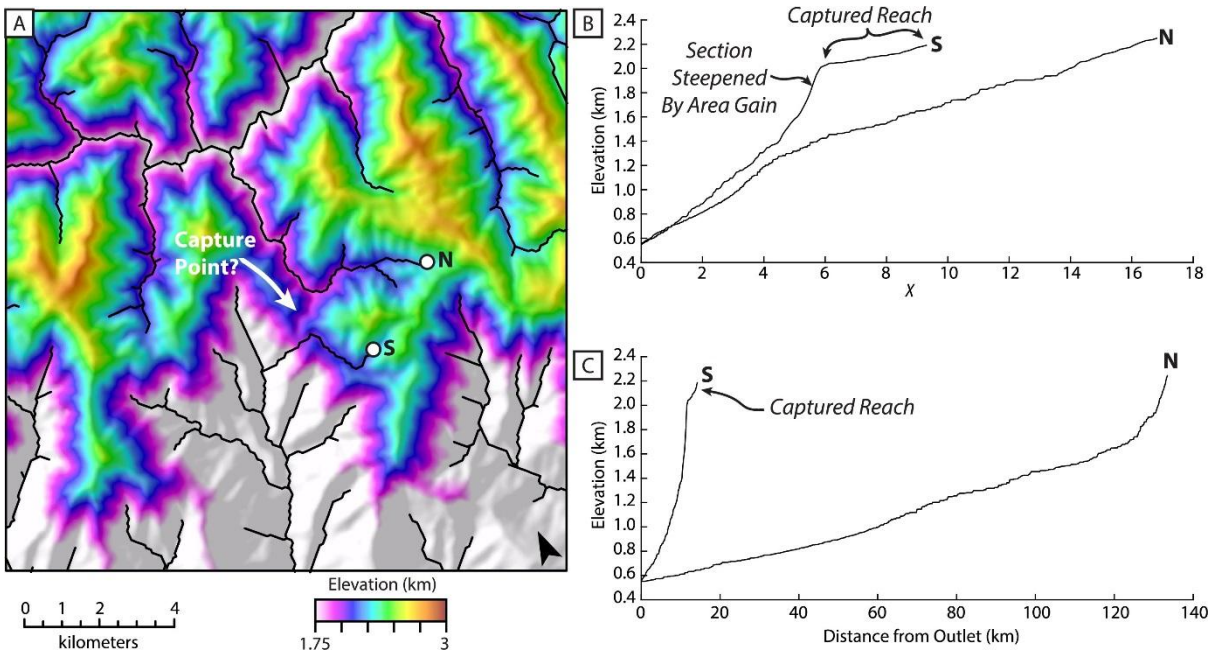


Figure 1.6: An example of topographic and χ evidences identified by Forte et al. (2015) of northward drainage divide migration in the eastern Greater Caucasus. A) A wind gap highlights a possible captured river section. B) χ–transformed river profiles of the two watersheds highlighted in panel A (note the north, N, and south, S, indications). C) A non–transformed river profile of the two drainages shown in panel 5A. Adapted from Forte and Whipple (2018).

## 1.5. Study areas

In the following subsections, I introduce the study areas used to investigate biases in detrital grain analysis (1.5.1) and the influence of rock properties in landscape development (1.5.2). I specify the details required to understand them in terms of the aims stated in the subsection 1.3, so some secondary information might not be included. The non–included information is detailed in the Chapters 2, 3 and 4.

### *1.5.1. For detrital grain analysis*

As stated in the justification of the study areas (1.2), two watersheds are used as natural laboratories to investigate the impact of rock properties in the characteristics of the sedimentary record. One of them is the Marsyandi watershed, in the central Himalaya, and the other is the

Tavignano watershed, in central Corsica Island (Mediterranean Sea). Below, I provide some information strictly useful for understanding the sources of detrital minerals in the investigated settings.

#### *1.5.1.1. Marsyandi watershed (Himalaya)*

The Marsyandi watershed, in the central Himalaya, has an area of approximately 4700 $km^2$, is 57 km wide and 170 km long. The Marsyandi flows into the Trishuli River, which later joins the Ganga River in the Himalayan foreland basin. Elevation varies from 200 m to 8000 m. The sediment source units can be grouped into five litho–structural units (Le Fort, 1975; Amidon et al., 2005; Attal and Lavé, 2006) (Fig. 1.7).

The uppermost source unit (Tethyan Series –"TTS") comprises Cambrian to Jurassic limestones, sandstones and shales. The Tethyan Series are intruded by a Miocene leucocratic granite (Manaslu granite –"MG") in its eastern section. The southern margin of the Tethyan Series is marked by a north–dipping, normal–sense shear zone known as the South Tibetan Detachment (STD). Below (south of) the STD lies the Greater Himalayan Series (GHS), a continuous sequence of amphibolite–grade schists and gneisses divided from south to north into three formations, grouped here as pelitic gneisses (Formation I –"FI") and Paleozoic augen gneiss intrusions in calc–silicate rocks (Formation II–III –"FII–III") (Le Fort, 1975). The series are in turn bounded to the south by the Main Central Thrust (MCT). The MCT is the structural boundary between the Greater Himalaya and Lesser Himalaya series. Lower–grade schists and meta–sediments of the Lesser Himalayan Series ("LH") occur in the MCT footwall.

Four parameters are essential to understand the provenance of sediments in the Marsyandi watershed: the empirically–derived information about erosion rates, pebble abrasion rates, zircon fertility and hillslope gravel supply.

Concerning the erosion rates, Garzanti et al. (2007) estimate relative erosion in three different sites along the main stem. In the uppermost site, they found relative erosion rates of 22.5 % (TTS) and 77.5 % (F II–III). At the intermediate site, they estimate relative erosion rates of 10 %, 34 % and 56 % for the TTS, F II–III and F I, respectively. In the Marsyandi outlet, relative erosion

rates are 28 %, 24 %, 10 %, 38 % for the TTS, F II–III, F I and LH, respectively. Other scientists found that modern erosion rates in the Himalaya have a spatial correlation with precipitation gradients, erosion and tectonic uplift of the MCT hanging–wall (Hodges et al., 2004; Deal et al., 2017; Olen et al., 2015).

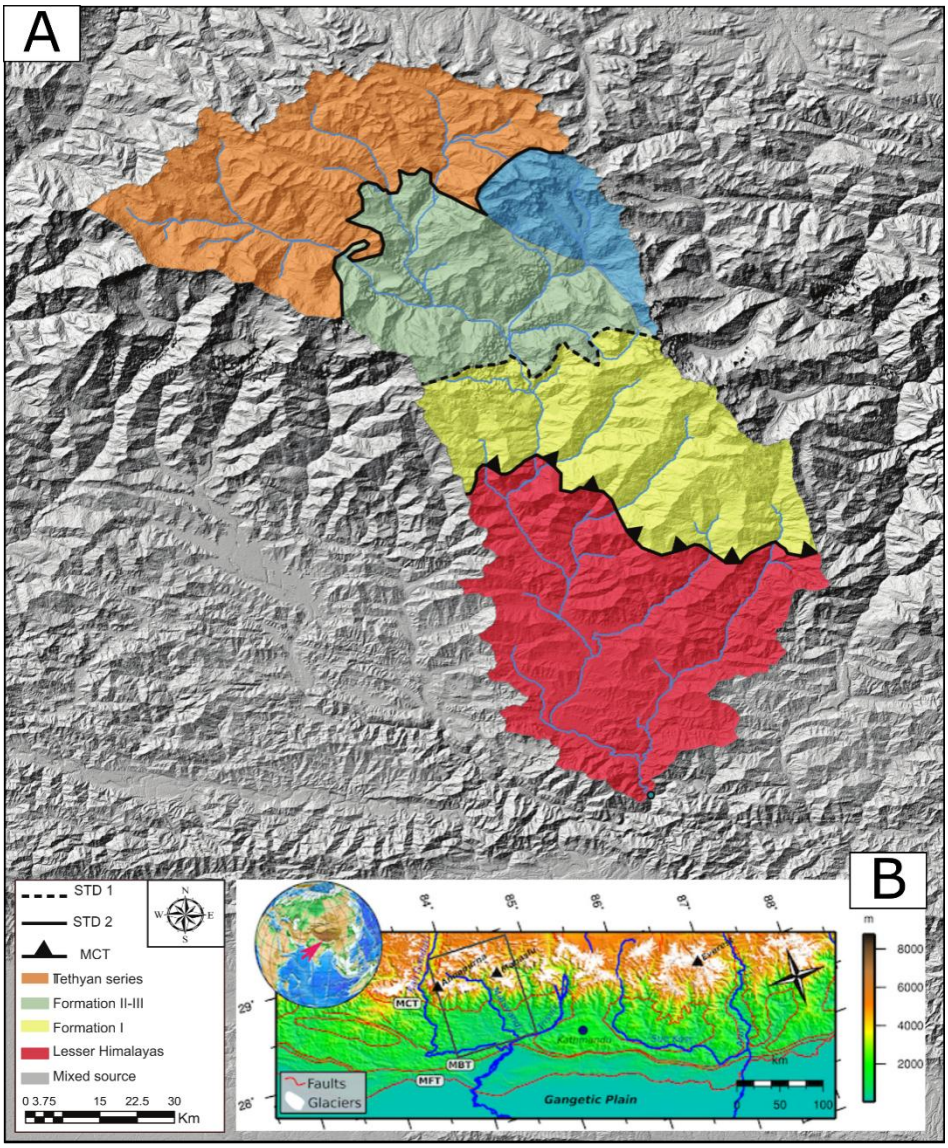


Figure 1.7: Source units of the Marsyandi watershed and its location in a regional and global scale. A) Geological map for the Marsyandi watershed superimposed on hillshade derived from 30–m resolution Shuttle Radar Topography Mission (SRTM) data. Geological units are derived from Le Fort (1975) (see also Amidon et al., 2005a, and 1403 Attal and Lavé, 2006). B) Location of the Marsyandi in the Himalaya and in a global context. Note that a black rectangle shows the Marsyandi watershed with the Himalaya and a red arrow show where it is in a global scale. The panel B is adapted from Godard et al. (2012).

Regarding pebble abrasion rates, Attal and Lave (2006) estimate values varying up to 10–fold depending on the rock type. For instance, quartzite from TTS has the lowest rate (0.4 % mass loss/km), while sandstones at the MCT has the highest (31 % mass loss/km) and schist (LH) has an intermediate one (23 % mass loss/km).

Regarding zircon fertility, Amidon et al. (2005) estimate that the relative concentration of zircons in the Marsyandi watershed is 1 grain/g (Formation II/ III), 3.2 grain/g (Lesser Himalaya), 5.7 grain/g (Tethyan Series), and 8.1 grain/g (Formation I). Importantly, the Manaslu granite has been estimated as containing no zircon. These approximately 8–fold variations strongly influence their predictions about zircon mixing proportions in mixed river samples.

Lastly, hillslope grain size supply data (Attal and Lave, 2006) estimated from landslides have $D_{50}$ (i.e., median grain size) of 32 mm. Among rock types, the $D_{50}$ varies from 64 mm (in quartzite) to 2 mm (in schist). Further details about the Marsyandi watershed is given in the study area section of the Chapter 2.

#### *1.5.1.2. Tavignano watershed (Corsica, Mediterranean Sea)*

Corsica is an island in the Western Mediterranean Sea that consists of two geological domains: Hercynian Corsica and Alpine Corsica (Fig. 1.8). In Hercynian Corsica, three main groups of intrusive rock types have been recognised: (i) an 'Mg–K' granite (U1 group) related to a collisional stage at ~ 320 –350 Ma; (ii) a 'calc–alkaline' granite U2 group related to crustal thinning at ~ 304 –280 Ma; (iii) and a U3 group composed of alkaline and metaluminous granites ranging from 238 to 259 Ma (see Orsini, 1980; Cocherie et al., 1992, 1994, 2005; Paquette et al., 2003; Rossi et al., 1988, 1993, 1995, 2001, 2005; Li et al., 2014). In Alpine Corsica, six main groups occur: (iv) external continental units with evidence of Hercynian deformation and magmatism (360 to 270 Ma), which are partly overlain by metasediments (260 to 50 Ma); (v) Schistes Lustrés made of Tethys–derived ophiolites and their metasedimentary cover (89–66 Ma); (vi) internal continental units are continental–derived slivers within the Schistes Lustrés complex (40–37 Ma); (vii) Nappes Supérieures made of deformed ophiolites, continental and sedimentary

units (286 –350 Ma); (viii) Pre–Hercynian basement rocks occur in scattered regions of Corsica (> 350 Ma); (ix) Miocene sedimentary plains occur at the north–eastern region of Corsica (see Ohnenstetter et al., 1981. Rieuf, 1980; Brovarone and Herwartz, 2013; Lin et al., 2018).

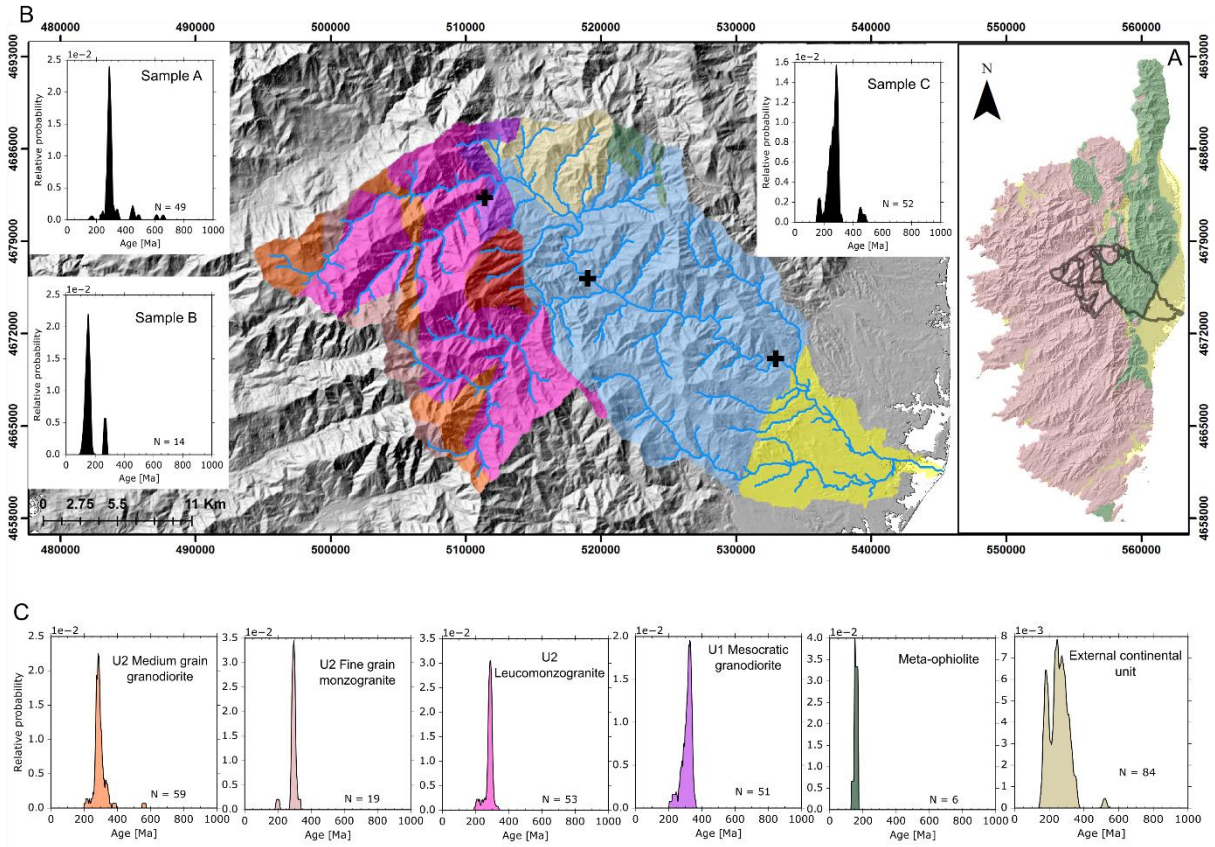


Figure 1.8: Source rocks and U–Pb zircon ages of the Tavignao watershed. A) Location of the Tavignano watershed in eastern Corsica. Pink rock types are granitoids of Hercynian Corsica, green rock types are from the Schistes Lustrés unit (Alpine Corsica), and yellow rock types are part of the Miocene sedimentary plains (Aleria and Marana). B) Source rocks and U–Pb age distributions of the downstream mixed sand samples in the uppermost (sample A), intermediate (sample B) and lowermost (sample C) sampling sites investigated in the Chapter 4. C) U–Pb age distributions of the source rocks of the Tavignano watershed. Note that the blue area represents the Schistes Lustrés unit, where no U–Pb age constrains exist. The yellow area represents the Aleria plain, which is not investigated in this work. The colours of the source rocks in panel B are equivalent to those U–Pb ages at panel C. The ages are in the papers: Cocherie et al. (2005), Rossi et al. (2006), Ohnesnstetter et al. (1981) and Cocherie et al. (1992) has grain morphology of U1. Rossi et al. (2015). Further information about this figure is given in the Chapter 4.

In the Tavignano watershed, nine major rock types are present. In the uppermost region, four formations from the U2 and U1 groups of Hercynian Corsica occur associated to two slices of

continental units (external continental units and Pre–Hercynian basement). They are: U1 mesocratic granites of 320 –350 Ma (U–Pb dating); and three rock types from the U2 group with U–Pb zircon ages varying ~ 302 –304 Ma (medium grain granodiorite), ~ 300.0 Ma (fine grain monzogranite) and ~ 280 –289 Ma (leucomonzogranite) (Cocherie et al., 1992; Rossi et al., 2006, 2015). The external continental unit named Santa–Lucia–Di–Mercurio has U–Pb zircon ages between 380 –140 Ma (Cocherie et al., 2005). The Pre–Hercynian basement have no published U–Pb age constrains but I believe they are older than the U1 mesocratic granites (i.e., > 320 –350 Ma) but lacks U–Pb age constrains. From the Alpine Corsica, two other units occur at the Tavignano: the Schistes Lustrés and meta–ophiolite units. For the Schistes Lustrés, the U–Pb zircon ages available are from continental slivers (granulites and plagiogranites) associated to ophiolite sequences, particularly from meta–ophiolites at the Inzecca Unit (142 –162 Ma) (Ohnenstetter et al., 1981). No U–Pb zircon age distribution has been published from supracrustal rocks of the Alpine Corsica (e.g., schist, quartzite or calcarenite).

Molliex et al. (2017) measured catchment–wide erosion rates ranging from 40 to 74 mm/kyr. No U–Pb zircon age distribution has been published from supracrustal rocks of the Alpine Corsica (e.g., schist, quartzite or calcarenite). Similarly, no information about zircon fertility, hillslope grain size supply and pebble abrasion rates are available to any of the sources of the Tavignano watershed. The limitations due to the absence of these constraints are explored in the Chapter 4 of this thesis.

### *1.5.2. For the influence of rock properties in the landscape*

To investigate the influence of rock properties in the landscape, Corsica Island is used as a study area. Below, I discuss the relevant aspects of its rock properties and environmental conditions in the investigation performed in the Chapter 3. As described in the previous subsection (1.5.1.2.), Corsica consists of two main geological units termed Hercynian and Alpine Corsica (Fig. 1.9).

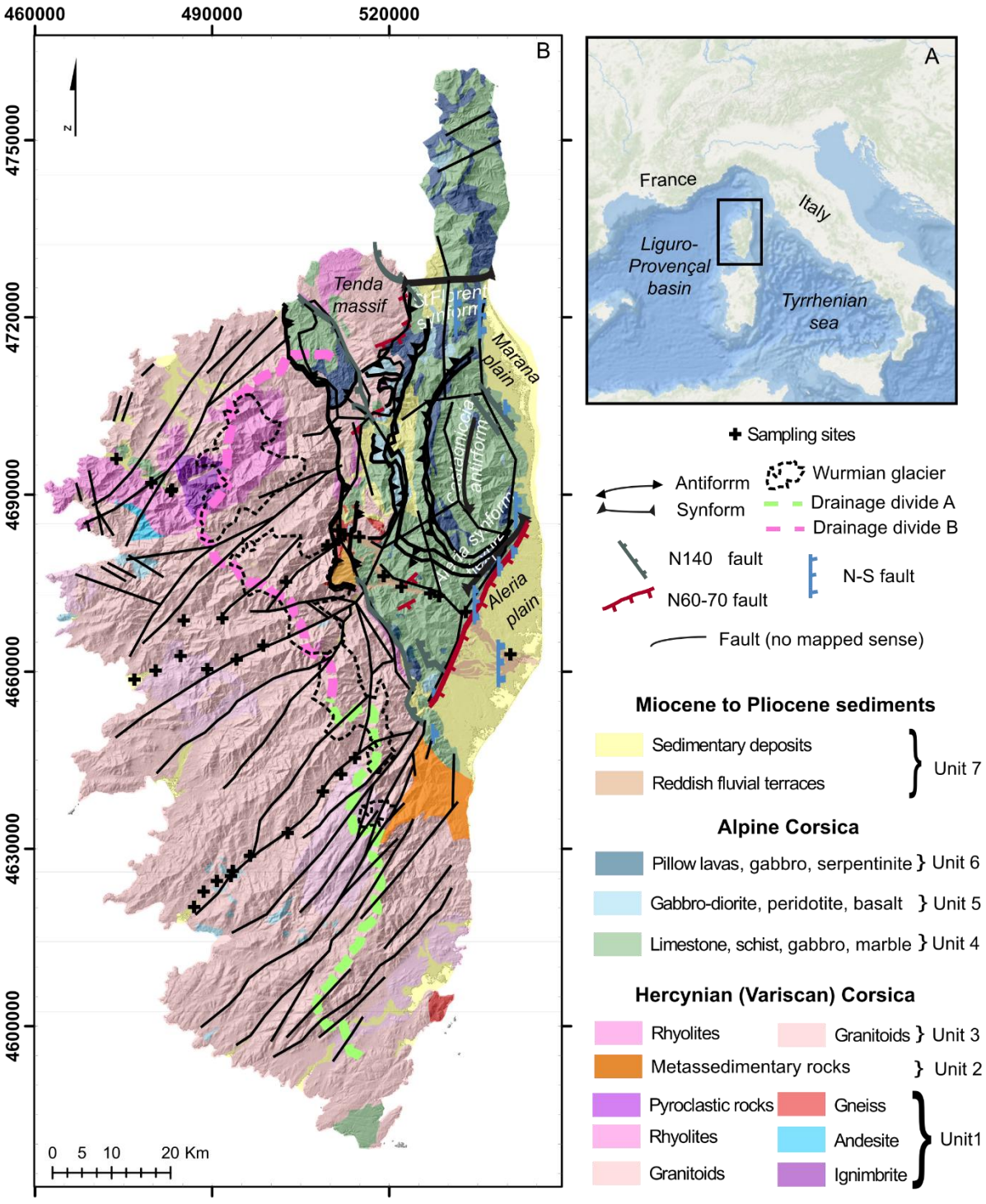


Figure 1.9: Geological map of Corsica, which includes mapped Alpine thrusts and extensional faulting related to the opening of the Tyrrhenian and Liguro–Provençal basins and sampling sites of gravel bars analysed in this work. The sub–division of the regional drainage divide in two sections (A and B) was done after analysing the χ and 'Gilbert' metrics. A) Location of Corsica in the Western Mediterranean Sea. B) Geological and structural units of Corsica. The geological units are adapted from Rossi et al. (1994a,b) and the tectonic units are from Gueydan et al. (2017). The regional drainage divide of Corsica was

segmented in this work between the southern (A) and northern (B) sections to ease morphometric analysis performed in the Chapter 3. The extension of the Wurmian glaciers in Corsica follows the mapping of Kuhlemann et al. (2005). Further information about this figure is given in the Chapter 3.

The Hercynian Corsica comprises three geological units that cover the majority of the island's onshore area. At the west, centre and south of Corsica, a non–metamorphosed basement made of Carboniferous to Early Permian granitoids, with pre–Hercynian metamorphic host rocks as well as Permian volcanic rocks occurs (Unit 1). These basement rocks are partly overlaid by continental and marine sedimentary rocks (Triassic to Paleocene) and by Eocene foredeep strata (mummulites–bearing flysch) that are strongly deformed (Unit 2). In the north, closer to the Alpine Corsica, Hercynian rhyolites, and granitoids metamorphosed into orthogneiss bearing blue amphibole occurs (Unit 3: Tenda massif units). In the Alpine Corsica, the Schistes Lustrés formation occurs as a thrust on top of the Eocene foredeep strata and of the metamorphosed Hercynian basement (i.e., over Tenda massif units).

The Schistes Lustrés is composed of metamorphosed oceanic rocks such as gabbros, peridodites, basalts and slices of continental basement that can be subdivided in three main units. The lowermost unit is made of marble, calcschist, schist, basalt and gabbro metamorphosed under high–pressure low–temperature conditions and has been referred as Castagniccia unit (Unit 4). The intermediate unit, named Lower oceanic unit is composed of basalt, gabbro and peridotite with slices of gneiss (Unit 5). On the top of the Schistes Lustrés formation, an upper oceanic unit (Unit 6) encapsulates several minor units (Pigno, Gratera, Centuri, Inzeca, Vecchio, Linguizzetta, Santa Lucia and Balagne units). Santa Lucia and Pigno units are continental slices with low to medium pressure metamorphism. The Balagne unit is a non–metamorphosed oceanic unit composed of serpentinite, gabbro, pillow lava and oceanic flysch material. The most recent onshore siliciclastic sedimentation basins (Miocene) are found over the Schistes Lustrés formation on east (Aleria and Marana), centre (Francardo) and north of Corsica (Saint Florent) (Unit 7). The Francardo and Saint Florent basins have depositional ages ranging from Burdigalian to Langhian. The Aleria and Marana sedimentary plains have formed during Burdigalian to Pliocene times and are made of sand and coarser material of river terraces.

Five main environmental conditions are required to understand the current topography of Corsica: the existence of former glaciers, sea level changes, structural boundaries, differential

erosion rates, and different exhumation rates. I will briefly summarise what is known about each for Corsica.

The climate has a very strong influence on the landscape of Corsica according to several workers. During the Marine Isotope Stages 4 (~ 18 ka), glaciers reached their maximum extension in the centre and north–western sections of the Corsica drainage divide, the rest of the island remained unglaciated (Kuhlemann et al., 2005). With warmer temperatures, these glaciers were removed in the Pleistocene.

Regarding sea level variation, two events are well–constrained: the Messinian crisis and Pleistocene changes. During the Messinian crisis (5.96 and 5.33 Ma) two phases of sea level lowering have been proposed by Gargani (2004). The first phase included a 600 – 700 m lowering over 400 kyr (i.e., ~ 1.45 mm/yr), while the second phase was marked by an 1300 – 1700 m of sea level lowering in 50 ky (i.e., 30 mm/yr). The base level returned to approximately its original position ~ 5.3 Ma. More recently, Waelbroeck et al. (2002) proposed that for the Pleistocene (130 ka), the Mediterranean Sea had a steady lowering of 120 m between 130 – 20 ka (i.e., 1.1 mm/yr) followed by a rising to the present (i.e., 6 mm/yr). However, there is no consensus on the literature about the rates and dates of sea level variation during the Messinian crisis (see Clauzon et al., 1996; Krijgsman et al., 1999; Rouchy and Caruso, 2006) and about the Mediterranean sea level during the Quaternary (see Lambeck and Purcell, 2005).

The influence of structural boundaries is visible in the spatial correlation with the drainage network. It is particularly important in the orientation of the drainage network in Western Corsica, where several structural boundaries (with no defined sense of motion) are spatially overlapping the river profiles.

According to Danišík et al. (2007), apatite fission–tracks (AFT) and (U–Th)/He (AHe) analysis reveal ages that corroborate a longitudinal asymmetric exhumation of Corsica (Fig. 1.10, Cavazza et al., 2001; Zarki–Jakni et al., 2004; Fellin et al., 2005; Danišík et al., 2007).

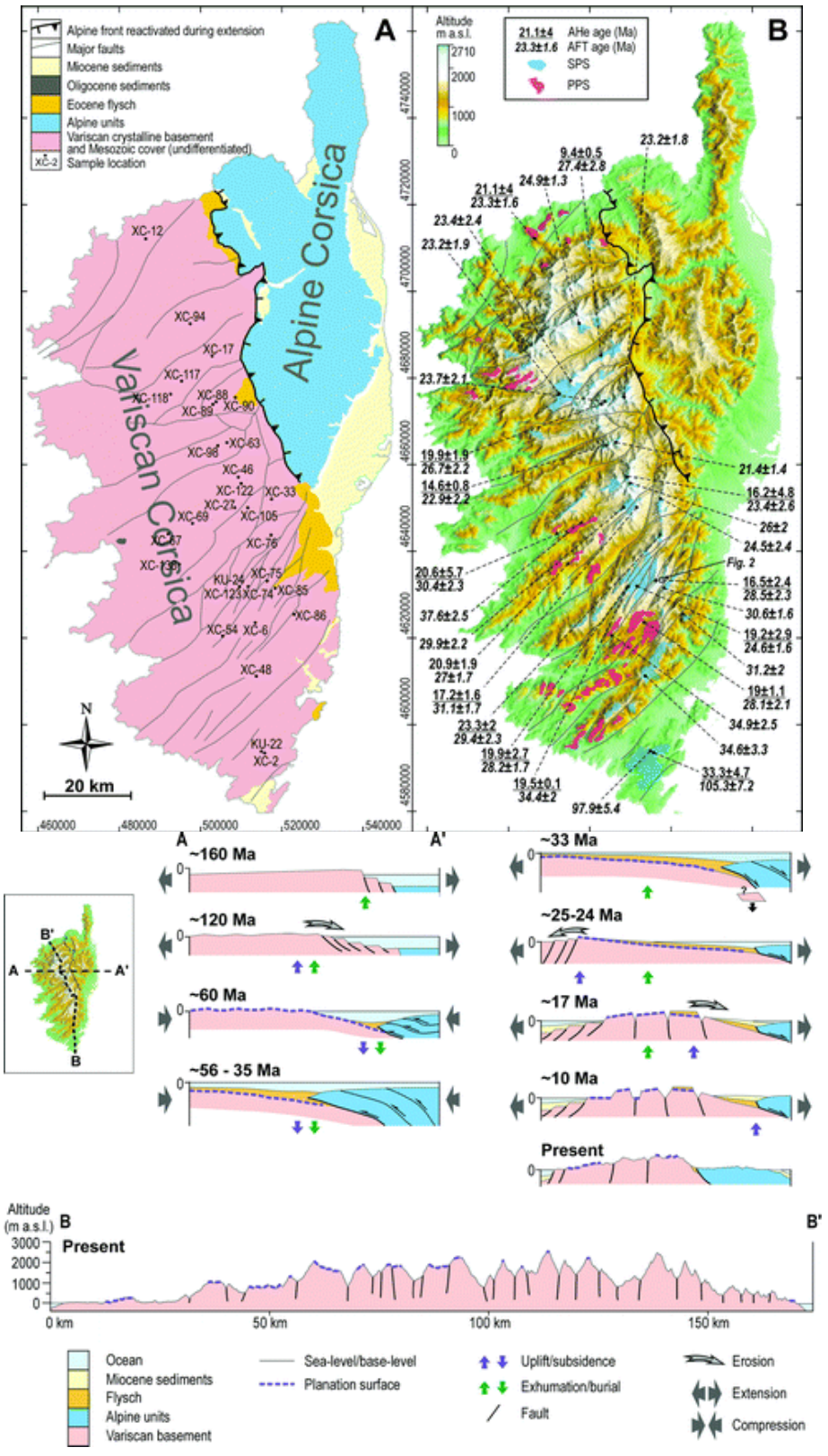
A
B
Alpine front reactivated during extension
Major faults
Miocene sediments
Oligocene sediments
Eocene flysch
Alpine units
Variscan crystalline basement and Mesozoic cover (undifferentiated)
Sample location
Alpine Corsica
Variscan Corsica
20 km
Altitude m a.s.l.
AHe age (Ma)
AFT age (Ma)
SPS
PPS
A
A'
~160 Ma
~120 Ma
~60 Ma
~56 - 35 Ma
~33 Ma
~25-24 Ma
~17 Ma
~10 Ma
Present
Altitude (m a.s.l.)
B
B'
Present
0 km
50 km
100 km
150 km
Ocean
Miocene sediments
Flysch
Alpine units
Variscan basement
Sea-level/base-level
Planation surface
Uplift/subsidence
Exhumation/burial
Fault
Erosion
Extension
Compression

Figure 1.10: Main geological units, thermochronometric ages and conceptual landscape evolution model of Hercynian Corsica in the geodynamic context depicted by Danisik et al. (2012). Panel A shows the geological map of Corsica, according to Rossi et al. 1980), with location of samples for thermochronometric analysis. In panel B, a map with summit planation surfaces (SPS; blue) and piedmont planation surfaces (PPS), according to the classification of Kuhlemann et al. (2005), with in situ apatite (U–Th)/He (AHe) and apatite fission track (AFT) ages is shown. Panel C represents a landscape evolution model of Corsica along a west to east transect (A–A') as proposed by Danisik et al. (2012). Adapted from Danisik et al. (2012).

Danišík et al. (2007) have proposed an exhumation model that starts in the Middle to Late Jurassic (~ 170 Ma – 145 Ma), when the Ligurian–Piedmont Ocean was generated between the Gondwana and Laurasian plates. In the Early Cretaceous (~ 120 Myr), the Hercynian basement was near–surface conditions and exposed to erosion due to a (i) continuous ocean–floor spreading and (ii) exhumation of the basement by removal of a Mesozoic cover strata (Danišík et al., 2012). From Early Cretaceous to Paleocene times (~ 120 Ma to ~ 60 Ma), the basement experienced a period of quiescence, probably linked to the formation of planation surfaces currently available at summits in Hercynian Corsica. In the Oligocene, several tectonic rearrangements happened. At ~ 33 Ma, due to a shear sense reversal (from compressional to extensional regime), the basement exhumed and a post–Eocene erosion surface was formed. The previously created planation surface was displaced by sub vertical faulting zones, defining differentially behaving structural units and the subsequent orientation of valleys. In the Late Oligocene (~ 25 Ma – 24 Ma), a new uplift occured, promoting the formation of continental alluviation. During the continental drift of Corsica–Sardinia in the Miocene, several differential structural uplifts occurred, triggering fluvial valley incision. At ~ 17 Ma, part of the basement becomes as a source for the Aleria and Marana Plains due to differential uplifts, tilting and flexural movements, which significantly destroyed the remnants of the existing planation surface. Finally, at ~ 11 Ma, Corsica was affected by another uplift phase, when deposition in the Miocene basins terminated and the Alpine part emerged above local base level. Important to note that, according to Danišík et al. (2007), exhumation started in the south of Corsica in the Late Oligocene (40–30 Ma), and propagated northward through early Miocene times, reaching the centre at 30–20 Ma, and the northern region at 20–17 Ma.

Finally, according to Molliex et al. (2017), ($^{10}$Be) catchment–wide erosion rates have a stronger correlation with rock strength than with any other morphometric (elevation, slope, relief,

river steepness) and climatic parameter (precipitation). Variations in the estimated erosion rates in Corsica are large over summit surfaces (8.1 to 140 mm/kyr), within catchment (e.g., 160 to 475 mm/kyr in the largest watershed of Corsica) and among catchments (15 to 95 mm/ky). However, while for Molliex et al. (2017) the relatively low catchment–wide erosion rates measured in their work indicate a condition approaching a large–scale erosional steady state, other scientists found that those strong variations of erosion in the river valleys and summit surface (and among catchments) is indicative of transience. I explore this debate further (Chapter 3), where a more detailed explanation on these variables (erosion rates, structural boundaries, sea level changes, the existence of former glaciers and different exhumation rates) is given.

## 1.6. Thesis outline

In a first chapter (2), I perform a series of experiments with an abrasion model to test if abrasion, which controls the release of minerals from gravel to sand, influences detrital age signatures and the erosion rates retrieved from them. In the study case (Marsyandi watershed, Himalaya), I use an extensive zircon age population dataset published by Amidon et al. (2005). The results demonstrate that pebble abrasion can change the zircon mixing proportions of upstream source units as well as the age distribution of mixed fluvial sands. This change is particularly significant when there is a strong contrast in rock resistance within the watershed. Pebble abrasion is one of many factors that can change the mixing proportion of sands, including hillslope gravel supply, erosion rates, and mineral fertility. In our study, the abrasion model predicts age distributions that are statistically indistinguishable from those predicted by a no–abrasion model. However, the relative erosion rates estimated by the model largely differ from the results of a no–abrasion model, and are closer to those from other studies that suggest a strong correlation between modern erosion rates, tectonics and precipitation intensity in the Marsyandi watershed. These findings suggest that pebble abrasion must be accounted to avoid uncorrected erosion rates estimated from detrital studies. This chapter has been published in the *Journal of Geophysical Research –Earth Surface* in 2018.

In the following chapter (3), I analyse the influence of rock types on the development of mountain topography on the young island of Corsica (Mediterranean Sea). I investigate the topographic state of both drainage network and regional drainage divide in response to post–Miocene tectonics combined with variations in sea–level. The results suggest that the northern section of the drainage divide is currently moving to the east, while the southern section is moving to the opposite direction (i.e., westward). These patterns reinforce that Corsica is currently in a transient topographic state. The analysis of the drainage network highlights both rock type and structural units as major controls on the modern river profiles. I found that knickpoints are preferentially located at a similar distance from sea level, which could suggest a common base level drop. However, given the existence of a strong structural control on the island, caution must be taken when interpreting spatial patterns of knickpoints in terms of external trigger. I have not found any correlation between the knickpoint metrics and the thermochonometric age domains compiled from other workers. These findings suggest that the current topographic state of the drainage network and divide of Corsica is controlled by both rock strength and structural boundaries rather than by long–term (and long–scale) exhumation patterns.

In the next chapter (4), I combine the techniques developed in the two previous chapters to assess what can be reliably retrieved from detrital studies, using the Tavignano watershed in Corsica (Mediterranean Sea) as a template. There, I find that the majority of the sampled zircon types are linked to the upstream sub–alkaline granites. The U–Pb ages of mixed samples show relatively similar peaks in the uppermost and lowermost sampling sites, while the intermediate site has several missing peaks. The main explanation for these results is the very small amount of grains collected for typology and U–Pb dating. The absence of zircon constraints in many of the contributing sources is also a major biasing factor. Through mineral mixing modelling, I demonstrate how analytical issues such as too few dated grains and age peak overlapping affects source–to–sink analysis have an important impact. I also demonstrate how mineral mixing proportion in poorly constrained settings can be equally explained by different natural bias (e.g., zircon fertility or erosion) without being able to disentangle them. These results reinforce the importance of choosing the proper mineral tracer and recognising the factors acting on it to assess what controls the information retained in the stratigraphic record.

The core chapters of this thesis (chapters 2–4) are written as research papers and have either already been, or will shortly be, submitted to scientific journals. Every chapter works as a stand–alone document covering separate topics, but all addressing the aims of this thesis.

In the following chapter (5), the results from the preceding three chapters (2–4) are integrated into a single discussion (section 1.2) regarding the research questions posed in the thesis approach (1.3). The implications and outcomes from these chapters are discussed, highlighting how their findings further our understanding of the influence of rock properties on both landscape and source–to–sink problems, including remaining gaps in our knowledge and revenues for future research.

Finally, in the last chapter (6), I provide a short conclusion emphasising the key results of this thesis.

# Chapter 2 –Does pebble abrasion influence detrital age population statistics? A numerical investigation of natural datasets

The work presented in this chapter was published in Journal of Geophysical Research –Earth Surface:

Lavarini, C., Attal, M., da Costa Filho, C. A., & Kirstein, L. A. (2018). Does Pebble Abrasion Influence Detrital Age Population Statistics? A Numerical Investigation of Natural Data Sets. Journal of Geophysical Research: Earth Surface, 123(10), 2577-2601.

The final version published in the Journal can be found in the Appendix A. This work was done in collaboration with the co-authors, who helped developing the code, analysing and writing the manuscript. C.L., M. A. and C.A.C.F. wrote the code for the abrasion model. C.L. run the simulations, plotted the figures, and wrote the manuscript with the collaboration of M. A. and L.K., who also designed simulations and analysis.

C. Lavarini, M. Attal, C. A. da Costa Filho, and L.A. Kirstein

Key Points:

- Pebble abrasion can distort the mineralogy of fluvial sands and ultimately the statistics of detrital age populations derived from them.

- Numerical simulations show that pebble abrasion is able to produce detrital age distortion but proportionally less than spatially variable erosion and mineral fertility.

- Simulations with empirical data shows that relative erosion rates derived from age populations are significantly different when accounting for abrasion.

**Keywords:** sediment, detrital methods, abrasion, provenance, bias, erosion, geochronology, zircon.

## Abstract

Pebble abrasion is a key factor controlling the release of minerals into sand, but few attempts have been made to model how it could influence the liberation of minerals into the size fraction used in detrital geochronology. I perform a series of experiments with an abrasion model to test this influence using natural and synthetic datasets. Our results demonstrate that pebble abrasion can change the zircon mixing proportions of upstream source units as well as the age distribution of mixed fluvial sands. This change is particularly significant when there is strong contrast in rock resistance within the watershed. Pebble abrasion is one of many factors that can change the mixing proportion of sands, including hillslope gravel supply, erosion rates, and mineral fertility. In our study case (Marsyandi watershed, Himalaya), the abrasion model predicts age distributions that are statistically indistinguishable from those predicted by a no–abrasion model. However, the relative erosion rates estimated by our model largely differ from the results of a no–abrasion model, and are closer to those from other studies that suggest a strong correlation between modern erosion rates, tectonics and precipitation intensity in the Marsyandi watershed. These findings highlight that, even in cases where there is no statistical evidence of change between the modelled age distributions, abrasion can affect the erosion rates estimated from them. Therefore, quantifying the influence of abrasion on sand production is an essential step not only to predict mixing proportions but also to accurately retrieve erosion rates from the measured grain age distributions.

## 2.1. Introduction

Minerals rich in uranium and thorium contain vital clues to unravelling Earth's history. More resistant minerals such as zircon behave as Earth's timekeepers as they can retain information even after crustal or sediment recycling, and so are key tools to reconstruct ancient geological events (e.g., Amelin et al., 1999; Mojzsis et al., 2001; Wilde et al., 2001). For this reason, detrital zircon has been extensively used in investigations about the growth and evolution of continents (e.g., Iizuka et al., 2010; Dhuime et al., 2012; Oliver et al., 2014), documenting sub–glacial erosion (e.g., Cox et al., 2010; Tochilin et al., 2012; Thomson et al., 2013) as well as reconstructing sediment provenance and drainage development (e.g., Singh et al., 2008; Kirstein et al., 2009, 2013; Alizai et al., 2011; Gehrels et al., 2011; Blum and Pecha, 2014).

But how representative are the sampled grains of the original system? We should not ignore this perennial question if we are to have confidence in our interpretation of preserved sedimentary deposits and what they represent. The importance of investigating source–to–sink processes that may have influenced the preservation of grains is increasingly being recognized (Garzanti et al., 2009; Lukens et al., 2016). Potential biases, if measurable, could have profound effects on the way in which we interpret the sedimentary record. As a result, a number of studies have focused on how different processes such as sediment generation on hillslopes (e.g., Riebe et al., 2015; Lukens et al., 2016), transport in river channels (e.g., Garzanti et al., 2008, 2009; Lawrence et al., 2011a) and sediment mixing in watersheds (Haddadchi et al., 2013, 2014) can affect the way we use detrital information.

At the same time, numerical models have increasingly been applied as a tool to unravel the source of zircons in modern rivers (Sundell and Saylor, 2017). Several of these models apply a forward mixing approach, whereby empirical observations such as exposure area and zircon fertility (i.e. the concentration of the mineral of interest in the source area) are used to generate an artificial grain age probability density function which is compared to the best fit of the measured grain age distribution (e.g., Saylor et al., 2013; Kimbrough et al., 2015; Licht et al., 2016; Sharman and Johnstone, 2017). There is often a mismatch between the model–predicted and best–fit age distributions that is typically explained by a variety of natural factors such as differences in erosion rates (e.g., Amidon et al., 2005a), mineral fertility over the study area (e.g.,

Moecher and Samson, 2006; Dickinson, 2008), and fractionation by transport processes (e.g., hydraulic sorting) (Lawrence et al., 2011b; Malusà et al., 2016).

In detrital studies, minerals of interest such as zircon and apatite are more likely to be found in the 63–250 micron sand fraction. Inherent in these studies is the assumption that this fraction is representative of the system under investigation and that the upstream source units are homogeneously mixed. Lukens et al. (2016) showed that detrital methods focusing on a given size fraction (cosmogenic nuclides in sand in their case) could be biased in steep terrain, as some parts of the catchment may generate more sand than others (see also Riebe et al., 2015). Further, implicit in this practice (and by extension in sediment mixing models) is an untested assumption that pebbles with different abrasion rates are not able to statistically change (i.e., distort) the detrital age distribution of sands. However, fluvial abrasion of clasts has long been considered as one of the main drivers of mineral liberation from coarser to finer size fractions and thus one of the processes which, along with selective transport, promote downstream fining along a river (Krumbein, 1941; Kuenen, 1956; Schumm and Stevens, 1973; Mills, 1979; Parker, 1991; Attal and Lavé, 2006, 2009; Le Bouteiller et al., 2011; Domokos and Gibbons, 2012; Miller et al., 2014). The importance of abrasion in generating sand was confirmed by recent studies combining both field and laboratory investigations, (e.g., Sklar and Dietrich, 2001; Lewin and Brewer, 2002; Attal et al., 2006; Attal and Lavé, 2006, 2009).

Here, I investigate whether pebble abrasion can statistically change (distort) the detrital age distribution recorded by fluvial sands. The Marsyandi watershed, central Nepal, is an abrasion–dominant setting with exceptional constraints on the parameters that are required to simulate the evolution of sediment grain size and mineralogy: published U–Pb detrital zircon age distributions and zircon fertility datasets (Amidon et al., 2005a) are used together with pebble abrasion rates and hillslope grain size supply data (Attal and Lavé, 2006) to simulate detrital age distortions along the Marsyandi River. In addition, our model predictions are compared to other independent published datasets of sediment mixing (e.g., Garzanti et al., 2007) and erosion rates (e.g., Pratt–Sitaula et al., 2004; Gabet et al., 2008; Burbank et al., 2003) from the study area.

I initially test if, by using specific pebble abrasion rates, I am able to simulate statistically significant changes on the U–Pb detrital zircon grain age population from sands by comparing model results with and without abrasion. I also compare our no–abrasion model results with

results from Amidon et al. (2005a)'s no–abrasion model as a test of our model's performance. I then assess the magnitude of the distortion other well–known controlling factors (i.e., differences in erosion rates, zircon fertility and hillslope gravel supply) are able to generate in the Marsyandi catchment, and assess if abrasion is able to produce distortions of a comparable magnitude. With these experiments, I test if pebble abrasion is a significant factor influencing the grains ultimately used in detrital studies, and the resultant grain age distributions used to investigate past landscape change.

## 2.2. Materials and Methods

### *2.2.1. Estimating the source mixing proportion in mixed sand samples*

Measuring the U–Pb zircon grain age distribution both in upstream source units and in a downstream mixed river sample should be sufficient to obtain the mixing proportions of these source units by iteratively solving the proportions in which they must be present to produce a best fit (Amidon et al., 2005a,b).

The best–fit age distribution $f(x)$ of a downstream sample $g(x)$ derived from $n$ source units, is given as:

$$f(x) = \sum_{i=1}^{n} \Phi_i f_i(x), \quad (1)$$

where $\Phi_i$ is the zircon mixing proportion, equal to $1/n$ if all source rocks are equally represented, and must satisfy:

$$\sum_{i=1}^{n} \Phi_i = 1. \quad (2)$$

In Equation (1), $f_i(x)$ is the U–Pb zircon age distribution from the source unit $i$, and is mathematically represented by the probability density function (PDF):

$$f_i(x) = \frac{1}{\sigma_i \sqrt{2\pi}} e^{-\frac{1}{2}\left(\frac{x-\mu_i}{\sigma_i}\right)^2}, \quad (3)$$

where $x$ is grain age, $\mu_i$ is the mean grain age and $\sigma_i$ is the analytical uncertainty of the dating method (c.f. Saylor and Sundell, 2016).

The zircon mixing proportions $\Phi_i$ are iteratively estimated by minimising the area mismatch ($M$) between the U–Pb zircon grain age distribution of the mixed sample $g(x)$ and the U–Pb zircon grain age best–fit $f(x)$ made of upstream source units $f_i(x)$. This minimisation is performed by a mathematical optimization, which is solved in this work through the Sequential Least SQuares Programming (SLSQP) method (Nocedal and Wright, 2000). Although PDF cross–plot maximisation and Monte Carlo modelling seems to generate more accurate mixing proportions (Saylor et al., 2013; Sundell and Saylor, 2017; Sharmanand Johnstone, 2017), I chose the area mismatch method to match the procedures adopted by Amidon et al. (2005a), as I am using their age populations and wish to produce results that are directly comparable with their no–abrasion model.

The area mismatch ($M$) accounts for discrepancies between the total areas of two discretised PDFs (Amidon et al., 2005a) and can be calculated as:

$$M = \sum_{k=1}^{n} \frac{|f(x_k) - g(x_k)|}{2}, \quad (4)$$

where $n$ represents the number of grain ages considered, $x_1$ and $x_n$ represent the minimum and maximum ages, respectively, and $f(x_k)$ and $g(x_k)$ are the modelled and mixed sample age distributions, respectively.

I also use area mismatch ($M$) as a metric to analyze the age distributions predicted by the sediment mixing models (see section 2.4).

### *2.2.2. Mixing models*

Both the abrasion and no–abrasion models that I apply in this work are 2D linear mixing models which predict fluvial sediment mixtures by a forward approach based on the characteristics of the zircons (i.e., age) and of the sediment sources units (e.g., fertility, exposure area and abrasion rate). Mixing models can also be used as inverse unmixing models to predict the erosion rates that match the age distributions and the best–fit fluvial sediment mixtures

described in Equation 1. The theoretical and quantitative details of both models and how the mixing proportions and U–Pb detrital zircon grain ages are used are described below.

### *2.2.2.1. No–abrasion model*

The no–abrasion model is a reproduction of the linear zircon (un)mixing model proposed by Amidon et al.(2005a). It predicts the mixing proportion of sands originating from upstream source units along any point on the river network. It is based on the exposure area and mineral fertility of the source units. In this model, the predicted zircon proportion $\Phi_i^P$ from a specific source *i* in a geological setting composed of *n* sources can be mathematically described as:

$$\Phi_i^P = \frac{A_i C_i}{\sum_{k=1}^{n} A_k C_k}, \quad (5)$$

where:

$$\sum_{k=1}^{n} A_k = 1, \quad (6)$$

$$\sum_{k=1}^{n} C_k = 1. \quad (7)$$

The predicted zircon mixing proportion ($\Phi_i^P$), equal to 1/*n* if all source rocks are equally represented, must satisfy:

$$\sum_{i=1}^{n} \Phi_i^P = 1. \quad (8)$$

$A_i$and $C_i$ refer, respectively, to relative exposure area and relative zircon concentration (fertility) of the source unit *i*. Multiplying the PDF of each source unit, $f_i(x)$, by its respective mixing proportion predicted by the model, $\Phi_i^P$, allows us to create an artificial PDF, $h(x)$, corresponding to the age distribution expected for a case where pebble abrasion is not considered. The expression for $h(x)$ is similar to Equation (1) and can be written as:

$$h(x) = \sum_{i=1}^{n} \Phi_i^P f_i(x). \quad (9)$$

The discrepancies between predicted and best–fit mixing proportions estimated in subsection 2.1 ($\Phi_i^P$ and $\Phi_i$, respectively) can then be attributed to different factors, including different relative erosion rates, $\Phi_i^R$, for the different units (Amidon et al., 2005a) (e.g., a unit being eroded

two times faster than other units will contribute twice the amount of zircon expected from the procedure above). These relative erosion rates, $\Phi_i^R$, for the no–abrasion model can be iteratively estimated by:

$$\Phi_i = \frac{\Phi_i^P \Phi_i^R}{\sum_{k=1}^{n} \Phi_k^P \Phi_k^R}, \quad (10)$$

where $\Phi_i^R$ is equal to $1/n$ if all source rocks are eroded at the same rate and must satisfy:

$$\sum_{i=1}^{n} \Phi_i^R = 1. \quad (11)$$

They can also be estimated by minimizing the area mismatch, $M$, between the age distributions created by the model, $h(x)$, and the best–fit solution, $f(x)$.

### *2.2.2.2. Abrasion model*

The abrasion model proposed in this work is also a linear (un)mixing model and its key assumptions are: (1) bedrock incision processes and downstream fining can be treated as steady state; (2) all particle sizes are moved downstream; (3) selective sorting as well as weathering are negligible on the considered timescale; (4) size reduction due to both breaking and attrition to sand is treated with a single abrasion rate; and (5) zircon proportion is homogeneously distributed in the generated sand fraction. Note that assumptions 1, 2, 3 and 5 are typically assumed in sediment mixing models. In this work, I also include assumption 4 because the abrasion experiments performed by Attal and Lavé (2006) do not discriminate abrasion products according to grain size (e.g., sand, silt, or gravel) and also because the abrasion rates they calculated encapsulate both breaking and attrition without distinguishing between these processes. The limitations imposed by our assumptions are discussed in section 4.4.

In the model, I assume each point across the catchment is a source of sediment belonging to a given rock unit $i$ (see model implementation, section 2.3). The sediment supplied to the river system by each source is made of sand and clasts ("gravel"); I set the initial gravel mass fraction, $F_{g0}$, to 75 % in our reference runs, an average value for landslides in the Marsyandi valley (Attal and Lavé, 2006). I then record the distance $d$ between each source point and a specific river site, and apply an empirically–defined version of the Sternberg's law to calculate the proportion of the

sediment initially supplied by the source unit that reaches the considered river site as gravel ($F_g$) (Dingle et al., 2017):

$$F_g = F_{g0}\, e^{-\alpha d} \quad (12)$$

According to Equation (12), the initial percentage of gravel mass $F_{g0}$ changes to a percentage $F_g$ at distance $d$ from the origin, at a rate given by the rock unit–dependent abrasion rate $\alpha$ (in $km^{-1}$). The percentage of sand mass $F_s$ at $d$ is inversely proportional to the gravel mass $F_g$:

$$F_s = 1 - F_g \quad (13)$$

Note that the Sternberg's law (Equation 12) as used in our work is a "generalized Sternberg's law" that refers to mass loss and not to grain size fining (Miller et al., 2014). It is important to make this distinction because recent work by Domokos et al. (2014) and Miller et al. (2014) suggests that grain size fining due to abrasion does not follow the original Sternberg's law: angular fragments initially experience a rounding phase during which mass is loss but grain size is not significantly reduced; once the grains have been rounded, both mass and grain size are reduced in concert. Their work suggests that mass loss described by Equation (12) applies to both abrasion phases, including the original rounding phase, and is therefore suitable to describe abrasion of fragments from their source, as in our model.

Given that every source unit $i$ has a specific zircon concentration $C_i$ (fertility), relative exposure area $A_i$ and relative supply rate by erosion $\Phi_i^{ZR}$, the zircon mixing proportion of the source unit $i$ in river sands $\Phi_i^{Z}$is given by:

$$\Phi_i^{Z} = F_s A_i C_i \Phi_i^{ZR} \quad (14)$$

at distance $d$.

Multiplying each single source unit PDF, $f_i(x)$, by the mixing proportion estimated by the model ($\Phi_i^{Z}$) allows us to create an artificial PDF, $z(x)$, corresponding to the age distribution of a downstream sand sample as expected when abrasion does occur. The expression of $z(x)$ is similar to Equation (1):

$$z(x) = \sum_{i=1}^{n} \Phi_i^{Z} f_i(x). \quad (15)$$

As in the no–abrasion model, the relative erosion rates ($\Phi_i^{ZR}$) can also be inversely estimated by minimizing the area mismatch ($M$) between the artificially created PDF, $z(x)$, and the best–fit sample age distribution, $f(x)$ (Fig. 2.1).

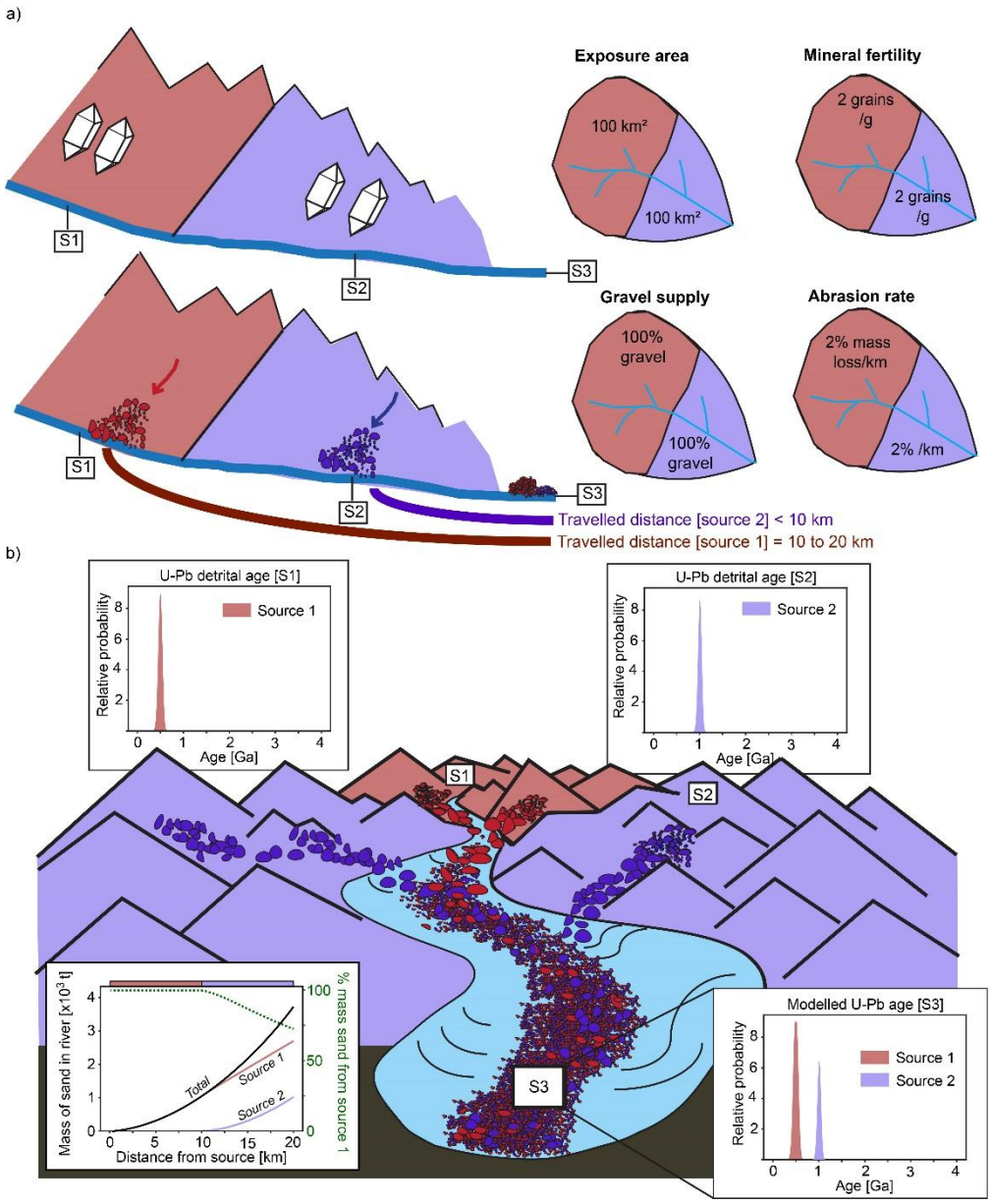


Figure 2.1: Conceptual representation of the variables used in the abrasion mixing model and the resulting impact on the modelled U–Pb detrital age distribution z(x) used to estimate erosion rates. In this representation, different travelled distances d impact the proportion of sand sourced from the two units. This leads to a change in the zircon mixing proportion $\Phi_i^Z$ that modifies the detrital age distribution z(x) in the 63–125 µm fraction used in geochronology. (a) Controlling factors of mass and zircon concentration of sands in the abrasion model: top –bedrock control: exposure area (km$^2$) and mineral fertility (grains/g); bottom –sediment control: hillslope gravel fraction (coarser than sand) and abrasion rate (% mass loss/km), with abrasion progressively transferring zircons from the gravel to the sand fraction as sediment is transported downstream. (b) On a spatial scale, two contributing single source units (S1 and S2) are

mixed downstream (S3). Sample S3 reflects the mixture of upstream controlling factors, including abrasion; in this case, source one is over–represented as the longer transport distance leads to a greater sand production from abrasion and therefore contribution in the mixed sand sample (S3). This is exemplified by the inset (bottom left) showing the mass of sand along a linear river system coming from sources 1 and 2 in a simple model based on Attal and Lavé's (2006, 2009): 1000 tons of sediment are supplied to the system every km (all gravel in this scenario), from source 1 over the first 10 km and from source 2 over the next 10 km. Gravel is abraded according to the Sternberg's law (see text) at a rate of 2 % mass loss/km. Total amount of sand (black) is sum of sand from sources 1 (pink) and 2 (purple). The contribution from source 1 in a sand sample is shown by green dashed line; it is 72% after a distance of 20 km (sample S3). As gravel from source 1 experienced greater transport distance, more sand has been released from source 1 compared to source 2.

### *2.2.3. Model implementation*

In our simulations, I use topographic data with ~ 90 m spatial resolution of the Marsyandi watershed from the Shuttle Radar Topography Mission (SRTM). From these elevation data, I define the river network (used to route sediment across the catchment) and extract flow length for each pixel across the watershed, using tools from the Geospatial Data Abstraction Library (GDAL). Flow length is used to calculate travel distance (km) from each pixel to a given river site ($d$ in Equation 12). The source units ($i$ in Equation 14) with their spatial extent [$km^2$] also feed the model as geographic layers. For a given "sampling" location along the river, each contributing pixel is assigned a transport distance $d$ and a source unit $i$; the relative exposure area of each unit $A_i$ is calculated based on this information. For each source unit $i$, the initial percentage of gravel supplied by the hillslopes to the river channel ($F_g$), zircon concentration ($C_i$) and supply rate by erosion ($\Phi_i^{ZR}$) are set by the user. After combining all those parameters and retrieving the zircon mixing proportion ($\Phi_i^{Z}$) of every source unitfor the river sands at the considered river site (Equation 14), I use $\Phi_i^{Z}$ as an input to create the artificial PDF ($z(x)$ in Equation 15). All the code used to perform our analysis as well as to generate the figures is open source and can be downloaded from GitHub at https://github.com/clavarini.

### *2.2.4 Statistical analysis of model predictions*

The PDFs constructed by the mixing models are statistically assessed by area mismatch ($M$), similarity coefficient ($S$), Kolmogorov–Smirnov test ($K$–$S$), PDF cross–plot analysis and Q–Q

plots. The main aim of these analyses is to quantify how different the model predictions are by comparing their resulting age distributions based on specified scenarios. Another reason to use all these goodness-of-fit metrics is due to their varying sensitivity to changes in age distributions. By combining several of them, I can provide a wide range of statistical analysis to answer my intial question about the influence of pebble abrasion on detrital geochronology.

Any statistically significant difference between the age distributions generated by the mixing models is hereafter named distortion.

### *2.2.4.1 Similarity coefficient (S)*

The similarity coefficient *S* measures if samples have overlapping modes as well as similar proportions of components in each of the modes. Gehrels (2000) defines it as:

$$S = \sum_{k=1}^{N} \sqrt{f(x_k)g(x_k)} \quad (16)$$

where $f(x_k)$ and $g(x_k)$ are the probability density functions (PDFs) of samples one and two, respectively, and $x_1$ and $x_N$ are the minimum and maximum ages for the population. An *S* value of 1 indicates that the PDFs are perfectly matched both in the modes and modal proportions, while a value of 0 indicates that the two age populations have no modes in common.

### *2.2.4.2 Kolmogorov–Smirnov (K–S) test*

Traditionally, the Kolmogorov–Smirnov (*K–S*) test assesses the null hypothesis that two samples are drawn from parent populations with the same distribution. It calculates the *K–S* statistic *Ds*, which is the maximum difference between the empirical cumulative distribution functions (CDFs) of the two analyzed samples, and returns a *p*–value that is inversely proportional to the confidence level at which the two samples fail the hypothesis. The *Ds* value is calculated as:

$$Ds_{1,2} = \sup_k |F_1(x_k) - F_2(x_k)|, \quad (17)$$

where sup($x$) is the supremum of the set of distances, and $F_1$ and $F_2$ are the CDFs of the two samples made from $n_1$ and $n_2$ observations, respectively.

The probability $p$ that the observed samples are from the same population was calculatedby Stephens (1970) as:

$$p(Ds_{observed} > Ds_{critical}) = Q_{KS}(\lambda) = 2\sum_{i=1}^{\infty}(-1)^{i-1} e^{-2i^2\lambda^2} \quad (18)$$

where

$$\lambda = \left(\sqrt{n_e} + 0.12 + \frac{0.11}{\sqrt{n_e}}\right) Ds \quad (19)$$

and

$$n_e = \frac{n_1 n_2}{n_1 + n_2} \quad (20)$$

with limiting values of $Q_{KS}(0) = 1$ and $Q_{KS}(\infty) = 0$.

The *K–S* statistic represents a useful metric to investigate the similarity in the shape of detrital age distributions and to assess our artificially created PDFs. In cases where the distance *Ds* between the investigated PDFs approaches zero, $p$ (or $Q_{KS}$) tends to 1, while extreme distances will tend to produce $p$ values approaching 0. In this work, I retrieve both *Ds* and $p$ values, since some studies have shown that in detrital geochronology *Ds* is more sensitive than its corresponding probability ($p$) (Satkoski et al., 2013; Vermeesch, 2013; Saylor and Sundell, 2016).

### *2.2.4.3 PDF cross–plot and quantile–quantile (Q–Q) plot*

In statistics and probability, quantiles refer to specific cut points dividing the range of a probability distribution (PDF) into contiguous intervals with equal probabilities. A quantile–quantile (Q–Q) plot is a plot where quantiles of two datasets are plotted against each other. In detrital studies, Q–Q plots are used to determine if two data sets come from populations with a common distribution. A PDF cross–plot is a Q–Q plot which, rather than using cumulative distribution functions (CDFs), is based on two PDFs (Saylor et al., 2012). The advantage of the cross–plot to examine detrital age distributions is that it is sensitive to the presence or absence of

age peaks (e.g., Saylor et al., 2013). Samples with identical age peaks, peak shapes and peak magnitudes have $R^2$ = 1, while for those sharing no age peaks $R^2$ approaches 0. PDFs that share either some, but not all, peaks, or have peaks of different magnitudes or shapes, will produce cross–plots with $R^2$ ranging between 0 and 1.

## *2.5. Study area and experimental setting*

### *2.5.1. The Marsyandi watershed*

The Marsyandi watershed, in the central Himalaya, has an area of approximately 4700 km$^2$, is 57 km wide and 170 km long. The Marsyandi flows into the Trishuli River, which later joins the Ganga River in the Himalayan foreland basin. Elevation varies from 200 m to 8000 m. The sediment source units can be grouped into five litho–structural units (Le Fort, 1975; Amidon et al., 2005a; Attal and Lavé, 2006) (Fig. 2.2).

The uppermost source unit (Tethyan Series –"TTS") comprises Cambrian to Jurassic limestones, sandstones and shales. The Tethyan Series are intruded by a Miocene leucocratic granite (Manaslu granite –"MG") in its eastern section. The southern margin of the Tethyan Series is marked by a north–dipping, normal–sense shear zone known as the South Tibetan Detachment (STD). Below (south of) the STD lies the Greater Himalayan Series (GHS), a continuous sequence of amphibolite–grade schists and gneisses divided from south to north into three formations, grouped here as pelitic gneisses (Formation I –"FI") and Paleozoic augen gneiss intrusions in calc–silicate rocks (Formation II–III –"FII–III") (Le Fort, 1975). The series are in turn bounded to the south by the Main Central Thrust (MCT). The MCT is the structural boundary between the Greater Himalaya and Lesser Himalaya series. Lower–grade schists and meta–sediments of the Lesser Himalayan Series ("LH") occur in the MCT footwall.

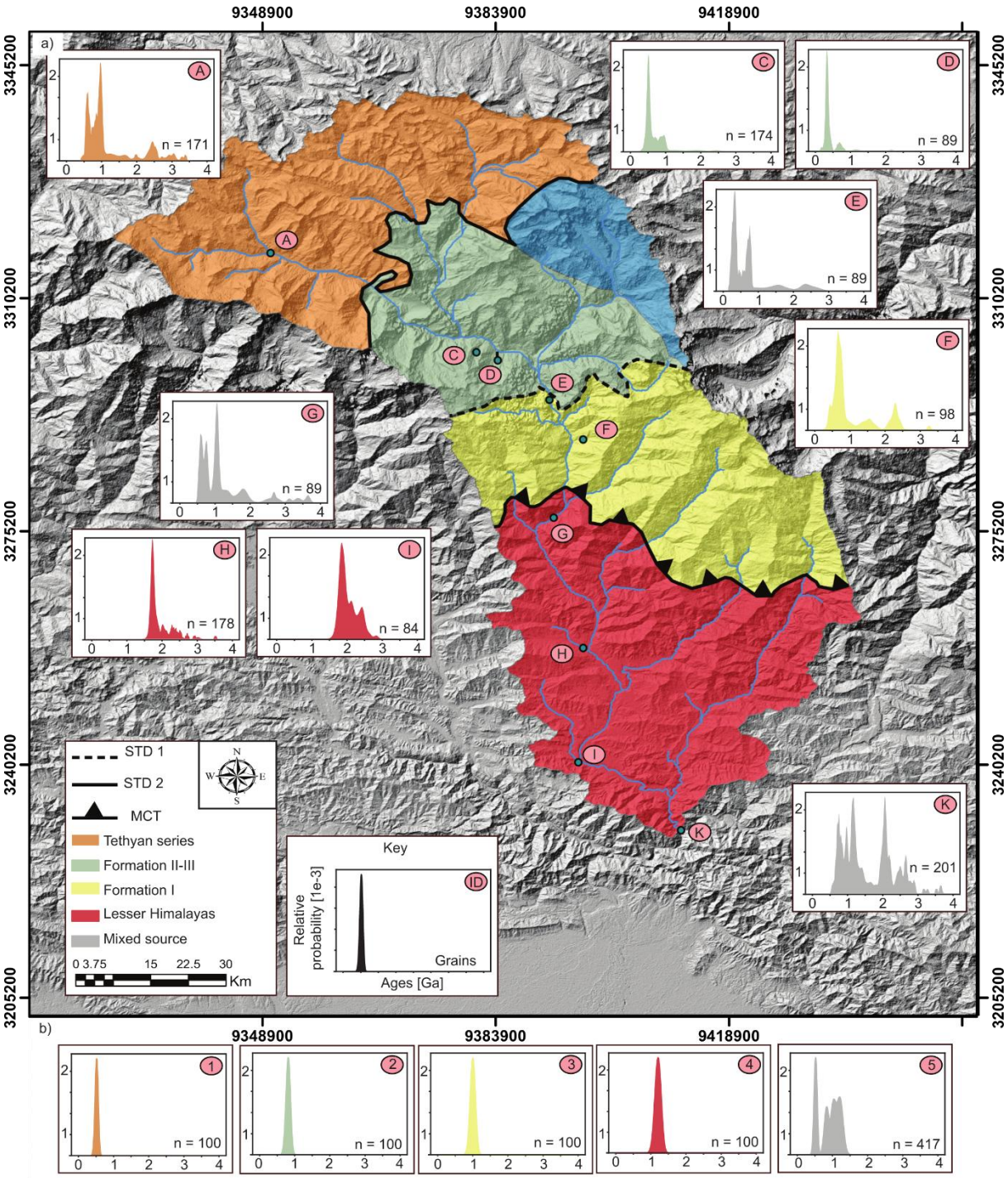


Figure 2.2: Source units of the Marsyandi watershed and their U–Pb detrital age distribution. (a) Geological map for the Marsyandi watershed superimposed on hillshade derived from 30–m resolution Shuttle Radar Topography Mission (SRTM) data. Geological units are derived from Le Fort (1975) (see also Amidon et al., 2005a, and Attal and Lavé, 2006). Sample locations and U–Pb detrital ages distributions (samples A to K) measured by Amidon et al. (2005a) are also indicated; they are used in this work as a study case and in the numerical simulations. Grey PDFs indicate mixed samples, whereas coloured PDFs represent source samples, with the colour relating to the unit in question. MCT is Main Central Thrust; STD 1 and 2 are South Tibetan Detachment as mapped by Searle and Godin (2003), and

Colchen et al. (1987), respectively. (b) Synthetic U–Pb age distributions (samples 1–5) created in this work to facilitate the statistical assessment of our numerical experiments: samples 1 to 4 are sources (indicated by colours) and sample 5 is mixed sand sample predicted at outlet without abrasion (location K in (a)). The vertical axis in the PDFs is relative probability (x $10^{-3}$) and the horizontal axis is U–Pb grain age (Ga).

### *2.5.2. The Marsyandi dataset*

In our study case, I test the effects of abrasion on detrital information using the Marsyandi catchment as a template. The mixing proportion of sands, pebble abrasion rates and zircon fertility of the source units are derived from Attal and Lavé (2006) and Amidon et al. (2005a). The abrasion rates for rock types (e.g., sandstone, schist, etc.) of Attal and Lavé (2006) (their Table 2) are converted to a representative value for the source units of Amidon et al. (2005a) by applying weighted arithmetic mean corrections (Table 2.1).

Table 2.1: Published parameters used in this work to predict the mixing proportion and relative distribution of erosion rates at sampling points in the Marsyandi watershed.

| **Source**[a] | **Zircon fertility (grains/g)** [b] | **Abrasion rate (% mass loss/km)** [c] | **Gravel supply (%)** [d] |
|---|---|---|---|
| TTS | 0.6 | 4.3 | 75 |
| MG | 0 | 0.4 | 75 |
| F II–III | 0.3 | 0.4 | 75 |
| F I | 0.8 | 1.4 | 75 |
| LH | 0.3 | 9.4 | 75 |

[a] TTS = Tethyan series, MG = Manaslu granite, F II–III = Formation II–III, F I = Formation I, LH = Lesser Himalaya.
[b] Estimated by Amidon et al. [2005a].
[c] Estimated from experimental abrasion rates by Attal and Lavé [2006].
[d] Average percentage of hillslope supply coarser than sand (i.e., > 2 mm), estimated by Attal and Lavé [2006].

The U–Pb detrital zircon grain ages are from Amidonet al. (2005a) (Supporting Information Table S1); age smoothing was applied prior to statistical analysis with the same age window interval (80 Ma) as used by Amidon et al. (2005a). I also performed statistical comparison (i.e., *S*, *M*, PDF cross–plot, Q–Q plot, and *K*–*S* statistics) between age distributions with and without smoothing to test if statistically significant changes occur and, therefore, biases the sediment

(un)mixing results. Our statistical comparison is in the Supporting Information (Tables S3 and S4) and is discussed in a section dedicated to methodological uncertainties (4.4).

Shuttle Radar Topography Mission (SRTM) elevation data with ~90 m of spatial resolution are used as topographic data in the mixing models. The modelling calculations are performed for three river locations where samples were collected (Fig. 2.2). The uppermost sampling point (E) has three contributing source units (TTS, MG and FII–III); the sampling point (G) has four (TTS, MG, FII–III and FI), and the Marsyandi outlet (K) has all five. Numerical tests of the minimizations were performed to solve for the relative erosion rates (presented in section 3).

### *2.5.3 Experimental setting*

In all numerical experiments where I test for factors controlling zircon mixing, I use synthetic U–Pb age distributions for the sources in addition to the natural age distributions of Amidonet al. (2005a). The synthetic distributions are normal, with specific age peaks ($\mu$) of 0.5, 0.8, 1 and 1.2 Ga for the Tethyan, Formation II–III, Formation I and Lesser Himalaya sequences, respectively, and a standard deviation ($\sigma$) of 5 % (Fig. 2.2, Equation 3, Supporting information Table S2). This spread of age is comparable to the spread in the real dataset. I adopted ages increasing downstream so that the relative contribution of the different sources is easier to identify in the mixed sample distributions; I also chose to have a distinct peak (Tethyan Series at 0.5 Ga) and three partly overlapping distributions, comparable to the real dataset. I performed additional experiments with four additional synthetic age distributions with various degrees of peak overlap to assess the influence of this factor (discussed hereafter and presented in the Supporting Information).

#### *2.5.3.1 Testing the influence of abrasion rates on age distributions*

In our first set of simulations, I test the influence of pebble abrasion rates on mixed sample age distributions (scenarios A1–A4). Zircon fertility is the same for all sources, except for the Manaslu granite for which zircon fertility is set to zero to reproduce the behaviour of a non–contributing source region to the age distribution, as Amidon et al. (2005a) found no zircon

within the Marsyandi watershed that they could unambiguously relate to the Manaslu granite. The hillslope gravel supply is also set to a uniform value of 75 %. The abrasion rates used in the simulations are based on experimental abrasion rates for rock types of the Marsyandi watershed from Attal and Lavé (2006) (Table 2.2).

Table 2.2: Parameters used in the numerical experiments testing the influence of pebble abrasion rates in the age distribution of sands. TTS = Tethyan Series, F II–III = Formation II–III, F I = Formation I, LH = Lesser Himalaya.

| Experiment | Zircon fertility (grains/g) [a] | Abrasion rate (% mass loss/km) [b] | | | |
|---|---|---|---|---|---|
| | | TTS | F II–III | F I | LH |
| A1 | 1 | 0.4 | 0.4 | 0.4 | 0.4 |
| A2 | 1 | 31 | 0.15 | 0.15 | 0.15 |
| A3 | 1 | 0.15 | 0.15 | 0.15 | 31 |
| A4 | 1 | 4.3 | 0.4 | 1.4 | 9.4 |

[a] Estimated by Amidon et al. [2005a].
[b] Estimated by Attal and Lavé [2006].

In the first scenario (A1), the effect of uniform abrasion is assessed by setting a single abrasion rate of 0.4 %/km, (equivalent to granite) for the whole watershed. In the second scenario (A2), I simulate the behaviour of a watershed with two extreme rock strengths: rocks from the Tethyan Series have a high abrasion rate of 31 %/km, (equivalent to poorly cemented sandstone) and the rest of the rocks are abraded at a low rate of 0.15 %/km (equivalent to quartzite). In the third experiment (A3), I assess how source location impacts fluvial sand composition by inverting the previous scenario: the Lesser Himalaya has the highest abrasion rate (31 %/km) while rocks from the upstream sources are abraded at 0.15 %/km. In the fourth scenario (A4), I apply abrasion rates representative of the different units in the Marsyandi watershed (Attal and Lavé, 2006). The main aim of this experiment is to simulate how the fluvial sand composition behaves in a complex scenario of rocks with multiple abrasion rates but decoupling it from other controlling factors that can bias the sand mixing proportion.

### *2.5.3.2 Comparing the influence of different controlling factors on age distributions*

In a second series of experiments, I test the sensitivity of the age distributions to abrasion rate (B2), erosion rate (B3), fertility (B4), and initial gravel fraction (B5). The experiments are run using both synthetic and natural datasets. The parameter values used to create the scenarios are chosen to emphasise the distortion in sand while keeping within a realistic range. Variations in erosion rate, abrasion rate, hillslope gravel supply and zircon fertility are applied based on values published by Garzanti et al. (2007), Attal and Lavé (2006) and Amidonet al. (2005a), respectively (Table 2.3). Scenario B1 is the reference scenario with all parameters spatially uniform and no abrasion (see Fig. 2.3, "no abrasion").

In scenario B2, abrasion rate for Tethyan Series gravel varies between 0.15 and 31 %/km while it is kept at 0.15 %/km for the other units; the experiment with the most extreme value (31 %/km) is the same as A2. In B3, the Tethyan Series are eroded between 1 and 5.1 times faster than the rest of the catchment. In B4, the fertility of rocks from the Tethyan Series is 0.8 grains/g while it is set to between 0 and 0.8 grains/g in the rest of the catchment; the experiment where all non–TTS units contributes no zircon (fertility = 0) simulates an extreme scenario with "invisible" units. In B5, sediment initially sourced from the Tethyan Series is made of between 60 and 90 % of gravel (i.e., between 10 and 40 % sand) while this number is 90 % in the rest of the catchment; this range of values encompasses values from landslides in different lithologies measured in the Marsyandi valley (Attal and Lavé, 2006). Scenario B5b is the same as B5, except that the initial gravel fraction varies between 60 and 90 % for the Lesser Himalaya sources (instead of TTS) while this number is 90 % in the rest of the catchment; this scenario tests the influence of peak overlap, as the LH peak in the synthetic dataset overlaps with the Formation I peak (see next section). Finally, I explore a scenario where Tethyan Series have both an extremely high abrasion rate (31 %/km) and the lowest initial gravel fraction (60 %) supplied to the river channel, while the other source units have low abrasion rates (0.15 %/km) and hillslopes with an extremely high gravel content (90 %) (scenario B6). The aim of this experiment is to test the influence of the known covariance between highly abradable source units and higher sand supply from hillslopes due to higher weathering rates in softer rocks (e.g., schist versus quartzite, see Attal and Lavé, 2006).

#### *2.5.3.3 Testing the ability of controlling factors to reproduce the distortion from others*

In these experiments, I test how well each controlling factor can mimic the distortion caused by another factor in the most extreme scenarios from experiments B2 to B5, using both synthetic and natural datasets. I use the maximum and minimum values used in the experiments B2 to B5 as bounds to iteratively solve for the best fit between the age distribution created from a factor being tested and a factor whose distortion is intended to be reproduced.

To test the ability of the method to cope with relative changes in partly overlapping age peaks, I explore a scenario where the Lesser Himalaya has the smallest gravel fraction (60 %) instead of the Tethyan Series (scenario B5b instead of B5, see Table 2.3) as the LH peak in the synthetic dataset overlaps with the Formation I peak (whereas the TTS peak is isolated).

#### *2.5.3.4 Testing the influence of abrasion on mixing proportions in the Marsyandi catchment*

Finally, I use the Marsyandi dataset to assess the influence of abrasion on both mixing proportions and age distributions in a real scenario, using the parameters described in Table 2.1. For the three mixed samples E, G and K (Fig. 2.2), I compare best–fit results using the iterative method described in section 2.1 with the results obtained from the mixing models with and without abrasion. At each site, I discuss the differences and their statistical significance.

## 2.6. Results

### *2.6.1. Simulations for sensitivity analysis*

#### *2.6.1.1. Influence of abrasion rates on age distributions*

Simulations A1 to A4 demonstrate how pebble abrasion affects the zircon mixing proportions of upstream sediment source units in the sand fraction and ultimately distorts the grain age distributions (PDPs) of the mixed samples derived from them (Fig. 2.3).

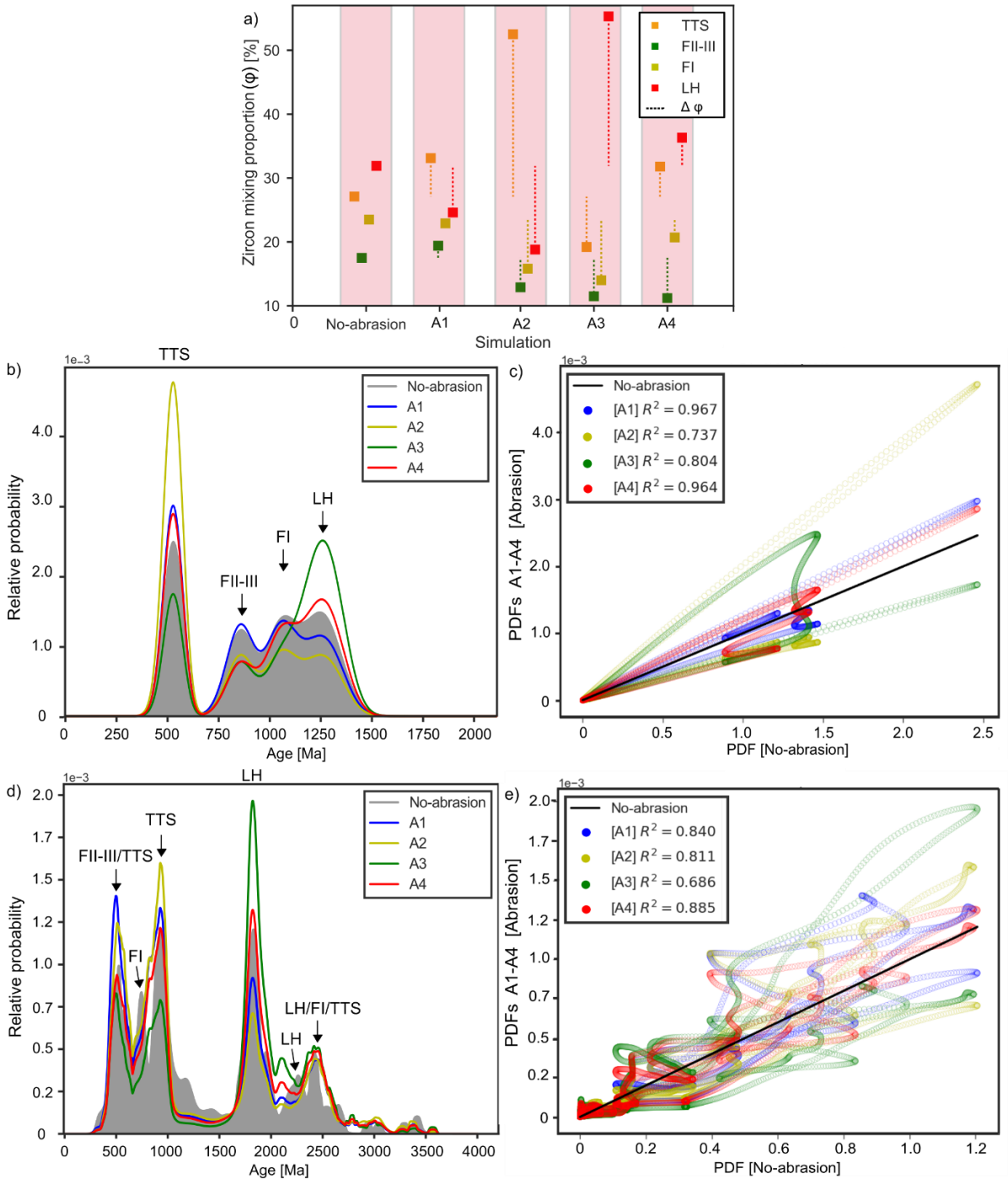


Figure 2.3: Results of the numerical simulations that tested the statistics of synthetic U–Pb zircon age populations (PDPs) derived from zircon mixing modelling using abrasion scenarios (Table 2.2): uniform abrasion rate (A1), very high abrasion rate for TTS (A2) or for LH (A3), and realistic values for the

different units based on Attal and Lavé (2006) (A4). (a) Percentage zircon from the different rock units in sand at the catchment outlet. Mixing proportions in the no–abrasion case reflect the relative exposure area of the different units; dashed lines indicate change with respect to the no–abrasion scenario. (b) and (d) Probability density plots (PDPs) generated using the mixing proportions predicted by the abrasion model on synthetic and natural age distribution, respectively. Arrows identify peaks associated with the four sources. (c) and (e) Statistical assessment of the PDPs through PDF cross–plots. Additional statistical assessment (e.g., Q–Q plots) can be found in the supporting information (Table S5, S6, Fig. S1). Note that scenarios A2 and A3 lead to the greatest amount of distortion with the synthetic dataset (see $R^2$ values in (c)), with greater distortion in case A2 due to the TTS peak being isolated compared to the LH peak. With the natural dataset, only scenario A3 leads to a significant amount of distortion compared to the other scenarios (see $R^2$ values in (e)), which I explain by LH having a unique peak at ~1.8 Ga; most TTS peaks are shared with other units.

Modifications in the zircon mixing proportions (Fig. 2.3a) and in the shape of the PDPs are recorded in all experiments but not all of them are significant (Fig. 2.3c, e). The experiments that simulate extreme contrast in abrasion rates (A2 and A3) have changes in the zircon mixing proportion that distort all U–Pb grain age distributions investigated (see the $R^2$ values of the PDF cross–plots). Extremely high abrasion rates (31 %/km versus 0.15 %/km) lead to rapid release of zircon from gravel to sand for the unit in question. The unit therefore ends up overly represented in the mixed sand sample: more than 50 % of the zircons in the mixed sample are sourced from TTS and LH in scenarios A2 and A3, respectively (Fig. 2.3a). In the synthetic datasets (Fig. 2.3b), this is shown by the clear growth of the TTS and LH source peaks, respectively.

The trends with the natural datasets are less clear, as peaks are not as well defined, overlap, and do not have a normal distribution; units are not characterised by a single peak neither (Fig. 2.2). All scenarios (A1–A4) show significant statistical changes in the age distributions, overall greater than with the synthetic datasets (Fig. 2.3d, e). The only exception is scenario A2, in which more distortion is observed with the synthetic dataset (Fig. 2.3c, e). This can be explained by the fact that TTS shares its major peaks (in range 0.5–1 Ga) with Formations I, II and III (Fig. 2.2): a relative increase in zircons from TTS in the range 0.5–1 Ga due to rapid abrasion is counterbalanced by a relative decrease in zircons from Formations I, II and III in the same age range. On the other hand, the dominant age peak from LH at ~1.8 Ga is unique, leading to the greatest amount of distortion ($R^2$ = 0.69, Fig. 2.3e) and a clear growth of this peak in experiment A3 (Fig. 2.3d).

Interestingly, numerical changes in the zircon mixing proportions and age distributions in the uniform abrasion scenario (A1) are comparable to when abrasion reflects the real variations of the rocks from the Marsyandi watershed (A4), both with synthetic and natural datasets. Statistically, however, in both cases (A1 and A4), the *K*–*S* tests and PDF cross–plots are not able to demonstrate that these populations are different from a no–abrasion scenario (with 95 % confidence) and therefore no statistically significant change (distortion) is identified. The similarity coefficient (*S*) and Q–Q plot statistics are less sensitive in detecting changes in the grain age distributions but also mirror the trends identified by the PDF cross–plots and area mismatch (*M*) (Supporting Information Table S5–S6 and Fig. S1). Finally, additional experiments with synthetic datasets characterised by peaks with various shapes and degrees of overlap provide very similar results overall (Fig. 2.4, and Supporting Information Fig. S1 and Table S11): $R^2$ values for experiments A1 and A4 are almost not affected by the changes (changes are within 5 %) and experiments A2 and A3 generate the greatest amount of distortion. However, the isolation and broadness of the peak targeted by the change in abrasion rate seem to affect the relative amount of distortion in scenarios A2 and A3: A3 generates greater distortion than A2 when peaks are well isolated (age distributions 1 and 2), and the opposite when there is significant overlap (age distributions 3–5). These variations demonstrates a sensitivity of the results to the shape of the age distributions, though the $R^2$ values for experiments A2 and A3 tend to be very close, no more than 16 % from each other.

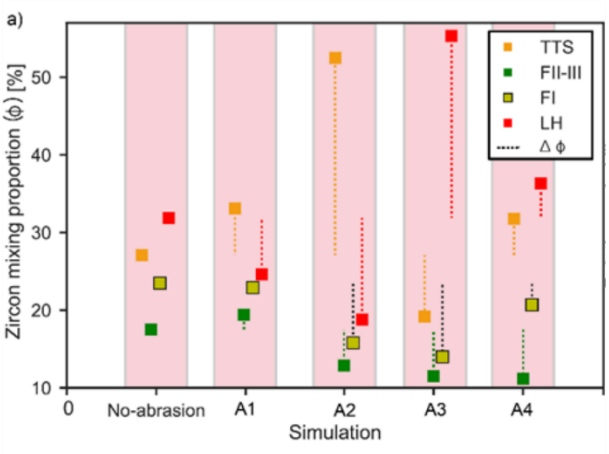
a)
Zircon mixing proportion (ϕ) [%]
TTS
FII-III
FI
LH
Δ ϕ
No-abrasion
A1
A2
A3
A4
Simulation

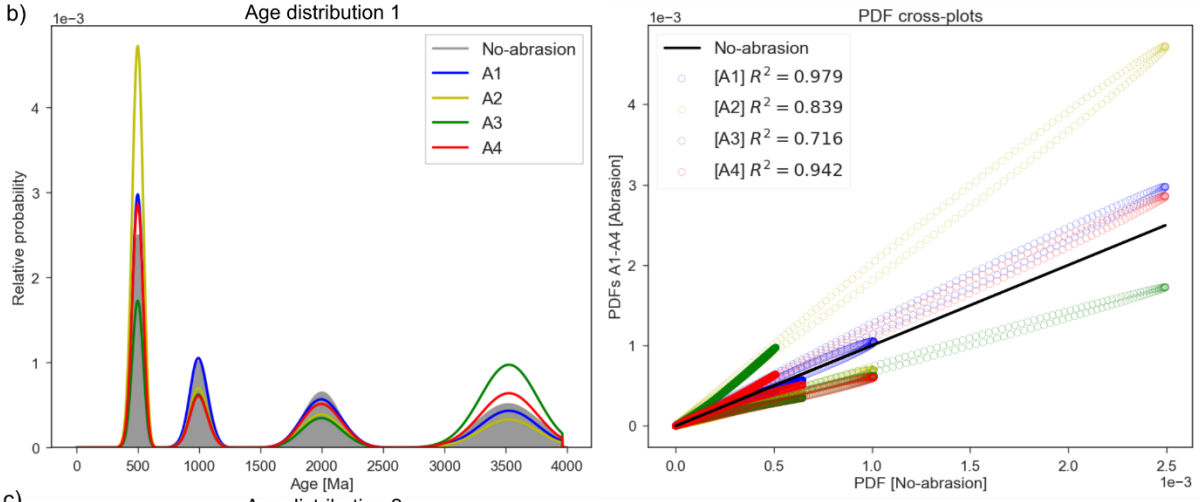
b)
Age distribution 1
Relative probability
Age [Ma]
No-abrasion
A1
A2
A3
A4
PDF cross-plots
PDFs A1-A4 [Abrasion]
PDF [No-abrasion]
[A1] $R^2$ = 0.979
[A2] $R^2$ = 0.839
[A3] $R^2$ = 0.716
[A4] $R^2$ = 0.942

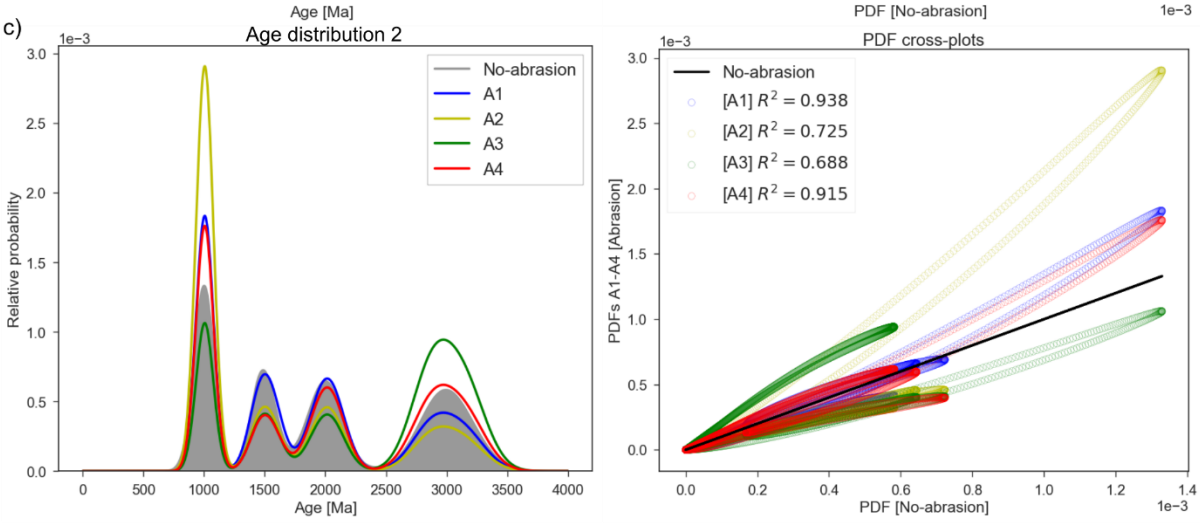
c)
Age distribution 2
Relative probability
Age [Ma]
No-abrasion
A1
A2
A3
A4
PDF cross-plots
PDFs A1-A4 [Abrasion]
PDF [No-abrasion]
[A1] $R^2$ = 0.938
[A2] $R^2$ = 0.725
[A3] $R^2$ = 0.688
[A4] $R^2$ = 0.915

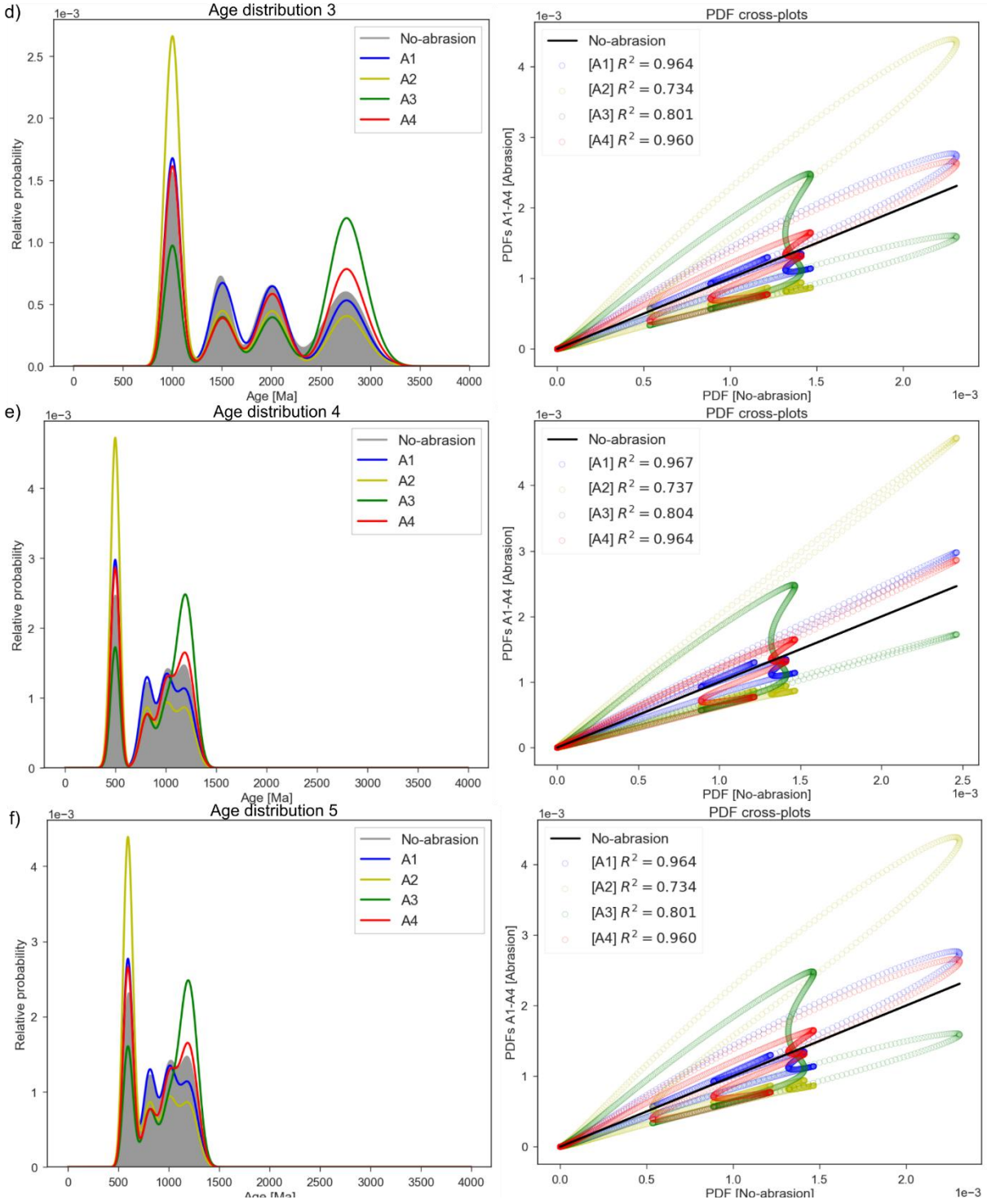
d)
Age distribution 3
1e−3
Relative probability
Age [Ma]
No-abrasion
A1
A2
A3
A4
PDF cross-plots
PDFs A1-A4 [Abrasion]
PDF [No-abrasion]
[A1] $R^2$ = 0.964
[A2] $R^2$ = 0.734
[A3] $R^2$ = 0.801
[A4] $R^2$ = 0.960
e)
Age distribution 4
[A1] $R^2$ = 0.967
[A2] $R^2$ = 0.737
[A3] $R^2$ = 0.804
[A4] $R^2$ = 0.964
f)
Age distribution 5

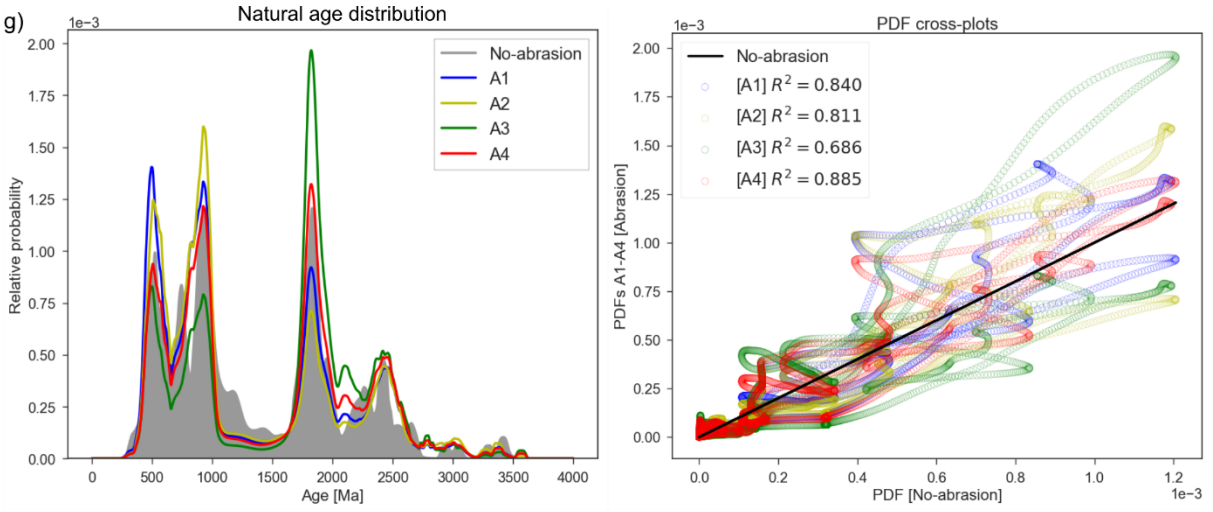


Figure 2.4. Results of the numerical simulations that tested the statistics of synthetic U–Pb zircon age populations (PDPs) derived from zircon mixing modelling using abrasion scenarios (Table 2.2): uniform abrasion rate (A1), very high abrasion rate for TTS (A2) or for LH (A3), and realistic values for the different units based on Attal and Lavé (2006) (A4). This figure display similar information to Fig. 2.3 but includes results for all synthetic age distributions (b–f). (a) Percentage zircon from the different rock units in sand at the catchment outlet. Mixing proportions in the no–abrasion case reflect the relative exposure area of the different units; dashed lines indicate change with respect to the no–abrasion scenario. (b–g) Probability density plots (left) and PDF cross–plots (right) generated using the mixing proportions predicted by the abrasion model; (g) show data using the natural age distribution. Statistical assessment of this complete dataset can be found in Fig. S1 (Q–Q plots) and Table S11.

#### *2.6.1.2. Influence of the different controlling factors on age distributions*

We produced age populations in a range of scenarios, whereby the Tethyan Series are assigned distinct values from all other units for abrasion rate, erosion rate, zircon fertility and gravel fraction in sediment supply (scenarios B2, B3, B4 and B5, respectively; Table 2.3). The results are populations where the peak at 0.5 Ga is enhanced with respect to the other peaks (Fig. 2.5a–d).

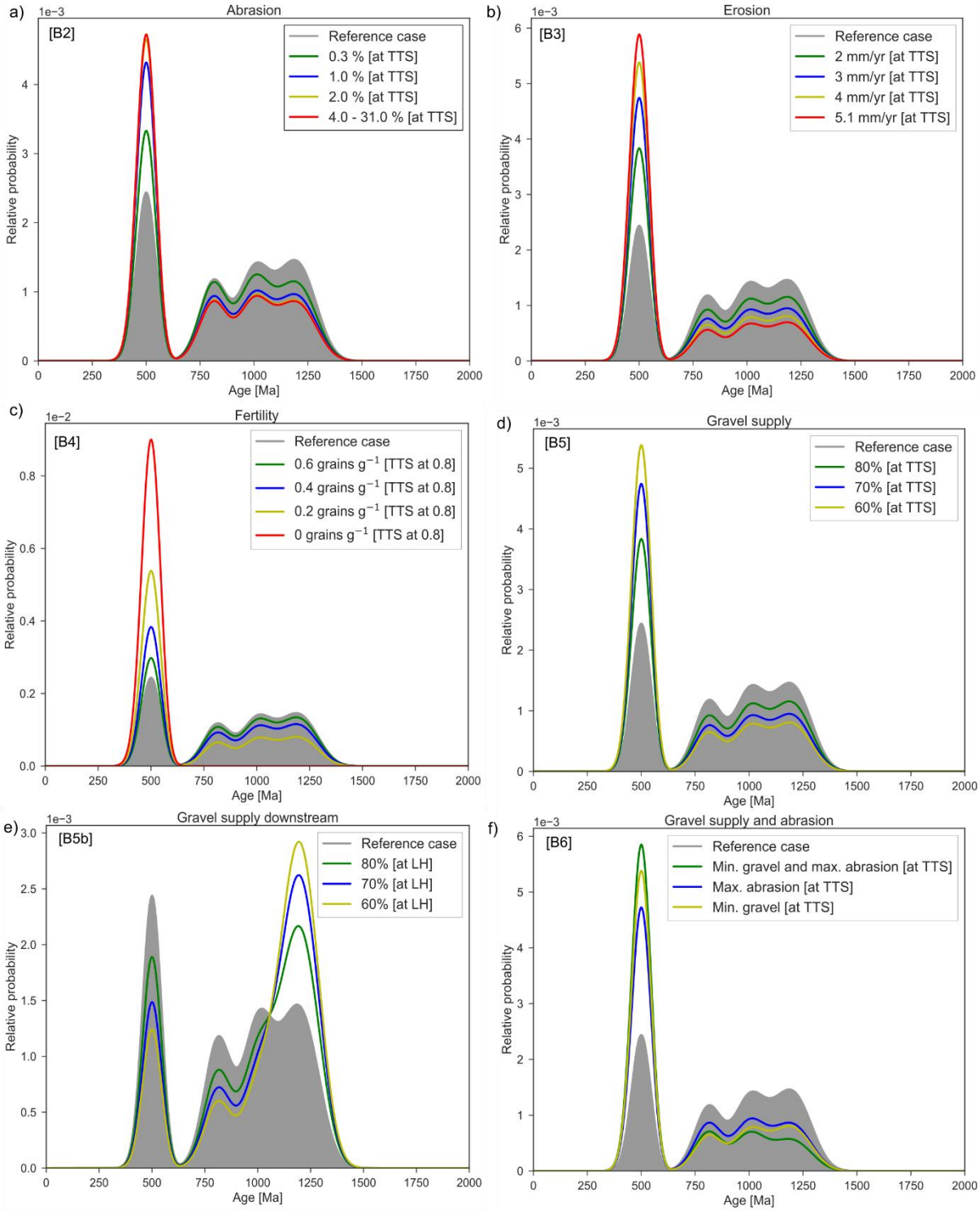


Figure 2.5: Synthetic zircon age populations (PDPs) derived from zircon mixing in numerical experiments B2–B6 (Table 3), showing sensitivity of PDPs to (a) abrasion (B2), (b) erosion rate (B3), (c) fertility (B4) and (d–e) hillslope gravel supply (B5–B5b). An additional experiment B6 has a low initial gravel supply and high abrasion rate for TTS (Table 3). B1 is the reference case (all factors uniform, no abrasion); B2 is the same as simulation A2. Note the quasi linear response to erosion rate, fertility and hillslope gravel

supply (b–e), in extreme contrast with the influence of abrasion rate (a). Combining low gravel supply with high abrasion rate leads to increased distortion (f): TTS is overrepresented in a sand sample at the outlet with respect to other units, due to both greater sand contribution at the source (hillslope) and greater release of sand through abrasion of gravel (high abrasion rate). Full statistical assessment can be found in the supporting information (Table S7–S8).

Table 2.3: Parameters used in the numerical experiments comparing the distortion caused by well–known controlling factors (erosion rate, zircon fertility, hillslope gravel supply and abrasion). TTS = Tethyan Series, F II–III = Formation II–III, F I = Formation I, LH = Lesser Himalaya. A sensitivity analysis was also carried out for experiments B2 to B5b, with results shown in Figure 4: TTS' abrasion rate was varied between 0.15 and 31 %/km in B2; TTS' erosion rate was varied between 1 and 5.1 mm/yr in B3; fertility of non–TTS units was varied between 0 and 0.8 grains/g in B4; gravel supply from TTS and LH was varied between 60 and 90 % in B5 and B5b, respectively.

| **Experiment** | **Factor** | **Coefficients** | | | |
|---|---|---|---|---|---|
| B1 | All uniform – no abrasion | TTS | F II–III | F I | LH |
| B2 | Abrasion rate (% mass loss/km) | 31 | 0.15 | 0.15 | 0.15 |
| B3 | Erosion rate (mm/a) | 5.1 | 1 | 1 | 1 |
| B4 | Zircon fertility (grains/g) | 0.8 | 0 | 0 | 0 |
| B5 | Gravel supply (%) | 60 | 90 | 90 | 90 |
| B5b* | Gravel supply (%) | 90 | 90 | 90 | 60 |
| B6 | Gravel supply (%) + | 60 | 90 | 90 | 90 |
| | Abrasion rate (% mass loss/km) | 31 | 0.15 | 0.15 | 0.15 |

* B5b is similar to B5 except that LH has the smallest gravel supply instead of TTS; see text for details.

The experiments highlight that all of these controlling factors affect the zircon mixing proportions and statistically distort the age distribution of modern river sands. The response is linear for erosion rate, fertility and initial gravel fraction (e.g., a doubling of erosion rate in the TTS units leads to twice more zircon from this unit); the response is strongly non–linear with respect to abrasion rates, with high sensitivity at low abrasion rates and no sensitivity at rates above 2 %/km (Fig. 2.5a). When combining both high abrasion rate and high initial sand content at the source (scenario B6), I observe increased distortion compared to scenarios with either high abrasion rate or high initial sand content at the source (Fig. 2.5f): the TTS unit is overrepresented in the sand sample due to a relatively greater proportion of zircons from other units being "retained" in gravel, as a comparatively greater amount of gravel from these units is supplied at the source and this gravel persists for longer (lower abrasion rate).

We find that, within the realistic range of values for the Marsyandi catchment, the factors that can produce the highest distortion are, from highest to lowest: fertility, erosion, hillslope gravel supply and, lastly, pebble abrasion (Fig. 2.6).

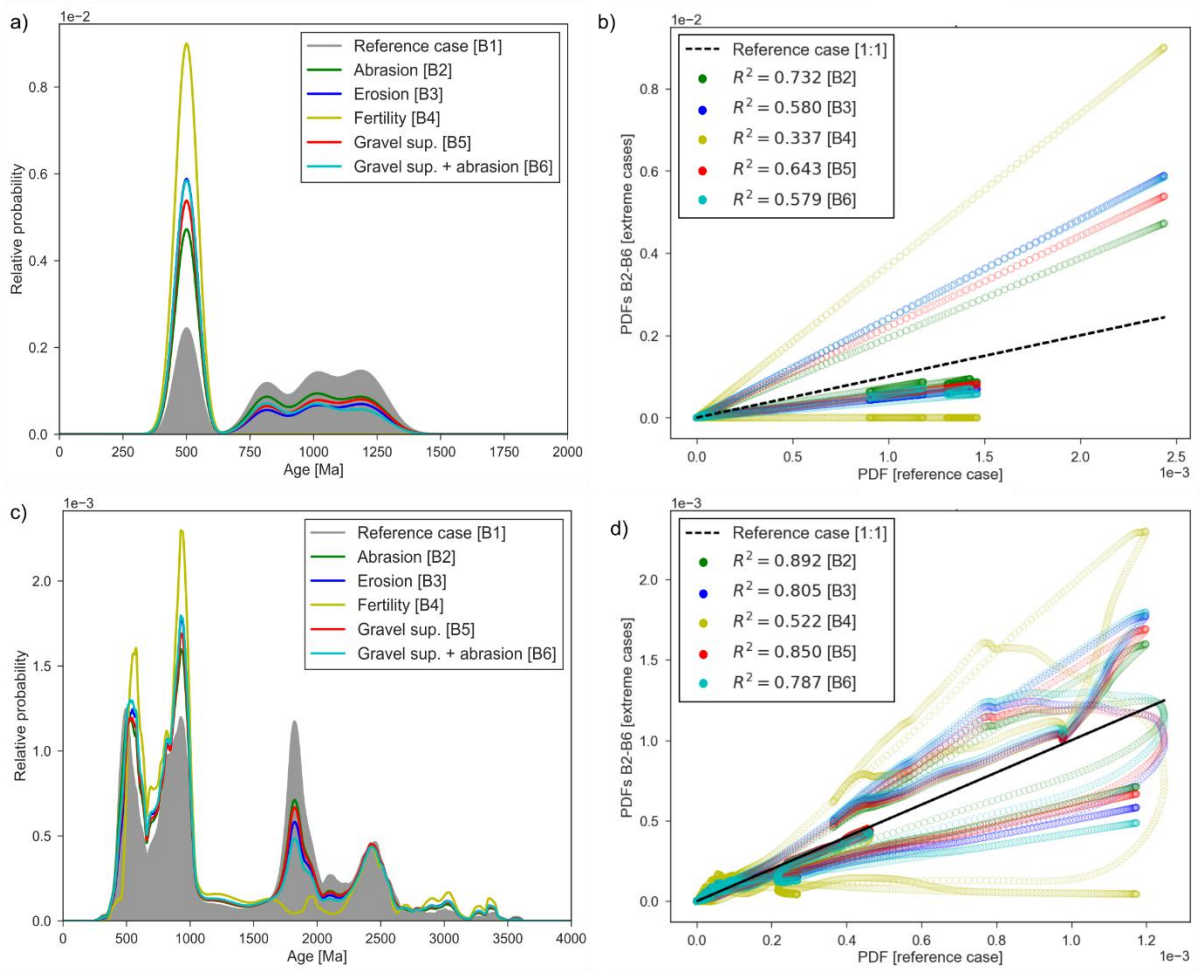


Figure 2.6: (a, c) Probability density plots (PDPs) and (b, d) PDF cross–plots of the end–member scenarios from experiments B2–B6 (Table 3). (a, b) are based on synthetic age distributions. (c, d) are based on natural age distributions. Additional statistical assessment can be found in the supporting information (Table S7–S8, Fig. S3). Note the clear distortion generated by the different parameters with the synthetic dataset (b); the distortion is not as significant with the natural dataset (d), which I explain as due to overlapping peaks, though the relative influence of the different parameters is the same in both datasets (with fertility having the greatest effect).

This order is valid for both synthetic and natural datasets, though the amount of distortion in the natural dataset tends to be lower, possibly due again to the fact that TTS shares peaks with other units (Fig. 2.6). I note that increasing peak overlap in the synthetic datasets leads to a

systematic increase in distortion (lower $R^2$ values in PDF cross–plots) for all scenarios (Supporting Information Fig. S2 and Table S11).

As in the previous section (3.1.1), metrics such as the similarity coefficient (*S*) and Q–Q plot statistics are the least sensitive to detecting changes in the grain age distributions but mirror the trends identified using the PDF cross–plots and area mismatch (*M*) (Supporting Information Table S7, S8 and Figure S2, S3).

#### *2.6.1.3. Ability of controlling factors to reproduce the distortion from others*

We assess the capability of different distorting factors to reproduce the distortion created in experiments B2–B6. I use the optimization method to assess whether, for example, the age distribution produced by scenario B2 (Tethyan Series rocks abraded at 31 %/km) can be mimicked by allowing other parameters (relative erosion rates, fertility and gravel supply) to vary, in turn, within the range of realistic values (Fig. 2.7, see also experiments with different synthetic datasets in Supporting Information Fig. S4).

I find that all the factors are able to perfectly reproduce the impact of abrasion on the zircon grain age distribution (B2) (Fig. 2.7; statistics in Supporting Information Table S9, S10). The effect of having Tethyan Series rocks abraded at 31 %/km while the others are abraded at 0.15 %/km can be replicated by having the Tethyan Series' erosion rate, fertility or initial sand supply (= 1 – initial gravel supply) around three times greater than that of the other units (Supporting Information Table S13). On the contrary, abrasion is not able to fully reproduce the distortions caused by any other controlling factor (Fig. 2.7). Changes in fertility are able to fully reproduce the distortion caused by differences in relative erosion rates (B3 –erosion of Tethyan Series five time faster than other units), but changes in abrasion rates or gravel fraction can produce distributions similar enough (not statistically distinct; Fig. 2.7). No factor can fully reproduce the distortion caused by extreme differences in fertility (B4); this occurs as a result of having three "invisible lithologies" with fertility = 0. Any lithology containing zircons will appear in the mixed sand sample, irrespective of their abrasion rate, initial gravel fraction or

relative erosion rate (except in an unimaginable scenario where erosion rate = 0 or gravel supply = 100 % and abrasion rate = 0). All factors except abrasion are able to reproduce the age distribution resulting from variation in hillslope gravel supply, even in a situation where the peak that is affected (i.e. Lesser Himalaya) partly overlaps with other peaks (scenario B5b, Table 3, Fig. 2.7). These results apply to both synthetic and natural datasets (Fig. 2.7).

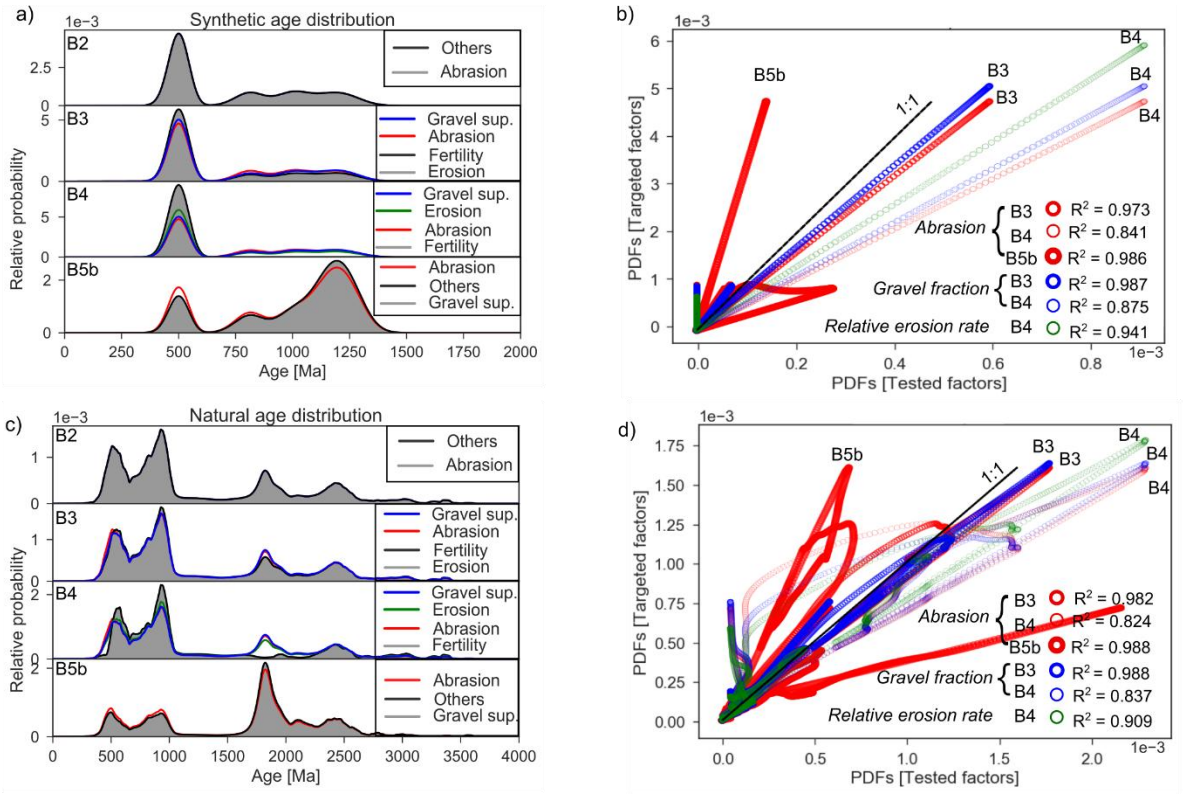


Figure 2.7: Results of the numerical simulations comparing the capability of each controlling factor to reproduce the distortions of abrasion (B2), erosion (B3), fertility (B4) and hillslope gravel supply (B5b) in the zircon age populations (PDPs). (a, c) Probability density plots (PDPs) of the experiments, comparing the distribution created by varying a given factor (grey) with the best fit distributions obtained by varying one of the other parameters (curves). Factors that can perfectly reproduce the distribution are grouped in "Others". (b, d) PDF cross–plots and their $R^2$ comparing how the (tested) factors can reproduce a distortion caused by a specific (targeted) factor; thickness of circles refers to scenario, whereas colour refers to tested factor. (a, b) are based on synthetic age distributions. (c, d) are based on natural age distributions. Note the similar performance ($R^2$) with both synthetic and natural datasets. Additional statistical assessment can be found in the supporting information (Table S9, S10).

It is interesting to note that in all cases, abrasion produces peaks that are not high enough to replicate the extreme distortion caused by the other factors. In other words, not enough sand is produced by abrasion from the Tethyan Series in experiments B3 and B4 and from the Lesser

Himalaya in experiment B5b. This results from abrasion rates being allowed to vary only between 0.15 and 31 %/km. When looking at the statistics of the results, however, I find that the "best fit" is given for abrasion rates of 3.5 and 3.3 %/km for the Tethyan Series for experiments B3 and B4, respectively, while the other lithologies are being abraded at 0.15 %/km (Table S6). This is unexpected as, in theory, more sand from the Tethyan Series could be generated with greater abrasion rates (up to 31 %/km). This occurs as a result of the termination threshold in the minimisation procedure in the model, as iterations stop when the minimisation does not reduce the misfit by more than 0.1 % in the cost function. In case B3, for example, I find that the proportions of zircon sourced from the Tethyan Series are 52.48 % and 52.54 % with abrasion rates of 3.5 and 31 %/km, respectively: mixing proportions are insensitive to abrasion rates beyond a given value, as shown in the sensitivity analysis (Fig. 2.4a). On the other hand, the best–fit abrasion rates in scenario B5b are 30.3 %/km for the Lesser Himalaya and 0.15 %/km for the other lithologies: in this case, the proximity of the Lesser Himalaya units to the outlet makes the mixing proportions more sensitive to changes in abrasion rates for these units. These results highlight the non–linear dependency of mixing proportions on abrasion rates, as opposed to the other factors (a doubling of fertility in one unit can be mimicked by a doubling of relative erosion rate for this unit). They also demonstrate the effectiveness, and limitations, of the optimization method.

### *2.6.2. Study case (Marsyandi watershed)*

In this last section of the analysis, I consider the real datasets to assess the importance of abrasion in controlling the age distribution of mixed samples and the relative erosion rates retrieved from them. In the following, I mix the real source age distributions to match the mixed sample age distributions measured in locations E, G and K (Fig. 2.2). I first produce a best–fit mixed sample distribution using the mismatch minimisation method described in section 2.1 and used in section 3.1.2. I then use our full mixing models (abrasion and no–abrasion, see section 2.2) that include field–derived parameters (Table 2.1) to attempt to replicate the best–fit distributions and retrieve relative erosion rates for the different units that make up the Marsyandi watershed. As mentioned earlier, the minimisation method is an iterative procedure that stops

when the iteration does not reduce the misfit by more than 0.1 % in the cost function. The cost function I use to produce the best–fit mixed sample distribution is the ratio of predicted to measured sums of squares of zircon ages (see section 2.1). The cost function I use for the full mixing models is area mismatch, to follow the procedure by Amidon et al. (2005a). Results for this section for the three sampling sites (E, G and K) are presented in figures 2.8, 2.9 and 2.10, respectively (see also Supporting Information Tables S14, S15, and S16). I find that the grain age distributions created with the abrasion and no–abrasion models are statistically indistinguishable in all river reaches analyzed. However, the zircon mixing proportions and the relative erosion rates estimated from the same ages are different.

In the uppermost sampling site (E), only two sources are contributing (Tethyan Series and Formation II–III). When trying to best fit the no–abrasion and abrasion models (Fig. 2.8), I find a difference of 6 % between the zircon mixing proportions estimated by the two models (Fig. 2.8a). In spite of this, the modelled ages have an indistinguishable distribution ($R^2$ = 0.988). However, the relative erosion rates derived from these two models are significantly different: the relative contribution of the FII–III rises from 58.3 to 71.3 % when abrasion is accounted for, to counterbalance the increased zircon contribution from the Tethyan Series due to its relatively high abrasion rates (4.3 %/km, compared to 0.4 %/km for FII–III) (Fig. 2.8). The strong contrast in rock resistance to abrasion in this case (an order of magnitude) leads to a strong difference in predicted relative erosion rates.

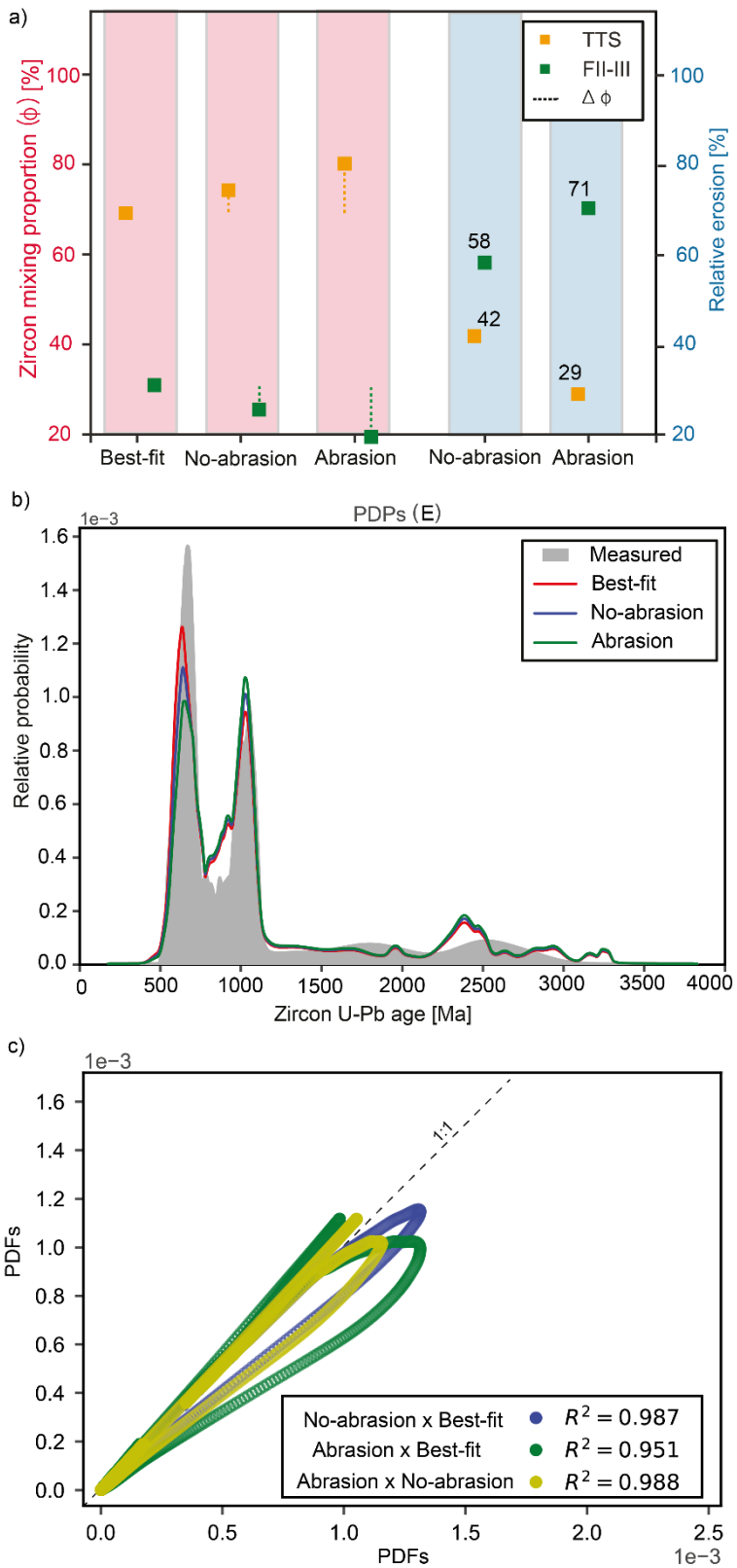


Figure 2.8: Results of the numerical mixing models for the Marsyandi uppermost sampling site (E): resulting U–Pb age distributions (PDPs), relative erosion rates and statistical assessment. (a) Percentage zircon from the different rock units in sand at site E (pink) and predicted relative erosion rates (blue) for

the no–abrasion and abrasion models; dashed lines indicate change with respect to the best–fit approach (see text). (b) PDPs of the measured grains, modelled best–fit, no–abrasion and abrasion models. (c) PDF cross–plots comparing the modelled PDFs (no abrasion and abrasion) to the best–fit PDF (in blue and green) as well as comparing the modelled PDFs among themselves (in yellow).

At the intermediate site (G), the influence of abrasion is mostly visible in the proportions of Tethyan Series and FI: the abrasion model predicts that the Tethyan Series contribute 12 % more zircon at the sampling site than the no–abrasion model (65 instead of 53 %), while the contribution of FI is reduced from 28 to 16 % (Fig. 2.9a). This may be the result of the two units sharing part of their peaks in their age distributions (Fig. 2.2). Interestingly, this change is accommodated by relative erosion rates with an opposite trend, as Tethyan Series rocks are the most erodible and thus release more sand (and zircons) as they are transported further downstream: relative erosion rate of FI increases from 25.6 to 39.3 % while it drops from 40 to 29.3 % for the Tethyan Series. All modelled distributions are statistically indistinguishable from each other (Fig. 2.9b, c).

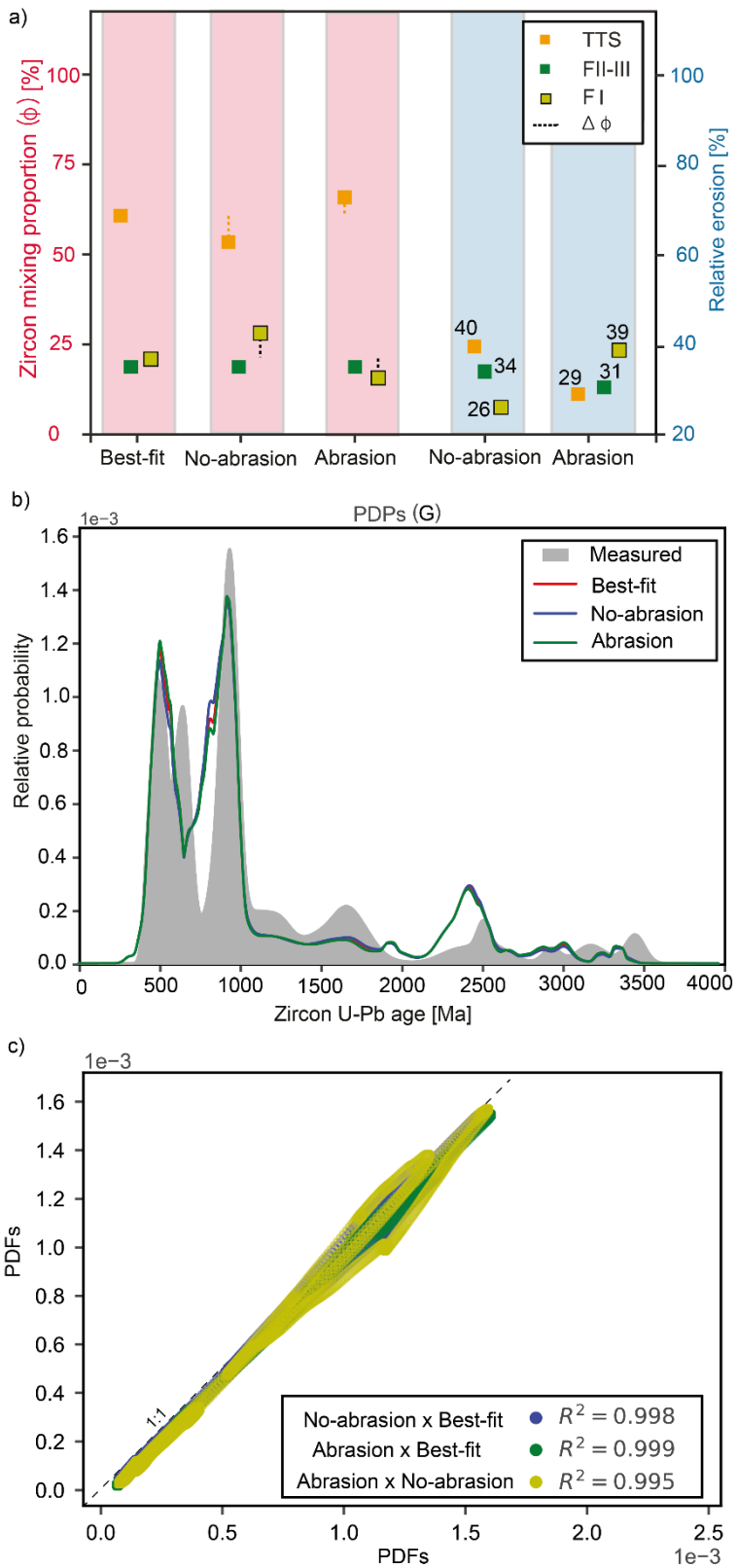


Figure 2.9: Results of the numerical mixing models for the intermediate Marsyandi sampling site (G): their resulting age distributions (PDPs), relative erosion and statistical assessment. (a) Percentage zircon from the different rock units in sand at site G (pink) and predicted relative erosion rates (blue) for the no–

abrasion and abrasion models; dashed lines indicate change with respect to the best–fit approach (see text). (b) PDPs of the measured grains, modelled best–fit, no–abrasion and abrasion models. (c) PDF cross–plots comparing the modelled PDFs (no–abrasion and abrasion) to the best–fit PDF (in blue and green) as well as comparing the modelled PDFs among themselves (in yellow).

At the outlet sampling site (K), the results are not consistent with results from previous sampling sites (Fig. 2.10). Firstly, the best–fit distribution predicts zircon mixing proportions that are significantly different from those derived from the no–abrasion and abrasion models: the mixing models (both abrasion and no–abrasion) predict a much lower contribution from Tethyan Series and Lesser Himalaya (by up to 10 % each) and a much greater contribution from FI (by 15–20 %). This highlights the non–uniqueness of the solutions and the sensitivity to the approach used, in particular when sources have distributions that partly overlap (Fig. 2.2). Secondly, the relative erosion rates predicted for the abrasion and no–abrasion scenarios are very similar, despite the significant differences at the sites upstream: differences in relative erosion rates for each unit do not exceed 2.2 % (Fig. 2.10a) and the distributions produced are nearly identical (Fig. 2.10b, c). In some circumstances, overlap of the distributions and spatial differences in abrasion rates may conspire to compensate for abrasion and erosion effects, leading to a limited influence on the inversion outcomes.

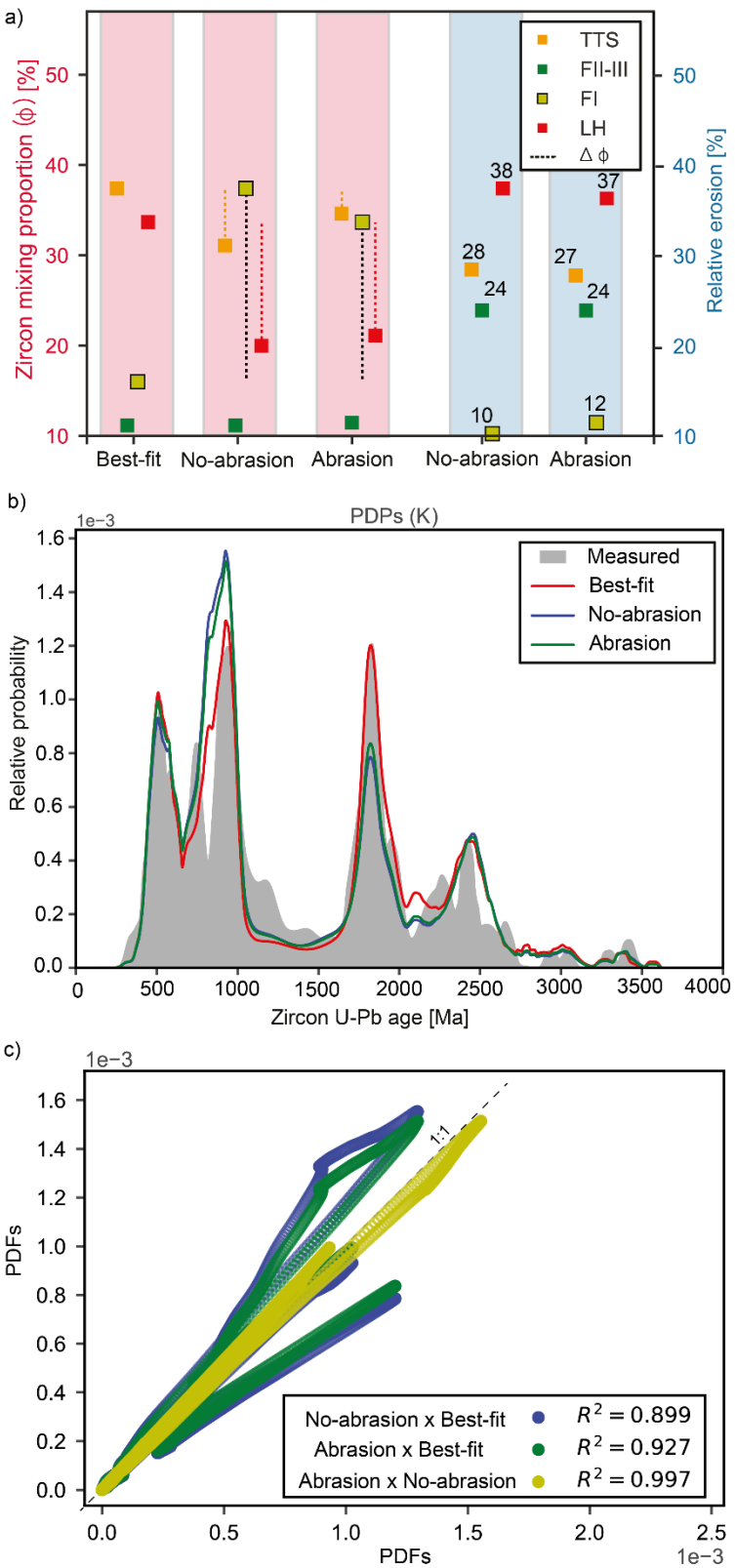


Figure 2.10: Results of the numerical mixing models for the Marsyandi outlet (K): their resulting age distributions (PDPs), relative erosion and statistical assessment. A) Percentage zircon from the different rock units in sand at site K (pink) and predicted relative erosion rates (blue) for the no–abrasion and

abrasion models; dashed lines indicate change with respect to the best–fit approach (see text). B) PDPs of the measured grains, modelled best–fit, no–abrasion and abrasion models. C) PDF cross–plots comparing the modelled PDFs (no–abrasion and abrasion) to the best–fit PDF (in blue and green) as well as comparing the modelled PDFs among themselves (in yellow).

## 2.7. Discussion

### *2.7.1. Abrasion as a distorting factor*

Our numerical simulations using empirically–derived abrasion rates agree with recent research that highlights grain size biasing as one of the factors controlling the mineralogy and, therefore, the grain information of sands transported by rivers (e.g., Aguilar et al., 2014; Codilean et al., 2014; Carretier et al., 2015). The importance of abrasion in distorting grain age distributions is, however, more debatable. Although changes in the zircon mixing proportion can occur in watersheds of homogeneous lithology (e.g, experiment A1) and of diverse abrasion rates (e.g., A4), the resulting age distributions may not appear significantly distorted. Recently, Saylor and Sundell (2016) highlighted the limitations in the current statistical methods to assess changes in PDFs and, earlier, Vermeesch (2012) discussed the low sensitivity of PDPs to changes in zircon proportions. In both cases, there is supporting evidence explaining why numerical changes in the zircon mixing proportions are not necessarily followed by distortions of the age distribution statistics.

However, in watersheds of very different rock strengths (e.g., experiments A2 and A3, and sampling site E in the Marsyandi watershed), the distortions caused by abrasion are unambiguous. These findings highlight that sources of different rock strengths such as quartzite and sandstone found in complex tectonic environments (e.g., pro– and retro–foreland basins) can have their detrital age signatures significantly changed in modern river sands. Moreover, distorted grain age distributions within sediment reaching continental platforms can be preserved in siliciclastic rocks and in the product of their recycling (e.g., metamorphic rocks) (Campbell et al., 2005; Perez and Horton, 2014; Sharman and Johnstone, 2017). Therefore, recognizing these distortions is important to more accurately (un)mix grain age distributions through modelling and inform provenance analysis from sedimentary archives.

The circumstances under which bias from abrasion is expected to be significant are summarised in Fig. 2.11. Even in the absence of contrasts in rock resistance to abrasion, bias will be expected if transport distance is short relative to abrasion rate (Fig. 2.11a, b). As sediment is transported downstream, the relative proportion of remaining gravel (and therefore "trapped" zircon) decreases downstream: in catchments where sediment has been transported over long distances, most of the gravel is turned into sand and most zircons have therefore been released in the sand fraction, limiting bias (Attal and Lavé, 2006, 2009; Dingle et al., 2017). What defines "long" or "short" distances is the abrasion rate (Fig. 2.11b): in a simple model where sediment is constantly supplied along a linear river system and gravel is abraded at a given rate (Attal and Lavé, 2006, 2009), I can calculate the amount of gravel that has been turned into sand at a given distance downstream. For very erodible gravel abrading at 20 %/km, more than 60 % of all gravel that has been supplied to the river has been turned into sand 10 km downstream from the river origin: I can therefore expect limited bias after distances in the order of 10–20 km. For gravel abrading at 2 %/km, this figure is 10 %: a significant amount of zircon remains "trapped" within gravel. The result is shown in Fig. 2.1b: at a point 20 km downstream of a river system made of half a lithology 1 and half a lithology 2, I find that 72 % of the sand sampled comes from the lithology exposed in the top half of the catchment due to greater transport distance, despite the fact that the river has been supplied the same amount of sediment from both units and that gravel from both units is abraded at the same rate of 2 %/km. For lithologies abrading at such rate, I expect limited bias after transport distance of the order of 100–200 km (Fig. 2.11a, b; Attal and Lavé, 2006, 2009; Dingle et al., 2017). Finally, gravel from resistant rocks (abrasion rate $\leq$ 0.2 %/km, e.g. quartzite, volcanics, mica–poor gneiss or granite, see Attal and Lavé, 2009) will persist for distances in excess of 1000 km (Fig. 2.11b): a significant amount of zircon from these units is therefore likely to remain trapped in gravel even in very large, continental–scale catchments, leading to their underrepresentation in sand samples. This is why strong contrasts in rock resistance to erosion and the presence of hard rocks will lead to bias from abrasion, irrespective of catchment size (Fig. 2.11a).

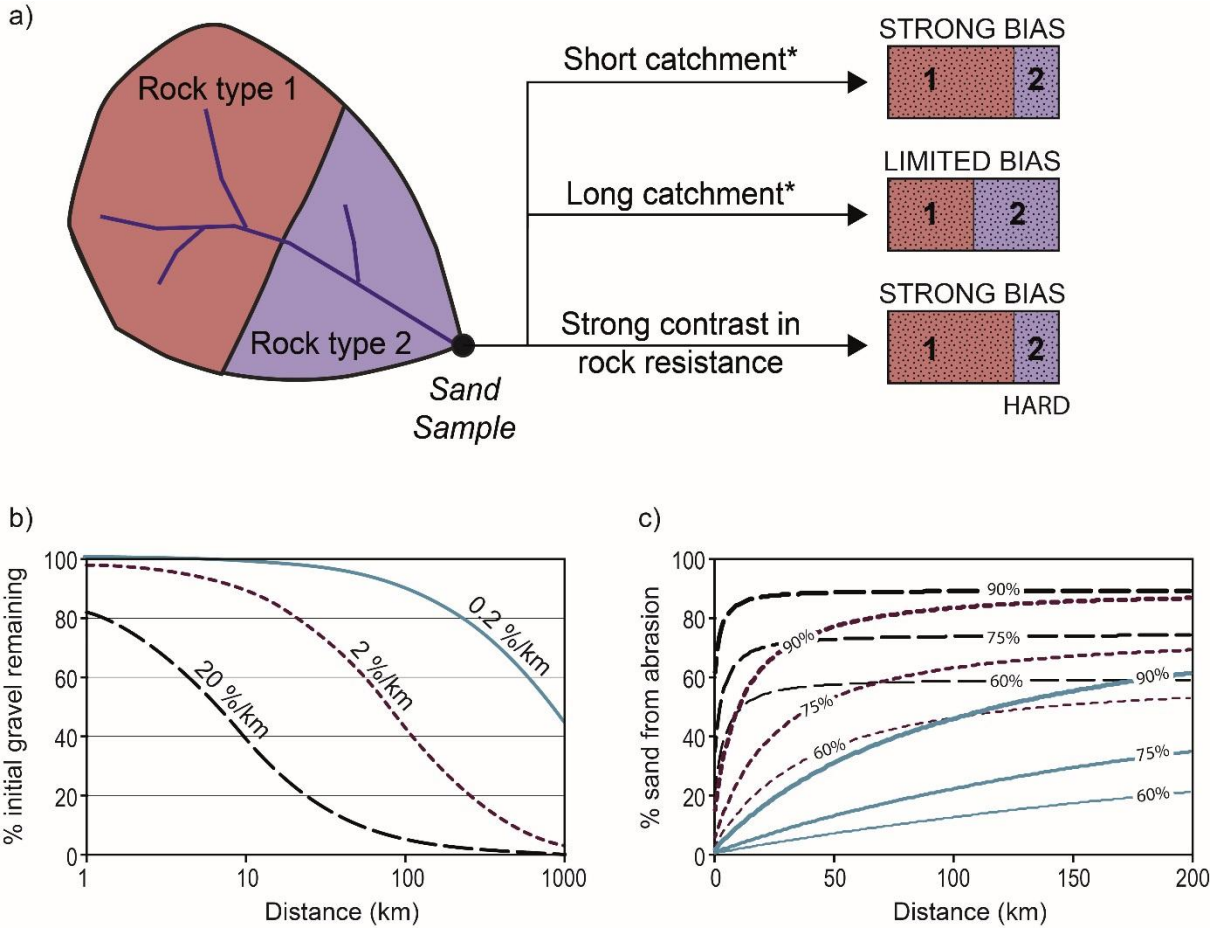


Figure 2.11: (a) Schematic diagram summarising the circumstances under which bias from abrasion can be expected in a sand sample. Bias is expected to decrease with increasing length of the river system, as the relative amount of sand (and therefore zircons or any other tracer minerals) retained in gravel decreases downstream. How quickly sand is released from gravel through abrasion is a function of the abrasion rate, so "short" and "long" have relative meanings for a catchment (*, see (b)). Strong contrast in rock resistance to abrasion will enhance bias, as gravel from hard lithologies will persist for long distances, therefore limiting the release of zircon or any other tracer minerals from this lithology (in the figure, rock type 2 is harder, leading to underrepresentation in sand sample). (b) Downstream conversion from gravel to sand as a function of abrasion rate (note log scale on x–axis). These results are based on a simple linear river model from Attal and Lavé's (2006, 2009) (see also Fig. 1b): a given amount of sediment is supplied to the system every km and gravel is abraded according to Sternberg's law. At a distance of 10 km downstream, 61 % of all gravel supplied to the system has been turned into sand for a mass loss of 20 %/km (39 % of gravel remaining). This figure is 10 % and 1 % for a mass loss of 2 and 0.2 %/km, respectively. At a distance of 100 km, nearly all gravel supplied to the system has been turned into sand for a mass loss of 20 %/km (4 % of gravel remaining). This figure is 58 % and 9 % for a mass loss of 2 and 0.2 %/km, respectively. Gravel from resistant lithologies can persist over hundreds of km. (c) Influence of abrasion rate and initial gravel fraction on relative contribution of abrasion to sand. Key is as in (b): abrasion rate of 0.2, 2 and 20 %/km are shown by solid (light blue), short dash (dark brown) and long dash (black) lines, respectively. % value on curves indicates initial gravel fraction from hillslopes. Curves show the relative contribution of sand from abrasion in a sand sample taken at a given distance downstream.

### *2.7.2. Abrasion versus other factors*

According to our simulations, abrasion is one of the factors with the lowest capability of distorting the detrital age distribution of sands among all currently considered controlling factors. Based on the Marsyandi's natural datasets, all considered factors are able to reproduce the distortion caused by abrasion in the age distribution, which may explain why abrasion has long been stated as a factor of minor influence in detrital geochronology (e.g., Malusà et al., 2013). Unlike abrasion, the other parameters tested have a linear relationship with the mixing proportions: for example, a doubling of erosion rate or fertility from one unit will lead to a doubling of the zircon contribution from this unit in a mixed sand sample further downstream. This is in stark contrast with our result showing that the effect of having Tethyan Series rocks abraded at 31 %/km while the other lithologies are abraded at 0.15 %/km can be replicated by having the Tethyan Series' erosion rate, fertility or initial sand supply (the converse of gravel supply in our study) around three times greater than that of the other units (Table S5 and S6). It is important to note, however, that this number is strongly controlled by the initial gravel (or sand) supply: in our reference scenarios, the initial sand supply is set to 25 % for all units. As a result, total abrasion of Tethyan Series gravel into sand (due to an extremely high abrasion rate) will lead to an extra 75 % of sand at the outlet, that is, a quadrupling of the amount of sand sourced from the Tethyan Series (compared to a scenario with no abrasion). This would lead to zircons from the Tethyan Series being four times more abundant in our mixed sample, if gravel from other lithologies were not abraded. I found Tethyan Series zircons around thrice more abundant in our scenario, due to gravel from other lithologies being abraded. The initial gravel fraction therefore puts an upper limit on the amount of distortion that can be generated through abrasion when strong differences in abrasion rates exist. Initial gravel supply of 90% could potentially generate abrasion–driven differences in mixing proportions of up to an order of magnitude, as discussed below.

Zircon fertility is a highly variable parameter, with some units potentially being devoid of zircon and therefore being invisible in subsequent mineral selective dating. In our simulations, zircon fertility of the source units has the largest control on grain age distortion. Recent research

on terrains of varied zircon fertility suggests that fertility is the main driver of natural bias in detrital geochronology, and that constraining this bias is an essential step in improving the reliability of dating techniques(Moecher and Samson, 2006; Glotzbach et al., 2017).

In our study, I vary hillslope gravel supply between 60 and 90 %, so sand supply varies within a factor of ~4, between 10 and 40 %. Whereas sources of sediment may have gravel supplies beyond these bounds (e.g., glacial sediment can have up to 70 % of its volume made of particles finer than 1 mm), I believe that this range is representative of most sediment sources in active mountain ranges (e.g., Attal and Lavé, 2006). Confirming this point, Casagli et al. (2003) measured grain size for 42 landslide dams in the Northern Apennines, Italy, and found that ~90 % of the studied deposits had a "gravel" fraction (> 2 mm) making up between 60 and 90 % of their volume. The lower potential variability in gravel supply compared to fertility limits the potential bias created by variations in this parameter. In addition, these variations will be irrelevant if the source units are abraded rapidly and/or if transport distance to the sampling point is long, as in these cases most of the gravel will have been turned into sand by the time it reaches the sampling point (Dingle et al., 2017). It is important however to recognize gravel supply as a potential source of bias for catchments with strong contrasts in gravel abrasion rates and/or short catchments, as illustrated in the following experiments (Fig. 2.11c).

Here, I use again the simple linear model of sediment supply and abrasion (Attal and Lavé, 2006, 2009) to calculate the amount of sand coming from the abrasion of gravel as a function of distance downstream, initial gravel supply and abrasion rate (Fig. 2.11c). Initial gravel supply controls the maximum amount of sand that can be released by abrasion (and therefore create bias), whereas abrasion rate dictates how quickly this sand is produced. If the initial sand supply (the converse of gravel supply) is low, then most sand will come from abrasion, leading to greater potential for bias. If the initial sand supply is high, then most of the sand in the river will originate from the source rather than from abrasion, at least in the upper part of the catchment (short transport distance = low amount of zircon released by abrasion); differences in relative zircon proportions from different lithologies will therefore more likely reflect differences in initial sand supply between the lithologies. I consider a point 50 km downstream from the river origin (Fig. 2.11c): if the lithologies exposed in the catchment are abrading at 20 %/km, then most of the gravel (> 90 %, see Fig. 2.11b) will have been turned into sand so there will be no

bias from abrasion, whatever the initial gravel fraction. If the lithologies exposed in the catchment are abrading at 0.2 %/km, then most of the sand will have originated from the initial supply (e.g., > 90 % of the sand if the initial gravel supply is 60 %, Fig. 2.11c); in this case, difference in relative zircon proportions will reflect differences in initial gravel supply (e.g., if one lithology has an initial 40 % sand fraction and the other 10 %, then there will be four times more sand from the former in the mixed sample, all else equal). The trade–offs between initial gravel supply and abrasion rate are not entirely intuitive and certainly require further work; however, the model highlights again the strong potential for bias by abrasion in the presence of highly resistant rocks.

### *2.7.2. Abrasion and erosion in the Marsyandi region*

Inverse modelling of sediment grain age distributions in the Marsyandi River using our mixing models reveals that the estimated relative erosion rates are highly sensitive to abrasion, despite the amount of grain age distortion not necessarily being statistically significant. For the sampling site E (upstream), calculated erosion rates are in rough agreement with those estimated by other studies (e.g., Burbank et al., 2003; Pratt–Sitaula et al., 2004; Garzanti et al., 2007; Gabet et al., 2008). For instance, Garzanti et al. (2007) found relative erosion rates of 22.5 % for Tethyan Series and 77.5 % for Formation II–III, against 29 % for Tethyan Series and 71 % for Formation II–III from our abrasion model (Fig. 2.8). The no–abrasion model yields distinct relative erosion rates, with 42 % and 58 % for the Tethyan Series and Formation II–III, respectively.

At sampling site G (intermediate), our relative erosion rates are again in good agreement with published research which tends to show a downstream increase in erosion rates (Fig. 2.9). For instance, when converted to relative erosion, Garzanti et al. (2007) found relative erosion rates of 10 %, 34 % and 56 %, while our abrasion model suggests 29 %, 32 % and 39 % for the Tethyan Series, Formation II–III and Formation I, respectively. The relative erosion rates estimated by the no–abrasion model suggest an upstream increase in relative erosion rates, with rates varying from 26 % (Formation I) to 40 % (Tethyan Series). Modern erosion rates in the Himalaya suggest a spatial correlation between precipitation gradients and erosion that is enhanced by the tectonic

uplift of the MCT hanging–wall (Hodges et al., 2004; Deal et al., 2017; Olen et al., 2015). Our modelling suggests that abrasion is also important as the no–abrasion model predicts different trends.

At the Marsyandi outlet (K), differences in relative erosion rates for each unit do not exceed 2.2 % and the distributions produced by the abrasion and no–abrasion models are nearly identical (Fig. 2.10). The abrasion model predicts relative erosion rates ~2 % greater for Formation I, but the difference is too small to be attributed it to any specific factor. Such a result would be expected if all gravel had been turned into sand, as in this case the mixing proportions would mimic a no–abrasion scenario. The transport distance over which around 90 % of the initial gravel is turned into sand by abrasion can be calculated as $250/\alpha$, where $\alpha$ is the abrasion rate in % mass loss / km (Equation (12)) (Attal and Lavé, 2006; Dingle et al., 2017). Based on the abrasion rates used in this study (Table 2.1), this distance is 58, 625, 179 and 27 km for the Tethyan Series, Formation II–III, Formation I and Lesser Himalaya, respectively. Tethyan Series gravels will have travelled at least 130 km (Fig. 2.2) so very few of them would have survived to the outlet (site K). Formation I sediment will have travelled between 70 and 120 km so I expect no more than a quarter of it to have reached site K as gravel. Lesser Himalaya units are exposed closest to the outlet but their high abrasion rate (9.4 %/km) means that a large part of the sediment derived from it will also reach site K as sand (the distance between MCT and site K is 80 km, see Fig. 2.2). However, transport distances for the resistant Formation II–III range between 100 and 140 km, meaning that between 40 and 50 % of the sediment sourced from this unit should reach site K as gravel. This should lead to a strong underrepresentation of the Formation II–III in the mixed sand sample and therefore greater calculated erosion rates to counterbalance this effect, which I do not observe. I hypothesize that this is a coincidence potentially resulting from overlapping source age distributions (e.g., shared peak at ~0.5 Ga in Tethyan Series and Formation II–III, see Fig. 2.2): in some circumstances, this overlap combined with spatial differences in abrasion rates may compensate for abrasion and erosion effects, leading to a limited influence on the inversion outcomes. In general however, I expect the effect of abrasion on mixing proportions to decrease with increasing transport distance in the absence of very strong lithologies.

Overall, with the exception of sampling site K, our predictions of relative erosion rates using an abrasion model are better correlated with documented rates and spatial variability found by

other studies. Pebble abrasion, based on lithology, can therefore be an important factor to consider when inversely solving for modern erosion rates.

### *2.7.3. Methodological uncertainties and limitations*

Inverse modelling to predict erosion rates is known to be difficult and subject to model specifications as well as uncertainties in grain age distributions. There is no consensus on how to choose statistical analyses to (un)mixing age distributions (Saylor and Sundell, 2016). In our case, I worked with area mismatch (*M*) to be able to compare our results directly with those from Amidon et al. (2005a). However, this metric is known to have limitations when used to unravel grain age distributions (Sundelland Saylor, 2017) and may not be the most sensitive method to identify the influence of abrasion rates in detrital grain age signatures. Furthermore, working with unique solutions of mixing proportions can be problematic (Saylor and Sundell, 2016; Sundelland Saylor, 2017; Sharman and Johnstone, 2017), since small variations in mixing proportions may produce statistically similar (and fitting) distributions but significantly impact the results of inverse erosion modelling (e.g., relative erosion rates). These issues can be dramatically enhanced when smoothing the age distributions (see Supporting Information Tables S3 and S4). In the natural age distributions (samples E, G and K), the smoothing procedure produces statistically significant changes in two samples (TTS and mixed sample, K). Additionally, by reducing age variability, it favours convergence when finding mixing proportions from source units (Amidon et al., 2005a). These differences in the sensitivity of the (un)mixing techniques can obscure detectable variations in the age distributions caused by pebble abrasion.

Another important consideration is the effect of intrinsic characteristics of age distributions (i.e., the ages and their relative probability) in statistical analyses. Our experiments with different age peaks show that the ability of statistical metrics to identify changes is affected by the spread, overlap and shape of the peaks. Thus, there is an intrinsic bias in any age distribution under investigation. Future research on this issue could bring significant contribution to minimize this bias in a quantitative way. It also reinforces the non–uniqueness of solutions to (un)mixing age distributions as highlighted by several authors (e.g., Sundell and Saylor, 2017).

It is important to consider the implications of some of our assumptions, in particular regarding the transfer of zircon from gravel to sand. In our model, I assume that all products of abrasion are in the sand fraction, and that the zircons are homogenously distributed in this sand. In reality, the fraction finer than 2 mm is far more heterogeneous than assumed here, both in the initial sediment supply from the hillslope to the river and in the fluvial sediment transported (Attal and Lavé, 2006, Attal et al., 2015; Riebe et al., 2015, Lukens et al., 2016, Sklar et al., 2017). In addition, abrasion will also produce fragments and particles in a wide range of sizes, leading to potentially different mineral compositions depending on the fraction sampled. For example, the abrasion of granite tends to produce sand, whereas abrasion of limestone will produce more silt and clay (Bradley, 1970; Attal and Lavé, 2009). However, given that no constraints about the grain size of abrasion products in the Marsyandi watershed exist, I cannot estimate quantitatively how distorted our own analyses can be due to this process. I must also mention that an important covariation exists between grain size of abrasion products, abrasion rates and hillslope grain size supply (Attal and Lavé, 2006). Less resistant bedrock types are more likely to have higher weathering rates and to produce regolith with higher content of fine material (i.e., sand, silt and clay) than hard rock types, leading to lower initial gravel supply to the river channels and consequently smaller amount of gravel available for abrasion. The covariation of hillslope grain size, grain size of abrasion products and abrasion rate associated with a given rock type can produce unusual effects, as shown in Section 4.2, and requires further attention. Because most detrital studies focus on a given sediment fraction (usually sand), it is becoming increasingly important to understand the production and evolution of the fine fraction of the sediment spectrum, from the hillslopes to the sedimentary basin, as a result of chemical and physical processes (Sklar et al., 2017); including abrasion during fluvial transport.

Hydrodynamic fractionation of grain sizes, whereby larger sediment grains travel slower than smaller ones, operates on a range of scales (bedload versus suspended load, as well as differences within bedload and within suspended load) in the majority of natural environments (e.g., Miller et al., 2014). Recent findings suggest potential bias from downstream hydraulic sorting in cases where a relationship between zircon grain age and size exists, e.g., larger grains are younger and smaller ones are older (Yang et al., 2012). The influence of grain density is also important, given that relative enrichment in gravel bars, river pools and other common sampling sites for detrital

studies can bias denser minerals such as zircon. However, because our work focuses only on one type of mineral (zircon) and uses the relative proportions of zircons from different units, it seems reasonable to assume that zircons from all units will be affected in a similar way and that the outcomes of our work would not be significantly affected by the processes mentioned above, except in a case where zircons from different units have different sizes, which I cannot assess.

Finally, although I applied the same procedure adopted by Amidon et al. (2005a) to directly compare our results with theirs and assess the influence of abrasion, our no–abrasion model produces mixing proportions and relative erosion rates that are slightly different from their no–abrasion model results. Our predictions are different by 2 % and 4 % in the mixing proportions and erosion rates estimated for site E. At the sampling site G, our predictions differ by up to 2 % and 5 % in the mixing proportion and erosion rates, respectively. At the outlet (K), these differences become higher, reaching up to 6 % in the mixing proportion and 5 % in the relative erosion rates. A possible explanation for these differences is small changes in the quality of the Digital Elevation Model and/or in the minimisation procedures adopted. In all cases, however, our no–abrasion model mirrors the same pattern of zircon mixing proportion and erosion estimated by the no–abrasion model of Amidon et al. (2005a).

## 2.8. Conclusion

Our numerical simulations provide evidence of the role of pebble abrasion in distorting detrital grain age information from modern sands. This distortion is significant in settings with large contrasts in rock strength or short catchments. In long catchments with no resistant lithologies, most of the gravel initially supplied from the hillslopes will have been turned into sand by the time it reaches the outlet, leading to the release of most detrital grains and limited bias potential from abrasion. Conversely, gravel from resistant lithologies (e.g., quartzite, volcanics, mica–poor granite or gneiss) can persist for transport distances of hundreds of km, locking detrital minerals within them and increasing the bias potential from abrasion: abrasion will likely lead to the underrepresentation of units characterised by such resistant rock in a sand sample. I find however that pebble abrasion is the factor with the lowest distortion capability

when compared with other well–known factors that might bias the preserved sedimentary record (i.e., relative erosion rates, zircon fertility and hillslope gravel supply). Abrasion has a non–linear impact on the mixing proportion of river sand, and this impact is modulated by the initial gravel supply: whereas a doubling a zircon fertility or erosion rate in a unit will lead to a doubling of the zircon contribution from this unit in a mixed sample, the impact of doubling the abrasion rate may be much lower. I find, in one of our scenarios, that the equivalent effect of havingrocks from one unit abraded 200 times faster than rocks from other units can be replicated by tripling the fertility or erosion rate of this unit.

The relative erosion rates of source units estimated by inverse modelling are impacted by abrasion, despite minimal (statistically insignificant) variations in the grain age distributions. In the Marsyandi catchment, our abrasion model predicts erosion rates that are closer to those found by the majority of previous studies, compared to a no–abrasion model. These results suggest that even when statistics are not able to identify significant changes in the age distribution of samples, the erosion rates deconvolved from them can still be significantly affected. Therefore, assessing the influence of abrasion on the evolution of the composition of river sediment is essential if I are to accurately estimate erosion rates from inverse modelling, using detrital methods based on a given sediment fraction (e.g., sand), in particular when the source units feature large variations in rock strength.

I identify research into the trade–offs between initial gravel supply and abrasion rates and into the size distribution of the products of abrasion for rocks of different lithologies as priorities to develop models that would better constrain the influence of abrasion and other factors on biases in detrital studies.

# Chapter 3 –Is it static or moving? Assessing drainage network and divide stability of an island in transience (Corsica, Mediterranean Sea)

Key points:

- I find that the main drainage divide of Corsica is moving in different directions in the north (eastward) and south (westward).
- Statistical analyses suggest topography is more sensitive to contrasts in rock strength and structural boundaries than to sea level variations and long–term exhumation rates.
- The metrics of knickpoints and divide stability indicate that Corsica is currently in transience.

**Key–words:** $\chi$ river profiles; Gilbert metrics; transient landscape; grain size distribution; river steepness

## Abstract

Corsica, an island in the western Mediterranean Sea, is a relevant setting to evaluate the effect of tectonic and climatic forcing on landscape evolution. It was rapidly exhumed up to late Miocene following accretion of an Alpine terrain to Hercynian Corsica. It is now believed to be at, or approaching, an exhumational, and, potentially, a topographic steady–state condition. However, published geological evidence of short–lived pulses enhancing incision rates contrasts with the very low long–term erosion rates measured using cosmogenic nuclides. In this work, I investigate drainage networks and the main regional drainage divide of Corsica by applying two tools of divide stability named χ and 'Gilbert' metrics. I complement the study of the divide with an assessment of the river profiles of Corsica by quantifying river steepness and locating knickpoints. Because the steepness of a river can also be affected by the grain size of the sediment it transports, I also present new grain size information for sediment transported by rivers across the island. The χ and 'Gilbert' results suggest that the northern section of the drainage divide is currently moving to the east, while the southern section is moving to the opposite direction (i.e., westward). These patterns suggest that Corsica is in a transient state, where the current direction of drainage divide motion mirrors the predicted trend required to reach a horizontal steady–state. River steepness, sediment grain size and knickpoints in the drainage network highlight the influence of both rock type and structural units as major controls on the modern river profiles. The drainage network over Hercynian Corsica has a higher density of knickpoints with greater values of slope, relief, length and magnitude (i.e., the elevation difference between the lip and the average steepness). These are followed by the Alpine Corsica with intermediate density and values of knickpoints' metrics, and, lastly, by the Miocene sedimentary plains, where knickpoints are rare. The range of grain size in modern gravel bars and knickpoints' metrics in Corsica reflects a similar pattern, with Hercynian rock types having larger ranges than those at the Alpine Corsica. Importantly, the spatial distribution of knickpoints, grain size coarsening and river steepness peaks show a preferential location around the boundaries of structural units (e.g., faulting zones). I have not identified any difference between the knickpoint metrics in the thermochonometric age domains compiled from other workers. These findings suggest that the current topographic state of the drainage network and divide in Corsica is

primarily controlled by rock strength and the structural boundaries than the long–term (and long–scale) exhumation patterns that last until the Pliocene.

## 3.1. Introduction

Understanding the topographic response of landscapes to changes in controlling factors such as sediment grain size, rock strength, uplift and climate is fundamental to unravel the dynamics of landscape evolution (Allen and Breshears, 1998; Forte et al., 2016; Snyder et al., 2000; Whipple and Tucker, 1999; Yanites et al., 2017). Under conditions where the controlling factors are invariant in time, steady erosion rates are the natural attractor of the landscape: topography is expected to evolve towards achieving steady–state, whereby the erosion rate at every point in the landscape matches uplift rate, so that the topography becomes time–invariant (e.g., Willett and Brandon, 2002; Whipple, 2001). Any perturbation, e.g., a temporal or spatial change in one of the controlling factors, will lead to disequilibrium between uplift and erosion and therefore to a topographic response: a landscape is considered to be in a transient state when readjusting to a new set of conditions (e.g., Ouimet et al., 2007; Prince et al., 2011; Willenbring et al., 2013). In terrestrial landscapes, rivers tend to be the drivers of transience: rivers can aggrade or incise into bedrock, promoting changes in channel slope and propagating signals upstream in the form of knickpoints reshaping the morphology of tributaries and hillslopes (see Mudd, 2017). The uppermost terminations of river profiles, the channel heads, are the last part of the fluvial network to respond to the changes downstream (i.e., a bottom-up process); delays in the response of channel heads in adjacent basins are responsible for plan–view adjustments of the river network which manifest via drainage divide migration (Whipple et al., 2017 a, b; Bonnet, 2009). On the other hand, channel heads may be the first elements of the river network to respond to changes in precipitation (e.g., climate change), leading to a cascade of adjustments downstream (Mudd, 2017). Recent studies (e.g., Pelletier, 2004) have demonstrated that this phenomenon of drainage reorganisation is more persistent and widespread than originally considered in landscape evolution models (e.g., those used by Howard (1994) and Willett et al. (2001)), with many highlighting that transient signals may be detected by assessing the stability of drainage divides and hillslopes (e.g., Giachetta et al., 2014; Willett et al., 2014).

Determining a landscape's topographic state has been done mainly by comparing morphometric parameters of river profiles and hillslopes, as well as constraining changes in erosion, exhumation and uplift rates over short ($10^4$ to $10^5$ years) and long ($10^6$ to $10^7$ years) term (Finnegan et al., 2014; Mudd, 2017; Whittaker et al., 2007). Among those morphometric parameters, river steepness has been used as a proxy for inferring spatial changes in rock uplift and erodibility (a coefficient that encapsulates climate, rock strength and sediment grain size) (e.g., Cyr et al., 2010; Vanacker et al., 2015). In particular, the identification of knickpoints has been a key element to infer temporal and spatial changes in erosion rates in response to varying environmental conditions (e.g., erodibility, structural boundaries, and uplift) (see Frankel et al., 2007; Brocard et al., 2016).

To assess drainage divide stability or, conversely, detect migration, two recent morphometric tools have been proposed. One method is based on a transformation of channel length by integrating drainage area, producing the variable $\chi$ (see Willett et al., 2014); this variable has a dimension of length and increases upstream. According to the theory, two rivers at topographic steady–state sharing a common drainage divide should have the same value of $\chi$ at the divide. Conversely, $\chi$–anomalies suggest disequilibrium, with the divide expected to migrate towards the basins with the highest $\chi$ values at the divide. Although numerical simulations and empirical data support that $\chi$–anomalies can correctly predict drainage divide migration (e.g., correlation between rivers predicted to expand and occurrence of higher erosion rates), some studies provide evidence that the choice of base–level for the integration, as well as spatial variations in erodibility, can significantly affect the $\chi$ values of rivers at divides and that $\chi$–anomalies may not necessarily be diagnostic of drainage instability (e.g., Forte and Whipple, 2018; Whipple et al., 2017 a, b).

As a means of constraining actual drainage divide stability rather than a potential migration direction, it has been proposed to work with morphometric parameters such as upstream gradient, relief and elevation at the channel heads; these parameters are expected to vary with short–term erosion rates ($10^3$–$10^5$ year) and would therefore be indicative of disequilibrium, as suggested by Gilbert (1877) (Whipple et al., 2017 b). Recent work (e.g., Forte and Whipple, 2018) suggests that the 'Gilbert metrics' are more sensitive to drainage divide instability than $\chi$–anomalies. They are also independent of assumptions that potentially invalidate the $\chi$–anomalies approach (i.e.,

chosen base–level and uniform conditions in uplift, rock erodibility and climate) and thus provide an independent assessment of divide stability. While the 'Gilbert metrics' represent a top–down assessment that reflects environmental conditions acting on the hillslopes of the drainage divide, the $\chi$ represents a bottom–up assessment that reflects spatial changes in rock strength, climate, and tectonics over a catchment.

In this work, I apply these new quantitative frameworks to evaluate the topographic state of Corsica, and assess whether both methods provide compatible results. Corsica, an island in the western Mediterranean Sea, is an excellent setting to evaluate the effect of tectonic and climatic forcing on landscape evolution. It was rapidly exhumed up to late Miocene times (~ 14 Ma) following accretion of an Alpine terrain to Hercynian Corsica (see Fellin et al., 2005a). It is now believed to be at, or approaching, an exhumational, and, potentially, a topographic steady–state condition given its very low long term ($^{10}$Be) erosion rates (e.g., Molliex et al., 2017). Following accretion, there is evidence of drainage reorganisation in the north such as Miocene basins now disconnected from their sources, indicative of drainage capture (Cavazza et al., 2007; Fellin et al., 2005b). Additional evidence testifying to a recent (post–14 Ma) transient history of the Corsican landscape include: large cut–and–fill Quaternary river terraces (Sømme et al., 2011); order of magnitude differences between long–term exhumation rates ($10^6$ to $10^7$ years) and short–term erosion rates ($10^4$ to $10^5$ years) (Fellin et al., 2005b; Molliex et al., 2017); marine records of sea–level variations during Quaternary and Messinian times (Pichevin et al., 2003); and extinct Würmian glaciers over an asymmetric drainage divide (Fig. 3.1) with variable erosion rates (Kuhlemann et al., 2009).

I investigate drainage networks and the main N–S regional drainage divide of Corsica. In order to assess whether the drainage divide is static (i.e., in a topographic steady–state) or moving (i.e., in a topographic transience), I perform both $\chi$ and 'Gilbert' metric analyses. I complement the study of the divide with an assessment of the river profiles of Corsica. To test the hypothesis of transience, I quantify river steepness and locate knickpoints which I then compare with geological databases in order to distinguish between static knickpoints (e.g., related to change on lithology or structure) and migrating knickpoints (i.e., not related to any lithological boundary or structure and therefore likely to represent a transient signal). Because the steepness of a river can also be affected by the grain size of the sediment it transports (Sklar and Dietrich, 1998, 2004), I

also present new grain size information for sediment transported by rivers across the island. These data are incorporated within the topographic analysis to constrain the influence of a range of drivers, including rock strength, on the dynamics of the Corsican landscape.

## 3.2. Study area

### *3.2.1. Major lithological units*

Corsica consists of two main geological units termed Hercynian (or Variscan) and Alpine Corsica (Fig. 3.1). Hercynian Corsica comprises three geological units that cover the majority of the island's onshore area (Rossi et al., 1994 a, b). It includes non–metamorphosed Carboniferous to Early Permian granitoids, Permian volcanic rocks and gneiss (Unit 1). The basement rocks are partly overlaid by continental and marine sedimentary rocks (Triassic to Paleocene) and by Eocene foredeep strata (nummulite–bearing flysch) that are strongly deformed (Unit 2) (Fig. 3.1). In the north, closer to Alpine Corsica, Hercynian rhyolites and granitoids are metamorphosed into orthogneiss bearing blue amphibole (Unit 3: Tenda massif units).

In Alpine Corsica, the Schistes Lustrés (literally, "shiny schists") formation occurs as a thrusted nappe on top of the Eocene foredeep strata and the metamorphosed Hercynian basement (i.e., over Tenda massif units). The Schistes Lustrés is composed of metamorphosed oceanic rocks such as gabbros, peridodites, basalts and slices of continental basement that can be subdivided in three main units. The lowermost unit is made of marble, calcschist, schist, basalt and gabbro metamorphosed under high–pressure low–temperature conditions and has been referred as the Castagniccia unit (Unit 4). The intermediate unit, named Lower oceanic unit, is composed of basalt, gabbro and peridotite with slices of gneiss (Unit 5). On the top of the Schistes Lustrés formation, an upper oceanic unit (Unit 6) encapsulates several minor units (Pigno, Gratera, Centuri, Inzeca, Vecchio, Linguizzetta, Santa Lucia and Balagne units). The Santa Lucia and Pigno units are continental slices with low to medium pressure metamorphism. The Balagne unit is a non–metamorphosed oceanic unit composed of serpentinite, gabbro, pillow lava and oceanic flysch material.

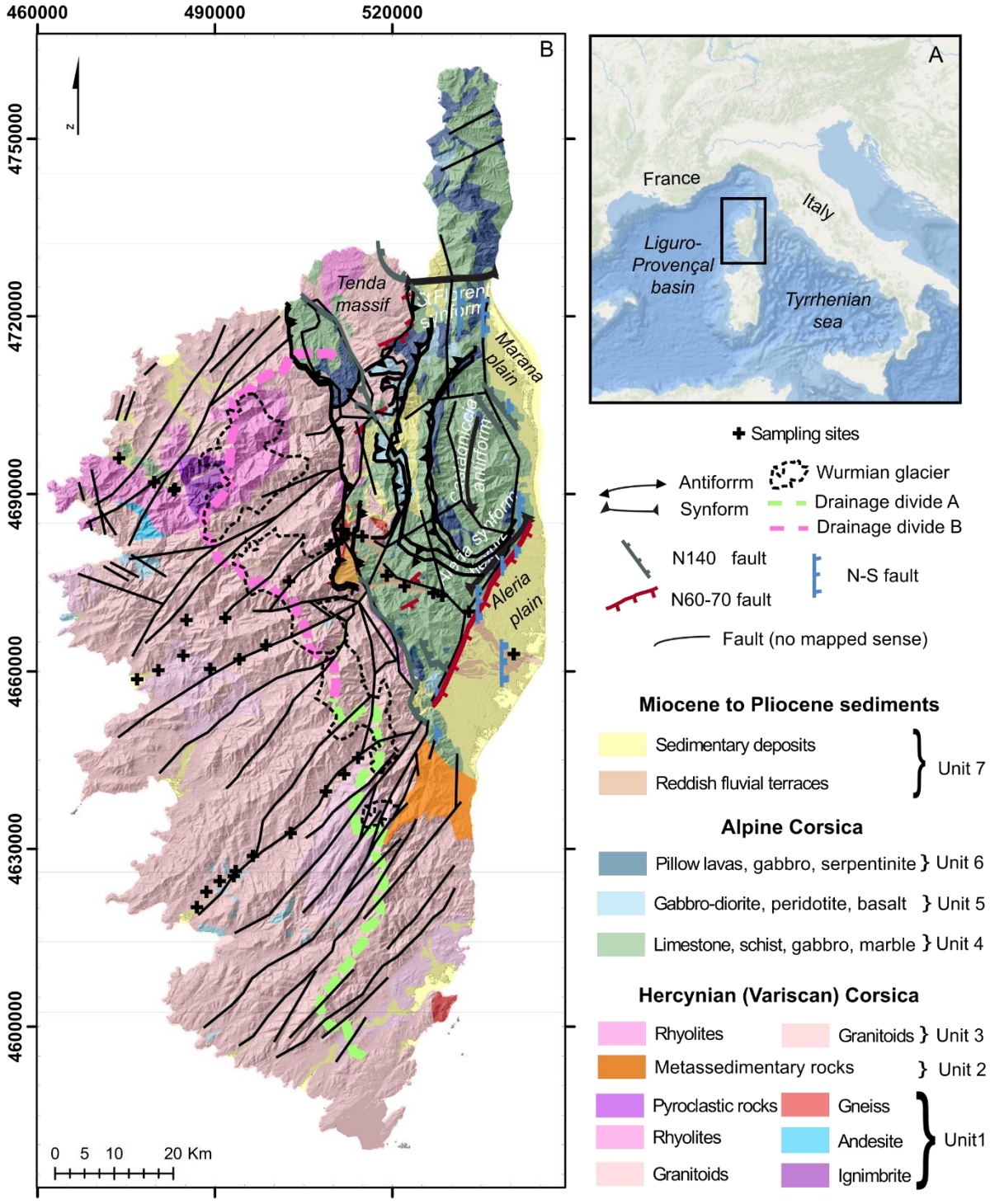


Figure 3.1: Geological map of Corsica, which includes mapped Alpine thrusts and extensional faults related to the opening of the Tyrrhenian and Liguro–Provençal basins, as well as the sampled gravel bars sites analysed in this work. The sub–division of the regional drainage divide in two sections (A and B) was done after analysing the χ and 'Gilbert' metrics (see results). A) Location of Corsica in the Western

Mediterranean Sea. B) Geological and structural units of Corsica. The geological units are adapted from Rossi et al. (1994 a, b) and the tectonic units are from Gueydan et al. (2017). The regional drainage divide of Corsica was segmented in this work between the southern (A) and northern (B) sections to ease morphometric analysis. The extension of the Würmian glaciers in Corsica follows the mapping of Kuhlemann et al. (2005b).

Malaveille et al. (1998) have proposed an evolutionary model of Alpine Corsica, which intra–oceanic subduction (after the Jurassic) was succeeded by subduction of the Hercynian Corsica units under an oceanic crust (Adriatic plate). During this continental–oceanic subduction, previously buried Hercynian and Alpine Corsica units, now high–pressure–low temperature (HP–LT) rocks (e.g., ophiolite and Schistes Lustrés), uplifted due to buoyancy of the plates. During exhumation, part of the Western Corsica units (e.g., allochthonous HP–LT gneiss) overthrust the older (autochthonous) Hercynian basement, while creating normal faulting along the Alpine contact. Lastly, in the Eocene, a closure of oceanic crust (Ligurian–Provençal basin) caused an orogenic phase that overthrust ophiollitic nappes (Schistes Lustrés units) over the previously uplifted and eroded Western Corsica units.

The most recent onshore siliciclastic sedimentation basins (Miocene) are found over the Schistes Lustrés formation to the east (Aleria and Marana), centre (Francardo) and north of Corsica (Saint–Florent) (Unit 7) (Fig. 3.1). The Francardo and Saint–Florent basins have depositional ages ranging from Burdigalian to Langhian. The Aleria and Marana sedimentary plains have formed during Burdigalian to Pliocene times and are made of sand and coarser material of river terraces. Miocene sediment is also found on the Hercynian basement at the southern tip of the island (Bonifacio basin).

### *3.2.2. Mesozoic to Cenozoic thermo–tectonic evolution*

Low temperature thermochronometers (e.g., zircon and apatite fission–tracks, (U–Th)/He) from Corsica have provided a unique opportunity to reconstruct crustal evolution of the western Mediterranean area over the long–term (244–10 Ma) (Fellin et al., 2005a). Compilations of several thermochronometers indicate for how long different parts of the lithosphere have crossed

a certain temperature (i.e., a closure temperature). These closure temperatures vary from 70 to 110 °C for apatite fission–tracks, and 230 to 250 °C for zircon fission–tracks. For (U–Th)/He technique, which is a lower temperature themochronometer, the closure temperature is < 40 for apatite (AHe), and between 140 and 210 °C for zircon (see Reiners et al., 2005; Reiners and Brandon, 2006).

Zircon fission–tracks (ZFT) ages, can be grouped in three domains (Danišík et al., 2007; Fellin et al., 2005a; Mailhé et al., 1986): ZFT zones 1, 2, 3 (Fig. 3.2 –A). ZFT zone 1 includes much of Hercynian Corsica with ages ranging from 244 to 147 Ma. It is characterised by a westward increase in age associated to the rifting of the Ligurian–Piemont Ocean. ZFT zone 2 is located along the Alpine deformation front with ages ranging from 120 to 58 Ma which have been associated with eastward subduction. ZFT zone 3 includes the Alpine units with ZFT ages ranging from 45 to 22 Ma associated with late Cenozoic metamorphism (see Danišík et al., 2007). These domains are spatially correlative to the actual regional drainage divide, which roughly approximates the border between the ZFT zones 1 and 2 (Fig. 3.1, 3.2–A).

Apatite fission–track (AFT) and (U–Th)/He (AHe) dating reveal cooling ages that corroborate a longitudinal asymmetric exhumation of Corsica (Cavazza et al., 2001; Danišík et al., 2007; Fellin et al., 2005 a,b; Zarki–Jakni et al., 2004) (Fig. 3.2–B). It has been proposed that exhumation started in the south of Corsica in the Late Oligocene (40–30 Ma) and propagated northward through early Miocene times, reaching the centre at 30–20 Ma, and the northern region at 20–17 Ma (see Danišík et al., 2007).

The majority of AFT ages in the central and western parts of Corsica are between 20 and 27 Ma (Fig. 3.2–B). To the south, a cluster of older ages (46 to 105 Ma) has been measured (Zarki–Jakni et al., 2004). The youngest ages (20–10 Ma) are within Alpine units and the former Alpine wedge in north–eastern Corsica. Danišík et al. (2007) proposed four domains (AFT 1 to 4) according to their age and genesis (Fig. 3.3–C). AFT domain 1 contains AFT ages ranging from 30.6 to 16.4 Ma. The largest domain (AFT domain 2) has been divided into three sub–domains (Fig. 3.3–D). In the southernmost extremity of Corsica (AFT domain 3) resides the oldest domain (105.3 to 46.4 Ma) (Danišík et al., 2007). Finally, in the NE region of Corsica (AFT domain 4) ages range from 24.9 to 16.4 Ma. They are indicative of high cooling rate (up to 60°C/Myr), equivalent to ~2 km/Myr of exhumation rate, which has been linked to tectonic denudation (Jolivet et al., 1990;

Fellin et al., 2005a; Fournier et al., 1991; Rosenbaum et al., 2005). Fellin et al. (2005a) argue that cooling trajectories were perturbed by a heating event (from 19 to 14 Ma) related to burial of up to ~2 km thick Miocene successions.

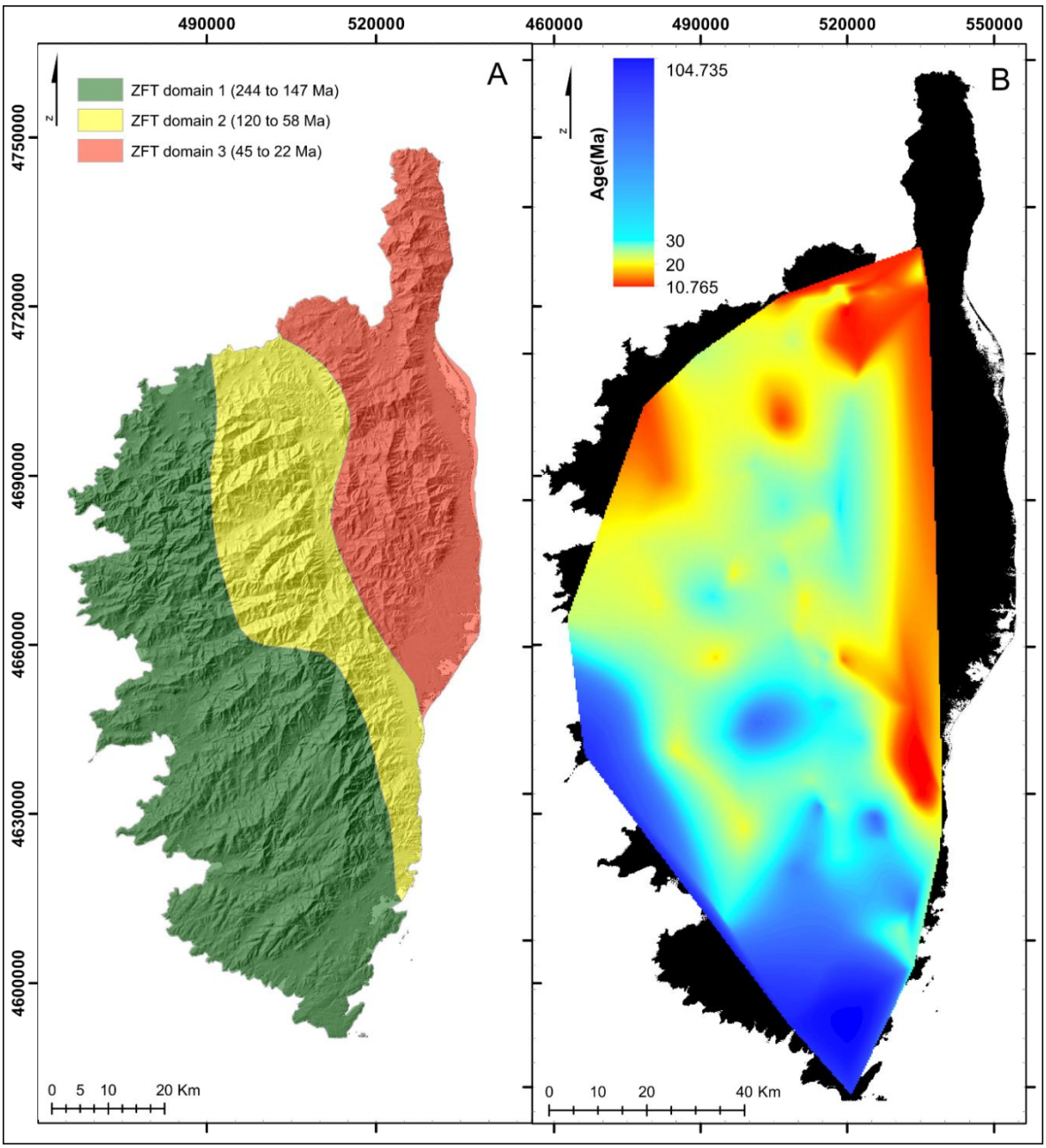


Figure 3.2: Spatial distribution of zircon (ZFT) and apatite fission–track (AFT) ages adapted from Danišík et al. (2007). The ages represented in those maps are compiled from the works of Cavazza et al. (2001), Zarki–Jakni et al. (2004), Fellin et al. (2005) and Danišík et al. (2007). A) Zircon fission track (ZFT) ages clustered in domains based on their age similarity. B) Spatial distribution of compiled AFT ages obtained by interpolation (nearest neighbour) and smoothing (30 m window) of the data set. Errors are not included.

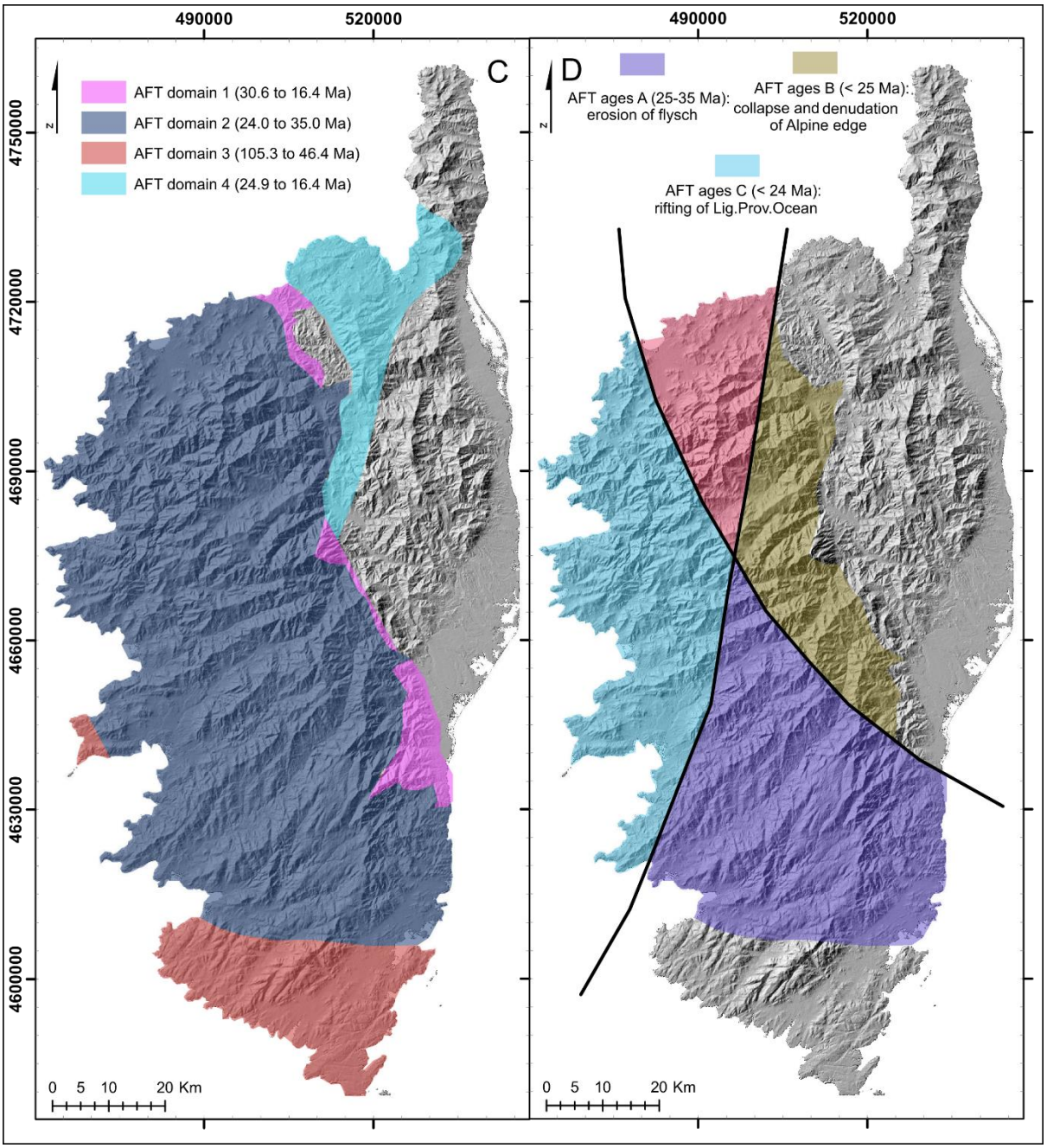


Figure 3.3: Spatial distribution of zircon (ZFT) and apatite fission–track (AFT) ages adapted from Danišík et al. (2007). The ages represented in those maps are compiled from the works of Cavazza et al. (2001), Zarki–Jakni et al. (2004), Fellin et al. (2005) and Danišík et al. (2007). C) Subdivision of Corsica into AFT domains based on their age similarity. D) Subdivision of AFT domain II into three subdivisions according to similarities in AFT ages and relations to geological features. The reddish zone in the panel D has not being referenced to any age group and it was displayed here just to keep the original format of the mapping made by from Danišík et al. (2007).

### *3.2.3. Miocene and post–Miocene landscape evolution*

After very high uplift rates (1.5 km/Myr) that lasted until Middle Miocene (~14 Ma), there is evidence of drainage reorganisation in the north such as Miocene basins now disconnected from their sources, indicative of drainage capture (Cavazza et al., 2007; Fellin et al., 2005b). Additional evidence testifying a recent (post–14 Ma) transient history of the Corsican landscape at low exhumation rates (0.2 km/Myr) include: large cut–and–fill Quaternary river terraces (Sømme et al., 2011); order of magnitude differences between long–term exhumation rates ($10^6$ to $10^7$ years) and short–term erosion rates ($10^4$ to $10^5$ years) (Fellin et al., 2005b; Molliex et al., 2017); marine records of sea–level variations during Quaternary and Messinian times (Pichevin et al., 2003); and extinct Würmian glaciers over an asymmetric drainage divide (Fig. 3.1) with variable erosion rates during the Quaternary (Kuhlemann et al., 2009).

Quaternary erosion rates have been derived from a range of techniques but the data are patchy, with most of the studies focused on the two largest catchments, both located to the east of the regional drainage divide: the Golo River watershed, which flows north–eastward, and the Tavignano River watershed, with its south–eastward drainage network (#3 and #7, respectively, in Fig. 3.4).

In the Golo River watershed, (U–Th)/He dating of apatite (AHe) provides a long–term erosion rate ranging from 25 to 220 mm/kyr over the last 7–3 Ma (Fellin et al., 2005b; Kuhlemann et al., 2009). Incision rates estimated from river terraces by optically stimulated luminescence (OSL) range from 160 to 475 mm/kyr (Fellin et al., 2005b), which is about one order of magnitude higher than long–term (AHe) erosion rates. Based on seismic reflection and analysis of offshore basins, Calvès et al. (2013) found catchment–wide erosion rates of 47–219 mm/kyr for the last 130 ka, while Molliex et al. (2017) estimated short–term erosion rates of 15–95 mm/kyr using detrital $^{10}$Be cosmogenic nuclides in the Golo watershed. Using high–resolution GPS and OSL in river terraces, Sømme et al. (2011) estimated rates of incision for the Golo River between 190 and 420 mm/kyr, with varying values for the different tectonic domains of Hercynian and Alpine Corsica.

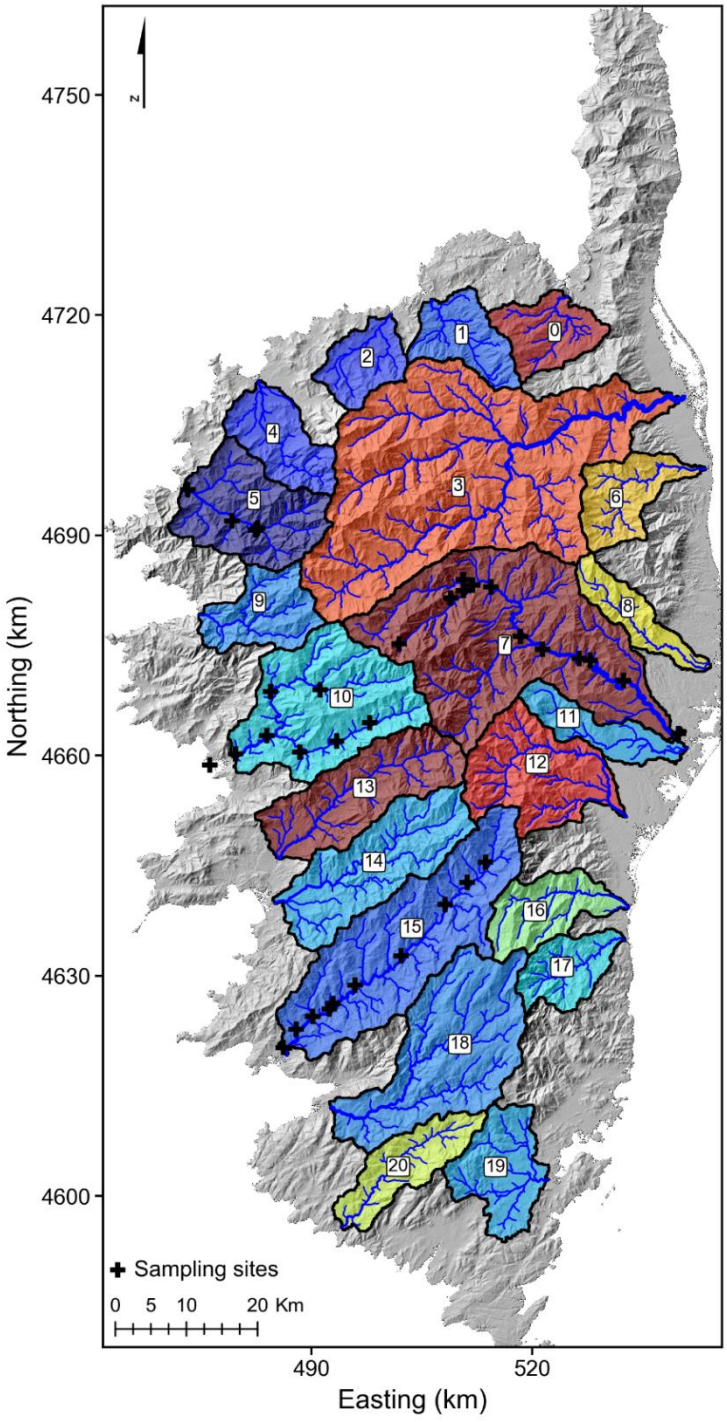


Figure 3.4: Watersheds of Corsica investigated in this work, including numbering and sites of analysed gravel bars (cross symbol) where pebble lithology and grain size were estimated (see section 3 for details). Numbers 3, 7, 5, 10 and 15 represent the Golo, Tavignano, Fango, Liamone and Taravo, respectively. Only watersheds with full coverage of elevation data (DEM) were used to perform $\chi$ analysis and extract the 'Gilbert' metrics. A plot of each complete watershed in Corsica can be found in the Fig. 3.15).

In the Tavignano River watershed, Molliex et al. (2017) measured catchment–wide erosion rates of 40 –74 mm/ky, which are between those found near the drainage divide (8 to 140 mm/kyr) by Kuhlemman et al. (2007, 2009) and catchment–wide erosion rates (15 –95 mm/kyr) in the Golo watershed. These catchment–wide erosion rates are much lower than the incision rates (160 –475 mm/kyr) of the Golo River from Fellin et al. (2005b).

Although there are no short–term catchment–wide erosion rates available to directly compare both sides of the drainage divide, some studies conducted by Kuhlemann et al. (2007, 2009) along summit surfaces using $^{10}$Be cosmogenic nuclides provide constrains for understanding the stability of the regional drainage divide. Erosion rates are low and range between 8.2 and 24 mm/kyr at the summits (Kuhlemann et al., 2009). However, they found a clear spatial distribution to the measured erosion rates, with a westward increase from 9.1 mm/kyr (east) to 13.6 mm/kyr (centre) to 17.6 mm/kyr (west); this was observed at the summits from the centre to the north of the island. Erosion rates varied from 15.2 mm/kyr (east) to 20.3 mm/kyr (west) in the centre of the island. They were relatively low at the southernmost summits (8.2 mm/kyr).

The influence of rock strength has been noticed by Molliex et al. (2017) when comparing short–term ($^{10}$Be) erosion rates and rebound values from different rock types in the two largest watersheds (Golo and Tavignano) of the island. Short–term ($^{10}$Be) catchment–wide erosion rates from Molliex et al. (2017) show a stronger correlation with rock strength and vegetation cover than with any other morphometric (elevation, slope, relief, river steepness) and climatic (precipitation) parameter. To understand the relation between rock strength and erosion rates, Molliex et al. (2017) measured rebound values (*Q*) from the different rock types in Corsica using a Schmidt hammer. Rock types from the Hercynian domain have higher rebound values (*Q*) than the Alpine units. For instance, within the Hercynian domain, rhyolite and pyroclastites (i.e., Permian volcanics) have the highest values (~ 67.5 *Q*), followed by granitoids (e.g., granodiorite and leucocratic granite) at intermediate values (~ 65.5 *Q*) and metamorphosed basement rocks (e.g., magmatic gneiss) with the lowest values (~ 63.5 *Q*). In the Alpine domain, the rebound values decrease from ophiolitic rocks (e.g., schist and gabbro, ~ 61 *Q*), to sedimentary rocks (e.g., sandstone and conglomerate, ~ 55 *Q*), with the lowest values obtained in the phyllite (~ 45 *Q*). Weathering rates estimated by measuring aluminium (Al) and potassium (K) in the regolith followed the same pattern of rock resistance mentioned above, i.e., higher weathering rates for

weaker rocks and lower for those harder. This strong lithological control on erosion rates suggests a likely strong influence on topography as well (e.g., hillslope and channel steepness), which will be investigated in this study.

The landscape of Corsica has been showed to be sensitive to the influence of climate. Glaciers reached their maximum extent ~18 ka in the centre and north–western sections of the Corsica drainage divide (Kuhlemann et al., 2005b) (Fig. 3.1). The southern region of the island experienced periglacial influence and glaciers were absent. Marine Isotope Stages (MIS) correlate with sediment yield which is up to twice higher (from 200 to 400 t $km^{-2}$/kyr) during changes from interglacial to glacial periods in Corsica (e.g., 18–35 ka). The short–term ($^{10}$Be) in–situ erosion rates estimated at the summits by Kuhlemann (2009) also correlate with modern precipitation rates, which are higher on the western side of the Corsican drainage divide, suggesting a potential influence, though it is important to note that the asymmetry and contrast in erosion rates could be driven by other factors.

Finally, it is relevant to mention the two phases of sea level lowering during the Messinian crisis (Gargani, 2004). The first phase, lasting 400 kyr, saw a 600 –700 m lowering at an average rate of ~ 1.45 mm/yr, while the second phase was marked by a 1300 –1700 m sea level drop over 50 ky (i.e., 30 mm/yr). The crisis was over around 5.3 Ma ago, with the sea level returning to a position close to present. More modest, yet significant sea level variations occurred over the Quaternary, associated with successive glacial and interglacial periods. Waelbroeck et al. (2002) proposed that, in the last 130 ka, the Mediterranean Sea level experienced a steady lowering of 120 m between 130–20 ka (i.e., 1.1 mm/yr), followed by a rise to the present level at a rate of ~6 mm/yr. Although there is no consensus on the literature about the rates and dates of sea level variation during the Messinian crisis (see Clauzon et al., 1996; Krijgsman et al., 1999; Rouchy and Caruso, 2006) and about the Mediterranean sea level during the Quaternary (see Lambeck and Purcell, 2005), the propposed sea level variation made by Gargani (2004) and Waelbroeck et al. (2002) are consistent with the sediment yield measured by Calvès et al. (2013), which showed that sea level drop was followed by an increase in the erosion rates. A summary of all major events that Corsica experienced during and after the Miocene (including their dates and rates) are given in the figure 3.5.

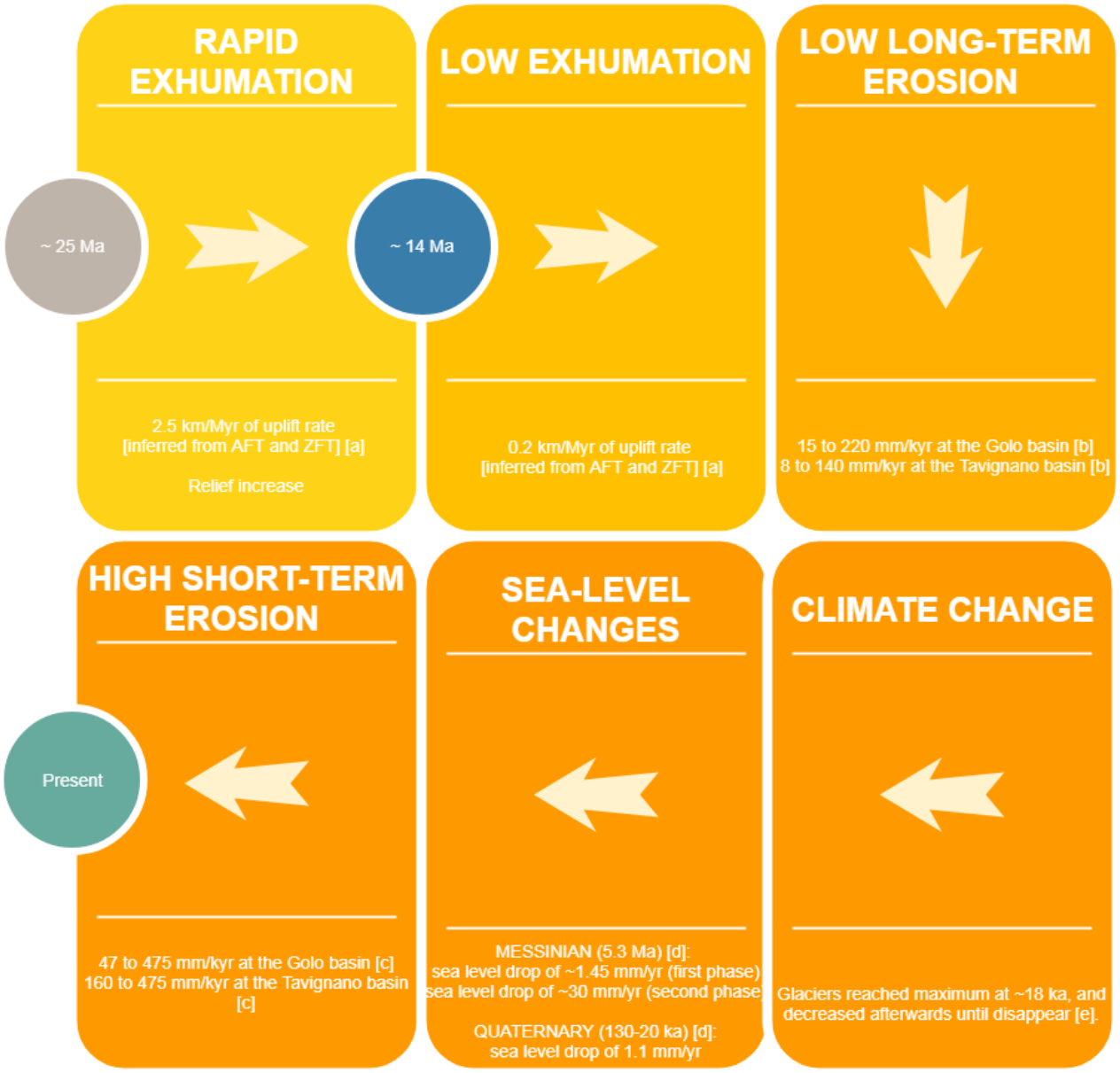


Figure 3.5: Summary of major events that Corsica experienced during and after the Miocene. A rapid exhumation between ~ 25 and 14 Ma generated the topographic wavelength and relief that was conserved afterwards due to low long-term erosion rates. However, these low long-term erosion rates have been interrupted by uplift pulses (that generated higher erosion rates in the river valleys), sea level drops (during the Messinian and Quaternary), and glacier retreat (after ~ 18 ka). The letters [a, b, c, d, e, f, g, h, i] are references for the rates and dates. a = Fellin et al. (2005a); b = Fellin et al. (2005b), Kuhlemann et al. (2007, 2009), Molliex et al. (2017); c = Calvès et al. (2013), Sømme et al. (2011), Fellin et al. (2005b); d = Gargani (2004), Waelbroeck et al. (2002); e = Kuhlemann et al. (2005b).

## 3.3. Methods

### *3.3.1. Background: the stream power incision model*

River profile evolution can be described based on what factors modulate the rate of channel incision. Incision in transport–limited systems occurs if and only if the local transport capacity of the river is greater than the sediment load delivered from upstream (Howard, 1980; Howard and Kerby, 1983). In detachment–limited systems, incision occurs because the local transport capacity of the river greatly exceeds the sediment supply (Howard, 1980; Whipple and Tucker, 1999). Hybrid systems are defined as those where both transport capacity and detachment control the channel incision (Sklar and Dietrich, 1998; Whipple and Tucker, 2002; Gasparini et al., 2007). In this work, I assume that river profile evolution can be fully reproduced by using the stream power incision model, which is routinely used to simulate detachment–limited system conditions due to its well–known capability in reproducing geomorphic features (e.g., knickpoint migration) as well as providing metrics to predict drainage divide stability (e.g., χ–transformation).

The most commonly used model of bedrock river incision, named stream power incision model (SPIM), expresses the erosion rate in terms of channel slope and drainage area, as follows:

$$\frac{\partial z}{\partial t} = U(x,t) - K(x,t)A(x,t)^m \left|\frac{\partial z}{\partial x}\right|^n, \quad (1)$$

where $z$ is elevation (L), $t$ is time (T), $x$ is horizontal upstream distance (L), $U$ is the rate of rock uplift (L $T^{-1}$) from a reference base–level, $K$ is an erodibility coefficient ($T^{-1}$ $L^{(1-2m)}$) that aggregates the influence of climate, lithology, and sediment supply, $A$ is drainage area ($L^2$), and $m$ and $n$ are empirical dimensionless constants (Howard and Kerby, 1983; Whipple and Tucker, 1999).

Assuming steady–state ($\partial z/\partial t = 0$), equation (1) can be simplified as:

$$\left|\frac{dz}{dx}\right| = \left(\frac{U}{K}\right)^{\frac{1}{n}} A(x)^{-\frac{m}{n}}. \quad (2)$$

Assuming spatial uniformity of $U$ and $K$, this equation (2) describes a power–law scaling between slope and drainage area. Plotting slope and drainage area of a given river in log–log scale may support this steady–state assumption by producing a straight line, the slope of which equals the channel concavity ($m/n$), whereas the vertical position of the line is an indicative of the ratio of uplift to erodibility ($U/K$) to the power $1/n$, often referred to as the steepness index, $k_{sn}$. Deviations from a power law slope–area relationship may be evidence of transience of the river channel, variations in bedrock erodibility, or non–uniform erosion and transport mechanisms (Synder et al., 2000; Kirby and Whipple, 2001). However, slope data tend to be noisy and sudden changes in drainage area at tributary junctions lead to gaps in a slope–area data; as a result, the ability to detect transient signals or quantify parameters from the SPIM using slope–area data has recently been questioned (see Wobus et al., 2006), although tributary junctions can be relevant features for understanding flow dynamics, sediment transport and bed morphology (see Best, 1987). A recent solution to these problems is the χ method, which is based on a transformation by integration, as explained below (Perron and Royden, 2013; Royden and Perron, 2013).

### 3.3.2. *Identifying the geomorphic (i.e., topographic) state of the landscape*

In order to identify the geomorphic state of Corsica, I investigate both river profiles and regional drainage divide. In the river profiles, I search for changes in river steepness, knickpoints and grain size pattern to unravel the influence of erodibility ($K$), uplift rates ($U$) and base level change that can have modulated the erosional response of Corsica. At the drainage divides, I apply $\chi$ analysis and 'Gilbert' metrics as a proxy for estimating relative erosion rates and identify potential drainage (in)stability.

### 3.3.3. *χ–transformation and river steepness*

I begin from the expression of the SPIM. To relax the steady–state assumption, I consider erosion rate instead of uplift rate and replace *U* by *E* in equation (2). Separating variables in the equation, assuming that *E* and *K* may be spatially variable, and integrating, yields:

$$\int dz = \int \left(\frac{E(x)}{K(x)A(x)^m}\right)^{\frac{1}{n}} dx. \quad (3)$$

Equation (3) may be integrated from some base level ($x_b$)to upstream:

$$z(x) = z(x_b) + \left(\frac{E(x)}{K(x)A(x)_0^m}\right)^{\frac{1}{n}} \chi, \quad (4a)$$

where

$$\chi = \int_{x_b}^{x} \left(\frac{A_0}{A(x)}\right)^{\frac{m}{n}} dx, \quad (4b)$$

and $A_0$ is a reference drainage area, introduced to make the integrand in equation (4b) dimensionless (Perron and Royden, 2013).

The transformed coordinate, $\chi$, has a dimension of length. In a situation where *K* and *E* are uniform in space and time, the elevation, *z(x)*, is a linear function of χ according to equation (4a). The slope of the $\chi$–transformed river profile is the equivalent of the channel steepness from the area–slope plot if $A_0 = 1$ m$^2$, and is hereafter named $k_{sn}$ (see Mudd et al., 2014). It can be written as:

$$k_{sn} = \left(\frac{E}{KA_0^m}\right)^{\frac{1}{n}}. \quad (5)$$

As $k_{sn}$ is physically dependent on the chosen concavity index (*m/n*), comparison of river steepness among watersheds can only be performed if the same reference concavity value is chosen for all river channels in the landscape under investigation. River channel concavity (*m/n*) was estimated for every complete watershed of Corsica using a maximum likelihood estimator (Mudd et al., 2018). Based on the distribution of channel concavity values found by the maximum likelihood estimator, I chose a concavity of 0.35, which is the mean value of all χ methods employed (i.e., χ all data, and χ Monte Carlo), to perform our analysis and compare all river steepness ($k_{sn}$) of Corsica (Fig. 3.6).

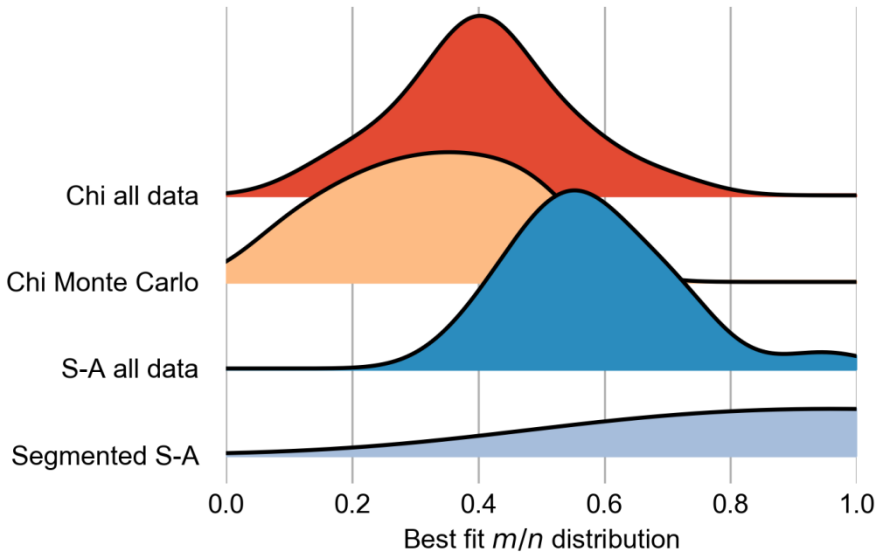


Figure 3.6: Comparison of methods used to find the best–fit concavity index (m/n) and their best–fit values. I chose 0.35 as an intermediate value of Monte Carlo simulations used to find the best concavity index (m/n).

Because the χ analysis tends to be applied to incising, bedrock rivers, I were concerned by the potential influence of the alluvial river reaches as rivers cross the Aleria and Marana sedimentary plains in the East before reaching the sea. Comparison of the analysis' results with and without the alluvial segments showed no significant differences: the alluvial segments in our case do not influence the results. All the analysis was performed using a Shuttle Radar Topography Mission (SRTM) digital elevation model with ~30 m of spatial resolution.

### *3.3.4. Knickpoint identification*

Knickpoints mark segments in the river profile where steepness is higher than expected for the associated contributing drainage area, thereby creating a positive deviation, or convexity, when plotting elevation as a function of distance (long profile) or slope as a function of drainage area on a log–log plot (Howard et al., 1994; Whipple and Tucker, 1999). Such convexities can be divided into three groups: locally steepened zones ("vertical step knickpoints"), if the river

steepness is identical upstream and downstream of a convexity; “slope–break knickpoints”, if the river steepness has a long–length increase downstream from a convexity (Kirby and Whipple, 2012); and “knickzone”, if several knickpoints are spaced closely together or if a knickpoint has diffused during upstream migration and became a single unit (see Neely et al., 2017). In this work, I refer as knickpoint to all classifications described above (Lague, 2014).

In order to systematically identify knickpoints along our rivers, I use the algorithm written by Neely et al. (2017), which has four required parameters: a smoothing window, knickpoint height pre–lumping, a lumping window size, and a knickpoint height post–lumping (Fig. 3.7).

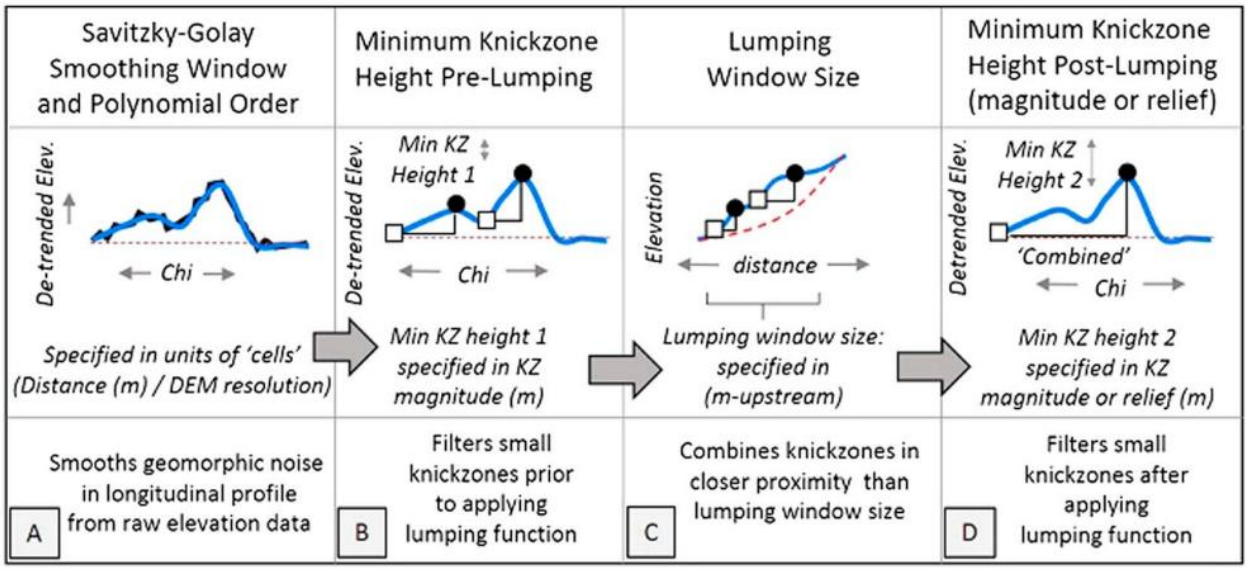


Figure 3.7: Representation of the parameters required in the algorithm developed by Neely et al. (2017) to extract knickpoints from DEMs. A) Represents a smoothing window reducing noise in the DEM; B) represents a knickpoint height pre–lumping where small knickpoints are removed; C) represents a lumping window size that combines knickpoints nearby and D) represents a final step where knickpoint height post–lumping removes small knickpoints. Adapted from Neely et al. (2017).

I take intermediate parameter values recommended by Neely et al. (2017) for DEMs with 30 m of spatial resolution, i.e., 7.5 units of cell as a smoothing window, a 2.5 m minimum knickpoint height pre–lumping, 75 m of lumping window size, and, finally, a 5 m of minimum knickpoint height post–lumping. The smoothing window removes geomorphic noise in raw elevation data. The selection of a knickpoint height filters small knickpoints (potentially insignificant or resulting from data noise) before applying the lumping function. The lumping

window size combines knickpoints in closer segments (i.e., in knickzones). Lastly, minimum knickpoint height post–lumping removes small knickpoints that remained after the previous steps.

Knickpoints can results from differences in rock resistant to erosion at lithological boundaries or tectonic structures ("static") or can reflect the propagation of transient signals ("migrating") (see Cook et al., 2013; Crosby and Whipple, 2006). The location of the latter ones should not coincide with lithological contacts or structures. I verify if the identified knickpoints are stationary or migrating by comparing their location with locations of geological boundaries on the geological map.

### *3.3.5. 'Gilbert' metrics for drainage divide stability*

I follow the same procedures adopted by Forte and Whipple (2018) to analyse upstream gradient, upstream relief, and elevation at channel heads (i.e., the 'Gilbert' metrics) for predicting drainage divide stability in natural landscapes. Stability should in theory be reflected by equal values of all metrics on both side of the divide. Disequilibrium would appear as systematic deviation. Greater erosion on one side of the divide (which would lead to migration of the divide towards the least erosive side) could be expressed in the landscape as: steeper gradient, greater relief and lower channel head elevation (implying steeper hillslopes connected the divide to the channel head). These metrics may be influenced by other parameters (e.g., bedrock lithology, rainfall) so results have to be carefully interpreted to rule out any other possible control. In the absence of other influences, systematic differences in all metrics are likely to reflect disequilibrium.

The location of the channel heads is based on a reference drainage area ($10^5$ $m^2$) for channel initiation, which has been used as a standard in many studies using the technique (e.g., Forte et al., 2015, 2016). A colour scale based on a normalisation of upstream gradient, upstream relief and elevation at channel heads is set to the whole drainage network for an initial visual comparison of anomalies along the divide (shown and discussed in part 4.1). Finally, after selecting a section of particular interest, histograms are used to compare the mean values of each metric on both sides of the drainage divide.

I perform four uncertainty analyses for the drainage divide metrics. Three have already been proposed by Forte and Whipple (2018), i.e., one standard error of the mean (s.e.), one standard deviation (s.d.), and 95% bootstrap confidence interval determined from a 1000 iteration resampling scheme. The s.d. measures the variability (or dispersion) of a set from the mean, while the s.e. estimates how far the set mean is likely to be from the true population mean. Both metrics (s.d. and s.e.) have 68% of confidence interval and the s.e. is always smaller than the s.d.. Bootstrapping is a statistical test in which very small samples are resampled to a much larger data set (1000 in our case) to reason about the real population with 95% of confidence. I also use a *t*–test to assess if the difference between the means is statistically significant (with 95% of confidence). By using different uncertainty estimators, I aim to provide a robust assessment of the drainage divide stability, given that different metrics can indicate stability or motion depending on the chosen uncertainty level (an illustration of how the Gilbert metrics work has already been given; see Fig. 1.5 in the Chapter 1).

I analyse all uncertainty levels independently but the criteria used to define a migrating drainage divide section is the rejection of at least 3 out of 4 uncertainty levels that the metrics of opposing sides are equal (i.e., the null hypothesis test).

### *3.3.6. Grain size distribution and rock type in modern gravel bars*

By analysing the grain size distribution of gravel bars, I can explore the relationship between them and river steepness. Alluvial material can armour the river bed (cover–effect) from erosion or can enhance river incision (tool–effect) (see Sklar and Dietrich, 1998). The former occurs in environments where bedload mobility is low and the sediments protect the river from stream power and particle energy impact. In the latter, the bedload behaves as an agent carving the river bed and thus promoting incision. Identifying possible correlation among river steepness and sediment grain size could help in finding mechanisms of river incision in Corsica beyond the well–known stream power incision model. Moreover, by coupling grain size analysis with rock type identification, I can compare how bedload changes according to the different rock strength transported by rivers.

We selected four representative watersheds (Tavignano, Liamone, Taravo and Fango) where 27 modern river gravel bars were analysed (Fig. 3.1). The criteria used to select the watersheds were length and lithological diversity so that I could have a fair representation of the geological units and transport processes of Corsica.

The methods used to determine the grain size distribution of fluvial sediment are similar to the ones used by Attal and Lavé (2006) and Attal et al. (2015). I selected only sediments that had been unambiguously transported by rivers. Surface and subsurface gravel bars were distinguished to infer armouring (Bunte and Abt, 2001). Surface grain size was determined in the field by identifying rock type and intermediate axes of 100 pebbles from the surface gravel bars, which has been a standard procedure in many works (e.g., Attal et al. (2015)). To confirm our field identification of pebble rock type, representative pebbles were prepared as thin–sections. Besides the field measurements, photos were also taken to estimate intermediate pebble axes following the procedures of grid counting from Kellerhals and Bray (1971).

Subsurface sediment was excavated from a pit after removing the surface sediments over approximately 0.5 $m^2$. As performed by Attal and Lavé (2006) and Attal et al. (2015), to analyse subsurface sediments, the surface gravel layer was removed to the thickness of the largest boulder. The material from the pits was sieved using 10, 20 and 40 mm mesh sieves. Each fraction was weighed using a scale of ~20 g precision, and fragments larger than 80 mm were weighed individually. The size of clasts larger than 80 mm was estimated by assuming that they were spheres with a density of 2650 kg $m^{-3}$, which is representative of quartz–dominated rocks. Around 1 kg of the fraction finer than 10 mm was sampled for further analysis. Its grain size distribution was determined in the lab using 8, 5.6, 4, 2.8, 2, 1.4 and 1 mm square mesh sieves. Restrictions found in the field were: some of the gravel bars were too small (< 2 $m^2$) and limited by bedrock, which reduced the amount of material for analysis. I was also unable to dig deep below the water table. The mass of sediment sieved and weighed at each site ranged between 45 and 319 kg. The unit of grain size analysis adopted in this chapter is ψ (psi), which is given by:

$$\psi = log_2 (D) \quad (6),$$

where D is the diameter of the particle in mm.

## 3.4. Results

### *3.4.1. Drainage divide stability*

After a visual inspection of Corsican rivers, I segmented the regional drainage divide in two parts (A and B) where a distinct contrast is observed in both χ and 'Gilbert' metrics (Fig. 3.8 and 3.9, data analysed hereafter). This segmentation procedure is recommended by Forte and Whipple (2018) to minimise the variance of metrics that could bias the prediction of motion into a stable position. Generally speaking. the southern section of the Corsica drainage divide (A) is marked by values of χ and 'Gilbert' metrics (more particularly, upstream gradient and relief) that suggest a westward divide migration trend (i.e., the eastward flowing rivers have lower χ and higher gradient and relief values closer to the divide than the westward ones). On the contrary, a clearer contrast in the values around the northern section of the drainage divide (B) highlights an eastward divide migration trend (i.e., the westward flowing rivers have lower χ and higher gradient and relief values closer to the divide than the eastward ones).

When quantitatively assessed, the majority of the southern drainage divide (A) metrics are indicative of drainage divide migration to the west in both 'Gilbert' and χ metrics (Fig. 3.10). Except for channel head elevation, χ as well as the other channel head metrics (upstream gradient and relief) show evidence of across drainage divide instability by having mean values that do not overlap in two out of three uncertainty estimation levels (95% bootstrap confidence interval and 1 s.e.). The *t*–tests are not statistically significant to reject that the means are different in two metrics (upstream relief and elevation at channel heads). Yet, under a more restrictive uncertainty condition (i.e., 1 s.d.), all metrics have means that are statistically undistinguishable. The quantitative assessment of the northern drainage divide (B) metrics has also confirmed the visual inspection (Fig. 3.11). Overall, both 'Gilbert' and χ metrics suggest a divide migration to the east in two out of three uncertainty estimation levels (95% bootstrap confidence interval and 1 s.e.). The *t*–tests are statistically significant to reject that the means are equal in all metrics. Under a more restrictive uncertainty condition (i.e., 1 s.d.), except for the χ, all metrics have means from both sides of the drainage divide that are statistically undistinguishable.

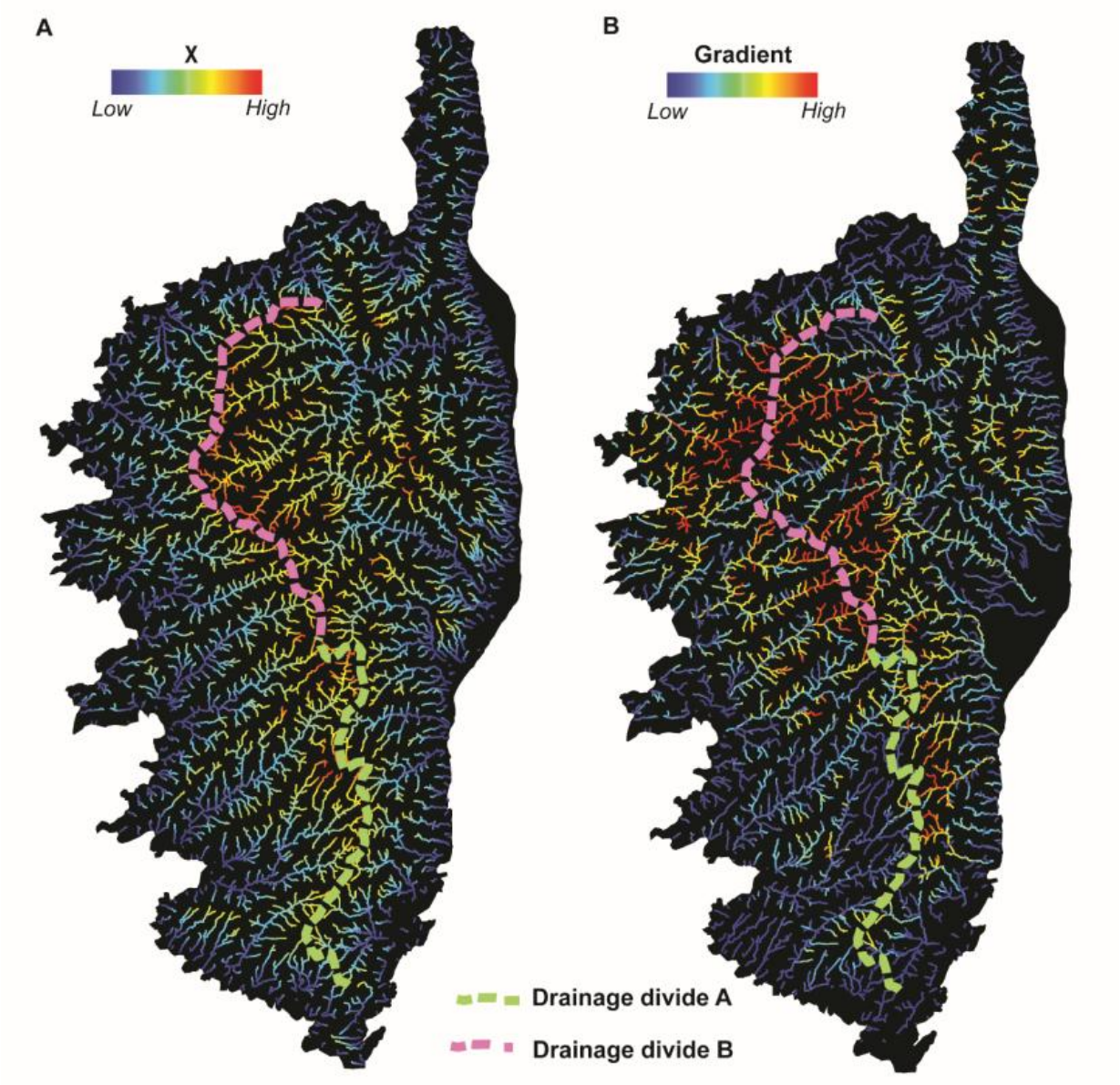


Figure 3.8: χ values (A) and the normalised values of upstream gradient (B) at channel heads of the drainage network across Corsica. The regional drainage divide was segmented in two shorter ones (A and B) based on the visual anomaly in χ, gradient and relief. Similar values for each of these metrics on both sides of the divide would indicate stability. In the presence of anomalies, the divide is expected to migrate towards the least erosive part, that is, the part with the greatest χ value and channel head elevation, and lowest gradient and relief.

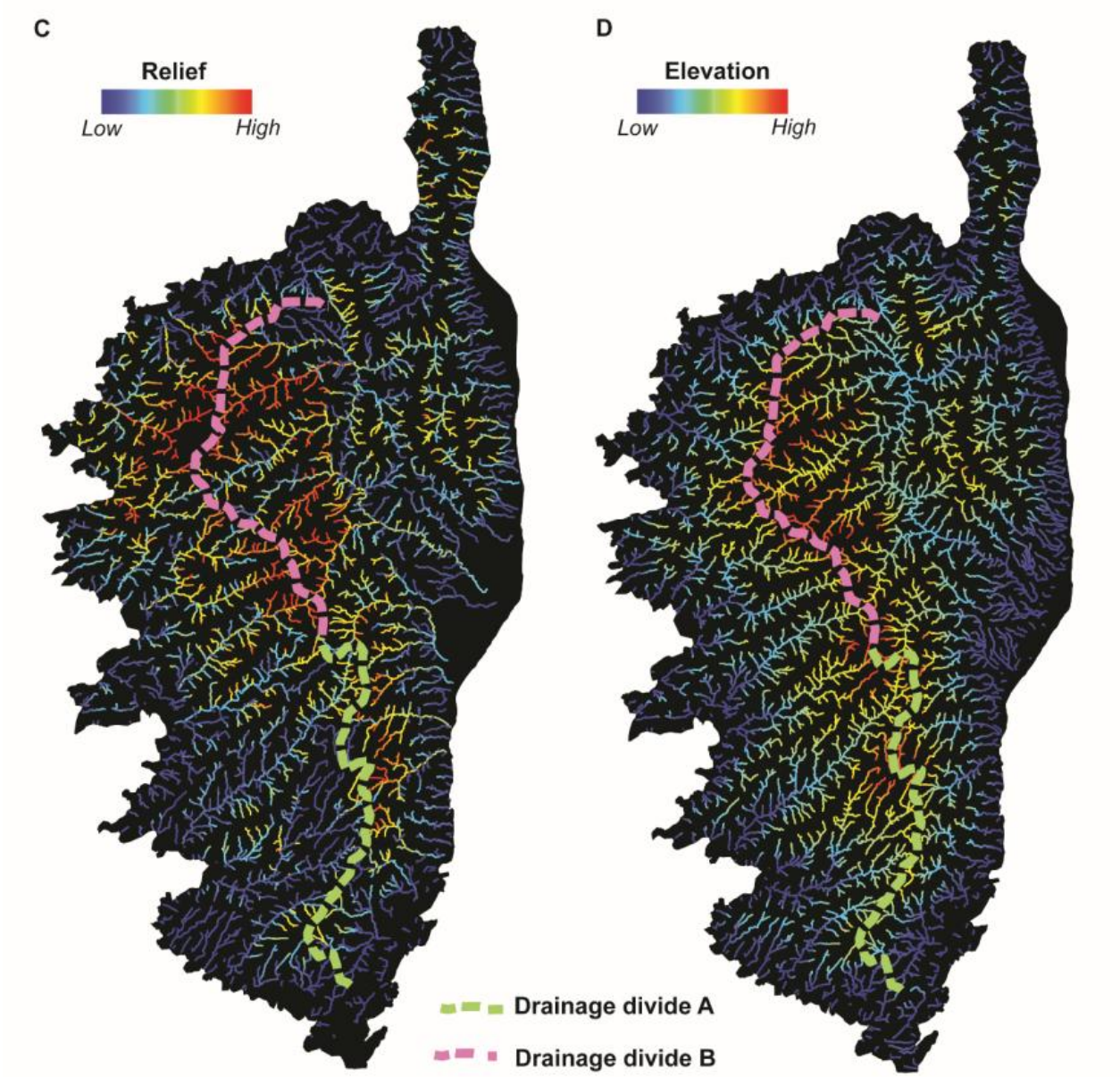


Figure 3.9: relief (C) and elevation (D) at channel heads of the drainage network across Corsica. The regional drainage divide was segmented in two shorter ones (A and B) based on the visual anomaly in $\chi$, gradient and relief. Similar values for each of these metrics on both sides of the divide would indicate stability. In the presence of anomalies, the divide is expected to migrate towards the least erosive part, that is, the part with the greatest $\chi$ value and channel head elevation, and lowest gradient and relief.

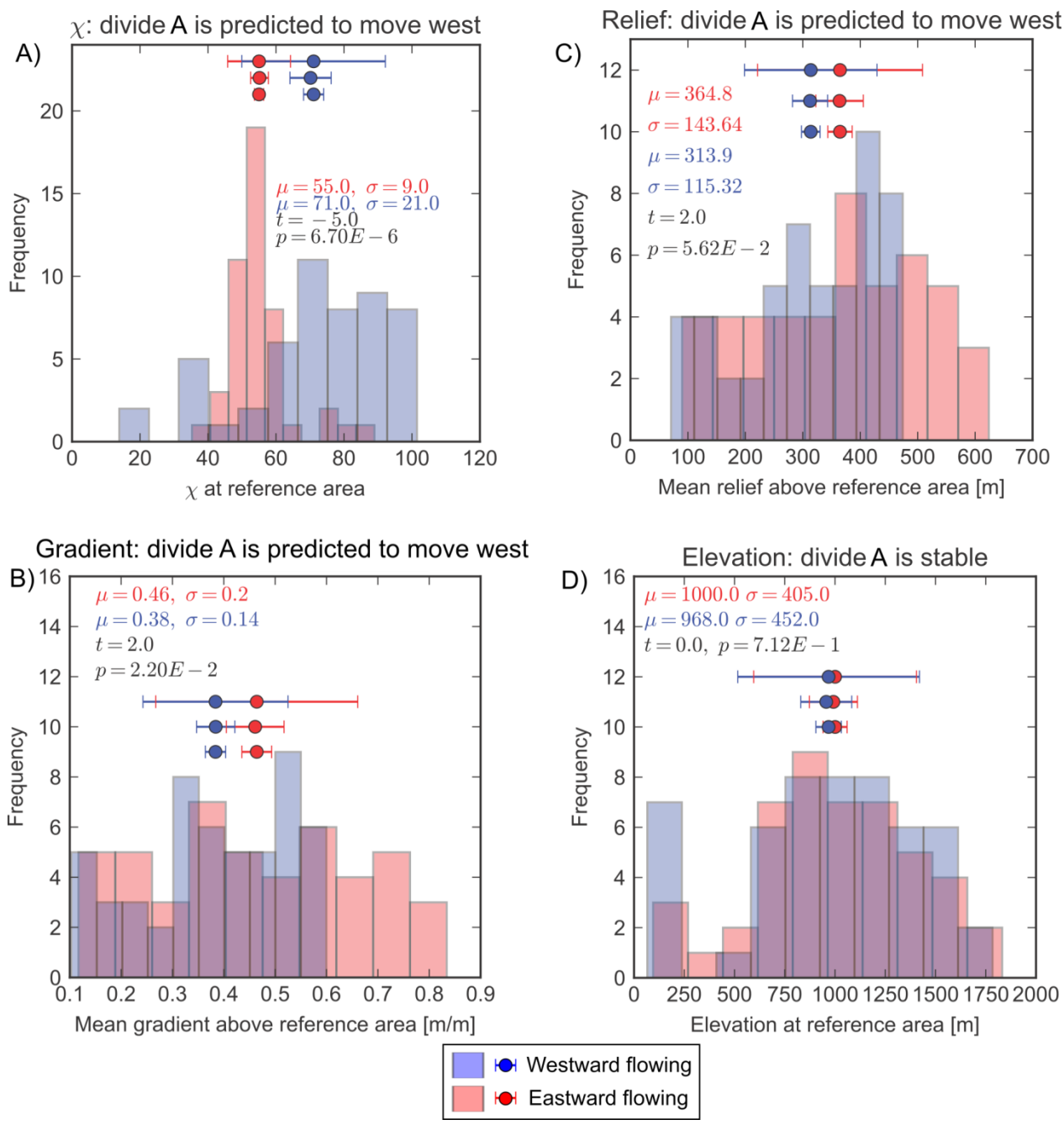


Figure 3.10: Drainage divide stability metrics collected from the channel heads in the southern section (A) of the Corsica regional divide. Frequency bars and data plots in red represent eastward flowing river catchments, while those in blue represent westward flowing river catchments. Mean (μ) and standard deviation (σ) of the channel heads metrics are also coloured accordingly. The t–tests (t) and their statistical significance (p) are also displayed (in black). The error bars represent, from top to bottom, 1 s.d., 95% bootstrap confidence interval and 1 s.e..

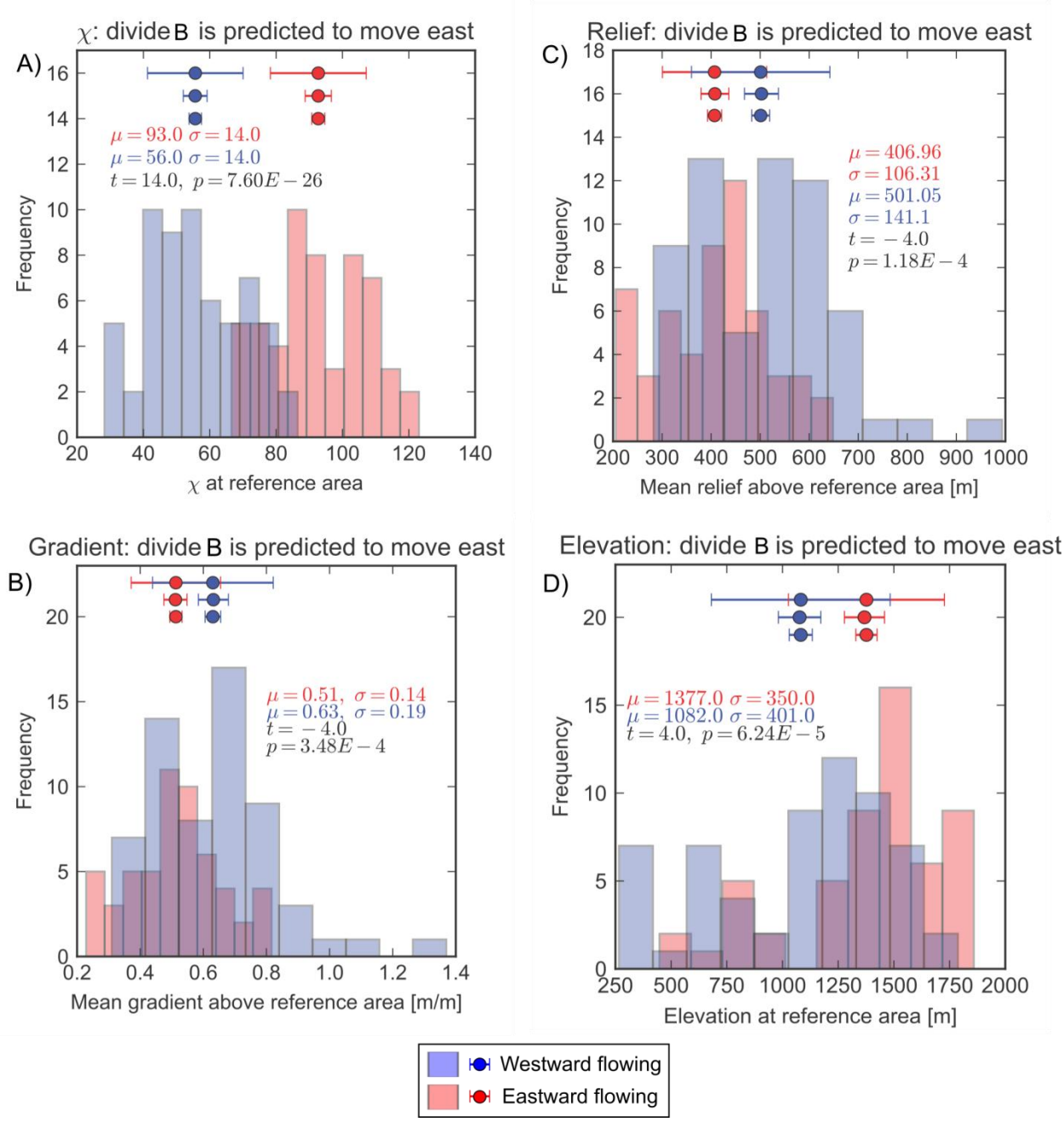


Figure 3.11: Drainage divide stability metrics collected from the channel heads in the southern section (B) of the Corsica regional divide. Frequency bars and uncertainty plots in red represent eastward flowing river catchments, while those in blue represent westward flowing river catchments. Mean (μ) and standard deviation (σ) of the channel heads metrics are also coloured accordingly. The t–tests (t) and their statistical significance (p) are also displayed (in black). The error bars represent, from top to bottom, 1 s.d., 95% bootstrap confidence interval and 1 s.e..

### *3.4.2. Drainage network analysis*

#### *3.4.2.1. Spatial distribution of knickpoints*

In this section, I locate and measure knickpoints using the automatic detection algorithm presented in section 3.2.2 and assess their spatial relationship with respect to a series of potential controlling factors. I assess the occurrence and magnitude of knickpoints with respect to geological units, geological structures (faults), side of regional drainage divide, extent of Würmian glaciers, thermochronological domains identified by previous studies (apatite and zircon FT), and distance from the coast. The occurrence of knickpoints shows an interesting spatial distribution with respect to tectonic structures and rock types in Corsica (Fig. 3.12 and 3.13).

The Miocene to modern sedimentary plains of Aleria and Marana have few knickpoints, and those few have the smallest values in the metrics that characterise their size (i.e., magnitude, relief, slope and length between lips and bases) (Fig. 3.14, Table 3.1). I identify 0.1 knickpoints/km$^2$ with an average magnitude of 13.0 m in this unit. The knickpoint metrics are among the ~ 48.0% lower values identified across the whole of Corsica (probability of occurrence [$Pr\ x$] $<\mu - 0.5\sigma$). In the Schistes Lustrés unit, where metasediments and ophiolites dominate, the amount and magnitude of knickpoints largely increases, with 0.2 knickpoints/km$^2$ and an average magnitude of 22.6 m. In this unit, the knickpoint metrics are between ~ 48.0% and 99.3% higher values in Corsica (i.e., $Pr\ \mu - 0.5\sigma < x < 2.5\sigma$). In the Hercynian Corsica units, where granitoids dominate, there are 0.23 knickpoints /km$^2$, with an average magnitude of 27.7 m. I identify that some metrics are among the highest 0.7% found in the whole Corsica (i.e., $Pr\ x > \mu + 2.5\sigma$) for this unit.

The *t*–tests are statistically significant to affirm that the three major geological units of Corsica (i.e., sedimentary plains, Schistes Lustrés and Hercynian Corsica units) have knickpoints with different means of magnitude, relief, and slope (with 95% of confidence, see Table S1). On the contrary, the *t*–tests do not allow us to reject the hypothesis that the means of lengths are equal among the knickpoints of those major geological units.

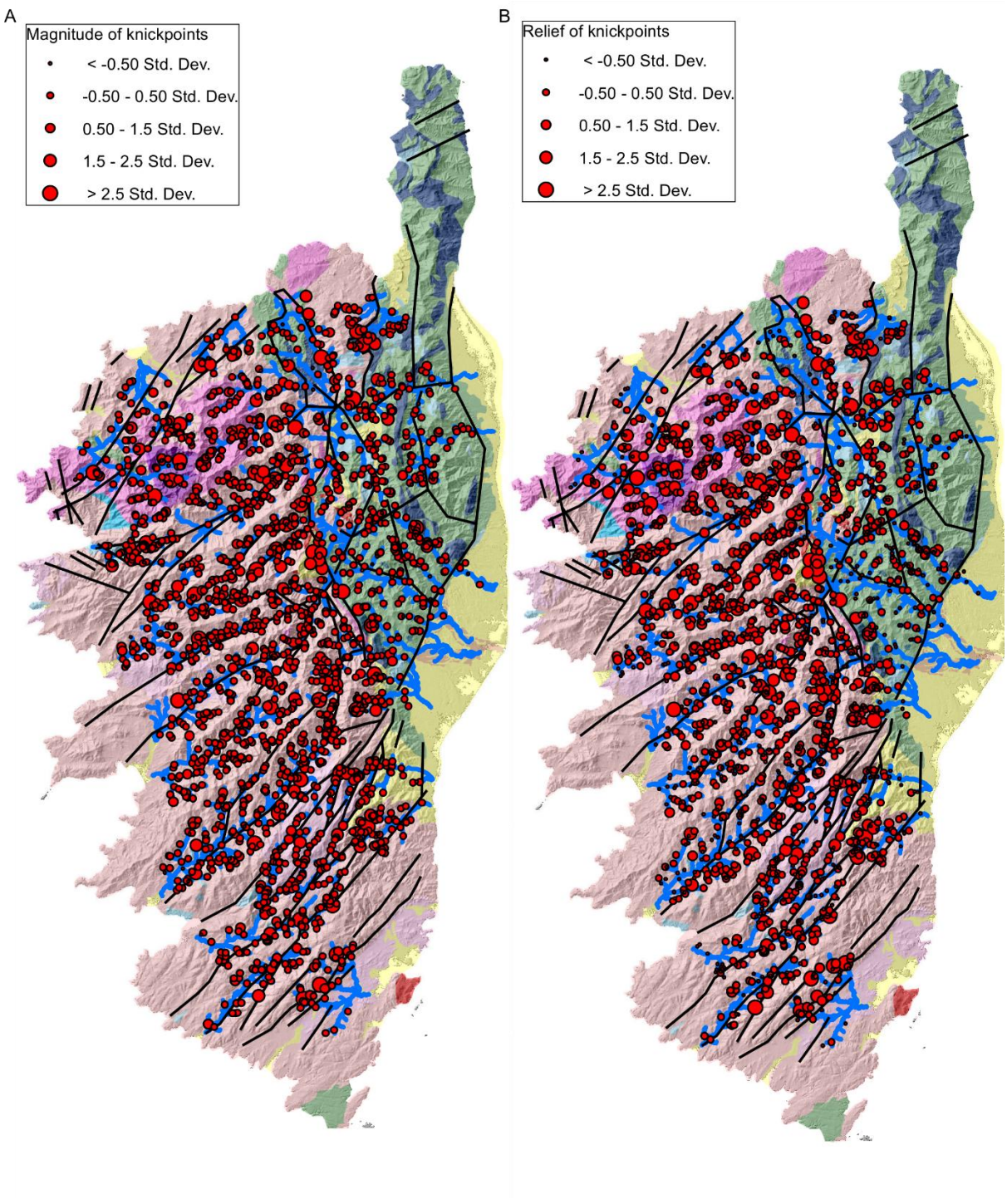


Figure 3.12: Metrics of knickpoints across the drainage network of Corsica, superimposed over a geological map. A) Magnitude of the knickpoints (i.e., vertical distance of the lip from channel steepness). B) Relief of the knickpoints (i.e vertical distance of the lip from the base). All the knickpoints' metrics are displayed according to their s.e.. All structural elements from Figure 3.1 are displayed here as continuous solid lines to ease visualisation, irrespective of their nature. The geological units are adapted from Rossi et al. (1994 a, b) and the tectonic units are from Gueydan et al. (2017).

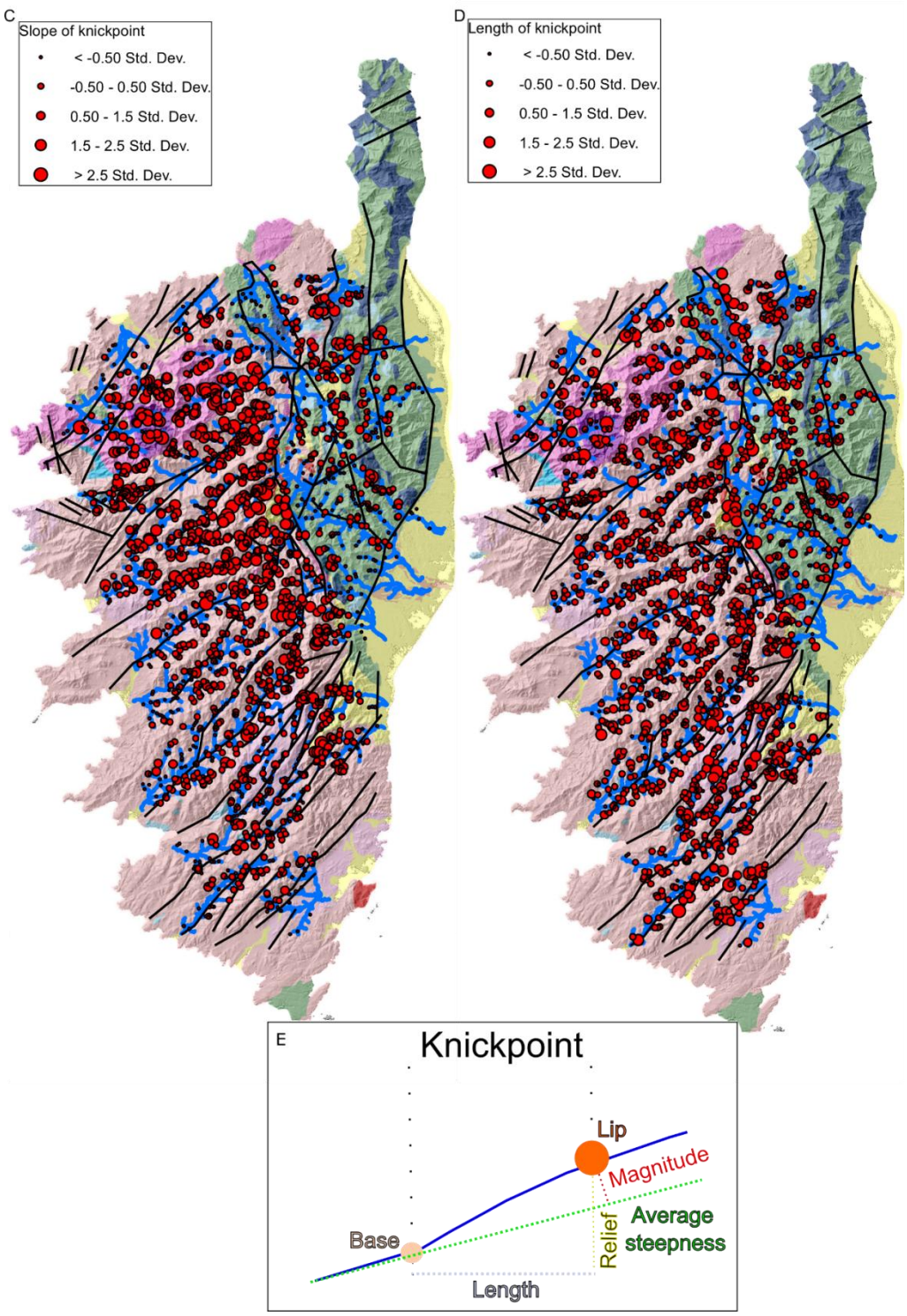


Figure 3.13: Metrics of knickpoints across the drainage network of Corsica, superimposed over a geological map. C) Slope of the knickpoint reach. D) Length of the knickpoint (i.e., horizontal distance from the lip to the base). All the knickpoints' metrics are displayed according to their SE. All structural elements from Figure 1 are displayed here as continuous solid lines to ease visualisation, irrespective of their nature. The geological units are adapted from Rossi et al. (1994 a, b) and the tectonic units are from

Gueydan et al. (2017). E) Sketch showing how knickpoint metrics of length (in grey), relief (in yellow), slope (the angle between average steepness and the lip, not included in thte skecth) and magnitude (in red) are extracted in this work. The blue line in the sketch represents the actual river profile.

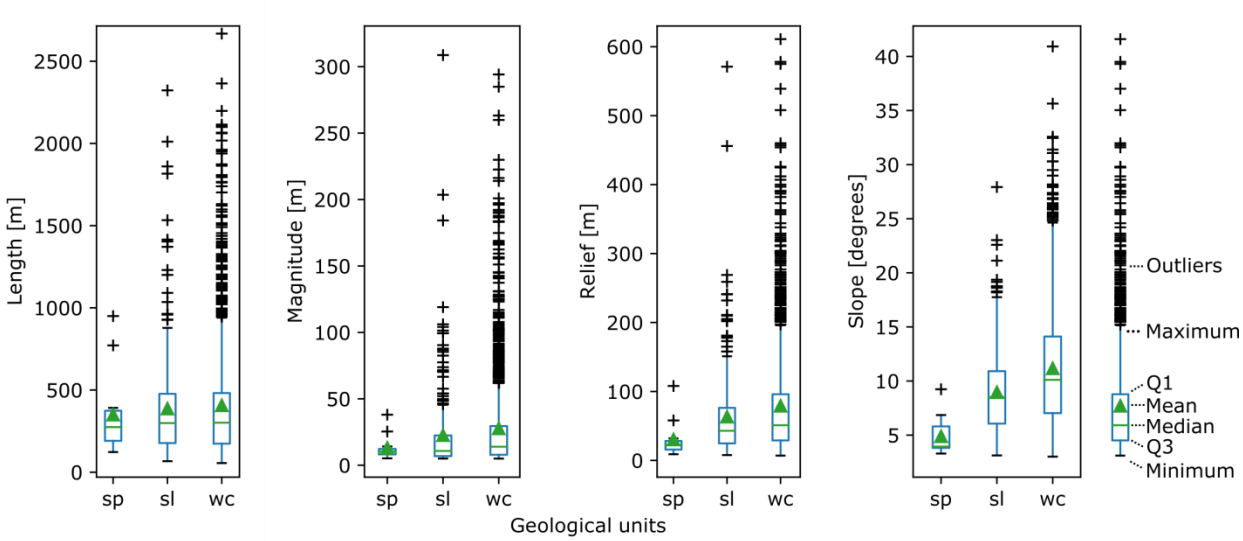


Figure 3.14: Knickpoint metrics measured according to the geological units of Corsica. *sp* = sedimentary plains; *sl* = Schistes Lustrés; *hc* = Hercynian Corsica; *maximum* = greatest value, excluding outliers; *Q1* = 25% of data greater than this value; *Q3* = 25% of data less than this value; *minimum* = lowest value, excluding outliers. *t*–tests comparing if the means of knickpoints' metrics can be found in the supporting information (Table S1).

Table 3.1: Characteristics of the knickpoints identified in Corsica with the automatic detection algorithm: density, magnitude, relief, slope and length measured from the base to the lip are given according to the geological unit.

| Rock type unit | # of kp | Density [kp/km$^2$] | Mean Magnitude [m] | Mean Relief [m] | Mean Slope [degrees] | Mean Length [m] |
|---|---|---|---|---|---|---|
| Sedimentary Plain | 12 | 0.1 | 13 | 30.4 | 4.9 | 350 |
| Schistes Lustrés | 316 | 0.2 | 22.7 | 63.4 | 9.0 | 387.2 |
| Hercynian Corsica | 1606 | 0.2 | 27.8 | 79.2 | 11.2 | 407.2 |

Besides the geological units, another important spatial correlation is the occurrence of knickpoints predominantly at or near fault zones. In Alpine Corsica, knickpoints tend to occur upstream of several fault zones trending 60–70°N that separates the Schistes Lustrés from the Aleria and Marana plains. The knickpoints are also concentrated around the thrust zones in the Castagniccia antiform and along faults parallel to where the Tavignano drainage network flows (see Fig. 3.1 for a detailed location of the Castagniccia antiform and other structures, and Figs. 3.12, and 3.13 for the knickpoints). In Hercynian Corsica, where rock strength is less variable due to the homogenous nature of the mostly intrusive rocks, the knickpoints occur along fault zones. In the Tenda massif, the knickpoints are concentrated along three fault zones. In the Golo and Tavignano rivers, the knickpoints become more abundant and larger upstream of the thrust zone that separates Hercynian and Alpine Corsica, even when flowing on the same rock type (e.g., granitoids). It is upstream of this major thrust zone that the largest knickpoints occur (i.e., the highest 0.7% of values). The drainage network flows parallel to fault zones in both the Golo and Tavignano river sections, as well as in the majority of rivers draining south–westward in Hercynian Corsica. Some rivers that flow perpendicular to the fault zones but within uniform rock type (e.g., watershed # 19 in the extreme south and # 2 in the extreme north) also show a preferential occurrence of knickpoints upstream of the fault zones.

Another important spatial trend is related to the regional drainage divide. In the headwaters of the rivers draining the southern section of the drainage divide (A), the majority of the knickpoints are larger along the eastward flowing rivers than along the rivers flowing to the west (see Fig. 3.15 and the knickpoints closer to the divide in the Figs 3.12, 3.13, and 3.16). This observation is supported by statistical analysis (*t*–test) comparing the metrics of both sides of the drainage divide, showing a statistically significant difference in relief and slope (Table S2).

In the headwaters of the northern section of the drainage divide (B), knickpoints closer to the channel heads of the westward flowing rivers are larger than those at the opposite side flowing to the east. This visual pattern is supported by one of the metrics (slope) through statistical analysis (*t*–test) comparing both sides of the drainage divide but the contrast is not as pronounced as across the southern section of the divide (A) (Table S2). This pattern resembles the drainage divide metrics, where instability was found in the northern drainage divide (B) and a

stable condition in the southern drainage divide (A). Although the statistical analysis (*t*–test) fails to reject that drainage divide has equal means in the northern and southern sections, this pattern is similar to that found by the drainage divide metrics, where the drainage networks in expansion have slightly higher 'Gilbert' (and lower $\chi$) values than those under retraction.

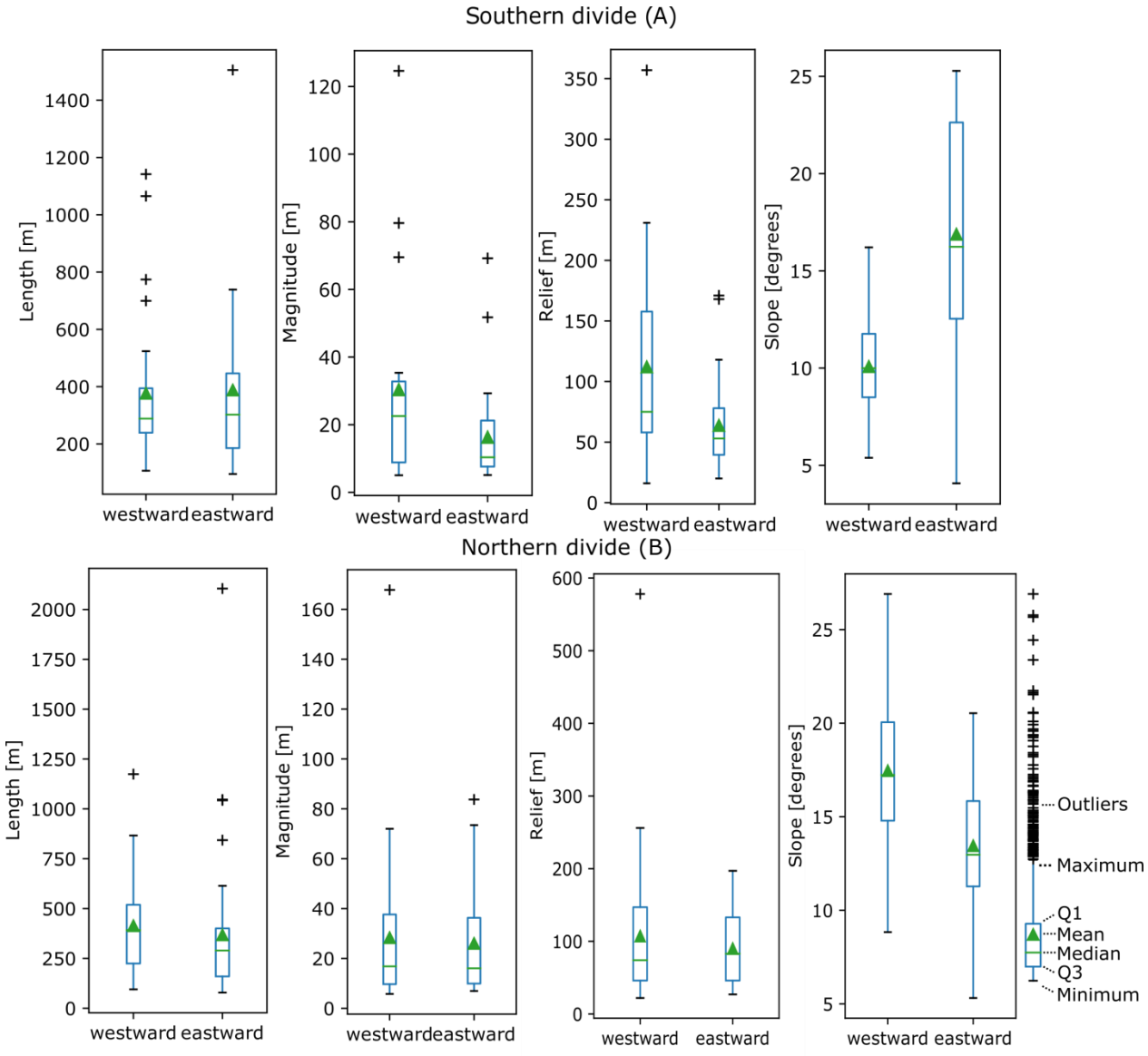


Figure 3.15: Metrics of knickpoints draining westward and eastward from the border of the drainage divide of Corsica. Only the closest knickpoint to each channel head was considered in this analysis. maximum = greatest value, excluding outliers; Q1 = 25% of data greater than this value; Q3 = 25% of data less than this value; minimum = lowest value, excluding outliers. *t*–tests comparing if the means of knickpoints' metrics can be found in the supporting information (Table S2).

The occurrence of large knickpoints is also statistically coincident with the extension of previous Würmian glaciers near the Corsican drainage divide (Fig. 3.1). The knickpoints in the area covered by Würmian glaciers have mean slope and relief greater than the average for Corsica (under 95% of confidence interval; see Fig. 3.16 and Tables S3 and S4 in supporting information). However, the other two knickpoint metrics (i.e., magnitude and length) have means that are statistically undistinguishable from the rest of the Corsica. In the area glaciated during the Würm, I found ~ 0.4 knickpoints/km$^2$, which is approximately twice the density in the Schistes Lustrés and Hercynian Corsica units, and four times that in the Aleria and Marana plains.

Thermochronological domains represent areas with different exhumation histories, which may be reflected in the characteristics of the knickpoints. Except for slope, I have not identified any statistically significant correlation between knickpoints' metrics and both apatite fission–track (AFT) ages and domains compiled from other studies (Fig. 3.17 and Table S4). On the contrary, zircon fission–track (ZFT) age domains 1 (244 to 147 Ma), 2 (120 to 58 Ma) and 3 (45 to 12 Ma) have means of metrics that are statistically different (with 95% of confidence), except for length (Table S4). This can potentially be related to the rough correlation between ZFT domains and the main three geological units that make up Corsica (Fig. 3.1).

Finally, I analyse the frequency of all identified knickpoints' horizontal distance from the rivers' outlets, which in Corsica are at the coast (Fig. 3.18).

The knickpoints over the Alpine Corsica also have three distance peaks but at ~ 15, 25 and 55 km from the sea level, with the largest peak ~ 25 km (Fig. 3.18-A).The knickpoints over the Hercynian Corsica have three distance peaks at ~ 20, 35 and 65 km from the sea level, with the largest peak at ~ 20 km (Fig. 3.18-B). Most knickpoints are within 40 –50 km of the coast, which may reflect the typical length of Corsican river systems, with very few knickpoints 40–50 km from the coast.

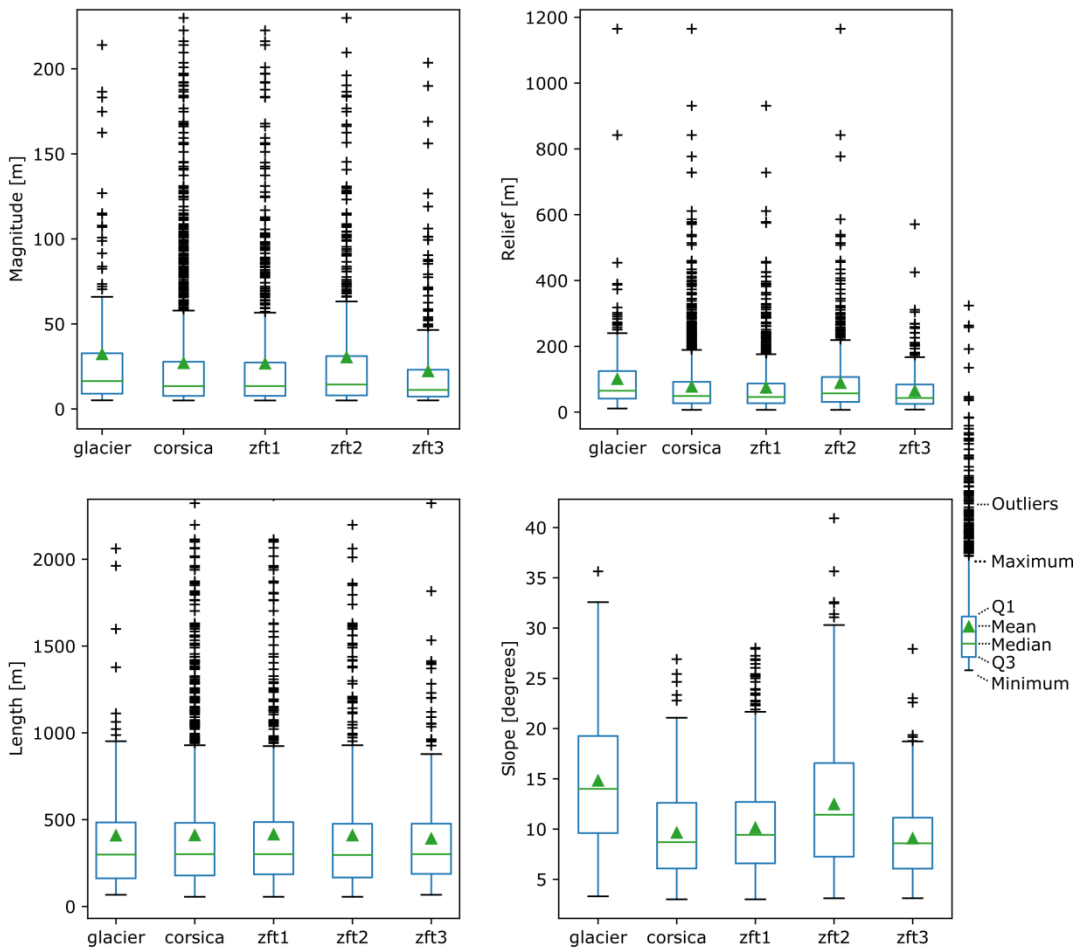


Figure 3.16: Metrics of knickpoints' are compared to the previous Würmian glaciers, apatite (AFT) and zircon fission–track (ZFT) domains compiled from the works of Cavazza et al. (2001), Zarki–Jakni et al. (2004), Fellin et al. (2005) and Danišík et al. (2007). These domains are displayed in the Figure 3.2A and C. The extension of the Würmian glaciers in Corsica follows the mapping of Kuhlemann et al. (2005b) displayed in the Figure 3.1. The ages were extracted from the figure Figure 3.2 using the function extract data to point in ArcGIS. *t*–tests comparing if the means of knickpoints' metrics can be found in the supporting information (Table S4).

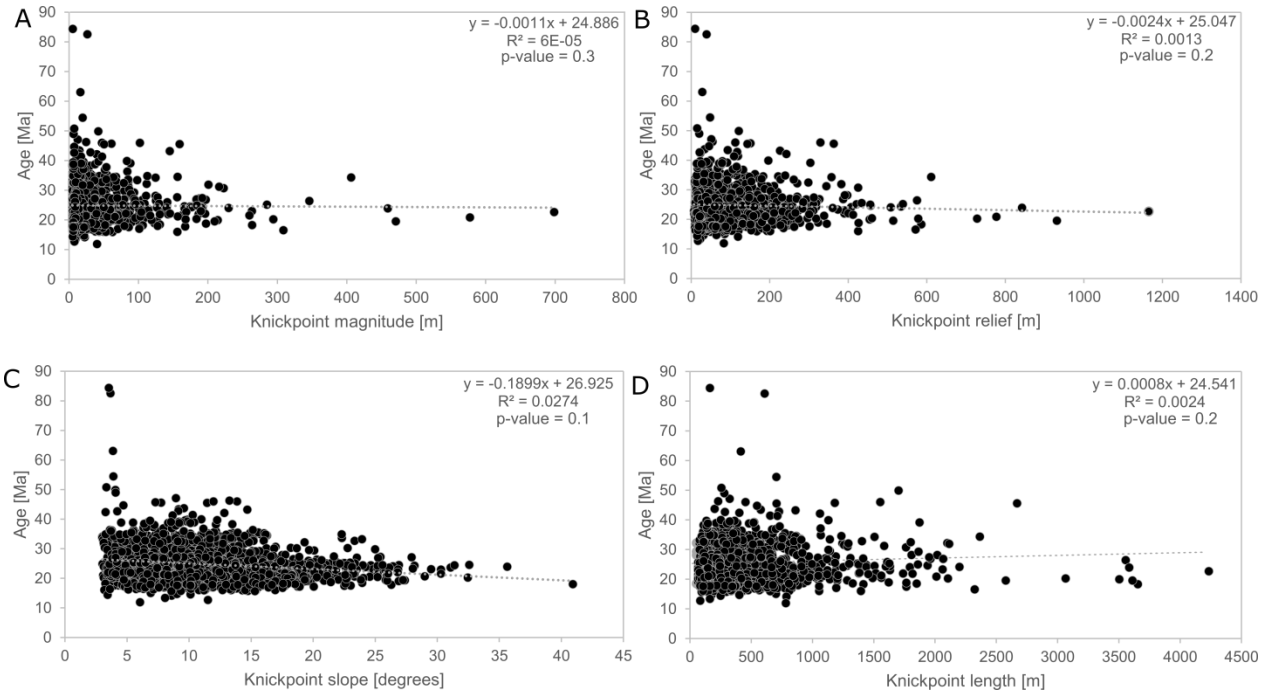


Fig. 3.17: Regression analysis performed with knickpoints' metrics and apatite–fission track (AFT) ages presented in Figure 3.2B (extrapolated from point data). Coefficient of determination ($R^2$) is extremely low, showing no correlation between age and any metric under investigation. The AFT ages were extracted from the figure Figure 3.2B using the function extract data to point in ArcGIS. Note that the uncertainty of the AFT ages was not considered in this work but can be found in the work of Danišík et al. (2007).

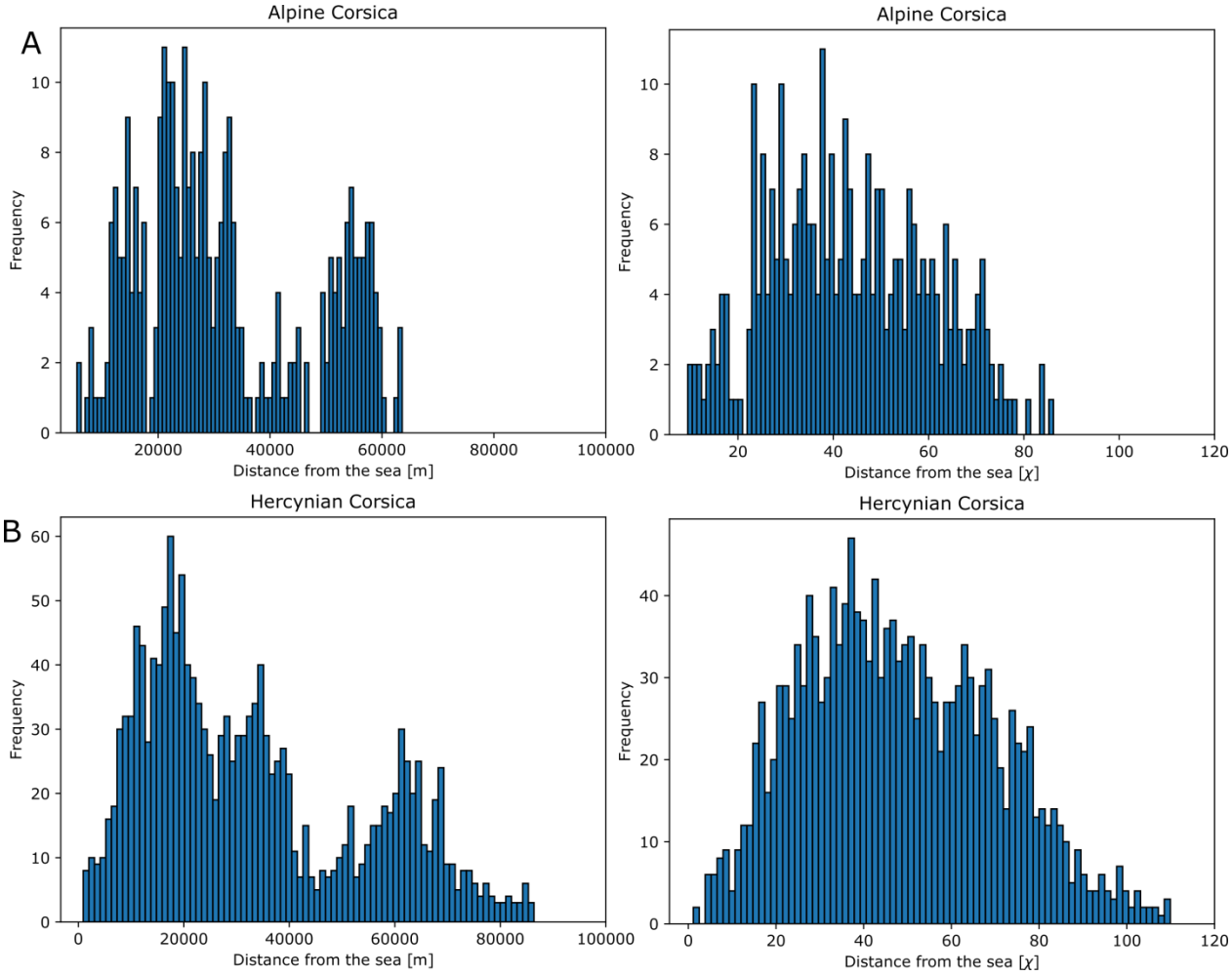


Fig. 3.18: Frequency of knickpoints' distance from the coast (in χ and m), for all knickpoints over the Alpine Corsica units (A) and Hercynian Corsica units (B). The distance from rivers' outlets was binned in 80 intervals to produce the frequency plots. Note that the largest peaks are slightly different in the Hercynian (~ 20 km and 36 χ), and Alpine Corsica units (~ 25 km and 36 χ).

### *3.4.2.2. River steepness, structures and rock types*

The χ map shows changes in river steepness over all draining sides of Corsica (Fig. 3.19 and 3.20).

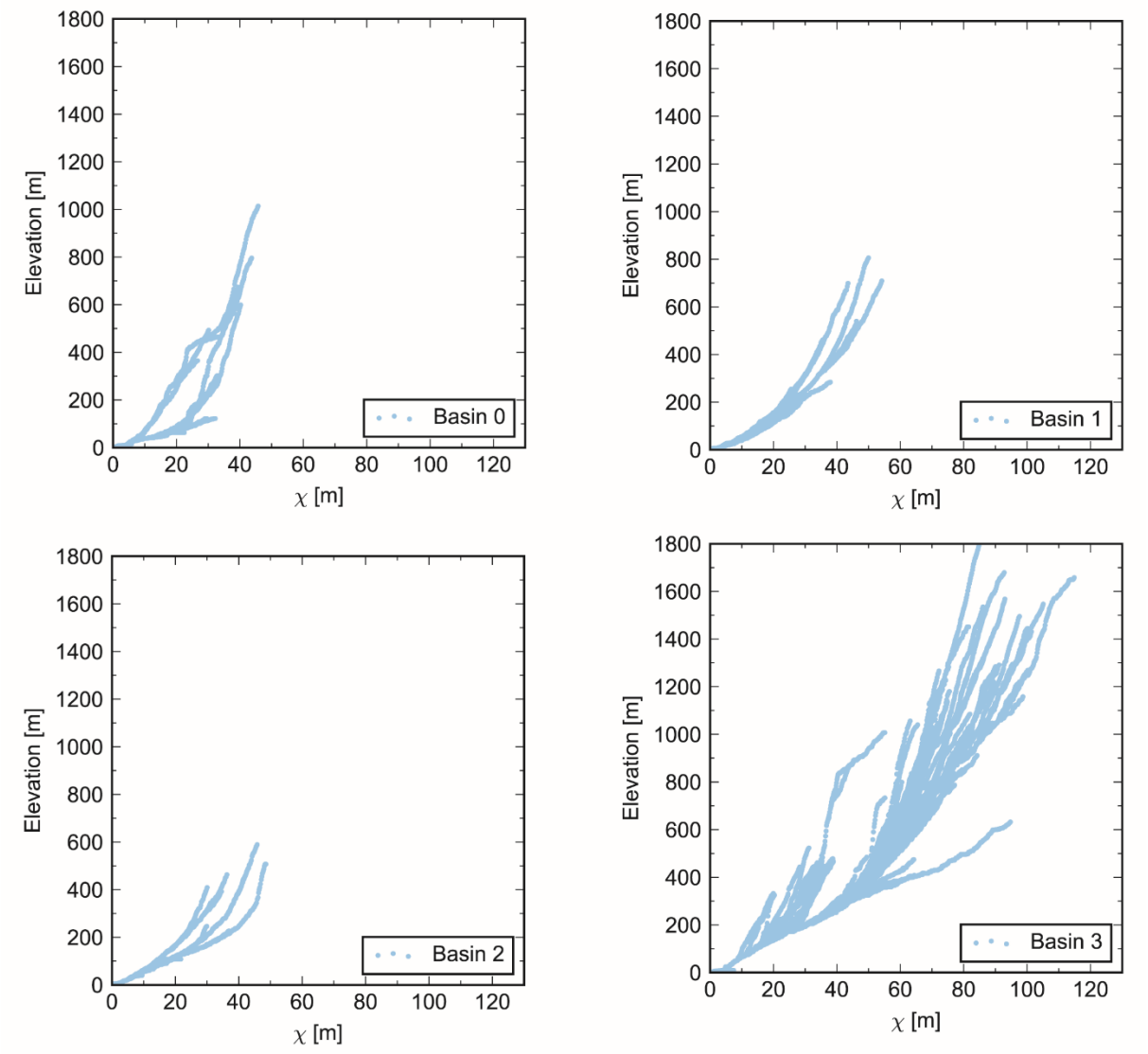
Elevation [m]
χ [m]
Basin 0
Basin 1
Basin 2
Basin 3

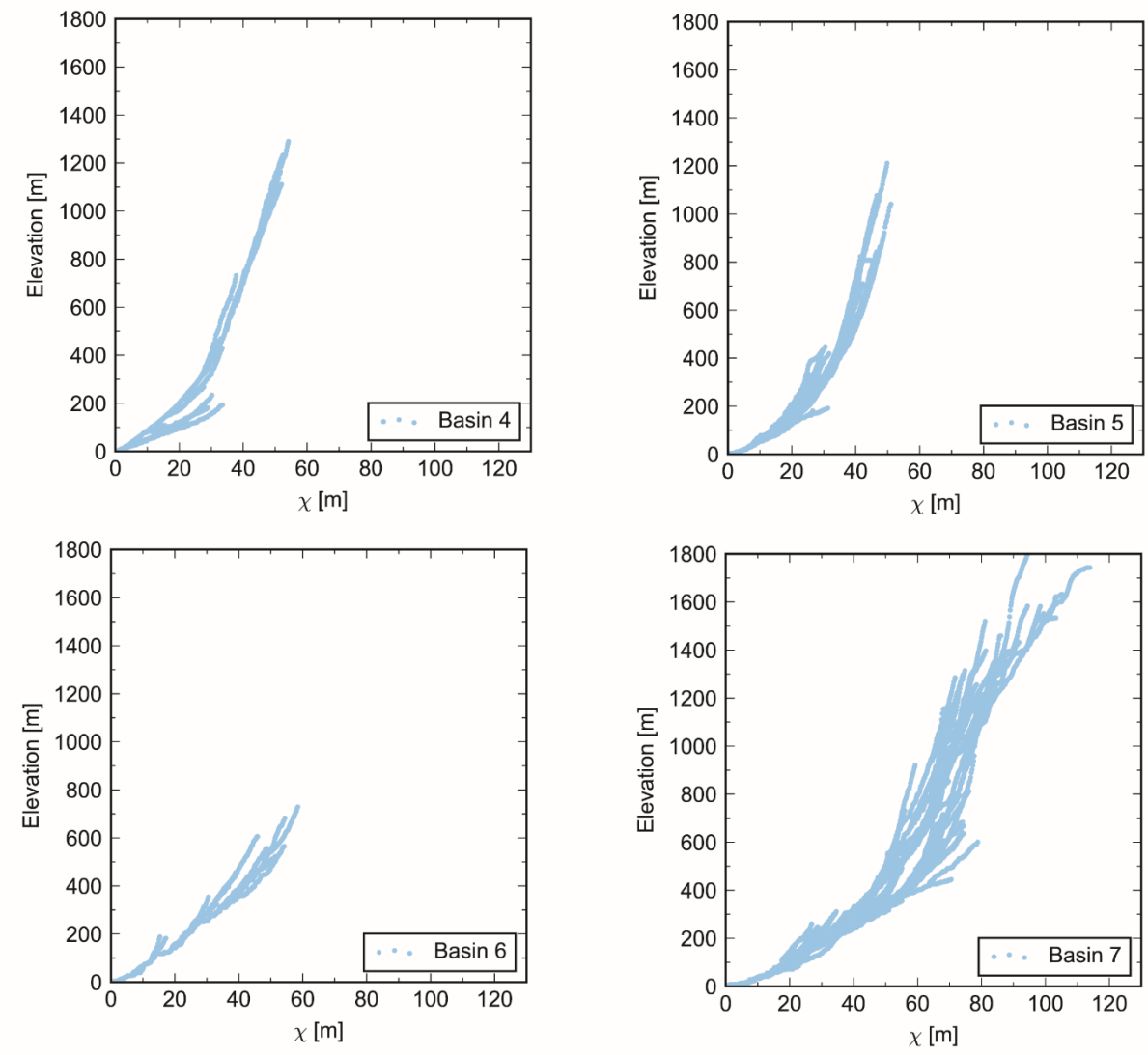
Elevation [m]
χ [m]
Basin 4
Basin 5
Basin 6
Basin 7

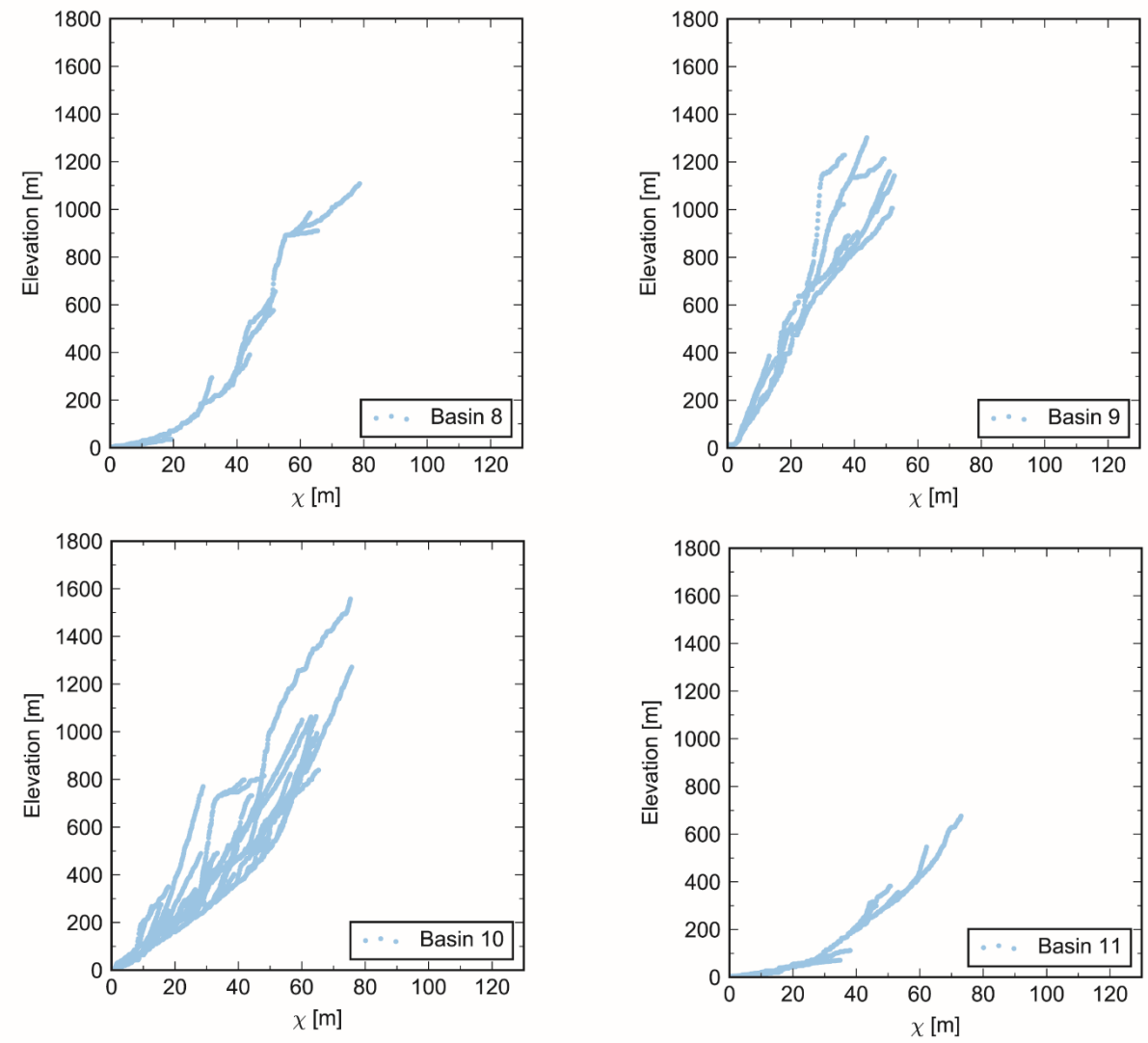
Elevation [m]
χ [m]
Basin 8
Basin 9
Basin 10
Basin 11

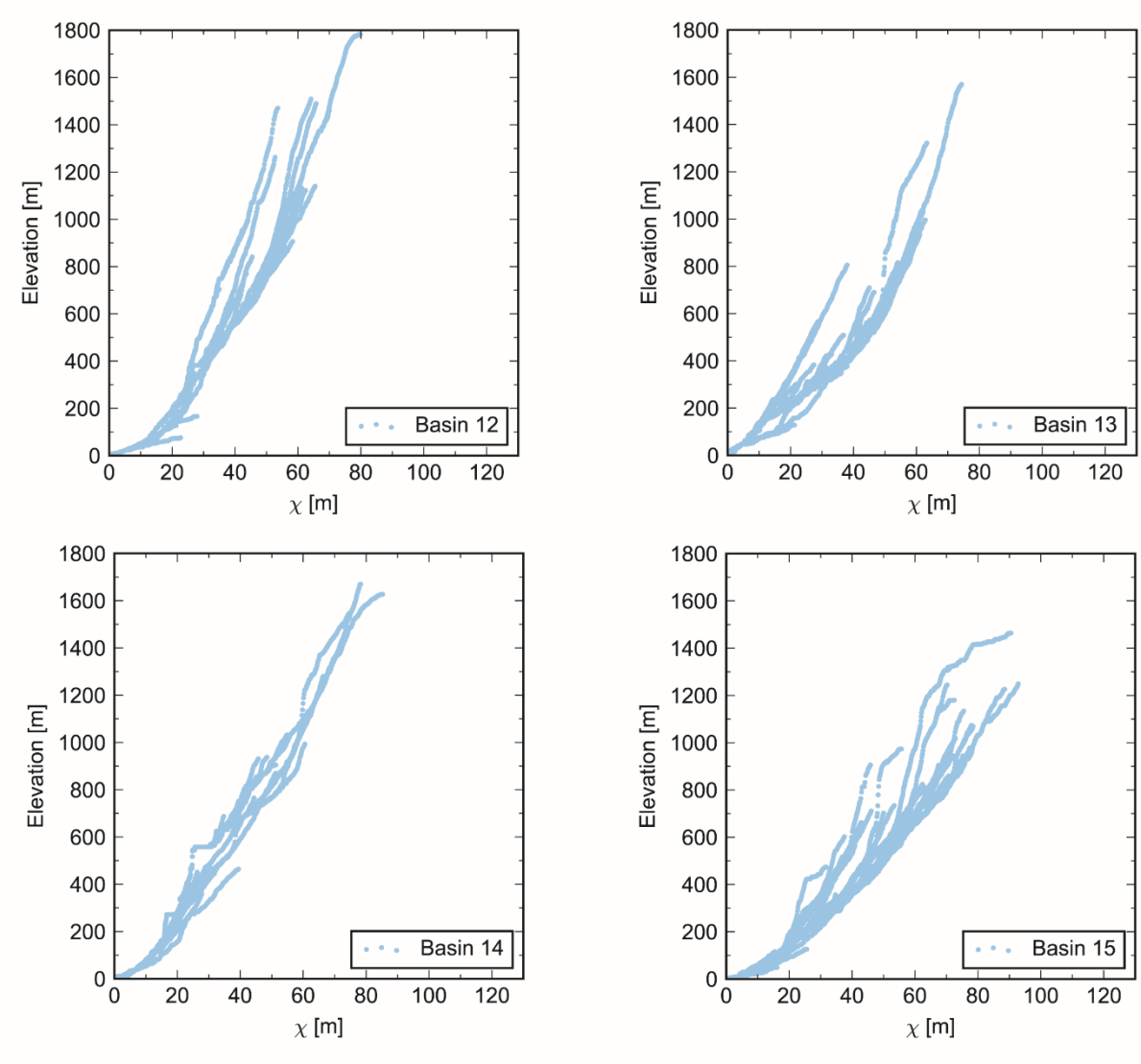
Elevation [m]
χ [m]
Basin 12
Basin 13
Basin 14
Basin 15

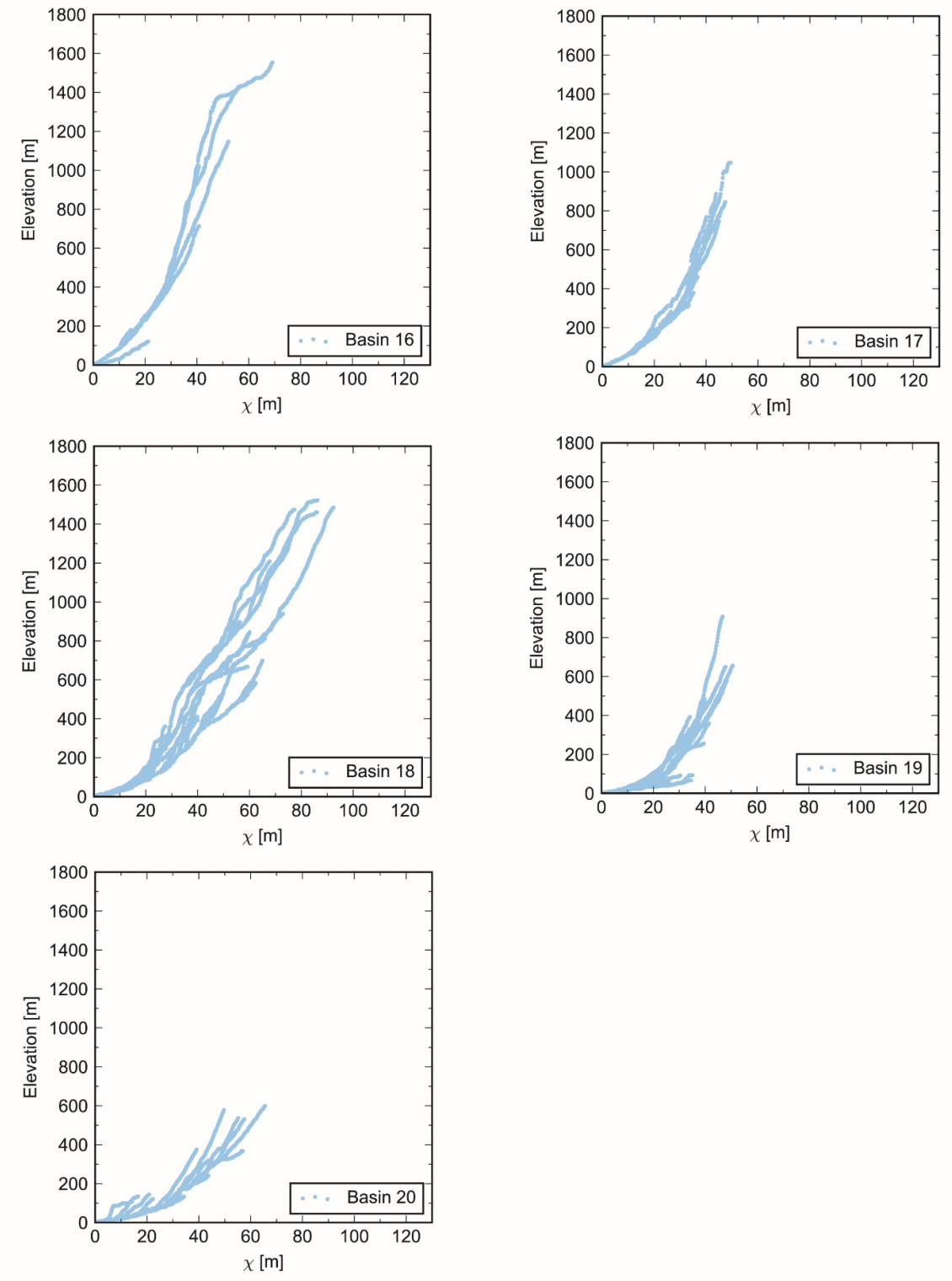


Figure 3.19: The χ river long–profiles of complete watersheds in Corsica. All the plots were generated using a concavity index (m/n) of 0.35.

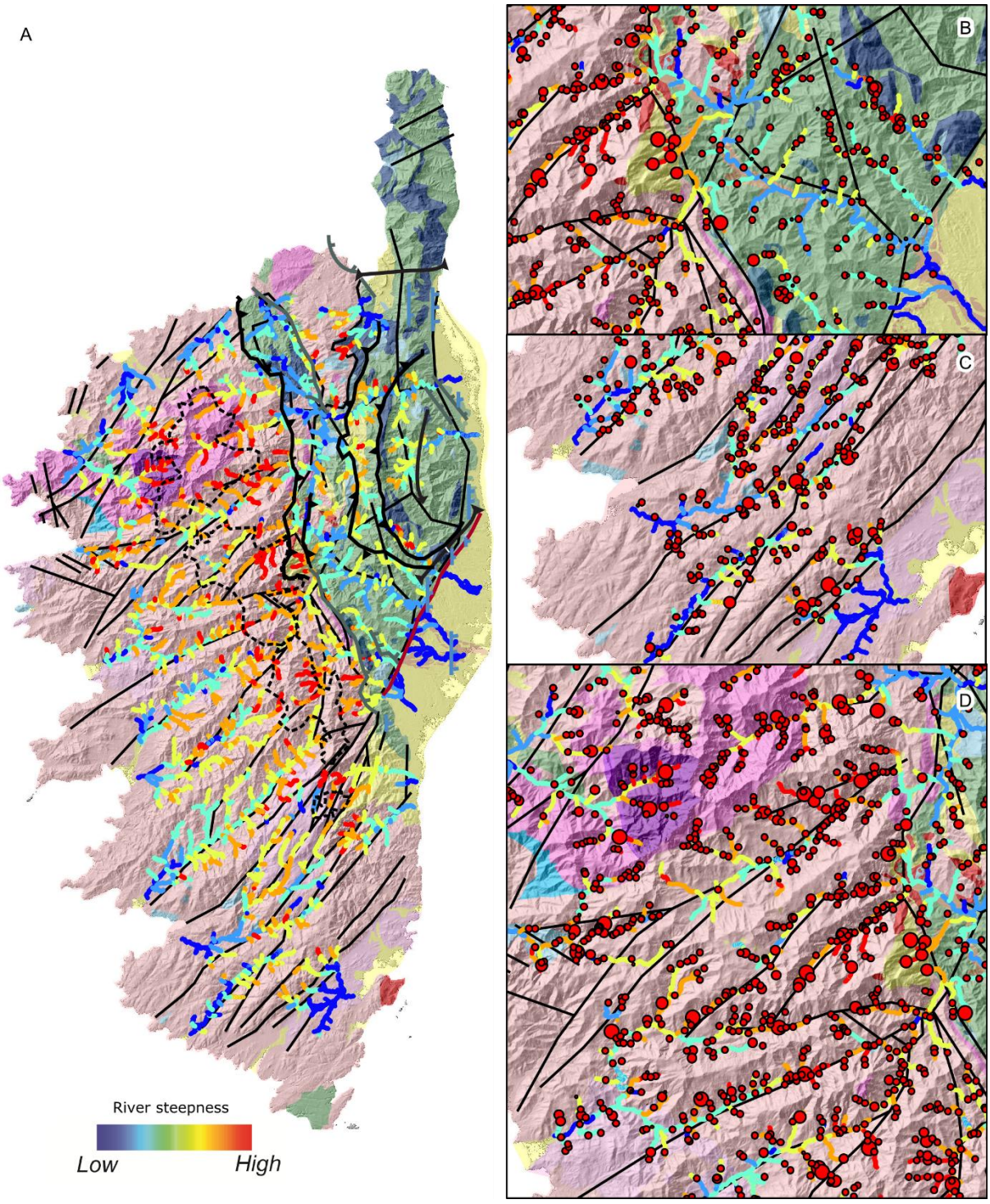


Fig. 3.20: River steepness ($k_{sn}$) map showing correlation (or lack of) between reaches of varied steepness and rock types, structures (e.g., fault zones), and the occurrence of knickpoints (circles). Background colours indicate geology whereas stream colours indicate steepness. The subplots B, C and D are zoomed

areas of interest from Corsica. The subplot B shows how the knickpoints are located at the structural and lithological boundaries of Hercynian and Alpine Corsica units. It also shows how the magnitude of knickpoints and river steepness change from the Aleria plain (in yellow) to the Alpine units (in green), and, finally, to the Hercynian Corsica. The subplot C shows how structural boundaries control the spatial distribution of knickpoints and the occurrence of low and high river steepness values. The subplot D shows that the main rivers in the Hercynian Corsica overlap the structural boundaries.

All watersheds have changes in river steepness that spatially correlate to rock types, which may undermine the method based on χ–anomalies to assess the stability of drainage divides (Fig. 3.20A and B). Some of the changes in river steepness also correlate to structural boundaries, where knickpoints occur at the contact or upstream (Fig. 3.20C and D). An important observation is that, for the m/n ratio used ($m/n$ = 0.35, see Fig. 3.6), almost all rivers show anomalously steep headwaters and anomalously low gradient reaches near their outlet. The $k_{sn}$ values tend to overall decrease downstream, but it is important to note that this is, in many cases, associated with lithological changes (e.g., east draining rivers originating in the Hercynian basement, cutting through the Schistes Lustrés and crossing the Aleria –Marana plains before reaching the sea).

A quantitative analysis of the river steepness ($k_{sn}$) shows a clear relation with rock types (Fig. 3.21A). Granitoids (i.e., granite, granodiorite), pyroclastites and rhyolites have relatively the highest river steepness averages ($k_{sn}$ = 18±3, 25±3 and 22±3, respectively) and the largest amount of outliers (ranging from $k_{sn}$ = 50 to 110). Clastic sedimentary rocks (conglomerate and sandstone), mafic/ultramafic (gabbro, gabbro–diorite, serpentinite, peridotite) and other volcanics (e.g., ignimbrite) have intermediate values of river steepness ($k_{sn}$ = 18±2, 18±2 and 10±1, respectively), and a relatively high amount of outliers (ranging from 40 to 70). The lowest river steepness values are found in the unconsolidated sediments (marl, sand and gravel) of the Aleria and Marana plain (depositional setting), as well as in the Schistes Lustrés formation (limestone, schist and breccia), with mean $k_{sn}$ = 8±1 and 10±2, respectively, and a relatively high amount of outliers (ranging from 20 to 50).

A quantitative analysis of river steepness ($k_{sn}$) also shows a relation with the watershed where they belong (Fig. 3.21B). Although east and westward draining watersheds have both a very large spread range of values, some have a less dispersed distribution around the mean (e.g., basins 6 and 20), while others have a large number of outliers (e.g., basins 7, 9 and 15). There is no correlation with basin size, as watersheds with a large amount of outliers include some of the shortest watersheds (e.g., 9) and some of the longest ones (e.g., basins 3, 7 and 15). In all cases of

intermediate and large spread of values, the watersheds are crosscut by fault zones and are made of contrasted rock type; this is observed across both Hercynian and Alpine Corsica units, highlighting again the strong lithological control.

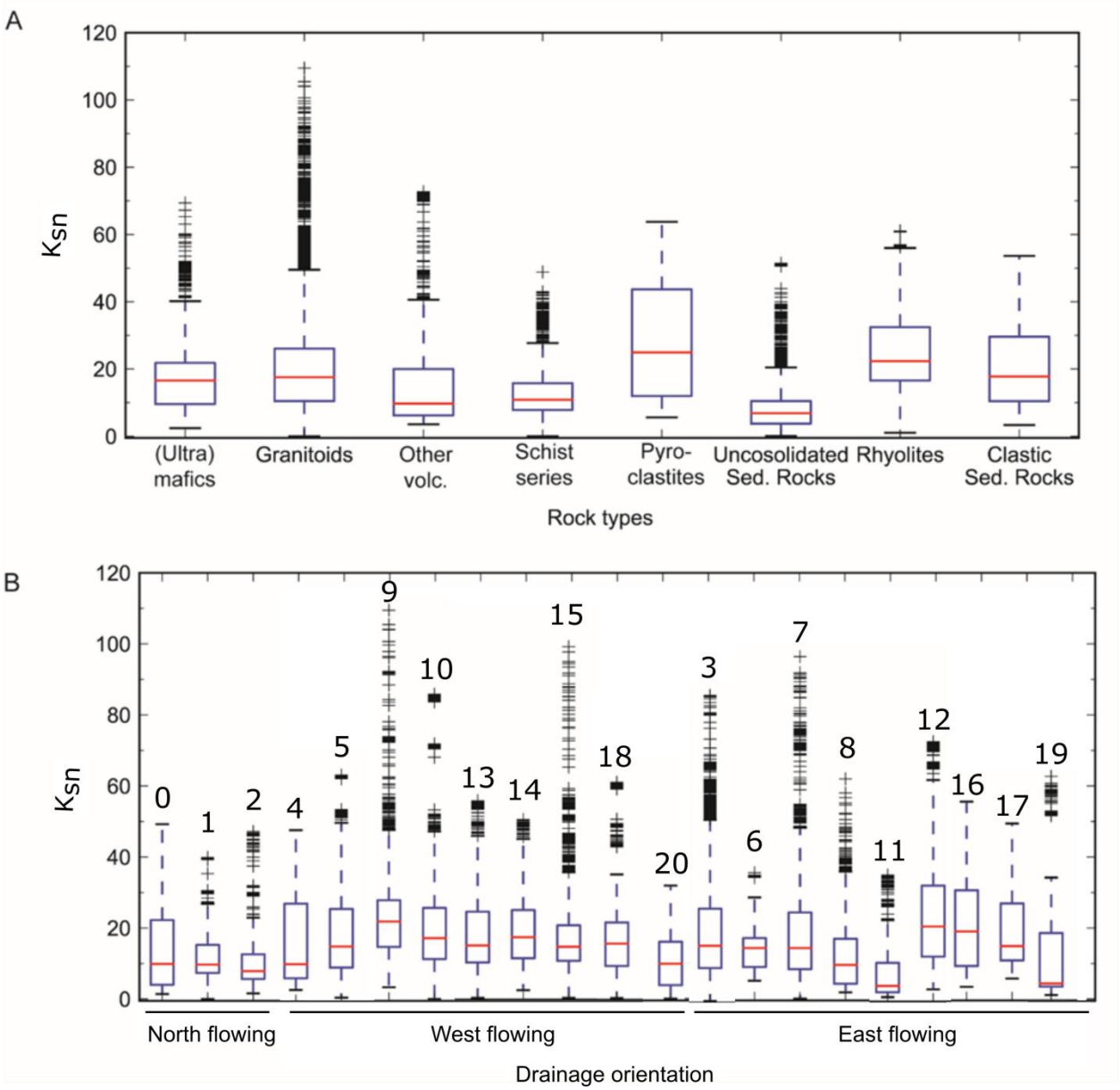


Figure 3.21: Boxplots showing how the river steepness ($k_{sn}$) varies according to rock type (A) and watershed (B). The Hercynian Corsica units comprise granitoids, other volcanics, rhyolites, pyroclastities and ultra–mafics. The Alpine Corsica units comprise Schist series and other clastic sedimentary rocks. The Aleria plain comprises unconsolidated sedimentary rocks. The red line in the boxplots represents the median; lower quartile in the box represents the limit of 25% of values lower than the median; the upper quartile in the box represents the limit of 25% of values higher than the median; the upper and lower whiskers represent values that are beyond the 50% of the values; the crosses are outliers, which are 1.5

times of upper quartile. The boxplots are grouped according to their drainage orientation (northward, eastward and westward flowing rivers). The numbers at the top of the box plots are the basin numbers presented in the Figure 3.4.

### *3.4.2.3. Sediment grain size along Corsican rivers*

The grain size distribution of river sediments shows two distinct patterns when the surface and subsurface gravel bars are analysed (Fig. S1 in the supporting information). I find that the subsurface gravel bars do not show obvious sensitivity to changes in river steepness and to the outcropping lithologies. This is in contrast with the surface sediment, especially with their mean diameter ($D_{50}$). In the Fango watershed, there is a downstream fining trend in the surface gravel bars analysed, with $D_{50}$ decreasing from 7.1±0.5 to 5.7±0.8 ψ, which is accompanied by a steady decrease in river steepness ($k_{sn}$) (Fig. 3.22C). However, the Liamone, Taravo and Tavignano watersheds show some increases in river steepness ($k_{sn}$) and sediment coarsening (Fig. 3.22A, B and D).

In the Tavignano, downstream coarsening associated with peaks in river steepness is observed in the upper half of the catchment, whereas the lower half show a clear downstream fining associated with a progressive reduction in channel steepness (Fig. 3.22A–B). In the Tavignano watershed, a $D_{50}$ coarsening from 6.8±0.4 to 7.5±0.6 ψ occurs after a change in river steepness from 50 to 90 $k_{sn}$ (between 70 and 55 χ[m]). In the Taravo watershed, the $D_{50}$ changes from 8.0±0.5 to 9.0±0.6 ψ after a river steepness peak of $k_{sn}$ = 50 to 100 and then it gets coarser downstream (between 0 and 30 χ[m), despite a steady decrease in river steepness from 30 to 0 $k_{sn}$. In the Liamone, a downstream fining trend is marked by coarsening after a peak in river steepness, with $D_{50}$ coarsening from 8.0±0.6 to 8.5±0.4 ψ (between 50 and 35 χ[m]) and 7.0±0.5 to 7.5±0.5 ψ (between 32.5 and 20 χ[m]) in two reaches after a river steepness change from 50 to 70 $k_{sn}$ and 50 to 85 $k_{sn}$, respectively.

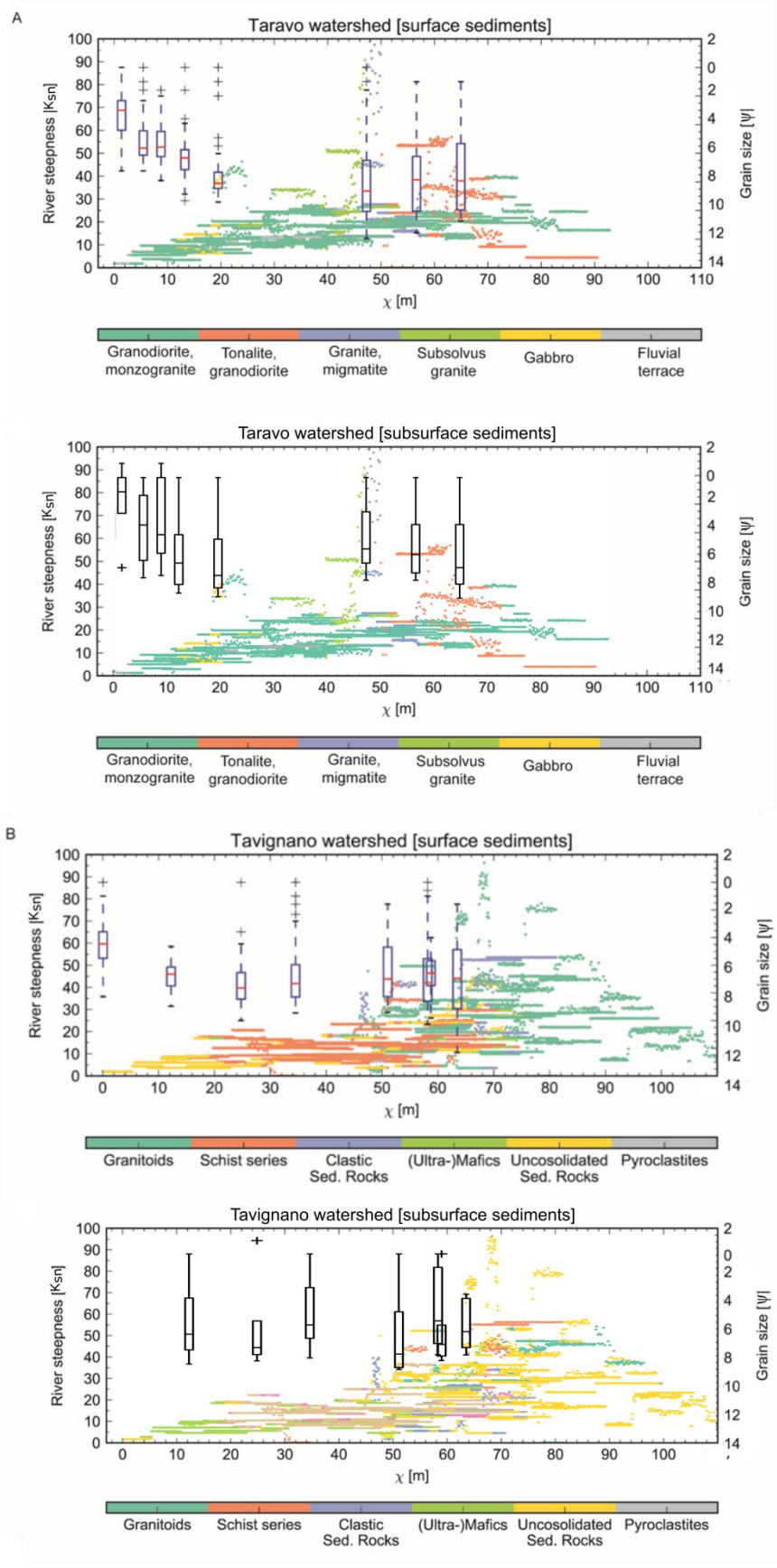
A
Taravo watershed [surface sediments]
River steepness [Ksn]
Grain size [ψ]
χ [m]
Granodiorite, monzogranite
Tonalite, granodiorite
Granite, migmatite
Subsolvus granite
Gabbro
Fluvial terrace
Taravo watershed [subsurface sediments]
River steepness [Ksn]
Grain size [ψ]
χ [m]
Granodiorite, monzogranite
Tonalite, granodiorite
Granite, migmatite
Subsolvus granite
Gabbro
Fluvial terrace
B
Tavignano watershed [surface sediments]
River steepness [Ksn]
Grain size [ψ]
χ [m]
Granitoids
Schist series
Clastic Sed. Rocks
(Ultra-)Mafics
Uncosolidated Sed. Rocks
Pyroclastites
Tavignano watershed [subsurface sediments]
River steepness [Ksn]
Grain size [ψ]
χ [m]
Granitoids
Schist series
Clastic Sed. Rocks
(Ultra-)Mafics
Uncosolidated Sed. Rocks
Pyroclastites

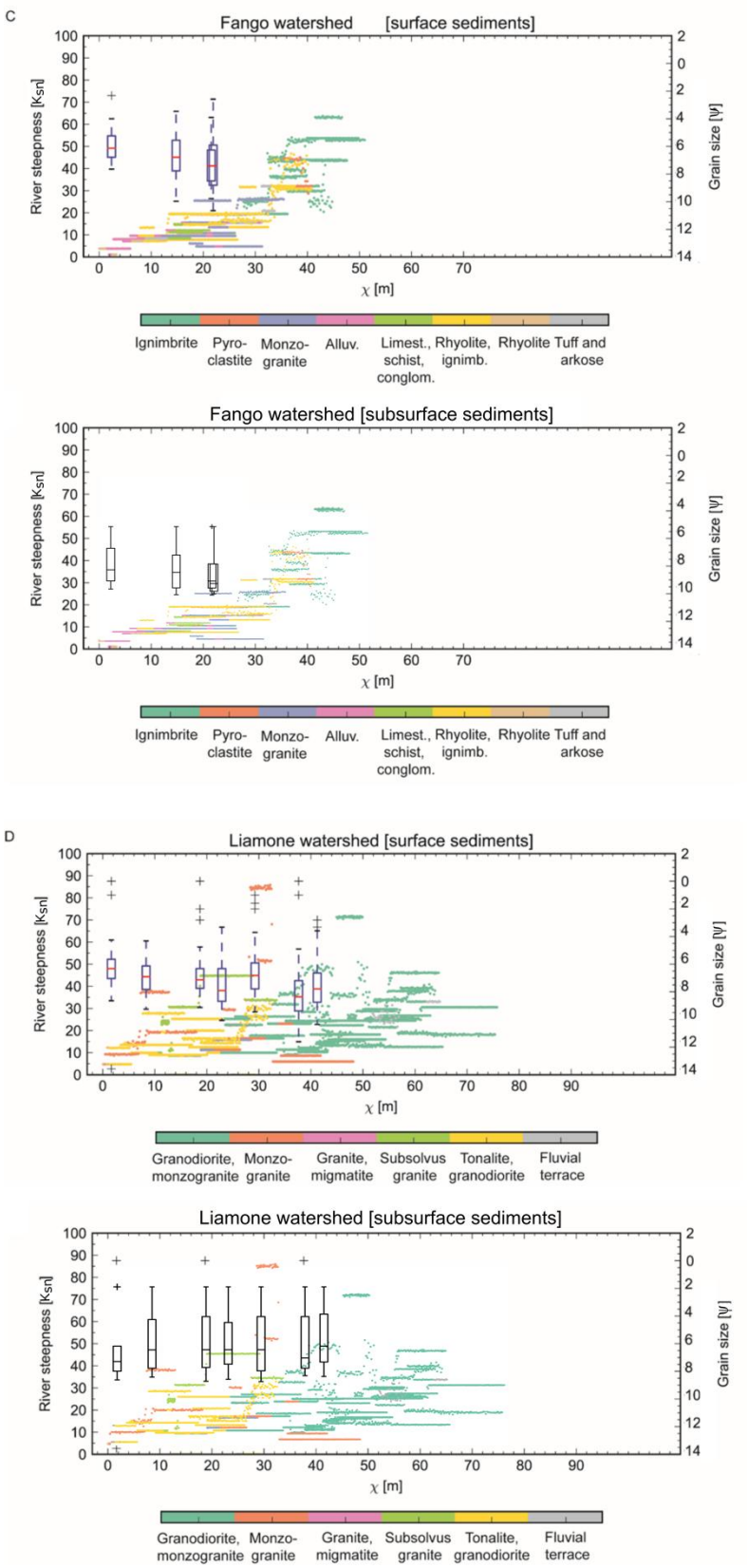
C
Fango watershed [surface sediments]
River steepness [Ksn]
Grain size [Ψ]
χ [m]
Ignimbrite
Pyro-clastite
Monzo-granite
Alluv.
Limest., schist, conglom.
Rhyolite, ignimb.
Rhyolite
Tuff and arkose
Fango watershed [subsurface sediments]
River steepness [Ksn]
Grain size [Ψ]
χ [m]
Ignimbrite
Pyro-clastite
Monzo-granite
Alluv.
Limest., schist, conglom.
Rhyolite, ignimb.
Rhyolite
Tuff and arkose
D
Liamone watershed [surface sediments]
River steepness [Ksn]
Grain size [Ψ]
χ [m]
Granodiorite, monzogranite
Monzo-granite
Granite, migmatite
Subsolvus granite
Tonalite, granodiorite
Fluvial terrace
Liamone watershed [subsurface sediments]
River steepness [Ksn]
Grain size [Ψ]
χ [m]
Granodiorite, monzogranite
Monzo-granite
Granite, migmatite
Subsolvus granite
Tonalite, granodiorite
Fluvial terrace

Figure 3.22: River steepness ($k_{sn}$) and surface grain size distribution (boxplots) of the surface sediments collected in gravel bars along $\chi$ distance (m) of the main stem. A, B, C and D are from Taravo, Tavignano, Fango and Liamone watersheds, respectively. The bedrock types are from Rossi et al. (1994 a, b). The red line in the boxplots represents the median; the lower quartile in the box represents the limit of 25% of values lower than the median; the upper quartile in the box represents the limit of 25% of values higher than the median; the upper and lower whiskers represent values that are beyond the 50% of the values; the crosses are outliers, which are 3/2 times of upper quartile.

A more diverse pebble material is observed in the surface than in the subsurface gravel bars of all analysed watersheds (Fig. 3.23). A comparison between source area and pebble rock type is not possible for the Taravo and Liamone watersheds because their sources have a coarser mapping resolution than the pebble rock type identification undertaken during this study. For instance, in the Taravo watershed, only two mapped units are identified as sources (e.g., granodiorite with tonalite and granodiorite with monzogranite) but up to eight pebble rock types are found (e.g., schist, rhyolite, granite, granodiorite, dacite, diorite and basalt). In the Liamone, there are also two mapped sources, but up to seven different pebble rock types identified in the gravel bars. Either geological mapping is too coarse, or past glaciers may have shifted lithologies across divides. On the other hand, the Tavignano watershed shows how different rock strengths impact the population of sediments. Schistes Lustrés represents 68% of the source area at the Tavignano outlet, but only 30% of the material coarser than sand in the surface gravel bars comes from this unit (Fig. 3.23A). This effect is also visible at two sampling sites upstream, where ~ 75% and 48% of the catchment is made of Schistes Lustrés but only ~ 10% and 22% of sub-surface sediment coarser than sand in the surface gravel bars comes from this formation.

Analysing the grain size also reveals that some rock types are in specific ranges (Fig. S2 in supporting information). Pebbles made of granite are found in a larger range of sizes than other rocks from Hercynian Corsica (e.g., rhyolite, basalt, diorite, andesite, dacite, and gabbro) in the Liamone and Taravo watersheds. In the Fango, rhyolite has a larger range of sizes than granite but is overall slightly finer. Quartz is primarily found in sizes approaching sand fraction, consistent with disintegration of quartz–bearing lithologies including granite. Granite is also generally coarser than supracrustal rocks (e.g., sandstone, conglomerate and schist) in the majority of cases. Specifically in the Tavignano, the largest pebbles found at two sampling sites are made of conglomerate, although granite has the largest average size and range of occurrence

than others. Schist has similar range and average size of granite at two sampling sites in the Tavignano but it is overall finer and shorter in terms of size range than granite in all the other sampling sites of this watershed.

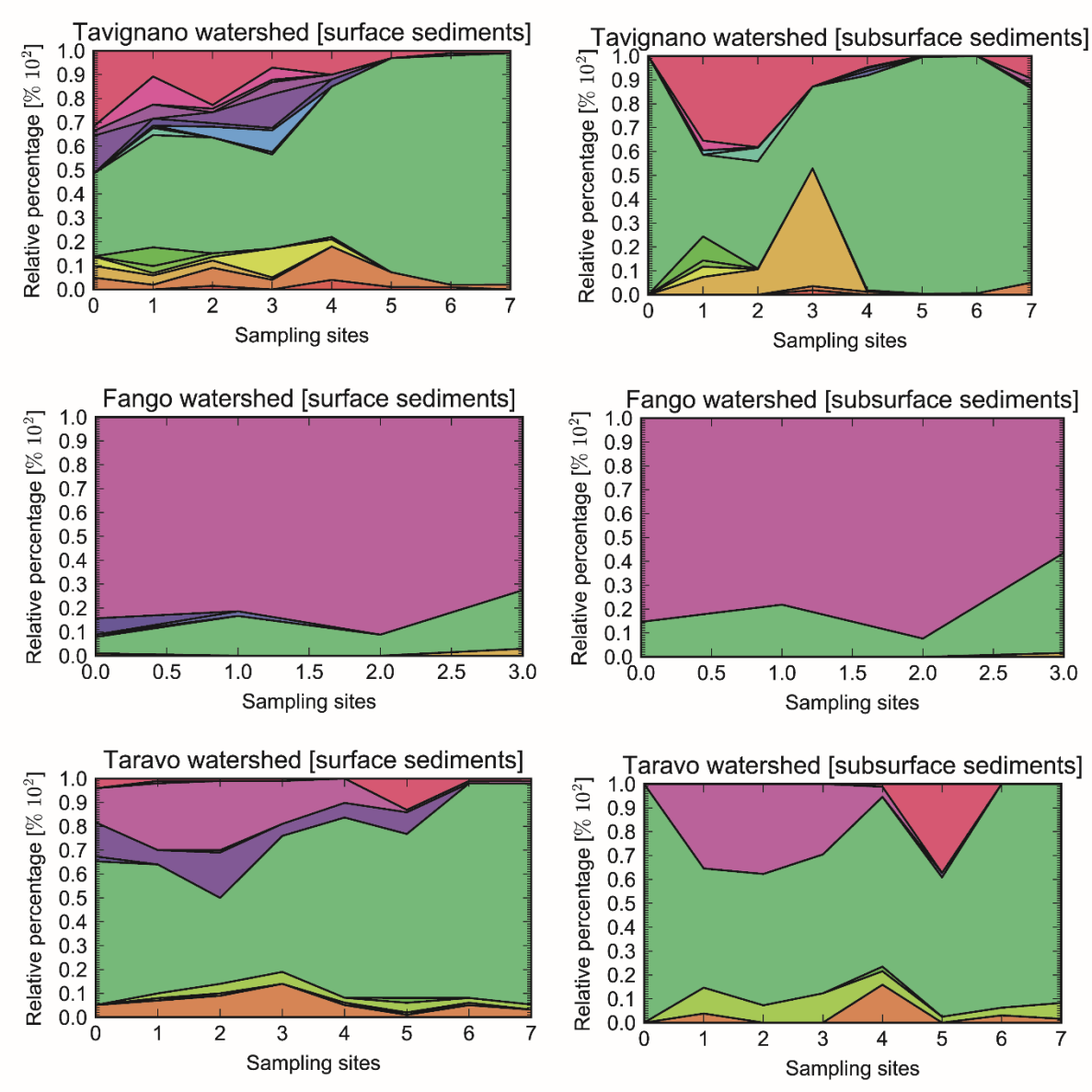

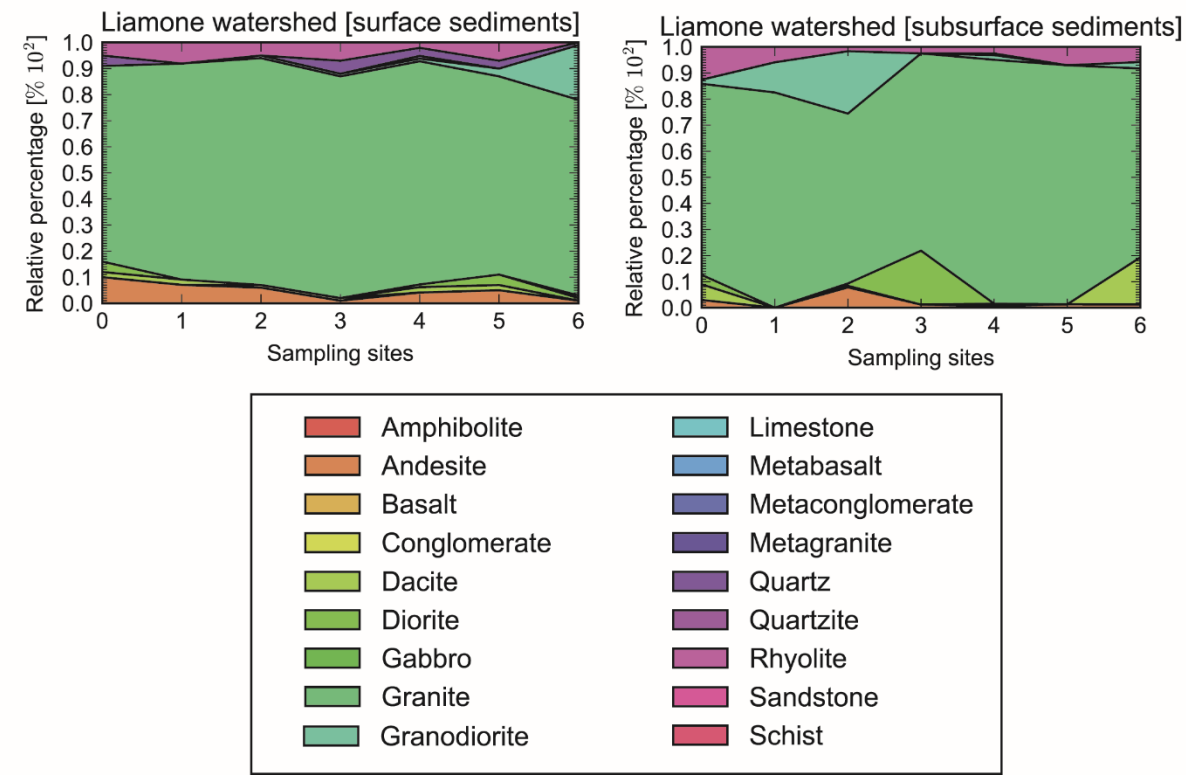


Figure 3.23: Relative percentage of rock type at the surface and subsurface of the gravel bars analysed in Corsica. The sampling sites numbers decrease downstream (i.e., headwaters are to the right and catchment outlet to the left). For a detailed description of the percentage of material identified and other characteristics of the gravel, please see the Fig. S4 in supporting information.

Bivariate analysis of river steepness ($k_{sn}$) and grain size (ψ) per lithology of surface gravel bars (which are the most sensitive to $k_{sn}$ variations, as shown in the Figs. 3.22 and 3.23) does not show any statistically significant correlation but still reveals interesting patterns that can be associated to rock strength (Fig. 3.24). Among all rock types, granite has the largest range of pebble sizes (from 10 to 2 ψ) and, at the same time, the second largest range of river steepness values (from $k_{sn}$ = 0 to 200) after rhyolite. For the other Hercynian Corsican rock types, the range of sizes decreases from rhyolite (10 to 4.0 ψ) to granodiorite (11 to 6 ψ), and approaches the shortest ranges in gabbro (7.8 to 5 ψ), which mirrors the trend in river steepness ($k_{sn}$ = 15 to 300, 0 to 220 and 10 to 180, respectively). The supracrustal rocks of Alpine Corsica units have an even smaller distribution of sizes, with values changing from conglomerate (8.8 to 3.8 ψ) to schist (9 to 3 ψ), and approaching the shortest range of all rock types in limestone (8 to 4.1 ψ). This trend is also followed by river steepness ($k_{sn}$ = 0 to 180, 5 to 100 and 0 to 80, respectively).

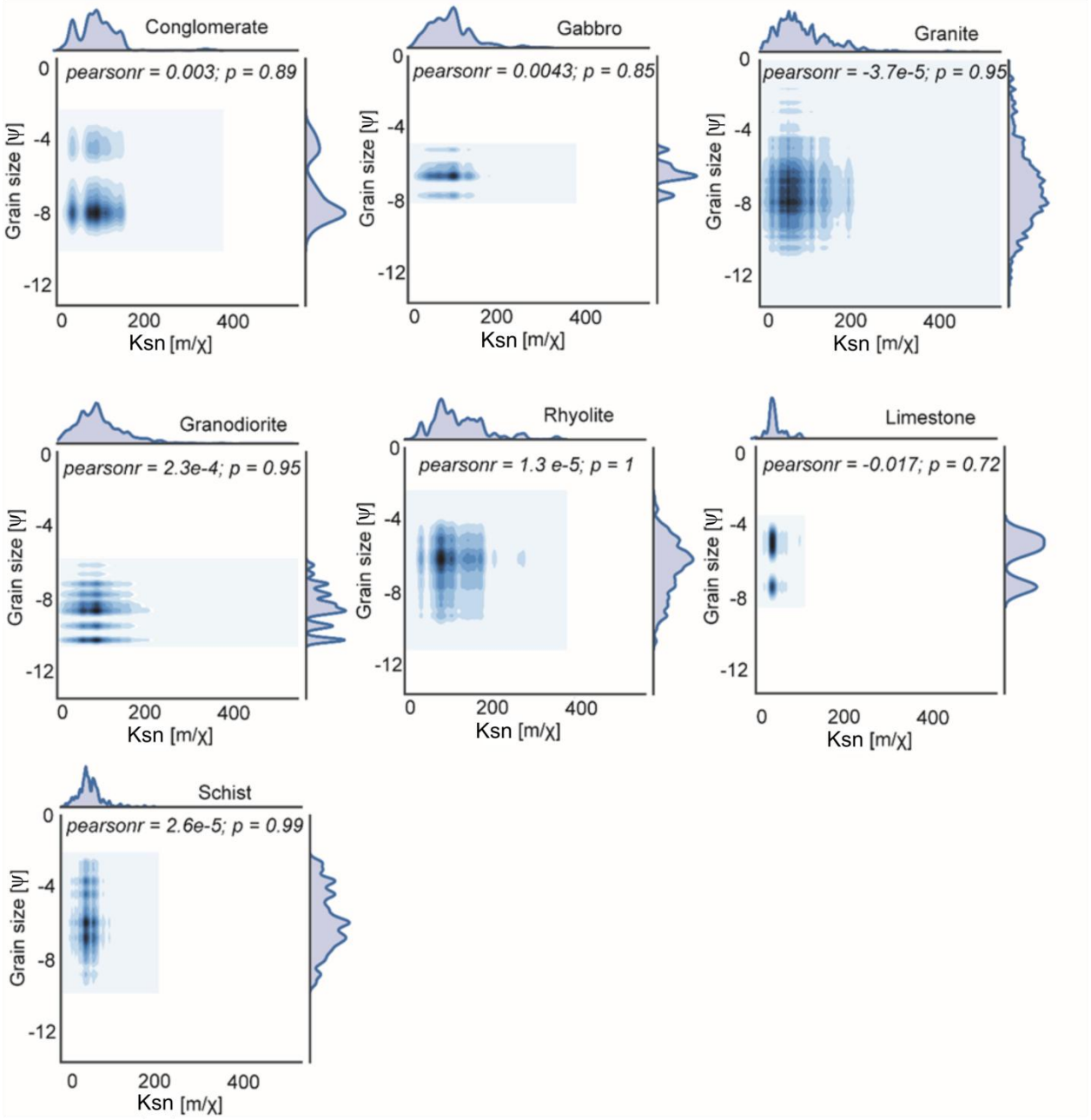


Figure 3.24: Bivariate analysis of grain size (φ) and river steepness ($k_{sn}$) per rock type. The population of values are probability density functions (PDFs) of $k_{sn}$ in the top and grain size in the right side. The frequency of each PDF is plotted in a blue scale, creating a density pattern. The frequency (density) of each value in this bivariate analysis is highlighted, so deeper blue represents a denser value than lighter ones. These PDFs were used as variables in the Pearson's correlation coefficient, so a coefficient approaching pearsonr = 1 indicates a perfect regression between grain size (ψ) and river steepness ($k_{sn}$). In this case (of pearsonr = 1), an increase in grain–size would be followed by a similar increase in river steepness. However, in our results, the Pearson's correlation coefficient is too low and does not show any

statistically significant correlation, although the distribution of grain–sizes and river steepness still varies according to the rock types. For instance, note the variation in the $k_{sn}$ and ψ of limestone and granite.

## 3.5. Discussion

Our analysis of a range of topographic metrics and sediment characteristics, and their relationship with geological units and structure, allow us to make a series of conclusive remarks regarding the topographic state of Corsica.

In terms of plan view development of topography, 'Gilbert' and χ metrics allow us to assess the stability of the drainage divide. As noted in the natural settings investigated by Forte and Whipple (2018), applying the most restrictive uncertainty measure (1 s.d.) does not allow us to evidence any disequilibrium at the divide. However the two other recommended uncertainty level (i.e., 1 s.e., 95% bootstrap confidence interval and *t*–tests) reveal a statistically significant migration trend in the majority of 'Gilbert' and χ metrics in Corsica. Similarly, I found that upstream gradient and relief in 'Gilbert' metrics were more efficient at detecting potential disequilibrium compared to channel head elevation; this difference in sensitivity was also noted in other natural settings (see Forte and Whipple, 2018). Our results are also in agreement with a series of empirical studies (e.g., Binnie, 2008; DiBiase et al., 2010; Forte et al., 2015) that Forte and Whipple (2018) find an agreement between the predicted direction of migration by using either 'Gilbert' or χ metrics, though the 'Gilbert' metrics seem to be more sensitive and therefore represent a better choice when assessing the stability of drainage divides.

The fact that the majority of 'Gilbert' and χ metrics shows the same migration direction (westward in the southern drainage divide and eastward in the northern drainage divide) indicate that the current erosion at the divide fits with the predicted long–term migration. Such agreement suggests that Corsica is undergoing a horizontal rearrangement of its drainage network and is not in steady–state. I do not find evidence of discrete river capture (e.g., change in $k_{sn}$ that does not correlate with lithological or uplift boundaries) in any of the analysed χ–elevation river profile. This lack of evidence despite evidence for modern disequilibrium may have two causes. Firstly, most of the changes in χ and $k_{sn}$ are spatially coincident with changes outcropping rock types and

boundaries of structural units: the very diverse nature of the rocks exposed in Corsica may have obscured any major reorganisation signal. Secondly, there may have been a shift in the nature of the reorganisation, potentially due to the reduced magnitude of the tectonic movements since the Miocene (Daníšík et al., 2007, 2010; Fellin et al., 2005 a, b). Miocene drainage reorganisation in northern Corsica is marked by massive river captures triggered by tectonic inversions, leaving geomorphic evidence including wind gaps and onshore sedimentary basins now disconnected from their sources (Cavazza et al., 2007; Fellin et al., 2005 a, b; Sømme et al., 2011). The absence of recent discrete river captures suggests that drainage expansion has happened primarily by continuous area gain/loss since the Pliocene, when the last discrete river captures are recorded in the north–eastern of Corsica (Daníšík et al., 2010; Fellin et al., 2005 a, b). The process of drainage expansion through continuous area gain does not leave, in general, topographic records in $\chi$–elevation profiles (Whipple et al., 2017 a, b) and is more likely to occur in tectonically quiescent and post–orogenic erosional settings, such as Corsica.

The metrics of the knickpoints near the drainage divide also mirror the migration direction identified by the 'Gilbert' and $\chi$ metrics, particularly in the southern section of the divide: near the divide, the largest knickpoints are found on the "expanding" side of the divide (east side in the south, west side in the north). This is surprising given that knickpoints associated with transient signals should, by definition, separate a relict upstream area from a downstream region where the wave of incision has propagated (Neely et al., 2017). A possible explanation is that the knickpoints were potentially driven by uplift and Quaternary (and Messinian?) sea level changes, and that some knickpoints on the expanding side of the divide have already reached the divide where they drive the competition between east– and west–flowing rivers. Higher precipitation over the expanding sides of the drainage divide (Kuhlemann et al., 2007, 2009) may have promoted a bottom–up process, accelerating the migration of previously existing knickpoints (that would have also reached the divide), or a top–down wave of erosion that is totally independent of a knickpoint propagation and solely controlled by precipitation intensity at the hillslopes of the drainage divide. In addition, I believe that former glaciers can have smoothed the landscape (e.g., by removing knickpoints) or lead to local steepening (e.g., by enhancing incision and knickpoints).

River steepness, knickpoints and grain size distribution have important spatial correlations with rock types, which roughly agree with rebound values and erosion rates measured by Molliex et al. (2017). By comparing knickpoints' metrics, grain size distribution and river steepness, I corroborate that rock types from the Hercynian domain might have higher resistance than the Alpine units. Differently from Molliex et al. (2017), I found that, among the Hercynian Corsica, granites might be more resistant, given their larger range of grain sizes, dominance in the coarse fraction of the gravel bar sediment, and higher values of river steepness than any other rock type. In the supracrustal rocks of the Alpine Corsica, the relative rock strength estimated by Molliex et al. (2017) is similar to the values found in our analysis: schist are more resistant than conglomerate, and limestone. These constraints suggest that, during the Quaternary, rock strength might have been a major control on the rates of river incision, sediment production and, potentially, in the response time of the landscape to changes in boundary conditions such as regional base level (sea level), precipitation intensity and uplift rates documented for Corsica.

In spite of the preferred occurrence of knickpoints and changes in river steepness along structural boundaries, I distinguish a clustering of knickpoints in three specific ranges of distance from sea level across all major units of Corsica. In particular, the largest cluster is at 20 and 25 km from the coast in the Hercynian and Alpine Corsica, respectively (Fig. 3.18), suggesting that they may have been triggered from a common base level fall, such as sea level and that they have propagated at different rates according to the rock strength (slower across Hercynian Corsica). This hypothesis could be plausible if associated with a major base level drop, such as the Messinian salinity crisis (e.g., Gargani, 2004; Waelbroeck et al., 2002). If those knickpoints had been triggered by this crisis, they would have migrated at rates of ~3.8 and 4.7 mm/yr over the last 5.3 Ma in the Hercynian and Alpine Corsica, respectively, which is consistent with rates documented around the Mediterranean domain for basins of similar sizes (e.g., Italy, Greece, Turkey: Whittaker and Boulton, 2010). However, there are important point to consider regarding the Messinian crisis: firstly, there is a strong asymmetry, with a deep Liguro–Provencal basin to the West and a much more juvenile, shallower Tyrrhenian Sea to the East: the signal may have been felt very differently on both sides of the island. Secondly, the drop in sea–level would have caused a similarly extreme migration of the rivers' base level, whereby the coastline would have migrated potentially tens of kilometres basin–ward. Any knickpoint triggered by the crisis would

have started migrating across what used to be the seafloor, at a pace depending on the nature of the relief now emerged (Snyder et al, 2002); whether these knickpoints would have reached what is now the modern coast before the rapid re–flooding of the Mediterranean Sea is difficult to assess and will require further work. Such work may include numerical modelling of landscape evolution to assess the response of topography made of a range of rock types to a major base level drop such as the Messinian's (e.g., Loget et al., 2006).

We are not able to detect any spatial correlation of thermochronometric ages on the river paramaters analysed. The zircon fission–track (ZFT) domains, where I found means of knickpoints' metrics that are statistically distinguishable, are partly coincident with the Hercynian and Alpine domains, which makes the correspondence between them and the river metrics potentially biased by the domains' rock strength. This lack of evidence about the influence of thermochronometric ages on the river paramaters suggest that local discontinuities are more effective on modulating the modern river profile than large–scale uplift/exhumation patterns that dominated the thermochronometric history of Corsica before the Pliocene.

Overall, the differences in river steepness and knickpoint metrics between the Hercynian and Alpine Corsica can be explained by the following main controlling factors: diversity of structural units, density of geological structures, and rock strength. The Hercynian Corsica has a larger amount of structural units than the Alpine Corsica, which are likely to differentially erode and consequently to generate knickpoints. There is also a similar orientation between drainage network and geological structures in Hercynian Corsica that is not predominant in the Alpine units, reinforcing the likely influence of structures on the drainage network pattern. The influence of rock strength in river profile evolution is another factor that can help explaining the statistically significant difference between knickpoints over distinct rock types. Knickpoints are more likely to propagate fast and even diffuse in the less resistant rock types, such as those from the Alpine Corsica (e.g., schist). On the other hand, harder rock types, such as the volcanics and igneous rocks of Hercynian Corsica, can reduce the response time (i.e., the propagation velocity) and maintain the knickpoint slope for longer. This distinct diffusional behaviour together with different grain sizes provided to the rivers can modulate the incision rates and processes according to the rock type. As attested by our analysis, the Hercynian Corsica has a higher density of knickpoints, which also tend to be larger, and coarser sediments than the Alpine units.

Although the majority of the knickpoints are at the main structural boundaries, potentially indicating a stationary condition, the large range between 20 and 25 km from the sea can be an indicative of possible migration. However, the presence of numerous geological boundaries limits the potential to associate knickpoints to a possible common base level fall that could be related to sea level variation.

## 3.6. Conclusion

Based on several statistical analyses of 'Gilbert' and χ metrics, I identify two major directions of drainage divide migration in Corsica. The northern section of the drainage divide is currently moving to the east, while the southern section is moving to the opposite direction (i.e., westward). These patterns suggest that Corsica is in a transient state, where the current direction of drainage divide motion mirrors the predicted trend required to reach a horizontal steady–state.

The analysis of the drainage network through river steepness, sediment grain size and knickpoints highlight the influence of both rock type and structural units as major controls on the modern river profiles. The drainage network over Hercynian Corsica has a higher density of knickpoints with larger metrics (magnitude [μ = 27.8 m], relief [μ = 79.2], slope [μ = 11.2$^{o}$], and length [μ = 407.2 m]). These are followed by the Alpine Corsica with intermediate density and values of knickpoints' metrics (magnitude [μ = 22.7 m], relief [μ = 63.4], slope [μ = 9.0$^{o}$], and length [μ = 387.2 m]), and, lastly, by the Miocene sedimentary plains (magnitude [μ = 13.0 m], relief [μ = 30.4], slope [μ = 4.9$^{o}$], and length [μ = 350.1 m]), where knickpoints are rare. The range of grain size in modern gravel bars in Corsica reflects a similar pattern, with Hercynian rock types having larger ranges than those at the Alpine Corsica (e.g., pebbles of granite from Hercynian Corsica vary from 10 to 2 ψ, while pebbles of limestone from Alpine Corsica vary from 8 to 4 ψ). River steepness follows a similar pattern of the knickpoints' metrics, with decreasing values from the Hercynian to the Alpine Corsica (e.g., from 0 to 300 $k_{sn}$ in Hercynian to 0 to 180 $k_{sn}$ in Alpine Corsica), reaching the lowest range of grain sizes in the sedimentary plains. Importantly, the spatial distribution of knickpoints, grain size coarsening and river steepness peaks show a preferential location around the boundaries of structural units (e.g.,

faulting zones). These structural boundaries control the direction of the drainage network and the river metrics (i.e., river steepness, slope, magnitude, length and relief of knickpoints) in the Hercynian and in the Alpine Corsica. Moreover, I have found that knickpoints are preferentially located at a relatively similar distance from the sea level, which could suggest a common base level drop. The majority of the knickpoints are located at ~ 20 km from the sea level in the Hercynian and ~ 25 km in the Alpine Corsica. However, given the existence of structural control in the genesis of knickpoints, caution must be taken. Future work (e.g., using numerical simulation) can properly analyse this hypothesis by testing how long it would take to a wave of incision to realistically propagate in the watersheds of Corsica.

I have not identified any difference between the knickpoint metrics in the thermochonometric age domains compiled from other workers. The only exception is the zircon fission–track age domains that, however, roughly coincide with the major rock types in Corsica (i.e., Hercynian and Alpine units) and cannot be discarded as biased by them. These findings suggest that the current topographic state of the drainage network and divide in Corsica is primarily controlled by rock strength and the structural boundaries than the long–term (and long–scale) exhumation patterns that last until the Pliocene.

# Chapter 4 –What information can we reliably retrieve from detrital studies? Insights from detrital zircons and sediment mixing modelling in Corsica (Mediterranean Sea)

Key points:

- Detrital zircons in the Tavignano River have typologies and U–Pb ages that indicate local sources of Hercynian granites, Alpine meta–ophiolites and granitoids.
- Unmixing of U–Pb zircon ages from river samples indicate source contribution proportions that largely differ from their exposure area.
- Simulations with controlling factors of detrital grains suggest that quantitatively estimating them is a non–trivial task.

**Key words:** Zircon typology; U–Pb ages; Provenance analysis; Tavignano watershed; Numerical simulation

## Abstract

Analysis of detrital mineralogy to link source areas with the sedimentary record is widely used in studies aiming to reconstruct erosional history, drainage development and, more broadly, landscape evolution over time. However, factors that change how different sources are preserved in detrital records (i.e., bias) are still poorly understood and often not considered when drawing conclusions in some case studies. Here, I use a combination of field observations, laboratory analyses and numerical modelling of the Tavignano watershed (Corsica, Mediterranean Sea) as an example of under–constrained system. I use typology, internal texture, U–Pb geochronology and sediment mixing modelling of zircons from three sampling sites along the main river to assess what information can be reliably extracted regarding their provenance. Our detrital analysis reveals a prevalence of euhedral zircon types with well–developed magmatic zoning and a typology that is similar both in the core and in the external surface of the grains, especially in the uppermost and lowermost sampling sites. The morphological signature of the euhedral zircons can be associated to a complex cooling history, with characteristics of sub–alkaline to alkaline granites. Non–euhedral grains are present in all samples but they have a greater occurrence in the intermediate site, where meta–ophiolites (Schistes Lustrés unit) and granitoids (an "External Continental" unit) are significant sources. Likewise, U–Pb zircon ages are more similar in the samples from the uppermost and lowermost sites than in the intermediate one. The unmixing of U–Pb zircon ages reveals that Hercynian granites, meta–ophiolites and granitoids are the predominant sources in the samples. Although our results fit with the known characteristics of their sources, many uncertainties arise from missing source ages, underrepresented grains, and misfits between predicted source proportions based on exposure area and their real (measured) percentage in the samples. I perform numerical simulations testing the influence of number of grains, overlapping ages, zircon fertility, hillslope gravel supply, erosion and pebble abrasion rates in our results using synthetic and empirical constrains. Our simulations demonstrate that more grains than have been used in this work are necessary to reduce uncertainty on source proportions in our river samples to an acceptable level. Additionally, biases are produced when the sources have overlapping ages that mirror some of the investigated sources (e.g., the U2 group from Hercynian Corsica). I also find that, while erosion, hillslope sand supply and pebble abrasion alone are not likely to create significant bias on the source proportions, changes in

zircon fertility can produce large bias without any additional influence. The empirical constrains available in our study area are not sufficient to disentangle the influence of each biasing factor. The simulations demonstrate that estimating the factors that control the characteristics of detrital samples in poorly constrained settings is a non–trivial task.

## 4.1. Introduction

Clastic sediments represent an integrated fingerprint of the erosion, transport and depositional processes that have contributed to their evolutionary history. The analysis of sediments has enabled many studies reconstructing source area (e.g., Ustaömer et al., 2016; Johnson et al., 2016), paleogeography (e.g., Zhang et al., 2017; Sharman et al., 2015), sediment dispersal evolution (e.g., Sharman et al., 2018; Malkowski et al., 2017), and rates of exhumation (e.g., Bush et al., 2016; Mark et al., 2016) and denudation (e.g., Han et al., 2016; Gemignani et al., 2018). The detrital mineral composition evolves during transport, deposition and diagenesis. Some detrital studies use this evolution to learn about the sediment production and transport processes (e.g., Garzanti et al., 2007). Other detrital studies rely on a single mineral provenance tool, such as zircon geochronology (see Roberts and Spencer, 2015). Zircon ($ZrSiO_4$) is a common accessory mineral in igneous rocks that tends to survive during sedimentary processing due to its hardness (~7.5 Mohs hardness scale) (Fedo et al., 2003). It also incorporates a range of trace elements including uranium and thorium, which allow dating using geochronological (e.g., U–Pb dating) and thermochronometric techniques (e.g., fission–track dating) (Garver, 2014; Gehrels, 2014). Morphological characteristics of zircon are also unique archives of geological processes. For instance, zircons can evolve from euhedral tetrahedral to metamict forms due to radiation damages over time (Balan et al., 2001). Metamorphic zircon, in particular, can have an ovoid external morphology and show characteristic features such as resorption when imaged (Corfu et al., 2003).

However, what are the assumptions made when using detrital zircon information to reconstruct past environments? These assumptions can be divided into those resulting from (i) the nature of the material being eroded and from processing during transport (i.e., natural biases), and

(ii) those that result from field sampling and processing to separate the zircon for dating in the laboratory (i.e., analytical biases). Common assumptions include, firstly, that zircon occurs as an accessory mineral and that the mineral fertility is similar in all the original sources (e.g., Mason et al., 2017; Sickmann et al., 2016). Secondly, that the abundance of zircon does not change significantly during sediment transport and abrasion processes (e.g., Saylor et al., 2013). Thirdly, that the age distribution in the source lithologies is unique, so different parts of the catchment can be identified through deconvolution of the grain age distribution, so that inversion leads to an understanding of erosion processes (e.g., Amidon et al., 2005a,b; Lavarini et al., 2018).

Nevertheless, it is known that not all rock types may contain zircon, including even some igneous rocks (e.g., the Manaslu granite in the Himalaya; see Amidon et al., 2005a), highlighting that a mono–mineralic approach may not be appropriate in studies where the aim is to reconstruct uplift, erosion and depositional histories, but some sources can be "invisible" in the sedimentary record (see Moecher and Samson, 2006; Malusà et al., 2016).

Natural biases have received increasing attention, with studies focusing on the influence of differential erosion rates (e.g., Spencer et al., 2018), zircon fertility (e.g., Malusà et al., 2013), hillslope gravel supply (e.g., Lukens et al., 2016) and pebble abrasion (e.g., Lavarini et al., 2018) on sediment composition. These studies have found evidence that, while hillslope gravel supply, erosion and pebble abrasion are more likely to change the percentage of target minerals, sources with very low fertility may even be invisible in the sedimentary record.

The recognition of analytical biases and the means of minimizing them from sample selection to deconvolution results have also improved. For instance, a recent statistical analysis, using probability and combinatory theory with synthetic grain ages, suggests an ideal number of grains to analyse ($n$ = 117) so that one can be 95% confident of not having missed a population (Vermeesch, 2004). Techniques such as cone splitting to avoid biasing during sample processing and improved fitting techniques to better unmix overlapping age peaks have been proposed (e.g., Vermeesch, 2012; Sundell and Saylor, 2017).

However, many settings where detrital studies are performed do not have sufficient empirical constraints to properly define their natural biasing factors and not even enough target minerals (e.g., zircon or apatite grains) for a statistically significant provenance study. Since workers

cannot define the relative importance of each factor in the detrital population in poorly constrained settings, disentangling them can become, due to uncertainty, quantitatively impractical.

Here, I examine capabilities and limitations of the detrital zircon approach for reconstructing provenance of modern sediments derived from catchments where the age and distribution of the source lithologies are known independently. I use the Tavignano watershed in Corsica (Mediterranean Sea), as a template for this analysis. I investigate the typology, internal texture, U–Pb ages and source mixing proportion of detrital zircons from three sampling sites along the main stem. Previous work has dated a range of zircon–bearing lithologies over the two main geological domains on the island, so investigating modern sediments should yield insights into the supply and transport processes that produce and potentially bias the detrital signature.

Through this work, I highlight the difficulties of finding causal factors when sources are not extremely well constrained, which often occurs in lithologically complex areas where provenance analysis is sometimes the only tool available for understanding past landscape change.

## 4.2. Study area

Corsica is an island in the Western Mediterranean Sea that consists of two geological domains: Hercynian Corsica and Alpine Corsica (Fig. 4.1). In Hercynian Corsica, three main groups of intrusive rock types have been recognised: (i) an ‘Mg–K’ granite (U1 group) related to a collisional stage at ~ 320 –350 Ma; (ii) a ‘calc–alkaline’ granite (U2 group) related to crustal thinning at ~ 304 –280 Ma; (iii) and alkaline and metaluminous granites (U3 group) ranging from 238 to 259 Ma (Cocherie et al., 1992, 1994, 2005; Paquette et al., 2003; Rossi et al., 1988, 1993, 1995, 2001, 2006; Li et al., 2014). In Alpine Corsica, six main groups occur: (iv) external continental units with evidence of Hercynian deformation and magmatism (360 to 270 Ma), which are partly overlain by metasediments (260 to 50 Ma); (v) Schistes Lustrés made of Tethys–derived ophiolites and their metasedimentary cover (89–66 Ma); (vi) internal continental units which are continental–derived slivers within the Schistes Lustrés complex (40–37 Ma); (vii) Nappes Supérieures made of deformed ophiolites, continental and sedimentary units (286 –350

Ma); (viii) Pre–Hercynian basement rocks occuring in scattered regions of Corsica (> 350 Ma); (ix) Miocene sedimentary plains occuring in the north–east of Corsica (Ohnenstetter et al., 1981; Rieuf, 1980; Brovarone and Herwartz, 2013; Lin et al., 2018).

In the Tavignano watershed, nine major rock types are present (Fig. 4.1). In the uppermost region, four formations from the U2 and U1 groups of Hercynian Corsica occur associated to two slices of continental units (external continental units and Pre–Hercynian basement). They are: U1 mesocratic granites aged 320 –350 Ma (U–Pb dating), and three rock types from the U2 group with U–Pb zircon ages ~ 302 –304 Ma (medium grained granodiorite), ~ 300.0 Ma (fine grained monzogranite) and ~ 280 –289 Ma (leucomonzogranite) (Cocherie et al., 1992; Rossi et al., 2006, 2015). To the north, the external continental unit named Santa–Lucia–Di–Mercurio has U–Pb zircon ages between 140 and 380 Ma (Cocherie et al., 2005). The Pre–Hercynian basement has no published U–Pb age constrains but I believe it is older than the U1 mesocratic granites (i.e., > 320 –350 Ma). From the Alpine Corsica, two other units occur within the Tavignano: the Schistes Lustrés and meta–ophiolite units. For the Schistes Lustrés, the U–Pb zircon ages available are from continental slivers (granulites and plagiogranites) associated to ophiolite sequences, particularly from meta–ophiolites at the Inzecca Unit (142 –162 Ma) (Ohnenstetter et al., 1981). No U–Pb zircon age distribution has been published from supracrustal rocks of the Alpine Corsica (e.g., schist, quartzite or calcarenite).

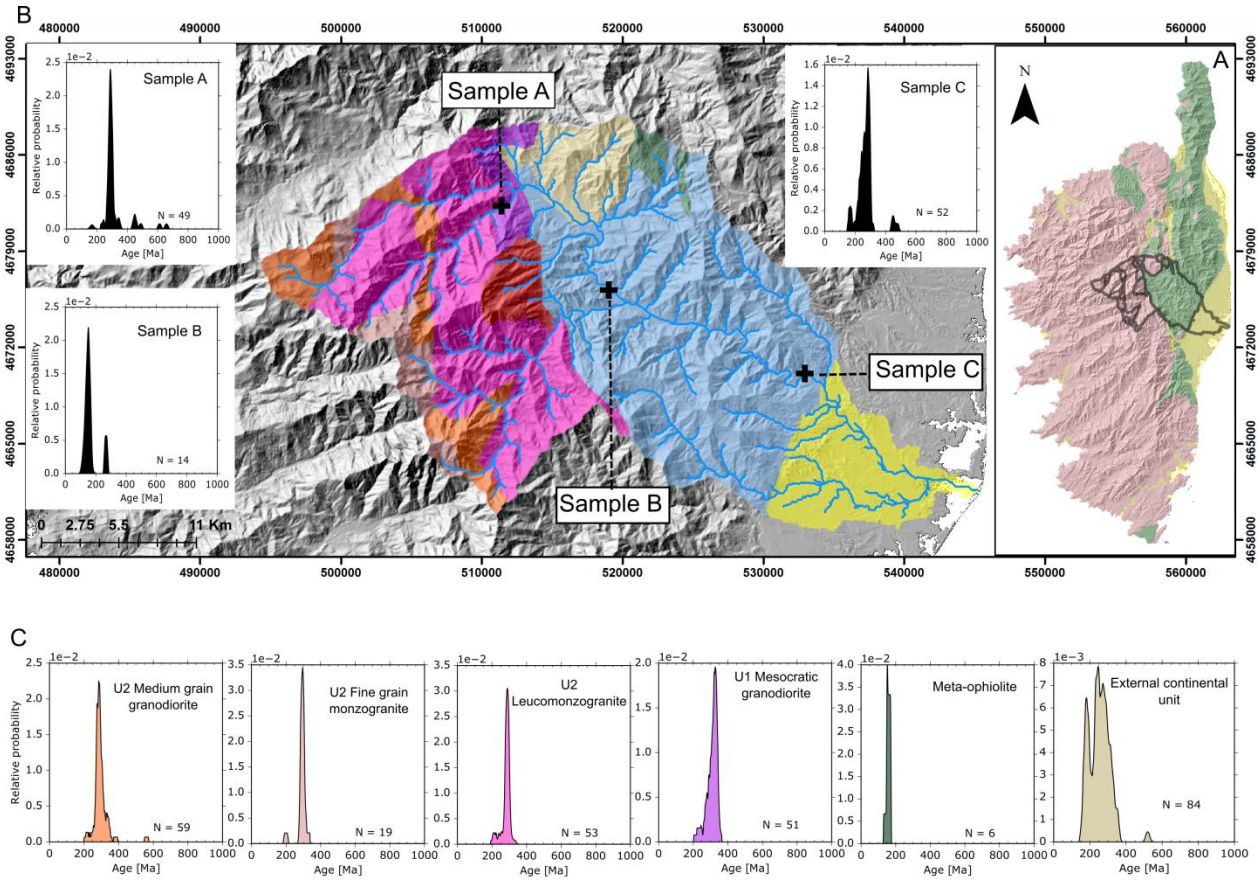


Figure 4.1: Source rocks and U–Pb zircon ages of the Tavignano watershed. A) Location of the Tavignano watershed in eastern Corsica. Pink rock types are granitoids of Hercynian Corsica, green rock types are from the Schistes Lustrés unit (Alpine Corsica), and yellow rock types are part of the Miocene sedimentary plains (Aleria and Marana). B) Source rocks and U–Pb age distributions of the downstream mixed sand samples in the uppermost (sample A), intermediate (sample B) and lowermost (sample C) sampling sites. C) U–Pb age distributions of the source rocks of the Tavignano watershed. Note that the blue area represents the Schistes Lustrés unit, where no U–Pb age constrains exist. The yellow area represents the Aleria plain, which is not investigated in this work. The colours of the source rocks in panel B are equivalent to those U–Pb ages at panel C. The ages in panel C are from Cocherie et al. (1992, 2005), Ohnesnstetter et al. (1981) and Rossi et al. (2006, 2015) and are available as supporting information (Tables S1 and S2).

## 4.3. Methods

### *4.3.1. Fieldwork sampling strategy*

Three modern gravel bars located in the uppermost (sample A), intermediate (sample B) and lowermost (sample C) reaches along the Tavignano River were sampled for zircon analysis

(Fig. 4.1). At the uppermost sampling site (A), 11.2% of the catchment is made of U2 medium grained granodiorite, 75% of U2 leucomonzogranite, 10.9% of U2 fine grained monzogranite, 2.3% of U1 mesocratic granite, and 0.3% of Pre–Hercynian basement. At the intermediate sampling site (B), 10.7% of the catchment is made of U2 medium grained granodiorite, 33.9% of U2 leucomonzogranite, 4.2% of U2 fine grained monzogranite, 6.2% of U1 mesocratic granite, 21.1% of Schiste Lustrés units, 4.8% of Pre–Hercynian basement, 3.5% of meta–ophiolite units, and 15.4% of external continental units. At the lowermost sampling site (C), 9.3% of the catchment is made ofU2 medium grained granodiorite, 33.3% of U2 leucomonzogranite, 5.1% of U2 fine grained monzogranite, 3.2% of U1 mesocratic granite, 35% of Schiste Lustrés units, 3.9% of Pre–Hercynian basement, 1.8% of meta–ophiolite units and 8% of external continental units. All else being equal (e.g., zircon fertility and erosion rates), these are the expected zircon proportions to be found at each sampling site. Deviations from these number can be interpreted in a range of ways, as will be discussed.

At each site, only sediment that had been unambiguously transported by fluvial processes was selected. Subsurface sediment was extracted from a pit after excavating the surface material over an area approximately 0.5 by 0.5 m, following the methods detailed by Bundt and Abt (2001), and Attal and Lavé (2006). The material extracted from the pits was then sieved in the field using 10, 20 and 40 mm square mesh sieves. Approximately 1 kg of the fraction finer than 10 mm was sampled for further processing in the laboratory.

### *4.3.2. Sample processing in the laboratory*

Samples were dried and then sieved into > 4 mm, 2 mm to 4 mm, 1 mm to 2 mm, 500 μm to 1 mm, 250 μm to 500 μm, 125 μm to 250 μm, 63 μm to 125 μm, and < 63 μm size fractions using stainless steel sieves (cleaned using a stiff brush and ultrasonic bath). To provide a concentrate of heavy minerals and ease the handpicking of zircon grains, density–gravity separation was performed with a Wilfley shaking table for the fraction of every sample collected between 125 to 63 μm. The sub–sample of concentrate of heavy minerals was then passed through a Frantz magnetic separator to remove grains with magnetic properties. Minerals were

separated at 0.4, 0.8, and 1.5 amperes using a side slope of 20$^{o}$ and a tilt of 25$^{o}$. The non–magnetic minerals at 1.5 ampere were then separated into heavier and lighter grains using lithium heteropolytungstate (LST) with a known density of 2.8 g/ml.

The final concentrate of minerals from the heavy liquid separation was analysed using an optical microscope for morphological and birefringence analysis. Those grains with zircon characteristics were selected to assess the presence of zirconium with a scanning electron microscopy (SEM) with energy dispersive x–ray spectroscopy (EDX). Finally, by using the EDX, I selected only grains with high content of zirconium for U–Pb dating and typology classification as a means to avoid mistakenly working with minerals other than zircon.

### *4.3.3. Zircon grain morphology*

The morphology of zircon grains was analysed using an optical microscope and a scanning electron microscope (SEM) mass spectrometry with cathodoluminescence detector (CL). I use the zircon typology of Pupin (1980), which is a combination of the most common crystalline faces of zircons (pyramids {101}, {211} and prisms {100}, {110}) (Fig. 4.2).

Main types and subtypes are reported according to two variables: the A (I.A.) and T indexes (I.T.). This classification scheme is based on the development of prismatic and pyramidal crystal faces of zircons. The A index (IA) has been associated to Al/(Na + K) ratio and pyramidal faces. The pyramids {211}, {101} and {301} are known to correlate well with aluminous, alkaline and peralkaline mediums, respectively. The T index (IT) is associated to the temperature of zircon crystallisation, which regulates the development of prismatic faces.

This classification scheme allows grouping zircon types into different environments of crystallisation. For instance, low A and T indices are typical of crustal origin (i.e., which crystallised in the crust) such as leucogranites and aluminous monzogranites. Large ranges of A and varying T indexes are associated to granitoids in between crustal and mantle origin (i.e., hybrid group) such as calc–alkaline and sub–alkaline monzogranites/granodiorites. The highest values of A and T indexes are typical of mantle origin, with prevalence of alkaline granitoids

(Pupin, 1980). Given the very small size of detrital zircons (63 –125 µm), morphological analysis are usually performed in optical microscopy and cathodoluminescence detector (CL).

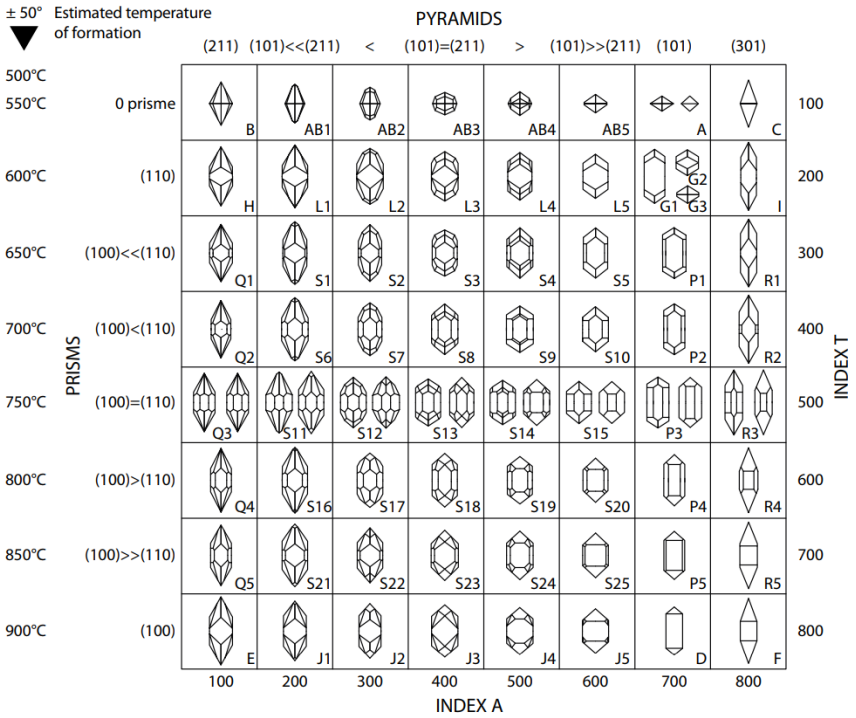


Figure 4.2: Zircon typological classification proposed by Pupin (1980). Index A is the Al/alkali ratio, controlling the development of pyramids in the crystals. Index T is the temperature on the development of prisms. Adapted from Martins et al. (2014).

After estimating the A and T indices of the grains, I calculate the mean points (*I.A. mean* and *I.T. mean*) of each index following Pupin (1980). They can be estimated as follows:

$$I.A.mean = \sum_{i=1}^{n} I.A.* n_{I.A.} \quad (1)$$

and

$$I.T.mean = \sum_{i=1}^{n} I.T.* n_{I.T.} \quad (2)$$

where $n_{I.A.}$ and $n_{I.T.}$ are the frequencies of each A (IA) and T indexes (IT), where $\sum n_{I.A.} =$ e $\sum n_{I.T.} = 1$. These mean points can be used to trace what Pupin (1980) calls "Typological Evolutionary Trend" (T.E.T.) of the zircon population and estimate their origin (i.e., if they are from crust, mantle or hybrid origin). The T.E.T. is plotted over the mean points and a slope (a). This slope (a) can be measured by:

$$a = \left(\frac{\sqrt{(A.I.mean - A.I.)^2}}{N}\right) / \left(\frac{\sqrt{(T.I.mean - T.I.)^2}}{N}\right) \quad (3)$$

where *N* is the total number of analysed grains.

By using CL images, I also identify internal structures, such as inclusions and different zoning patterns from core to the external morphology. The same typology classification for the external morphology proposed by Pupin (1980) is used to classify the zircon cores (when they exist) and to identify growth patterns from the zoning pattern. Identifying these characteristics can provide clues about the magmatic history of the grains, such as changes in the magma composition and in temperature of the mantle/crust. All the CL images of detrital zircons analysed in this work are available as supporting information (Fig. S1).

Cocherie et al. (2005) provided a large data set of zircon types classified within the framework proposed by Pupin (1980) for the U2 leucomonzogranites of Corsica, whose zircons are the main source of our samples. Therefore, by classifying the detrital zircons in our sample, I can try linking the sediments to their sources.

### *4.3.4. U–Pb detrital zircon age estimation*

I used secondary ion mass spectrometry (SIMS) to quantify the amount of $^{206}$Pb, $^{207}$Pb, $^{208}$Pb, $^{238}$U, $^{232}$Th, $^{204}$Pb in each zircon grain. I then calculated the ratios $^{238}$U/$^{206}$Pb to estimate the crystallisation age of the grains. It is known that $^{206}$Pb is produced by radioactive decay of $^{238}$U at a constant rate (half of the $^{238}$U mass is lost in 4.47 billion years) so measuring the masses of these isotopes is sufficient to obtain the zircon age. SIMS use an internal beam of positive or negative ions to reach a sample surface and generate secondary ions that transfer into a mass spectrometer for measuring trace elements and isotopic compositions in minerals. The sample processing (i.e., sieving, shaking table, magnetic and heavy liquid separation), optical microscopy and SIMS analyses were performed in the laboratories of the University of Edinburgh. The SEM with energy dispersive x–ray spectroscopy (EDX) and CL analyses were performed at the laboratories of the Heriot–Watt University. The U–Pb grains analysis was performed through excavation of the zircon cores by a primary ion beam and comparison with a

standard–sample bracketing. The ages have precision and accuracy of 1–2 %. Other parts of the zircon grains (e.g., recrystallised domains and zoning) are not dated.

### *4.3.5. Unmixing U–Pb age distributions*

I perform an unmixing procedure of U–Pb age distributions of mixed downstream river samples to find the best–fit of upstream contributing sources. By using this technique, I can compare the measured proportion of each contributing source in the sample with its exposure area and infer if any variability in mineral fertility, erosion rates, pebble abrasion rates or grain size hillslope (or any other variable) can explain the measured mineral proportion. The unmixing procedure performed in this work is similar to the one described in Chapter 2, more precisely, in equations 1 to 9. These equations are fundamental to produce probability density functions (PDFs) of age U–Pb distributions from different potential sources and to compare them with a mixed downstream sand sample using statistical parameters.

### *4.3.6. Testing analytical and natural biasing factors*

After unmixing U–Pb age distributions of our river samples, I perform a series of numerical experiments to test the ability of natural and analytical biasing factors to produce the U–Pb age distribution and zircon mixing proportions empirically estimated from the mixed fluvial samples (A, B, and C) of the Tavignano River. Biasing factors such as size–density sorting of heavy minerals and biasing by different grain sizes produced by pebble abrasion are not considered. I do not test these factors because no constraints were available in the literature that could be used as bounds in our simulations, and because I am considering only the relative proportions of one type of mineral; sorting processes should affect all zircons in a similar way, except if grains from different units have different sizes (Malusà et al., 2013). However, I do discuss how those factors may influence our results (discussion section (6)).

Regarding analytical biases, I focus on two factors: the influence of reducing the number of analysed grains and the influence of sources with overlapping ages. Overlapping ages are tested because they seem relevant to understand the mismatch that is presented in the result section (5) about the U2 group of granites. The number of analysed grains is tested as a biasing factor because our samples have less than minimum required according to the works of Vermeesch (2014). The details of the simulated scenarios (e.g., the number of grains used, the chosen overlapping age peaks) are given further in the results section (6). To analyse the sensitivity of each factor tested, I use the same statistical parameters described in Chapter 2 (i.e., area mismatch (*M*), similarity coefficient (*S*), Kolmogorov–Smirnov test (*K–S*), PDF cross–plot analysis and Q–Q plots).

Regarding the natural biases, I focus specifically on four factors that can have affected the zircon mixing proportions in our samples: hillslope gravel supply, zircon fertility, erosion rates and pebble abrasion rates.

We use a 2D linear sediment mixing model, which predicts fluvial sediment mixtures based on the characteristics of the zircons (i.e., age) and of the sediment sources units (e.g., zircon fertility, exposure area and abrasion rate). This model is identical to the one presented in Chapter 2, particularly in equations 6 to 14. To analyse the sensitivity of each factor tested, I use the sum of squared errors (SSE). In a model with a single explanatory variable, which is our case, SSE is given by:

$$SSE = \sum_{i=1}^{n} (y_i - f(x_i))^2, \quad (4)$$

where $y_i$ is the $i^{th}$ value of the variable to be predicted (i.e., zircon mixing proportion found in our empirical data), $x_i$ is the $i^{th}$ value of the explanatory variable (i.e., hillslope gravel supply, pebble abrasion rates and erosion rates), and $f(x_i)$ is the predicted value of $y_i$ (i.e., predicted zircon mixing proportion using the tested factor). In cases of good fit between the predicted and the "measured" (real or synthetic) zircon mixing proportions, the SSE approaches zero, so lower values are indicative of good fitness of the model. Mixing models are used here to predict how well the controlling factors can match the best–fit fluvial sediment mixtures. The simulated scenarios are given further in the results section (6). Tables (S3 to S7) containing the synthetic data used in our simulations can be found in the supporting information.

In our simulations, I use topographic data with ~ 90 m spatial resolution from the Tavignano watershed from the Shuttle Radar Topography Mission (SRTM). From these elevation data, I define the river network (used to route sediment across the catchment) and extract flow length for each pixel across the watershed, using tools from the Geospatial Data Abstraction Library (GDAL). Flow length is used to calculate travel distance (km) from each pixel to a given river site ($d$ in equation 12 in Chapter 2). The source units ($i$ in equation 14 in Chapter 2) with their spatial extent [$km^2$] also feed the model as geographic layers. For a given "sampling" location along the river, each contributing pixel is assigned a transport distance $d$ and a source unit $i$; the relative exposure area of each unit $A_i$ is calculated based on this information. For each source unit $i$, the initial percentage of gravel supplied by the hillslopes to the river channel ($F_g$), zircon concentration ($C_i$) and supply rate by erosion ($\Phi_i^{ZR}$) are set by the user. All the code used to perform our analysis as well as to generate the figures is open source and can be downloaded from GitHub at https://github.com/clavarini.

## 4.4. Results

### *4.4.1. Typological classification of zircon grains*

At the uppermost sampling site (A), I identify 13 zircon types of external morphology that follow the classification of Pupin (1980). From all dated grains ($n$ = 49), 31 % ($n$ = 15) could not be classified because they were broken, had lost euhedral characteristics (e.g., by rounding), or could not be distinguished in the CL images (Fig. 4.3). Of the 34 remaining euhedral zircons that could have their external morphology classified, the majority has an external morphological type D (26 % of them i.e. 9 grains from the 34), G1 (12% and $n$ = 4), P2 (12 % and $n$ = 4), and S5 (12 % and $n$ = 4), while the remaining types (G2, J3, J5, P1, P4, P5, S10, S15 and S8) are represented by one or two crystals (Fig. 4.4). Based on Pupin (1980), the external morphological signature of this sample is of sub–alkaline granite origin, with a typological evolutionary trend that crosses the domains of sub–alkaline granites to calc–alkaline granites origins (Fig. 4.5). The internal zoning of the grains reveals that 70% ($n$ = 24) of the zircons have the same typology from the core to the rim. In the remaining grains, where external morphology is not the same as in the core (30% of the total grains and $n$ = 10), J5 (63% of the zircons [$n$ = 5] with core morphology different from external) is the predominant core type.

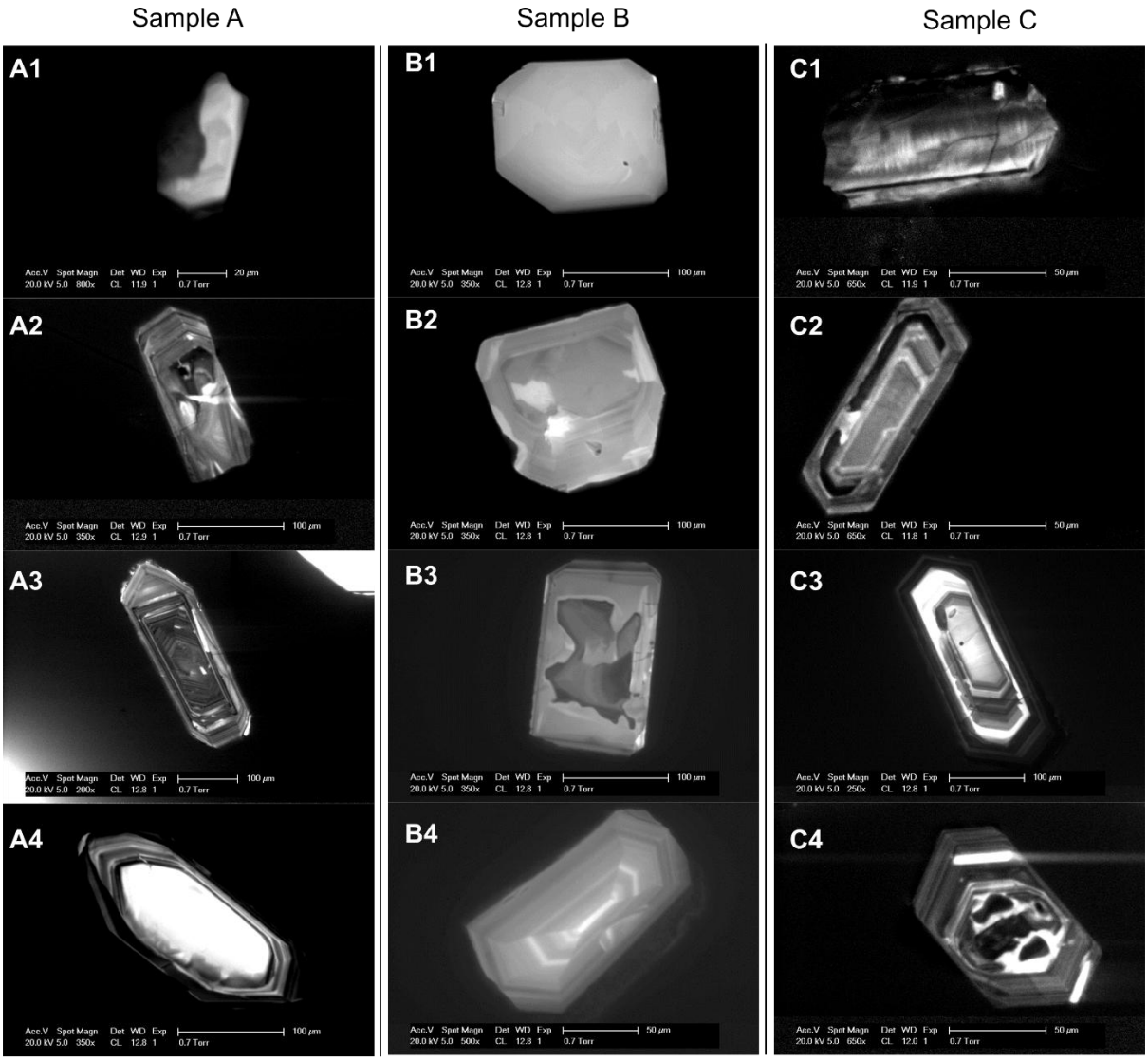


Figure 4.3: Zircon grains from the uppermost (A), intermediate (B) and lowermost (C) sampling sites. A1, B1 and C1 are examples of zircon grains that could not be classified due to non–euhedral shape. A2 is an example of a zircon type D, with oscillatory zoning from core to the rim, presence of fracturing and corrosion (by resorption or dissolution). A3 is an example of a zircon type G1, with oscillatory zoning from core to the rim and no fracturing or corrosion. A4 is an example of a zircon type P2, with oscillatory zoning from core to the rim, recrystallised domains, and corrosion. B2 is an example of a zircon type G2, with oscillatory zoning from core to the rim and corrosion. B3 is an example of a zircon type J5, with oscillatory zoning from core to the rim, recrystallised domains, corrosion, fracturing, inclusion and alteration. B4 is an example of a zircon type R3, with oscillatory zoning from core to the rim but no evidences of recrystallised domains, corrosion, fracturing, and other kind of alteration. C2 is an example of a zircon type P1, with oscillatory zoning from core to the rim, recrystallised domains, corrosion, and fracturing. C3 is an example of a zircon type P5, with oscillatory zoning from core to the rim, recrystallised and mitamictised domains. C4 is an example of a zircon type S10, with oscillatory zoning from core to the rim, recrystallised domains and corrosion. All the CL images of detrital zircons analysed in this work are available as supporting information (Fig. S1).

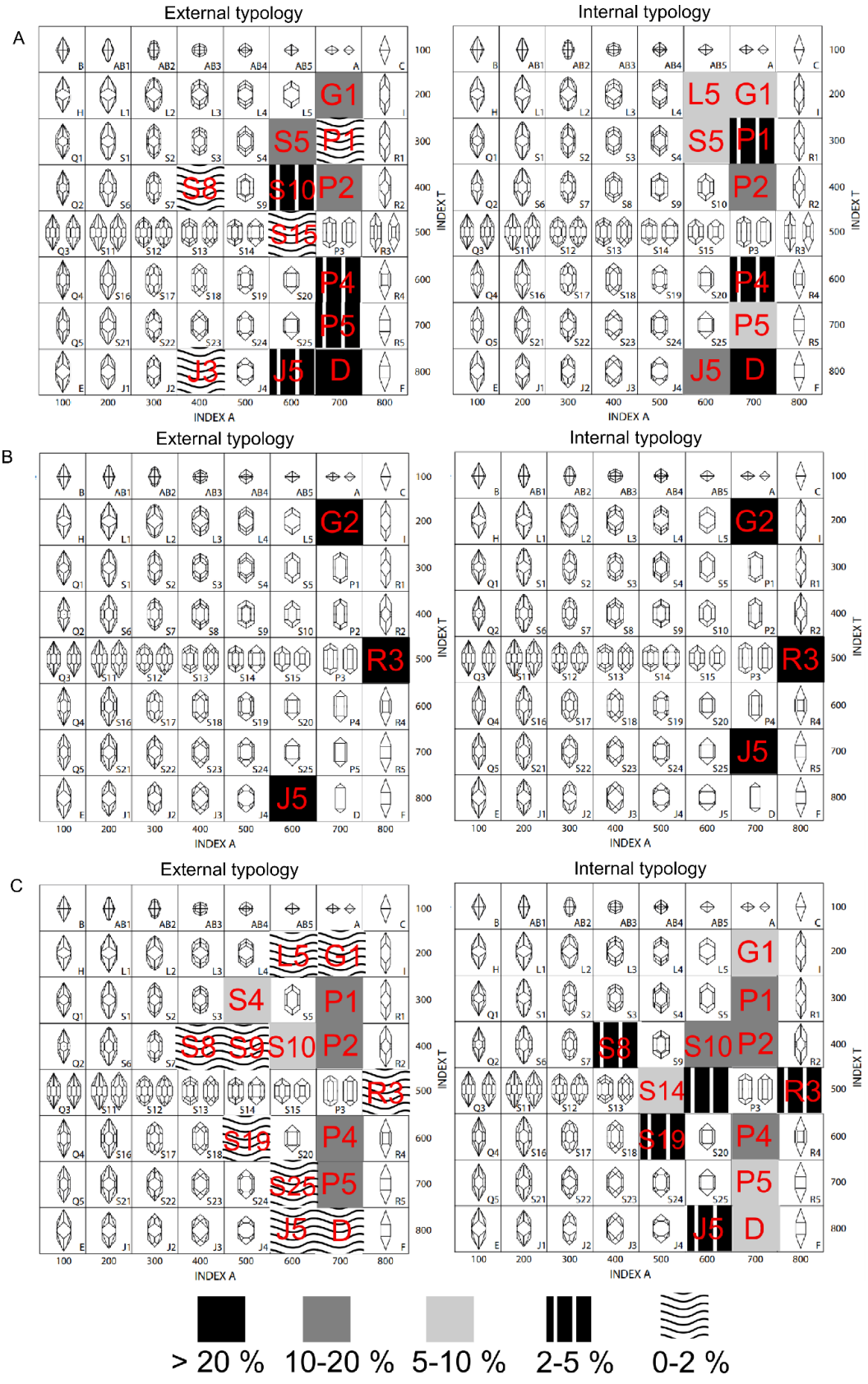
A
External typology
Internal typology
INDEX A
INDEX T
B
External typology
Internal typology
INDEX A
INDEX T
C
External typology
Internal typology
INDEX A
INDEX T
> 20 %
10-20 %
5-10 %
2-5 %
0-2 %

Figure 4.4: Zircon typology from the uppermost (A), intermediate (B) and lowermost (C) sampling sites according to the classification proposed by Pupin (1980). Index A reflects the Al/alkali ratio, controlling the development of pyramids in the crystals. Index T reflects the effects of temperature on the development of prisms.

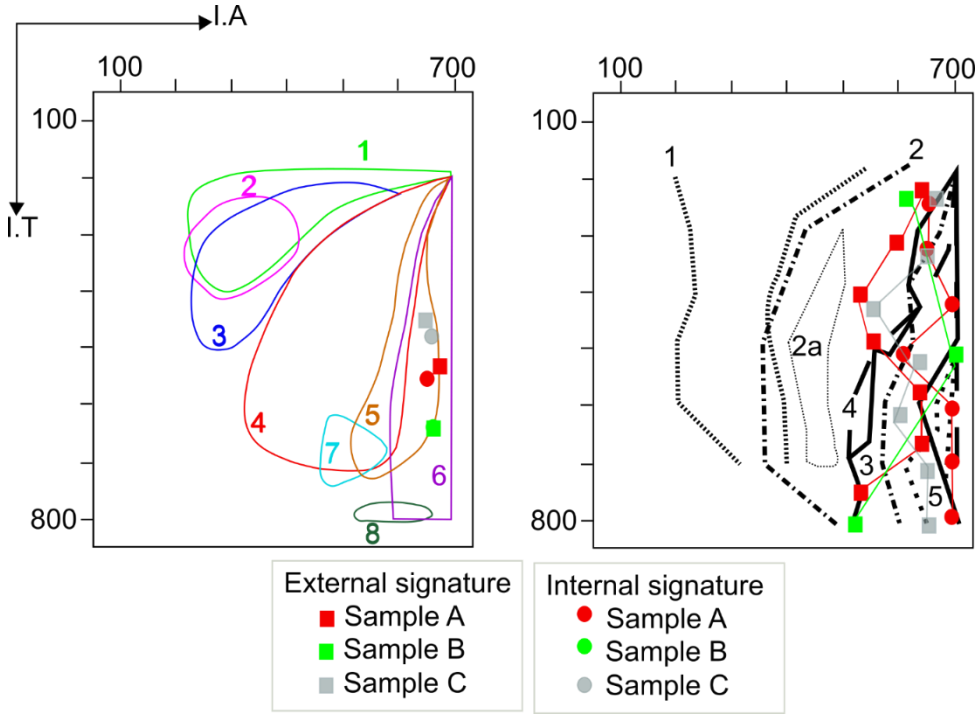


Figure 4.5: Morphological signatures of zircon populations from the uppermost (A), intermediate (B) and lowermost (C) sampling sites in the (A, T) morphological diagram of Pupin (1980). a. Distribution of the mean point; granitic domains: (1) aluminous leucogranites; (2) (sub) autochthonous anatectic granites; (3) intrusive aluminous monzogranites–granodiorites; (4) calc–alkaline and K–calc–alkaline series; (5) sub–alkaline series; (6) alkaline series; (7) continental tholeiitic series; (8) oceanic plagiogranites. b. Typological evolutionary trends (TET) represent lines that fall in specific domains calculated with mean points and standard deviations of zircon grains in a Pupin (1980)'s diagram. There are five main groups: Granitic domains: (1) crustal or mainly crustal origin; (2) calc–alkaline granites; (2a) K calc–alkaline granites; (3) sub–alkaline granites; (4) alkaline subsolvus granites; (5) alkaline hypersolvus granites. In cases when both external and internal zircon morphological signatures are identical, only the external signature is displayed.

From all grains where the internal morphology could be analysed (67% of the total grains or *n* = 33), the proportion of identified core types decreases from D (36% of them i.e. 12 grains from the 33), followed by P2 and J5 (12% and *n* = 4 each), to several other types represented by two grains (L5, P5, S5 and G1) and one grain (P1, G2, and P4). The core morphological signature of the grains is of sub–alkaline to alkaline granite origin, with a typological evolutionary trend that crosses the domains of alkaline subsolvus granites to calc–alkaline granites origin.

At the intermediate sampling site (B), I identify only 3 zircon types of external and internal morphology that follow the classification of Pupin (1980) (Fig. 4.3). From all dated grains (*n* = 14), 71 % (*n* = 10) could not be classified because they were broken, had lost euhedral characteristics (e.g., by rounding) or could not be distinguished in the CL images. Of the four euhedral grains that could be classified (29 % of the total grains), two grains have an external morphological type of J5 (50 % and *n* = 2), one grain is classified as R3 (25 % and *n* = 1) and another is G2 (25 % and *n* = 1) (Fig. 4.4). The analysis of the internal morphology of the grains shows the same classification of the external morphology in 100 % of cases. The morphological signature of the core and of the crystal grains are between sub–alkaline and alkaline granite origin, with a typological evolutionary trend that crosses the domains of alkaline subsolvus granite to calc–alkaline granites origin (Fig. 4.5).

At the lowermost sampling site (C), I identify 19 zircon types of external and internal morphology that follow the classification of Pupin (1980). From all dated grains (*n* = 52), 25 % (*n* = 13) could not be classified because they were broken, had lost euhedral characteristics (e.g., by rounding) or could not be distinguished in the CL images (Fig. 4.3). Of the 39 euhedral grains that could be classified (75 % of the total grains), the majority has an external morphological type of P4 (18 % and *n* =7), followed by P1 and P2 (13 % with *n* = 5, each), P5 (10 % with *n* = 4), S14 and S10 (8 % with *n* = 3, each), while the 9 other types are only represented by one grain each (Fig. 4.4). Based on Pupin (1980), the external morphological signature of this sample is of sub–alkaline granite origin, with a typological evolutionary trend that crosses sub–alkaline granite to calc–alkaline granites origin (Fig. 5). The internal zoning of the grains reveals that 85% (*n* = 33) of the euhedral zircons have the same typology from the core to the external morphology. In the remaining ones, where external morphology is not the same as in the core (15 % of the total grains and *n* = 6), G2 occurs twice as core type, and P5, S10, P1 and D occurs once each. From all grains where the internal morphology could be analysed (75 % of the total grains or *n* = 39), the majority are subtypes of P (P4 (18 % and *n* = 7)), P1 (15 % and *n* = 6), P2 (10 % and *n* = 4)), followed by S10 (10 %, and *n* = 4), P5 (8 %, and *n* = 3), and several types with two grains (S14, G1, D and G2) or one grain (S15, S8, S19, R3 and J5) each. The core morphological signature of the grains is of sub–alkaline granite origin, with a typological evolutionary trend that crosses sub–alkaline granite to calc–alkaline granites origin.

### *4.4.2. Internal and external structures of zircon grains*

The structures (internal and external) of the zircon grains in the uppermost (A) and lowermost sampling sites (C) are similar, while a very different pattern occurs in the intermediate sampling site (B) (Fig. 4.6).

At the uppermost (A) and lowermost sampling sites (C), the large majority of the grains (88 %) have a well–developed magmatic oscillatory zoning from the core to the grain surface, and a minority (12 %) have no internal structures (i.e., an opaque pattern). Cores are also predominant (76 to 94%). Recrystallised domains and traces of corrosion (by resorption or dissolution) are present in less than half of the grains (19 to 35%) (Fig. 4.3). Evidence that resembles metamictised domains vary from 22% to 38% of the grains, 38 to 45% have fracturing, 8 to 31% are only fragments, and mineral inclusions are rate found (2 to 8%). The width–to–length ratio of the zircon grains has a mean indicating an overall prevalence of elongated grains (i.e., a ratio larger than approaching 1).

At the intermediate sampling site (B), the majority of the total grains (57 %, $n$ = 8) have no internal structures (i.e., are opaque). The remaining grains have faint (21%, $n$ = 3) and broad (21%, $n$ = 3) magmatic oscillatory zoning from the core to the rim. Recrystallised domains and traces of corrosion (by resorption or dissolution) are visible in only 2 grains (14.2%) (Fig. 4.3). Evidence that resembles metamictised domains are found in 57% ($n$ = 8) of the grains, while 43 % ($n$ = 6) have fracturing and 57% ($n$ = 8) are only fragments. Evidences of inclusion are found 28% ($n$ = 4) of the grains. Less than half of the zircon grains (43 %, $n$ = 6) has an identifiable core. The width–to–length ratio of the zircon grains has a mean of 1.9 ($\sigma$ = 1.1), indicating an overall prevalence of zircon grains with similar length and width metrics (i.e., a ratio approaching 1).

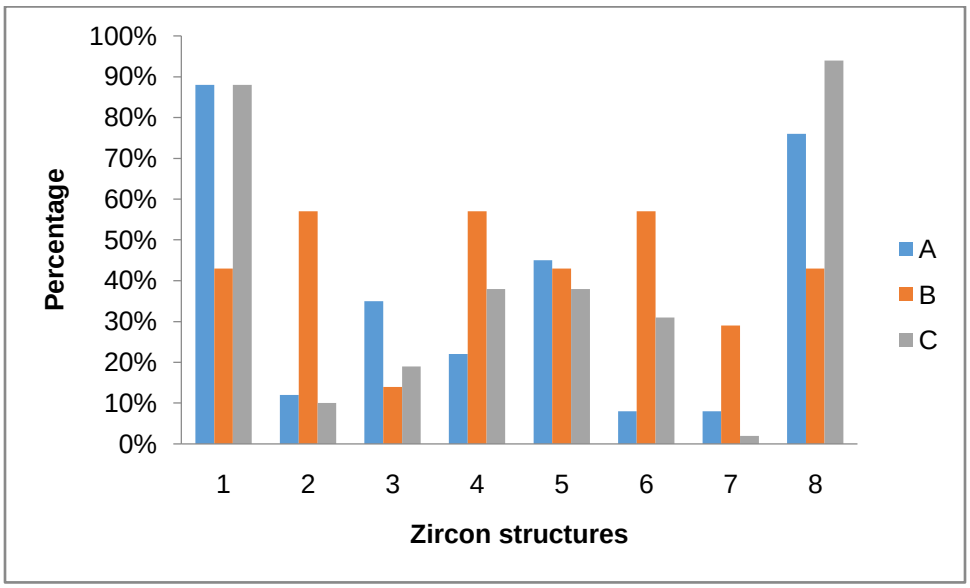


Figure 4.6: Summary of internal and external structures of zircon grains in the samples A, B and C. % = the percentage of each characteristic. The numbers on the x-axis correspond to the presence of (1) well–developed magmatic oscillatory zoning; (2) no internal structures; (3) recrystallised domains and/or corrosion; (4) metamictised domains; (5) fracturing; (6) grains are fragments; (7) inclusions; and (8) cores. Note the difference between the uppermost (A) and lowermost (C) sampling sites characteristics and those from the intermediate sampling site (B).

### *4.4.3. U–Pb ages*

In total, only 49 zircon grains from the uppermost sampling site (A) in the Tavignano watershed were dated, followed by 14 in the sampling site at the intermediate part of the watershed (B), and 54 in the lowermost sampling site (C) (Fig 4.1). Despite the significant amount of sediment sampled (~ 1 kg/sample), the number of analysed grains is far below the minimum of 117 required to a statistically significant analysis. By using the uncertainty estimation of Vermeesch (2004), the uppermost sample (A) has 5% of probability (*p*) that one particular fraction of the population (*f*) is missed if this fraction is greater than 11 %; the intermediate sampling site (B) has 5% of probability (*p*) that one particular fraction of the population (*f*) is missed if this fraction is greater than 26 %; and the lowermost sample (C) has 5% of probability (*p*) that one particular fraction of the population (*f*) is missed if this fraction is greater than 10 %. The limitations introduced by the amount of zircon grains in our analysis are discussed in the section 5 of this work.

In the uppermost sampling site (A), the U–Pb age distribution has several short peaks (150, 250, 375, 500, 625 and 650 Ma) and a large well–defined peak at ~ 300 Ma. In the intermediate sampling site (B), the U–Pb age distribution has only two peaks (~ 150 and 260 Ma), with the largest peak at ~ 150 Ma (Fig 4.1). In the lowermost sampling site (C), the U–Pb age distribution has the largest peak at ~ 300 Ma with a decreasing series of peaks from ~ 250 to 200 Ma, and small peaks from 150 to 200 Ma and from 450 to 500 Ma. The mean (μ) and standard deviation (σ) values of the $^{238}U$ and $^{206}Pb$ isotopes of each sampling site are displayed in the Table 4.1 and their mean masses show a drastic reduction from the uppermost (A) and lowermost (C) sampling sites to the intermediate sampling site (B).

Table 4.1: Mean (μ) and standard deviation (σ) values of each zircon sample. Note how the average values of $^{238}U$ and $^{206}Pb$ change according to the sampling site. The individual grain ages and their uncertainty can be found in the supporting information section (Table S2).

| | Sample A | | Sample B | | Sample C | |
|---|---|---|---|---|---|---|
| | μ (Ma) | σ (Ma) | μ (Ma) | σ (Ma) | μ (Ma) | σ (Ma) |
| $^{238}U$ | 855.8 | 610.7 | 131.0 | 325.9 | 1118.1 | 853.4 |
| $^{206}Pb$ | 35.5 | 23.5 | 4.6 | 12.1 | 39.5 | 27.6 |

### *4.4.4. Correlation between type, texture and age of zircons*

Here, I combine all zircon grain information presented in the previous sections about type and U–Pb ages to provide an overview of them. When grouping the zircons by types (i.e., S, J, D, P and G, see Fig. 4.2), the U–Pb ages show different average values (Fig. 4.7).

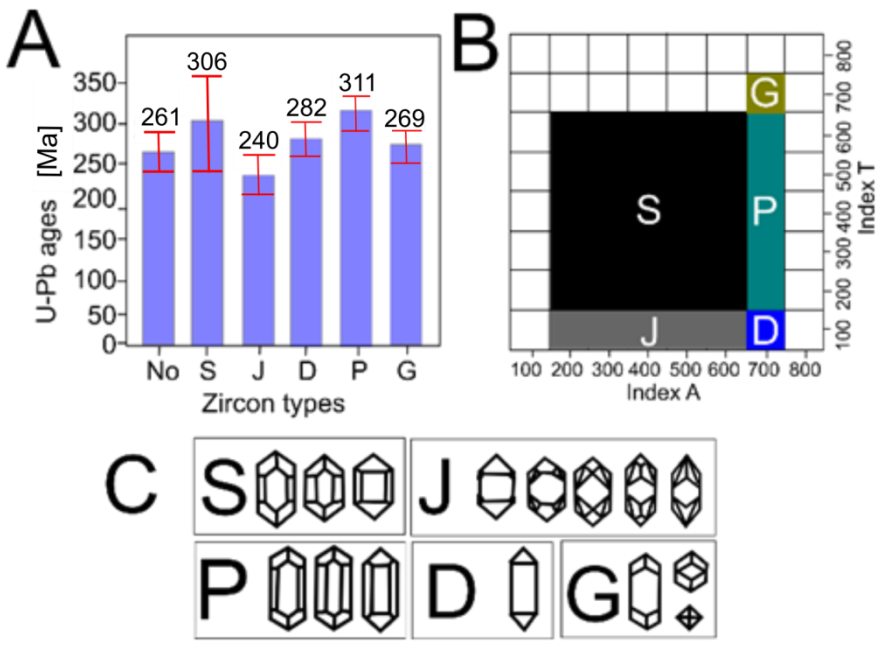


Figure 4.7: The U–Pb ages of zircon types, their average U–Pb ages, and indexes A and T found in the uppermost, intermediate and lowermost sampling sites of the Tavignano watershed. A) U–Pb ages by zircon types. B) Location of the previous zircon types in the classification of Pupin (1980) diagram. C) Main subtypes found in our samples. The zircon types S, J, P and G include all subtypes found. The term "no" refers to zircon that could not be classified due to non–euhedral characteristics or image limitations. The error bars (in red) are the uncertainty of the means, and at their top there are the mean age values (in Ma). Note that some zircon types with low index T have younger U–Pb ages than some zircon types with high index T.

The types at the bottom, i.e. with lower index T (temperature), in the classification of Pupin (1980), have higher U–Pb ages than those with a higher index, at the top of the classification scheme. For instance, the zircon types P (311 Ma) and S (306 Ma) are the oldest zircons in the samples and have an index T ranging from 300 to 700$^{o}$C, while the J and D types have younger U–Pb ages (240 and 282 Ma, respectively) and the highest index T of the samples (i.e., 800$^{o}$C). An exception to this pattern is the zircon type G that has a young U–Pb age (269 Ma) and a low index T (200$^{o}$C). The zircons that could not be classified have relatively young U–Pb ages (260). However, I performed a test (an analysis of variance [ANOVA]) to check if the ages of the zircon types are statistically different. The results indicate that there are no statistically significant differences on U–Pb ages between the zircon types described above (according to one–way ANOVA $F(5,106) = 1.3$, $p = 0.26$, see Table 4.2).

Table 4.2: Analysis of variance (ANOVA) of the main types of zircon found in our samples. Note that the p–value is not below 0.05 so I cannot reject the hypothesis that the groups have equal means. SS = sum of the squares, df = degrees of freedom, MS = mean square, F ratio (MS between groups/ MS within groups), P–value = probability of rejecting that the distance between the means of groups is small relative to the random error within each group (i.e., the null hypothesis). F critical = the minimum value of F required to reject the null hypothesis.

| *Source of Variation* | *SS* | *df* | *MS* | *F* | *P–value* | *F crit* |
|---|---|---|---|---|---|---|
| Between Groups | 45779.6 | 5 | 9155.9 | 1.3 | 0.2 | 2.3 |
| Within Groups | 744307.2 | 106 | 7021.7 | | | |
| Total | 790086.8 | 111 | | | | |

## *4.4.5. Zircon mixing models*

### *4.4.5.1. Best–fit of zircon sources in the mixed samples*

The U–Pb age unmixing of the downstream mixed sand samples (A, B and C) reveals varying sensitivities to find the best–fit of the U–Pb source ages (Fig. 4.8). It also reveals a large variation in the proportion of each source in the zircon mixing.

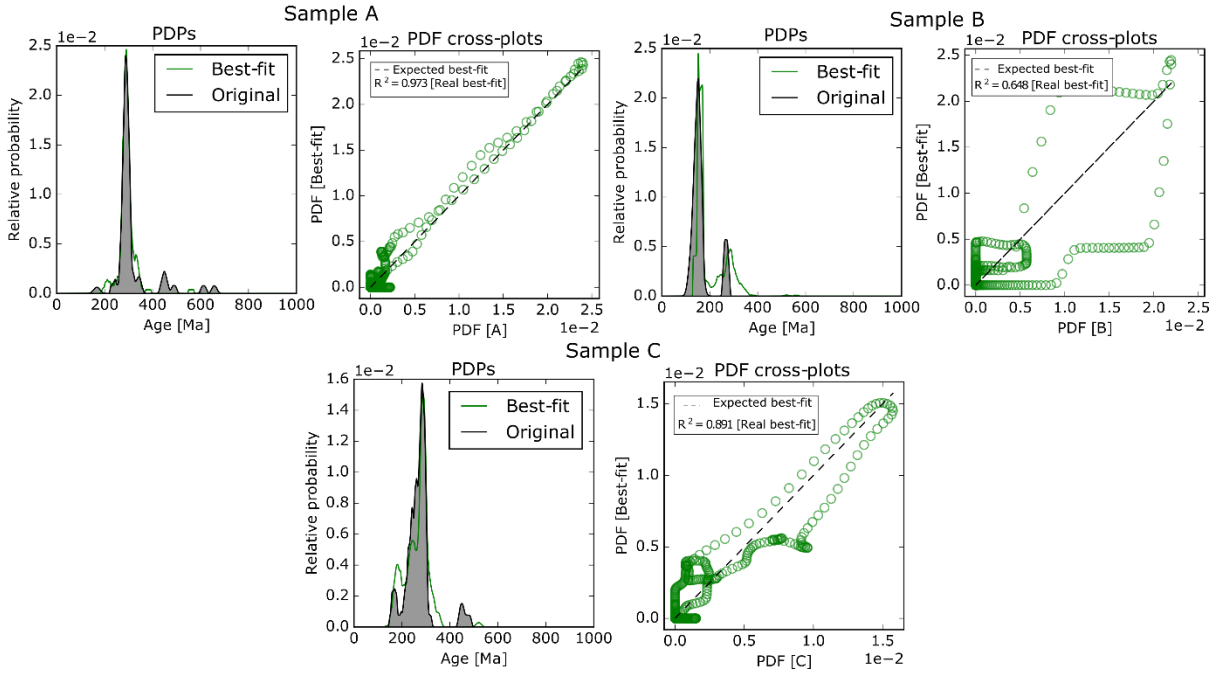

Figure 4.8: Real U–Pb age distributions and their best–fit of source mixing in the sand samples collected along the Tavignano watershed. Sample A, B and C are the uppermost, intermediate and lowermost sampling sites investigated in this work, respectively. Green plots represent the best–fit solutions; black and gray plots are the measured (real) age distributions.

At the uppermost sampling site (A), the best–fit solution was able to fit relatively well the main peak at ~ 300 Ma (U2) but it was unable to fit to the smaller peak ages at ~ 150 Ma, 400–500 Ma, and 600–700 Ma. The sediment mixing proportion deconvolved from the best–fit solution is 16.7 % from U2 leucomonzogranite, 21.3 % from U2 fine grain monzogranite, 56.7 % from U2 medium grain granodiorite and 5.3 % from U1 mesocratic granite. The percentage of exposure area of these source units are 75.0 % from U2 leucomonzogranite, 10.9 % from U2 fine grain monzogranite, 11.3 % from U2 medium grain granodiorite and 2.6 % from U1 mesocratic granite (Fig. 4.9). Everything else being equal (e.g., zircon fertility and erosion), the proportions of each source in the river sample should match the exposure area, but that is not the case. The statistical parameters show a relatively good agreement between the best–fit and the detrital mixed sample (A), according to the similarity (90 %), mismatch (15.1 %), likeliness (84.8 %), Kolmogorov–Smirnov ($D$ = 0.1, $p$ = 0.4), Q–Q plot ($R^2$ = 0.9) and PDF cross–plot ($R^2$ = 0.9) coefficients.

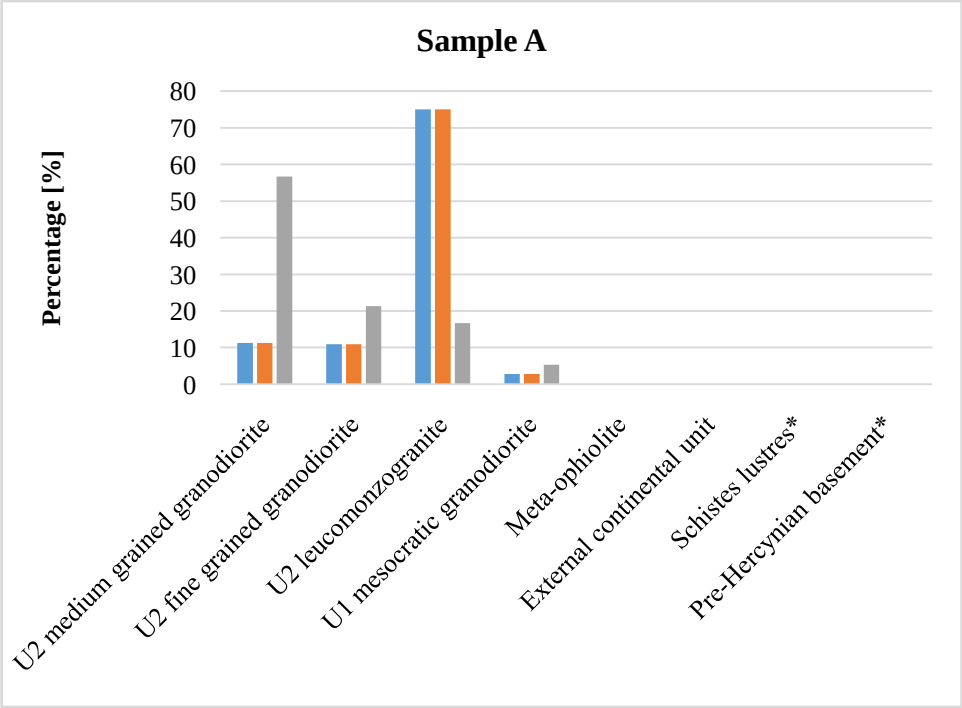

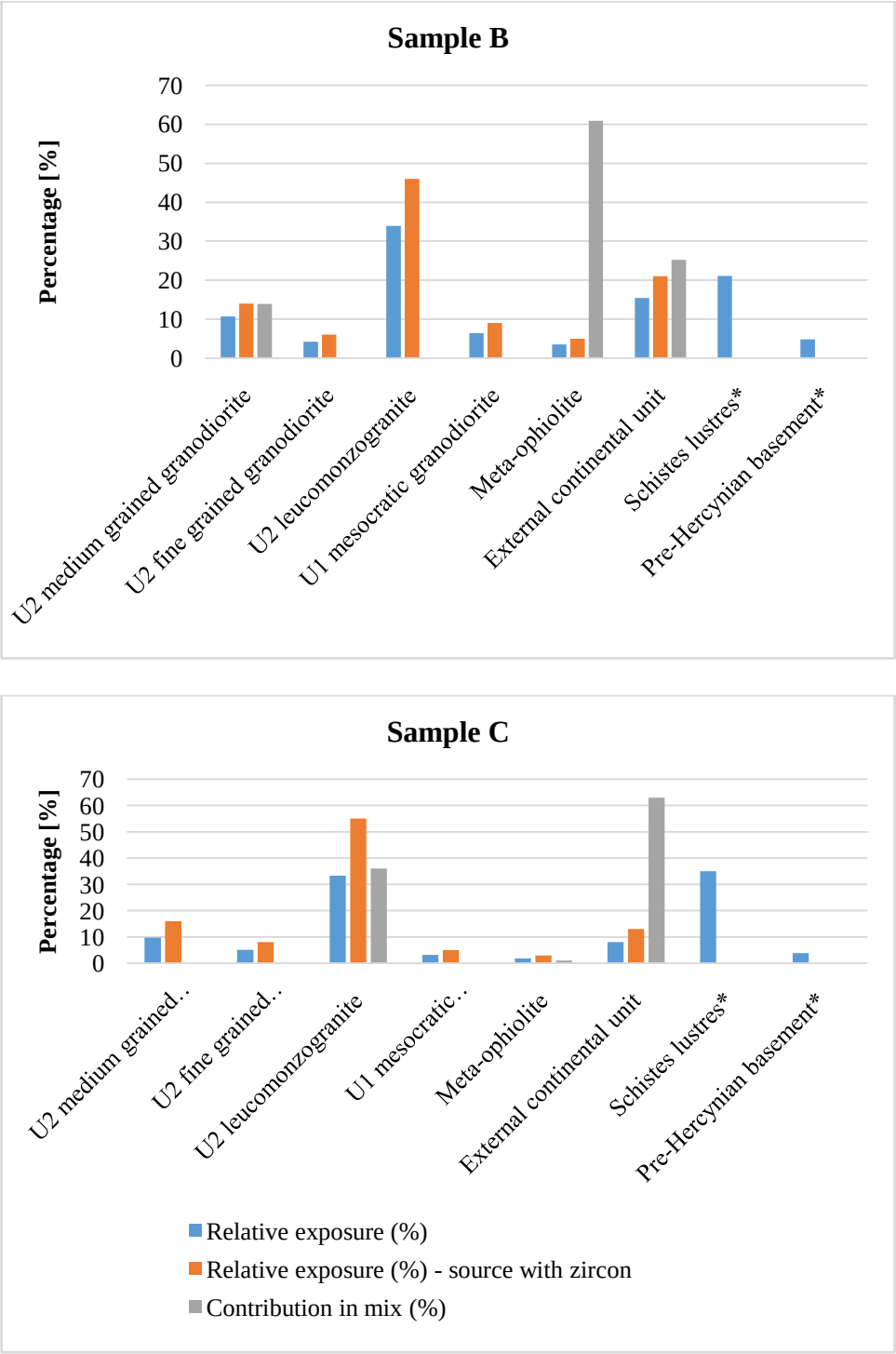


Fig. 4.9: Relative proportion of detrital zircons expected based on exposure area only ("relative exposure (%)" in blue); relative proportion of detrital zircons expected based on the exposure area but restricted to those with zircon fertility ("relative exposure (%) –source with zircon" in orange); and the measured contribution in mixed samples A, B and C estimated using the unmixing results shown in subsection 4.5.1 ("contribution in mix (%)" in grey).

At the intermediate sampling site (B), where only 14 grains were analysed, the best–fit solution was unable to fit well all age peaks at ~ 150 and ~ 275 Ma: offset is observed, and some ages that were not sampled are predicted by the best–fit solution (e.g., older than 300 Ma). The sediment mixing proportion deconvolved from the best–fit solution is 60.9 % from meta–ophiolite, 25.2 % from external continental unit and 13.9 % from U2 medium grain granodiorite. The percentage of exposure area of these source units are 3.5 % from meta–ophiolite units, 15.4 % from external continental units, 10.7 % from U2 medium grain granodiorite, 4.2 % from U2 fine grain monzogranite, 33.9 % from U2 leucomonzogranite, 6.2 % from U1 mesocratic granite, 21.1 % from Schiste Lustrés units and 4.8 % from Pre–Hercynian basement. This means that 25.9 % (Schiste Lustrés and Pre–Hercynian) of the source units are undetectable due to absence of zircon U–Pb age constrains. Everything else being equal (e.g., zircon fertility and erosion), the proportions of each source in the river sample should match the exposure area only of those with U–Pb age constrains but, again, that is not the case. The statistical parameters show a relatively high disagreement between the best–fit and the downstream mixed sample (B), according to the similarity (78.8 %), mismatch (38.5 %), likeliness (61.4 %), Kolmogorov–Smirnov ($D$ = 0.4, $p$ = 4 x $10^{-3}$), Q–Q plot ($R^2$ = 0.9) and PDF cross–plot ($R^2$ = 0.6) coefficients.

At the lowermost sampling site (C), the best–fit solution was able to fit relatively well the peaks between ~ 150 and 300 Ma but it was unable to fit the peak ages 350–500 Ma. The sediment mixing proportion deconvolved from the best–fit solution is 1.0 % from meta–ophiolite, 63.0 % from external continental unit and 37.0 % from U2 leucomonzogranite. The percentage of exposure area of these source units are 1.8 % from meta–ophiolite units, 8.0 % from external continental units, 33.3 % from U2 leucomonzogranite, 5.1 % from U2 Fine grain monzogranite, 3.2 % from U1 Mesocratic granite, 35.0 % from Schistes Lustrés units, 3.9 % from Pre–Hercynian basement. This means that 38.9 % (Schiste Lustrés and Pre–Hercynian) of the source units are undetectable due to absence of zircon U–Pb age constrains. Everything else being equal (e.g., zircon fertility and erosion), the proportions of each source in the river sample should match the exposure area only of those with U–Pb age constrains but this largely contrasts with our results. The statistical parameters show a relatively high disagreement between the best–fit and the downstream mixed sample (C) as evidenced by the similarity (91.9 %), mismatch (20.5 %),

likeliness (79.4 %), Kolmogorov–Smirnov ($D$ = 0.1, $p$ = 0.51), Q–Q plot ($R^2$ = 0.9) and PDF cross–plot ($R^2$ = 0.8) coefficients.

## 4.5. Discussion

### *4.5.1. Typological classification of zircon grains*

In the uppermost sampling site (A), only 34 grains could be typologically classified, which gives, according to Vermeesch (2004), 20 %, 10 % and 5% of probability of missing at least one source larger than 11 %, 12 % and 14 %, respectively. This means that except for the U2 leucomonzogranite (75.0 % of the exposure area), all the remaining sources (i.e., U2 fine grain monzogranite, U2 medium grain granodiorite and U1 mesocratic granite) have less than 80 % of confidence to be represented in our sample. In the intermediate sampling site (B), only 4 grains were analysed, which gives 96% of probability of missing at least one fraction larger than 20 %. This poses a serious limitation to the interpretation of the zircon types from this sample, given that even the largest sources have a high risk to be missed (e.g., U2 leucomonzogranite with 33.9 % of exposure area). In the lowermost sampling site (C), only 39 grains were analysed, which gives 96 % and 14 % of probability of missing at least one fraction larger than 5 % and 10 %, respectively. In this case, only U2 leucomonzogranite (54.8 % of exposure area), U2 medium grained granodiorite (15.3 % of exposure area) and external continental unit (13.1 % of exposure area) are larger than 10 % of the total population, so they have a lower probability (14 %) of being missed from the provenance analysis.

In spite of this severe statistical limitation, relevant information can be retrieved from the zircon typology. Regarding the morphological signature, the diversity of zircon types increases from the uppermost (A) to the lowermost sampling site (C) where more calc–alkaline types such as S subtypes are found. The majority of the samples indicates a sub–alkaline to alkaline granite origin, which fits the broad classification scheme of the contributing source rocks studied by Cocherie et al. (1992, 2005), Ohnesnstetter et al. (1981) and Rossi et al. (2006, 2015) (i.e., ‘Mg–K’ U1 and a ‘calc–alkaline’ U2 group). In addition, our detrital zircon typology also reflects

known characteristics of source areas such as the orogenic calc–alkaline Hercynian granites and anorogenic alkaline Permian granites of Corsica identified in the seminal work of Pupin (1980).

The spread of zircon types in our samples are large, from high (800$^{o}$C) to low temperatures (200$^{o}$C). According to several workers (e.g., Pupin, 1980; Vavra, 1990, 1993) large variation in index T are indicative of a complex crystallisation history of the zircon grains. According to Cocherie et al. (2005), the zircon typology of the U2 leucomonzogranites of Corsica, whose zircons are the main source of our samples, reflects this complex crystallisationhistory. Published zircon typology from the U2 leucomonzogranites includes a P5 majority (65 %) with an average AT index of 684–700 (Punta di Carbone outcrop); a range of zircon types from G1 to P5 with an average AT index of 464–597 (Coti Chiavari outcrop); mainly P4–P5 zircon types, with an average AT index of 614–681 (Cima a Forca outcrop); predominantly S2 to S23 types, with an average AT index of 342–477 (Verde pass outcrop); and G1 to P3–S23 types (Tana outcrop). The meta–ophiolite of Schistes Lustrés (Inzecca unit) has zircons with characteristics of tholeiitic series, with types predominantly J5 and D, and AT index of 624–785. The zircon types identified for the U2 and meta–ophiolite units, which are the main sources of zircon in our samples, are in rough agreement with those I found in the uppermost (e.g., D, G1, S5, P2), intermediate (e.g., G2, R3 and J5), and lowermost sampling sites (e.g., P1, P2, P4, P5) in this work.

### *4.5.2. Internal and external structures of zircon grains*

The fact that the majority of zircon grains have a similar typology on both core and external morphology reinforces, among other things, their origin from a chemically stable environment (Miller et al., 2007; Vavra et al., 1996, 1999).

Another relevant information from the structure of zircon grains is the varying percentage of recrystallised domains and of rounded/opaque grains from sampling sites. The percentage of grains with recrystallised domains is larger in the uppermost sampling site (A) closer to the Alpine wedge (39.5 %), than in the lowermost one (C) near the Aleria plain (19.2 %). The intermediate sampling site (B) has a majority (57.1 %) of grains with no internal structures (i.e.,

are opaque) and an overall prevalence (42.8 %) of zircon grains with similar length and width metrics, typical of rounded grains (i.e., approaching 1). These characteristics, together with the very small number of grains ($n$ = 14) that were collected from the same amount of sand sampled (~ 1 kg) at site B, suggest that zircon grains of the intermediate sampling site (B) may come from sources with lower zircon fertility and different crystallisation histories. The two distinct U–Pb age peaks (~ 150 and 260 Ma) are consistent with the suggestion that these zircons are mainly from meta–ophiolites (Inzecca unit) and external continental slivers (Santa–Lucia–Di–Mercurio) rather than U1 and U2 group rock types found in the other samples (A and C). The internal and external structure of these zircon grains highlight they can have experienced a higher grade of metamorphism during the Alpine orogeny that altered the original euhedral characteristics into non–euhedral ones, including loss of zoning, and/or morphological changes made by abrasion during transport (potentially enhanced by metamorphism of the grains). Another possibility is that size–density sorting, as reported in previous works (e.g., Garzanti et al., 2008, 2009), may have biased the information retrieved from this sample by favouring the transport/deposition into placers and lag deposits of the lighter/smaller grains (from meta–ophiolites and external continental slivers) against the heavier/larger ones (associated to the U2–U1 groups of granites). The discontinuous transmission of provenance zircon signals has been noticed in other settings (e.g., in the Nile river; see Garzanti et al., 2018), where detrital age compositions are lost repeatedly, altered or replaced over long distances due to size–density sorting of younger, denser and non–metamictised zircon grains rather than lighter, older, and metamictised grains. However, I cannot discard the limited number of grains (< 117) as one of the most likely biasing factors to weaken a proper identification of the sources through grain analysis.

### *4.5.3. Best–fit of zircon sources in the mixed samples*

Our U–Pb unmixing procedures to predict zircon mixing proportions have relatively higher mismatch values than similar studies using the same technique. For instance, Amidon et al. (2005) found area mismatch values ranging from 6.0 % to 12.4 % in a well–constrained watershed in the Himalayas. In our case, the area mismatch between the real (measured) zircon

age distribution and the best–fit made of contributing source ages at the intermediate sampling site (B) is ~ one fold higher (38.5 % of area mismatch) than in the lowermost (C) sampling site (20.5 % of area mismatch). The area mismatch in the intermediate sampling site (B) is ~ 2.5 times higher than the uppermost sampling site (A), which is our best–fitted scenario (with 15.1 % of mismatch).

The other statistical analyses (similarity coefficient, likeliness, Kolmogorov–Smirnov, Q–Q plot and PDF cross–plot) mirror the same trend diagnosed using the area mismatch. Several hypothesis can explain these statistical misfits: limited number of analysed grains, local size–density sorting condition, missing U–Pb ages from some sources and overlapping ages.

The U–Pb age distribution at the intermediate sampling site (B), contrary to what happens in the uppermost (A) and lowermost sampling sites (C), does not record the age peaks at ~ 300 Ma (U2 group) and from 450 to 500 Ma (Pre–Hercynian?). If a source age is identified upstream and downstream from a sample, it is likely that an analytical bias (e.g., the number of dated grains) or natural biases (e.g., local size–density sorting condition) can have caused the disappearance of those age peaks in an intermediate sample, which should have recorded them (e.g., Garzanti et al., 2018). Although I do not have any constraint about local size–density sorting to test this hypothesis, I know the number of analysed grains is far below the recommended amount of 117 (see Veermech, 2007). By analysing only few grains (e.g., 6 grains from the meta–ophiolites and 14 grains from the sampling site B), some source ages can be missed in a downstream mixed sample, which seriously affects the inversion scheme that finds the best–fit solution of contributing sources (Veermesch, 2007; Sundell and Saylor, 2017). Therefore, I test the hypothesis of limited number of zircon grains in one of the following section (4.6.1).

Two relevant aspects can be highlighted about missing possible sources using a U–Pb provenance analysis tool. Firstly, the absence of U–Pb zircon ages from units with very large exposure areas (e.g., Schistes Lustrés and Pre–Hercynian basement) violates the assumption that zircons can be used as a tracer to estimate sediment mixing proportions in the Tavignano watershed. Therefore, in our case, U–Pb zircon ages can only be used as a proxy to investigate zircon mixing proportions instead. This reinforces that the choice of a tracer mineral should be based on the mineralogy of the rock types in the investigated area, given that mineral

concentration is the most important factors in detrital studies and all further analysis are grain–dependent. Secondly, the missing U–Pb ages of Schistes Lustrés and Pre–Hercynian basement may explain the missing peaks older than 600 Ma and ~ 500 Ma in the samples B and C (and by extension their statistical misfits).

Another key aspect to be highlighted is the misfit between the zircon proportions estimated from the U–Pb age unmixing and what would be expected based on the current exposure area of each source rock, as it is assumed in some detrital studies (e.g., Saylor et al., 2013) (Fig. 8). In the uppermost sampling site (A), there is a misfit of 2.7 % between granites of groups U1 and U2. Within these groups, deviation between predicted contribution in the mixed sample and what would be expected based on exposure area (everything else equal) reaches up to 58.3 % (U2 leucomonzogranite). At the intermediate sampling site (B), excluding those source rocks with no U–Pb zircon ages (i.e., Schistes Lustrés and Pre–Hercynian basement), there is a misfit of 52.2 % between the exposure area of the U2 granites (66.1 %) and the zircon proportion estimated from them (14 %). Also at the intermediate sampling site (B), a misfit of 56.3 % is recorded between the exposure area of the meta–ophiolite (4.6 %) and the percentage of zircon estimated from the U–Pb age unmixing (61.0 %). At the lowermost sampling site (C), excluding those source rocks with no U–Pb zircon ages, the main misfit (49.0 %) is between the exposure area of the external continental unit (13.0 %) and the percentage of zircon estimated from the U–Pb age unmixing (63.0 %). Also at the lowermost sampling site (C), the misfit between the exposure area of the U2 groups and their estimated zircon proportion is 42.1 %. A potential analytical explanation for these misfits is that overlapping ages from the U2 groups (e.g., U2 leucocratic granite, U2 fine grained granodiorite, etc.) around 280 Ma can have biased the predicted zircon proportions during the unmixing procedures. This overlapping can help explaining why some source rocks from the U2 group are set as contributing 0 % (e.g., U2 leucocratic granite) while others have a relatively high percentage (e.g., U2 fine grained granodiorite) at the intermediate (B) and lowermost sampling sites (C). One hypothesis is that the U–Pb age unmixing can select specific age populations that increase the best–fit solution while setting similar age sources as contributing with zero grains, therefore biasing the predicted mixing proportions. I test the hypothesis of overlapping ages in one of the following section (4.6.2).

Lastly, the U1 group is invisible in the estimated mixing proportions in the intermediate (B) and lowermost sampling sites (C), despite having an isolated age peak (320–350 Ma) and a considerable exposure area (varying from 5.3 % to 8.4 %, if only sources with U–Pb ages are considered). In this case, due to the isolated peak, age overlapping seems less significant than in the U2 units, so the most likely explanation is the number of analysed grains. Besides the biases caused by analytical and size–density sorting previously mentioned, four factors can also change the zircon proportions in mixed samples: gravel hillslope supply, zircon fertility, erosion rates and abrasion rates. In two of the following sections (4.6.3 to 4.6.4), I use simple numerical experiments to simulate how these factors can cause the biases in the detrital information retrieved in our work and to explain why it may be difficult to disentangle them.

## 4.6. Testing analytical and natural biasing factors

### *4.6.1. Number of analysed grains*

In these experiments, I perform two scenarios (A1–A2) where I analyse if there is a statistically significant difference between the U–Pb age distributions created using the minimum required number of zircon grains per sample ($n$ = 117) and the number of grains analysed in this work (i.e., between 6 and 84. See Fig. 4.1).

In scenario A1, I generate synthetic ages with normal distributions for each contributing source of the uppermost sampling site (A). Following Vermeesch (2005), I create 117 synthetic grain ages with peaks at 300, 400, 500 and 600 Ma ($\sigma$ = 6). These age peaks were created to avoid the influence of overlapping in the final results and, therefore, to capture only the influence of the tested factor (i.e., number of grains). I also create a synthetic mixed sample that represents the sampling site (A) as a combination that matches the percentage exposure area of each source and by consequence the amount of grains that are expected if everything else is equal. The number of synthetic grains at the mixed sample equals the sum of the upstream sources (i.e., $n$ = 468).

In scenario A1, the PDF cross–plot shows that the statistical misfit between best–fit solution of contributing sources and the synthetic mixed sample age distribution is not significant

to reject that they are equal (Fig. 4.10a). Although there is 11.0% of area mismatch (M), the other parameters show a relatively good agreement between the best–fit solution and the synthetic age distribution (S = 0.9, M = 0.1, L = 0.9, Ks = 0.05, $p$ = 0.5, Q–Q plot [$R^2$ = 0.929]).

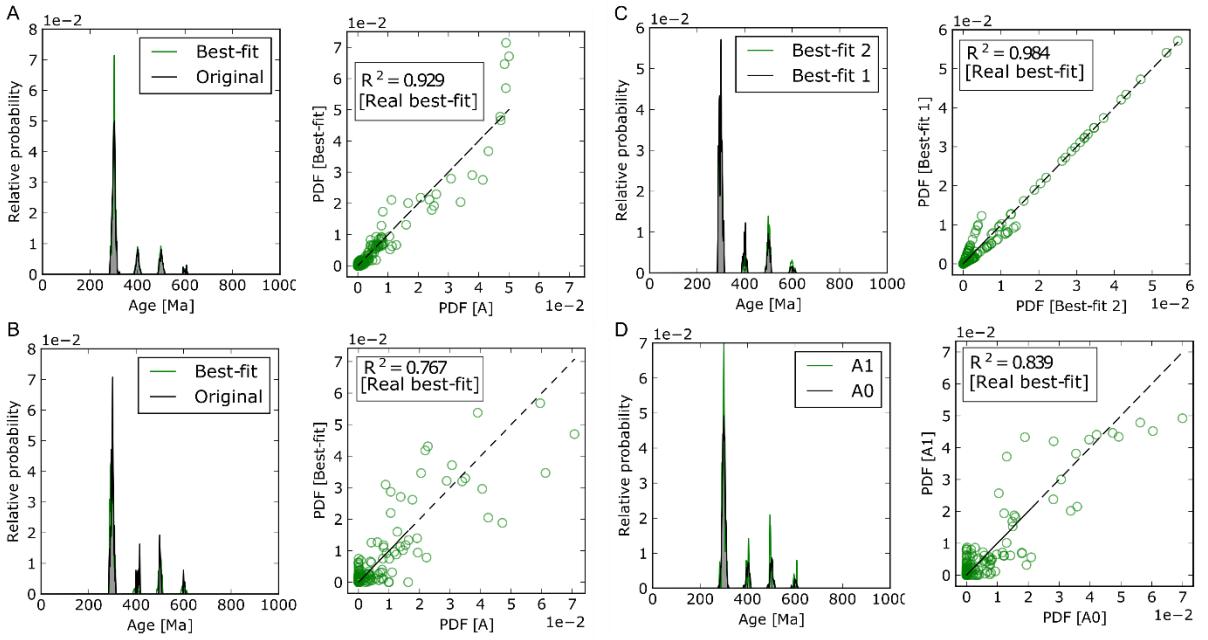


Figure 4.10: Synthetic U–Pb age distributions, best–fit solutions and their PDF cross–plots in the simulations A1–A2. Panels A and B are comparing the synthetic age distributions and their best–fits in the scenarios A1 and A2, respectively. Panel C represents a comparison of the best fits solutions of A1 and A2. Panel D represents a comparison of the synthetic age distributions of A1 and A2.

In scenario A2, I randomly select from the previous scenario (A1) the amount of grains used in reality to characterise the sources (i.e., 59, 19, 53 and 51 grains in the U2 Medium grain granodiorite, U2 fine grain monzogranite, U2 leucomonzogranite and U1 mesocratic granite extracted from the works of Cocherie et al. (1992, 2005), Ohnesnstetter et al. (1981) and Rossi et al. (2006, 2015), respectively) and the mixed sample of the river sample A (49 grains from this work). In the scenario A2, the misfit largely increases as attested by the statistical metrics (S = 0.9, M = 0.3, L = 0.7, Ks = 0.15, $p$ = 0.4, Q–Q plot [$R^2$ = 0.767]). In this case, the PDF cross–plot shows that hypothesis that the best–fit age distribution and the synthetic age distribution are equal can be rejected with more than 95% confidence ($R^2$ = 0.767, i.e., only 76.7 % of the variance in one age distribution fit to the other; see Fig. 4.10b). This result suggests that by using the amount of grains analysed in our work, I have a significantly biased best–fit age distribution.

I perform a statistical comparison between the best–fit age distributions of the scenarios A1 ($n$ = 467) and A2 ($n$ = 49) (Fig. 4.10c). The comparison reveals that the mismatch between the two best fits is not significant enough to reject that the two distributions are equal (S = 0.9, M = 0.1, L = 0.9, Ks = 0.09, $p$ = 0.3, Q–Q plot [$R^2$ = 0.9]). This suggests that the best–fit generated from the amount of grains analysed in our work would not be statistically different if I had used the minimum recommended number of zircon grains instead.

I also perform a statistical comparison between the synthetic age distributions that simulates the mixed sampling site (A) in scenarios A1 ($n$ = 467) and A2 ($n$ = 49) (Fig. 4.10d). The comparison reveals that they are largely different (S = 0.9, M = 0.2, L = 0.7, Ks = 0.14, $p$ = 0.4, Q–Q plot [$R^2$ = 0.84]) and, according to the PDF cross–plot, the hypothesis that they are equal can be rejected (with 95 % confidence). This result suggests that the real (measured) age distribution is significantly biased if the amount of grains changes from the recommended number (i.e., $n$ = 117) to the amount used in this work.

Our simulations suggest that reducing the number of analysed grains to the amount I used in this work induces a statistically significant bias on the U–Pb age distribution of the mixed sediment sample. Although the best–fit age distributions do not differ from each other, the age distributions from synthetic mixed sand sample (A4) using our number of grains are significantly affected. These simulations reinforce that the amount of grains I used can have biased the interpretations of our work (i.e., typology, internal texture, U–Pb age distribution and mixing proportions of zircons) since every result is grain–dependent. It also reinforces the importance of following Veermesch (2007)'s recommendation about the number of grains in provenance analysis.

### *4.6.2. Overlapping age peaks*

In these experiments, I test the influence of overlapping age peaks in the estimated U–Pb best–fit age distribution and in the zircon mixing proportions. I start the experiments (B1) with the same ages of the scenario A1 of the previous experiment (i.e., peaks at 300 [U2 leucomonzogranite], 400 [U2 Fine grain granodiorite], 500 [U2 Medium fine granodiorite] and

600 Ma [U1 Mesocratic granite]). I then perform simulations with different age intervals and record their changes in the statistical parameters until they fully overlap each other (Fig. 4.11). These age peaks are: 300, 350, 400, and 450 Ma in the second simulation (B2); 300, 325, 350, and 400 Ma in the third simulation (B3); 300, 310, 320 and 330 Ma in the fourth simulation (B4); and all sources with 300 Ma in the fifth simulation (B5).

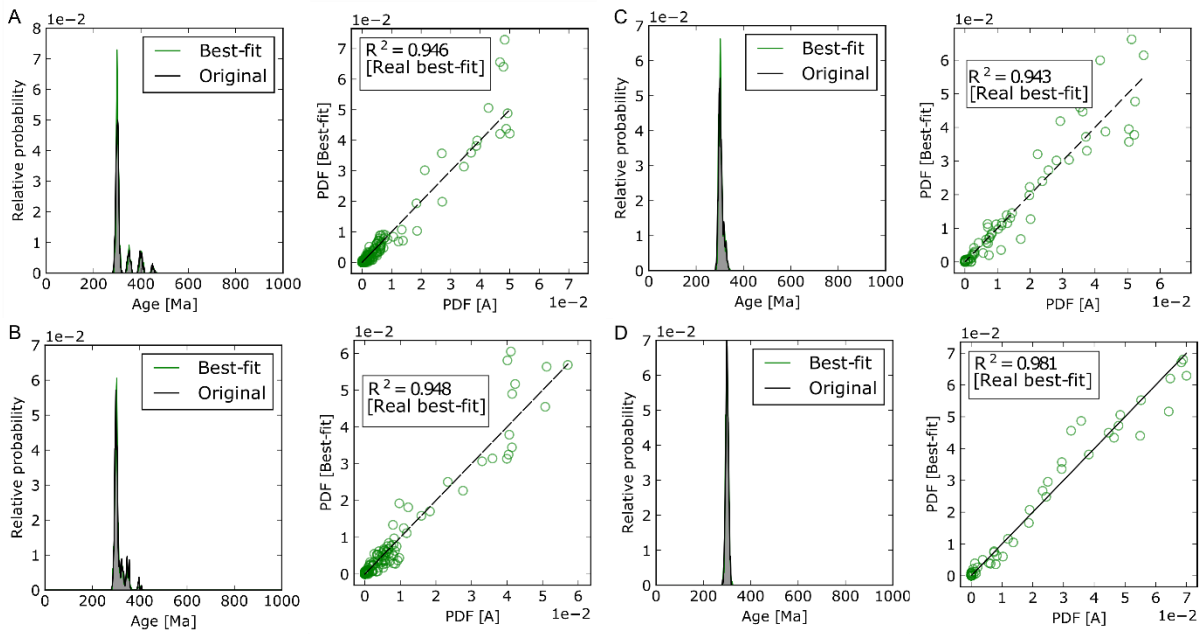


Figure 4.11: Synthetic U–Pb age distributions, best–fit solutions and their PDF cross–plots in the simulations: B2–B5. Panels A, B, C and D are comparing the synthetic age distributions and their best–fits in the scenarios B2, B3, B4 and B5, respectively. The simulation B1 is the same as the plot A1 in figure 4.9 and for this reason is not portrayed here.

These simulations suggest an increase in statistical misfit as the age peaks progressively approaches the other (B1 to B3), but then it starts to decrease when they progressively overlap (B4 to B5). In the scenarioswhere the age peaks are very distant (B1) until the peaks start overlapping each other (B3), the statistical parameters highlight an increase in the misfit between the best–fit and the synthetic age distribution. According to the PDF cross–plot, the best–fit and synthetic age distribution can be rejected as equal (Fig. 4.11a, b; Table 4.3). In the scenarios B4 and B5, where the age peaks sharply overlap, there is a decrease in the misfit of the best–fit solution and the synthetic age distribution, but, according to the PDF cross–plot only the scenario B4 can still be rejected as equal (Fig. 4.11c and d).

Table 4.3: Statistical parameters retrieved in each simulated scenario (B1 to B5) using different age peaks for each lithology. Note how the K–S tests (and their p–values) and M increase in the first three scenarios (B1–B3) and then decrease in the last two (B4–B5). S = similarity coefficient. M = area mismatch. L = likeliness. K–S = Kolmogorov–Smirnov (distance value) and its *p*–value (i.e., the probability of rejecting the hull hypothesis, i.e., they age distributions are equal).

| Scenario | S | M | L | K–S | p–value | Q–Q plot |
|---|---|---|---|---|---|---|
| B1 | 0.9 | 0.1 | 0.9 | 0.05 | 0.5 | 1.0 |
| B2 | 0.9 | 0.1 | 0.9 | 0.07 | 0.2 | 1.0 |
| B3 | 0.9 | 0.2 | 0.9 | 0.1 | 0.006 | 1.0 |
| B4 | 0.9 | 0.1 | 0.9 | 0.01 | 0.001 | 1.0 |
| B5 | 0.9 | 0.06 | 0.9 | 0.01 | 0.0011 | 0.9 |

However, by analysing the predicted zircon proportions of the previous simulations, I identify an inverted pattern where the misfit between the synthetic and predicted percentage of grains from the sources progressively increases with increasing overlap. In the first three scenarios (B1–B3), when the age peaks get closer and an increase in statistical misfit occurs, the maximum misfit between the synthetic zircon proportion and the predicted zircon proportion is 2.9 % per contributing source (U2 leucomonzogranite in scenario B3) (Fig. 4.12). In the last two scenarios (B4–B5), when the age peaks strongly overlap and a decrease in statistical misfit occurs, the maximum misfit between the synthetic zircon proportion and the predicted zircon proportion can be up to 64.1 % per contributing source (U2 leucomonzogranite in the scenario B5).

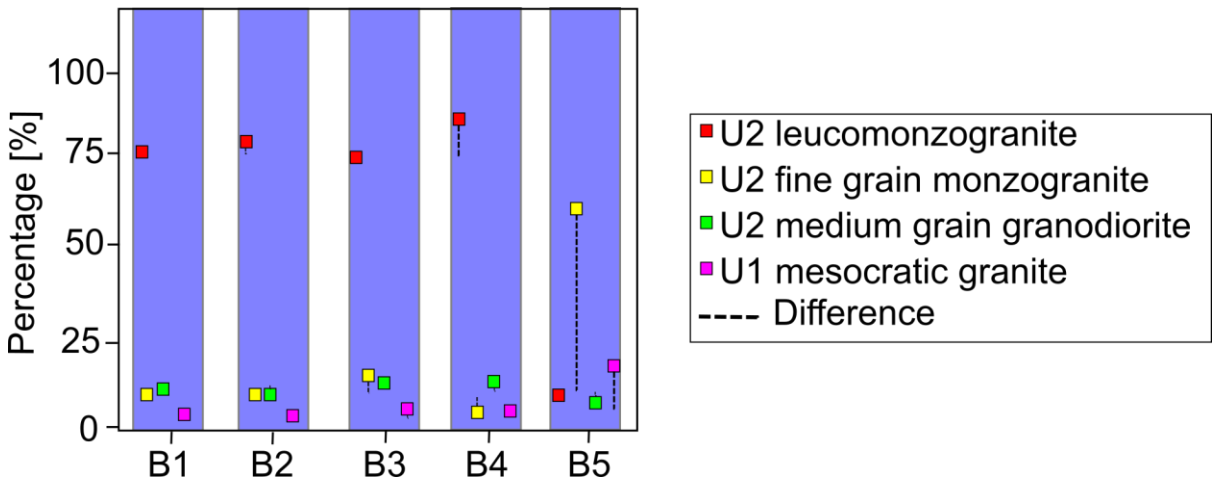


Figure 4.12: Zircon mixing proportion predicted in every simulation (B1–B5) compared to the percentage of exposure area per source. Note that the differences increase particularly in the experiments B4 and B5.

These simulations suggest that, even though the statistical misfit reduces in situations with age overlapping, the misfit between the predicted and real zircon mixing proportion can be extremely high. This is particularly important in cases where the variability of age peaks around the mean can cause significant overlapping (B4–B5). It is important to note that in the case of nearly complete overlap of peaks for two sources, attributing a grain to either of these sources will not lead to change in mismatch. Therefore, the relative best–fit proportions between these two sources will almost be random, as the algorithm will not be able to use change in mismatch to attribute a grain to the source it actually comes from. Large differences between real and predicted proportions for the source with overlapping peaks will be expected in these circumstances, as the algorithm will likely put all the grains in the same source (once a grain has been attached to one of these two sources, moving it to the second source will not improve mismatch). For this reason, I believe that different sources with overlapping age peaks should be treated as a single source rather than varying sources in U–Pb detrital zircon analysis. In our case, the U2 group (with overlapping ages from 200 to 400 Ma) should be analysed as a single source to minimise the misfit on their predicted zircon mixing proportions. However, this approach would not work for sources that are made of more than one peak, even if one of the peaks significantly overlaps with the peak from another source. Assessing the overlap effect in these circumstances would require further experiments.

### *4.6.3. Hillslope sand supply*

In these experiments, I simulate four scenarios (C1–C4) with varying values of hillslope sand supply to measure their capability of reproducing the same zircon mixing proportions of the uppermost sampling site (A) estimated from the U–Pb age deconvolution (as shown in the section 4.5.1). Because I do not consider abrasion here, all sand is initially delivered from hillslopes. Here, I test the influence of having differences in sand fraction initially supplied: if a rock unit has an initial sand fraction of 20 % (of all sediment supplied from the hillslopes), and another 10 %, then the former is expected to relatively contribute twice the amount of zircon compared to

the latter. No empirical constrains are available for the Tavignano watershed about grain size supplied from the hillslopes, I use a wide range of possible scenarios.

In the scenarios C1 and C2, I use an extreme scenario where the sand supply from hillslopes can very between 0% and 100% and between 0% and 50% for all contributing lithologies, respectively. The results indicate that these scenarios (C1 and C2) can almost perfectly reproduce the measured zircon mixing proportions according to the sum of squares due to error (SSE = 3.0 x $10^{-2}$ and SSE = 2.1 x $10^{-5}$, for C1 and C2, respectively) (Fig. 4.13).

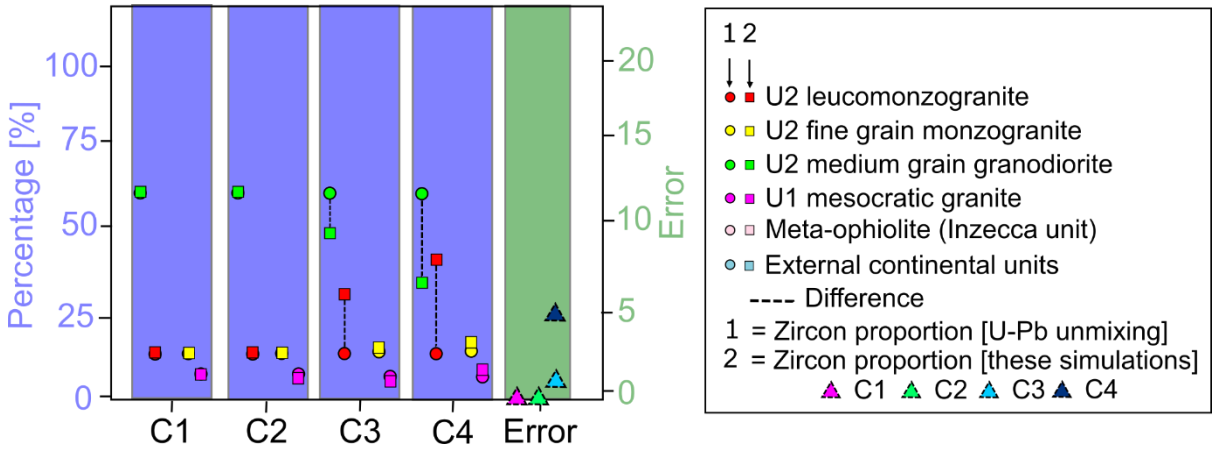


Figure 4.13: Comparing the ability of sand hillslope supply to produce the zircon mixing proportions in the scenarios C1 to C4. The error is the sum of squares due to error (SSE) between the zircon mixing proportions calculated using zircon fertility and U–Pb age unmixing. Note that the simulations C1 and C2 can reproduce the zircon mixing proportions that match the proportions of the uppermost sampling site (A), while C3 and C4 cannot. The squared dots (1) represent the zircon mixing proportion estimated in this work using U–Pb unmixing techniques. The circled dots (2) represent the zircon mixing proportion estimated using the parameters of scenarios E1 to E4.

In the scenarios C3 and C4, I use a more restrictive condition, with values from 10 to 100% and from 10 to 50% of sand supply per source as bounds, respectively. The results indicate that these scenarios (C3 and C4) cannot properly reproduce the measured zircon mixing proportions according to the sum of squares due to error (SSE = 1.3 and SSE = 5.3 for C3 and C4, respectively).

With these simulations, I demonstrate that only in unrealistic cases where no sand supply occurs, the amount of zircon from the source fits the measured zircon mixing proportion. These

results suggest that by varying hillslope sand supply from sources, I cannot explain the characteristics of our detrital samples.

### *4.6.4. Zircon fertility*

In the Tavignano watershed, both Schistes Lustrés and Pre–Hercynian basement have no age constraints available. In these experiments I simulate four scenarios (D1–D4) where I test if by making small variations of zircon fertility in the sources, they can reproduce the measured zircon mixing proportions in the uppermost sampling site (A) estimated with the U–Pb age unmixing (shown in the section 4.5.1). In scenario D1, I use 1 to 2 grain/g of zircon fertility per source as bounds. The results indicate that this scenario (D1) cannot properly reproduce the measured zircon mixing proportions (SSE = 14.3) (Fig. 4.14). In the scenario D2, I use 0.5 to 2 grain/g of zircon fertility per source as bounds. The results also indicate that this scenario (D2) cannot properly reproduce the measured zircon mixing proportions (SSE = 6.9). In the scenario D3, I use 0.5 to 5 grain/g of zircon fertility per source as bounds. The results also indicate that this scenario (D3) cannot properly reproduce the measured zircon mixing proportions (SSE = 1.3). In the scenario D4, I use 0.1 to 5 grain/g of zircon fertility per source as bounds. The results indicate that this scenario (D4) can perfectly reproduce the measured zircon mixing proportions (SSE = 1.8 x $10^{-2}$).

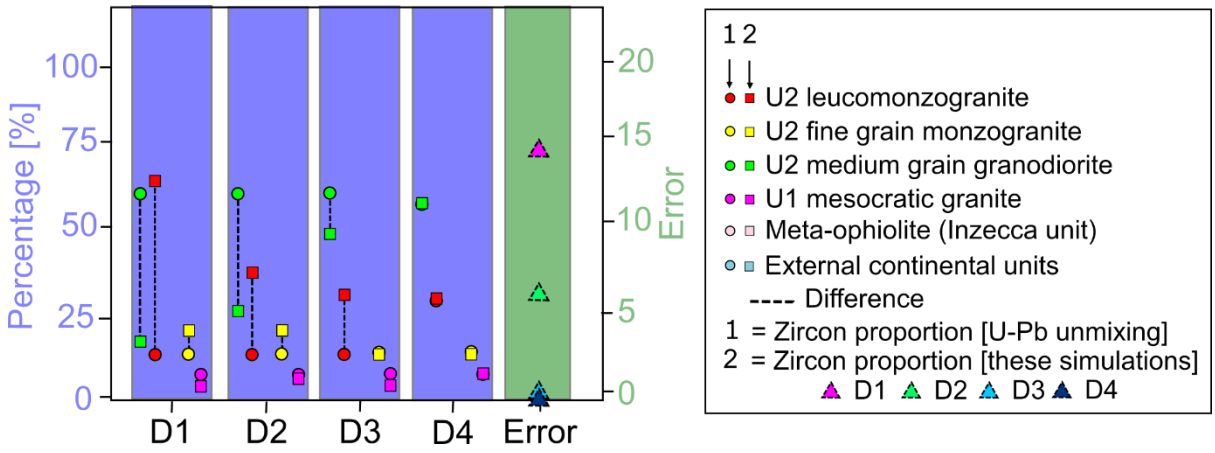

Figure 4.14: Comparing the best–fit of zircon mixing proportions using zircon fertility and the zircon mixing proportions estimated using U–Pb age unmixing in the scenarios D1 to D4. The error is the sum of squares due to error (SSE) between the zircon mixing proportions calculated using zircon fertility and U–Pb age unmixing. Note that the simulation D4 can reproduce the zircon mixing proportions that match the proportions of the uppermost sampling site (A), while D1 to D3 cannot. The squared dots (1) represent the zircon mixing proportion estimated in this work using U–Pb unmixing techniques. The circled dots (2) represent the zircon mixing proportion estimated using the parameters of scenarios D1 to D4.

These simulations suggest that if the difference between zircon fertility in the sources is large enough (D4), it can reproduce our measured (real) zircon proportion without calling for any further controlling factor. In other words, if U2 leucomonzogranite has zircon fertility approaching zero (0.1 grain/g) and U2 medium grain granodiorite can have up to 5 grains/g, zircon variability can fully explain the measured age distribution of the uppermost sampling site. As zircon fertility can fully explain the measured age population, no other variable may be required to explain our data (e.g., erosion or abrasion).

### *4.6.5. Relative erosion rates*

In these experiments (E1–E3), I simulate the capability of erosion rates to reproduce the same zircon mixing proportions measured from U–Pb age unmixing for the uppermost sampling site (A) (shown in the section 4.5.1).

In the first scenario (E1), I use 40 to 80 mm/kyr as erosion rates per source as bounds, which is the range of $^{10}$Be catchment–wide erosion rates found by Molliex et al. (2017) in the Tavignano watershed. The results indicate that this scenario (E1) cannot reproduce the measured zircon mixing proportions (SSE = 14.5) (Fig. 4.15). In the second scenario (E2), I use 8 mm/kyr as the lowest bound and 80 mm/kyr (from the previous scenario) as the maximum bound. The lowest bound corresponds to the lowest *in situ*$^{10}$Be erosion rates estimated from summit surfaces in the Tavignano by Kuhlemann et al. (2007). The upper bound corresponds to the highest $^{10}$Be catchment–wide erosion rate calculated by Molliex et al. (2017). The simulations indicate that this scenario (E2) cannot reproduce the measured zircon mixing proportions (SSE = 1.3). In the third scenario (E3), I use 8 mm/kyr as the lowest bound (from the previous scenario). The

maximum bound used in this simulation is 475 mm/kyr, which is the highest value of river incision found in the Golo River in Corsica using optically stimulated luminescence (Fellin et al., 2005a; Sømme et al., 2011). The results indicate that this scenario (E3) can perfectly reproduce the measured zircon mixing proportions (SSE = 0.2).

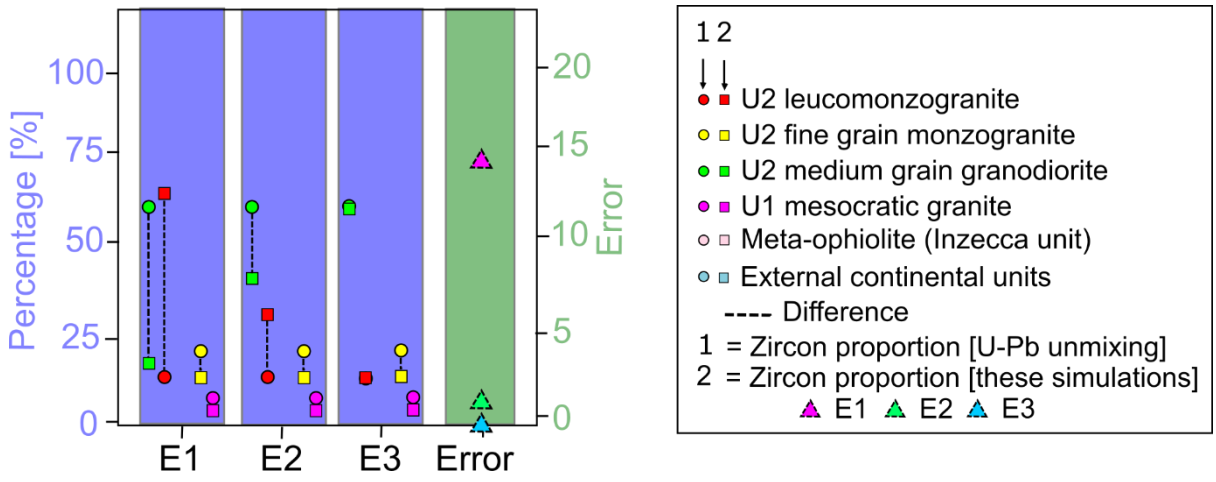


Figure 4.14: Comparing the best–fit of zircon mixing proportions using erosion rates and the zircon mixing proportions estimated using U–Pb age unmixing in the scenarios E1 to E3. The error is the sum of squares due to error (SSE) between the zircon mixing proportions calculated using zircon fertility and U–Pb age unmixing. The squared dots (1) represent the zircon mixing proportion estimated in this work using U–Pb unmixing techniques. The circled dots (2) represent the zircon mixing proportion estimated using the parameters of scenarios E1 to E3.

These simulations suggest that by using a range of empirical erosion rates determined for the Tavignano watershed and its surroundings, it is possible to reproduce, without any further controlling factor, practically the same measured zircon mixing proportions. However, given that the bounds that reproduce the appropriate zircon mixing proportions are not located in the Tavignano watershed (E3), I cannot discard that the influence of erosion rate can be significant only if combined with any other controlling factor (e.g., zircon fertility or hillslope gravel supply).

### *4.6.6. Pebble abrasion rates*

In these experiments (F1–F3), I simulate the capability of pebble abrasion rates to reproduce the same zircon mixing proportions measured from U–Pb age unmixing (shown in the section 4.5.1) for the uppermost (A), intermediate (B) and lowermost (C) sampling sites.

In the first scenario (F1), I use the range of 0.4 to 1.4 mass loss/km found by Attal and Lavé (2006), as bounds in the uppermost sampling site (A). These values are within the range of granite and gneisses in the Himalaya and are used here as proxies. The results indicate that this scenario (F1) cannot reproduce the measured zircon mixing proportions (SSE = 19.9) (Fig. 4.16). In the second scenario (F2), I use the same range of abrasion rates but for the intermediate sampling site (B). The results also indicate that this scenario (F2) cannot reproduce the measured zircon mixing proportions properly (SSE = 11.7). In the third scenario (F3), I use the same range of abrasion rates but for the lowermost sampling site (C). The results also indicate that this scenario (F3) cannot reproduce the measured zircon mixing proportions properly (SSE = 5.1).

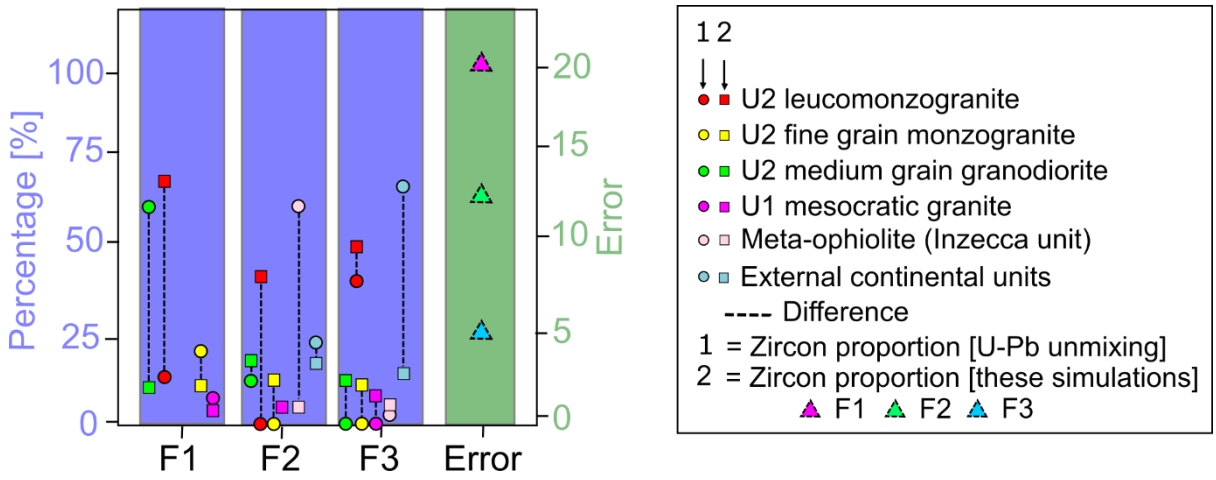


Figure 4.15: Comparing the best–fit of zircon mixing proportions using pebble abrasion rates and the zircon mixing proportions estimated using U–Pb age unmixing in the scenarios F1 to F3. The error is the sum of squares due to error between the zircon mixing proportions calculated using pebble abrasion rates and U–Pb age unmixing. The squared dots (1) represent the zircon mixing proportion estimated in this work using U–Pb unmixing techniques. The circled dots (2) represent the zircon mixing proportion estimated using the parameters of scenarios F1 to F3.

These simulations suggest that by using the published range of abrasion rates for similar rock types I cannot reproduce the measured zircon proportion. If abrasion were to influence the expected zircon mixing proportion based on exposure area, it would occur only if associated to any of the previously tested controlling factors (i.e., hillslope grain size supply, zircon fertility

and erosion rates) and not alone. Below, in the Table 4.4., I summarise the values used in the simulations A1 to F3.

Table 4.4: Summary of all simulations performed, including their age distribution characteristics, number of grains per sample, and the testing variable.

| Simulation | Age peaks [Ma] | # of grains | Testing variable |
|---|---|---|---|
| A1 | 300, 400, 500, 600 | 117 per sample | # of grains |
| A2 | 300, 400, 500, 600 | 59, 19, 53, 51, 49 | # of grains |
| B1 | 300, 400, 500, 600 | 117 per sample | Age peaks |
| B2 | 300, 350, 400, 450 | 117 per sample | Age peaks |
| B3 | 300, 325, 350, 400 | 117 per sample | Age peaks |
| B4 | 300, 310, 320, 330 | 117 per sample | Age peaks |
| B5 | 300 per sample | 117 per sample | Age peaks |
| C1 | Age peaks of sample A | 59, 19, 53, 51, 49 | Sand: 0 to 100% |
| C2 | Age peaks of sample A | 59, 19, 53, 51, 49 | Sand: 0 to 50% |
| C3 | Age peaks of sample A | 59, 19, 53, 51, 49 | Sand: 10 to 100% |
| C4 | Age peaks of sample A | 59, 19, 53, 51, 49 | Sand: 10 to 50% |
| D1 | Age peaks of sample A | 59, 19, 53, 51, 49 | Grains: 1 to 2g/g |
| D2 | Age peaks of sample A | 59, 19, 53, 51, 49 | Grains: 0.5 to 2g/g |
| D3 | Age peaks of sample A | 59, 19, 53, 51, 49 | Grains: 0.5 to 5g/g |
| D4 | Age peaks of sample A | 59, 19, 53, 51, 49 | Grains: 0.1 to 5g/g |
| E1 | Age peaks of sample A | 59, 19, 53, 51, 49 | Erosion: 40 to 80 mm/kyr |
| E2 | Age peaks of sample A | 59, 19, 53, 51, 49 | Erosion: 8 to 80 mm/kyr |
| E3 | Age peaks of sample A | 59, 19, 53, 51, 49 | Erosion: 8 to 475 mm/kyr |
| F1 | Age peaks of sample A | 59, 19, 53, 51, 49 | Abrasion: 0.4 to 1.4 mass loss/km |
| F2 | Age peaks of sample B | 59, 19, 53, 51, 6, 84, 14 | Abrasion: 0.4 to 1.4 mass loss/km |
| F3 | Age peaks of sample C | 59, 19, 53, 51, 6, 84, 52 | Abrasion: 0.4 to 1.4 mass loss/km |

### *4.6.7. Are the simulated biasing factors able to explain our detrital information results?*

Our simulations demonstrate that any analytical controlling factor (overlapping ages and number of analysed grains) can cause misfits between the predicted and real zircon mixing proportions of our samples. Similarly, any natural controlling factor (hillslope sand supply, abrasion, erosion and zircon fertility) can also cause statistically significant changes between the predicted and real zircon mixing proportions of our samples. From the natural biasing factors, our simulations demonstrate that only zircon fertility can individually cause the observed changes in both the zircon mixing proportions and U–Pb age distributions of the Tavignano without the necessity of any further explanatory variable. The zircon fertility, however, can only reproduce the measured ages of the mixed sample if one of the sources can approach zero grains/g and the others have a much higher content (5 grains/g). However, the understanding of zircon proportion and U–Pb ages is limited because available empirical constrains does not allow discriminating the actual contribution of each factor to the measured source proportion. I believe that if only poorly–constrained factors are available, disentangle and test their influence is an intrinsic limiting condition in detrital studies.

## 4.7. Conclusion

We identify from the zircon typology of three different sampling sites in the Tavignano watershed a prevalence of a sub–alkaline to alkaline granite as morphological signature, which fits with the calc–alkaline granite sources. The zircon typologies have a large variation in the associated temperature of crystallisation. Zircons with non–euhedral characteristics are predominant in the intermediate sampling site and can be associated to external continental slivers (Santa–Lucia–di–Mercurio nappe) and/or meta–ophiolites (Inzecca unit). The core and the external surface of grains have, in general, a similar typology, indicating a chemically stable condition for crystallisation.

The zircon mixing modelling predicts a proportion of each contributing source that does not fit their exposure area. I demonstrate with numerical simulations that many biases can have caused these discrepancies. The analytical biases include (1) reducing the number of dated U–Pb zircon grains from an ideal quantity ($n$ = 117) to the same amount used in this work; and (2) issues on predicting zircon mixing proportions from sources with overlapping age peaks. The natural biases include different hillslope grain size supply, zircon fertility in the sources, erosion and pebble abrasion rates per source. The possibility of size–density sorting cannot also be discarded as biasing factor of zircon grains, especially in the intermediate sampling site (B) where smaller zircons overcome the larger ones.

Our results demonstrate that recognising which factors contribute to zircon mixing proportions and U–Pb age distributions is not trivial, given that many of them can occur and separating their influence can be impractical. New research about the bounds of bias produced by each factor using a more controlled environment (e.g., a lab) or a better constrained natural setting could provide a clearer overview on the limits of distortion they can provoke in detrital geochronology. Similarly, estimating the uncertainty involved in every step of collecting information from detrital studies (e.g., from zircon fertility estimation to the number of analysed grains) could also improve the reliability of the technique by giving an estimative of cumulative uncertainty in the measurements performed to get detrital ages from sediment samples.

# Chapter 5 –Discussion

Although the previous three chapters are individual papers that can be read as standalone works, investigation drawn from them provide an important contribution towards a wider understanding concerning the influence of rock properties on surface processes and the sedimentary record. Moreover, although some of the results are directly linked to specific settings (e.g., Himalayas (Chapter 2); Corsica Island (Chapter 3 and 4)), a key aspect of this thesis is to pose research questions that are not only site–specific (i.e., where the findings are only of local interest) but that advance our understanding of the influence of rock properties. As stated in the introduction (1.3), I have focused on three main research questions during this thesis:

1. Does pebble abrasion influence detrital age population statistics?
2. Is the landscape of Corsica Island (Mediterranean Sea) in a steady topographic or transient state?
3. What can we reliably retrieve from detrital grains in poorly constrained settings?

Below, I summarise the fundamental outcomes and the consequences of the investigation of the previous three chapters. I also discuss their uncertainties, limitations, and possible future research programmes.

## 5.1. Does pebble abrasion influence detrital age population statistics?

Overall, yes. In cases where there is a large contrast in rock resistance to abrasion or the distance travelled by the pebbles is short, a statistically significant change in the detrital age population statistics can occur due to abrasion. In long watersheds with soft bedrock, most of the gravel initially supplied from the hillslopes will have been turned into sand by the time it reaches the outlet (leading to the release of most detrital grains and limited bias potential from abrasion).

On the contrary, coarser sediments from resistant rock types (e.g., quartzite, volcanics, mica–poor granite or gneiss) can persist for transport distances of hundreds of kilometers, locking detrital minerals within them and increasing the bias potential from abrasion (i.e., leading to the underrepresentation of units characterized by such resistant rock types).

However, it is relevant to note that pebble abrasion is the factor with the lowest distortion capability when compared with other well–known factors that might bias the preserved sedimentary record (i.e., relative erosion rates, zircon fertility and hillslope gravel supply). A possible explanation is that pebble abrasion has a non–linear impact on the mixing proportion of river sand, and this impact is modulated by the initial gravel supply. For instance, by doubling the zircon fertility or erosion rate of a unit will lead to a doubling of the zircon contribution from this unit in a mixed sample, the impact of doubling the abrasion rate may be much lower. In one of the tested scenarios, the equivalent effect of having rocks from one unit abraded 200 times faster than rocks from other units can be replicated by tripling the fertility or erosion rate of the unit.

Lastly, it is important to note that the relative erosion rates of source units estimated by inverse modelling are impacted by abrasion, despite minimal (statistically insignificant) variations in the grain age distributions. In the Marsyandi watershed of the Himalayas, the abrasion model predicts erosion rates that are closer to those found by the majority of previous studies, compared to a no–abrasion model. These results suggest that even when statistics are not able to identify significant changes in the age distribution of samples, the erosion rates deconvolved from them can still be significantly affected.

### *5.1.1. Limitations*

It is important to consider the implications of some of the assumptions in my work, in particular regarding the transfer of zircon from gravel to sand. In the model, I assume that all products of abrasion are in the sand fraction, and that the zircons are homogenously distributed in this sand. In reality, the fraction finer than 2 mm is far more heterogeneous than assumed in Chapter 2, both in the initial sediment supply from the hillslope to the river and in the fluvial

sediment transported (Attal and Lavé, 2006, Attal et al., 2015; Riebe et al., 2015, Lukens et al., 2016, Sklar et al., 2017). In addition, abrasion will also produce fragments and particles in a wide range of sizes, leading to potentially different mineral compositions depending on the fraction sampled. For example, the abrasion of granite tends to produce sand, whereas abrasion of limestone will produce more silt and clay (Bradley, 1970; Attal and Lavé, 2009). However, given that no constraints about the grain size of abrasion products in the Marsyandi watershed exist, I cannot estimate quantitatively how distorted our own analyses can be due to this process but am cognisant of the fact that only the granite will provide zircon.

I must also mention that an important covariation exists between grain size of abrasion products, abrasion rates and hillslope grain size supply (Attal and Lavé, 2006). Less resistant bedrock types are more likely to have higher weathering rates and to produce regolith with higher content of fine material (i.e., sand, silt and clay) than hard rock types, leading to lower initial gravel supply to the river channels and consequently smaller amount of gravel available for abrasion. It is also relevant to mention the influence of uplift and erosion rates in setting weathering rates and, therefore, in modulating the initial size fraction supplied from the hillslopes to the rivers (Anderson and Dietrich, 2002; Hren et al., 2007). The covariation of hillslope grain size, grain size of abrasion products and abrasion rate associated with a given rock type can produce unusual effects and requires further attention. Because most detrital studies focus on a given sediment fraction (usually sand), it is becoming increasingly important to understand the production and evolution of the fine fraction of the sediment spectrum, from the hillslopes to the sedimentary basin, as a result of chemical and physical processes (Sklar et al., 2017); including abrasion during fluvial transport.

Hydrodynamic fractionation of grain sizes, whereby larger sediment grains travel slower than smaller ones, operates on a range of scales (bedload versus suspended load, as well as differences within bedload and within suspended load) in the majority of natural environments (e.g., Miller et al., 2014). Recent findings suggest potential bias from downstream hydraulic sorting in cases where a relationship between zircon grain age and size exists, e.g., larger grains are younger and smaller ones are older (Yang et al., 2012). The influence of grain density is also important, given that relative enrichment in gravel bars, river pools and other common sampling sites for detrital studies can bias denser minerals such as zircon. However, because our work

focuses only on one type of mineral (zircon) and uses the relative proportions of zircons from different units, it seems reasonable to assume that zircons from all units will be affected in a similar way and that the outcomes of our work would not be significantly affected by the processes mentioned above, except in a case where zircons from different units have different sizes, which I cannot assess.

### *5.1.2. Future research*

I believe that two main research programmes can contribute to clarify these limitations.

Firstly, experimental research on the grain sizes produced by different rock types during pebble abrasion could provide a more reliable constraint on how target detrital minerals (e.g., zircon and apatite) are incorporated into the size fraction used in geo–thermochrology (63–125 μm). Similar experimental research could also help understanding cosmogenic nuclide concentration in detrital quartz used in catchment–wide erosion research. A potential research design to test the impact of pebble abrasion in the fraction used in detrital studies could be done by experimenting with a circular flume where bedload transport in mountain rivers can be realistically simulated. Attal et al. (2005) and Domokos et al. (2014) performed similar experiments to investigate rates of abrasion and final shapes of pebbles in mountain settings. By simulating an environment where pebble abrasion is controllable and the rock characteristics are known a priori (e.g., target mineral fertility, U–Pb ages and cosmogenic nuclide concentration), it is possible to disentangle the final impact of pebble abrasion on the characteristics of grains used in detrital studies. This novel research would bring the first empirical quantification of grain size by–products influence in detrital geo–thermochronology ever made.

Secondly, the problem of predicting grain size supply from hillslopes needs a clear mathematical approach. Sklar et al. (2017) have provided the first steps for a mechanistic model that captures the influence of lithology, life, erosion and topography in the grain size available in the hillslopes. Their simulations demonstrate that size reduction is a function of residence time on hillslopes and their path to the river channel. By including their hillslope grain size equations in the pebble abrasion model used in this work (Chapter 2 and 4), it could be possible to create a

framework for scientists to test for the influence of hillslope grain size on the detrital information retrieved in their geo–thermochronology data set. Future work providing a simple user–friendly algorithm (e.g., with a graphical user interface) that combines both numerical models (hillslope grain size supply model of Sklar et al. (2017) and sediment mixing model of Lavarini et al. (2018)) would be an extremely useful tool for field geoscientists who want to test for the influence of possible factors on their detrital information.

## 5.2. Is the landscape of Corsica Island (Mediterranean Sea) in topographic steady or transient–state?

The collected results provide evidence of transience (i.e., varying elevation over time) in rivers and in the regional drainage divide of Corsica. 'Gilbert' and $\chi$ metrics predict that the northern section of the divide is currently migrating to the east, while the southern section is moving to the opposite direction (i.e., westward). These predictions suggest that Corsica is in a transient topographic state at the present and, potentially, since the Miocene (~ 14 Ma) when the last drainage reorganisation occurred.

The analysis of the drainage network through river steepness, sediment grain size and knickpoints also demonstrate the influence of both rock type resistance and structural units in the modern river profiles of Corsica. For example, Hercynian rock types have a higher resistance to erosion, higher density of knickpoints, and knickpoints with larger metrics of change (e.g., slope, relief, length and magnitude) than those over softer rock types in the Alpine Corsica and Miocene sedimentary plains.

The range of grain size in modern gravel bars in Corsica reflects a similar influence of rock resistance, with Hercynian rock types representing larger grain size ranges than those from Alpine Corsica. River steepness follows a similar pattern to rock resistance, with decreasing values from Hercynian to Alpine Corsica regions.

Importantly, the spatial distribution of knickpoints, grain size coarsening and river steepness peaks show a preferential location around the boundaries of structural units (e.g., faulting zones).

These structural boundaries exert a spatial control on the direction of the drainage network and on the river metrics (i.e., river steepness, slope, magnitude, length and relief of knickpoints) in Hercynian and Alpine Corsica.

Finally, knickpoints are preferentially located at a relatively similar distance from modern sea level, which could suggest a common base level drop. However, given that rivers in Corsica have a similar length (potentially making knickpoints clustered at similar distance from base level) and that knickpoint migration should vary according to the drainage area (i.e., disturbing an uniform distance from base level; see Berlin and Anderson, 2007), and the existence of possible structural controls in the genesis of knickpoints, caution must be taken to consider base level drop as a plausible hypothesis for knickpoint generation in Corsica. For this reason, I suggest that the base level change hypothesis should be investigated in a future work.

My results suggest that river steepness and grain size are strongly influenced by rock strength which is in accordance to several other studies (e.g., Attal et al., 2015; Forte and Yanites, 2016). Another contribution is regarding the response times of geomorphic transience, which, in the case of Corsica, has been occuring since the Miocene uplift and is beyond the Quaternary.

### *5.2.1. Limitations*

Several limitations arise from the results presented in Chapter 3, particularly in three key aspects.

Firstly, the geological maps of Corsica have a resolution that does not fit with the detailed gravel bar analysis performed. This means that a straightforward comparison between sources and sediment clast types is not possible and that estimations of abrasion rates (or rock resistance) can be severely influenced by the large–scale of lithologies in my base map. Due to this limitation, and the impossibility of assessing uncertainty, the results presented in Chapter 3 comparing rock percentage in gravel bars and their sources can be seen only as an approximation.

Secondly, the algorithms that extract information about knickpoints and drainage divide stability require choosing parameters that can produce bias (e.g., smoothing window in the

knickpoint finder and best–fit river concavity index in χ –transformation), even if a careful prior selection is performed (see Mudd et al., 2014, 2018). By choosing a single value that represents the average of all river concavities in Corsica, for example, deviations in the prediction of knickpoints can occur. Similarly, any change in the window size of the knickpoint finder can find more or less changes in the river profile (see Neely et al., 2017), while reducing the selection of channel head metrics can indicate a different divide motion (see Forte and Whipple, 2018). Particularly in the metrics of divide stability, the absence of spatial statistics and the user–dependent choice of channel heads can increase even further the uncertainty inherited from the choice of chi and Gilbert metrics parameters.

Thirdly, the hypothesis that knickpoints between 20 and 25 km from the coast were produced by sea level drop needs further investigation considering the preferential location near structural boundaries. Distinguishing between the factors that drive knickpoint formation is important but has not been resolved here.

### *5.2.2. Further questions*

Besides better geological maps to investigate source to sink problems in Corsica, I believe that two main improvements for geomorphology and sedimentology can be proposed from the outcomes of this chapter.

Firstly, an enormous development in uncertainty estimation has occurred with χ and knickpoint metrics, but progress in predicting drainage divide migration from topography can be further enhanced with spatial statistics. The current analysis of divide stability using the 'Gilbert' and χ metrics is based on comparing their values across the drainage divide through some uncertainty analysis (e.g., bootstrap, 1 standard deviation of the mean, etc.) that do not consider spatial dimensions. For example, by coupling the spatial dimensionality, visualising divide stability through vectors of divide migration trends (with direction and magnitude) could provide a clearer assessment than contrasting Gilbert' and χ metric anomaly maps. This new visualisation could also avoid the necessity of selecting a shorter–range of channel head values as proposed by

Forte and Whipple (2018), thus minimising selection bias by the user. Moreover, by applying spatial metrics (e.g., spatial autocorrelation, and stratified heterogeneity), it is possible to test for the relationship between causal factors (e.g., rock type, uplift) and drainage divide stability in routine analysis. It also allows clustering of divide stability patterns in the landscape (e.g., mapping stable and unstable divide sections based on a window search). Therefore, coupling spatial statistics in algorithms of drainage divide analysis would enhance the reliability of 'Gilbert' and $\chi$ metrics in future works in geomorphology.

Secondly, future numerical simulations with empirical constraints can test if the knickpoints were caused by base level drop. By incorporating in a landscape evolution model the rates of sea level drop and rise estimated for the Messinian crisis, it is possible to provide a relatively well–calibrated test for the influence of global base level change in the formation of knickpoints in Corsica. Robl et al. (2017) when investigating the controls in landscape evolution of the Southern Alps performed a similar approach. I strongly believe that a future assessment using empirical constrains on sea level variation within a surface process model (e.g., pyBadlands, LithoChild, etc.) that account for spatially variable rock properties can reliably confirm or reject this hypothesis.

## 5.3. What can we reliably retrieve from detrital grains in poorly constrained settings?

The analysis I performed demonstrate that in settings where there is limited information on the source material, recognising which factors reliably explain zircon mixing proportions and U–Pb age distributions is not trivial. In other words, the causes of detrital information can be estimated but quantifying uncertainty is rarely possible.

It is particularly relevant to mention that often zircon mixing modelling predicts a proportion of contributing sources that does not fit their exposure area and that many analytical and natural biases can explain these changes. The analytical biases include (1) reducing the number of dated U–Pb zircon grains from an ideal quantity (n >100 grains) to the same amount used in this work; (2) issues on predicting zircon mixing proportions from sources with overlapping age peaks. The

natural biases include (3) different hillslope grain size supply, (4) zircon fertility in the sources, (5) erosion and (6) pebble abrasion rates per source. The possibility of size–density sorting, although not explicitly tested, cannot also be discarded as biasing factor of zircon grains, especially in the intermediate sampling site (B), where lighter and more rounded grains are prevalent. Overall, the numerical experiments performed demonstrate that only zircon fertility is able to produce the measured zircon mixing proportions of the investigated setting (Tavignano watershed, Corsica) without any further causal factor. At the same time, a combination of the remaining controlling factors (i.e., 1 to 6) can together contribute to the measured zircon mixing proportions, although I cannot quantify them.

Despite the uncertainty in the reliability of the zircon data analysed, I identify in the Tavignano watershed a prevalence of zircons with a sub–alkaline to alkaline granite as morphological signature in the uppermost and lowermost sampling sites (A and B, respectively), which fits with their calc–alkaline granite sources. The identified zircon typologies have a large variation in the temperature of crystallisation. Zircons with non–euhedral characteristics are predominant in the intermediate sampling site (B) and can be associated to external continental slivers (Santa–Lucia–di–Mercurio nappe) and/or meta–ophiolites (Inzecca unit). The core and the external surface of grains have, in general, a similar typology, which suggest a chemically stable geological condition during crystal growth. On the other hand, non–euhedral grains, especially in the intermediate sampling site, can indicate metamorphism and metamictisation of source terranes as well as possible physical breaking during fluvial transport.

### *5.3.1. Limitations and further research*

I believe that two research programmes can be proposed from the remaining gaps of the work.

Firstly, the results presented in Chapter 4 do not have a combined statistical uncertainty that show how the final sediment characteristics are determined by the sum of all the potential sources of uncertainty. In other words, the distortion in discovering the source characteristics from detrital samples is assessed separately on a case–specific basis. So, future work quantifying the

accumulated biases and uncertainties from all analytical and natural biases involved in detrital studies (e.g., using probability theory) could bring relevant information for scientists when analysing results of mineralogical composition, detrital ages and other characteristics of the stratigraphic record. A similar approach for investigating uncertainty propagation from data acquisition to result estimation was performed by Wheaton et al. (2010) with a focus on DEMs. A major progress was made with the statistical limitations of analysing less than the minimum number of grains (e.g., Vermeesch, 2004), and by showing how to minimise biases in sampling (e.g., Sharman and Johnstone, 2017; Sundell and Saylor, 2017) but quantifying how much the sequence of uncertainties from source to sink influence the reliability of the final information retrieved from sediments has never been done. Consequently, by providing a user–friendly interactive interface tool that estimates cumulative biases in the sedimentary record, future work could improve many inferences of field–based scientists about surface processes.

Secondly, to understand sediment transfer to the offshore basins in the Mediterranean Sea it is crucial to quantify long–term erosion rates in the rivers of Corsica more accurately. Despite several studies that already performed investigations with this focus (e.g., Calvès et al., 2013; Fellin et al., 2005 a, b; Kuhlemann et al., 2007, 2009; Molliex et al., 2017; Sømme et al., 2011), conflicting results do not allow an overview on how Corsica rivers provide sediments to the ongoing sedimentary basins. Novel research combining detrital minerals (e.g., quartz, apatite and zircon) and different methods (e.g., $^{10}$Be cosmogenic nuclides, fission–track) could provide a broader assessment of sediment flux over a range of timescales than currently available data sets. However, to understand the mechanism of sediment transfer from source to sink in Corsica, it is still required a proper estimation of mineral fertility, grain size hillslope supply and abrasion rates of the source areas. I believe that new studies combining remote estimations of grain size hillslope supply (e.g., Sklar et al., 2017), and new field–based data (e.g., source ages) can contribute to unravel past landscape changes in Corsica.

# Chapter 6 –Conclusion

The key–conclusions of this thesis are:

1. *Pebble abrasion can bias detrital mineral information in the sedimentary record*. Numerical simulations with empirically derived controlling factors show evidences that detrital geochronology suffers statistically significant distortion caused by abrasion and other known factors (e.g., erosion rates, hillslope grain size supply, and target mineral fertility). The impact of pebble abrasion in detrital geochronology is enhanced when sediments have short travel distances and if catchments are made of contrasting rock strengths.

2. *The landscape of Corsica is currently in transience*. The $\chi$ and 'Gilbert' metrics used to investigate drainage divide stability indicate that the northern section of the regional drainage divide of Corsica is moving to the east, while the southern section is moving to the opposite direction (i.e., westward). Equally important, analysis of drainage network using river steepness, sediment grain size and knickpoint metrics highlight an influence of both rock type and structural units as major controls on the unsteady modern river profiles.

3. *Quantifying the factors that influence the sedimentary record is a non–trivial task*. Analysis of detrital zircons from a large Corsican watershed reveals important information about their sub–alkaline to alkaline granite origin, crystallisation environments and, eventually, metamorphism. However, absence of many constraints required to quantify the detrital population does not allow discriminating how much each controlling factor can have affected the sedimentary record.

# Chapter 7 –References


Abrahami, R., van der Beek, P., Huyghe, P., Hardwick, E., & Carcaillet, J. (2016). Decoupling of long–term exhumation and short–term erosion rates in the Sikkim Himalaya. Earth and Planetary Science Letters, 433, 76–88.

Aguilar, G., S. Carretier, V. Regard, R. Vassallo, R. Riquelme, and J. Martinod (2014), Grain size–dependent 10 be concentrations in alluvial stream sediment of the Huasco valley, a semi–arid andes region, *Quaternary Geochronology*, *19*, 163–172, doi:10.1016/j.quageo.2013.01.011

Alizai, A., A. Carter, P. D. Clift, S. VanLaningham, J. C. Williams, and R. Kumar (2011), Sediment provenance, reworking and transport processes in the Indus River by U–Pb dating of detrital zircon grains, *Global and Planetary Change*, *76*(1), 33–55.

Allen, C. D., & Breshears, D. D. (1998). Drought–induced shift of a forest–woodland ecotone: rapid landscape response to climate variation. Proceedings of the National Academy of Sciences, 95(25), 14839–14842.

Allen, P. A., J. J. Armitage, A. C. Whittaker, N. A. Michael, D. Roda–Boluda, and M. D'Arcy (2015), Fragmentation model of the grain size mix of sediment supplied to basins, *The Journal of Geology*, *123*(5), 405–427.

Amelin, Y., D.–C. Lee, A. N. Halliday, and R. T. Pidgeon (1999), Nature of the Earth's earliest crust from hafnium isotopes in single detrital zircons, *Nature*, *399*(6733), 252–255.

Amidon, W. H., D. W. Burbank, and G. E. Gehrels (2005a), Construction of detrital mineral populations: insights from mixing of U–Pb zircon ages in Himalayan rivers, *BasinResearch*, *17*(4), 463–485.

Amidon, W. H., D. W. Burbank, and G. E. Gehrels (2005b), U–Pb zircon ages as a sediment mixing tracer in the Nepal Himalaya, *Earth and Planetary Science Letters*, *235*(1), 244–260.

Anderson, S. P., Dietrich, W. E., & Brimhall Jr, G. H. (2002). Weathering profiles, mass-balance analysis, and rates of solute loss: Linkages between weathering and erosion in a small, steep catchment. Geological Society of America Bulletin, 114(9), 1143-1158.

Attal, M., & Lavé, J. (2006). Changes of bedload characteristics along the Marsyandi River (central Nepal): Implications for understanding hillslope sediment supply, sediment load evolution along fluvial networks, and denudation in active orogenic belts. Geological Society of America Special Papers, 398, 143–171.

Attal, M., & Lavé, J. (2009). Pebble abrasion during fluvial transport: Experimental results and implications for the evolution of the sediment load along rivers. Journal of Geophysical Research, 114, F04023. https://doi.org/10.1029/2009jf001328

Attal, M., J. Lavé, and J.–P. Masson (2006), New facility to study river abrasion processes, *Journal of Hydraulic Engineering*, *132*(6), 624–628.

Attal, M., S. M. Mudd, M. D. Hurst, B. Weinman, K. Yoo, and M. Naylor (2015), Impact of change in erosion rate and landscape steepness on hillslope and fluvial sediments grain size in the Feather River basin (Sierra Nevada, California), *Earth Surface Dynamics*, 3(1), 201–222, doi: 10.5194/esurf–3–201–2015

Balan, E., Neuville, D. R., Trocellier, P., Fritsch, E., Muller, J. P., & Calas, G. (2001). Metamictization and chemical durability of detrital zircon. American Mineralogist, 86(9), 1025–1033.

Berlin, M. M., & Anderson, R. S. (2007). Modeling of knickpoint retreat on the Roan Plateau, western Colorado. Journal of Geophysical Research: Earth Surface, 112(F3).

Best, J. L. (1987). Flow dynamics at river channel confluences: implications for sediment transport and bed morphology.

Binnie, S. A., Phillips, W. M., Summerfield, M. A., Fifield, L. K., & Spotila, J. A. (2008). Patterns of denudation through time in the San Bernardino Mountains, California: Implications for early–stage orogenesis. Earth and Planetary Science Letters, 276(1–2), 62–72.

Blum, M., and M. Pecha (2014), Mid–Cretaceous to Paleocene North American drainage reorganization from detrital zircons, *Geology*, *42*(7), 607–610.

Bonnet, S. (2009). Shrinking and splitting of drainage basins in orogenic landscapes from the migration of the main drainage divide. Nature Geoscience, 2(11), 766.

Bracciali, L., Najman, Y., Parrish, R. R., Akhter, S. H., & Millar, I. (2015). The Brahmaputra tale of tectonics and erosion: Early Miocene river capture in the Eastern Himalaya. Earth and Planetary Science Letters, 415, 25–37.

Bradley, W. C. (1970), Effect of weathering on abrasion of granitic gravel, Colorado River (Texas), *Geological Society of America Bulletin*, 81, 61–80, doi:10.1130/

Bradley, W. C. (1970). Effect of weathering on abrasion of granitic gravel, Colorado River (Texas). Geological Society of America Bulletin, 81, 61–80. https://doi.org/10.1130/0016-7606(1970)81(61:EOWOAO)2.0.CO;2

Bressan, F., Papanicolaou, A. N., & Abban, B. (2014). A model for knickpoint migration in first-and second-order streams. Geophysical Research Letters, 41(14), 4987–4996.

Brocard, G. Y., Willenbring, J. K., Miller, T. E., & Scatena, F. N. (2016). Relict landscape resistance to dissection by upstream migrating knickpoints. Journal of Geophysical Research: Earth Surface, 121(6), 1182–1203.

Brovarone, A. V., & Herwartz, D. (2013). Timing of HP metamorphism in the Schistes Lustrés of Alpine Corsica: New Lu–Hf garnet and lawsonite ages. Lithos, 172, 175–191.

Bunte, K., & Abt, S. R. (2001). Sampling surface and subsurface particle–size distributions in wadable gravel–and cobble–bed streams for analyses in sediment transport, hydraulics, and streambed monitoring. Gen. Tech. Rep. RMRS–GTR–74. Fort Collins, CO: US Department of Agriculture, Forest Service, Rocky Mountain Research Station. 428 p., 74.

Burbank, D., A. Blythe, J. Putkonen, B. Pratt–Sitaula, et al. (2003), Decoupling of erosion and precipitation in the Himalaya, *Nature*, *426*(6967), 652.

Bush, M. A., Saylor, J. E., Horton, B. K., & Nie, J. (2016). Growth of the Qaidam Basin during Cenozoic exhumation in the northern Tibetan Plateau: Inferences from depositional patterns and multiproxy detrital provenance signatures. Lithosphere, 8(1), 58–82.

Calvès G, Toucanne S, Jouet G, Charrier S, Thereau E, Etoubleau J, Marsset T, Droz L, Bez M, Jorry S, Mulder T, Lericolais G. 2013. Inferring denudation variations from the sediment

record; an example of the last glacial cycle record of the Golo basin and watershed, East Corsica, Western Mediterranean Sea. Basin Research 24: 1–22.

Campbell, I. H., P. W. Reiners, C. M. Allen, S. Nicolescu, and R. Upadhyay (2005), He–Pb double dating of detrital zircons from the Ganges and Indus rivers: implication for quantifying sediment recycling and provenance studies, *Earth and Planetary ScienceLetters*, *237*(3), 402–432, doi: 10.1016/j.epsl.2005.06.043

Carretier, S., V. Regard, R. Vassallo, G. Aguilar, J. Martinod, R. Riquelme, F. Christophoul, R. Charrier, E. Gayer, M. Farías, L. Audin, and C. Lagane (2015), Differences in $^{10}$Be concentrations between river sand, gravel and pebbles along the western side of the central Andes, *Quaternary Geochronology*, *27*, 33–51, doi: 10.1016/j.quageo.2014.12.002

Casagli, N., L. Ermini, L., and G. Rosati (2003), Determining grain size distribution of the material composing landslide dams in the Northern Apennines: sampling and processing methods, *Engineering Geology*, 69, 83–97, doi:10.1016/S0013–7952(02)00249–1

Cavazza W, Zattin M, Ventura B, Zuffa GG. 2001. Apatite fission–track analysis of Neogene exhumation in northern Corsica (France). Terra Nova 13: 51–57.

Cavazza, W., DeCelles, P. G., Fellin, M. G., & Paganelli, L. (2007). The Miocene Saint–Florent Basin in northern Corsica: stratigraphy, sedimentology, and tectonic implications. Basin Research, 19(4), 507–527.

Chew, D. M., & Donelick, R. A. (2012). Combined apatite fission track and U–Pb dating by LA–ICP–MS and its application in apatite provenance analysis. Quantitative mineralogy and microanalysis of sediments and sedimentary rocks: Mineralogical Association of Canada Short Course, 42, 219–247.

Clauzon, G., Suc, J. P., Gautier, F., Berger, A., & Loutre, M. F. (1996). Alternate interpretation of the Messinian salinity crisis: Controversy resolved?. Geology, 24(4), 363-366.

Clift, P. D., Blusztajn, J., & Nguyen, A. D. (2006). Large- scale drainage capture and surface uplift in eastern Tibet–SW China before 24 Ma inferred from sediments of the Hanoi Basin, Vietnam. Geophysical Research Letters, 33(19).

Cocherie, A., Guerrot, C., & Rossi, P. H. (1992). Single–zircon dating by step–wise Pb evaporation: comparison with other geochronological techniques applied to the Hercynian granites of Corsica, France. Chemical Geology: Isotope Geoscience section, 101(1–2), 131–141.

Cocherie, A., Rossi, P., & Le Bel, L. (1984). The Variscan calc–alkalic plutonism of western Corsica: mineralogy and major and trace element geochemistry. Physics of the earth and planetary interiors, 35(1–3), 145–178.

Cocherie, A., Rossi, P., Fanning, C. M., & Guerrot, C. (2005). Comparative use of TIMS and SHRIMP for U–Pb zircon dating of A–type granites and mafic tholeiitic layered complexes and dykes from the Corsican Batholith (France). Lithos, 82(1–2), 185–219.

Cocherie, A., Rossi, P., Fouillac, A. M., & Vidal, P. (1994). Crust and mantle contributions to granite genesis—An example from the Variscan batholith of Corsica, France, studied by trace–element and Nd–Sr–O–isotope systematics. Chemical Geology, 115(3–4), 173–211.

Codilean, A. T., C. R. Fenton, D. Fabel, P. Bishop, and S. Xu (2014), Discordance between cosmogenic nuclide concentrations in amalgamated sands and individual fluvial pebbles in an arid zone catchment, *Quaternary Geochronology*, *19*, 173–180, doi: 10.1016/j.quageo.2012.04.007

Cook, K. L., Turowski, J. M., & Hovius, N. (2013). A demonstration of the importance of bedload transport for fluvial bedrock erosion and knickpoint propagation. Earth Surface Processes and Landforms, 38(7), 683–695.

Corfu, F., Hanchar, J. M., Hoskin, P. W., & Kinny, P. (2003). Atlas of zircon textures. Reviews in mineralogy and geochemistry, 53(1), 469–500.

Cowie, P. A., Whittaker, A. C., Attal, M., Roberts, G., Tucker, G. E., & Ganas, A. (2008). New constraints on sediment–flux–dependent river incision: Implications for extracting tectonic signals from river profiles. Geology, 36(7), 535–538.

Cox, S. E., S. N. Thomson, P. W. Reiners, S. R. Hemming, and T. van de Flierdt (2010), Extremely low long–term erosion rates around the Gamburtsev mountains in interior east Antarctica, *Geophysical Research Letters*, *37*(22), L22307.

Crosby, B. T., & Whipple, K. X. (2006). Knickpoint initiation and distribution within fluvial networks: 236 waterfalls in the Waipaoa River, North Island, New Zealand. Geomorphology, 82(1–2), 16–38.

Cyr, A. J., Granger, D. E., Olivetti, V., & Molin, P. (2010). Quantifying rock uplift rates using channel steepness and cosmogenic nuclide–determined erosion rates: Examples from northern and southern Italy. Lithosphere, 2(3), 188–198.

Daníšík M, Kuhlemann J, Dunkl I, Evans NJ, Székely B, Frisch W. 2012. Survival of ancient landforms in a collisional setting as revealed by combined fission track and (U–Th)/He thermochronometry: a case study from Corsica (France). Journal of Geology 120(2): 155–173

Daníšík M, Kuhlemann J, Dunkl I, Székely B, Frisch W. 2007. Burial and exhumation of Corsica (France) in the light of fission track data. Tectonics 26 .TC1001

Deal, E., A.–C. Favre, and J. Braun (2017), Rainfall variability in the Himalayan orogeny and its relevance to erosion processes, Water Resources Research, 53(5), 4004–4021, doi:10.1002/2016WR020030

Dhuime, B., C. J. Hawkesworth, P. A. Cawood, and C. D. Storey (2012), A change in the geodynamics of continental growth 3 billion years ago, *Science*, *335*(6074), 1334–1336.

DiBiase, R. A., Whipple, K. X., Heimsath, A. M., & Ouimet, W. B. (2010). Landscape form and millennial erosion rates in the San Gabriel Mountains, CA. Earth and Planetary Science Letters, 289(1–2), 134–144.

Dickinson, W. R. (2008), Impact of differential zircon fertility of granitoid basement rocks in North America on age populations of detrital zircons and implications for granite petrogenesis, *Earth and Planetary Science Letters*, *275*(1), 80–92, doi: 10.1016/j.epsl.2008.08.003

Dingle, E. H., M. Attal, and H. D. Sinclair (2017), Abrasion–set limits on Himalayan gravel flux, *Nature*, *544*(7651), 471–474, doi: 10.1038/nature22039

Domokos, G., and G. W. Gibbons (2012), The evolution of pebble size and shape in space and time, *Proceedings of the Royal Society of London A: Mathematical, Physical and EngineeringSciences*, *468*(2146), 3059–3079.

Domokos, G., D. J. Jerolmack, A. Á. Sipos, and Á. Török, (2014), How river rocks round: resolving the shape–size paradox, *PloS One*, 9(2), e8865, https://doi.org/10.1371/journal.pone.0088657

Dosseto, A., Buss, H. L., & Chabaux, F. (2014). Age and weathering rate of sediments in small catchments: The role of hillslope erosion. Geochimica et Cosmochimica Acta, 132, 238–258.

Farley, K. A. (2000). Helium diffusion from apatite: General behavior as illustrated by Durango fluorapatite. Journal of Geophysical Research: Solid Earth, 105(B2), 2903–2914.

Fedo, C. M., Sircombe, K. N., & Rainbird, R. H. (2003). Detrital zircon analysis of the sedimentary record. Reviews in Mineralogy and Geochemistry, 53(1), 277–303.Garver J.I. (2014) Thermochronology, Detrital Zircon. In: Rink W., Thompson J. (eds) Encyclopedia of Scientific Dating Methods. Springer, Dordrecht

Fellin MG, Picotti V, Zattin M. 2005b. Neogene to Quaternary rifting and inversion in Corsica: retreat and collision in the western Mediterranean. Tectonics 24 . DOI:10.1029/2003TC001613.TC1011

Fellin MG, Vance JA, Garver JI, Zattin M. 2006. The thermal evolution of Corsica as recorded by zircon fission–tracks. Tectonophysics 421: 299–317.

Fellin MG, Zattin M, Picotti V, Reiners PW, Nicolescu S. 2005a. Relief evolution in northern Corsica (western Mediterranean): Constraints on uplift and erosion on long–term and short–term timescales. Journal of Geophysical Research 110. DOI:10.1029/ 2004JF000167.F01016

Fernández–Suárez, J., Gutiérrez–Alonso, G., Pastor–Galán, D., Hofmann, M., Murphy, J. B., & Linnemann, U. (2014). The Ediacaran–Early Cambrian detrital zircon record of NW Iberia: Possible sources and paleogeographic constraints. International Journal of Earth Sciences, 103(5), 1335–1357.

Finnegan, N. J., Schumer, R., & Finnegan, S. (2014). A signature of transience in bedrock river incision rates over timescales of 10 4–10 7 years. Nature, 505(7483), 391.

Flint, J. J. (1974). Stream gradient as a function of order, magnitude, and discharge. Water Resources Research, 10(5), 969–973.

Forte, A. M., & Whipple, K. X. (2018). Criteria and tools for determining drainage divide stability. Earth and Planetary Science Letters, 493, 102–117.

Forte, A. M., Whipple, K. X., & Cowgill, E. (2015). Drainage network reveals patterns and history of active deformation in the eastern Greater Caucasus. Geosphere, 11(5), 1343–1364.

Forte, A. M., Whipple, K. X., Bookhagen, B., & Rossi, M. W. (2016). Decoupling of modern shortening rates, climate, and topography in the Caucasus. Earth and Planetary Science Letters, 449, 282–294.

Forte, A. M., Yanites, B. J., & Whipple, K. X. (2016). Complexities of landscape evolution during incision through layered stratigraphy with contrasts in rock strength. Earth Surface Processes and Landforms, 41(12), 1736–1757.

Fournier, M., Jolivet, L., Goffé, B., & Dubois, R. (1991). Alpine Corsica metamorphic core complex. Tectonics, 10(6), 1173–1186.

Frankel, K. L., Pazzaglia, F. J., & Vaughn, J. D. (2007). Knickpoint evolution in a vertically bedded substrate, upstream–dipping terraces, and Atlantic slope bedrock channels. Geological Society of America Bulletin, 119(3–4), 476–486.

Gabet, E. J., D. W. Burbank, B. Pratt–Sitaula, J. Putkonen, and B. Bookhagen (2008), Modern erosion rates in the high Himalayas of Nepal, *Earth and Planetary Science Letters*, *267*(3), 482 – 494.

Gabet, E. J., Mudd, S. M., Milodowski, D. T., Yoo, K., Hurst, M. D., & Dosseto, A. (2015). Local topography and erosion rate control regolith thickness along a ridgeline in the Sierra Nevada, California. Earth Surface Processes and Landforms, 40(13), 1779–1790.

Gargani, J. (2004). Modelling of the erosion in the Rhone valley during the Messinian crisis (France). Quaternary International, 121(1), 13–22.

Garzanti, E. (2016). From static to dynamic provenance analysis—Sedimentary petrology upgraded. Sedimentary Geology, 336, 3–13.

Garzanti, E., G. Vezzoli, S. Andò, J. Lavé, M. Attal, C. France–Lanord, and P. DeCelles (2007), Quantifying sand provenance and erosion (Marsyandi River, Nepal Himalaya), *Earth and Planetary Science Letters*, *258*(3), 500–515.

Garzanti, E., Resentini, A., Andò, S., Vezzoli, G., Pereira, A., & Vermeesch, P. (2015). Physical controls on sand composition and relative durability of detrital minerals during ultra- long distance littoral and aeolian transport (N amibia and southern A ngola). Sedimentology, 62(4), 971–996.

Garzanti, E., Resentini, A., Vezzoli, G., Andò, S., Malusà, M., & Padoan, M. (2012). Forward compositional modelling of Alpine orogenic sediments. Sedimentary Geology, 280, 149–164.

Garzanti, E., S. Andò, and G. Vezzoli (2008), Settling equivalence of detrital minerals and grain size dependence of sediment composition, *Earth and Planetary Science Letters*, *273*(1), 138–151.

Garzanti, E., S. Andò, and G. Vezzoli (2009), Grain size dependence of sediment composition and environmental bias in provenance studies, *Earth and Planetary Science Letters*, *277*(3), 422–432.

Garzanti, E., Vermeesch, P., Rittner, M., & Simmons, M. (2018). The zircon story of the Nile: Time- structure maps of source rocks and discontinuous propagation of detrital signals. Basin Research.

Gasparini, N. M., Whipple, K. X., & Bras, R. L. (2007). Predictions of steady state and transient landscape morphology using sediment-flux-dependent river incision models. Journal of Geophysical Research: Earth Surface, 112(F3).

Gehrels, G. (2014). Detrital zircon U–Pb geochronology applied to tectonics. Annual Review of Earth and Planetary Sciences, 42, 127–149.

Gehrels, G. E. (2000), Introduction to detrital zircon studies of Paleozoic and Triassic strata in western Nevada and northern California, *Special Paper of the Geological Societyof America*, *347*, 1–17.

Gehrels, G., P. Kapp, P. DeCelles, A. Pullen, R. Blakey, A. Weislogel, L. Ding, J. Guynn, A. Martin, N. McQuarrie, et al. (2011), Detrital zircon geochronology of pre–Tertiary strata in the Tibetan–Himalayan orogen, *Tectonics*, *30*(5).

Gemignani, L., van der Beek, P. A., Braun, J., Najman, Y., Bernet, M., Garzanti, E., & Wijbrans, J. R. (2018). Downstream evolution of the thermochronologic age signal in the Brahmaputra catchment (eastern Himalaya): Implications for the detrital record of erosion. Earth and Planetary Science Letters, 499, 48–61.

Giachetta, E., Refice, A., Capolongo, D., Gasparini, N. M., & Pazzaglia, F. J. (2014). Orogen-scale drainage network evolution and response to erodibility changes: insights from numerical experiments. Earth Surface Processes and Landforms, 39(9), 1259–1268.

Gilbert, G. K. (1877). Report on the Geology of the Henry Mountains. US Government Printing Office.

Glotzbach, C., F. Busschers, and J. Winsemann (2017), Detrital thermochronology of Rhine, Elbe and Meuse river sediment (central Europe): Implications for provenance, erosion and mineral fertility, *International Journal of Earth Sciences*, doi: 10.1007/s00531–017–1502–9

Godard, V., Bourlès, D. L., Spinabella, F., Burbank, D. W., Bookhagen, B., Fisher, G. B., ... & Léanni, L. (2014). Dominance of tectonics over climate in Himalayan denudation. Geology, 42(3), 243–246.

Godard, V., Burbank, D. W., Bourlès, D. L., Bookhagen, B., Braucher, R., & Fisher, G. B. (2012). Impact of glacial erosion on 10Be concentrations in fluvial sediments of the Marsyandi catchment, central Nepal. Journal of Geophysical Research: Earth Surface, 117(F3).

Gosse, J. C., & Phillips, F. M. (2001). Terrestrial in situ cosmogenic nuclides: theory and application. Quaternary Science Reviews, 20(14), 1475–1560.

Gueydan, F., Brun, J. P., Phillippon, M., & Noury, M. (2017). Sequential extension as a record of Corsica Rotation during Apennines slab roll–back. Tectonophysics, 710, 149–161.

Guo, L., Zhang, H. F., Harris, N., Xu, W. C., & Pan, F. B. (2017). Detrital zircon U–Pb geochronology, trace–element and Hf isotope geochemistry of the metasedimentary rocks in the

Eastern Himalayan syntaxis: tectonic and paleogeographic implications. Gondwana Research, 41, 207–221

Hack, J. T. (1957). Studies of longitudinal stream profiles in Virginia and Maryland (Vol. 294). US Government Printing Office.

Haddadchi, A., D. S. Ryder, O. Evrard, and J. Olley (2013), Sediment fingerprinting in fluvial systems: review of tracers, sediment sources and mixing models, *InternationalJournal of Sediment Research*, *28*(4), 560 –578.

Haddadchi, A., J. Olley, and P. Laceby (2014), Accuracy of mixing models in predicting sediment source contributions, *Science of The Total Environment*, *497*, 139 –152.

Han, Y., Zhao, G., Sun, M., Eizenhöfer, P. R., Hou, W., Zhang, X., & Wang, B. (2016). Detrital zircon provenance constraints on the initial uplift and denudation of the Chinese western Tianshan after the assembly of the southwestern Central Asian Orogenic Belt. Sedimentary geology, 339, 1–12.

Hanks, T. C. (2000). The age of scarplike landforms from diffusion-equation analysis. Quaternary geochronology, 4, 313–338.

Heimsath, A. M., Dietrich, W. E., Nishiizumi, K., & Finkel, R. C. (1997). The soil production function and landscape equilibrium. *Nature*, *388*(6640), 358.

Helland–Hansen, W., Sømme, T. O., Martinsen, O. J., Lunt, I., & Thurmond, J. (2016). Deciphering earth's natural hourglasses: perspectives on source–to–sink analysis. Journal of Sedimentary Research, 86(9), 1008–1033.

Hodges, K., C. Wobus, K. Ruhl, T. Schildgen, and K. Whipple (2004), Quaternary deformation, river steepening, and heavy precipitation at the front of the higher Himalayan ranges, Earth and Planetary Sciences Letters, 220(3–4), 379–389, doi: 10.1016/S0012–821X(04)00063–9

Howard, A. D. (1980). Thresholds in river regimes. Thresholds in geomorphology, 227–258.

Howard, A. D., & Kerby, G. (1983). Channel changes in badlands. Geological Society of America Bulletin, 94(6), 739–752.

Howard, A. D., Dietrich, W. E., & Seidl, M. A. (1994). Modeling fluvial erosion on regional to continental scales. Journal of Geophysical Research: Solid Earth, 99(B7), 13971–13986.

Hren, M. T., Hilley, G. E., & Chamberlain, C. P. (2007). The relationship between tectonic uplift and chemical weathering rates in the Washington Cascades: field measurements and model predictions. American Journal of Science, 307(9), 1041-1063.

Hurford, A. J. (2019). An Historical Perspective on Fission–Track Thermochronology. In Fission–Track Thermochronology and its Application to Geology (pp. 3–23). Springer, Cham.

Hurst, M. D., Mudd, S. M., Walcott, R., Attal, M., & Yoo, K. (2012). Using hilltop curvature to derive the spatial distribution of erosion rates. Journal of Geophysical Research: Earth Surface, 117(F2).

Iizuka, T., T. Komiya, S. Rino, S. Maruyama, and T. Hirata (2010), Detrital zircon evidence for hf isotopic evolution of granitoid crust and continental growth, *Geochimica etCosmochimica Acta*, *74*(8), 2450 –2472.

Ireland, T. R., & Williams, I. S. (2003). Considerations in zircon geochronology by SIMS. Reviews in mineralogy and geochemistry, 53(1), 215–241.

J.L. Paquette, R.P. Ménot, C. Pin, J.B. Orsini. Episodic and short–lived granitic pulses in a post–collisional setting: evidence from precise U–Pb zircon dating through a crustal cross–section in Corsica. Chemical Geology, 198 (2003), pp. 1–20

Jackson, S. E., Pearson, N. J., Griffin, W. L., & Belousova, E. A. (2004). The application of laser ablation–inductively coupled plasma–mass spectrometry to in situ U–Pb zircon geochronology. Chemical Geology, 211(1–2), 47–69.

Johnson, T. E., Kirkland, C. L., Reddy, S. M., Evans, N. J., & McDonald, B. J. (2016). The source of Dalradian detritus in the Buchan Block, NE Scotland: application of new tools to detrital datasets. Journal of the Geological Society, jgs2016–019.

Jolivet, L., R. Dubois, M. Fournier, B. Goffé, A. Michard, and C. Jourdan (1990), Ductile extension in Alpine Corsica, Geology, 18, 1007–1010.

Kellerhals, R., & Bray, D. I. (1971). Sampling procedures for coarse fluvial sediments. Journal of the Hydraulics Division, 97(8), 1165-1180.

Kimbrough, D. L., M. Grove, G. E. Gehrels, R. J. Dorsey, K. A. Howard, O. Lovera, A. Aslan, P. K. House, and P. A. Pearthree (2015), Detrital zircon U–Pb provenance of the Colorado River: A 5 m.y. record of incision into cover strata overlying the Colorado plateau and adjacent regions, Geosphere, 11(6), 1719, doi: 10.1130/GES00982.1

Kirby, E., & Whipple, K. (2001). Quantifying differential rock–uplift rates via stream profile analysis. Geology, 29(5), 415–418.

Kirby, E., & Whipple, K. X. (2012). Expression of active tectonics in erosional landscapes. Journal of Structural Geology, 44, 54–75.

Kirstein, L.A., A. Carter, Y.G. Chen (2013), Impacts of arc collision on small orogens: New insights from the Coastal Range detrital record, Taiwan, *Journal of the Geological Society, London,* 171(1), 5–8, DOI: 10.1144/jgs2013–046

Kirstein, L.A., M.G. Fellin, S.D. Willett, A. Carter, Y.G. Chen, J.I. Garver, D–C. Lee (2009), Pliocene onset of rapid exhumation in Taiwan during arc–continent collision: New insights from detrital thermochronometry, Basin Research, 22(3), 270 –285 DOI: 10.1111/j.1365–2117.2009.00426.x

Krijgsman, W., Hilgen, F. J., Raffi, I., Sierro, F. J., & Wilson, D. S. (1999). Chronology, causes and progression of the Messinian salinity crisis. Nature, 400(6745), 652.

Krumbein, W. C. (1941), The effects of abrasion on the size, shape and roundness of rock fragments, *The Journal of Geology*, *49*(5), 482–520.

Kuenen, P. H. (1956), Experimental abrasion of pebbles: 2. rolling by current, *The Journal of Geology*, *64*(4), 336–368.

Kuhlemann J, Frisch W, Székely B, Dunkl I, Daníšík M, Krumrei I. 2005b. Würmian maximum glaciation in Corsica: glacier extent, amplifying paleorelief, and mesoscale climate. Austrian Journal of Earth Science 97: 68–81.

Kuhlemann J, Krumrei I, Daníšík M, Van der Borg K. 2009. Weathering of granite and granitic regolith in Corsica: short–term 10Be versus long–term thermochronological constraints. In Thermochronological Methods: From Palaeotemperature Constraints to Landscape Evolution Models, Lisker F, Ventura B, Glasmacher UA (eds), Vol. 324. Geological Society of London Special Publication; 217–235.

Kuhlemann J, Rohling EJ, Krumrei I, Kubik P, Ivy–Ochs S, Kucera M. 2008. Regional synthesis of Mediterranean atmospheric circulation during the Last Glacial Maximum. Science 321: 1338–1340.

Kuhlemann J, Székely B, Frisch W, Daníšík M, Dunkl I, Molnar G, Timar G. 2005a. DEM analysis of mountaineous relief in a crystalline basement block:Cenozoic relief generations in Corsica (France). Zeitschrift für Geomorphologie N. F 49(1): 1–21.

Kuhlemann J, Van der Borg K, Daníšík M, Frisch W. 2007. In situ 10Be–rosion rates in granites of subalpine Miocene paleosurfaces in the western Mediterranean (Corsica, France). International Journal of Earth Science 97: 549–564.

Kuhlemann J, Van der Borg K, Daníšík M, Frisch W. 2007. In situ 10Be–rosion rates in granites of subalpine Miocene paleosurfaces in the western Mediterranean (Corsica, France). International Journal of Earth Science 97: 549–564.

Kuhlemann, J., Krumrei, I., Danišík, M., & van der Borg, K. (2009). Weathering of granite and granitic regolith in Corsica: short–term 10Be versus long–term thermochronological constraints. Geological Society, London, Special Publications, 324(1), 217–235.

Kuhlemann, J., van der Borg, K., Bons, P. D., Danišík, M., & Frisch, W. (2008). Erosion rates on subalpine paleosurfaces in the western Mediterranean by in–situ 10 Be concentrations in granites: implications for surface processes and long–term landscape evolution in Corsica (France). International Journal of Earth Sciences, 97(3), 549–564.

Lague, D. (2014). The stream power river incision model: evidence, theory and beyond. Earth Surface Processes and Landforms, 39(1), 38–61.

Lambeck, K., & Purcell, A. (2005). Sea-level change in the Mediterranean Sea since the LGM: model predictions for tectonically stable areas. Quaternary Science Reviews, 24(18-19), 1969-1988.

Lambeck, K., Antonioli, F., Purcell, A., & Silenzi, S. (2004). Sea–level change along the Italian coast for the past 10,000 yr. Quaternary Science Reviews, 23(14–15), 1567–1598.

Lambert, D., Mallet, M., Ducrocq, V., Dulac, F., Gheusi, F., & Kalthoff, N. (2011). CORSiCA: a Mediterranean atmospheric and oceanographic observatory in Corsica within the framework of HyMeX and ChArMEx. Advances in Geosciences, 26, 125–131.

Lavarini, C., Attal, M., da Costa Filho, C. A., & Kirstein, L. A. (2018). Does pebble abrasion influence detrital age population statistics? A numerical investigation of natural datasets. Journal of Geophysical Research: Earth Surface.

Lawrence, R. L., R. Cox, R. W. Mapes, and D. S. Coleman (2011a), Hydrodynamic fractionation of zircon age populations, *Geological Society of America Bulletin*, *123*(1–2), 295–305.

Le Bouteiller, C., F. Naaim–Bouvet, N. Mathys, and J. Lavé (2011), A new framework for modeling sediment fining during transport with fragmentation and abrasion, *Journal ofGeophysical Research: Earth Surface*, *116*(F3), F03002.

Le Fort, P. (1975). Himalayas: the collided range. Present knowledge of the continental arc. American Journal of Science, 275(1), 1–44.

Lease, R. O., Burbank, D. W., Gehrels, G. E., Wang, Z., & Yuan, D. (2007). Signatures of mountain building: Detrital zircon U/Pb ages from northeastern Tibet. Geology, 35(3), 239–242.

Lease, R. O., Haeussler, P. J., & O'Sullivan, P. (2016). Changing exhumation patterns during Cenozoic growth and glaciation of the Alaska Range: Insights from detrital thermochronology and geochronology. Tectonics, 35(4), 934–955.

Lewin, J., & Macklin, M. G. (2003). Preservation potential for Late Quaternary river alluvium. Journal of Quaternary Science: Published for the Quaternary Research Association, 18(2), 107–120.

Lewin, J., and P. A. Brewer (2002), Laboratory simulation of clast abrasion, *Earth Surface Processes and Landforms*, *27*(2), 145–164.

Li, X. H., Faure, M., & Lin, W. (2014). From crustal anatexis to mantle melting in the Variscan orogen of Corsica (France): SIMS U–Pb zircon age constraints. Tectonophysics, 634, 19–30.

Licht, A., A. Pullen, P. Kapp, J. Abell, and N. Giesler (2016), Eolian cannibalism: Reworked loess and fluvial sediment as the main sources of the Chinese Loess plateau, *Geological Society of America Bulletin*, *128*(5–6), 944, doi: 10.1130/B31375.1

Lin, W., Rossi, P., Faure, M., Li, X. H., Ji, W., & Chu, Y. (2018). Detrital zircon age patterns from turbidites of the Balagne and Piedmont nappes of Alpine Corsica (France): Evidence for an European margin source. Tectonophysics, 722, 69–105.

Litty, C., Lanari, P., Burn, M., & Schlunegger, F. (2017). Climate–controlled shifts in sediment provenance inferred from detrital zircon ages, western Peruvian Andes. Geology, 45(1), 59–62.

Liu, L. (2014). Rejuvenation of Appalachian topography caused by subsidence–induced differential erosion. Nature Geoscience, 7(7), 518.

Loget, N., Davy, P., & Van den Driessche, J. (2006). Mesoscale fluvial erosion parameters deduced from modeling the Mediterranean sea level drop during the Messinian (late Miocene). Journal of Geophysical Research: Earth Surface, 111(F3).

Lukens, C. E., C. S. Riebe, L. S. Sklar, and D. L. Shuster (2016), Grain size bias in cosmogenic nuclide studies of stream sediment in steep terrain, *Journal of Geophysical Research:Earth Surface*, *121*(5), 978–999, doi: 10.1002/2016JF003859

Maher, E., Harvey, A. M., & France, D. (2007). The impact of a major Quaternary river capture on the alluvial sediments of a beheaded river system, the Rio Alias SE Spain. Geomorphology, 84(3–4), 344–356.

Mailhé, D., Lucazeau, F., & Vasseur, G. (1986). Uplift history of thrust belts: An approach based on fission track data and thermal modelization. Tectonophysics, 124(1–2), 177–191.

Malavieille, J., Chemenda, A., & Larroque, C. (1998). Evolutionary model for Alpine Corsica: mechanism for ophiolite emplacement and exhumation of high–pressure rocks. TERRA NOVA–OXFORD–, 10, 317–322.

Malkowski, M. A., Schwartz, T. M., Sharman, G. R., Sickmann, Z. T., & Graham, S. A. (2017). Stratigraphic and provenance variations in the early evolution of the Magallanes–Austral foreland basin: Implications for the role of longitudinal versus transverse sediment dispersal during arc–continent collision. Bulletin, 129(3–4), 349–371.

Malusà, M. G., A. Carter, M. Limoncelli, I. M. Villa, and E. Garzanti (2013), Bias in detrital zircon geochronology and thermochronometry, *Chemical Geology*, *359*, 90–107.

Malusà, M. G., A. Resentini, and E. Garzanti (2016), Hydraulic sorting and mineral fertility bias in detrital geochronology, *Gondwana Research*, *31*, 1–19.

Malusà, M. G., Faccenna, C., Baldwin, S. L., Fitzgerald, P. G., Rossetti, F., Balestrieri, M. L., ... & Piromallo, C. (2015). Contrasting styles of (U) HP rock exhumation along the Cenozoic Adria- Europe plate boundary (Western Alps, Calabria, Corsica). Geochemistry, Geophysics, Geosystems, 16(6), 1786–1824.

Malusà, M. G., Resentini, A., & Garzanti, E. (2016). Hydraulic sorting and mineral fertility bias in detrital geochronology. Gondwana Research, 31, 1–19.

Mandal, S. K., Lupker, M., Burg, J. P., Valla, P. G., Haghipour, N., & Christl, M. (2015). Spatial variability of 10 Be–derived erosion rates across the southern Peninsular Indian escarpment: A key to landscape evolution across passive margins. Earth and Planetary Science Letters, 425, 154–167.

Mark, C., Cogné, N., & Chew, D. (2016). Tracking exhumation and drainage divide migration of the Western Alps: A test of the apatite U–Pb thermochronometer as a detrital provenance tool. Bulletin, 128(9–10), 1439–1460.

Martins, H. C. B., Simões, P. P., & Abreu, J. (2014). Zircon crystal morphology and internal structures as a tool for constraining magma sources: Examples from northern Portugal Variscan biotite–rich granite plutons. Comptes Rendus Geoscience, 346(9–10), 233–243.

Mason, C. C., Fildani, A., Gerber, T., Blum, M. D., Clark, J. D., & Dykstra, M. (2017). Climatic and anthropogenic influences on sediment mixing in the Mississippi source–to–sink system using detrital zircons: Late Pleistocene to recent. Earth and Planetary Science Letters, 466, 70–79.

Mather, A. E. (2000). Adjustment of a drainage network to capture induced base–level change: an example from the Sorbas Basin, SE Spain. *Geomorphology*, *34*(3–4), 271–289.

Miller, K. L., Szabó, T., Jerolmack, D. J., & Domokos, G. (2014). Quantifying the significance of abrasion and selective transport for downstream fluvial grain size evolution. Journal of Geophysical Research: Earth Surface, 119, 2412–2429. https://doi.org/10.1002/2014JF003156

Mills, H. H. (1979), Downstream rounding of pebbles–A quantitative review, *Journal of Sedimentary Research*, *49*(1).

Moecher, D. P., & Samson, S. D. (2006). Differential zircon fertility of source terranes and natural bias in the detrital zircon record: Implications for sedimentary provenance analysis. Earth and Planetary Science Letters, 247(3–4), 252–266.

Mojzsis, S. J., T. M. Harrison, and R. T. Pidgeon (2001), Oxygen–isotope evidence from ancient zircons for liquid water at the Earth's surface 4,300 Myr ago, *Nature, 409*(6817), 178–181.

Molli, G. (2008). Northern Apennine–Corsica orogenic system: an updated overview. Geological Society, London, Special Publications, 298(1), 413–442.

Molli, G., Tribuzio, R., & Marquer, D. (2006). Deformation and metamorphism at the eastern border of the Tenda Massif (NE Corsica): a record of subduction and exhumation of continental crust. Journal of Structural Geology, 28(10), 1748–1766.

Molliex, S., Jouet, G., Freslon, N., Bourlès, D. L., Authemayou, C., Moreau, J., & Rabineau, M. (2017). Controls on Holocene denudation rates in mountainous environments under Mediterranean climate. Earth Surface Processes and Landforms, 42(2), 272–289.

Morton, A. C. (1985). Heavy minerals in provenance studies. In Provenance of arenites (pp. 249–277). Springer, Dordrecht.

Mudd, S. M. (2017). Detection of transience in eroding landscapes. Earth Surface Processes and Landforms, 42(1), 24–41.

Mudd, S. M., Attal, M., Milodowski, D. T., Grieve, S. W., & Valters, D. A. (2014). A statistical framework to quantify spatial variation in channel gradients using the integral method of channel profile analysis. Journal of Geophysical Research: Earth Surface, 119(2), 138–152.

Mudd, S. M., Clubb, F. J., Gailleton, B., & Hurst, M. D. (2018). How concave are river channels?. Earth Surface Dynamics, 6(2), 505–523.

Murphy, B. P., Johnson, J. P., Gasparini, N. M., & Sklar, L. S. (2016). Chemical weathering as a mechanism for the climatic control of bedrock river incision. Nature, 532(7598), 223.

Naylor, M., Sinclair, H. D., Bernet, M., van der Beek, P., & Kirstein, L. A. (2015). Bias in detrital fission track grain–age populations: Implications for reconstructing changing erosion rates. Earth and Planetary Science Letters, 422, 94–104.

Neely, A. B., Bookhagen, B., & Burbank, D. W. (2017). An automated knickzone selection algorithm (KZ-Picker) to analyze transient landscapes: Calibration and validation. Journal of Geophysical Research: Earth Surface, 122(6), 1236–1261.

Nesbitt, H. W., Young, G. M., McLennan, S. M., & Keays, R. R. (1996). Effects of chemical weathering and sorting on the petrogenesis of siliciclastic sediments, with implications for provenance studies. The Journal of Geology, 104(5), 525–542.

Nocedal, J., and S. Wright (2000), *Numerical Optimization (Springer Series in Operations*

Oh, N. H., & Richter, D. D. (2005). Elemental translocation and loss from three highly weathered soil–bedrock profiles in the southeastern United States. Geoderma, 126(1–2), 5–25.

Ohnenstetter, M., Ohnenstetter, D., Vidal, P., Cornichet, J., Hermitte, D., & Mace, J. (1981). Crystallization and age of zircon from Corsican ophiolitic albitites: consequences for oceanic expansion in Jurassic times. Earth and Planetary Science Letters, 54(3), 397–408.

Olen, S. M., B. Bookhagen, B. Hoffmann, D. Sachse, D. P. Adhikari, and M. R. Strecker (2015), Understanding erosion rates in the Himalayan orogen: A case study from the Arun valley. Journal of Geophysical Research: Earth Surface, 120(10), 2080–2102, doi: 10.1002/2014JF003410

Olen, S. M., B. Bookhagen, B. Hoffmann, D. Sachse, D. P. Adhikari, and M. R. Strecker (2015), Understanding erosion rates in the Himalayan orogen: A case study from the Arun valley, *Journal of Geophysical Research: Earth Surface*, *120*(10), 2080–2102, doi: 10.1002/2014JF003410

Oliver, G., K. Zaw, M. Hotson, S. Meffre, and T. Manka (2014), U–Pb zircon geochronology of Early Permian to Late Triassic rocks from Singapore and Johor: A plate tectonic reinterpretation, *Gondwana Research*, *26*(1), 132–143.

Ouimet, W. B., Whipple, K. X., Royden, L. H., Sun, Z., & Chen, Z. (2007). The influence of large landslides on river incision in a transient landscape: Eastern margin of the Tibetan Plateau (Sichuan, China). Geological Society of America Bulletin, 119(11–12), 1462–1476.

P. Rossi, M. Durand–Delga, J.–C. Lahondère, D. Lahondère. Carte géologique de la France au 1/50000. Carte et Notice explicative de la feuille Santo–Pietro–di–Tenda, BRGM, Orléans, France (2001).

Paquette, J.L., R.P. Ménot, C. Pin, J.B. Orsini. Episodic and short–lived granitic pulses in a post–collisional setting: evidence from precise U–Pb zircon dating through a crustal cross–section in Corsica. Chemical Geology, 198 (2003), pp. 1–20

Parker, G. (1991), Selective sorting and abrasion of river gravel. I: Theory, *Journal of Hydraulic Engineering*, *117*(2), 131–147.

Pelletier, J. D. (2004). Persistent drainage migration in a numerical landscape evolution model. Geophysical Research Letters, 31(20).

Pelletier, J. D. (2008). Quantitative modelling of earth surface processes (Vol. 304). Cambridge University Press.

Perez, N. D., and B. K. Horton (2014), Oligocene–miocene deformational and depositional history of the andean hinterland basin in the northern Altiplano plateau, southern Peru, *Tectonics*, *33*(9), 1819–1847, doi: 10.1002/2014TC003647

Perron, J. T., & Royden, L. (2013). An integral approach to bedrock river profile analysis. Earth Surface Processes and Landforms, 38(6), 570–576.

Pichevin, L., Mulder, T., Savoye, B., Gervais, A., Cremer, M., & Piper, D. J. W. (2003). The Golo submarine turbidite system (east Corsica margin): morphology and processes of terrace formation from high–resolution seismic reflection profiles. Geo–Marine Letters, 23(2), 117–124.

Pratt–Sitaula, B., D. W. Burbank, A. Heimsath, and T. Ojha (2004), Landscape disequilibrium on 1000–10,000 year scales Marsyandi river, Nepal, central Himalaya, *Geomorphology*, *58*(1), 223 –241.

Prince, P. S., Spotila, J. A., & Henika, W. S. (2011). Stream capture as driver of transient landscape evolution in a tectonically quiescent setting. Geology, 39(9), 823–826.

Priyatkina, N., Khudoley, A. K., Collins, W. J., Kuznetsov, N. B., & Huang, H. Q. (2016). Detrital zircon record of Meso–and Neoproterozoic sedimentary basins in northern part of the Siberian Craton: Characterizing buried crust of the basement. Precambrian Research, 285, 21–38.

Reiners, P. W., & Brandon, M. T. (2006). Using thermochronology to understand orogenic erosion. Annu. Rev. Earth Planet. Sci., 34, 419–466.

Reiners, P. W., Ehlers, T. A., & Zeitler, P. K. (2005). Past, present, and future of thermochronology. Reviews in Mineralogy and Geochemistry, 58(1), 1–18.

Riebe, C. S., L. S. Sklar, C. E. Lukens, and D. L. Shuster (2015), Climate and topography control the size and flux of sediment produced on steep mountain slopes, *Proceedings of the National Academy of Sciences*, *112*(51), 15,574–15,579, doi: 10.1073/pnas.1503567112

Rieuf, M., 1980. Étude stratigraphique et structurale des unités au Nord–Est de Corte (Corse) (Ph.D. thesis). Univ. Toulouse.

Roberts, G. G., & White, N. (2010). Estimating uplift rate histories from river profiles using African examples. Journal of Geophysical Research: Solid Earth, 115(B2).

Roberts, N. M., & Spencer, C. J. (2015). The zircon archive of continent formation through time. Geological Society, London, Special Publications, 389(1), 197–225.

Robl, J., Heberer, B., Prasicek, G., Neubauer, F., & Hergarten, S. (2017). The topography of a continental indenter: The interplay between crustal deformation, erosion, and base level changes in the eastern Southern Alps. Journal of Geophysical Research: Earth Surface, 122(1), 310–334.

Rosenbaum, G., K. Regenauer-Lieb, and R. Weinberg (2005), Continental extension: From core complexes to rigid block faulting, Geology, 33, 609–612.

Rossi Ph. Cocherie A. Fanning C.M. Deloule E. (2006). –Variscan to Eo–Alpine events recorded in European lower–crust zircons sampled from the French Massif Central and Corsica, France –Lithos , 87, 235–260.

Rossi, P, et al. (1994b). — Carte géol. France (1/50000), feuille Corte (1110). Orléans: BRGM. Notice explicative par P. Rossi et al. (1994), 150 p.

Rossi, P., & Cocherie, A. (1991). Genesis of a Variscan batholith: Field, petrological and mineralogical evidence from the Corsica–Sardinia batholith. Tectonophysics, 195(2–4), 319–346.

Rossi, P., Calvez, J. Y., & Cocherie, A. (1988). Age varisque précoce du plutonisme magnésio–potassique en Corse occidentale: conséquences géodynamiques. Comptes rendus de l'Académie des sciences. Série 2, Mécanique, Physique, Chimie, Sciences de l'univers, Sciences de la Terre, 307(13), 1541–1547.

Rossi, P., Cocherie, A., & Fanning, C. M. (2015). Evidence in Variscan Corsica of a brief and voluminous Late Carboniferous to Early Permian volcanic–plutonic event contemporaneous with a high–temperature/low–pressure metamorphic peak in the lower crust. Bulletin de la Société Géologique de France, 186(2–3), 171–192.

Rossi, P., Cocherie, A., Fanning, C. M., & Deloule, É. (2006). Variscan to eo–Alpine events recorded in European lower–crust zircons sampled from the French Massif Central and Corsica, France. Lithos, 87(3–4), 235–260.

Rossi, P., Durand–Delga, M., & Cocherie, A. (1993). Caractère volcano–plutonique du magmatisme calco–alcalin composite d'âge stéphanien supérieur–permien inférieur en Corse.

Comptes rendus de l'Académie des sciences. Série 2, Mécanique, Physique, Chimie, Sciences de l'univers, Sciences de la Terre, 316(12), 1779–1788.

Rossi, P., Durand–Delga, M., & Cocherie, A. (1995). Identification en Corse d'un socle panafricain (cadomien), conséquences sur la paléogéographie de l'orogène varisque sud–européen. CR Acad. Sci. Paris, 321(II A), 983–992.

Rossi, P., Lahondère, J.C., Lluch, D., Loye–Pilot, M.D., Jacquet (1994a). – Carte géol. France (1/50000), feuille Saint–FIorent (1103). Orléans: BRGM. Notice explicative par Rossi et al. (1994),93p.

Rouchy, J. M., & Caruso, A. (2006). The Messinian salinity crisis in the Mediterranean basin: a reassessment of the data and an integrated scenario. Sedimentary Geology, 188, 35-67.

Royden, L., & Perron, J. T. (2013). Solutions of the stream power equation and application to the evolution of river longitudinal profiles. Journal of Geophysical Research: Earth Surface, 118(2), 497–518.

Satkoski, A. M., Wilkinson, B. H., Hietpas, J., & Samson, S. D. (2013). Likeness among detrital zircon populations–An approach to the comparison of age frequency data in time and space. Bulletin, 125(11–12), 1783–1799. https://doi.org/10.1130/B30888.1

Saylor, J. E., and K. E. Sundell (2016), Quantifying comparison of large detrital geochronology data sets, *Geosphere*, *12*(1), 203–220, doi: 10.1130/GES01237.1

Saylor, J. E., D. F. Stockli, B. K. Horton, J. Nie, and A. Mora (2012), Discriminating rapid exhumation from syndepositional volcanism using detrital zircon double dating: Implications for the tectonic history of the Eastern Cordillera, Colombia, *Geological Society of America Bulletin*, *124*(5–6), 762–779.

Saylor, J. E., J. N. Knowles, B. K. Horton, J. Nie, and A. Mora (2013), Mixing of source populations recorded in detrital zircon U-Pb age spectra of modern river sands, J. Geol., 121(1), 17–33.

Scherler, D., Bookhagen, B., & Strecker, M. R. (2014). Tectonic control on 10Be- derived erosion rates in the Garhwal Himalaya, India. Journal of Geophysical Research: Earth Surface, 119(2), 83–105.

Schumm, S., and M. Stevens (1973), Abrasion in place: a mechanism for rounding and size reduction of coarse sediments in rivers, *Geology*, *1*(1), 37–40.

Sharman, G. R., & Johnstone, S. A. (2017). Sediment unmixing using detrital geochronology. Earth and Planetary Science Letters, 477, 183–194. https://doi.org/10.1016/j.epsl.2017.07.044

Sharman, G. R., Graham, S. A., Grove, M., Kimbrough, D. L., & Wright, J. E. (2015). Detrital zircon provenance of the Late Cretaceous–Eocene California forearc: Influence of Laramide low–angle subduction on sediment dispersal and paleogeography. Bulletin, 127(1–2), 38–60.

Sharman, G. R., Hubbard, S. M., Covault, J. A., Hinsch, R., Linzer, H. G., & Graham, S. A. (2018). Sediment routing evolution in the North Alpine Foreland Basin, Austria: interplay of transverse and longitudinal sediment dispersal. Basin Research, 30(3), 426–447.

Shaw, J., Gutiérrez–Alonso, G., Johnston, S. T., & Galán, D. P. (2014). Provenance variability along the Early Ordovician north Gondwana margin: Paleogeographic and tectonic implications of U–Pb detrital zircon ages from the Armorican Quartzite of the Iberian Variscan belt. Bulletin, 126(5–6), 702–719.

Shobe, C. M., Tucker, G. E., & Barnhart, K. R. (2017). The SPACE 1.0 model: a Landlab component for 2-D calculation of sediment transport, bedrock erosion, and landscape evolution. Geoscientific Model Development, 10(12), 4577-4604.

Sickmann, Z. T., Paull, C. K., & Graham, S. A. (2016). Detrital–zircon mixing and partitioning in fluvial to deep marine systems, Central California, USA. Journal of Sedimentary Research, 86(11), 1298–1307.

Sinclair, H. D., Mudd, S. M., Dingle, E., Hobley, D. E. J., Robinson, R., & Walcott, R. (2017). Squeezing river catchments through tectonics: Shortening and erosion across the Indus Valley, NW Himalaya. Bulletin, 129(1–2), 203–217.

Singh, S. K., S. K. Rai, and S. Krishnaswami (2008), Sr and Nd isotopes in river sediments from the Ganga basin: Sediment provenance and spatial variability in physical erosion, *Journal of Geophysical Research: Earth Surface*, *113*(F3), F03006.

Sircombe, K. N., & Stern, R. A. (2002). An investigation of artificial biasing in detrital zircon U–Pb geochronology due to magnetic separation in sample preparation. Geochimica et Cosmochimica Acta, 66(13), 2379–2397.

Sklar, L. S., and W. E. Dietrich (2001), Sediment and rock strength controls on river incision into bedrock, *Geology*, *29*(12), 1087–1090.

Sklar, L. S., and W. E. Dietrich (2004), A mechanistic model for river incision into bedrock by saltating bed load, *Water Resources Research*, *40*(6).

Sklar, L. S., C. S. Riebe, J. A. Marshall, J. Genetti, S. Leclere, C. L. Lukens, and V. Merces (2017), The problem of predicting the size distribution of sediment supplied by hillslopes to rivers, *Geomorphology*, *277*, 31–49, doi: 10.1016/j.geomorph.2016.05.005

Sklar, L., & Dietrich, W. E. (1998). River longitudinal profiles and bedrock incision models: Stream power and the influence of sediment supply. Rivers over rock: fluvial processes in bedrock channels, 107, 237–260.

Sklar, Leonard S., and William E. Dietrich. "A mechanistic model for river incision into bedrock by saltating bed load." Water Resources Research 40, no. 6 (2004).

Sláma, J., & Košler, J. (2012). Effects of sampling and mineral separation on accuracy of detrital zircon studies. Geochemistry, Geophysics, Geosystems, 13(5).

Snyder, N. P., Whipple, K. X., Tucker, G. E., & Merritts, D. J. (2000). Landscape response to tectonic forcing: Digital elevation model analysis of stream profiles in the Mendocino triple junction region, northern California. Geological Society of America Bulletin, 112(8), 1250–1263.

Snyder, N. P., Whipple, K. X., Tucker, G. E., & Merritts, D. J. (2002). Interactions between onshore bedrock–channel incision and nearshore wave–base erosion forced by eustasy and tectonics. Basin Research, 14(2), 105–127.

Sømme TO, Piper DJW, Deptuck ME, Helland–Hansen W. 2011. Linking onshore–offshore sediment dispersal in the Golo source–to–sink system (Corsica, France) during late Quaternary. Journal of Sedimentary Research 81(2): 118–137. DOI:10.2110/jsr.2011.11.

Spencer, C. J., Kirkland, C. L., & Roberts, N. M. (2018). Implications of erosion and bedrock composition on zircon fertility: Examples from South America and Western Australia. Terra Nova.

Stephens, M. A. (1970), Use of the Kolmogorov–Smirnov, Cramér–Von Mises and related statistics without extensive tables, *Journal of the Royal Statistical Society. SeriesB (Methodological)*, pp. 115–122.

Stokes, M., Mather, A. E., & Harvey, A. M. (2002). Quantification of river–capture–induced base–level changes and landscape development, Sorbas Basin, SE Spain. Geological Society, London, Special Publications, 191(1), 23–35.

Sundell, K. E., & Saylor, J. E. (2017). Unmixing detrital geochronology age distributions. Geochemistry, Geophysics, Geosystems, 18, 2872–2886. https://doi.org/10.1002/2016GC006774

Thomson, S. N., Reiners, P. W., Hemming, S. R., & Gehrels, G. E. (2013). The contribution of glacial erosion to shaping the hidden landscape of East Antarctica. Nature Geoscience, 6(3), 203.

Tochilin, C. J., Reiners, P. W., Thomson, S. N., Gehrels, G. E., Hemming, S. R., & Pierce, E. L. (2012). Erosional history of the Prydz Bay sector of East Antarctica from detrital apatite and zircon geo- and thermochronology multidating. Geochemistry, Geophysics, Geosystems, 13(11).

Ustaömer, T., Ustaömer, P.A., Robertson, A.H.F. et al. Int J Earth Sci (Geol Rundsch) (2016) 105: 7. https://doi.org/10.1007/s00531–015–1225–8

van der Beek, P., Litty, C., Baudin, M., Mercier, J., Robert, X., & Hardwick, E. (2016). Contrasting tectonically driven exhumation and incision patterns, western versus central Nepal Himalaya. Geology, 44(4), 327–330.

Vanacker, V., von Blanckenburg, F., Govers, G., Molina, A., Campforts, B., & Kubik, P. W. (2015). Transient river response, captured by channel steepness and its concavity. Geomorphology, 228, 234–243.

Vavra, G. (1990). On the kinematics of zircon growth and its petrogenetic significance: a cathodoluminescence study. Contributions to Mineralogy and Petrology, 106(1), 90–99.

Vavra, G. (1993). A guide to quantitative morphology of accessory zircon. Chemical Geology, 110(1–3), 15–28.

Vavra, G., Gebauer, D., Schmid, R., & Compston, W. (1996). Multiple zircon growth and recrystallization during polyphase Late Carboniferous to Triassic metamorphism in granulites of the Ivrea Zone (Southern Alps): an ion microprobe (SHRIMP) study. Contributions to Mineralogy and Petrology, 122(4), 337–358.

Vavra, G., Schmid, R., & Gebauer, D. (1999). Internal morphology, habit and U–Th–Pb microanalysis of amphibolite–to–granulite facies zircons: geochronology of the Ivrea Zone (Southern Alps). Contributions to Mineralogy and Petrology, 134(4), 380–404.

Vermeesch, P. (2004). How many grains are needed for a provenance study?. Earth and Planetary Science Letters, 224(3–4), 441–451.

Vermeesch, P. (2012). On the visualisation of detrital age distributions. Chemical Geology, 312, 190–194.

Waelbroeck, C., Labeyrie, L., Michel, E., Duplessy, J. C., McManus, J. F., Lambeck, K., ... & Labracherie, M. (2002). Sea–level and deep water temperature changes derived from benthic foraminifera isotopic records. Quaternary Science Reviews, 21(1–3), 295–305.

Weissel, J. K., & Seidl, M. A. (1998). Inland propagation of erosional escarpments and river profile evolution across the southeast Australian passive continental margin. Geophysical Monograph–American Geophysical Union, 107, 189–206.

Wheaton, J. M., Brasington, J., Darby, S. E., & Sear, D. A. (2010). Accounting for uncertainty in DEMs from repeat topographic surveys: improved sediment budgets. Earth surface

processes and landforms: the journal of the British Geomorphological Research Group, 35(2), 136–156.

Whipple, K. X. (2001). Fluvial landscape response time: How plausible is steady–state denudation?. American Journal of Science, 301(4–5), 313–325.

Whipple, K. X., & Tucker, G. E. (1999). Dynamics of the stream-power river incision model: Implications for height limits of mountain ranges, landscape response timescales, and research needs. Journal of Geophysical Research: Solid Earth, 104(B8), 17661–17674.

Whipple, K. X., & Tucker, G. E. (2002). Implications of sediment-flux-dependent river incision models for landscape evolution. Journal of Geophysical Research: Solid Earth, 107(B2), ETG–3.

Whipple, K. X., DiBiase, R. A., Ouimet, W. B., & Forte, A. M. (2017b). Preservation or piracy: Diagnosing low–relief, high–elevation surface formation mechanisms. Geology, 45(1), 91–94.

Whipple, K. X., Forte, A. M., DiBiase, R. A., Gasparini, N. M., & Ouimet, W. B. (2017a). Timescales of landscape response to divide migration and drainage capture: Implications for the role of divide mobility in landscape evolution. Journal of Geophysical Research: Earth Surface, 122(1), 248–273.

Whittaker, A. C., & Boulton, S. J. (2012). Tectonic and climatic controls on knickpoint retreat rates and landscape response times. Journal of Geophysical Research: Earth Surface, 117(F2).

Whittaker, A. C., Cowie, P. A., Attal, M., Tucker, G. E., & Roberts, G. P. (2007). Contrasting transient and steady–state rivers crossing active normal faults: new field observations from the Central Apennines, Italy. Basin Research, 19(4), 529–556.

Wilde, S. A., Valley, J. W., Peck, W. H., & Graham, C. M. (2001). Evidence from detrital zircons for the existence of continental crust and oceans on the Earth 4.4 Gyr ago. Nature, 409(6817), 175.

Willenbring, J. K., Gasparini, N. M., Crosby, B. T., & Brocard, G. (2013). What does a mean mean? The temporal evolution of detrital cosmogenic denudation rates in a transient landscape. Geology, 41(12), 1215–1218.

Willett, S. D., & Brandon, M. T. (2002). On steady states in mountain belts. Geology, 30(2), 175–178.

Willett, S. D., McCoy, S. W., Perron, J. T., Goren, L., & Chen, C. Y. (2014). Dynamic reorganization of river basins. Science, 343(6175), 1248765.

Willgoose, G., Bras, R. L., & Rodriguez-Iturbe, I. (1991). Results from a new model of river basin evolution. Earth Surface Processes and Landforms, 16(3), 237–254.

Wobus C, Whipple KX, Kirby E, Snyder N, Johnson J, Spyropolou K, Crosby B, Sheehan D. 2006. Tectonics from topography: procedures, promise, and pitfalls. In Tectonics, Climate, and Landscape Evolution, Willett SD, Hovius N, Brandon MT, Fisher DM (eds), Geological Society of America Special Paper 398, Penrose Conference Series. Geological Society of America: Boulder, CO; 55–74.

Wobus, C., Whipple, K. X., Kirby, E., Snyder, N., Johnson, J., Spyropolou, K., ... & Willett, S. D. (2006). Tectonics from topography: Procedures, promise, and pitfalls. Special papers–geological society of america, 398, 55.

Yang, S., Zhang, F., & Wang, Z. (2012). Grain size distribution and age population of detrital zircons from the Changjiang (Yangtze) River system, China. Chemical Geology, 296, 26–38.

Yanites, B. J., Becker, J. K., Madritsch, H., Schnellmann, M., & Ehlers, T. A. (2017). Lithologic effects on landscape response to base level changes: a modeling study in the context of the Eastern Jura Mountains, Switzerland. Journal of Geophysical Research: Earth Surface, 122(11), 2196–2222.

Zarki-Jakni, B., P. Van der Beek, G. Poupeau, M. Sosson, E. Labrin, P. Rossi, and J. Ferrandini (2004), Cenozoic denudation of Corsica in response to Ligurian and Tyrrhenian extension: Results from apatite fission-track thermochronology, Tectonics, 23, TC1003, doi:10.1029/2003TC001535.

Zattin, M., M. G. Fellin, W. Cavazza, V. Picotti, J. A. Vance, and G. G. Zuffa (2001), Exhumation of northern Corsica (France), Geophys. Res. Abstr., 3, 531.

Zhang, Z., Xiao, W., Majidifard, M.R. et al. Int J Earth Sci (Geol Rundsch) (2017) 106: 1223. https://doi.org/10.1007/s00531–016–1314–3

Zhong, Y., Zhai, M., Peng, P., Santosh, M., & Ma, X. (2015). Detrital zircon U–Pb dating and whole–rock geochemistry from the clastic rocks in the northern marginal basin of the North China Craton: Constraints on depositional age and provenance of the Bayan Obo Group. Precambrian Research, 258, 133–145.

# Chapter 8 –Supporting information

## 8.1. Chapter 2

Table S1. Real U-Pb ages from the Marsyandi published by Amidon et al. (2005a).

| TTS (A) | | Formation III (C) | | Formation II (D) | | Formation I (F) | | Lesser Himalaya (H) | | Lesser Himalaya (I) | | Sample E | | Sample G | | Sample K | |
|---|---|---|---|---|---|---|---|---|---|---|---|---|---|---|---|---|---|
| Age (Ma) | Error (Ma) | Age (Ma) | Error (Ma) | Age (Ma) | Error (Ma) | Age (Ma) | Error (Ma) | Age (Ma) | Error (Ma) | Age (Ma) | Error (Ma) | Age (Ma) | Error (Ma) | Age (Ma) | Error (Ma) | Age (Ma) | Error (Ma) |
| 408.3 | 9.3 | 328.2 | 27.1 | 314.5 | 24.9 | 547.4 | 50.5 | 1746 | 63.9 | 1717 | 98.1 | 398.9 | 4.7 | 431.8 | 18.3 | 336.8 | 18.2 |
| 461.4 | 26.4 | 386.3 | 16.1 | 332.3 | 12.6 | 583.8 | 29 | 1751 | 26.7 | 1729 | 45.3 | 430.8 | 5.8 | 439.1 | 18.5 | 356.7 | 16.2 |
| 505.4 | 25.6 | 398.2 | 12.5 | 398.9 | 15.2 | 598.2 | 19.8 | 1753 | 10.7 | 1768 | 116.6 | 435 | 7.2 | 448.4 | 10.0 | 415.8 | 16.9 |
| 511.5 | 9.1 | 406.9 | 14.2 | 402.0 | 8.5 | 611.4 | 35.6 | 1763 | 55 | 1777 | 114.5 | 439.2 | 12.8 | 452.8 | 15.5 | 430.8 | 25.0 |
| 517.3 | 12.1 | 423.6 | 20.7 | 405.5 | 8.9 | 614.1 | 29.7 | 1765 | 27.8 | 1778 | 110.3 | 439.8 | 11.8 | 466.4 | 31.0 | 432.0 | 24.3 |
| 518.1 | 13.5 | 432 | 23.8 | 427.6 | 13.0 | 641.6 | 32.9 | 1773 | 67.4 | 1780 | 93.5 | 447.7 | 15 | 470.1 | 17.1 | 446.2 | 5.6 |
| 518.6 | 5.5 | 455.5 | 29.8 | 427.6 | 8.9 | 651.4 | 46.9 | 1773 | 14.6 | 1782 | 77.4 | 469.3 | 8.6 | 495.3 | 26.0 | 448.4 | 7.1 |
| 521.8 | 9.2 | 458.6 | 13.8 | 432.9 | 11.6 | 675.6 | 31 | 1776 | 37.8 | 1787 | 71.2 | 477.1 | 21.5 | 499.2 | 15.1 | 455.6 | 7.9 |
| 531.2 | 2.3 | 461.8 | 25.7 | 439.2 | 9.4 | 716.8 | 27.2 | 1777 | 37.6 | 1793 | 69.9 | 480.1 | 1.5 | 499.4 | 18.6 | 466.7 | 24.2 |
| 532.1 | 25.2 | 467.3 | 24.5 | 439.7 | 8.2 | 725.5 | 42.9 | 1783 | 19 | 1805 | 68.4 | 485.1 | 7.4 | 502.8 | 15.7 | 485.8 | 19.9 |
| 535.7 | 25.4 | 467.4 | 9.7 | 441.8 | 13.4 | 728.2 | 24.2 | 1787 | 22.7 | 1809 | 57.9 | 486 | 10.2 | 505.4 | 19.7 | 490.6 | 13.6 |
| 539.3 | 13.9 | 468.8 | 12.6 | 442.5 | 14.6 | 732.3 | 41.5 | 1787 | 9.6 | 1816 | 58.1 | 488.3 | 7.5 | 521.9 | 7.9 | 494.2 | 4.6 |
| 539.9 | 3.6 | 472.1 | 26.2 | 445.8 | 9.2 | 732.8 | 37.4 | 1788 | 37.8 | 1817 | 56.6 | 494 | 9.6 | 522.4 | 24.5 | 500.1 | 19.7 |
| 540.8 | 11.9 | 476.2 | 10.6 | 449.1 | 15.2 | 747.2 | 43.8 | 1793 | 83.3 | 1818 | 33.6 | 495.1 | 17.5 | 523.6 | 29.5 | 500.9 | 11.4 |
| 541.8 | 5.2 | 476.5 | 33.3 | 449.4 | 12.7 | 751.6 | 23.6 | 1808 | 17.1 | 1819 | 68.5 | 499.8 | 5.4 | 530.3 | 21.2 | 502.5 | 5.2 |
| 546.0 | 4.6 | 481.1 | 26.4 | 453.0 | 11.7 | 782.2 | 29.2 | 1809 | 23.5 | 1830 | 70.6 | 504.6 | 4.8 | 560.6 | 22.9 | 514.2 | 7.0 |
| 546.4 | 7.9 | 481.5 | 25.5 | 453.5 | 15.9 | 790.6 | 29.8 | 1810 | 75.9 | 1836 | 26.4 | 514.4 | 37.7 | 563.3 | 28.4 | 515.4 | 17.9 |
| 553.6 | 31.1 | 481.5 | 27.2 | 453.8 | 9.4 | 793.7 | 35.4 | 1812 | 25 | 1843 | 68.4 | 516.3 | 3.6 | 581.3 | 20.9 | 515.5 | 17.4 |
| 555.2 | 29.9 | 483.5 | 31.7 | 455.5 | 8.9 | 794.6 | 13.4 | 1815 | 11 | 1843 | 61.6 | 528.1 | 8.2 | 584.7 | 49.2 | 515.6 | 15.5 |
| 560.1 | 15.4 | 483.8 | 27.5 | 458.4 | 13.8 | 811.1 | 17.6 | 1817 | 19.4 | 1845 | 83.1 | 530.3 | 6.5 | 596.9 | 50.0 | 519.5 | 21.4 |
| 561.0 | 2.6 | 484 | 16.2 | 458.4 | 7.9 | 817.6 | 30.4 | 1819 | 12.8 | 1846 | 130.6 | 535.2 | 17.3 | 616.9 | 23.9 | 528.6 | 34.3 |
| 564.8 | 12.3 | 486.5 | 27.5 | 460.2 | 12.3 | 822.7 | 17.4 | 1820 | 45.9 | 1847 | 73.6 | 535.7 | 25.1 | 617.6 | 25.8 | 529.6 | 28.3 |
| 580.8 | 4.5 | 486.9 | 15.6 | 461.7 | 9.8 | 827.5 | 19.1 | 1820 | 17.4 | 1847 | 79.5 | 536.1 | 8.4 | 622.2 | 19.0 | 551.5 | 5.9 |
| 583.1 | 19.9 | 488 | 27.2 | 462.4 | 14.4 | 830 | 18.4 | 1820 | 24.2 | 1848 | 74.4 | 538.6 | 10.8 | 638.6 | 15.9 | 557.3 | 4.0 |
| 587.9 | 11.6 | 489.5 | 12.5 | 463.2 | 18.2 | 833.5 | 45 | 1820 | 52.5 | 1850 | 66.5 | 542.6 | 7.8 | 647.8 | 28.7 | 560.1 | 18.2 |
| 588.8 | 33.5 | 491.8 | 32.3 | 464.6 | 5.5 | 833.6 | 46.1 | 1821 | 36.2 | 1853 | 158.7 | 543.2 | 11.3 | 647.8 | 23.7 | 566.6 | 26.5 |
| 591.0 | 21.3 | 493.6 | 27.8 | 464.8 | 5.5 | 834.8 | 16.3 | 1821 | 81.1 | 1856 | 90 | 547.9 | 8.7 | 661.3 | 21.5 | 568.9 | 29.9 |

| | | | | | | | | | | | | | | | | | |
|---|---|---|---|---|---|---|---|---|---|---|---|---|---|---|---|---|---|
| 593.6 | 21.8 | 496 | 22 | 465.1 | 6.6 | 841.1 | 29.3 | 1821 | 24 | 1858 | 60.3 | 554.4 | 5 | 669.2 | 27.2 | 571.3 | 44.3 |
| 596.0 | 4.4 | 500.1 | 12.9 | 465.6 | 10.8 | 848.9 | 25.2 | 1822 | 15.2 | 1858 | 107.6 | 557.3 | 2.6 | 679.2 | 23.6 | 579.9 | 28.3 |
| 602.1 | 9.1 | 500.3 | 32.4 | 466.5 | 9.6 | 850 | 37.2 | 1823 | 34.9 | 1859 | 76 | 564.2 | 3.5 | 683.6 | 27.6 | 600.2 | 11.3 |
| 605.1 | 7.1 | 502.1 | 25.6 | 469.5 | 12.9 | 852.8 | 31 | 1823 | 27.9 | 1860 | 58.7 | 568.2 | 6.9 | 687.7 | 24.8 | 603.5 | 34.3 |
| 608.1 | 3.1 | 502.8 | 27.9 | 471.1 | 23.8 | 859.2 | 43.9 | 1823 | 24.7 | 1863 | 67.7 | 569.9 | 7.6 | 693.3 | 26.9 | 605.4 | 23.1 |
| 612.7 | 3.8 | 503.4 | 20.2 | 471.7 | 11.2 | 862.3 | 42.3 | 1825 | 24.7 | 1867 | 89.8 | 575.2 | 10.3 | 734.5 | 41.5 | 608.4 | 6.5 |
| 613.8 | 3.6 | 504.6 | 10.2 | 472.2 | 19.8 | 867 | 41.2 | 1826 | 43.1 | 1868 | 70.8 | 575.3 | 8.5 | 801.0 | 30.2 | 614.1 | 12.5 |
| 625.8 | 33.1 | 506.1 | 35.5 | 476.1 | 12.3 | 868.6 | 50 | 1827 | 58.5 | 1886 | 67.9 | 578.4 | 12 | 849.4 | 29.0 | 615.1 | 32.5 |
| 639.5 | 18.9 | 506.6 | 18.7 | 476.1 | 9.7 | 869.6 | 53.3 | 1828 | 31.1 | 1892 | 65 | 580.6 | 6.7 | 858.5 | 46.6 | 635.4 | 9.2 |
| 645.8 | 17.7 | 507.8 | 27.6 | 476.4 | 4.9 | 870.4 | 49.9 | 1829 | 19.4 | 1892 | 49.6 | 585.5 | 5.4 | 886.5 | 34.7 | 641.8 | 12.7 |
| 656.3 | 8.4 | 508.8 | 38.5 | 476.7 | 11.1 | 873 | 31.7 | 1830 | 19 | 1893 | 78 | 610.8 | 19.8 | 895.6 | 29.6 | 660.4 | 12.6 |
| 660.5 | 13.8 | 509 | 28.9 | 477.1 | 7.6 | 880.1 | 43.8 | 1831 | 54 | 1905 | 39.7 | 639 | 2 | 898.3 | 31.1 | 679.0 | 41.6 |
| 681.0 | 11.3 | 509.2 | 15.8 | 477.4 | 8.1 | 884.5 | 75.5 | 1835 | 8.2 | 1912 | 58.7 | 669.8 | 8.6 | 910.6 | 36.9 | 698.8 | 24.5 |
| 689.3 | 49.5 | 509.9 | 27.4 | 479.4 | 12.0 | 887.6 | 66.3 | 1837 | 40.6 | 1930 | 13.8 | 676.8 | 23.2 | 921.2 | 33.4 | 700.9 | 32.8 |
| 691.8 | 22.0 | 515.1 | 27.6 | 479.5 | 21.1 | 897.2 | 42.6 | 1837 | 40.4 | 1935 | 172.3 | 682 | 5.2 | 922.1 | 46.2 | 711.4 | 10.9 |
| 699.6 | 10.2 | 521.8 | 20.6 | 480.4 | 12.9 | 901.2 | 46.2 | 1839 | 23.3 | 1947 | 67.6 | 724.3 | 5.4 | 924.0 | 38.2 | 716.0 | 14.3 |
| 702.3 | 5.1 | 524.4 | 16.7 | 480.9 | 8.6 | 901.5 | 48.2 | 1841 | 38.9 | 1951 | 59.6 | 761.7 | 11.1 | 925.2 | 35.4 | 725.4 | 14.1 |
| 710.3 | 7.9 | 525 | 18.8 | 481.7 | 9.5 | 903.6 | 22.2 | 1842 | 35 | 1971 | 36.6 | 784.9 | 17.3 | 927.8 | 30.9 | 732.0 | 11.7 |
| 715.5 | 26.1 | 526.8 | 34 | 481.9 | 13.8 | 904.9 | 65.8 | 1844 | 35.7 | 1972 | 95.2 | 785.1 | 6.8 | 928.9 | 33.4 | 733.5 | 27.8 |
| 718.1 | 15.2 | 537 | 24 | 481.9 | 21.6 | 906.3 | 29.7 | 1844 | 76.6 | 1985 | 80.5 | 787 | 34.5 | 933.8 | 35.3 | 740.2 | 27.8 |
| 728.9 | 10.8 | 538 | 17.6 | 482.9 | 12.5 | 907.4 | 32.8 | 1845 | 36.1 | 1992 | 90.3 | 833 | 11.2 | 940.6 | 151.0 | 741.7 | 19.0 |
| 736.6 | 21.6 | 538.2 | 30 | 483.3 | 9.4 | 910.6 | 47.5 | 1845 | 55 | 2005 | 69.1 | 856.1 | 8.8 | 944.0 | 34.3 | 746.3 | 25.3 |
| 740.8 | 11.5 | 549.3 | 33.2 | 484.0 | 6.5 | 931.9 | 35 | 1853 | 27.9 | 2015 | 62.7 | 878.1 | 5.1 | 944.3 | 36.6 | 750.7 | 15.9 |
| 758.8 | 8.4 | 550.4 | 13 | 484.3 | 18.7 | 936.2 | 26.4 | 1854 | 18 | 2020 | 104 | 880.3 | 10.2 | 948.6 | 32.5 | 757.0 | 5.3 |
| 777.7 | 6.2 | 573.8 | 20.1 | 484.6 | 12.8 | 940.6 | 35.9 | 1854 | 25.5 | 2021 | 98.8 | 881.4 | 18.5 | 948.8 | 31.4 | 758.2 | 28.5 |
| 780.4 | 17.9 | 575.8 | 27.9 | 485.4 | 21.3 | 943.4 | 34.9 | 1856 | 34.9 | 2079 | 63.7 | 885.5 | 18 | 958.8 | 31.6 | 771.4 | 19.3 |
| 785.1 | 6.7 | 608.3 | 22.7 | 491.0 | 10.6 | 958.6 | 48.1 | 1877 | 70.4 | 2080 | 80.3 | 893.9 | 6.8 | 959.5 | 23.8 | 775.2 | 10.9 |
| 792.0 | 8.7 | 619.3 | 26.6 | 491.3 | 13.3 | 961.7 | 68.3 | 1893 | 13.3 | 2095 | 66.6 | 896.9 | 9.5 | 971.8 | 28.1 | 785.1 | 10.8 |
| 795.9 | 12.9 | 635.7 | 36 | 492.6 | 11.3 | 965.1 | 12.9 | 1906 | 21.4 | 2096 | 28.2 | 921.5 | 13 | 977.7 | 31.1 | 801.3 | 39.0 |
| 798.7 | 6.2 | 644.3 | 23.8 | 496.8 | 15.9 | 967.5 | 175.3 | 1909 | 20.1 | 2129 | 86.9 | 923.6 | 8 | 978.0 | 35.4 | 833.1 | 47.0 |

| | | | | | | | | | | | | | | | | | |
|---|---|---|---|---|---|---|---|---|---|---|---|---|---|---|---|---|---|
| 804.3 | 18.9 | 665.4 | 20.4 | 497.3 | 19.0 | 971.3 | 82.2 | 1918 | 19.4 | 2137 | 27.4 | 930.1 | 5.5 | 982.0 | 31.4 | 862.1 | 20.3 |
| 806.0 | 21.0 | 683.4 | 37.2 | 497.5 | 16.7 | 973.9 | 28.2 | 1940 | 39.6 | 2152 | 68.7 | 943.8 | 39.8 | 982.9 | 31.2 | 866.2 | 22.4 |
| 809.5 | 19.7 | 711.4 | 8.5 | 500.6 | 13.1 | 974 | 48.5 | 1957 | 89.1 | 2167 | 71.2 | 944 | 8.7 | 990.5 | 37.4 | 868.9 | 19.8 |
| 818.2 | 48.3 | 713.8 | 38.3 | 504.2 | 20.6 | 978.3 | 28.3 | 1957 | 54 | 2179 | 41.2 | 963.1 | 7.4 | 1022.6 | 122.0 | 869.4 | 32.8 |
| 830.5 | 21.1 | 715.6 | 27.5 | 504.7 | 11.0 | 985.4 | 35 | 1968 | 19.4 | 2184 | 51.8 | 964.8 | 26.9 | 1080.6 | 101.9 | 870.1 | 30.6 |
| 833.3 | 4.4 | 739.6 | 21.5 | 508.5 | 15.9 | 991.4 | 57.1 | 1977 | 11.6 | 2209 | 56.1 | 967.1 | 22 | 1106.1 | 160.5 | 871.9 | 34.1 |
| 836.1 | 23.1 | 803.2 | 29.6 | 509.6 | 25.2 | 1024 | 162.9 | 1982 | 11.5 | 2227 | 74.5 | 971.2 | 8 | 1132.2 | 115.5 | 873.9 | 34.8 |
| 837.6 | 45.4 | 805.3 | 35 | 516.8 | 13.9 | 1073 | 132.8 | 2064 | 16.9 | 2228 | 136.2 | 977 | 11 | 1148.8 | 101.8 | 880.6 | 9.6 |
| 838.8 | 25.4 | 824.1 | 53.1 | 520.0 | 17.5 | 1077 | 162.5 | 2094 | 50.9 | 2268 | 65.4 | 979.3 | 14.8 | 1164.4 | 192.7 | 883.9 | 29.8 |
| 845.5 | 9.7 | 831 | 46.1 | 524.2 | 20.0 | 1115 | 132.2 | 2097 | 8.3 | 2304 | 62.1 | 988.7 | 15.5 | 1166.5 | 117.4 | 897.5 | 20.5 |
| 847.8 | 36.9 | 837.1 | 27.5 | 532.6 | 11.6 | 1159 | 92.5 | 2102 | 47.6 | 2322 | 59.9 | 988.8 | 5.8 | 1252.8 | 245.4 | 899.6 | 20.6 |
| 861.6 | 10.0 | 847.6 | 46.3 | 536.1 | 26.3 | 1178 | 163.3 | 2115 | 9.3 | 2333 | 58.7 | 988.9 | 4.9 | 1269.5 | 59.6 | 911.3 | 11.1 |
| 867.4 | 11.7 | 899.1 | 48.3 | 547.7 | 15.2 | 1214 | 180.9 | 2134 | 59.8 | 2366 | 68.1 | 990.9 | 31.7 | 1436.9 | 155.8 | 915.0 | 7.6 |
| 876.5 | 14.0 | 899.7 | 47.2 | 549.4 | 16.6 | 1462 | 102.7 | 2139 | 40.1 | 2381 | 67.5 | 1086 | 132 | 1531.0 | 115.0 | 917.1 | 9.1 |
| 878.4 | 25.5 | 902.6 | 56.7 | 555.0 | 19.0 | 1557 | 89.4 | 2173 | 40 | 2399 | 134.5 | 1111 | 150 | 1558.9 | 224.9 | 917.2 | 11.2 |
| 886.3 | 7.3 | 918.7 | 48.3 | 574.8 | 12.4 | 1559 | 81.8 | 2193 | 8.7 | 2409 | 64.6 | 1376 | 258 | 1603.8 | 192.3 | 927.2 | 41.1 |
| 887.9 | 12.9 | 937.4 | 28.7 | 577.2 | 20.3 | 1576 | 128.8 | 2250 | 24.3 | 2425 | 65.1 | 1515 | 168 | 1613.5 | 103.1 | 931.5 | 37.9 |
| 888.8 | 4.4 | 938.9 | 48.2 | 591.9 | 15.0 | 1603 | 155.1 | 2273 | 37.7 | 2433 | 52.3 | 1535 | 291 | 1662.6 | 64.1 | 933.4 | 14.1 |
| 891.7 | 13.8 | 946.8 | 45.9 | 604.2 | 17.7 | 1699 | 85.1 | 2331 | 11.8 | 2442 | 63.5 | 1604 | 201 | 1690.3 | 183.0 | 937.1 | 30.8 |
| 900.5 | 8.7 | 968.3 | 61.2 | 731.6 | 7.2 | 1732 | 62.6 | 2338 | 11.9 | 2448 | 43.7 | 1706 | 208 | 1705.7 | 113.1 | 944.9 | 24.7 |
| 903.2 | 8.8 | 983.2 | 22.1 | 785.4 | 20.9 | 1735 | 60.8 | 2361 | 7 | 2453 | 71.7 | 1762 | 135 | 1748.9 | 90.4 | 947.8 | 7.9 |
| 905.7 | 7.7 | 983.6 | 23.2 | 788.2 | 13.7 | 1820 | 129.3 | 2384 | 20.1 | 2492 | 62.4 | 1771 | 123 | 1761.5 | 87.7 | 949.4 | 22.2 |
| 908.4 | 4.8 | 1163 | 204 | 788.8 | 20.1 | 1847 | 96.1 | 2385 | 6 | 2496 | 63.4 | 1866 | 123 | 2354.8 | 106.0 | 953.0 | 44.9 |
| 910.1 | 7.0 | 1199 | 206 | 816.6 | 46.7 | 1893 | 83 | 2428 | 51 | 2529 | 67.8 | 2050 | 121 | 2415.8 | 134.3 | 957.2 | 33.1 |
| 910.1 | 15.0 | 1364 | 241 | 847.1 | 15.8 | 2266 | 44.8 | 2442 | 5 | 2549 | 146.3 | 2401 | 150 | 2529.9 | 26.0 | 957.3 | 51.4 |
| 915.6 | 5.9 | 1847 | 159 | 849.5 | 20.5 | 2372 | 67.4 | 2443 | 23.1 | 2650 | 53.6 | 2475 | 119 | 2544.7 | 88.2 | 963.5 | 37.5 |
| 919.0 | 6.0 | 1952 | 172 | 855.2 | 12.6 | 2384 | 158.9 | 2486 | 23 | 2841 | 56.4 | 2522 | 108 | 2652.7 | 93.2 | 968.2 | 7.6 |
| 920.4 | 19.1 | 2454 | 97.4 | 916.7 | 27.4 | 2434 | 101.2 | 2494 | 14.6 | | | 2527 | 127 | 2956.8 | 50.7 | 974.9 | 50.0 |
| 923.6 | 4.6 | 314.5 | 24.9 | 939.8 | 30.8 | 2434 | 101.2 | 2555 | 16.7 | | | 2546 | 101 | 3169.9 | 73.0 | 975.4 | 37.8 |
| 923.8 | 56.6 | 332.3 | 12.6 | ##### | 71.3 | 2444 | 117.7 | 2590 | 25.4 | | | 2716 | 114 | 3254.1 | 86.6 | 981.5 | 16.5 |

| | | | | | | | | | |
|---|---|---|---|---|---|---|---|---|---|
| 925.2 | 16.1 | 398.9 | 15.2 | ##### | 76.0 | 2450 | 105 | 2598 | 5.6 |
| 927.6 | 11.6 | 402.0 | 8.5 | ##### | 51.2 | 2454 | 52 | 2632 | 59.1 |
| 930.0 | 8.7 | 405.5 | 8.9 | | | 2454 | 84 | 2764 | 4.9 |
| 935.5 | 7.0 | 427.6 | 13.0 | | | 2456 | 115.4 | 2803 | 6.3 |
| 936.5 | 20.7 | 427.6 | 8.9 | | | 2458 | 41.7 | 2978 | 8.6 |
| 942.4 | 8.7 | 432.9 | 11.6 | | | 2465 | 37.7 | 3079 | 42.1 |
| 944.1 | 5.3 | 439.2 | 9.4 | | | 2471 | 174.7 | 3567 | 11.1 |
| 949.5 | 16.6 | 439.7 | 8.2 | | | 2485 | 34.2 | 1717 | 98.1 |
| 950.1 | 153.2 | 441.8 | 13.4 | | | 2525 | 69.7 | 1729 | 45.3 |
| 952.1 | 164.6 | 442.5 | 14.6 | | | 2612 | 34.6 | 1768 | 116.6 |
| 952.4 | 9.5 | 445.8 | 9.2 | | | 3423 | 34.9 | 1777 | 114.5 |
| 954.3 | 10.5 | 449.1 | 15.2 | | | | | 1778 | 110.3 |
| 955.9 | 23.8 | 449.4 | 12.7 | | | | | 1780 | 93.5 |
| 956.2 | 5.0 | 453.0 | 11.7 | | | | | 1782 | 77.4 |
| 957.8 | 8.0 | 453.5 | 15.9 | | | | | 1787 | 71.2 |
| 958.1 | 12.0 | 453.8 | 9.4 | | | | | 1793 | 69.9 |
| 959.9 | 5.1 | 455.5 | 8.9 | | | | | 1805 | 68.4 |
| 961.5 | 12.7 | 458.4 | 13.8 | | | | | 1809 | 57.9 |
| 964.9 | 19.8 | 458.4 | 7.9 | | | | | 1816 | 58.1 |
| 965.5 | 41.5 | 460.2 | 12.3 | | | | | 1817 | 56.6 |
| 974.0 | 11.9 | 461.7 | 9.8 | | | | | 1818 | 33.6 |
| 976.5 | 8.4 | 462.4 | 14.4 | | | | | 1819 | 68.5 |
| 979.3 | 8.6 | 463.2 | 18.2 | | | | | 1830 | 70.6 |
| 980.4 | 36.7 | 464.6 | 5.5 | | | | | 1836 | 26.4 |
| 987.6 | 14.1 | 464.8 | 5.5 | | | | | 1843 | 68.4 |
| 989.2 | 7.2 | 465.1 | 6.6 | | | | | 1843 | 61.6 |
| 990.5 | 11.7 | 465.6 | 10.8 | | | | | 1845 | 83.1 |
| 997.5 | 9.2 | 466.5 | 9.6 | | | | | 1846 | 130.6 |
| 998.1 | 38.8 | 469.5 | 12.9 | | | | | 1847 | 73.6 |
| #### | 36.9 | 471.1 | 23.8 | | | | | 1847 | 79.5 |

| | | | | | |
|---|---|---|---|---|---|
| 2754 | 99.6 | 3478.6 | 55.1 | 987.1 | 18.3 |
| 2916 | 99.8 | 3478.6 | 55.1 | 987.7 | 39.1 |
| | | | | 990.2 | 29.9 |
| | | | | 1011.9 | 36.6 |
| | | | | 1027.8 | 96.5 |
| | | | | 1040.3 | 41.2 |
| | | | | 1040.9 | 86.2 |
| | | | | 1056.2 | 37.9 |
| | | | | 1071.2 | 57.2 |
| | | | | 1076.0 | 133.6 |
| | | | | 1088.6 | 40.8 |
| | | | | 1100.8 | 159.9 |
| | | | | 1101.6 | 106.4 |
| | | | | 1143.9 | 65.5 |
| | | | | 1146.5 | 193.8 |
| | | | | 1148.1 | 78.7 |
| | | | | 1154.1 | 49.9 |
| | | | | 1187.0 | 37.2 |
| | | | | 1195.3 | 35.5 |
| | | | | 1213.4 | 54.6 |
| | | | | 1216.3 | 95.7 |
| | | | | 1251.1 | 148.9 |
| | | | | 1294.3 | 151.6 |
| | | | | 1349.8 | 98.8 |
| | | | | 1367.0 | 69.9 |
| | | | | 1375.6 | 96.0 |
| | | | | 1394.7 | 147.8 |
| | | | | 1449.6 | 45.4 |
| | | | | 1488.3 | 67.2 |
| | | | | 1572.0 | 43.7 |

| | | | |
|---|---|---|---|
| #### | 139.4 | 471.7 | 11.2 |
| #### | 149.5 | 472.2 | 19.8 |
| #### | 123.6 | 476.1 | 12.3 |
| #### | 133.0 | 476.1 | 9.7 |
| #### | 224.2 | 476.4 | 4.9 |
| #### | 101.1 | 476.7 | 11.1 |
| #### | 135.9 | 477.1 | 7.6 |
| #### | 169.6 | 477.4 | 8.1 |
| #### | 143.2 | 479.4 | 12.0 |
| #### | 132.0 | 479.5 | 21.1 |
| #### | 259.6 | 480.4 | 12.9 |
| #### | 177.6 | 480.9 | 8.6 |
| #### | 210.1 | 481.7 | 9.5 |
| #### | 102.2 | 481.9 | 13.8 |
| #### | 132.9 | 481.9 | 21.6 |
| #### | 66.2 | 482.9 | 12.5 |
| #### | 70.0 | 483.3 | 9.4 |
| #### | 47.3 | 484.0 | 6.5 |
| #### | 61.6 | 484.3 | 18.7 |
| #### | 13.1 | 484.6 | 12.8 |
| #### | 48.3 | 485.4 | 21.3 |
| #### | 136.2 | 491.0 | 10.6 |
| #### | 205.3 | 491.3 | 13.3 |
| #### | 138.4 | 492.6 | 11.3 |
| #### | 53.0 | 496.8 | 15.9 |
| #### | 36.3 | 497.3 | 19.0 |
| #### | 26.1 | 497.5 | 16.7 |
| #### | 80.2 | 500.6 | 13.1 |
| #### | 43.4 | 504.2 | 20.6 |
| #### | 18.0 | 504.7 | 11.0 |

| | |
|---|---|
| 1848 | 74.4 |
| 1850 | 66.5 |
| 1853 | 158.7 |
| 1856 | 90 |
| 1858 | 60.3 |
| 1858 | 107.6 |
| 1859 | 76 |
| 1860 | 58.7 |
| 1863 | 67.7 |
| 1867 | 89.8 |
| 1868 | 70.8 |
| 1886 | 67.9 |
| 1892 | 65 |
| 1892 | 49.6 |
| 1893 | 78 |
| 1905 | 39.7 |
| 1912 | 58.7 |
| 1930 | 13.8 |
| 1935 | 172.3 |
| 1947 | 67.6 |
| 1951 | 59.6 |
| 1971 | 36.6 |
| 1972 | 95.2 |
| 1985 | 80.5 |
| 1992 | 90.3 |
| 2005 | 69.1 |
| 2015 | 62.7 |
| 2020 | 104 |
| 2021 | 98.8 |
| 2079 | 63.7 |

| | |
|---|---|
| 1600.1 | 38.9 |
| 1684.8 | 15.3 |
| 1697.0 | 43.4 |
| 1710.7 | 5.4 |
| 1714.3 | 47.7 |
| 1738.6 | 31.2 |
| 1739.9 | 34.1 |
| 1741.6 | 56.2 |
| 1759.1 | 37.8 |
| 1773.4 | 34.5 |
| 1776.3 | 31.9 |
| 1790.1 | 53.9 |
| 1796.8 | 42.2 |
| 1797.9 | 36.7 |
| 1797.9 | 48.3 |
| 1800.2 | 10.8 |
| 1805.0 | 13.2 |
| 1806.8 | 36.7 |
| 1807.2 | 36.5 |
| 1809.4 | 24.6 |
| 1813.2 | 78.7 |
| 1823.0 | 34.0 |
| 1824.4 | 59.5 |
| 1825.4 | 66.4 |
| 1839.9 | 16.2 |
| 1842.1 | 11.4 |
| 1842.9 | 15.4 |
| 1844.1 | 25.1 |
| 1848.0 | 16.0 |
| 1848.5 | 44.4 |

| | | | |
|---|---|---|---|
| #### | 98.9 | 508.5 | 15.9 |
| #### | 63.2 | 509.6 | 25.2 |
| #### | 40.0 | 516.8 | 13.9 |
| #### | 19.6 | 520.0 | 17.5 |
| #### | 52.9 | 524.2 | 20.0 |
| #### | 201.5 | 532.6 | 11.6 |
| #### | 82.9 | 536.1 | 26.3 |
| #### | 28.0 | 547.7 | 15.2 |
| #### | 85.2 | 549.4 | 16.6 |
| #### | 30.9 | 555.0 | 19.0 |
| #### | 9.2 | 574.8 | 12.4 |
| #### | 25.1 | 577.2 | 20.3 |
| #### | 19.9 | 591.9 | 15.0 |
| #### | 46.2 | 604.2 | 17.7 |
| #### | 83.0 | 731.6 | 7.2 |
| #### | 23.8 | 785.4 | 20.9 |
| #### | 27.4 | 788.2 | 13.7 |
| #### | 31.1 | 788.8 | 20.1 |
| #### | 31.1 | 816.6 | 46.7 |
| #### | 53.0 | 847.1 | 15.8 |
| #### | 194.6 | 849.5 | 20.5 |
| #### | 17.0 | 855.2 | 12.6 |
| #### | 34.1 | 916.7 | 27.4 |
| #### | 7.8 | 939.8 | 30.8 |

| | |
|---|---|
| 2080 | 80.3 |
| 2095 | 66.6 |
| 2096 | 28.2 |
| 2129 | 86.9 |
| 2137 | 27.4 |
| 2152 | 68.7 |
| 2167 | 71.2 |
| 2179 | 41.2 |
| 2184 | 51.8 |
| 2209 | 56.1 |
| 2227 | 74.5 |
| 2228 | 136.2 |
| 2268 | 65.4 |
| 2304 | 62.1 |
| 2322 | 59.9 |
| 2333 | 58.7 |
| 2366 | 68.1 |
| 2381 | 67.5 |
| 2399 | 134.5 |
| 2409 | 64.6 |
| 2425 | 65.1 |
| 2433 | 52.3 |
| 2442 | 63.5 |
| 2448 | 43.7 |

| | |
|---|---|
| 1848.6 | 24.8 |
| 1852.3 | 19.5 |
| 1855.6 | 24.7 |
| 1859.0 | 19.1 |
| 1860.3 | 18.7 |
| 1861.6 | 17.3 |
| 1867.3 | 55.5 |
| 1918.7 | 10.3 |
| 1919.2 | 35.6 |
| 1923.4 | 18.3 |
| 1953.8 | 15.3 |
| 1970.9 | 33.4 |
| 1971.9 | 25.2 |
| 1972.0 | 27.4 |
| 1988.5 | 22.7 |
| 1995.7 | 34.5 |
| 1997.3 | 30.7 |
| 2008.7 | 62.4 |
| 2068.2 | 311.6 |
| 2095.8 | 30.1 |
| 2150.5 | 36.9 |
| 2167.3 | 28.1 |
| 2178.1 | 27.5 |
| 2228.8 | 44.0 |

| TTS (A) | | Formation III (C) | | Formation II (D) | | Formation I (F) | | Lesser Himalaya (H) | | Lesser Himalaya (I) | | Lowet Marsyandi (K) | |
|---|---|---|---|---|---|---|---|---|---|---|---|---|---|
| Age (Ma) | Error (Ma) | Age (Ma) | Error (Ma) | Age (Ma) | Error (Ma) | Age (Ma) | Error (Ma) | Age (Ma) | Error (Ma) | Age (Ma) | Error (Ma) | Age (Ma) | Error (Ma) |
| | | | | | | 2148. | | 3562. | | 3247. | | | |
| 493.1 | 25.0 | 891.8 | 50.0 | 956.2 | 50.0 | 7 | 100.0 | 3 | 175.0 | 1 | 175.0 | 493.1 | 25 |
| | | 1057. | | | | 2002. | | 3834. | | 3541. | | | |
| 518.5 | 25.0 | 6 | 50.0 | 998.4 | 50.0 | 4 | 100.0 | 9 | 175.0 | 9 | 175.0 | 518.5 | 25 |
| | | | | | | 2065. | | 3701. | | 3438. | | | |
| 487.3 | 25.0 | 868.3 | 50.0 | 997.6 | 50.0 | 8 | 100.0 | 5 | 175.0 | 9 | 175.0 | 487.3 | 25 |
| | | | | | | 1896. | | 3542. | | 3649. | | | |
| 528.0 | 25.0 | 997.1 | 50.0 | 969.8 | 50.0 | 1 | 100.0 | 7 | 175.0 | 1 | 175.0 | 528.0 | 25 |
| | | | | | | 1885. | | 3624. | | 3706. | | | |
| 490.4 | 25.0 | 956.6 | 50.0 | 984.9 | 50.0 | 7 | 100.0 | 5 | 175.0 | 5 | 175.0 | 490.4 | 25 |
| | | 1036. | | | | 2157. | | 3643. | | 3643. | | | |
| 548.5 | 25.0 | 4 | 50.0 | 915.5 | 50.0 | 9 | 100.0 | 7 | 175.0 | 8 | 175.0 | 548.5 | 25 |
| | | | | 1031. | | 1905. | | 3692. | | 3379. | | | |
| 475.5 | 25.0 | 993.5 | 50.0 | 6 | 50.0 | 6 | 100.0 | 0 | 175.0 | 7 | 175.0 | 475.5 | 25 |
| | | 1017. | | 1057. | | 1988. | | 3429. | | 3545. | | | |
| 555.9 | 25.0 | 5 | 50.0 | 6 | 50.0 | 5 | 100.0 | 4 | 175.0 | 7 | 175.0 | 555.9 | 25 |
| | | | | | | 2022. | | 3320. | | 3618. | | | |
| 518.9 | 25.0 | 945.8 | 50.0 | 942.8 | 50.0 | 4 | 100.0 | 2 | 175.0 | 2 | 175.0 | 518.9 | 25 |
| | | | | 1039. | | 2020. | | 3575. | | 3146. | | | |
| 496.8 | 25.0 | 900.8 | 50.0 | 8 | 50.0 | 8 | 100.0 | 6 | 175.0 | 4 | 175.0 | 496.8 | 25 |
| | | 1014. | | | | 2143. | | 3374. | | 3470. | | | |
| 494.2 | 25.0 | 7 | 50.0 | 992.6 | 50.0 | 2 | 100.0 | 9 | 175.0 | 8 | 175.0 | 494.2 | 25 |
| | | 1000. | | | | 2032. | | 3477. | | 3171. | | | |
| 510.8 | 25.0 | 7 | 50.0 | 847.5 | 50.0 | 2 | 100.0 | 4 | 175.0 | 0 | 175.0 | 510.8 | 25 |
| | | | | | | 1961. | | 3548. | | 3572. | | | |
| 510.2 | 25.0 | 975.2 | 50.0 | 961.0 | 50.0 | 7 | 100.0 | 8 | 175.0 | 6 | 175.0 | 510.2 | 25 |
| | | | | | | 1968. | | 3381. | | 3317. | | | |
| 515.2 | 25.0 | 936.9 | 50.0 | 997.4 | 50.0 | 1 | 100.0 | 4 | 175.0 | 9 | 175.0 | 515.2 | 25 |
| | | | | | | 1885. | | 3421. | | 3362. | | | |
| 495.5 | 25.0 | 934.6 | 50.0 | 954.1 | 50.0 | 0 | 100.0 | 1 | 175.0 | 2 | 175.0 | 495.5 | 25 |
| | | | | | | 1944. | | 3391. | | 3328. | | | |
| 527.4 | 25.0 | 965.9 | 50.0 | 980.8 | 50.0 | 6 | 100.0 | 8 | 175.0 | 7 | 175.0 | 527.4 | 25 |
| | | | | | | 2018. | | 3568. | | 3542. | | | |
| 513.6 | 25.0 | 909.7 | 50.0 | 914.2 | 50.0 | 3 | 100.0 | 0 | 175.0 | 8 | 175.0 | 513.6 | 25 |
| | | 1023. | | | | 2072. | | 3611. | | 3650. | | | |
| 536.8 | 25.0 | 3 | 50.0 | 939.2 | 50.0 | 4 | 100.0 | 0 | 175.0 | 3 | 175.0 | 536.8 | 25 |
| | | | | 1081. | | 2004. | | 3151. | | 3548. | | | |
| 487.6 | 25.0 | 997.8 | 50.0 | 6 | 50.0 | 3 | 100.0 | 1 | 175.0 | 3 | 175.0 | 487.6 | 25 |
| | | 1005. | | 1101. | | 2057. | | 3613. | | 3542. | | | |
| 514.8 | 25.0 | 3 | 50.0 | 3 | 50.0 | 9 | 100.0 | 7 | 175.0 | 2 | 175.0 | 514.8 | 25 |
| | | | | 1011. | | 1804. | | 3402. | | 3663. | | | |
| 506.8 | 25.0 | 902.2 | 50.0 | 5 | 50.0 | 2 | 100.0 | 0 | 175.0 | 4 | 175.0 | 506.8 | 25 |
| | | 1067. | | 1044. | | 2094. | | 3087. | | 3391. | | | |
| 523.4 | 25.0 | 9 | 50.0 | 7 | 50.0 | 9 | 100.0 | 3 | 175.0 | 3 | 175.0 | 523.4 | 25 |
| | | | | 1024. | | 1980. | | 3378. | | 3372. | | | |
| 485.1 | 25.0 | 958.6 | 50.0 | 1 | 50.0 | 5 | 100.0 | 1 | 175.0 | 5 | 175.0 | 485.1 | 25 |
| | | 1044. | | 1092. | | 2109. | | 3476. | | 3506. | | | |
| 479.2 | 25.0 | 2 | 50.0 | 7 | 50.0 | 5 | 100.0 | 3 | 175.0 | 8 | 175.0 | 479.2 | 25 |
| | | | | | | 2039. | | 3597. | | 3557. | | | |
| 503.6 | 25.0 | 909.1 | 50.0 | 989.9 | 50.0 | 1 | 100.0 | 3 | 175.0 | 2 | 175.0 | 503.6 | 25 |
| | | 1010. | | 1047. | | 1897. | | 3672. | | 3581. | | | |
| 493.4 | 25.0 | 2 | 50.0 | 0 | 50.0 | 1 | 100.0 | 1 | 175.0 | 4 | 175.0 | 493.4 | 25 |
| | | 1057. | | | | 2039. | | 3555. | | 3616. | | | |
| 530.1 | 25.0 | 6 | 50.0 | 948.9 | 50.0 | 5 | 100.0 | 4 | 175.0 | 4 | 175.0 | 530.1 | 25 |

| | | | | | | | | | | | | | |
|---|---|---|---|---|---|---|---|---|---|---|---|---|---|
| | | 1020. | | 1043. | | 2138. | | 3548. | | 3473. | | | |
| 431.4 | 25.0 | 0 | 50.0 | 8 | 50.0 | 7 | 100.0 | 9 | 175.0 | 3 | 175.0 | 431.4 | 25 |
| | | | | | | 1854. | | 3452. | | 3751. | | | |
| 477.2 | 25.0 | 960.6 | 50.0 | 956.2 | 50.0 | 4 | 100.0 | 2 | 175.0 | 8 | 175.0 | 477.2 | 25 |
| | | 1002. | | | | 2018. | | 3578. | | 3453. | | | |
| 525.3 | 25.0 | 9 | 50.0 | 954.0 | 50.0 | 1 | 100.0 | 5 | 175.0 | 6 | 175.0 | 525.3 | 25 |
| | | | | 1039. | | 1974. | | 3519. | | 3564. | | | |
| 478.1 | 25.0 | 991.5 | 50.0 | 1 | 50.0 | 2 | 100.0 | 9 | 175.0 | 3 | 175.0 | 478.1 | 25 |
| | | 1000. | | | | 1968. | | 3793. | | 3554. | | | |
| 468.2 | 25.0 | 1 | 50.0 | 944.2 | 50.0 | 1 | 100.0 | 7 | 175.0 | 7 | 175.0 | 468.2 | 25 |
| | | 1034. | | 1021. | | 2175. | | 3566. | | 3768. | | | |
| 485.7 | 25.0 | 4 | 50.0 | 1 | 50.0 | 2 | 100.0 | 6 | 175.0 | 8 | 175.0 | 485.7 | 25 |
| | | 1118. | | 1047. | | 1969. | | 3586. | | 3608. | | | |
| 520.2 | 25.0 | 0 | 50.0 | 3 | 50.0 | 0 | 100.0 | 8 | 175.0 | 0 | 175.0 | 520.2 | 25 |
| | | | | 1003. | | 1881. | | 3641. | | 3386. | | | |
| 510.4 | 25.0 | 894.8 | 50.0 | 1 | 50.0 | 5 | 100.0 | 8 | 175.0 | 2 | 175.0 | 510.4 | 25 |
| | | 1046. | | | | 1948. | | 3500. | | 3655. | | | |
| 475.3 | 25.0 | 9 | 50.0 | 948.8 | 50.0 | 6 | 100.0 | 7 | 175.0 | 4 | 175.0 | 475.3 | 25 |
| | | 1015. | | 1017. | | 2001. | | 3540. | | 3158. | | | |
| 542.9 | 25.0 | 1 | 50.0 | 4 | 50.0 | 1 | 100.0 | 9 | 175.0 | 8 | 175.0 | 542.9 | 25 |
| | | 1057. | | 1013. | | 1994. | | 3649. | | 3362. | | | |
| 538.0 | 25.0 | 8 | 50.0 | 6 | 50.0 | 5 | 100.0 | 5 | 175.0 | 7 | 175.0 | 538.0 | 25 |
| | | | | | | 1985. | | 3682. | | 3764. | | | |
| 484.4 | 25.0 | 930.6 | 50.0 | 971.6 | 50.0 | 3 | 100.0 | 9 | 175.0 | 2 | 175.0 | 484.4 | 25 |
| | | 1034. | | | | 2063. | | 3315. | | 3707. | | | |
| 478.0 | 25.0 | 6 | 50.0 | 954.3 | 50.0 | 5 | 100.0 | 0 | 175.0 | 2 | 175.0 | 478.0 | 25 |
| | | 1060. | | 1011. | | 2002. | | 3664. | | 3344. | | | |
| 513.6 | 25.0 | 7 | 50.0 | 3 | 50.0 | 3 | 100.0 | 8 | 175.0 | 6 | 175.0 | 513.6 | 25 |
| | | | | 1052. | | 1998. | | 3263. | | 3533. | | | |
| 521.4 | 25.0 | 941.5 | 50.0 | 3 | 50.0 | 1 | 100.0 | 8 | 175.0 | 5 | 175.0 | 521.4 | 25 |
| | | 1048. | | 1056. | | 2096. | | 3175. | | 3288. | | | |
| 494.6 | 25.0 | 7 | 50.0 | 4 | 50.0 | 3 | 100.0 | 9 | 175.0 | 6 | 175.0 | 494.6 | 25 |
| | | 1071. | | | | 1920. | | 3332. | | 3704. | | | |
| 503.3 | 25.0 | 4 | 50.0 | 954.3 | 50.0 | 2 | 100.0 | 7 | 175.0 | 6 | 175.0 | 503.3 | 25 |
| | | 1036. | | 1016. | | 1861. | | 3474. | | 3531. | | | |
| 491.3 | 25.0 | 2 | 50.0 | 2 | 50.0 | 7 | 100.0 | 4 | 175.0 | 6 | 175.0 | 491.3 | 25 |
| | | 1092. | | | | 1945. | | 3323. | | 3654. | | | |
| 504.6 | 25.0 | 9 | 50.0 | 956.5 | 50.0 | 7 | 100.0 | 8 | 175.0 | 2 | 175.0 | 504.6 | 25 |
| | | | | 1034. | | 1976. | | 3327. | | 3439. | | | |
| 513.3 | 25.0 | 980.5 | 50.0 | 8 | 50.0 | 0 | 100.0 | 6 | 175.0 | 4 | 175.0 | 513.3 | 25 |
| | | 1022. | | 1070. | | 2036. | | 3291. | | 3507. | | | |
| 457.1 | 25.0 | 9 | 50.0 | 4 | 50.0 | 8 | 100.0 | 2 | 175.0 | 2 | 175.0 | 457.1 | 25 |
| | | | | 1047. | | 2305. | | 3453. | | 3382. | | | |
| 514.5 | 25.0 | 934.3 | 50.0 | 5 | 50.0 | 5 | 100.0 | 8 | 175.0 | 6 | 175.0 | 514.5 | 25 |
| | | | | 1061. | | 1981. | | | | 3387. | | | |
| 460.4 | 25.0 | | | 9 | 50.0 | 3 | 100.0 | | | 1 | 175.0 | 460.4 | 25 |
| | | | | | | 1994. | | | | | | | |
| 474.3 | 25.0 | | | | | 2 | 100.0 | | | | | 474.3 | 25 |
| | | | | | | 2014. | | | | | | | |
| 490.6 | 25.0 | | | | | 9 | 100.0 | | | | | 490.6 | 25 |
| | | | | | | 2361. | | | | | | | |
| 539.3 | 25.0 | | | | | 9 | 100.0 | | | | | 539.3 | 25 |
| | | | | | | 2048. | | | | | | | |
| 521.2 | 25.0 | | | | | 1 | 100.0 | | | | | 521.2 | 25 |
| | | | | | | 1890. | | | | | | | |
| 493.5 | 25.0 | | | | | 9 | 100.0 | | | | | 493.5 | 25 |
| | | | | | | 2094. | | | | | | | |
| 515.2 | 25.0 | | | | | 6 | 100.0 | | | | | 515.2 | 25 |
| | | | | | | 1877. | | | | | | | |
| 481.0 | 25.0 | | | | | 4 | 100.0 | | | | | 481.0 | 25 |
| 456.9 | 25.0 | | | | | 2041. | 100.0 | | | | | 456.9 | 25 |

| | | | | | |
|---|---|---|---|---|---|
| | | 3 | | | |
| 492.9 | 25.0 | 1878.4 | 100.0 | 492.9 | 25 |
| 441.2 | 25.0 | 2049.9 | 100.0 | 441.2 | 25 |
| 465.3 | 25.0 | 2045.4 | 100.0 | 465.3 | 25 |
| 505.3 | 25.0 | 2077.8 | 100.0 | 505.3 | 25 |
| 448.0 | 25.0 | 1831.8 | 100.0 | 448.0 | 25 |
| 537.5 | 25.0 | 1847.7 | 100.0 | 537.5 | 25 |
| 467.1 | 25.0 | 1987.9 | 100.0 | 467.1 | 25 |
| 467.8 | 25.0 | 1998.1 | 100.0 | 467.8 | 25 |
| 493.6 | 25.0 | 2140.3 | 100.0 | 493.6 | 25 |
| 517.5 | 25.0 | 2056.2 | 100.0 | 517.5 | 25 |
| 453.0 | 25.0 | 2009.3 | 100.0 | 453.0 | 25 |
| 471.3 | 25.0 | 2024.8 | 100.0 | 471.3 | 25 |
| 506.0 | 25.0 | 1824.8 | 100.0 | 506.0 | 25 |
| 524.2 | 25.0 | 2112.2 | 100.0 | 524.2 | 25 |
| 509.9 | 25.0 | 2016.9 | 100.0 | 509.9 | 25 |
| 509.9 | 25.0 | 1945.9 | 100.0 | 509.9 | 25 |
| 491.5 | 25.0 | 1915.2 | 100.0 | 491.5 | 25 |
| 473.9 | 25.0 | 2095.8 | 100.0 | 473.9 | 25 |
| 490.0 | 25.0 | 2095.8 | 100.0 | 490.0 | 25 |
| 480.7 | 25.0 | 1881.4 | 100.0 | 480.7 | 25 |
| 469.8 | 25.0 | 1936.0 | 100.0 | 469.8 | 25 |
| 489.6 | 25.0 | 1904.8 | 100.0 | 489.6 | 25 |
| 528.7 | 25.0 | 1984.2 | 100.0 | 528.7 | 25 |
| 409.9 | 25.0 | 2041.6 | 100.0 | 409.9 | 25 |
| 496.6 | 25.0 | 1963.6 | 100.0 | 496.6 | 25 |
| 487.0 | 25.0 | 2016.7 | 100.0 | 487.0 | 25 |
| 557.8 | 25.0 | 1979.0 | 100.0 | 557.8 | 25 |
| 459.4 | 25.0 | 2006.9 | 100.0 | 459.4 | 25 |
| 510.9 | 25.0 | 2003.6 | 100.0 | 510.9 | 25 |
| 460.4 | 25.0 | 2030.2 | 100.0 | 460.4 | 25 |

| | | | | | | | | | | | | | |
|---|---|---|---|---|---|---|---|---|---|---|---|---|---|
| | | | | | | 1955.3 | 100.0 | | | | | 496.0 | 25 |
| 496.0 | 25.0 | | | | | | | | | | | | |
| | | | | | | 1965.0 | 100.0 | | | | | 533.6 | 25 |
| 533.6 | 25.0 | | | | | | | | | | | | |
| | | | | | | 2008.5 | 100.0 | | | | | 520.0 | 25 |
| 520.0 | 25.0 | | | | | | | | | | | | |
| | | | | | | 2083.1 | 100.0 | | | | | 529.3 | 25 |
| 529.3 | 25.0 | | | | | | | | | | | | |
| | | | | | | 2231.0 | 100.0 | | | | | 445.9 | 25 |
| 445.9 | 25.0 | | | | | | | | | | | | |
| | | | | | | 2024.0 | 100.0 | | | | | 498.0 | 25 |
| 498.0 | 25.0 | | | | | | | | | | | | |
| | | | | | | 1993.3 | 100.0 | | | | | 500.1 | 25 |
| 500.1 | 25.0 | | | | | | | | | | | | |
| | | | | | | 1918.7 | 100.0 | | | | | 504.8 | 25 |
| 504.8 | 25.0 | | | | | | | | | | | | |
| | | | | | | 1914.1 | 100.0 | | | | | 517.2 | 25 |
| 517.2 | 25.0 | | | | | | | | | | | | |
| | | | | | | 2033.2 | 100.0 | | | | | 526.2 | 25 |
| 526.2 | 25.0 | | | | | | | | | | | | |
| | | | | | | 1957.5 | 100.0 | | | | | 516.5 | 25 |
| 516.5 | 25.0 | | | | | | | | | | | | |

| TTS (A) | | Formation III (C) | | Formation II (D) | | Formation I (F) | | Lesser Himalaya (H) | | Lesser Himalaya (I) | | Lowet Marsyandi (K) | |
|---|---|---|---|---|---|---|---|---|---|---|---|---|---|
| Age (Ma) | Error (Ma) | Age (Ma) | Error (Ma) | Age (Ma) | Error (Ma) | Age (Ma) | Error (Ma) | Age (Ma) | Error (Ma) | Age (Ma) | Error (Ma) | Age (Ma) | Error (Ma) |
| | | 1444.4 | 75.0 | 1467.5 | 75.0 | 2022.4 | 100.0 | 3017.8 | 150.0 | 3026.9 | 150.0 | 1019.2 | 50.0 |
| 925.0 | 50.0 | | | | | | | | | | | | |
| | | 1522.9 | 75.0 | 1442.6 | 75.0 | 1927.2 | 100.0 | 3253.5 | 150.0 | 3077.8 | 150.0 | 927.7 | 50.0 |
| 932.4 | 50.0 | | | | | | | | | | | | |
| | | 1366.3 | 75.0 | 1514.5 | 75.0 | 2024.7 | 100.0 | 3121.3 | 150.0 | 2776.7 | 150.0 | 960.3 | 50.0 |
| 932.3 | 50.0 | | | | | | | | | | | | |
| | | 1451.1 | 75.0 | 1532.1 | 75.0 | 1818.4 | 100.0 | 3026.1 | 150.0 | 2854.8 | 150.0 | 990.6 | 50.0 |
| 971.5 | 50.0 | | | | | | | | | | | | |
| | | 1527.3 | 75.0 | 1487.8 | 75.0 | 1937.3 | 100.0 | 2833.0 | 150.0 | 2795.5 | 150.0 | 1010.8 | 50.0 |
| 1045.4 | 50.0 | | | | | | | | | | | | |
| | | 1483.1 | 75.0 | 1510.5 | 75.0 | 2149.1 | 100.0 | 3333.1 | 150.0 | 3014.9 | 150.0 | 957.5 | 50.0 |
| 977.1 | 50.0 | | | | | | | | | | | | |
| | | 1575.5 | 75.0 | 1390.9 | 75.0 | 2005.6 | 100.0 | 3089.7 | 150.0 | 3111.4 | 150.0 | 1016.8 | 50.0 |
| 996.5 | 50.0 | | | | | | | | | | | | |
| | | 1599.0 | 75.0 | 1446.3 | 75.0 | 2109.1 | 100.0 | 2889.0 | 150.0 | 2771.2 | 150.0 | 1064.3 | 50.0 |
| 1019.0 | 50.0 | | | | | | | | | | | | |
| | | 1460.4 | 75.0 | 1515.7 | 75.0 | 2093.4 | 100.0 | 3240.2 | 150.0 | 2734.1 | 150.0 | 965.7 | 50.0 |
| 999.1 | 50.0 | | | | | | | | | | | | |
| | | 1614.3 | 75.0 | 1521.7 | 75.0 | 2113.7 | 100.0 | 2611.7 | 150.0 | 3057.7 | 150.0 | 921.2 | 50.0 |
| 964.7 | 50.0 | | | | | | | | | | | | |
| | | 1407.2 | 75.0 | 1573.0 | 75.0 | 1937.1 | 100.0 | 3035.8 | 150.0 | 3066.8 | 150.0 | 980.2 | 50.0 |
| 942.0 | 50.0 | | | | | | | | | | | | |
| | | 1539.9 | 75.0 | 1547.5 | 75.0 | 1988.6 | 100.0 | 3110.0 | 150.0 | 3108.0 | 150.0 | 1022.1 | 50.0 |
| 1001.3 | 50.0 | | | | | | | | | | | | |
| | | 1603.0 | 75.0 | 1400.0 | 75.0 | 2185.4 | 100.0 | 3091.5 | 150.0 | 3096.5 | 150.0 | 1094.7 | 50.0 |
| 960.4 | 50.0 | | | | | | | | | | | | |
| | | 1564.9 | 75.0 | 1608.0 | 75.0 | 2033.2 | 100.0 | 3236.3 | 150.0 | 3104.7 | 150.0 | 965.7 | 50.0 |
| 1054.3 | 50.0 | | | | | | | | | | | | |
| | | 1541.9 | 75.0 | 1487.9 | 75.0 | 2292.5 | 100.0 | 3231.6 | 150.0 | 2766.8 | 150.0 | 1059.2 | 50.0 |
| 911.4 | 50.0 | | | | | | | | | | | | |
| | | 1525.8 | 75.0 | 1494.7 | 75.0 | 1935.9 | 100.0 | 2873.1 | 150.0 | 2978.2 | 150.0 | 1025.4 | 50.0 |
| 977.0 | 50.0 | | | | | | | | | | | | |

| | | | | | | | | | | | | | |
|---|---|---|---|---|---|---|---|---|---|---|---|---|---|
| | | 1543. | | 1561. | | 2068. | | 2709. | | 3110. | | | |
| 983.1 | 50.0 | 2 | 75.0 | 0 | 75.0 | 2 | 100.0 | 7 | 150.0 | 7 | 150.0 | 994.6 | 50.0 |
| | | 1467. | | 1391. | | 1897. | | 3010. | | 2949. | | 1085. | |
| 976.0 | 50.0 | 6 | 75.0 | 9 | 75.0 | 7 | 100.0 | 4 | 150.0 | 8 | 150.0 | 0 | 50.0 |
| | | 1605. | | 1488. | | 2037. | | 3036. | | 2654. | | | |
| 967.1 | 50.0 | 6 | 75.0 | 9 | 75.0 | 0 | 100.0 | 0 | 150.0 | 6 | 150.0 | 924.4 | 50.0 |
| 1034. | | 1378. | | 1509. | | 2065. | | 3194. | | 2964. | | 1018. | |
| 3 | 50.0 | 4 | 75.0 | 4 | 75.0 | 2 | 100.0 | 2 | 150.0 | 7 | 150.0 | 6 | 50.0 |
| 1072. | | 1490. | | 1564. | | 1838. | | 3020. | | 3014. | | | |
| 7 | 50.0 | 1 | 75.0 | 7 | 75.0 | 4 | 100.0 | 3 | 150.0 | 9 | 150.0 | 998.7 | 50.0 |
| 1044. | | 1361. | | 1533. | | 2118. | | 3011. | | 2902. | | 1042. | |
| 8 | 50.0 | 8 | 75.0 | 8 | 75.0 | 0 | 100.0 | 8 | 150.0 | 3 | 150.0 | 6 | 50.0 |
| | | 1678. | | 1457. | | 2161. | | 3202. | | 3012. | | | |
| 939.3 | 50.0 | 5 | 75.0 | 4 | 75.0 | 4 | 100.0 | 4 | 150.0 | 2 | 150.0 | 898.5 | 50.0 |
| 1016. | | 1561. | | 1539. | | 1925. | | 2887. | | 3091. | | 1082. | |
| 3 | 50.0 | 5 | 75.0 | 5 | 75.0 | 5 | 100.0 | 7 | 150.0 | 6 | 150.0 | 5 | 50.0 |
| | | 1530. | | 1482. | | 1995. | | 2906. | | 2787. | | | |
| 985.5 | 50.0 | 7 | 75.0 | 9 | 75.0 | 6 | 100.0 | 6 | 150.0 | 0 | 150.0 | 958.0 | 50.0 |
| 1073. | | 1626. | | 1484. | | 1881. | | 3006. | | 2864. | | | |
| 6 | 50.0 | 3 | 75.0 | 0 | 75.0 | 4 | 100.0 | 0 | 150.0 | 1 | 150.0 | 935.7 | 50.0 |
| | | 1542. | | 1494. | | 1927. | | 2848. | | 3152. | | 1061. | |
| 995.3 | 50.0 | 6 | 75.0 | 8 | 75.0 | 4 | 100.0 | 6 | 150.0 | 6 | 150.0 | 9 | 50.0 |
| | | 1547. | | 1539. | | 2016. | | 2959. | | 3034. | | | |
| 991.4 | 50.0 | 3 | 75.0 | 4 | 75.0 | 1 | 100.0 | 4 | 150.0 | 4 | 150.0 | 978.4 | 50.0 |
| | | 1601. | | 1500. | | 2029. | | 2918. | | 3025. | | 1154. | |
| 975.4 | 50.0 | 5 | 75.0 | 2 | 75.0 | 4 | 100.0 | 7 | 150.0 | 4 | 150.0 | 8 | 50.0 |
| | | 1522. | | 1432. | | 2090. | | 3055. | | 2835. | | | |
| 971.1 | 50.0 | 1 | 75.0 | 7 | 75.0 | 4 | 100.0 | 9 | 150.0 | 7 | 150.0 | 973.1 | 50.0 |
| 1046. | | 1555. | | 1493. | | 1980. | | 2927. | | 2730. | | 1054. | |
| 1 | 50.0 | 4 | 75.0 | 1 | 75.0 | 7 | 100.0 | 8 | 150.0 | 4 | 150.0 | 8 | 50.0 |
| | | 1459. | | 1504. | | 2056. | | 3346. | | 2819. | | | |
| 986.7 | 50.0 | 1 | 75.0 | 8 | 75.0 | 3 | 100.0 | 6 | 150.0 | 6 | 150.0 | 990.1 | 50.0 |
| 1059. | | 1388. | | 1588. | | 2071. | | 3219. | | 3058. | | 1016. | |
| 4 | 50.0 | 6 | 75.0 | 2 | 75.0 | 4 | 100.0 | 7 | 150.0 | 4 | 150.0 | 8 | 50.0 |
| 1038. | | 1481. | | 1541. | | 1890. | | 2968. | | 2995. | | 1058. | |
| 3 | 50.0 | 4 | 75.0 | 9 | 75.0 | 7 | 100.0 | 3 | 150.0 | 0 | 150.0 | 9 | 50.0 |
| 1065. | | 1485. | | 1620. | | 2057. | | 2985. | | 2947. | | 1100. | |
| 6 | 50.0 | 4 | 75.0 | 9 | 75.0 | 8 | 100.0 | 0 | 150.0 | 5 | 150.0 | 4 | 50.0 |
| | | 1498. | | 1530. | | 2093. | | 2895. | | 2911. | | | |
| 981.4 | 50.0 | 3 | 75.0 | 8 | 75.0 | 1 | 100.0 | 1 | 150.0 | 2 | 150.0 | 929.6 | 50.0 |
| 1029. | | 1467. | | 1528. | | 2166. | | 3060. | | 3005. | | 1012. | |
| 6 | 50.0 | 1 | 75.0 | 1 | 75.0 | 2 | 100.0 | 1 | 150.0 | 2 | 150.0 | 0 | 50.0 |
| | | 1465. | | 1538. | | 1946. | | 2980. | | 2939. | | 1012. | |
| 949.5 | 50.0 | 6 | 75.0 | 5 | 75.0 | 2 | 100.0 | 7 | 150.0 | 0 | 150.0 | 7 | 50.0 |
| | | 1498. | | 1484. | | 1783. | | 3073. | | 2879. | | | |
| 935.4 | 50.0 | 9 | 75.0 | 0 | 75.0 | 8 | 100.0 | 5 | 150.0 | 0 | 150.0 | 969.3 | 50.0 |
| 1067. | | 1529. | | 1453. | | 2148. | | 2867. | | 3225. | | | |
| 9 | 50.0 | 3 | 75.0 | 9 | 75.0 | 4 | 100.0 | 2 | 150.0 | 0 | 150.0 | 990.7 | 50.0 |
| | | 1709. | | 1502. | | 2033. | | 2840. | | 3026. | | 1013. | |
| 993.1 | 50.0 | 1 | 75.0 | 0 | 75.0 | 1 | 100.0 | 7 | 150.0 | 4 | 150.0 | 5 | 50.0 |
| 1074. | | 1501. | | 1455. | | 2054. | | 3048. | | 3133. | | | |
| 7 | 50.0 | 8 | 75.0 | 7 | 75.0 | 8 | 100.0 | 9 | 150.0 | 8 | 150.0 | 957.8 | 50.0 |
| 1056. | | 1486. | | 1572. | | 1924. | | 2807. | | 3020. | | 1013. | |
| 8 | 50.0 | 8 | 75.0 | 8 | 75.0 | 7 | 100.0 | 3 | 150.0 | 5 | 150.0 | 8 | 50.0 |
| 1020. | | 1432. | | 1405. | | 2005. | | 2835. | | 3131. | | 1030. | |
| 7 | 50.0 | 1 | 75.0 | 9 | 75.0 | 3 | 100.0 | 3 | 150.0 | 4 | 150.0 | 8 | 50.0 |
| | | 1445. | | 1553. | | 2136. | | 2953. | | 3074. | | | |
| 961.6 | 50.0 | 5 | 75.0 | 3 | 75.0 | 6 | 100.0 | 1 | 150.0 | 3 | 150.0 | 986.9 | 50.0 |
| | | 1476. | | 1399. | | 1919. | | 2958. | | 2972. | | | |
| 975.4 | 50.0 | 4 | 75.0 | 6 | 75.0 | 6 | 100.0 | 7 | 150.0 | 6 | 150.0 | 998.2 | 50.0 |
| 988.7 | 50.0 | 1617. | 75.0 | 1548. | 75.0 | 2043. | 100.0 | 3032. | 150.0 | 3092. | 150.0 | 967.7 | 50.0 |

| | | | | | | | | | | | | | |
|---|---|---|---|---|---|---|---|---|---|---|---|---|---|
| | | 1 | | 3 | | 3 | | 2 | | 4 | | | |
| 1020.4 | 50.0 | 1589.1 | 75.0 | 1491.3 | 75.0 | 1941.7 | 100.0 | 3104.0 | 150.0 | 2909.8 | 150.0 | 1047.0 | 50.0 |
| 930.8 | 50.0 | 1437.4 | 75.0 | 1431.3 | 75.0 | 1943.3 | 100.0 | 3023.9 | 150.0 | 3100.1 | 150.0 | 1005.3 | 50.0 |
| 1056.8 | 50.0 | | | 1573.5 | 75.0 | 1992.5 | 100.0 | | | 3240.2 | 150.0 | 994.4 | 50.0 |
| 962.2 | 50.0 | | | | | 1886.7 | 100.0 | | | | | 997.1 | 50.0 |
| 949.4 | 50.0 | | | | | 2024.0 | 100.0 | | | | | 983.6 | 50.0 |
| 1067.5 | 50.0 | | | | | 1953.2 | 100.0 | | | | | 974.1 | 50.0 |
| 931.6 | 50.0 | | | | | 1940.0 | 100.0 | | | | | 882.1 | 50.0 |
| 940.9 | 50.0 | | | | | 1898.4 | 100.0 | | | | | 1021.4 | 50.0 |
| 1032.2 | 50.0 | | | | | 1955.2 | 100.0 | | | | | 946.2 | 50.0 |
| 1020.0 | 50.0 | | | | | 1967.3 | 100.0 | | | | | 1072.7 | 50.0 |
| 1047.0 | 50.0 | | | | | 1947.8 | 100.0 | | | | | 1039.7 | 50.0 |
| 1029.1 | 50.0 | | | | | 2147.7 | 100.0 | | | | | 1068.5 | 50.0 |
| 980.5 | 50.0 | | | | | 1792.0 | 100.0 | | | | | 1039.4 | 50.0 |
| 1052.0 | 50.0 | | | | | 1824.3 | 100.0 | | | | | 1065.5 | 50.0 |
| 936.5 | 50.0 | | | | | 1945.9 | 100.0 | | | | | 1052.2 | 50.0 |
| 1021.0 | 50.0 | | | | | 2032.5 | 100.0 | | | | | 1004.3 | 50.0 |
| 942.4 | 50.0 | | | | | 2041.0 | 100.0 | | | | | 1055.6 | 50.0 |
| 1041.3 | 50.0 | | | | | 1980.8 | 100.0 | | | | | 1064.3 | 50.0 |
| 1022.0 | 50.0 | | | | | 1997.7 | 100.0 | | | | | 914.9 | 50.0 |
| 997.1 | 50.0 | | | | | 1947.7 | 100.0 | | | | | 919.9 | 50.0 |
| 1040.1 | 50.0 | | | | | 2011.2 | 100.0 | | | | | 925.8 | 50.0 |
| 1031.8 | 50.0 | | | | | 2038.1 | 100.0 | | | | | 993.8 | 50.0 |
| 962.6 | 50.0 | | | | | 1881.9 | 100.0 | | | | | 881.6 | 50.0 |
| 979.8 | 50.0 | | | | | 1823.2 | 100.0 | | | | | 931.1 | 50.0 |
| 1020.3 | 50.0 | | | | | 2240.5 | 100.0 | | | | | 980.9 | 50.0 |
| 1019.0 | 50.0 | | | | | 2105.7 | 100.0 | | | | | 1070.7 | 50.0 |
| 1030.0 | 50.0 | | | | | 1974.7 | 100.0 | | | | | 1028.0 | 50.0 |
| 932.6 | 50.0 | | | | | 1765.1 | 100.0 | | | | | 981.8 | 50.0 |
| 1014.4 | 50.0 | | | | | 2100.8 | 100.0 | | | | | 1031.4 | 50.0 |
| 988.8 | 50.0 | | | | | 1899.1 | 100.0 | | | | | 960.4 | 50.0 |

| | | | | | | | | | | | | | |
|---|---|---|---|---|---|---|---|---|---|---|---|---|---|
| | | | | | | 1972.2 | 100.0 | | | | | 1076.8 | 50.0 |
| 974.9 | 50.0 | | | | | | | | | | | | |
| | | | | | | 1838.1 | 100.0 | | | | | 934.9 | 50.0 |
| 997.8 | 50.0 | | | | | | | | | | | | |
| | | | | | | 1977.9 | 100.0 | | | | | 988.7 | 50.0 |
| 945.9 | 50.0 | | | | | | | | | | | | |
| | | | | | | 1883.5 | 100.0 | | | | | 1034.5 | 50.0 |
| 1036.5 | 50.0 | | | | | | | | | | | | |
| | | | | | | 1950.6 | 100.0 | | | | | 970.9 | 50.0 |
| 1050.3 | 50.0 | | | | | | | | | | | | |
| | | | | | | 2176.0 | 100.0 | | | | | 869.8 | 50.0 |
| 1030.7 | 50.0 | | | | | | | | | | | | |
| | | | | | | 2043.4 | 100.0 | | | | | 980.1 | 50.0 |
| 1085.3 | 50.0 | | | | | | | | | | | | |
| | | | | | | 2023.1 | 100.0 | | | | | 1067.7 | 50.0 |
| 1015.5 | 50.0 | | | | | | | | | | | | |
| | | | | | | 1972.3 | 100.0 | | | | | 1090.7 | 50.0 |
| 869.0 | 50.0 | | | | | | | | | | | | |
| | | | | | | 2052.3 | 100.0 | | | | | 1031.5 | 50.0 |
| 971.7 | 50.0 | | | | | | | | | | | | |
| | | | | | | 1830.4 | 100.0 | | | | | 908.3 | 50.0 |
| 1048.8 | 50.0 | | | | | | | | | | | | |
| | | | | | | 1897.5 | 100.0 | | | | | 956.4 | 50.0 |
| 1000.7 | 50.0 | | | | | | | | | | | | |
| | | | | | | 1971.5 | 100.0 | | | | | 948.5 | 50.0 |
| 939.7 | 50.0 | | | | | | | | | | | | |
| | | | | | | 2085.4 | 100.0 | | | | | 986.0 | 50.0 |
| 913.5 | 50.0 | | | | | | | | | | | | |
| | | | | | | 1962.6 | 100.0 | | | | | 935.8 | 50.0 |
| 1005.1 | 50.0 | | | | | | | | | | | | |
| | | | | | | 2203.8 | 100.0 | | | | | 1048.3 | 50.0 |
| 1027.1 | 50.0 | | | | | | | | | | | | |
| | | | | | | 1922.4 | 100.0 | | | | | 1016.6 | 50.0 |
| 990.4 | 50.0 | | | | | | | | | | | | |
| | | | | | | 1998.1 | 100.0 | | | | | 1044.4 | 50.0 |
| 979.3 | 50.0 | | | | | | | | | | | | |
| | | | | | | 1946.0 | 100.0 | | | | | 926.9 | 50.0 |
| 986.3 | 50.0 | | | | | | | | | | | | |
| | | | | | | 2053.0 | 100.0 | | | | | 833.1 | 50.0 |
| 989.1 | 50.0 | | | | | | | | | | | | |
| | | | | | | 1781.2 | 100.0 | | | | | 1132.0 | 50.0 |
| 969.4 | 50.0 | | | | | | | | | | | | |
| | | | | | | 2049.1 | 100.0 | | | | | 1015.2 | 50.0 |
| 1019.7 | 50.0 | | | | | | | | | | | | |

| TTS (A) | | Formation III (C) | | Formation II (D) | | Formation I (F) | | Lesser Himalaya (H) | | Lesser Himalaya (I) | | Lowet Marsyandi (K) | |
|---|---|---|---|---|---|---|---|---|---|---|---|---|---|
| Age (Ma) | Error (Ma) | Age (Ma) | Error (Ma) | Age (Ma) | Error (Ma) | Age (Ma) | Error (Ma) | Age (Ma) | Error (Ma) | Age (Ma) | Error (Ma) | Age (Ma) | Error (Ma) |
| | | 1508.2 | 75.0 | 1594.1 | 75.0 | 1955.5 | 100.0 | 2964.2 | 137.5 | 2593.5 | 137.5 | | |
| 989.3 | 50.0 | | | | | | | | | | | 980.4 | 50.0 |
| | | 1609.7 | 75.0 | 1415.6 | 75.0 | 2031.9 | 100.0 | 2793.7 | 137.5 | 2702.1 | 137.5 | | |
| 999.5 | 50.0 | | | | | | | | | | | 978.1 | 50.0 |
| | | 1495.0 | 75.0 | 1549.3 | 75.0 | 2019.8 | 100.0 | 2382.5 | 137.5 | 2762.1 | 137.5 | | |
| 976.8 | 50.0 | | | | | | | | | | | 982.8 | 50.0 |
| 1014.1 | 50.0 | 1496.2 | 75.0 | 1484.9 | 75.0 | 1915.0 | 100.0 | 2683.0 | 137.5 | 2595.8 | 137.5 | 1005.2 | 50.0 |

| | | | | | | | | | | | | | |
|---|---|---|---|---|---|---|---|---|---|---|---|---|---|
| 1046.2 | 50.0 | 1518.3 | 75.0 | 1505.9 | 75.0 | 1803.0 | 100.0 | 2774.3 | 137.5 | 2750.2 | 137.5 | 1032.0 | 50.0 |
| 1042.6 | 50.0 | 1647.1 | 75.0 | 1652.2 | 75.0 | 1978.5 | 100.0 | 2674.8 | 137.5 | 2709.6 | 137.5 | 1015.0 | 50.0 |
| 1056.6 | 50.0 | 1460.4 | 75.0 | 1658.7 | 75.0 | 2100.1 | 100.0 | 2905.7 | 137.5 | 2847.8 | 137.5 | 1004.5 | 50.0 |
| 992.2 | 50.0 | 1587.5 | 75.0 | 1382.5 | 75.0 | 2037.9 | 100.0 | 2951.9 | 137.5 | 2927.6 | 137.5 | 989.0 | 50.0 |
| 1004.1 | 50.0 | 1567.7 | 75.0 | 1516.2 | 75.0 | 1823.5 | 100.0 | 2902.9 | 137.5 | 2851.2 | 137.5 | 951.5 | 50.0 |
| 1023.3 | 50.0 | 1626.0 | 75.0 | 1529.9 | 75.0 | 1807.5 | 100.0 | 2538.1 | 137.5 | 2928.4 | 137.5 | 993.6 | 50.0 |
| 1037.0 | 50.0 | 1529.8 | 75.0 | 1416.8 | 75.0 | 1948.4 | 100.0 | 2536.4 | 137.5 | 2985.5 | 137.5 | 1020.0 | 50.0 |
| 937.6 | 50.0 | 1500.5 | 75.0 | 1371.0 | 75.0 | 2017.1 | 100.0 | 2581.3 | 137.5 | 2366.9 | 137.5 | 1045.8 | 50.0 |
| 1028.9 | 50.0 | 1439.8 | 75.0 | 1523.2 | 75.0 | 2189.4 | 100.0 | 2803.8 | 137.5 | 2665.0 | 137.5 | 954.9 | 50.0 |
| 1080.2 | 50.0 | 1478.4 | 75.0 | 1446.7 | 75.0 | 1934.6 | 100.0 | 2680.2 | 137.5 | 2908.6 | 137.5 | 1015.8 | 50.0 |
| 1013.3 | 50.0 | 1491.5 | 75.0 | 1413.4 | 75.0 | 2131.2 | 100.0 | 2711.8 | 137.5 | 2804.1 | 137.5 | 966.0 | 50.0 |
| 954.1 | 50.0 | 1489.8 | 75.0 | 1632.6 | 75.0 | 2157.5 | 100.0 | 2707.2 | 137.5 | 2800.5 | 137.5 | 1002.7 | 50.0 |
| 999.4 | 50.0 | 1452.3 | 75.0 | 1623.8 | 75.0 | 2012.1 | 100.0 | 2852.3 | 137.5 | 2674.0 | 137.5 | 1011.7 | 50.0 |
| 945.8 | 50.0 | 1588.2 | 75.0 | 1409.5 | 75.0 | 2158.6 | 100.0 | 2758.1 | 137.5 | 2695.2 | 137.5 | 987.3 | 50.0 |
| 1030.7 | 50.0 | 1537.5 | 75.0 | 1421.3 | 75.0 | 1992.4 | 100.0 | 2527.2 | 137.5 | 2538.8 | 137.5 | 1024.7 | 50.0 |
| 998.8 | 50.0 | 1652.4 | 75.0 | 1445.5 | 75.0 | 1886.9 | 100.0 | 2601.7 | 137.5 | 2632.3 | 137.5 | 1017.3 | 50.0 |
| 1004.1 | 50.0 | 1522.4 | 75.0 | 1415.1 | 75.0 | 2014.1 | 100.0 | 2845.9 | 137.5 | 2505.9 | 137.5 | 989.6 | 50.0 |
| 968.4 | 50.0 | 1324.4 | 75.0 | 1429.5 | 75.0 | 1922.4 | 100.0 | 2670.3 | 137.5 | 2648.0 | 137.5 | 1068.9 | 50.0 |
| 1099.9 | 50.0 | 1549.4 | 75.0 | 1534.8 | 75.0 | 2025.4 | 100.0 | 2861.8 | 137.5 | 2860.1 | 137.5 | 924.6 | 50.0 |
| 879.7 | 50.0 | 1610.9 | 75.0 | 1534.9 | 75.0 | 2004.7 | 100.0 | 2901.8 | 137.5 | 2741.4 | 137.5 | 959.7 | 50.0 |
| 934.0 | 50.0 | 1477.6 | 75.0 | 1466.3 | 75.0 | 2172.1 | 100.0 | 2803.7 | 137.5 | 2624.5 | 137.5 | 1028.0 | 50.0 |
| 934.1 | 50.0 | 1426.3 | 75.0 | 1436.7 | 75.0 | 1895.0 | 100.0 | 2773.9 | 137.5 | 2723.1 | 137.5 | 888.9 | 50.0 |
| 1067.8 | 50.0 | 1393.5 | 75.0 | 1605.9 | 75.0 | 2003.9 | 100.0 | 2942.6 | 137.5 | 2580.1 | 137.5 | 1024.9 | 50.0 |
| 999.9 | 50.0 | 1479.8 | 75.0 | 1454.2 | 75.0 | 2195.2 | 100.0 | 2631.2 | 137.5 | 2779.2 | 137.5 | 896.4 | 50.0 |
| 1070.3 | 50.0 | 1486.8 | 75.0 | 1441.1 | 75.0 | 1829.9 | 100.0 | 2709.3 | 137.5 | 2807.6 | 137.5 | 1006.9 | 50.0 |
| 1049.9 | 50.0 | 1442.6 | 75.0 | 1542.3 | 75.0 | 1766.5 | 100.0 | 2850.8 | 137.5 | 2619.1 | 137.5 | 997.6 | 50.0 |
| 999.4 | 50.0 | 1595.7 | 75.0 | 1558.7 | 75.0 | 2030.5 | 100.0 | 2809.0 | 137.5 | 2624.8 | 137.5 | 1037.1 | 50.0 |
| 1117.4 | 50.0 | 1422.0 | 75.0 | 1463.1 | 75.0 | 2059.6 | 100.0 | 2904.5 | 137.5 | 3003.4 | 137.5 | 993.0 | 50.0 |
| 1013.4 | 50.0 | 1447.6 | 75.0 | 1480.6 | 75.0 | 1838.8 | 100.0 | 2553.5 | 137.5 | 2825.9 | 137.5 | 972.4 | 50.0 |
| 951.0 | 50.0 | 1593.3 | 75.0 | 1431.7 | 75.0 | 2027.7 | 100.0 | 2893.3 | 137.5 | 2790.3 | 137.5 | 963.2 | 50.0 |
| 1005. | 50.0 | 1527. | 75.0 | 1463. | 75.0 | 1790. | 100.0 | 2827. | 137.5 | 2599. | 137.5 | 927.9 | 50.0 |

| | | | | | | | | | | | | | |
|---|---|---|---|---|---|---|---|---|---|---|---|---|---|
| 1 | | 3 | | 6 | | 3 | | 7 | | 0 | | | |
| 992.8 | 50.0 | 1513.6 | 75.0 | 1397.8 | 75.0 | 1964.9 | 100.0 | 2809.8 | 137.5 | 2797.6 | 137.5 | 971.3 | 50.0 |
| 957.5 | 50.0 | 1443.5 | 75.0 | 1548.2 | 75.0 | 2036.1 | 100.0 | 2393.9 | 137.5 | 2760.9 | 137.5 | 1015.5 | 50.0 |
| 1064.0 | 50.0 | 1415.7 | 75.0 | 1472.0 | 75.0 | 2023.1 | 100.0 | 2828.4 | 137.5 | 2665.1 | 137.5 | 995.4 | 50.0 |
| 1000.7 | 50.0 | 1467.9 | 75.0 | 1501.4 | 75.0 | 1961.5 | 100.0 | 2916.9 | 137.5 | 2829.4 | 137.5 | 993.0 | 50.0 |
| 1058.2 | 50.0 | 1482.2 | 75.0 | 1479.1 | 75.0 | 1963.7 | 100.0 | 2740.2 | 137.5 | 2849.1 | 137.5 | 1075.5 | 50.0 |
| 988.7 | 50.0 | 1334.5 | 75.0 | 1483.1 | 75.0 | 1942.2 | 100.0 | 2754.2 | 137.5 | 2877.2 | 137.5 | 984.0 | 50.0 |
| 1027.9 | 50.0 | 1497.5 | 75.0 | 1630.5 | 75.0 | 1953.3 | 100.0 | 2484.1 | 137.5 | 2644.1 | 137.5 | 1044.8 | 50.0 |
| 942.8 | 50.0 | 1394.0 | 75.0 | 1592.8 | 75.0 | 1955.4 | 100.0 | 2830.2 | 137.5 | 2850.5 | 137.5 | 1060.5 | 50.0 |
| 1124.5 | 50.0 | 1486.7 | 75.0 | 1412.3 | 75.0 | 2118.4 | 100.0 | 2738.4 | 137.5 | 2561.7 | 137.5 | 972.4 | 50.0 |
| 1041.9 | 50.0 | 1552.4 | 75.0 | 1504.1 | 75.0 | 2033.1 | 100.0 | 2945.0 | 137.5 | 2772.7 | 137.5 | 1044.8 | 50.0 |
| 1024.7 | 50.0 | 1617.0 | 75.0 | 1593.6 | 75.0 | 2021.7 | 100.0 | 2558.9 | 137.5 | 2644.5 | 137.5 | 1014.6 | 50.0 |
| 944.1 | 50.0 | 1541.1 | 75.0 | 1574.9 | 75.0 | 2004.9 | 100.0 | 2854.7 | 137.5 | 2766.2 | 137.5 | 951.8 | 50.0 |
| 1031.4 | 50.0 | 1455.8 | 75.0 | 1566.2 | 75.0 | 1972.3 | 100.0 | 2461.0 | 137.5 | 2745.2 | 137.5 | 1013.6 | 50.0 |
| 1016.2 | 50.0 | 1474.7 | 75.0 | 1485.1 | 75.0 | 2087.5 | 100.0 | 2939.5 | 137.5 | 2833.9 | 137.5 | 998.5 | 50.0 |
| 1052.3 | 50.0 | | | 1515.0 | 75.0 | 2092.6 | 100.0 | | | 2672.1 | 137.5 | 970.6 | 50.0 |
| 980.8 | 50.0 | | | | | 1994.8 | 100.0 | | | | | 1006.6 | 50.0 |
| 990.4 | 50.0 | | | | | 1952.5 | 100.0 | | | | | 1010.1 | 50.0 |
| 981.8 | 50.0 | | | | | 1890.7 | 100.0 | | | | | 998.6 | 50.0 |
| 1051.3 | 50.0 | | | | | 1960.0 | 100.0 | | | | | 967.1 | 50.0 |
| 1006.9 | 50.0 | | | | | 2257.0 | 100.0 | | | | | 963.0 | 50.0 |
| 1010.2 | 50.0 | | | | | 1905.2 | 100.0 | | | | | 997.4 | 50.0 |
| 945.0 | 50.0 | | | | | 1957.7 | 100.0 | | | | | 900.5 | 50.0 |
| 1047.7 | 50.0 | | | | | 1954.8 | 100.0 | | | | | 954.7 | 50.0 |
| 962.3 | 50.0 | | | | | 1974.6 | 100.0 | | | | | 891.8 | 50.0 |
| 1102.9 | 50.0 | | | | | 2212.3 | 100.0 | | | | | 1048.0 | 50.0 |
| 978.2 | 50.0 | | | | | 1861.3 | 100.0 | | | | | 1048.8 | 50.0 |
| 1000.2 | 50.0 | | | | | 2064.4 | 100.0 | | | | | 1112.6 | 50.0 |
| 1010.4 | 50.0 | | | | | 1922.8 | 100.0 | | | | | 998.5 | 50.0 |
| 1045.0 | 50.0 | | | | | 1862.6 | 100.0 | | | | | 1038.3 | 50.0 |
| 984.4 | 50.0 | | | | | 2117.4 | 100.0 | | | | | 993.5 | 50.0 |

| | | | | | |
|---|---|---|---|---|---|
| 1019.8 | 50.0 | 1928.0 | 100.0 | 989.9 | 50.0 |
| 1014.4 | 50.0 | 2077.8 | 100.0 | 951.3 | 50.0 |
| 1002.9 | 50.0 | 2173.4 | 100.0 | 909.9 | 50.0 |
| 1105.1 | 50.0 | 1855.7 | 100.0 | 918.6 | 50.0 |
| 922.5 | 50.0 | 1954.4 | 100.0 | 1010.2 | 50.0 |
| 1047.6 | 50.0 | 1976.7 | 100.0 | 956.9 | 50.0 |
| 1031.8 | 50.0 | 1903.1 | 100.0 | 1001.7 | 50.0 |
| 1093.2 | 50.0 | 1825.4 | 100.0 | 955.5 | 50.0 |
| 1063.7 | 50.0 | 1993.3 | 100.0 | 1021.8 | 50.0 |
| 1052.5 | 50.0 | 1947.3 | 100.0 | 975.1 | 50.0 |
| 932.4 | 50.0 | 2058.6 | 100.0 | 1010.8 | 50.0 |
| 948.1 | 50.0 | 1948.2 | 100.0 | 1010.6 | 50.0 |
| 1087.1 | 50.0 | 2206.3 | 100.0 | 916.1 | 50.0 |
| 994.5 | 50.0 | 1956.2 | 100.0 | 1072.1 | 50.0 |
| 1020.9 | 50.0 | 2031.3 | 100.0 | 988.5 | 50.0 |
| 914.8 | 50.0 | 2043.9 | 100.0 | 1025.6 | 50.0 |
| 977.5 | 50.0 | 2179.9 | 100.0 | 950.5 | 50.0 |
| 960.1 | 50.0 | 2158.4 | 100.0 | 980.5 | 50.0 |
| 1035.5 | 50.0 | 1750.1 | 100.0 | 924.7 | 50.0 |
| 982.4 | 50.0 | 1904.8 | 100.0 | 1038.1 | 50.0 |
| 1063.5 | 50.0 | 2075.6 | 100.0 | 995.4 | 50.0 |
| 1014.6 | 50.0 | 2027.4 | 100.0 | 959.2 | 50.0 |
| 966.0 | 50.0 | 1908.3 | 100.0 | 987.8 | 50.0 |
| 1030.9 | 50.0 | 1950.3 | 100.0 | 1091.8 | 50.0 |
| 1016.7 | 50.0 | 1890.3 | 100.0 | 903.1 | 50.0 |
| 1051.8 | 50.0 | 1991.6 | 100.0 | 951.6 | 50.0 |
| 986.4 | 50.0 | 1980.5 | 100.0 | 971.8 | 50.0 |
| 928.1 | 50.0 | 2037.0 | 100.0 | 1015.4 | 50.0 |
| 914.4 | 50.0 | 2272.9 | 100.0 | 998.5 | 50.0 |
| 978.4 | 50.0 | 2054.7 | 100.0 | 972.1 | 50.0 |
| 919.2 | 50.0 | 1940. | 100.0 | 995.9 | 50.0 |

| | | | | | | | | | | | | | |
|---|---|---|---|---|---|---|---|---|---|---|---|---|---|
| 990.2 | 50.0 | | | | | 2059.1 | 100.0 | | | | | 924.9 | 50.0 |
| 1105.9 | 50.0 | | | | | 2118.5 | 100.0 | | | | | 999.7 | 50.0 |
| 981.6 | 50.0 | | | | | 2124.8 | 100.0 | | | | | 1000.1 | 50.0 |

| TTS (A) | | Formation III (C) | | Formation II (D) | | Formation I (F) | | Lesser Himalaya (H) | | Lesser Himalaya (I) | | Lowet Marsyandi (K) | |
|---|---|---|---|---|---|---|---|---|---|---|---|---|---|
| Age (Ma) | Error (Ma) | Age (Ma) | Error (Ma) | Age (Ma) | Error (Ma) | Age (Ma) | Error (Ma) | Age (Ma) | Error (Ma) | Age (Ma) | Error (Ma) | Age (Ma) | Error (Ma) |
| 493.1 | 25.0 | 824.7 | 40.0 | 768.5 | 40.0 | 1005.6 | 50.0 | 1192.0 | 60.0 | 1154.5 | 60.0 | 493.1 | 25.0 |
| 518.5 | 25.0 | 848.5 | 40.0 | 737.1 | 40.0 | 943.4 | 50.0 | 1125.4 | 60.0 | 1320.4 | 60.0 | 518.5 | 25.0 |
| 487.3 | 25.0 | 848.0 | 40.0 | 850.9 | 40.0 | 1056.7 | 50.0 | 1275.7 | 60.0 | 1299.0 | 60.0 | 487.3 | 25.0 |
| 528.0 | 25.0 | 773.5 | 40.0 | 753.3 | 40.0 | 1026.0 | 50.0 | 1046.0 | 60.0 | 1153.0 | 60.0 | 528.0 | 25.0 |
| 490.4 | 25.0 | 864.4 | 40.0 | 797.4 | 40.0 | 1025.4 | 50.0 | 1230.9 | 60.0 | 1136.8 | 60.0 | 490.4 | 25.0 |
| 548.5 | 25.0 | 828.3 | 40.0 | 752.6 | 40.0 | 1035.0 | 50.0 | 1133.1 | 60.0 | 1153.3 | 60.0 | 548.5 | 25.0 |
| 475.5 | 25.0 | 790.7 | 40.0 | 825.9 | 40.0 | 992.7 | 50.0 | 1237.5 | 60.0 | 1236.3 | 60.0 | 475.5 | 25.0 |
| 555.9 | 25.0 | 764.9 | 40.0 | 857.5 | 40.0 | 891.2 | 50.0 | 1169.1 | 60.0 | 1206.0 | 60.0 | 555.9 | 25.0 |
| 518.9 | 25.0 | 833.1 | 40.0 | 779.7 | 40.0 | 1084.7 | 50.0 | 1182.5 | 60.0 | 1190.4 | 60.0 | 518.9 | 25.0 |
| 496.8 | 25.0 | 845.7 | 40.0 | 821.8 | 40.0 | 996.4 | 50.0 | 1265.8 | 60.0 | 1199.7 | 60.0 | 496.8 | 25.0 |
| 494.2 | 25.0 | 813.5 | 40.0 | 751.7 | 40.0 | 960.2 | 50.0 | 1115.4 | 60.0 | 1219.6 | 60.0 | 494.2 | 25.0 |
| 510.8 | 25.0 | 805.0 | 40.0 | 843.7 | 40.0 | 1066.6 | 50.0 | 1164.2 | 60.0 | 1117.1 | 60.0 | 510.8 | 25.0 |
| 510.2 | 25.0 | 794.9 | 40.0 | 737.0 | 40.0 | 1005.2 | 50.0 | 1303.5 | 60.0 | 1171.3 | 60.0 | 510.2 | 25.0 |
| 515.2 | 25.0 | 788.9 | 40.0 | 858.0 | 40.0 | 963.2 | 50.0 | 1205.6 | 60.0 | 1185.6 | 60.0 | 515.2 | 25.0 |
| 495.5 | 25.0 | 842.4 | 40.0 | 803.5 | 40.0 | 1049.0 | 50.0 | 1050.1 | 60.0 | 1228.7 | 60.0 | 495.5 | 25.0 |
| 527.4 | 25.0 | 813.4 | 40.0 | 714.2 | 40.0 | 1025.2 | 50.0 | 1168.4 | 60.0 | 1152.5 | 60.0 | 527.4 | 25.0 |
| 513.6 | 25.0 | 785.9 | 40.0 | 786.5 | 40.0 | 1003.1 | 50.0 | 1127.6 | 60.0 | 1080.1 | 60.0 | 513.6 | 25.0 |
| 536.8 | 25.0 | 792.5 | 40.0 | 830.6 | 40.0 | 935.7 | 50.0 | 1209.5 | 60.0 | 1227.8 | 60.0 | 536.8 | 25.0 |
| 487.6 | 25.0 | 752.0 | 40.0 | 753.4 | 40.0 | 1007.5 | 50.0 | 1139.5 | 60.0 | 1200.6 | 60.0 | 487.6 | 25.0 |
| 514.8 | 25.0 | 783.7 | 40.0 | 729.4 | 40.0 | 1061.6 | 50.0 | 1147.7 | 60.0 | 1227.0 | 60.0 | 514.8 | 25.0 |
| 506.8 | 25.0 | 715.1 | 40.0 | 763.3 | 40.0 | 990.1 | 50.0 | 1276.4 | 60.0 | 1169.9 | 60.0 | 506.8 | 25.0 |
| 523.4 | 25.0 | 840.6 | 40.0 | 742.2 | 40.0 | 992.3 | 50.0 | 1184.5 | 60.0 | 1244.4 | 60.0 | 523.4 | 25.0 |
| 485.1 | 25.0 | 804.5 | 40.0 | 770.9 | 40.0 | 964.1 | 50.0 | 1174.3 | 60.0 | 1144.7 | 60.0 | 485.1 | 25.0 |
| 479.2 | 25.0 | 809.3 | 40.0 | 784.5 | 40.0 | 1050.6 | 50.0 | 1238.1 | 60.0 | 1213.6 | 60.0 | 479.2 | 25.0 |
| 503.6 | 25.0 | 876.0 | 40.0 | 725.4 | 40.0 | 987.2 | 50.0 | 1150.5 | 60.0 | 1171.1 | 60.0 | 503.6 | 25.0 |
| 493.4 | 25.0 | 820.7 | 40.0 | 803.3 | 40.0 | 1016.0 | 50.0 | 1292.2 | 60.0 | 1128.1 | 60.0 | 493.4 | 25.0 |
| 530.1 | 25.0 | 789.4 | 40.0 | 851.1 | 40.0 | 1018.2 | 50.0 | 1242.6 | 60.0 | 1094.4 | 60.0 | 530.1 | 25.0 |
| 431.4 | 25.0 | 832.0 | 40.0 | 809.6 | 40.0 | 1089.9 | 50.0 | 1205.4 | 60.0 | 1097.0 | 60.0 | 431.4 | 25.0 |
| 477.2 | 25.0 | 883.4 | 40.0 | 835.9 | 40.0 | 1113.7 | 50.0 | 1176.3 | 60.0 | 1291.0 | 60.0 | 477.2 | 25.0 |
| 525.3 | 25.0 | 713.4 | 40.0 | 805.4 | 40.0 | 1049.0 | 50.0 | 1284.5 | 60.0 | 1351.0 | 60.0 | 525.3 | 25.0 |
| 478.1 | 25.0 | 775.4 | 40.0 | 829.8 | 40.0 | 1013.0 | 50.0 | 1196.6 | 60.0 | 1209.3 | 60.0 | 478.1 | 25.0 |
| 468.2 | 25.0 | 789.7 | 40.0 | 797.7 | 40.0 | 926.0 | 50.0 | 1105.6 | 60.0 | 1135.6 | 60.0 | 468.2 | 25.0 |

| | | | | | | | | | | | | | |
|---|---|---|---|---|---|---|---|---|---|---|---|---|---|
| 485.7 | 25.0 | 771.4 | 40.0 | 729.6 | 40.0 | 951.3 | 50.0 | 1225.6 | 60.0 | 1186.6 | 60.0 | 485.7 | 25.0 |
| 520.2 | 25.0 | 820.9 | 40.0 | 823.7 | 40.0 | 1004.1 | 50.0 | 1103.0 | 60.0 | 1222.4 | 60.0 | 520.2 | 25.0 |
| 510.4 | 25.0 | 822.3 | 40.0 | 808.9 | 40.0 | 960.3 | 50.0 | 1181.9 | 60.0 | 1250.3 | 60.0 | 510.4 | 25.0 |
| 475.3 | 25.0 | 835.1 | 40.0 | 742.0 | 40.0 | 998.5 | 50.0 | 1240.8 | 60.0 | 1215.0 | 60.0 | 475.3 | 25.0 |
| 542.9 | 25.0 | 854.9 | 40.0 | 793.1 | 40.0 | 1004.8 | 50.0 | 1133.6 | 60.0 | 1188.3 | 60.0 | 542.9 | 25.0 |
| 538.0 | 25.0 | 780.2 | 40.0 | 846.3 | 40.0 | 1060.5 | 50.0 | 1274.2 | 60.0 | 1236.8 | 60.0 | 538.0 | 25.0 |
| 484.4 | 25.0 | 794.2 | 40.0 | 745.1 | 40.0 | 990.1 | 50.0 | 1164.0 | 60.0 | 1285.6 | 60.0 | 484.4 | 25.0 |
| 478.0 | 25.0 | 735.6 | 40.0 | 854.9 | 40.0 | 929.3 | 50.0 | 1237.8 | 60.0 | 1171.9 | 60.0 | 478.0 | 25.0 |
| 513.6 | 25.0 | 736.2 | 40.0 | 776.4 | 40.0 | 1013.0 | 50.0 | 1172.8 | 60.0 | 1249.4 | 60.0 | 513.6 | 25.0 |
| 521.4 | 25.0 | 735.5 | 40.0 | 794.0 | 40.0 | 1002.9 | 50.0 | 1234.6 | 60.0 | 1084.1 | 60.0 | 521.4 | 25.0 |
| 494.6 | 25.0 | 819.0 | 40.0 | 847.4 | 40.0 | 1026.2 | 50.0 | 1122.6 | 60.0 | 1191.3 | 60.0 | 494.6 | 25.0 |
| 503.3 | 25.0 | 780.2 | 40.0 | 816.4 | 40.0 | 1054.1 | 50.0 | 1220.0 | 60.0 | 1165.6 | 60.0 | 503.3 | 25.0 |
| 491.3 | 25.0 | 769.0 | 40.0 | 856.6 | 40.0 | 1023.0 | 50.0 | 1232.4 | 60.0 | 1206.7 | 60.0 | 491.3 | 25.0 |
| 504.6 | 25.0 | 886.9 | 40.0 | 813.4 | 40.0 | 884.8 | 50.0 | 1213.7 | 60.0 | 1114.9 | 60.0 | 504.6 | 25.0 |
| 513.3 | 25.0 | 832.9 | 40.0 | 752.9 | 40.0 | 935.0 | 50.0 | 1228.2 | 60.0 | 1208.8 | 60.0 | 513.3 | 25.0 |
| 457.1 | 25.0 | 852.9 | 40.0 | 832.7 | 40.0 | 957.1 | 50.0 | 1276.6 | 60.0 | 1153.3 | 60.0 | 457.1 | 25.0 |
| 514.5 | 25.0 | 823.2 | 40.0 | 727.6 | 40.0 | 985.4 | 50.0 | 1158.8 | 60.0 | 1163.4 | 60.0 | 514.5 | 25.0 |
| 460.4 | 25.0 | | | 799.7 | 40.0 | 1039.5 | 50.0 | | | 1153.9 | 60.0 | 460.4 | 25.0 |
| 474.3 | 25.0 | | | | | 932.3 | 50.0 | | | | | 474.3 | 25.0 |
| 490.6 | 25.0 | | | | | 948.6 | 50.0 | | | | | 490.6 | 25.0 |
| 539.3 | 25.0 | | | | | 1113.3 | 50.0 | | | | | 539.3 | 25.0 |
| 521.2 | 25.0 | | | | | 1115.6 | 50.0 | | | | | 521.2 | 25.0 |
| 493.5 | 25.0 | | | | | 1009.3 | 50.0 | | | | | 493.5 | 25.0 |
| 515.2 | 25.0 | | | | | 932.5 | 50.0 | | | | | 515.2 | 25.0 |
| 481.0 | 25.0 | | | | | 934.8 | 50.0 | | | | | 481.0 | 25.0 |
| 456.9 | 25.0 | | | | | 1024.4 | 50.0 | | | | | 456.9 | 25.0 |
| 492.9 | 25.0 | | | | | 972.7 | 50.0 | | | | | 492.9 | 25.0 |
| 441.2 | 25.0 | | | | | 984.2 | 50.0 | | | | | 441.2 | 25.0 |
| 465.3 | 25.0 | | | | | 1006.9 | 50.0 | | | | | 465.3 | 25.0 |
| 505.3 | 25.0 | | | | | 953.9 | 50.0 | | | | | 505.3 | 25.0 |
| 448.0 | 25.0 | | | | | 1053.5 | 50.0 | | | | | 448.0 | 25.0 |
| 537.5 | 25.0 | | | | | 1037.6 | 50.0 | | | | | 537.5 | 25.0 |
| 467.1 | 25.0 | | | | | 906.7 | 50.0 | | | | | 467.1 | 25.0 |
| 467.8 | 25.0 | | | | | 923.1 | 50.0 | | | | | 467.8 | 25.0 |
| 493.6 | 25.0 | | | | | 1001.9 | 50.0 | | | | | 493.6 | 25.0 |
| 517.5 | 25.0 | | | | | 1004.5 | 50.0 | | | | | 517.5 | 25.0 |
| 453.0 | 25.0 | | | | | 959.2 | 50.0 | | | | | 453.0 | 25.0 |
| 471.3 | 25.0 | | | | | 1068.4 | 50.0 | | | | | 471.3 | 25.0 |
| 506.0 | 25.0 | | | | | 1020.9 | 50.0 | | | | | 506.0 | 25.0 |
| 524.2 | 25.0 | | | | | 919.4 | 50.0 | | | | | 524.2 | 25.0 |
| 509.9 | 25.0 | | | | | 1009.4 | 50.0 | | | | | 509.9 | 25.0 |
| 509.9 | 25.0 | | | | | 1004.5 | 50.0 | | | | | 509.9 | 25.0 |

| | | | | |
|---|---|---|---|---|
| 491.5 | 25.0 | 942.4 | 50.0 | 491.5 | 25.0 |
| 473.9 | 25.0 | 1008.6 | 50.0 | 473.9 | 25.0 |
| 490.0 | 25.0 | 1059.1 | 50.0 | 490.0 | 25.0 |
| 480.7 | 25.0 | 845.5 | 50.0 | 480.7 | 25.0 |
| 469.8 | 25.0 | 1038.2 | 50.0 | 469.8 | 25.0 |
| 489.6 | 25.0 | 1017.0 | 50.0 | 489.6 | 25.0 |
| 528.7 | 25.0 | 962.1 | 50.0 | 528.7 | 25.0 |
| 409.9 | 25.0 | 953.6 | 50.0 | 409.9 | 25.0 |
| 496.6 | 25.0 | 1053.5 | 50.0 | 496.6 | 25.0 |
| 487.0 | 25.0 | 1004.8 | 50.0 | 487.0 | 25.0 |
| 557.8 | 25.0 | 1031.8 | 50.0 | 557.8 | 25.0 |
| 459.4 | 25.0 | 1023.4 | 50.0 | 459.4 | 25.0 |
| 510.9 | 25.0 | 960.7 | 50.0 | 510.9 | 25.0 |
| 460.4 | 25.0 | 944.8 | 50.0 | 460.4 | 25.0 |
| 496.0 | 25.0 | 986.4 | 50.0 | 496.0 | 25.0 |
| 533.6 | 25.0 | 990.2 | 50.0 | 533.6 | 25.0 |
| 520.0 | 25.0 | 969.6 | 50.0 | 520.0 | 25.0 |
| 529.3 | 25.0 | 978.0 | 50.0 | 529.3 | 25.0 |
| 445.9 | 25.0 | 1083.0 | 50.0 | 445.9 | 25.0 |
| 498.0 | 25.0 | 981.3 | 50.0 | 498.0 | 25.0 |
| 500.1 | 25.0 | 974.4 | 50.0 | 500.1 | 25.0 |
| 504.8 | 25.0 | 948.6 | 50.0 | 504.8 | 25.0 |
| 517.2 | 25.0 | 969.0 | 50.0 | 517.2 | 25.0 |
| 526.2 | 25.0 | 1001.8 | 50.0 | 526.2 | 25.0 |
| 516.5 | 25.0 | 1030.7 | 50.0 | 516.5 | 25.0 |

| TTS (A) | | Formation III (C) | | Formation II (D) | | Formation I (F) | | Lesser Himalaya (H) | | Lesser Himalaya (I) | | Lowet Marsyandi (K) | |
|---|---|---|---|---|---|---|---|---|---|---|---|---|---|
| Age (Ma) | Error (Ma) | Age (Ma) | Error (Ma) | Age (Ma) | Error (Ma) | Age (Ma) | Error (Ma) | Age (Ma) | Error (Ma) | Age (Ma) | Error (Ma) | Age (Ma) | Error (Ma) |
| 618 | 30 | 824.7 | 40 | 768.51 | 40 | 1005.64 | 50 | 1192.01 | 60 | 1154.52 | 60 | 603.34075 | 30 |
| 610 | 30 | 848.5 | 40 | 737.05 | 40 | 943.37 | 50 | 1125.42 | 60 | 1320.35 | 60 | 634.41219 | 30 |
| 589 | 30 | 848 | 40 | 850.88 | 40 | 1056.74 | 50 | 1275.65 | 60 | 1299 | 60 | 609.01328 | 30 |
| 610 | 30 | 773.5 | 40 | 753.34 | 40 | 1026.04 | 50 | 1045.98 | 60 | 1152.97 | 60 | 609.70472 | 30 |
| 572 | 30 | 864.4 | 40 | 797.4 | 40 | 1025.41 | 50 | 1230.9 | 60 | 1136.77 | 60 | 603.26067 | 30 |
| 639 | 30 | 828.3 | 40 | 752.63 | 40 | 1035.04 | 50 | 1133.08 | 60 | 1153.31 | 60 | 568.86601 | 30 |
| 629 | 30 | 790.7 | 40 | 825.87 | 40 | 992.68 | 50 | 1237.45 | 60 | 1236.33 | 60 | 586.97305 | 30 |
| 584 | 30 | 764.9 | 40 | 857.52 | 40 | 891.16 | 50 | 1169.1 | 60 | 1206.01 | 60 | 591.06139 | 30 |
| 643 | 30 | 833.1 | 40 | 779.74 | 40 | 1084.73 | 50 | 1182.53 | 60 | 1190.41 | 60 | 602.54622 | 30 |

| | | | | | | | | | | | | | |
|---|---|---|---|---|---|---|---|---|---|---|---|---|---|
| | | 845. | | 821.8 | | | | 1265.7 | | 1199.7 | | 653.2839 | |
| 594 | 30 | 7 | 40 | 2 | 40 | 996.35 | 50 | 7 | 60 | 2 | 60 | 5 | 30 |
| | | 813. | | 751.6 | | | | | | 1219.6 | | 593.9103 | |
| 610 | 30 | 5 | 40 | 6 | 40 | 960.19 | 50 | 1115.4 | 60 | 4 | 60 | 4 | 30 |
| | | | | 843.7 | | 1066.6 | | 1164.1 | | 1117.0 | | 561.3108 | |
| 607 | 30 | 805 | 40 | 3 | 40 | 3 | 50 | 7 | 60 | 7 | 60 | 6 | 30 |
| | | 794. | | 736.9 | | 1005.2 | | 1303.5 | | 1171.2 | | 624.1670 | |
| 583 | 30 | 9 | 40 | 6 | 40 | 1 | 50 | 3 | 60 | 5 | 60 | 8 | 30 |
| | | 788. | | 858.0 | | | | 1205.6 | | | | 611.9612 | |
| 604 | 30 | 9 | 40 | 2 | 40 | 963.15 | 50 | 4 | 60 | 1185.6 | 60 | 2 | 30 |
| | | 842. | | | | 1048.9 | | 1050.0 | | | | 589.0812 | |
| 663 | 30 | 4 | 40 | 803.5 | 40 | 8 | 50 | 8 | 60 | 1228.7 | 60 | 7 | 30 |
| | | 813. | | 714.2 | | 1025.2 | | 1168.3 | | 1152.5 | | | |
| 594 | 30 | 4 | 40 | 1 | 40 | 2 | 50 | 9 | 60 | 3 | 60 | 631.7341 | 30 |
| | | 785. | | 786.5 | | 1003.1 | | 1127.5 | | 1080.0 | | | |
| 611 | 30 | 9 | 40 | 3 | 40 | 1 | 50 | 8 | 60 | 8 | 60 | 529.7073 | 30 |
| | | 792. | | | | | | 1209.4 | | 1227.8 | | | |
| 607 | 30 | 5 | 40 | 830.6 | 40 | 935.68 | 50 | 8 | 60 | 3 | 60 | 559.3399 | 30 |
| | | | | | | 1007.5 | | 1139.4 | | 1200.5 | | 601.7030 | |
| 569 | 30 | 752 | 40 | 753.4 | 40 | 3 | 50 | 5 | 60 | 6 | 60 | 1 | 30 |
| | | 783. | | 729.3 | | 1061.5 | | 1147.6 | | 1226.9 | | 552.8033 | |
| 592 | 30 | 7 | 40 | 6 | 40 | 8 | 50 | 7 | 60 | 8 | 60 | 9 | 30 |
| | | 715. | | 763.3 | | | | 1276.3 | | 1169.8 | | 659.7293 | |
| 624 | 30 | 1 | 40 | 3 | 40 | 990.13 | 50 | 9 | 60 | 9 | 60 | 4 | 30 |
| | | 840. | | 742.2 | | | | 1184.5 | | 1244.4 | | 589.1033 | |
| 633 | 30 | 6 | 40 | 1 | 40 | 992.34 | 50 | 1 | 60 | 2 | 60 | 4 | 30 |
| | | 804. | | 770.9 | | | | 1174.3 | | 1144.7 | | 614.8248 | |
| 651 | 30 | 5 | 40 | 4 | 40 | 964.08 | 50 | 4 | 60 | 4 | 60 | 5 | 30 |
| | | 809. | | 784.4 | | 1050.6 | | | | 1213.6 | | | |
| 636 | 30 | 3 | 40 | 6 | 40 | 4 | 50 | 1238.1 | 60 | 3 | 60 | 623.9659 | 30 |
| | | | | 725.4 | | | | 1150.5 | | 1171.1 | | 655.3919 | |
| 624 | 30 | 876 | 40 | 2 | 40 | 987.24 | 50 | 3 | 60 | 1 | 60 | 2 | 30 |
| | | 820. | | 803.2 | | 1015.9 | | 1292.1 | | 1128.0 | | | |
| 593 | 30 | 7 | 40 | 8 | 40 | 5 | 50 | 6 | 60 | 5 | 60 | 597.154 | 30 |
| | | 789. | | 851.1 | | 1018.2 | | 1242.6 | | 1094.3 | | 620.3708 | |
| 631 | 30 | 4 | 40 | 2 | 40 | 4 | 50 | 1 | 60 | 6 | 60 | 3 | 30 |
| | | | | 809.5 | | 1089.8 | | 1205.4 | | 1096.9 | | 558.4066 | |
| 696 | 30 | 832 | 40 | 8 | 40 | 8 | 50 | 4 | 60 | 6 | 60 | 6 | 30 |
| | | 883. | | 835.8 | | 1113.6 | | 1176.3 | | 1290.9 | | 646.0254 | |
| 628 | 30 | 4 | 40 | 7 | 40 | 7 | 50 | 4 | 60 | 6 | 60 | 9 | 30 |
| | | 713. | | 805.3 | | 1048.9 | | 1284.4 | | 1350.9 | | | |
| 611 | 30 | 4 | 40 | 5 | 40 | 9 | 50 | 6 | 60 | 9 | 60 | 608.2071 | 30 |
| | | 775. | | 829.7 | | 1013.0 | | 1196.5 | | 1209.2 | | 601.5886 | |
| 581 | 30 | 4 | 40 | 9 | 40 | 1 | 50 | 5 | 60 | 9 | 60 | 1 | 30 |
| | | 789. | | 797.6 | | | | 1105.5 | | | | 589.5367 | |
| 579 | 30 | 7 | 40 | 7 | 40 | 925.95 | 50 | 6 | 60 | 1135.6 | 60 | 1 | 30 |
| | | 771. | | 729.5 | | | | 1225.5 | | 1186.5 | | 596.0733 | |
| 535 | 30 | 4 | 40 | 6 | 40 | 951.26 | 50 | 5 | 60 | 8 | 60 | 5 | 30 |
| | | 820. | | 823.6 | | 1004.1 | | 1103.0 | | 1222.4 | | 612.6909 | |
| 593 | 30 | 9 | 40 | 8 | 40 | 4 | 50 | 4 | 60 | 3 | 60 | 4 | 30 |
| | | 822. | | 808.8 | | | | 1181.8 | | 1250.3 | | 593.7023 | |
| 633 | 30 | 3 | 40 | 6 | 40 | 960.27 | 50 | 8 | 60 | 4 | 60 | 5 | 30 |
| | | 835. | | 741.9 | | | | 1240.7 | | 1214.9 | | 646.3833 | |
| 635 | 30 | 1 | 40 | 5 | 40 | 998.51 | 50 | 7 | 60 | 7 | 60 | 1 | 30 |
| | | 854. | | | | 1004.7 | | 1133.5 | | 1188.3 | | | |
| 566 | 30 | 9 | 40 | 793.1 | 40 | 5 | 50 | 7 | 60 | 3 | 60 | 605.1607 | 30 |
| | | 780. | | 846.3 | | | | 1274.1 | | 1236.7 | | 602.3565 | |
| 589 | 30 | 2 | 40 | 1 | 40 | 1060.5 | 50 | 8 | 60 | 6 | 60 | 7 | 30 |
| | | 794. | | 745.1 | | | | 1164.0 | | 1285.5 | | 607.6621 | |
| 622 | 30 | 2 | 40 | 3 | 40 | 990.11 | 50 | 1 | 60 | 7 | 60 | 6 | 30 |
| 590 | 30 | 735. | 40 | 854.8 | 40 | 929.29 | 50 | 1237.8 | 60 | 1171.8 | 60 | 594.1138 | 30 |

| | | | | | | | | | | | | | |
|---|---|---|---|---|---|---|---|---|---|---|---|---|---|
| | | 6 | | 9 | | | | 1 | | 5 | | 4 | |
| 623 | 30 | 736.2 | 40 | 776.39 | 40 | 1012.98 | 50 | 1172.84 | 60 | 1249.39 | 60 | 527.7407 | 30 |
| 573 | 30 | 735.5 | 40 | 794.02 | 40 | 1002.92 | 50 | 1234.62 | 60 | 1084.11 | 60 | 642.3364 | 30 |
| 635 | 30 | 819 | 40 | 847.42 | 40 | 1026.21 | 50 | 1122.61 | 60 | 1191.33 | 60 | 629.2961 | 30 |
| 585 | 30 | 780.2 | 40 | 816.42 | 40 | 1054.12 | 50 | 1220.03 | 60 | 1165.63 | 60 | 627.6401 | 30 |
| 588 | 30 | 769 | 40 | 856.63 | 40 | 1023.02 | 50 | 1232.38 | 60 | 1206.73 | 60 | 622.2716 | 30 |
| 591 | 30 | 886.9 | 40 | 813.41 | 40 | 884.75 | 50 | 1213.67 | 60 | 1114.87 | 60 | 602.7659 | 30 |
| 596 | 30 | 832.9 | 40 | 752.88 | 40 | 935 | 50 | 1228.18 | 60 | 1208.81 | 60 | 611.2169 | 30 |
| 609 | 30 | 852.9 | 40 | 832.67 | 40 | 957.05 | 50 | 1276.6 | 60 | 1153.31 | 60 | 659.2592 | 30 |
| 611 | 30 | 823.2 | 40 | 727.63 | 40 | 985.44 | 50 | 1158.78 | 60 | 1163.37 | 60 | 626.7948 | 30 |
| 668 | 30 | | | 799.65 | 40 | 1039.54 | 50 | | | 1153.93 | 60 | 610.5961 | 30 |
| 616 | 30 | | | | | 932.3 | 50 | | | | | 594.07618 | 30 |
| 577 | 30 | | | | | 948.61 | 50 | | | | | 574.85617 | 30 |
| 590 | 30 | | | | | 1113.3 | 50 | | | | | 565.72249 | 30 |
| 582 | 30 | | | | | 1115.64 | 50 | | | | | 644.10997 | 30 |
| 573 | 30 | | | | | 1009.28 | 50 | | | | | 603.36098 | 30 |
| 589 | 30 | | | | | 932.46 | 50 | | | | | 554.223 | 30 |
| 643 | 30 | | | | | 934.76 | 50 | | | | | 584.85595 | 30 |
| 604 | 30 | | | | | 1024.4 | 50 | | | | | 605.82003 | 30 |
| 613 | 30 | | | | | 972.73 | 50 | | | | | 571.79643 | 30 |
| 602 | 30 | | | | | 984.23 | 50 | | | | | 604.35526 | 30 |
| 611 | 30 | | | | | 1006.88 | 50 | | | | | 647.26754 | 30 |
| 625 | 30 | | | | | 953.86 | 50 | | | | | 607.90552 | 30 |
| 560 | 30 | | | | | 1053.49 | 50 | | | | | 598.34889 | 30 |
| 504 | 30 | | | | | 1037.6 | 50 | | | | | 616.88757 | 30 |
| 592 | 30 | | | | | 906.66 | 50 | | | | | 660.34657 | 30 |
| 557 | 30 | | | | | 923.05 | 50 | | | | | 578.3765 | 30 |
| 567 | 30 | | | | | 1001.9 | 50 | | | | | 614.52482 | 30 |
| 618 | 30 | | | | | 1004.53 | 50 | | | | | 596.87994 | 30 |
| 594 | 30 | | | | | 959.16 | 50 | | | | | 622.30474 | 30 |
| 642 | 30 | | | | | 1068.4 | 50 | | | | | 600.37025 | 30 |
| 576 | 30 | | | | | 1020.8 | 50 | | | | | 570.7431 | 30 |

| | | | | | |
|---|---|---|---|---|---|
| | | 6 | | 1 | |
| 633 | 30 | 919.38 | 50 | 607.81547 | 30 |
| 597 | 30 | 1009.37 | 50 | 573.75401 | 30 |
| 595 | 30 | 1004.54 | 50 | 523.86711 | 30 |
| 631 | 30 | 942.41 | 50 | 623.64536 | 30 |
| 618 | 30 | 1008.63 | 50 | 597.17895 | 30 |
| 579 | 30 | 1059.08 | 50 | 642.79338 | 30 |
| 619 | 30 | 845.46 | 50 | 626.79534 | 30 |
| 615 | 30 | 1038.15 | 50 | 611.93847 | 30 |
| 556 | 30 | 1017.02 | 50 | 633.93337 | 30 |
| 611 | 30 | 962.13 | 50 | 600.90678 | 30 |
| 587 | 30 | 953.61 | 50 | 555.11049 | 30 |
| 575 | 30 | 1053.53 | 50 | 644.9663 | 30 |
| 619 | 30 | 1004.84 | 50 | 597.3179 | 30 |
| 586 | 30 | 1031.8 | 50 | 630.14284 | 30 |
| 630 | 30 | 1023.36 | 50 | 583.23112 | 30 |
| 627 | 30 | 960.65 | 50 | 577.43899 | 30 |
| 581 | 30 | 944.75 | 50 | 569.29909 | 30 |
| 616 | 30 | 986.36 | 50 | 586.65914 | 30 |
| 542 | 30 | 990.19 | 50 | 633.55041 | 30 |
| 596 | 30 | 969.63 | 50 | 564.04286 | 30 |
| 567 | 30 | 978 | 50 | 612.88499 | 30 |
| 598 | 30 | 1083.03 | 50 | 600.49226 | 30 |
| 549 | 30 | 981.3 | 50 | 616.78784 | 30 |
| 652 | 30 | 974.41 | 50 | 583.3232 | 30 |
| 658 | 30 | 948.63 | 50 | 608.34239 | 30 |
| 591 | 30 | 968.96 | 50 | 608.97706 | 30 |
| 629 | 30 | 1001.77 | 50 | 589.4535 | 30 |
| 588 | 30 | 1030.68 | 50 | 581.43026 | 30 |

Table S2.Synthetic U–Pb ages of Marsyandi watershed. Note that the synthetic age distribution displayed throughout the manuscript (Fig. 2–6) is the age distribution 4.

| **Sample** | *M* (% $10^2$) | *S* (% $10^2$) | *K–S* | | Q–Q plot ($R^2$) | PDF cross–plot ($R^2$) |
|---|---|---|---|---|---|---|
| | | | *Ds* | *p* (% $10^2$) | | |
| A | 0.001 | 0.990 | 0.089 | 0.532 | 1.000 | 0.922 |
| C | 0.002 | 0.994 | 0.099 | 0.430 | 1.000 | 0.956 |
| F | 0.001 | 0.999 | 0.090 | 0.512 | 1.000 | 0.993 |
| H | 0.001 | 0.994 | 0.118 | 0.525 | 1.000 | 0.984 |
| K | 0.000 | 0.992 | 0.084 | 0.520 | 1.000 | 0.917 |

Table S3.Statistical analysis comparing the natural ages with and without smoothing (see section 2.5.2 in main text). "Sample" refers to location of sample of which the distributions are investigated (Fig. 2). Statistics in the table evaluate the similarity between the raw and the smoothed distributions.

| **Sample** | *M* (% $10^2$) | *S* (% $10^2$) | *K–S* | | Q–Q plot ($R^2$) | PDF cross–plot ($R^2$) |
|---|---|---|---|---|---|---|
| | | | *Ds* | *p* (% $10^2$) | | |
| A | 0.00 | 0.99 | 0.13 | 0.45 | 1.00 | 0.98 |
| C | 0.00 | 1.00 | 0.17 | 0.53 | 1.00 | 1.00 |
| F | 0.00 | 1.00 | 0.16 | 0.54 | 1.00 | 1.00 |
| H | 0.00 | 1.00 | 0.12 | 0.53 | 1.00 | 1.00 |

| | | | | | | | |
|---|---|---|---|---|---|---|---|
| K | 0.00 | 1.00 | 0.06 | | 0.50 | 1.00 | 0.99 |

Table S4.Statistical analysis comparing the synthetic ages (distribution 4) with and without smoothing (see section 2.5.2 in main text). "Sample" refers to location of sample of which the distributions are investigated (Fig. 2). Statistics in the table evaluate the similarity between the raw and the smoothed distributions.

| X–axis | Y–axis | *M* (% $10^2$) | *S* (% $10^2$) | *K–S* | | Q–Q plot ($R^2$) | PDF cross–plot ($R^2$) |
|---|---|---|---|---|---|---|---|
| | | | | *Ds* | *p* (% $10^2$) | | |
| A1 | No–abr. (A) | 0.07 | 0.99 | 0.10 | 0.18 | 0.99 | 0.96 |
| A2 | No–abr. (A) | 0.25 | 0.96 | 0.26 | 1.64E–06 | 0.90 | 0.73 |
| A3 | No–abr. (A) | 0.20 | 0.97 | 0.21 | 7.36E–05 | 0.96 | 0.80 |
| A4 | No–abr. (A) | 0.09 | 0.99 | 0.08 | 0.26 | 0.98 | 0.96 |

Table S5.Statistical analysis of the experiments A1–A4 with synthetic age distributions (distribution 4) showing the PDFs analyzed (X–axis and Y–axis), area mismatch (M (% $10^2$)), similarity coefficient (S (% $10^2$)), distance (Ds) and probability (p (% $10^2$)) of K–S tests, and regression analysis of Q–Q plots and PDF cross–plots ($R^2$).

| X–axis | Y–axis | *M* (% $10^2$) | *S* (% $10^2$) | *K–S* | |
|---|---|---|---|---|---|
| | | | | *Ds* | *p* (% $10^2$) |
| A1 | No–abr. (A) | 0.16 | 0.98 | 0.12 | 0.10 |
| A2 | No–abr. (A) | 0.19 | 0.97 | 0.14 | 0.05 |
| A3 | No–abr. (A) | 0.25 | 0.95 | 0.23 | 0.00 |

| | | | | | |
|---|---|---|---|---|---|
| A4 | No–abr. (A) | 0.14 | 0.98 | 0.10 | 0.20 |

Table S6.Statistical analysis of the experiments A1–A4 with natural age distributions (Amidon et al., 2005a) showing the PDFs analyzed (X–axis and Y–axis), area mismatch (M (% $10^2$)), similarity coefficient (S (% $10^2$)), and distance (Ds) and probability (p (% $10^2$)) of K–S tests.

| Experiment | X–axis | Y–axis | | *M* (% $10^2$) | *S* (% $10^2$) | *K–S* | | Q–Q plot ($R^2$) | PDF cross–plot ($R^2$) |
|---|---|---|---|---|---|---|---|---|---|
| | | | | | | *Ds* | *p* (% $10^2$) | | |
| B2 | PDF [0.3 % mass loss] | PDF | [reference case] | 0.10 | 0.99 | 0.128 | 8.30E–02 | 0.99 | 0.94 |
| | PDF [1.0 % mass loss] | PDF | [reference case] | 0.20 | 0.97 | 0.222 | 4.00E–04 | 0.97 | 0.79 |
| | PDF [2.0 % mass loss] | PDF | [reference case] | 0.24 | 0.97 | 0.256 | 1.69E–05 | 0.96 | 0.74 |
| | PDF [4.0–31 % mass loss] | PDF | [reference case] | 0.25 | 0.96 | 0.262 | 1.77E–05 | 0.96 | 0.73 |
| B3 | PDF [ 2 mm/yr] | PDF | [reference case] | 0.15 | 0.99 | 0.166 | 1.30E–02 | 0.99 | 0.87 |
| | PDF [ 3 mm/yr] | PDF | [reference case] | 0.26 | 0.97 | 0.261 | 2.05E–05 | 0.96 | 0.73 |
| | PDF [ 4 mm/yr] | PDF | [reference case] | 0.33 | 0.94 | 0.332 | 6.65E–09 | 0.94 | 0.64 |
| | PDF [ 5.1 mm/yr] | PDF | [reference case] | 0.38 | 0.92 | 0.385 | 2.85E–13 | 0.91 | 0.58 |

| | | | | | | | | | |
|---|---|---|---|---|---|---|---|---|---|
| B4 | PDF [ 0.6 grain g–1] | PDF case] | [reference | 0.05 | 0.99 | 0.089 | 3.10E–01 | 1.00 | 0.98 |
| | PDF [ 0.4 grain g–1] | PDF case] | [reference | 0.15 | 0.98 | 0.168 | 1.00E–02 | 0.99 | 0.87 |
| | PDF [ 0.2 grain g–1] | PDF case] | [reference | 0.32 | 0.94 | 0.33 | 1.34E–08 | 0.94 | 0.64 |
| | PDF [ 0 grain g–1] | PDF case] | [reference | 0.72 | 0.52 | 0.728 | 1.01E–55 | 0.66 | 0.34 |
| B5 | 80% of gravel [at TTS] | PDF case] | [reference | 0.15 | 0.98 | 0.167 | 1.30E–02 | 0.99 | 0.87 |
| | 70% of gravel [at TTS] | PDF case] | [reference | 0.26 | 0.96 | 0.264 | 6.48E–06 | 0.96 | 0.73 |
| | 60% of gravel [at TTS] | PDF case] | [reference | 0.32 | 0.94 | 0.334 | 2.10E–08 | 0.94 | 0.64 |
| B5b | 80% of gravel [at LH] | PDF case] | [reference | 0.13 | 0.98 | 0.163 | 1.51E–02 | 0.99 | 0.90 |
| | 70% of gravel [at LH] | PDF case] | [reference | 0.22 | 0.97 | 0.246 | 1.30E–04 | 0.98 | 0.76 |

| | | | | | | | | |
|---|---|---|---|---|---|---|---|---|
| | 60% of gravel [at LH] | PDF [reference case] | 0.28 | 0.95 | 0.302 | 8.34E–07 | 0.97 | 0.66 |
| B6 | 60% of gravel + 31% mass loss [at TTS] | PDF [reference case] | 0.38 | 0.92 | 0.385 | 2.17E–13 | 0.91 | 0.58 |
| | 60% of gravel + 31% mass loss [at TTS] | 31% mass loss [at TTS] | 0.12 | 0.99 | 0.143 | 4.50E–02 | 0.99 | 0.97 |
| | 60% of gravel + 31% mass loss [at TTS] | 60% of gravel [at TTS] | 0.06 | 0.99 | 0.093 | 2.66E–01 | 1.00 | 0.99 |

Table S7.Statistical analysis of the experiments B2–B6 with synthetic age distributions (distribution 4) showing the PDFs analyzed (X–axis and Y–axis), area mismatch (M (% $10^2$)), similarity coefficient (S (% $10^2$)), and distance (Ds) and probability (p (% $10^2$)) of K–S tests.

| Experiment | X–axis | Y–axis | M (% $10^2$) | S (% $10^2$) | K–S | | Q–Q plot ($R^2$) | PDF cross–plot ($R^2$) |
|---|---|---|---|---|---|---|---|---|
| | | | | | Ds | p (% $10^2$) | | |
| B2 | PDF [0.3 % mass loss] | PDF [reference case] | 0.05 | 1.00 | 0.067 | 2.48E–01 | 1.00 | 0.97 |
| | PDF [1.0 % mass loss] | PDF [reference case] | 0.10 | 0.99 | 0.087 | 8.40E–02 | 0.99 | 0.92 |
| | PDF [2.0 % mass loss] | PDF [reference case] | 0.11 | 0.99 | 0.099 | 4.00E–02 | 0.99 | 0.90 |
| | PDF [4.0–31 % mass loss] | PDF [reference case] | 0.12 | 0.99 | 0.1 | 3.90E–02 | 0.99 | 0.89 |
| B3 | PDF [ 2 mm/yr] | PDF [reference case] | 0.06 | 1.00 | 0.065 | 2.62E–01 | 1.00 | 0.96 |
| | PDF [ 3 mm/yr] | PDF [reference case] | 0.11 | 0.99 | 0.086 | 8.70E–02 | 0.99 | 0.90 |
| | PDF [ 4 mm/yr] | PDF [reference case] | 0.14 | 0.99 | 0.103 | 2.90E–02 | 0.99 | 0.85 |
| | PDF [ 5.1 mm/yr] | PDF [reference case] | 0.17 | 0.98 | 0.118 | 9.60E–03 | 0.98 | 0.81 |
| B4 | PDF [ 0.6 grain g–1] | PDF [reference case] | 0.03 | 1.00 | 0.05 | 4.56E–01 | 1.00 | 0.99 |
| | PDF [ 0.4 grain g–1] | PDF [reference case] | 0.06 | 1.00 | 0.064 | 2.73E–01 | 1.00 | 0.96 |
| | PDF [ 0.2 grain g–1] | PDF [reference case] | 0.14 | 0.99 | 0.103 | 2.90E–02 | 0.99 | 0.85 |
| | PDF [ 0 grain g–1] | PDF [reference case] | 0.31 | 0.90 | 0.218 | 5.40E–07 | 0.94 | 0.52 |
| B5 | 80% of gravel [at TTS] | PDF [reference case] | 0.07 | 1.00 | 0.063 | 2.80E–01 | 1.00 | 0.96 |

| | | | | | | | | |
|---|---|---|---|---|---|---|---|---|
| | 70% of gravel [at TTS] | PDF [reference case] | 0.11 | 0.99 | 0.085 | 9.20E–02 | 0.99 | 0.90 |
| | 60% of gravel [at TTS] | PDF [reference case] | 0.14 | 0.99 | 0.102 | 3.20E–02 | 0.99 | 0.85 |
| B5b | 80% of gravel [at LH] | PDF [reference case] | 0.13 | 0.99 | 0.14 | 1.00E–03 | 0.98 | 0.86 |
| | 70% of gravel [at LH] | PDF [reference case] | 0.22 | 0.97 | 0.223 | 1.35E–08 | 0.96 | 0.69 |
| | 60% of gravel [at LH] | PDF [reference case] | 0.28 | 0.95 | 0.275 | 1.80E–13 | 0.94 | 0.57 |
| B6 | 60% of gravel + 31% mass loss [at TTS] | PDF [reference case] | 0.18 | 0.98 | 0.145 | 1.35E–03 | 0.98 | 0.79 |
| | 60% of gravel + 31% mass loss [at TTS] | 31% mass loss [at TTS] | 0.06 | 1.00 | 0.064 | 2.71E–01 | 1.00 | 0.98 |
| | 60% of gravel + 31% mass loss [at TTS] | 60% of gravel [at TTS] | 0.04 | 1.00 | 0.063 | 2.93E–01 | 1.00 | 0.99 |

Table S8.Statistical analysis of the experiments B2–B6 with natural age distributions (Amidon et al., 2005a) showing the PDFs analyzed (X–axis and Y–axis), area mismatch (M (% $10^2$)), similarity coefficient (S (% $10^2$)), and distance (Ds) and probability (p (% $10^2$)) of K–S tests.

| X–axis | Y–axis | *M* (% $10^2$) | *S* (% $10^2$) | *K–S* | |
|---|---|---|---|---|---|
| | | | | *Ds* | *p* (% $10^2$) |
| B2 [Others] | B2 [Abrasion] | 0 | 1 | 0 | 1 |
| B3 [Gravel fraction] | B3 [Erosion] | 0.09 | 0.99 | 0.11 | 0.14 |
| B3 [Abrasion] | B3 [Erosion] | 0.128 | 0.99 | 0.14 | 4.00E–02 |
| B3 [Fertility] | B3 [Erosion] | 0 | 1 | 0 | 1 |
| B4 [Gravel fraction] | B4 [Fertility] | 0.43 | 0.74 | 0.44 | 1.26E–18 |
| B4 [Erosion] | B4 [Fertility] | 0.34 | 0.809 | 0.352 | 3.31E–12 |
| B4 [Abrasion] | B4 [Fertility] | 0.8 | 0.43 | 0.8 | 4.78E–75 |
| B5b [Abrasion] | B5b [Gravel fraction] | 0.05 | 0.99 | 0.08 | 0.3 |
| B5b [Others] | B5b [Gravel fraction] | 0 | 1 | 0 | 1 |
| B6 [Gravel fraction] | B6 [Abr + Grav] | 0.05 | 0.99 | 0.085 | 3.30E–01 |
| B6 [Abrasion] | B6 [Abr + Grav] | 0.074 | 0.99 | 0.101 | 0.219 |
| B6 [Others] | B6 [Abr + Grav] | 0 | 1 | 0 | 1 |

Table S9.Statistical analysis of the ability of a given "tested" factor (X–axis) to reproduce the distortion created by a given "targeted" factor (Y–axis) using synthetic age distributions (distribution 4). The two PDFs are compared and the table show area mismatch (M (% $10^2$)), similarity coefficient (S (% $10^2$)), and distance (Ds) and probability (p (% $10^2$)) of K–S tests.

| X–axis | Y–axis | *M* (% $10^2$) | *S* (% $10^2$) | *K–S* | |
|---|---|---|---|---|---|
| | | | | *Ds* | *p* (% $10^2$) |
| B2 [Others] | B2 [Abrasion] | 0 | 1 | 0 | 1 |
| B3 [Gravel fraction] | B3 [Erosion] | 0.044 | 0.99 | 0.05 | 0.361 |
| B3 [Abrasion] | B3 [Erosion] | 0.04 | 0.99 | 0.05 | 4.10E–01 |
| B3 [Fertility] | B3 [Erosion] | 0 | 1 | 0 | 1 |

| | | | | | |
|---|---|---|---|---|---|
| B4 [Gravel fraction] | B4 [Fertility] | 0.195 | 0.95 | 0.14 | 0.00127 |
| B4 [Erosion] | B4 [Fertility] | 0.151 | 0.96 | 0.1 | 1.60E–02 |
| B4 [Abrasion] | B4 [Fertility] | 0.47 | 0.821 | 0.4 | 6.57E–33 |
| B5b [Abrasion] | B5b [Gravel fraction] | 0.04 | 0.99 | 0.066 | 0.26 |
| B5b [Others] | B5b [Gravel fraction] | 0 | 1 | 0 | 1 |
| B6 [Gravel fraction] | B6 [Abr + Grav] | 0.04 | 0.99 | 0.06 | 0.27 |
| B6 [Abrasion] | B6 [Abr + Grav] | 0.03 | 0.99 | 0.05 | 0.41 |
| B6 [Others] | B6 [Abr + Grav] | 0 | 1 | 0 | 1 |

Table S10.Statistical analysis of the ability of a given "tested" factor (X–axis) to reproduce the distortion created by a given "targeted" factor (Y–axis) using natural age distributions (Amidon et al., 2006a). The two PDFs are compared and the table show area mismatch (M (% $10^2$)), similarity coefficient (S (% $10^2$)), and distance (Ds) and probability (p (% $10^2$)) of K–S tests.

Table S11. Statistical analysis of the experiments A1–A4 and end–members of B2–B6 for all age distributions, including the five synthetic distributions (one sheet / distribution). Tables show the PDFs analyzed (X–axis and Y–axis), area mismatch (M (% $10^2$)), similarity coefficient (S (% $10^2$)), and distance (Ds) and probability (p (% $10^2$)) of K–S tests. Top four rows show similar information to Tables S5 and S6; bottom four rows show similar information to Tables S7 and S8 but for end–member scenarios for each experiment.

< Table S11> Table too large and uploaded as a separate file.

Table S12.Statistical analysis of the ability of a given "tested" factor (X–axis) to reproduce the distortion created by a given "targeted" factor (Y–axis) for all age distributions, including the five synthetic distributions (one sheet / distribution). Tables show the PDFs analyzed (X–axis and Y–axis), area mismatch (M (% $10^2$)), similarity coefficient (S (% $10^2$)), and distance (Ds) and probability (p (% $10^2$)) of K–S tests. These tables show similar information to Tables S9–S10 but for all synthetic distributions.

< Table S12> Table too large and uploaded as a separate file.

Table S13.Relative values (%) and error (% $10^2$) of optimizations trying to reproduce the distortion caused by abrasion in scenario B2 (Tethyan Series rocks abraded at 31 %/km while others are abraded at 0.15 %/km) by varying each of the other factors (relative erosion rate, fertility and gravel supply) within a range of realistic values.

| Source unit | Erosion rate (%) | Fertility (%) | Gravel supply (%) |
|---|---|---|---|
| Tethyan Series | 49 | 49 | 49 |
| Formation II–III | 19 | 19 | 19 |
| Formation I | 17 | 17 | 17 |
| Lesser Himalaya | 15 | 15 | 15 |
| Minimisation error | 1.8E–05 | 0.00023 | 1.2E–05 |

Table S14.Zircon mixing proportion and erosion rates estimated for the sampling site E (Marsyandi).

| Source unit | Best–fit | No–abrasion | | Abrasion | |
|---|---|---|---|---|---|
| | Mixing proportio | Mixing proportio | Relative erosion | Mixing proportio | Relative erosion |

| | n (%) | n (%) | (%) | n (%) | (%) |
|---|---|---|---|---|---|
| Tethyan Series | 68 | 75 | 42 | 81 | 29 |
| Formation II–III | 31 | 25 | 58 | 19 | 71 |

Table S15.Zircon mixing proportion and erosion rates estimated for the sampling site G (Marsyandi).

| Source unit | Best–fit | No–abrasion | | Abrasion | |
|---|---|---|---|---|---|
| | Mixing proportion (%) | Mixing proportion (%) | Relative erosion (%) | Mixing proportion (%) | Relative erosion (%) |
| Tethyan Series | 60 | 53 | 40 | 65 | 29 |
| Formation II–III | 19 | 19 | 34 | 19 | 31 |
| Formation I | 21 | 28 | 26 | 16 | 39 |

Table S16.Zircon mixing proportion and erosion rates estimated for the sampling site K (Marsyandi).

| Source unit | Best–fit | No–abrasion | | Abrasion | |
|---|---|---|---|---|---|
| | Mixing proportion (%) | Mixing proportion (%) | Relative erosion (%) | Mixing proportion (%) | Relative erosion (%) |
| Tethyan Series | 38 | 31 | 28 | 34 | 27 |
| Formation II–III | 11 | 11 | 24 | 12 | 24 |
| Formation I | 16 | 38 | 10 | 33 | 12 |
| Lesser Himalaya | 33 | 20 | 38 | 22 | 37 |

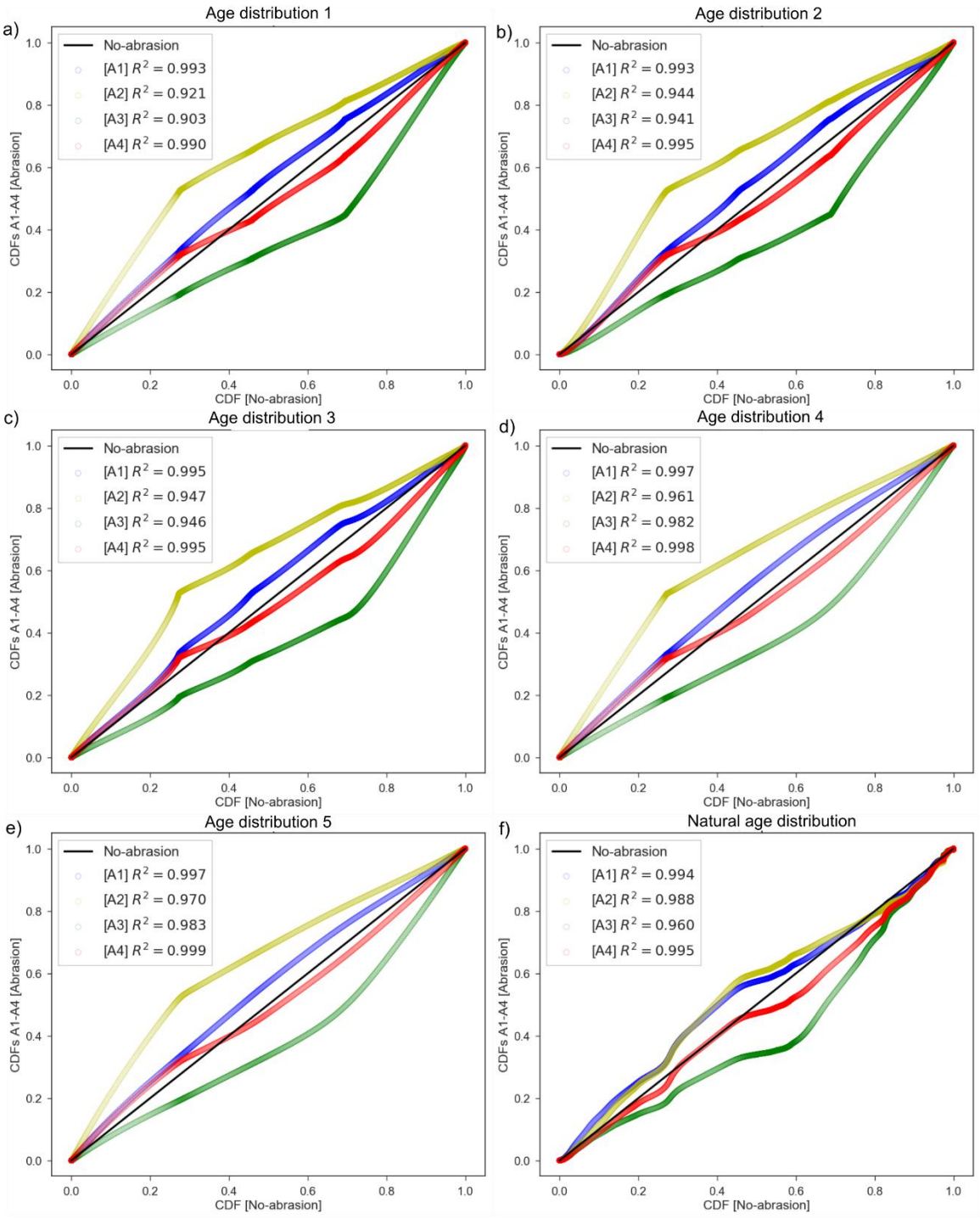


Figure S1.Q–Q plots of experiments A1–A4 with the five synthetic U–Pb age distributions (a–e) and the natural one (f). Results from these experiments are presented in Fig. 2.4.

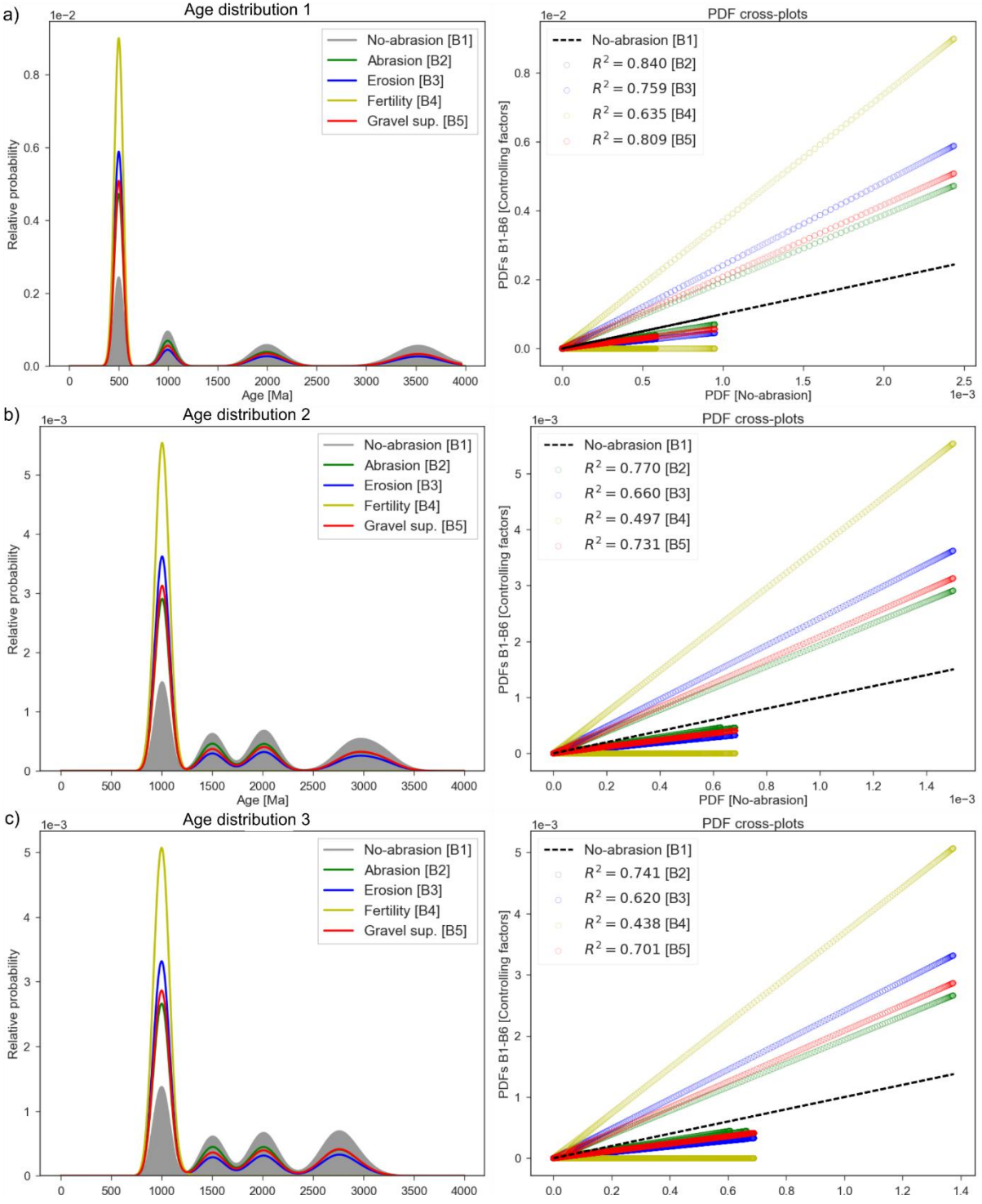
a)
Age distribution 1
1e−2
Relative probability
Age [Ma]
No-abrasion [B1]
Abrasion [B2]
Erosion [B3]
Fertility [B4]
Gravel sup. [B5]
PDF cross-plots
PDFs B1-B6 [Controlling factors]
PDF [No-abrasion]
1e−3
$R^2$ = 0.840 [B2]
$R^2$ = 0.759 [B3]
$R^2$ = 0.635 [B4]
$R^2$ = 0.809 [B5]
b)
Age distribution 2
1e−3
$R^2$ = 0.770 [B2]
$R^2$ = 0.660 [B3]
$R^2$ = 0.497 [B4]
$R^2$ = 0.731 [B5]
c)
Age distribution 3
$R^2$ = 0.741 [B2]
$R^2$ = 0.620 [B3]
$R^2$ = 0.438 [B4]
$R^2$ = 0.701 [B5]

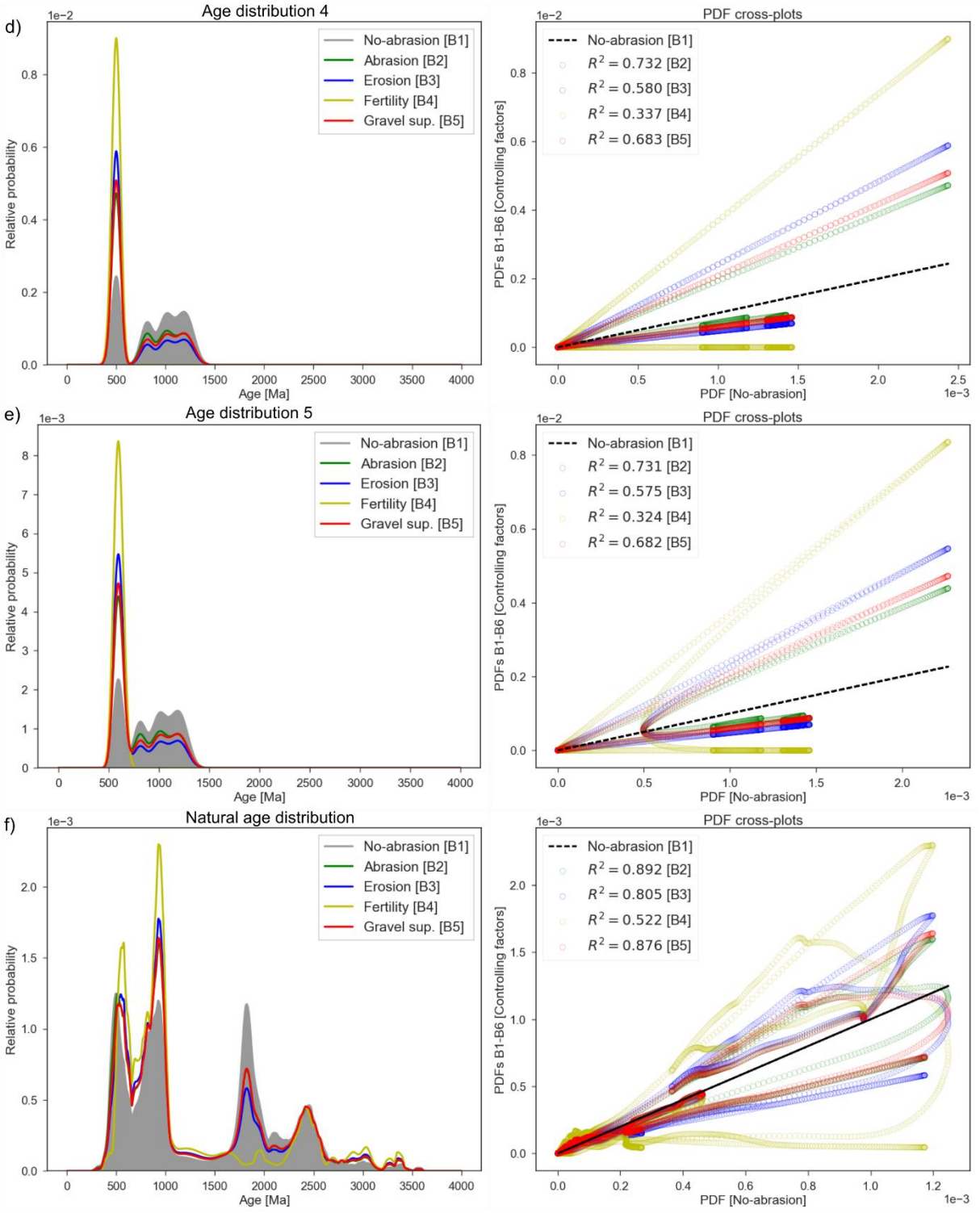


Figure S2.Probability density plots (left) and PDF cross–plots (right) of the end–member scenarios from experiments B2–B5 (Table 2.3). This figure display similar information to Fig. 2.6 but includes results for all synthetic age distributions (a–e). Statistical assessment of this complete dataset can be found in Fig. S3 (Q–Q plots) and Table S11.

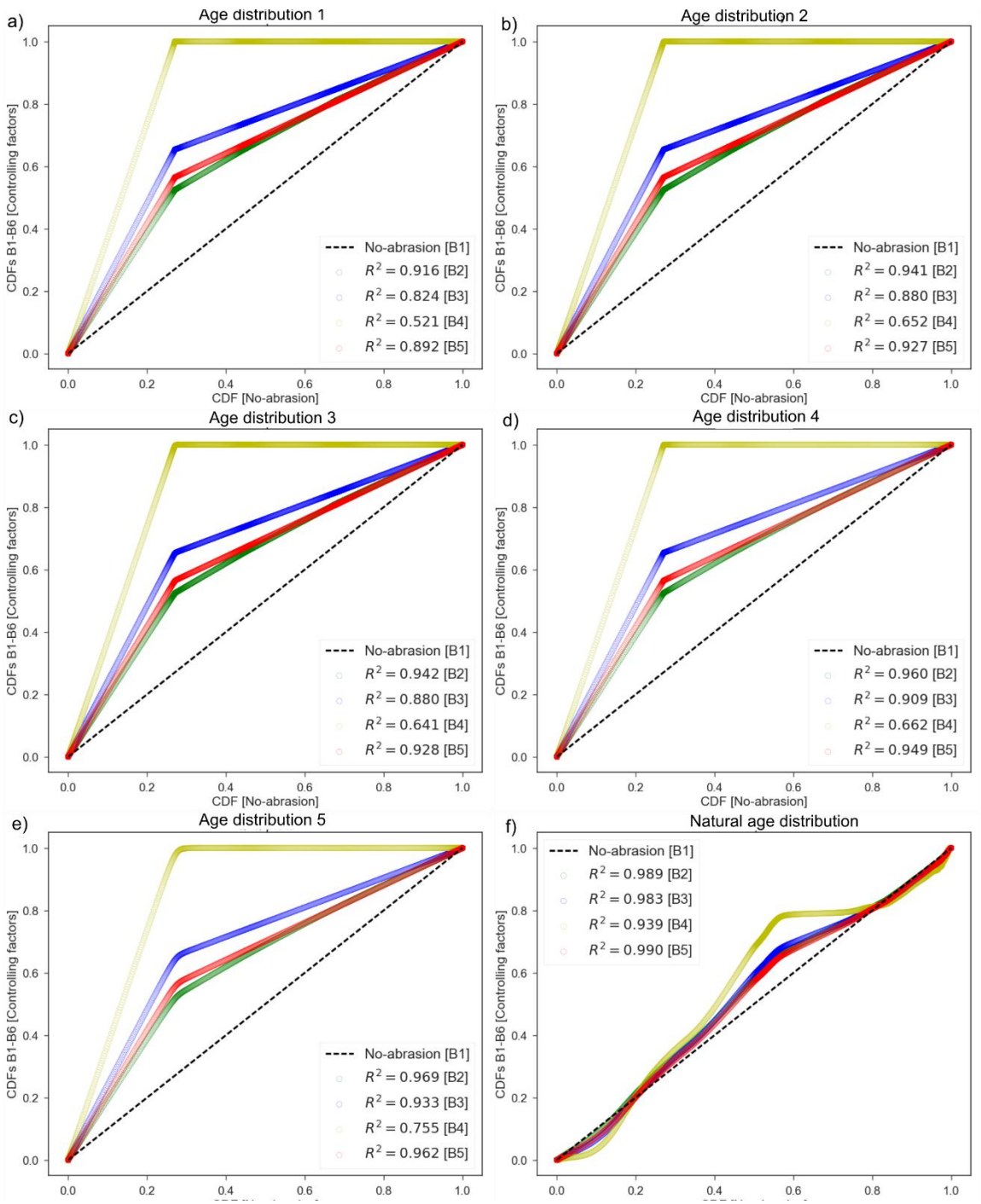


Figure S3.Q–Q plots of end–member scenarios in the experiments B2–B5 with the five synthetic U–Pb age distributions (a–e) and the natural one (f). Results from these experiments are presented in Fig. S2.

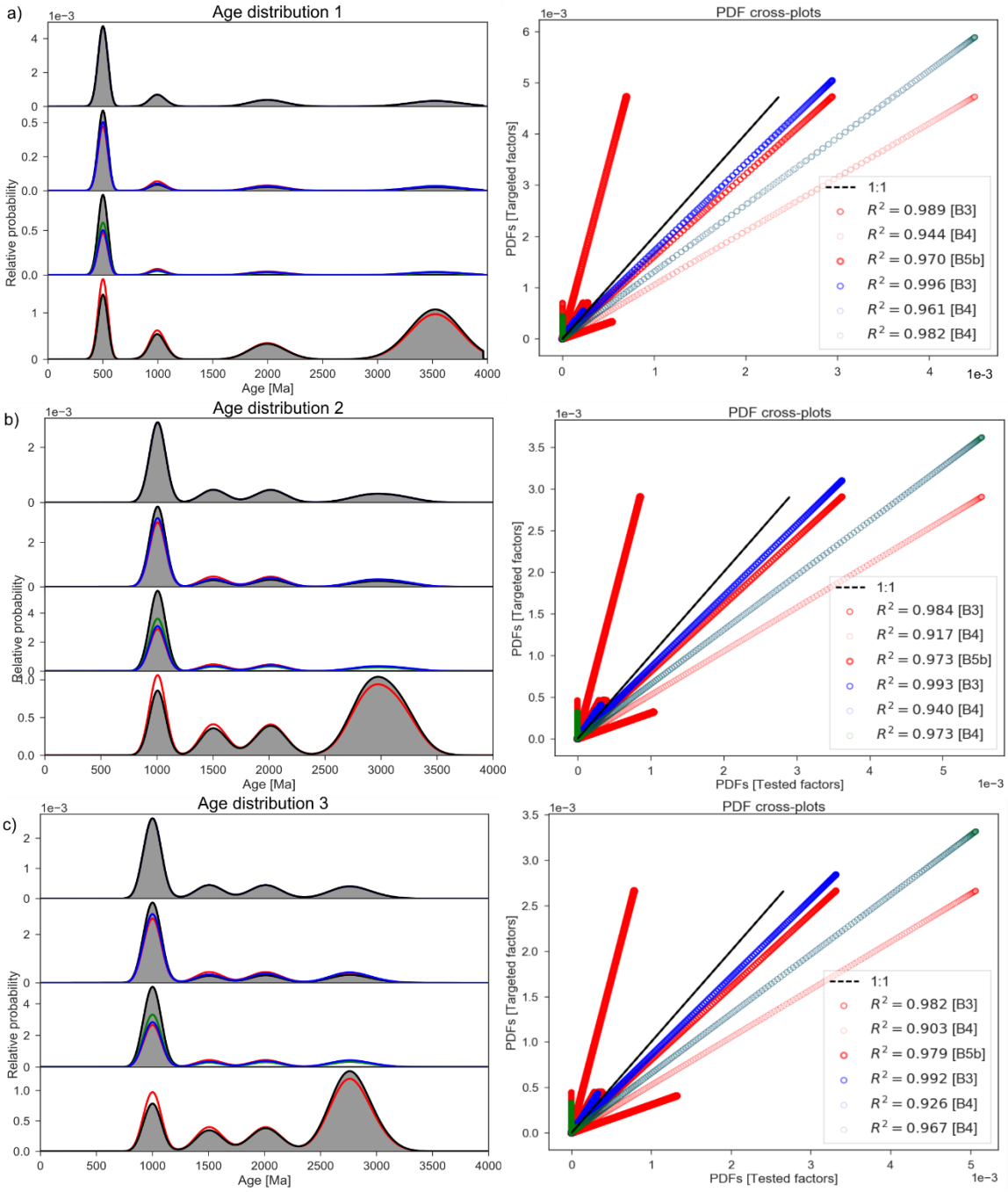
a)
Age distribution 1
1e−3
Relative probability
Age [Ma]
PDF cross-plots
PDFs [Targeted factors]
PDFs [Tested factors]
1:1
$R^2$ = 0.989 [B3]
$R^2$ = 0.944 [B4]
$R^2$ = 0.970 [B5b]
$R^2$ = 0.996 [B3]
$R^2$ = 0.961 [B4]
$R^2$ = 0.982 [B4]
b)
Age distribution 2
$R^2$ = 0.984 [B3]
$R^2$ = 0.917 [B4]
$R^2$ = 0.973 [B5b]
$R^2$ = 0.993 [B3]
$R^2$ = 0.940 [B4]
$R^2$ = 0.973 [B4]
c)
Age distribution 3
$R^2$ = 0.982 [B3]
$R^2$ = 0.903 [B4]
$R^2$ = 0.979 [B5b]
$R^2$ = 0.992 [B3]
$R^2$ = 0.926 [B4]
$R^2$ = 0.967 [B4]

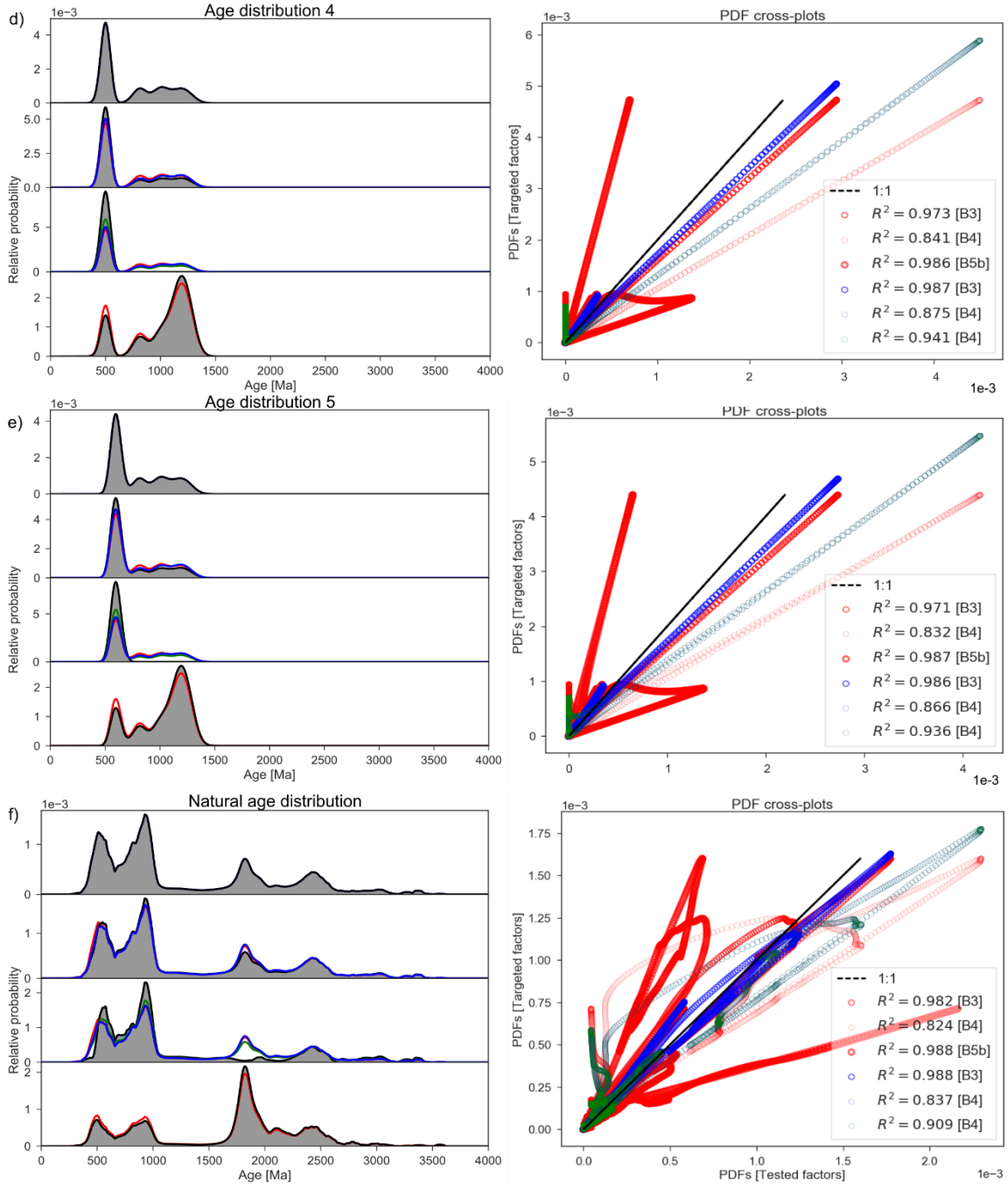


Figure S4: Results of the numerical simulations comparing the ability of each controlling factor to reproducing the distortions of abrasion (B2), erosion (B3), fertility (B4), hillslope gravel supply (B5b) and the coupled effect of abrasion and hillslope gravel supply (B6) in the zircon age populations (PDPs). Probability density plots (PDPs, left) and PDF cross–plots (right) of the experiments. This figure display similar information to Fig. 6 but includes results for all synthetic age distributions (a–e). PDPs compare the distribution created by varying a given factor (grey) with the best fit distributions obtained by varying the other parameters (curves). Factors that can perfectly reproduce the distribution are grouped in "Others". PDF cross–plots and compare how the (tested) factors can reproduce a distortion caused by a specific (targeted) factor; thickness of circles refers to scenario, whereas colour refers to tested factor. Statistical assessment of this complete dataset can be found in Table S12.

## 8.2.Chapter 3

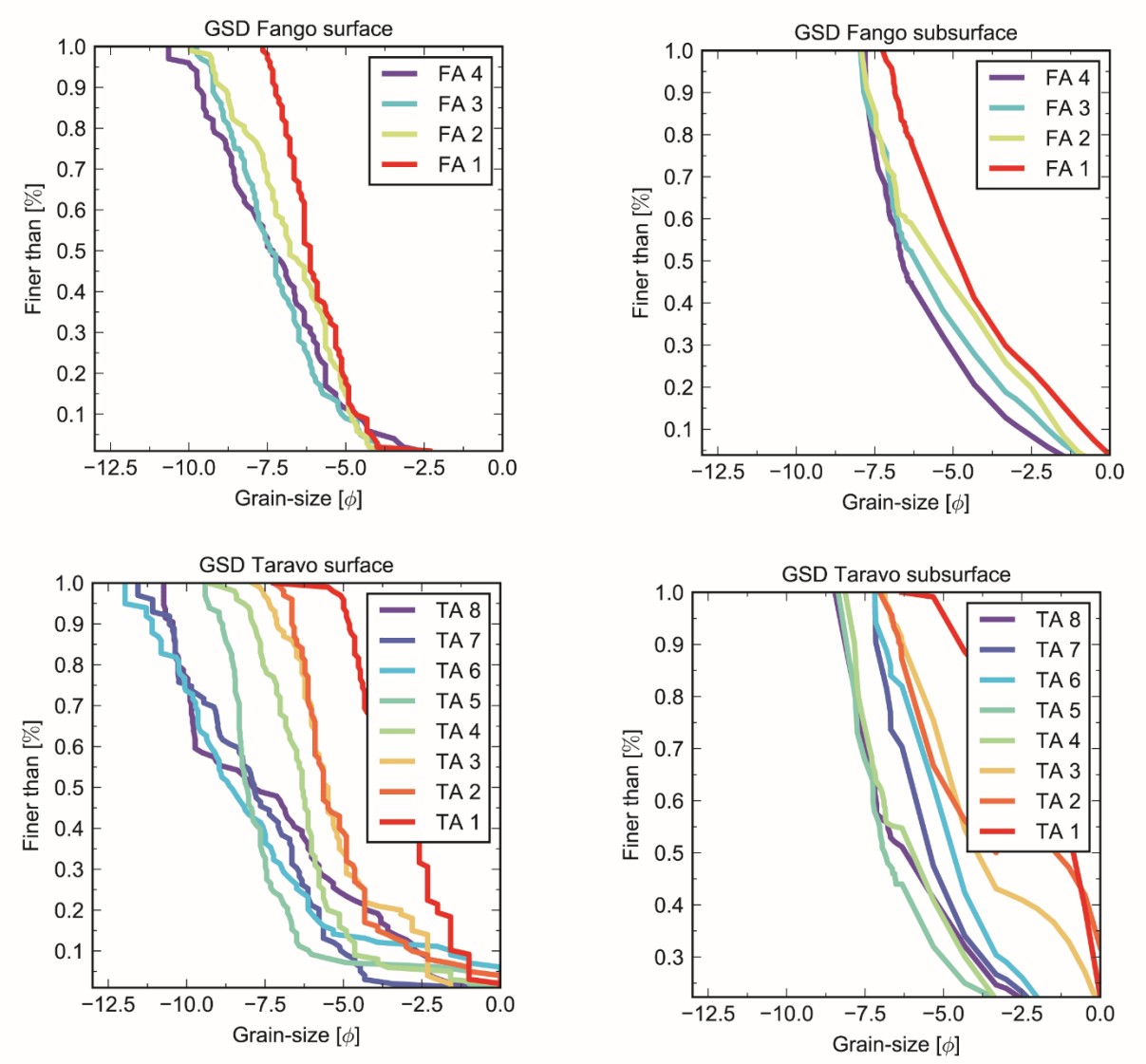


Figure S1: Cumulative grain size distribution (GSD) of the analysed gravel bars in Corsica. Higher numbers (e.g., FA 4) refer to upstream samples, while decreasing numbers (e.g., FA 1) are closer to the catchment outlet.

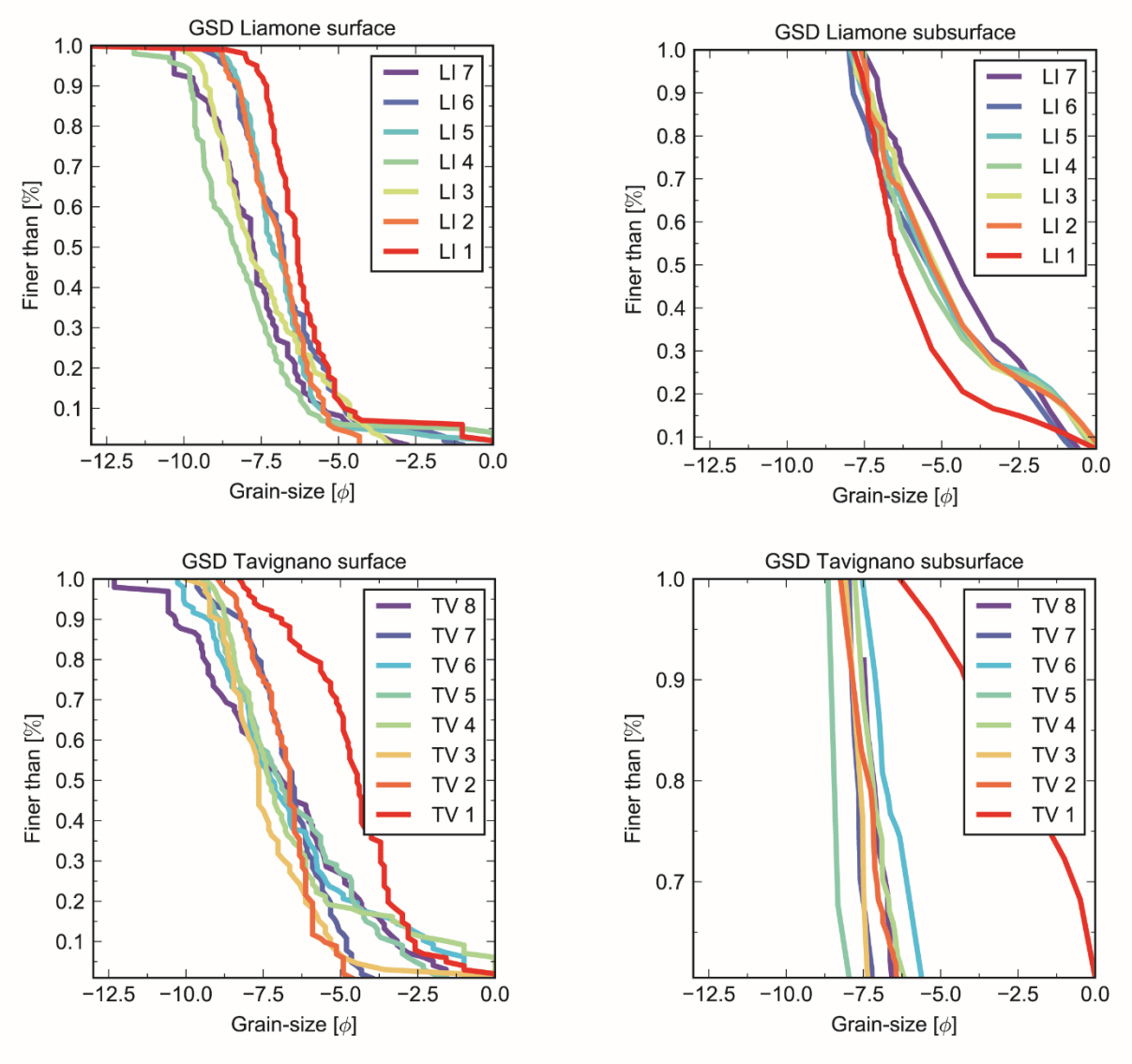


Figure S2: Grain size distribution per rock type in every sampling site analysed in the Fango, Liamone, Taravo and Tavignano watersheds (displayed in A, B, C and D plots, respectively).

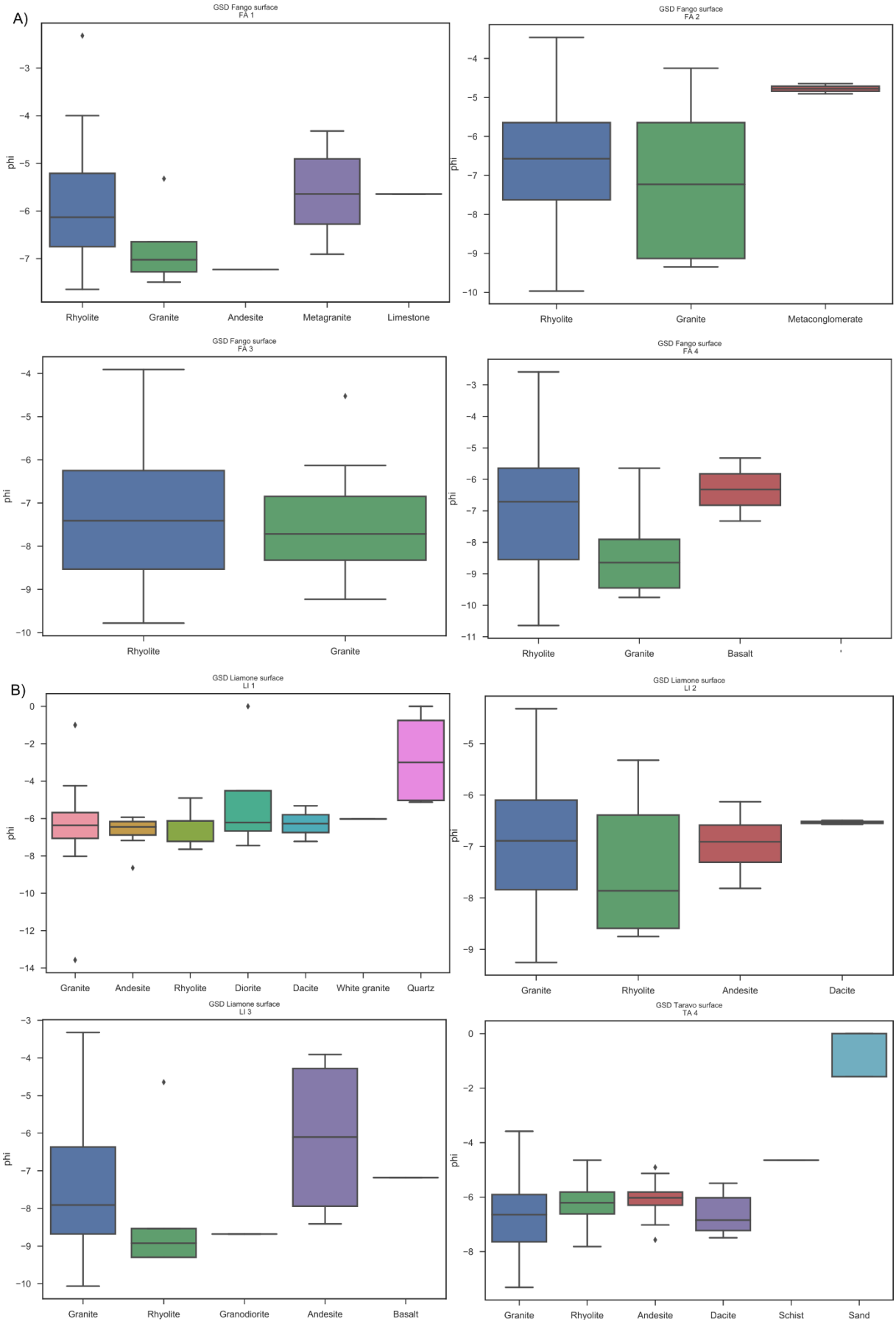
A)
GSD Fango surface
FA 1
phi
Rhyolite
Granite
Andesite
Metagranite
Limestone
GSD Fango surface
FA 2
phi
Rhyolite
Granite
Metaconglomerate
GSD Fango surface
FA 3
phi
Rhyolite
Granite
GSD Fango surface
FA 4
phi
Rhyolite
Granite
Basalt
B)
GSD Liamone surface
LI 1
phi
Granite
Andesite
Rhyolite
Diorite
Dacite
White granite
Quartz
GSD Liamone surface
LI 2
phi
Granite
Rhyolite
Andesite
Dacite
GSD Liamone surface
LI 3
phi
Granite
Rhyolite
Granodiorite
Andesite
Basalt
GSD Taravo surface
TA 4
phi
Granite
Rhyolite
Andesite
Dacite
Schist
Sand

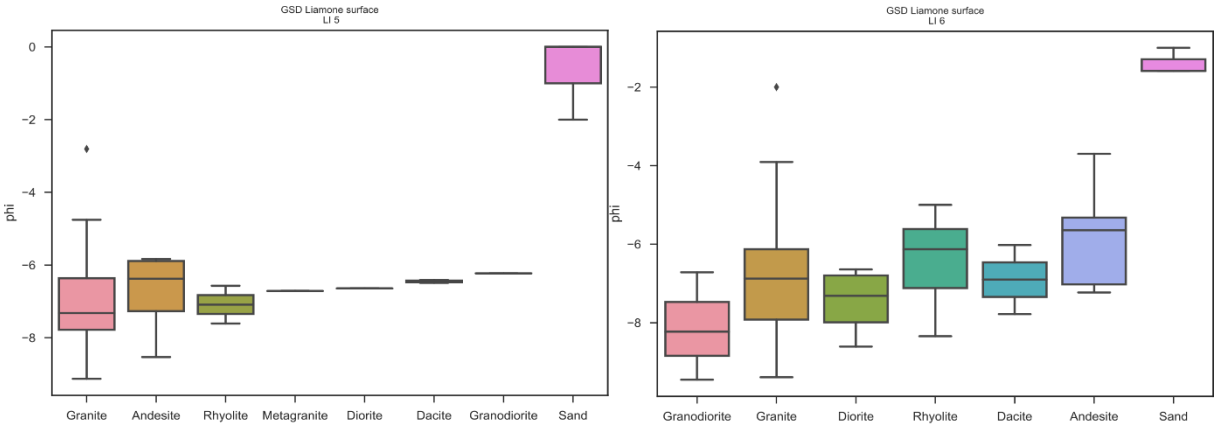
GSD Liamone surface
LI 5
phi
Granite
Andesite
Rhyolite
Metagranite
Diorite
Dacite
Granodiorite
Sand
GSD Liamone surface
LI 6
phi
Granodiorite
Granite
Diorite
Rhyolite
Dacite
Andesite
Sand

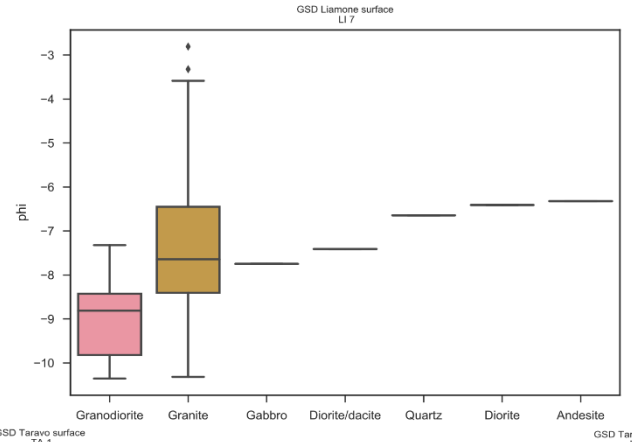
GSD Liamone surface
LI 7
phi
Granodiorite
Granite
Gabbro
Diorite/dacite
Quartz
Diorite
Andesite

C)

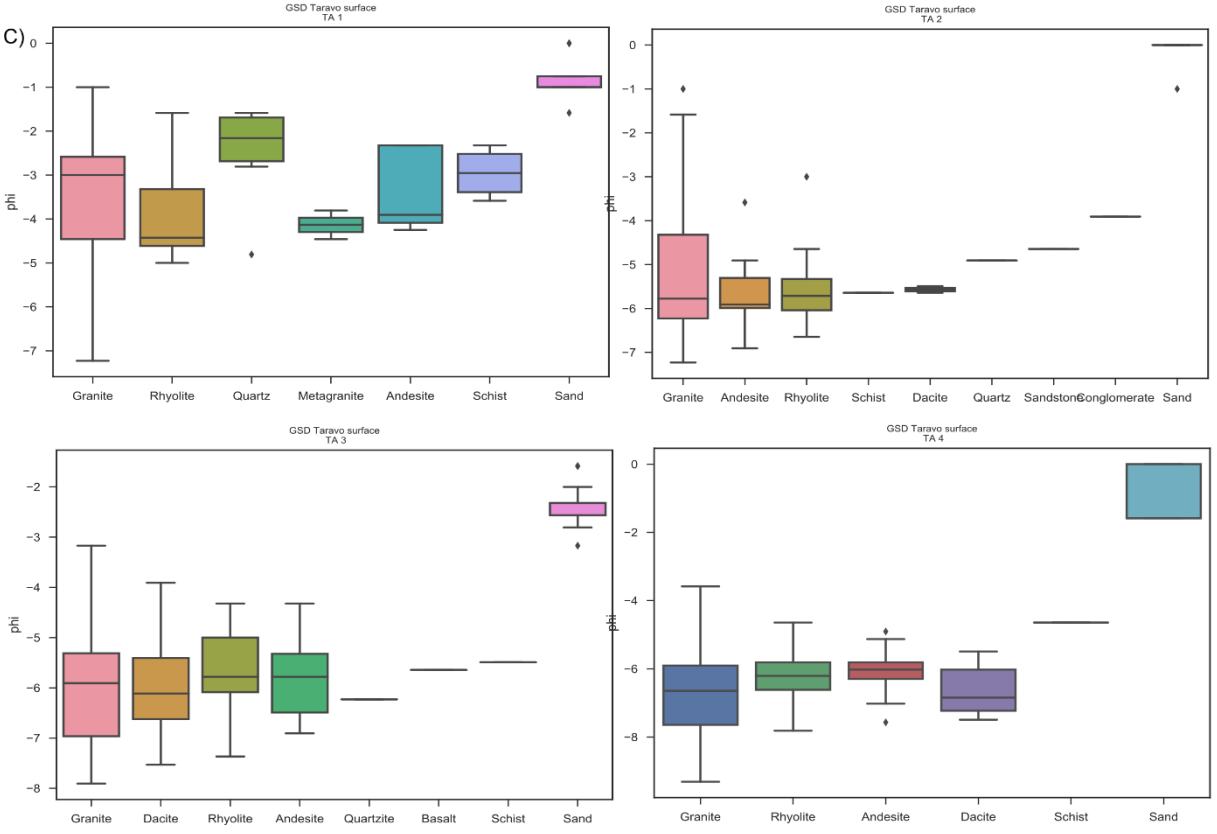
GSD Taravo surface
TA 1
phi
Granite
Rhyolite
Quartz
Metagranite
Andesite
Schist
Sand
GSD Taravo surface
TA 2
phi
Granite
Andesite
Rhyolite
Schist
Dacite
Quartz
Sandstone
Conglomerate
Sand


GSD Taravo surface
TA 3
phi
Granite
Dacite
Rhyolite
Andesite
Quartzite
Basalt
Schist
Sand
GSD Taravo surface
TA 4
phi
Granite
Rhyolite
Andesite
Dacite
Schist
Sand

D)

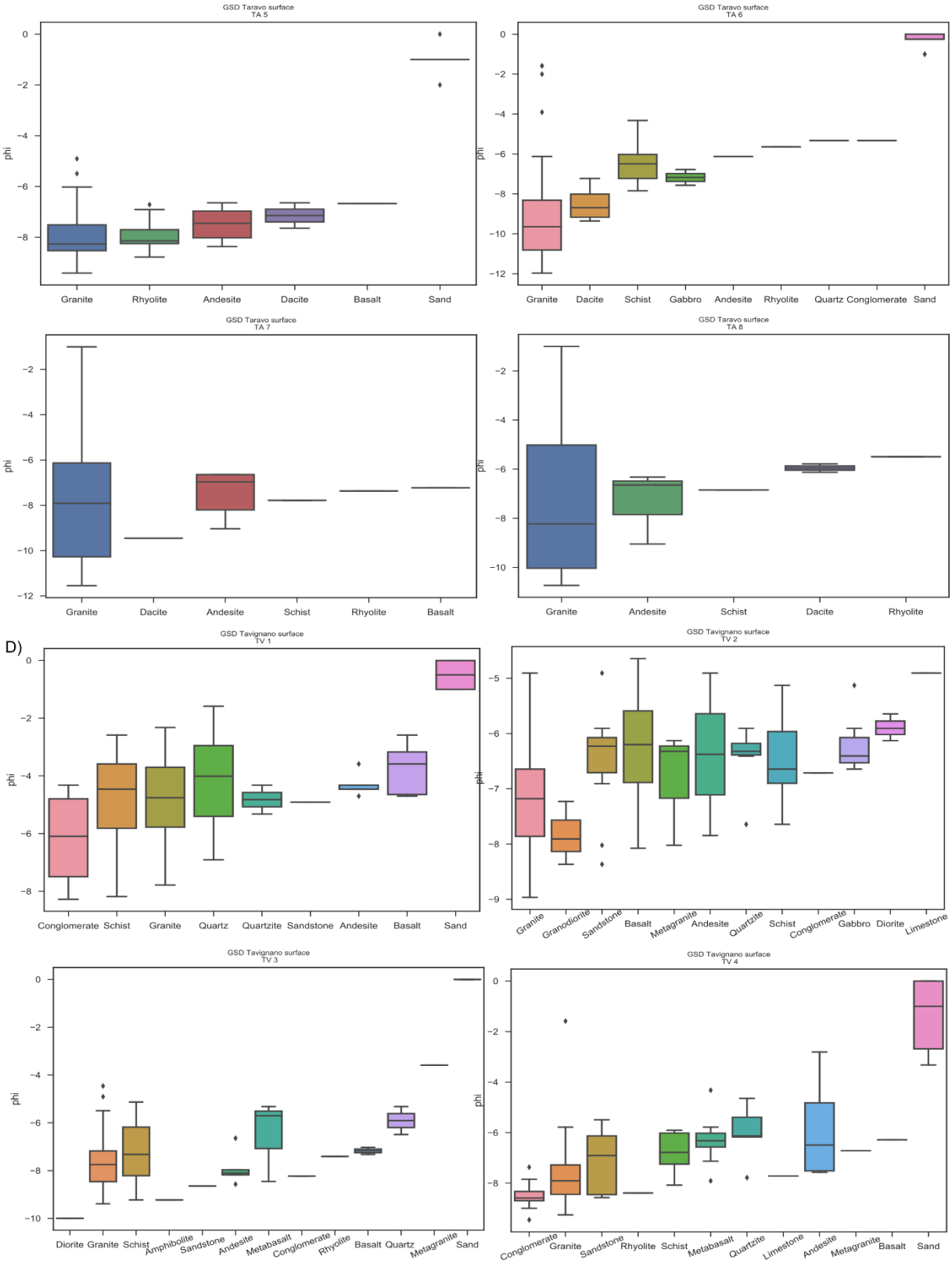
GSD Taravo surface
TA 5
phi
Granite
Rhyolite
Andesite
Dacite
Basalt
Sand
GSD Taravo surface
TA 6
phi
Granite
Dacite
Schist
Gabbro
Andesite
Rhyolite
Quartz Conglomerate
Sand
GSD Taravo surface
TA 7
phi
Granite
Dacite
Andesite
Schist
Rhyolite
Basalt
GSD Taravo surface
TA 8
phi
Granite
Andesite
Schist
Dacite
Rhyolite
GSD Tavignano surface
TV 1
phi
Conglomerate
Schist
Granite
Quartz
Quartzite
Sandstone
Andesite
Basalt
Sand
GSD Tavignano surface
TV 2
phi
Granite
Granodiorite
Sandstone
Basalt
Metagranite
Andesite
Quartzite
Schist
Conglomerate
Gabbro
Diorite
Limestone
GSD Tavignano surface
TV 3
phi
Diorite
Granite
Schist
Amphibolite
Sandstone
Andesite
Metabasalt
Conglomerate
Rhyolite
Basalt
Quartz
Metagranite
Sand
GSD Tavignano surface
TV 4
phi
Conglomerate
Granite
Sandstone
Rhyolite
Schist
Metabasalt
Quartzite
Limestone
Andesite
Metagranite
Basalt
Sand

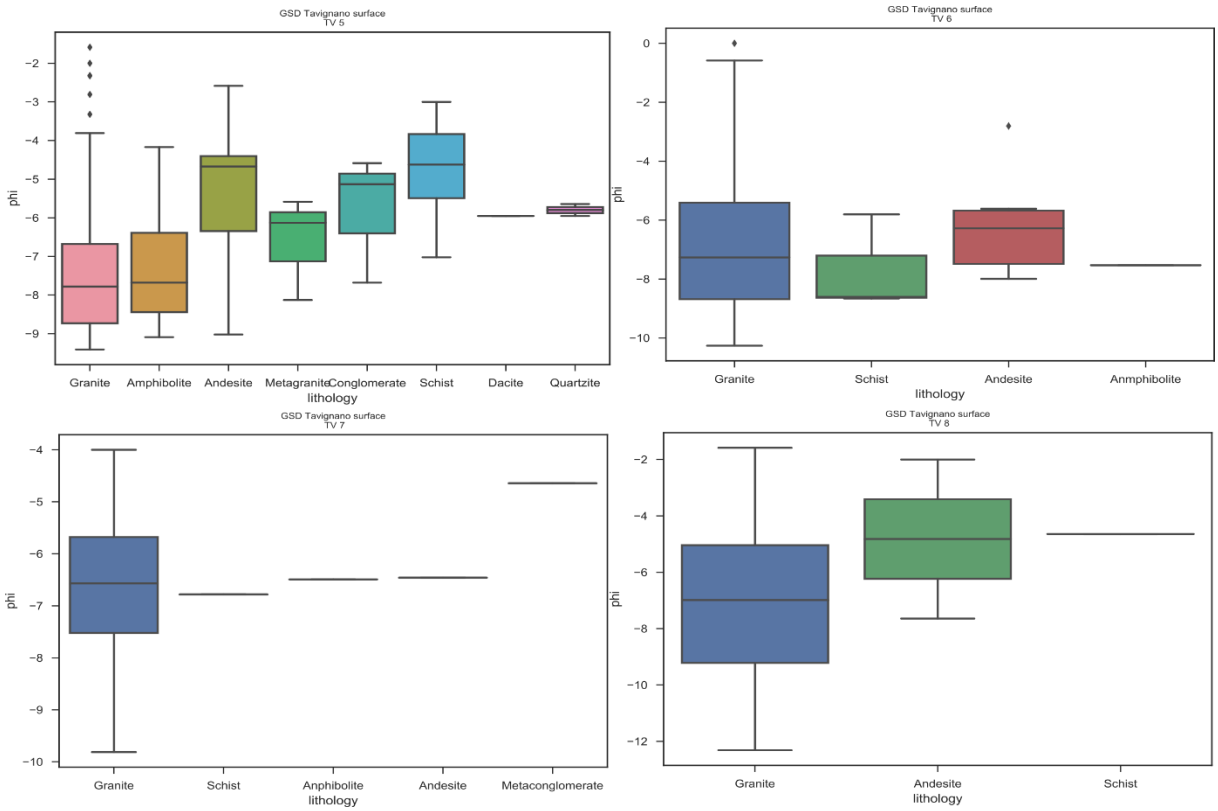


Figure S3: Grain size distribution per rock type in every sampling site analysed in the Fango, Liamone, Taravo and Tavignano watersheds (displayed in A, B, C and D plots, respectively).

Table S1: *t*–tests comparing if the means of knickpoints' metrics are statistically equal among the major rock type units of Corsica. SP refers to Sedimentary plains (Marana and Aleria), SL refers to the Schistes Lustrés units, and HC refers to the Hercynian Corsica. Note that in cases where $p < 0.05$, I can reject that the compared groups have equal means. For example, the magnitude of the knickpoints in SP and SL can be reject as equal, because of their $p < 0.001$, with 95% of confidence.

| Rock type unit | Magnitude [m] | | Relief [m] | | Slope [degrees] | | Length [m] | |
|---|---|---|---|---|---|---|---|---|
| | *p* | *t-test* | *p* | *t-test* | *p* | *t-test* | *p* | *t-test* |
| SP x SL | 1.24E-02 | 9.90E-01 | 1.81E-03 | 9.99E-01 | 2.55814E-06 | 1.00E+00 | 6.35E-01 | 5.26E-01 |
| SP x WC | 1.65E-04 | 1.00E+00 | 5.84E-05 | 1.00E+00 | 3.99925E-08 | 1.00E+00 | 4.59E-01 | 6.46E-01 |
| SL x WC | 5.46E-02 | 9.56E-01 | 7.84E-04 | 9.99E-01 | 3.26361E-16 | 1.00E+00 | 3.19E-01 | 7.49E-01 |

Table S2: Metrics of knickpoints draining westward and eastward from the border of the drainage divide of Corsica. Only the closest knickpoint to each channel head was considered in this analysis.

| Control group | Magnitude [m] | | Relief [m] | | Slope [degrees] | | Length [m] | |
|---|---|---|---|---|---|---|---|---|
| | *p* | *t*–test | *p* | *t*–test | *p* | *t*–test | *p* | *t*–test |
| Southern drainage divide (A) | 8.97E–02 | 9.29E–01 | 3.82E–02 | 9.70E–01 | 1.81E–04 | 1.00E+00 | 9.01E–01 | 3.68E–01 |
| Northern drainage divide (B) | 0.717805 | 4.73E–01 | 0.338555 | 7.35E–01 | 0.000202 | 1.00E+00 | 0.548529 | 5.83E–01 |

Table S3: Average values of magnitude, relief, slope and length of knickpoints according to their location. The groups analysed here are those knickpoints on former glacier extension, on the whole Corsica, and in the zircon fission track groups mapped by Danisik et al. (2007) and displayed in the Fig.3.2.

| Control group | Magnitude [m] | Relief [m] | Slope [degrees] | Length [m] |
|---|---|---|---|---|
| Former glaciers | 32.2 | 100.4 | 14.8 | 408.7 |
| Whole Corsica | 27.0 | 77.2 | 10.7 | 410.1 |
| ZFT 1 | 26.7 | 74.3 | 10.1 | 414.7 |
| ZFT 2 | 30.3 | 88.5 | 12.5 | 409.2 |
| ZFT 3 | 22.2 | 64.5 | 9.1 | 390.5 |

Table S4: Metrics of knickpoints' are compared to the previous Würmian glaciers, apatite (AFT) and zircon fission–track (ZFT) domains compiled from the works of Cavazza et al. (2001), Zarki–Jakni et al. (2004), Fellin et al. (2005) and Danišík et al. (2007). These domains are displayed in the Figure 2A and C. The extension of the Würmian glaciers in Corsica follows the mapping of Kuhlemann et al. (2005b) displayed in the Figure 3.1. The ages were extracted from the figure Figure 3.2 using the function extract data to point in ArcGIS.

| Control group | Magnitude [m] | | Relief [m] | | Slope [degrees] | | Length [m] | |
|---|---|---|---|---|---|---|---|---|
| | *p* | *t*–test | *p* | *t*–test | *p* | *t*–test | *p* | *t*–test |
| Former glaciers vs Corsica | 1.99E–01 | 8.43E–01 | 2.67E–03 | 9.98E–01 | 2.09E–18 | 1.00E+00 | 9.66E–01 | 3.34E–01 |
| | 9.89E– | 3.24E | 5.96E | 5.52E– | 1.17E | 9.07E– | 3.30E | 7.42E |

| | | | | | | | | |
|---|---|---|---|---|---|---|---|---|
| | 01 | –01 | –01 | 01 | –01 | 01 | –01 | –01 |
| AFT 1 x AFT 3 | 3.67E–01 | 7.15E–01 | 6.07E–01 | 5.46E–01 | 5.22E–02 | 9.58E–01 | 6.91E–02 | 9.45E–01 |
| AFT 1 x AFT 4 | 4.64E–01 | 6.43E–01 | 9.18E–01 | 3.60E–01 | 6.19E–01 | 5.37E–01 | 7.01E–01 | 4.85E–01 |
| AFT 2 x AFT 4 | 2.73E–01 | 7.85E–01 | 2.46E–01 | 8.06E–01 | 1.63E–04 | 1.00E+00 | 3.10E–02 | 9.75E–01 |
| AFT 2 x AFT 3 | 2.09E–01 | 8.34E–01 | 1.33E–01 | 8.94E–01 | 8.52E–07 | 1.00E+00 | 2.78E–03 | 9.98E–01 |
| AFT 3 x AFT 4 | 8.14E–01 | 4.17E–01 | 5.73E–01 | 5.68E–01 | 3.76E–02 | 9.70E–01 | 8.09E–02 | 9.36E–01 |
| ZFT 1 x ZFT 2 | 1.23E–01 | 9.02E–01 | 2.88E–03 | 9.98E–01 | 3.31E–16 | 1.00E+00 | 7.86E–01 | 4.32E–01 |
| ZFT 1 x ZFT 3 | 3.20E–02 | 9.75E–01 | 2.45E–02 | 9.80E–01 | 5.63E–05 | 1.00E+00 | 2.35E–01 | 8.14E–01 |
| ZFT 2 x ZFT 3 | 1.89E–03 | 9.98E–01 | 6.64E–06 | 1.00E+00 | 1.68E–24 | 1.00E+00 | 4.14E–01 | 6.79E–01 |

## 8.3. Chapter 4

Table S1: U–Pb ages of the Tavignano sources.

| Meta–ophiolite | |
|---|---|
| Age (Ma) | Error (Ma) |
| 162 | 1 |
| 159 | 1 |
| 162 | 1 |
| 161 | 1 |
| 159 | 1 |
| 142 | 1 |

| External continental units | | | | | | | | | |
|---|---|---|---|---|---|---|---|---|---|
| Age (Ma) | Error (Ma) | Age (Ma) | Error (Ma) | Age (Ma) | Error (Ma) | Age (Ma) | Error (Ma) | Age (Ma) | Error (Ma) |
| 321 | 5 | 242 | 2 | 182 | 2 | 281 | 10 | 157 | 3 |
| 270 | 7 | 186 | 3 | 281 | 8 | 181 | 3 | 174 | 2 |
| 235 | 2 | 303 | 5 | 325 | 5 | 271 | 5 | 304 | 4 |
| 293 | 8 | 356 | 5 | 188 | 3 | 309 | 7 | 224 | 3 |
| 216 | 6 | 168 | 3 | 281 | 4 | 305 | 6 | 283 | 4 |
| 323 | 4 | 256 | 5 | 277 | 12 | 270 | 5 | 234 | 3 |
| 324 | 5 | 323 | 4 | 310 | 5 | 223 | 8 | 253 | 3 |
| 298 | 4 | 295 | 9 | 176 | 4 | 254 | 5 | 261 | 2 |
| 350 | 5 | 282 | 3 | 200 | 5 | 187 | 3 | 208 | 3 |
| 240 | 2 | 265 | 4 | 240 | 5 | 194 | 5 | 240 | 3 |
| 228 | 5 | 247 | 10 | 246 | 4 | 258 | 4 | 237 | 3 |
| 243 | 3 | 295 | 6 | 199 | 5 | 282 | 14 | 228 | 2 |
| 174 | 4 | 270 | 4 | 237 | 11 | 265 | 15 | 186 | 2 |
| 164 | 3 | 346 | 3 | 196 | 4 | 284 | 11 | 221 | 3 |
| 270 | 8 | 331 | 7 | 239 | 6 | 520 | 7 | 199 | 2 |
| 183 | 3 | 247 | 7 | 254 | 4 | 173 | 3 | 279 | 4 |
| 2479 | 23 | 2653 | 24 | | | | | 290 | 5 |

| U2 leucomonzogranite | | | | | | | |
|---|---|---|---|---|---|---|---|
| Age (Ma) | Error (Ma) | Age (Ma) | Error (Ma) | Age (Ma) | Error (Ma) | Age (Ma) | Error (Ma) |
| 289.1 | 5.5 | 292.2 | 2.1 | 287.2 | 2.1 | 287.7 | 2.4 |
| 280.7 | 5.5 | 288.2 | 3.1 | 247 | 1.7 | 287.1 | 2.4 |
| 288.8 | 5.3 | 286.3 | 3 | 291 | 2.6 | 287.5 | 2.5 |
| 299.1 | 5.6 | 281.5 | 2 | 279.6 | 2.5 | 285.1 | 2.5 |

| | | | | | | | |
|---|---|---|---|---|---|---|---|
| 295.2 | 16.8 | 290.1 | 1.9 | 288.8 | 4 | 287.5 | 2.4 |
| 283.5 | 5.3 | 296.2 | 2 | 299 | 2.6 | 284 | 2.8 |
| 249 | 4.5 | 305.8 | 3.6 | 287.1 | 1.9 | 289.8 | 2.5 |
| 276.7 | 6.4 | 327.4 | 3.3 | 232 | 1.4 | 284.9 | 2.4 |
| 272.4 | 5.5 | 301.2 | 2.8 | 277.4 | 2 | | |
| 290.8 | 3.4 | 298.3 | 2.6 | 282 | 1.7 | | |
| 292.4 | 2.6 | 204.6 | 1.3 | 262.3 | 2 | | |
| 286.7 | 2.2 | 292.1 | 3.3 | 287.5 | 3.1 | | |
| 296 | 2.1 | 290.7 | 2.8 | 285.1 | 1.8 | | |
| 290.1 | 2.3 | 216.9 | 2.1 | 288.3 | 1.6 | | |
| 294.9 | 2.7 | 213.5 | 1.4 | 289.8 | 2.5 | | |

| U2 Fine grain granodiorite | |
|---|---|
| Age (Ma) | Error (Ma) |
| 288.5 | 5 |
| 291.6 | 4.9 |
| 291.4 | 5.1 |
| 288.8 | 4.8 |
| 295.7 | 4.9 |
| 294.7 | 4.9 |
| 292.4 | 4.8 |
| 292.8 | 4.8 |
| 199.1 | 3.2 |
| 294.3 | 5 |
| 292 | 4.7 |
| 294 | 4.9 |
| 303 | 1 |
| 300 | 1 |
| 296 | 1 |
| 294 | 1 |
| 292 | 1 |
| 307 | 1 |
| 326 | 1 |

| U2 Medium fine grain monzongranite | | | | | | | |
|---|---|---|---|---|---|---|---|
| Age (Ma) | Error (Ma) | Age (Ma) | Error (Ma) | Age (Ma) | Error (Ma) | Age (Ma) | Error (Ma) |
| 303 | 1 | 298 | 1 | 300 | 1 | 254 | 1 |
| 300 | 1 | 303 | 1 | 296 | 1 | 280 | 1 |
| 296 | 1 | 297 | 1 | 294 | 1 | 279 | 1 |
| 295 | 1 | 293 | 1 | 292 | 1 | 279 | 1 |
| 310 | 1 | 286 | 1 | 307 | 1 | 284 | 1 |
| 331 | 1 | 282 | 1 | 326 | 1 | 283 | 1 |
| 280 | 1 | 277 | 1 | 242 | 1 | 282 | 1 |

| | | | | | | | |
|---|---|---|---|---|---|---|---|
| 279 | 1 | 322 | 1 | 264 | 1 | 284 | 1 |
| 279 | 1 | 312 | 1 | 274 | 1 | 287 | 1 |
| 284 | 1 | 308 | 1 | 278 | 1 | 286 | 1 |
| 283 | 1 | 340 | 1 | 212 | 1 | 350 | 1 |
| 282 | 1 | 333 | 1 | 222 | 1 | 339 | 1 |
| 284 | 1 | 273 | 1 | 278 | 1 | 382 | 1 |
| 287 | 1 | 266 | 1 | 275 | 1 | 561 | 1 |
| 286 | 1 | 303 | 1 | 273 | 1 | | |

| U1 Mesocratic granite | | | | | | | |
|---|---|---|---|---|---|---|---|
| Age (Ma) | Error (Ma) | Age (Ma) | Error (Ma) | Age (Ma) | Error (Ma) | Age (Ma) | Error (Ma) |
| 302.8 | 4.5 | 337.7 | 5.0 | 303.0 | 1.0 | 308.0 | 1.0 |
| 320.0 | 4.7 | 339.9 | 5.2 | 310.0 | 1.0 | 324.0 | 1.0 |
| 320.9 | 4.7 | 343.8 | 5.0 | 298.0 | 1.0 | 278.0 | 1.0 |
| 324.2 | 4.8 | 310.0 | 1.0 | 334.0 | 1.0 | 290.0 | 1.0 |
| 325.8 | 4.8 | 318.0 | 1.0 | 353.0 | 1.0 | 332.0 | 1.0 |
| 326.6 | 4.9 | 326.0 | 1.0 | 240.0 | 1.0 | 310.0 | 1.0 |
| 328.5 | 4.9 | 331.0 | 1.0 | 284.0 | 1.0 | | |
| 328.5 | 4.8 | 297.0 | 1.0 | 215.0 | 1.0 | | |
| 329.0 | 4.8 | 300.0 | 1.0 | 270.0 | 1.0 | | |
| 331.5 | 4.9 | 300.0 | 1.0 | 321.0 | 1.0 | | |
| 332.0 | 4.9 | 323.0 | 1.0 | 280.0 | 1.0 | | |
| 333.8 | 4.9 | 327.0 | 1.0 | 305.0 | 1.0 | | |
| 334.4 | 4.9 | 233.0 | 1.0 | 315.0 | 1.0 | | |
| 335.1 | 4.9 | 257.0 | 1.0 | 330.0 | 1.0 | | |
| 335.2 | 4.9 | 281.0 | 1.0 | 272.0 | 1.0 | | |

Table S2: U–Pb ages measured in this work using SIMS.

| Sample A | | | | | | | |
|---|---|---|---|---|---|---|---|
| Age (Ma) | Error (Ma) | Age (Ma) | Error (Ma) | Age (Ma) | Error (Ma) | Age (Ma) | Error (Ma) |
| 612.6 | 5.4 | 279.5 | 2.7 | 313.2 | 2.7 | 456.9 | 4.4 |
| 296.5 | 3.3 | 338.7 | 3.6 | 275.0 | 2.4 | 292.4 | 4.1 |
| 286.0 | 2.8 | 315.5 | 14.0 | 292.0 | 2.5 | 297.1 | 2.6 |
| 289.0 | 3.2 | 288.3 | 2.6 | 273.1 | 2.4 | 167.7 | 10.4 |
| 235.2 | 2.3 | 294.3 | 2.9 | 489.2 | 4.8 | | |
| 280.5 | 2.5 | 299.6 | 2.6 | 293.3 | 3.1 | | |
| 284.6 | 2.7 | 347.7 | 4.7 | 300.4 | 3.0 | | |
| 287.7 | 2.6 | 273.3 | 2.4 | 294.6 | 2.9 | | |
| 283.4 | 2.7 | 297.7 | 2.7 | 297.4 | 2.6 | | |
| 288.7 | 13.1 | 284.9 | 2.8 | 657.6 | 6.4 | | |
| 284.1 | 2.7 | 293.7 | 2.9 | 252.2 | 5.4 | | |

| | | | | | | | |
|---|---|---|---|---|---|---|---|
| 275.4 | 2.9 | 448.6 | 4.9 | 284.5 | 2.6 | | |
| 441.7 | 4.4 | 298.3 | 2.7 | 275.8 | 2.8 | | |
| 277.4 | 5.9 | 289.8 | 3.2 | 310.3 | 3.4 | | |
| 291.4 | 2.7 | 296.9 | 2.7 | 294.6 | 2.5 | | |

| Sample B | |
|---|---|
| Age (Ma) | Error (Ma) |
| 140.1 | 10.0 |
| 154.0 | 6.5 |
| 157.6 | 6.6 |
| 131.9 | 12.6 |
| 122.1 | 8.8 |
| 144.0 | 5.8 |
| 158.5 | 5.4 |
| 160.9 | 3.8 |
| 138.3 | 6.8 |
| 157.7 | 10.4 |
| 144.5 | 5.0 |
| 271.1 | 2.4 |
| 264.8 | 2.6 |
| 158.4 | 12.0 |

| Sample C | | | | | | | |
|---|---|---|---|---|---|---|---|
| Age (Ma) | Error (Ma) | Age (Ma) | Error (Ma) | Age (Ma) | Error (Ma) | Age (Ma) | Error (Ma) |
| 286.8 | 3.0 | 260.9 | 2.5 | 243.6 | 2.3 | 249.7 | 2.3 |
| 267.0 | 2.3 | 290.3 | 2.8 | 166.1 | 1.5 | 445.9 | 4.1 |
| 287.3 | 4.0 | 235.8 | 2.2 | 266.3 | 2.4 | 277.1 | 2.7 |
| 295.5 | 2.6 | 159.6 | 2.0 | 262.1 | 2.5 | 289.6 | 4.4 |
| 477.8 | 4.2 | 291.9 | 2.6 | 236.2 | 2.1 | 216.5 | 2.6 |
| 296.6 | 2.6 | 250.0 | 2.3 | 220.7 | 2.6 | 264.1 | 2.6 |
| 184.0 | 3.6 | 207.0 | 2.4 | 232.9 | 2.1 | 282.2 | 2.8 |
| 294.3 | 2.6 | 252.8 | 2.1 | 286.0 | 2.5 | | |
| 227.0 | 2.0 | 292.1 | 2.7 | 288.9 | 2.6 | | |
| 234.9 | 2.8 | 258.8 | 5.5 | 249.7 | 2.1 | | |
| 286.6 | 4.0 | 168.9 | 1.5 | 284.4 | 2.7 | | |
| 452.9 | 4.3 | 287.2 | 2.8 | 273.1 | 2.6 | | |
| 272.4 | 2.9 | 263.9 | 2.3 | 271.7 | 2.3 | | |
| 291.2 | 2.7 | 312.5 | 3.0 | 290.3 | 2.8 | | |
| 279.8 | 7.0 | 243.9 | 2.4 | 282.8 | 6.1 | | |

Table S3: Artificial U–Pb created for the scenario A1.

| Artificial U2 leucomonzogranite | | | | | |
|---|---|---|---|---|---|
| Age (Ma) | Error (Ma) | Age (Ma) | Error (Ma) | Age (Ma) | Error (Ma) |
| 293.9 | 1.0 | 300.7 | 1.0 | 305.6 | 1.0 |
| 291.1 | 1.0 | 294.9 | 1.0 | 297.3 | 1.0 |
| 295.2 | 1.0 | 303.0 | 1.0 | 303.6 | 1.0 |
| 304.9 | 1.0 | 304.0 | 1.0 | 302.6 | 1.0 |
| 308.7 | 1.0 | 300.7 | 1.0 | 307.8 | 1.0 |
| 293.6 | 1.0 | 290.8 | 1.0 | 305.3 | 1.0 |
| 293.3 | 1.0 | 297.7 | 1.0 | 293.9 | 1.0 |
| 306.1 | 1.0 | 307.5 | 1.0 | 297.6 | 1.0 |
| 289.8 | 1.0 | 296.4 | 1.0 | 297.5 | 1.0 |
| 294.7 | 1.0 | 303.1 | 1.0 | 293.8 | 1.0 |
| 297.5 | 1.0 | 296.0 | 1.0 | 294.2 | 1.0 |
| 291.9 | 1.0 | 284.5 | 1.0 | 309.3 | 1.0 |
| 299.4 | 1.0 | 299.6 | 1.0 | 298.9 | 1.0 |
| 299.4 | 1.0 | 308.2 | 1.0 | 297.6 | 1.0 |
| 303.5 | 1.0 | 311.0 | 1.0 | 317.9 | 1.0 |
| 301.5 | 1.0 | 297.4 | 1.0 | 302.2 | 1.0 |
| 295.8 | 1.0 | 294.6 | 1.0 | 303.3 | 1.0 |
| 293.6 | 1.0 | 302.4 | 1.0 | 302.7 | 1.0 |
| 299.7 | 1.0 | 291.8 | 1.0 | 288.4 | 1.0 |
| 291.3 | 1.0 | 285.5 | 1.0 | 302.3 | 1.0 |
| 294.0 | 1.0 | 295.8 | 1.0 | 305.5 | 1.0 |
| 307.3 | 1.0 | 288.5 | 1.0 | 304.4 | 1.0 |
| 302.0 | 1.0 | 305.0 | 1.0 | 319.4 | 1.0 |
| 307.0 | 1.0 | 304.1 | 1.0 | 301.0 | 1.0 |
| 295.4 | 1.0 | 296.7 | 1.0 | 303.1 | 1.0 |
| 297.7 | 1.0 | 315.1 | 1.0 | 304.6 | 1.0 |
| 292.6 | 1.0 | 303.3 | 1.0 | 302.8 | 1.0 |
| 302.1 | 1.0 | 289.2 | 1.0 | 313.8 | 1.0 |
| 304.8 | 1.0 | 290.4 | 1.0 | 309.8 | 1.0 |
| 311.4 | 1.0 | 296.1 | 1.0 | 308.1 | 1.0 |
| 300.2 | 1.0 | 301.6 | 1.0 | 296.6 | 1.0 |
| 304.1 | 1.0 | 303.3 | 1.0 | 294.8 | 1.0 |
| 296.7 | 1.0 | 288.1 | 1.0 | 293.2 | 1.0 |
| 296.4 | 1.0 | 303.4 | 1.0 | 301.6 | 1.0 |
| 297.3 | 1.0 | 305.4 | 1.0 | 289.9 | 1.0 |
| 304.4 | 1.0 | 291.2 | 1.0 | 299.3 | 1.0 |
| 299.5 | 1.0 | 302.0 | 1.0 | 303.0 | 1.0 |
| 309.7 | 1.0 | 300.6 | 1.0 | 286.6 | 1.0 |
| 303.1 | 1.0 | 293.8 | 1.0 | 310.3 | 1.0 |

| Artificial U2 Fine grain granodiorite | | | | | |
|---|---|---|---|---|---|
| Age (Ma) | Error (Ma) | Age (Ma) | Error (Ma) | Age (Ma) | Error (Ma) |
| 399.1 | 1.0 | 401.4 | 1.0 | 408.4 | 1.0 |
| 398.8 | 1.0 | 396.0 | 1.0 | 393.5 | 1.0 |
| 408.8 | 1.0 | 398.8 | 1.0 | 400.4 | 1.0 |
| 397.8 | 1.0 | 395.7 | 1.0 | 389.3 | 1.0 |
| 403.8 | 1.0 | 409.7 | 1.0 | 399.6 | 1.0 |
| 401.9 | 1.0 | 407.5 | 1.0 | 399.1 | 1.0 |
| 392.8 | 1.0 | 401.1 | 1.0 | 404.6 | 1.0 |
| 401.8 | 1.0 | 393.7 | 1.0 | 399.1 | 1.0 |
| 409.1 | 1.0 | 398.8 | 1.0 | 406.7 | 1.0 |
| 401.5 | 1.0 | 389.1 | 1.0 | 395.3 | 1.0 |
| 398.1 | 1.0 | 400.8 | 1.0 | 398.9 | 1.0 |
| 410.0 | 1.0 | 402.5 | 1.0 | 397.1 | 1.0 |
| 392.0 | 1.0 | 392.8 | 1.0 | 401.4 | 1.0 |
| 399.2 | 1.0 | 391.4 | 1.0 | 400.3 | 1.0 |
| 403.0 | 1.0 | 391.8 | 1.0 | 395.3 | 1.0 |

| Artificial U2 Medium grain monzongranite | | | | | |
|---|---|---|---|---|---|
| Age (Ma) | Error (Ma) | Age (Ma) | Error (Ma) | Age (Ma) | Error (Ma) |
| 501.0 | 1.0 | 504.1 | 1.0 | 495.8 | 1.0 |
| 496.2 | 1.0 | 500.1 | 1.0 | 498.4 | 1.0 |
| 494.4 | 1.0 | 497.7 | 1.0 | 501.5 | 1.0 |
| 500.1 | 1.0 | 502.4 | 1.0 | 496.4 | 1.0 |
| 493.9 | 1.0 | 491.7 | 1.0 | 496.0 | 1.0 |
| 495.6 | 1.0 | 508.4 | 1.0 | 492.5 | 1.0 |
| 485.7 | 1.0 | 498.4 | 1.0 | 499.5 | 1.0 |
| 502.2 | 1.0 | 508.3 | 1.0 | 512.4 | 1.0 |
| 493.9 | 1.0 | 503.4 | 1.0 | 503.8 | 1.0 |
| 501.7 | 1.0 | 502.4 | 1.0 | 497.0 | 1.0 |
| 500.0 | 1.0 | 493.6 | 1.0 | 498.4 | 1.0 |
| 497.9 | 1.0 | 496.1 | 1.0 | 500.3 | 1.0 |
| 503.9 | 1.0 | 499.3 | 1.0 | 497.8 | 1.0 |
| 494.1 | 1.0 | 494.8 | 1.0 | 509.8 | 1.0 |
| 505.7 | 1.0 | 505.3 | 1.0 | 500.8 | 1.0 |
| 502.8 | 1.0 | 491.3 | 1.0 | 496.0 | 1.0 |
| 495.1 | 1.0 | 497.0 | 1.0 | 504.8 | 1.0 |
| 494.3 | 1.0 | 507.4 | 1.0 | 498.3 | 1.0 |
| 499.0 | 1.0 | 505.8 | 1.0 | 504.4 | 1.0 |
| 501.2 | 1.0 | 508.0 | 1.0 | 500.1 | 1.0 |
| 494.4 | 1.0 | 500.9 | 1.0 | 496.8 | 1.0 |
| 502.9 | 1.0 | 499.0 | 1.0 | 489.3 | 1.0 |
| 497.1 | 1.0 | 501.2 | 1.0 | 507.2 | 1.0 |

| | | | | | |
|---|---|---|---|---|---|
| 499.6 | 1.0 | 507.0 | 1.0 | 501.0 | 1.0 |
| 498.5 | 1.0 | 502.1 | 1.0 | 494.5 | 1.0 |
| 497.0 | 1.0 | 499.9 | 1.0 | 510.8 | 1.0 |
| 500.6 | 1.0 | 511.4 | 1.0 | 503.2 | 1.0 |
| 500.5 | 1.0 | 503.6 | 1.0 | 491.9 | 1.0 |
| 509.3 | 1.0 | 495.9 | 1.0 | 506.8 | 1.0 |
| 500.3 | 1.0 | 510.2 | 1.0 | 491.2 | 1.0 |
| 503.8 | 1.0 | 495.4 | 1.0 | 492.7 | 1.0 |
| 490.9 | 1.0 | 493.2 | 1.0 | 508.3 | 1.0 |
| 504.9 | 1.0 | 497.7 | 1.0 | 501.6 | 1.0 |
| 498.7 | 1.0 | 498.5 | 1.0 | 505.0 | 1.0 |
| 496.6 | 1.0 | 506.3 | 1.0 | 490.7 | 1.0 |
| 497.7 | 1.0 | 502.2 | 1.0 | 505.3 | 1.0 |
| 492.0 | 1.0 | 509.9 | 1.0 | 491.8 | 1.0 |
| 499.9 | 1.0 | 499.8 | 1.0 | 504.3 | 1.0 |
| 496.2 | 1.0 | 504.2 | 1.0 | 501.3 | 1.0 |

| Artificial U1 Mesocratic granite | | | | | |
|---|---|---|---|---|---|
| Age (Ma) | Error (Ma) | Age (Ma) | Error (Ma) | Age (Ma) | Error (Ma) |
| 597.6 | 1.0 | 599.3 | 1.0 | 593.2 | 1.0 |
| 608.2 | 1.0 | 599.5 | 1.0 | 604.0 | 1.0 |
| 593.4 | 1.0 | 595.3 | 1.0 | 610.4 | 1.0 |
| 603.5 | 1.0 | 605.8 | 1.0 | 582.5 | 1.0 |
| 608.2 | 1.0 | 603.1 | 1.0 | 600.8 | 1.0 |
| 606.5 | 1.0 | 598.9 | 1.0 | 601.2 | 1.0 |
| 602.7 | 1.0 | 604.4 | 1.0 | 594.7 | 1.0 |
| 600.8 | 1.0 | 601.9 | 1.0 | 596.0 | 1.0 |
| 604.7 | 1.0 | 590.0 | 1.0 | 598.0 | 1.0 |
| 600.4 | 1.0 | 589.4 | 1.0 | 594.3 | 1.0 |
| 604.5 | 1.0 | 599.4 | 1.0 | 607.0 | 1.0 |
| 602.5 | 1.0 | 596.2 | 1.0 | 601.1 | 1.0 |
| 606.5 | 1.0 | 590.4 | 1.0 | 594.2 | 1.0 |
| 603.8 | 1.0 | 599.4 | 1.0 | 598.8 | 1.0 |
| 608.4 | 1.0 | 589.6 | 1.0 | 603.1 | 1.0 |
| 605.9 | 1.0 | 611.0 | 1.0 | 603.3 | 1.0 |
| 597.3 | 1.0 | 598.3 | 1.0 | 586.2 | 1.0 |
| 611.8 | 1.0 | 601.1 | 1.0 | 594.5 | 1.0 |
| 597.0 | 1.0 | 599.1 | 1.0 | 596.7 | 1.0 |
| 608.1 | 1.0 | 595.9 | 1.0 | 599.1 | 1.0 |
| 610.0 | 1.0 | 604.1 | 1.0 | 604.2 | 1.0 |
| 608.3 | 1.0 | 612.4 | 1.0 | 610.8 | 1.0 |
| 601.0 | 1.0 | 591.6 | 1.0 | 598.6 | 1.0 |
| 597.9 | 1.0 | 602.1 | 1.0 | 605.2 | 1.0 |

| | | | | | |
|---|---|---|---|---|---|
| 602.4 | 1.0 | 594.7 | 1.0 | 618.3 | 1.0 |
| 605.7 | 1.0 | 592.5 | 1.0 | 605.9 | 1.0 |
| 614.8 | 1.0 | 592.1 | 1.0 | 602.4 | 1.0 |
| 603.2 | 1.0 | 603.3 | 1.0 | 599.4 | 1.0 |
| 597.1 | 1.0 | 606.2 | 1.0 | 609.0 | 1.0 |
| 607.5 | 1.0 | 594.7 | 1.0 | 593.7 | 1.0 |
| 594.5 | 1.0 | 604.4 | 1.0 | 604.2 | 1.0 |
| 594.6 | 1.0 | 603.0 | 1.0 | 604.7 | 1.0 |
| 597.8 | 1.0 | 600.5 | 1.0 | 596.9 | 1.0 |
| 610.9 | 1.0 | 588.5 | 1.0 | 599.9 | 1.0 |
| 602.4 | 1.0 | 609.1 | 1.0 | 594.6 | 1.0 |
| 615.9 | 1.0 | 588.9 | 1.0 | 595.6 | 1.0 |
| 598.8 | 1.0 | 595.9 | 1.0 | 599.9 | 1.0 |
| 595.2 | 1.0 | 596.5 | 1.0 | 604.1 | 1.0 |
| 604.3 | 1.0 | 606.0 | 1.0 | 598.4 | 1.0 |

| Artificial sample A | | | | | |
|---|---|---|---|---|---|
| Age (Ma) | Error (Ma) | Age (Ma) | Error (Ma) | Age (Ma) | Error (Ma) |
| 307.1 | 1.0 | 294.4 | 1.0 | 306.9 | 1.0 |
| 305.6 | 1.0 | 301.4 | 1.0 | 304.0 | 1.0 |
| 299.4 | 1.0 | 293.6 | 1.0 | 297.3 | 1.0 |
| 299.6 | 1.0 | 306.3 | 1.0 | 310.0 | 1.0 |
| 305.7 | 1.0 | 298.7 | 1.0 | 300.3 | 1.0 |
| 299.3 | 1.0 | 292.3 | 1.0 | 296.9 | 1.0 |
| 294.6 | 1.0 | 306.0 | 1.0 | 291.5 | 1.0 |
| 293.3 | 1.0 | 304.7 | 1.0 | 292.7 | 1.0 |
| 302.5 | 1.0 | 303.4 | 1.0 | 300.9 | 1.0 |
| 306.2 | 1.0 | 303.1 | 1.0 | 309.6 | 1.0 |
| 299.9 | 1.0 | 289.8 | 1.0 | 297.1 | 1.0 |
| 298.2 | 1.0 | 305.1 | 1.0 | 300.3 | 1.0 |
| 301.5 | 1.0 | 304.0 | 1.0 | 307.0 | 1.0 |
| 302.5 | 1.0 | 307.1 | 1.0 | 294.4 | 1.0 |
| 302.4 | 1.0 | 304.9 | 1.0 | 304.2 | 1.0 |
| 307.1 | 1.0 | 302.5 | 1.0 | 294.4 | 1.0 |
| 282.7 | 1.0 | 302.6 | 1.0 | 305.0 | 1.0 |
| 304.2 | 1.0 | 300.6 | 1.0 | 303.0 | 1.0 |
| 297.5 | 1.0 | 297.6 | 1.0 | 286.2 | 1.0 |
| 309.5 | 1.0 | 302.3 | 1.0 | 293.8 | 1.0 |
| 301.9 | 1.0 | 304.0 | 1.0 | 308.1 | 1.0 |
| 291.4 | 1.0 | 302.5 | 1.0 | 293.2 | 1.0 |
| 300.7 | 1.0 | 292.9 | 1.0 | 309.4 | 1.0 |
| 303.4 | 1.0 | 303.8 | 1.0 | 294.4 | 1.0 |
| 302.6 | 1.0 | 297.2 | 1.0 | 307.4 | 1.0 |
| 298.2 | 1.0 | 300.6 | 1.0 | 298.2 | 1.0 |

| | | | | | |
|---|---|---|---|---|---|
| 298.4 | 1.0 | 300.2 | 1.0 | 293.7 | 1.0 |
| 303.6 | 1.0 | 287.7 | 1.0 | 305.1 | 1.0 |
| 309.4 | 1.0 | 301.5 | 1.0 | 287.2 | 1.0 |
| 299.2 | 1.0 | 303.0 | 1.0 | 307.1 | 1.0 |
| 286.7 | 1.0 | 303.3 | 1.0 | 294.9 | 1.0 |
| 297.1 | 1.0 | 292.9 | 1.0 | 306.3 | 1.0 |
| 306.0 | 1.0 | 301.6 | 1.0 | 299.0 | 1.0 |
| 300.5 | 1.0 | 291.7 | 1.0 | 286.1 | 1.0 |
| 311.4 | 1.0 | 292.1 | 1.0 | 301.4 | 1.0 |
| 302.7 | 1.0 | 293.2 | 1.0 | 300.5 | 1.0 |
| 296.0 | 1.0 | 305.5 | 1.0 | 311.8 | 1.0 |
| 303.9 | 1.0 | 291.9 | 1.0 | 302.1 | 1.0 |
| 297.1 | 1.0 | 306.5 | 1.0 | 296.6 | 1.0 |
| 303.7 | 1.0 | 308.3 | 1.0 | 295.4 | 1.0 |
| 308.8 | 1.0 | 297.2 | 1.0 | 302.5 | 1.0 |
| 303.6 | 1.0 | 297.3 | 1.0 | 305.6 | 1.0 |
| 294.3 | 1.0 | 298.6 | 1.0 | 300.6 | 1.0 |
| 299.6 | 1.0 | 297.5 | 1.0 | 307.8 | 1.0 |
| 301.9 | 1.0 | 305.4 | 1.0 | 299.4 | 1.0 |
| 299.6 | 1.0 | 287.9 | 1.0 | 299.0 | 1.0 |
| 294.8 | 1.0 | 308.5 | 1.0 | 302.1 | 1.0 |
| 306.1 | 1.0 | 292.1 | 1.0 | 303.0 | 1.0 |
| 295.7 | 1.0 | 298.9 | 1.0 | 308.6 | 1.0 |
| 299.7 | 1.0 | 305.8 | 1.0 | 307.2 | 1.0 |
| 307.0 | 1.0 | 295.9 | 1.0 | 301.6 | 1.0 |
| 299.8 | 1.0 | 308.3 | 1.0 | 297.6 | 1.0 |
| 295.3 | 1.0 | 302.7 | 1.0 | 300.0 | 1.0 |
| 296.8 | 1.0 | 292.3 | 1.0 | 294.8 | 1.0 |
| 304.1 | 1.0 | 299.5 | 1.0 | 304.9 | 1.0 |
| 307.6 | 1.0 | 306.3 | 1.0 | 298.7 | 1.0 |
| 299.6 | 1.0 | 300.0 | 1.0 | 306.0 | 1.0 |
| 296.7 | 1.0 | 297.0 | 1.0 | 300.1 | 1.0 |
| 290.8 | 1.0 | 308.2 | 1.0 | 309.3 | 1.0 |
| 299.6 | 1.0 | 300.9 | 1.0 | 306.2 | 1.0 |
| 294.3 | 1.0 | 293.4 | 1.0 | 294.5 | 1.0 |
| 308.0 | 1.0 | 297.1 | 1.0 | 300.0 | 1.0 |
| 300.2 | 1.0 | 288.8 | 1.0 | 302.7 | 1.0 |
| 296.3 | 1.0 | 304.7 | 1.0 | 291.8 | 1.0 |
| 295.1 | 1.0 | 301.4 | 1.0 | 305.1 | 1.0 |
| 296.9 | 1.0 | 302.3 | 1.0 | 291.9 | 1.0 |
| 294.5 | 1.0 | 301.8 | 1.0 | 304.1 | 1.0 |
| 302.2 | 1.0 | 299.1 | 1.0 | 297.1 | 1.0 |
| 305.7 | 1.0 | 290.2 | 1.0 | 283.8 | 1.0 |
| 297.0 | 1.0 | 299.9 | 1.0 | 304.5 | 1.0 |

| | | | | | |
|---|---|---|---|---|---|
| 289.9 | 1.0 | 305.9 | 1.0 | 297.6 | 1.0 |
| 302.9 | 1.0 | 293.6 | 1.0 | 306.7 | 1.0 |
| 304.0 | 1.0 | 300.5 | 1.0 | 295.7 | 1.0 |
| 299.0 | 1.0 | 303.1 | 1.0 | 507.5 | 1.0 |
| 304.1 | 1.0 | 296.9 | 1.0 | 501.1 | 1.0 |
| 309.4 | 1.0 | 297.4 | 1.0 | 498.0 | 1.0 |
| 300.9 | 1.0 | 299.2 | 1.0 | 493.0 | 1.0 |
| 301.2 | 1.0 | 296.0 | 1.0 | 494.4 | 1.0 |
| 300.4 | 1.0 | 303.2 | 1.0 | 490.0 | 1.0 |
| 300.3 | 1.0 | 305.4 | 1.0 | 507.4 | 1.0 |
| 297.8 | 1.0 | 308.3 | 1.0 | 498.4 | 1.0 |
| 295.1 | 1.0 | 298.4 | 1.0 | 507.9 | 1.0 |
| 300.6 | 1.0 | 302.5 | 1.0 | 494.9 | 1.0 |
| 293.5 | 1.0 | 301.3 | 1.0 | 489.5 | 1.0 |
| 296.1 | 1.0 | 303.2 | 1.0 | 495.9 | 1.0 |
| 294.1 | 1.0 | 301.4 | 1.0 | 498.0 | 1.0 |
| 302.9 | 1.0 | 295.3 | 1.0 | 501.3 | 1.0 |
| 297.5 | 1.0 | 299.8 | 1.0 | 507.6 | 1.0 |
| 309.7 | 1.0 | 299.4 | 1.0 | 491.1 | 1.0 |
| 296.9 | 1.0 | 295.4 | 1.0 | 503.8 | 1.0 |
| 298.4 | 1.0 | 298.5 | 1.0 | 497.8 | 1.0 |
| 306.5 | 1.0 | 306.9 | 1.0 | 500.1 | 1.0 |
| 303.2 | 1.0 | 292.3 | 1.0 | 506.1 | 1.0 |
| 282.2 | 1.0 | 304.4 | 1.0 | 504.9 | 1.0 |
| 306.3 | 1.0 | 406.0 | 1.0 | 496.7 | 1.0 |
| 287.0 | 1.0 | 395.7 | 1.0 | 491.0 | 1.0 |
| 305.0 | 1.0 | 404.4 | 1.0 | 496.9 | 1.0 |
| 287.2 | 1.0 | 391.4 | 1.0 | 600.4 | 1.0 |
| 308.5 | 1.0 | 392.4 | 1.0 | 599.2 | 1.0 |
| 304.6 | 1.0 | 401.4 | 1.0 | 597.7 | 1.0 |
| 305.5 | 1.0 | 405.7 | 1.0 | 601.5 | 1.0 |
| 303.9 | 1.0 | 404.8 | 1.0 | 609.8 | 1.0 |
| 305.4 | 1.0 | 402.8 | 1.0 | 596.6 | 1.0 |
| 296.5 | 1.0 | 384.2 | 1.0 | 601.1 | 1.0 |
| 299.9 | 1.0 | 395.8 | 1.0 | 597.7 | 1.0 |
| 297.0 | 1.0 | 400.0 | 1.0 | 597.8 | 1.0 |
| 286.8 | 1.0 | 401.0 | 1.0 | 594.2 | 1.0 |
| 307.2 | 1.0 | 415.2 | 1.0 | 594.7 | 1.0 |
| 299.4 | 1.0 | 403.8 | 1.0 | 593.5 | 1.0 |
| 298.5 | 1.0 | 404.1 | 1.0 | 295.3 | 1.0 |
| 300.7 | 1.0 | 405.2 | 1.0 | 302.6 | 1.0 |
| 295.8 | 1.0 | 387.7 | 1.0 | 302.0 | 1.0 |
| 310.2 | 1.0 | 408.3 | 1.0 | 302.3 | 1.0 |
| 287.2 | 1.0 | 406.3 | 1.0 | 310.0 | 1.0 |

| | | | | | |
|---|---|---|---|---|---|
| 307.2 | 1.0 | 402.3 | 1.0 | 302.1 | 1.0 |
| 299.9 | 1.0 | 403.0 | 1.0 | 294.1 | 1.0 |
| 311.5 | 1.0 | 400.5 | 1.0 | 305.8 | 1.0 |
| 314.1 | 1.0 | 394.6 | 1.0 | 306.7 | 1.0 |
| 308.2 | 1.0 | 402.1 | 1.0 | 298.4 | 1.0 |
| 310.1 | 1.0 | 402.9 | 1.0 | 314.7 | 1.0 |
| 294.4 | 1.0 | 401.5 | 1.0 | 299.4 | 1.0 |
| 300.9 | 1.0 | 408.8 | 1.0 | 408.3 | 1.0 |
| 293.8 | 1.0 | 400.6 | 1.0 | 399.0 | 1.0 |
| 295.4 | 1.0 | 399.4 | 1.0 | 401.6 | 1.0 |
| 307.5 | 1.0 | 395.1 | 1.0 | 406.4 | 1.0 |
| 306.6 | 1.0 | 402.5 | 1.0 | 402.6 | 1.0 |
| 300.5 | 1.0 | 403.8 | 1.0 | 399.8 | 1.0 |
| 301.4 | 1.0 | 403.6 | 1.0 | 386.8 | 1.0 |
| 296.3 | 1.0 | 406.4 | 1.0 | 411.1 | 1.0 |
| 305.3 | 1.0 | 392.5 | 1.0 | 402.0 | 1.0 |
| 293.9 | 1.0 | 401.0 | 1.0 | 387.3 | 1.0 |
| 308.8 | 1.0 | 399.2 | 1.0 | 402.0 | 1.0 |
| 304.6 | 1.0 | 406.6 | 1.0 | 399.3 | 1.0 |
| 286.4 | 1.0 | 511.6 | 1.0 | 292.5 | 1.0 |
| 296.0 | 1.0 | 502.4 | 1.0 | 293.7 | 1.0 |
| 300.9 | 1.0 | 501.8 | 1.0 | 295.1 | 1.0 |
| 303.7 | 1.0 | 501.3 | 1.0 | 308.3 | 1.0 |
| 302.9 | 1.0 | 492.4 | 1.0 | 303.6 | 1.0 |
| 303.7 | 1.0 | 498.0 | 1.0 | 305.8 | 1.0 |
| 313.9 | 1.0 | 490.4 | 1.0 | 305.8 | 1.0 |
| 298.3 | 1.0 | 501.3 | 1.0 | 293.5 | 1.0 |
| 305.6 | 1.0 | 503.4 | 1.0 | 300.8 | 1.0 |
| 306.7 | 1.0 | 491.3 | 1.0 | 301.7 | 1.0 |
| 298.0 | 1.0 | 501.6 | 1.0 | 485.8 | 1.0 |
| 301.0 | 1.0 | 505.2 | 1.0 | 493.5 | 1.0 |
| 286.4 | 1.0 | 499.8 | 1.0 | 499.5 | 1.0 |
| 303.5 | 1.0 | 509.8 | 1.0 | 490.2 | 1.0 |
| 300.4 | 1.0 | 501.6 | 1.0 | 503.6 | 1.0 |
| 306.6 | 1.0 | 500.4 | 1.0 | 304.0 | 1.0 |
| 298.7 | 1.0 | 507.9 | 1.0 | 294.8 | 1.0 |
| 311.4 | 1.0 | 502.8 | 1.0 | 308.8 | 1.0 |
| 285.8 | 1.0 | 493.3 | 1.0 | 309.3 | 1.0 |
| 299.5 | 1.0 | 498.9 | 1.0 | 303.0 | 1.0 |
| 292.9 | 1.0 | 510.4 | 1.0 | 494.9 | 1.0 |
| 295.8 | 1.0 | 501.6 | 1.0 | 498.4 | 1.0 |
| | | 310.3 | 1.0 | 296.5 | 1.0 |

Table S4: Artificial U–Pb created for the scenario A2.

| Artificial U2 leucomonzogranite | | | | | |
|---|---|---|---|---|---|
| Age (Ma) | Error (Ma) | Age (Ma) | Error (Ma) | Age (Ma) | Error (Ma) |
| 301.3 | 1.0 | 288.7 | 1.0 | 301.4 | 1.0 |
| 305.1 | 1.0 | 301.4 | 1.0 | 294.2 | 1.0 |
| 298.8 | 1.0 | 294.0 | 1.0 | 295.8 | 1.0 |
| 297.4 | 1.0 | 294.6 | 1.0 | 305.2 | 1.0 |
| 304.6 | 1.0 | 297.4 | 1.0 | 302.1 | 1.0 |
| 304.9 | 1.0 | 307.2 | 1.0 | 305.9 | 1.0 |
| 293.3 | 1.0 | 301.7 | 1.0 | 302.3 | 1.0 |
| 306.2 | 1.0 | 295.2 | 1.0 | 298.7 | 1.0 |
| 300.9 | 1.0 | 305.7 | 1.0 | 299.2 | 1.0 |
| 311.8 | 1.0 | 299.2 | 1.0 | 294.1 | 1.0 |
| 313.4 | 1.0 | 306.6 | 1.0 | 302.2 | 1.0 |
| 311.9 | 1.0 | 299.9 | 1.0 | 294.5 | 1.0 |
| 301.6 | 1.0 | 291.3 | 1.0 | 312.3 | 1.0 |
| 298.8 | 1.0 | 295.6 | 1.0 | 293.9 | 1.0 |
| 301.2 | 1.0 | 299.2 | 1.0 | 298.7 | 1.0 |
| 299.8 | 1.0 | 299.0 | 1.0 | 288.6 | 1.0 |
| 303.0 | 1.0 | 304.9 | 1.0 | 307.0 | 1.0 |
| 313.7 | 1.0 | 296.1 | 1.0 | 298.6 | 1.0 |
| 312.3 | 1.0 | 300.8 | 1.0 | 309.2 | 1.0 |
| 296.4 | 1.0 | 309.8 | 1.0 | 298.8 | 1.0 |
| 308.5 | 1.0 | 305.4 | 1.0 | 290.5 | 1.0 |
| 295.3 | 1.0 | 302.3 | 1.0 | 289.1 | 1.0 |
| 300.3 | 1.0 | 290.2 | 1.0 | 308.1 | 1.0 |
| 297.7 | 1.0 | 310.4 | 1.0 | 300.7 | 1.0 |
| 299.1 | 1.0 | 295.0 | 1.0 | 294.0 | 1.0 |
| 292.1 | 1.0 | 294.9 | 1.0 | 305.3 | 1.0 |
| 300.0 | 1.0 | 310.9 | 1.0 | 293.6 | 1.0 |
| 307.0 | 1.0 | 298.3 | 1.0 | 301.6 | 1.0 |
| 306.2 | 1.0 | 285.0 | 1.0 | 302.1 | 1.0 |
| 311.5 | 1.0 | 303.8 | 1.0 | 309.7 | 1.0 |
| 297.6 | 1.0 | 298.4 | 1.0 | 299.2 | 1.0 |
| 288.9 | 1.0 | 299.7 | 1.0 | 301.6 | 1.0 |
| 310.1 | 1.0 | 298.1 | 1.0 | 310.7 | 1.0 |
| 304.0 | 1.0 | 294.9 | 1.0 | 286.8 | 1.0 |
| 298.5 | 1.0 | 296.6 | 1.0 | 293.8 | 1.0 |
| 297.5 | 1.0 | 304.0 | 1.0 | 298.4 | 1.0 |
| 295.8 | 1.0 | 310.0 | 1.0 | 299.6 | 1.0 |
| 303.4 | 1.0 | 298.6 | 1.0 | 290.6 | 1.0 |
| 297.7 | 1.0 | 307.3 | 1.0 | 309.9 | 1.0 |

| Artificial U2 Fine grain granodiorite |
|---|

| Age (Ma) | Error (Ma) | Age (Ma) | Error (Ma) | Age (Ma) | Error (Ma) |
|---|---|---|---|---|---|
| 357.8 | 1.0 | 344.6 | 1.0 | 361.3 | 1.0 |
| 352.6 | 1.0 | 353.6 | 1.0 | 355.2 | 1.0 |
| 346.0 | 1.0 | 351.7 | 1.0 | 346.5 | 1.0 |
| 349.2 | 1.0 | 348.3 | 1.0 | 346.9 | 1.0 |
| 345.0 | 1.0 | 352.8 | 1.0 | 353.3 | 1.0 |
| 346.4 | 1.0 | 361.2 | 1.0 | 348.5 | 1.0 |
| 340.5 | 1.0 | 352.3 | 1.0 | 340.6 | 1.0 |
| 346.1 | 1.0 | 347.2 | 1.0 | 357.9 | 1.0 |
| 353.7 | 1.0 | 349.2 | 1.0 | 350.0 | 1.0 |
| 352.7 | 1.0 | 342.6 | 1.0 | 346.7 | 1.0 |
| 344.4 | 1.0 | 351.7 | 1.0 | 349.4 | 1.0 |
| 348.5 | 1.0 | 349.5 | 1.0 | 356.1 | 1.0 |
| 351.5 | 1.0 | 349.6 | 1.0 | 353.6 | 1.0 |
| 359.5 | 1.0 | 343.0 | 1.0 | 355.2 | 1.0 |
| 352.2 | 1.0 | 363.0 | 1.0 | 347.8 | 1.0 |
| 341.5 | 1.0 | 351.8 | 1.0 | 347.7 | 1.0 |
| 356.8 | 1.0 | 345.2 | 1.0 | 352.4 | 1.0 |
| 362.5 | 1.0 | 353.3 | 1.0 | 351.9 | 1.0 |
| 345.4 | 1.0 | 339.8 | 1.0 | 347.4 | 1.0 |
| 352.7 | 1.0 | 349.9 | 1.0 | 355.5 | 1.0 |
| 364.8 | 1.0 | 355.2 | 1.0 | 349.2 | 1.0 |
| 352.4 | 1.0 | 341.1 | 1.0 | 356.0 | 1.0 |
| 343.0 | 1.0 | 358.0 | 1.0 | 346.0 | 1.0 |
| 345.8 | 1.0 | 348.4 | 1.0 | 335.9 | 1.0 |
| 354.1 | 1.0 | 351.3 | 1.0 | 347.5 | 1.0 |
| 350.1 | 1.0 | 346.2 | 1.0 | 346.3 | 1.0 |
| 339.1 | 1.0 | 354.9 | 1.0 | 346.4 | 1.0 |
| 345.0 | 1.0 | 354.1 | 1.0 | 356.9 | 1.0 |
| 347.8 | 1.0 | 348.1 | 1.0 | 346.6 | 1.0 |
| 351.9 | 1.0 | 336.6 | 1.0 | 350.5 | 1.0 |
| 355.0 | 1.0 | 347.7 | 1.0 | 353.2 | 1.0 |
| 350.7 | 1.0 | 339.3 | 1.0 | 347.8 | 1.0 |
| 352.2 | 1.0 | 345.7 | 1.0 | 349.9 | 1.0 |
| 354.3 | 1.0 | 359.6 | 1.0 | 353.0 | 1.0 |
| 349.3 | 1.0 | 347.1 | 1.0 | 347.0 | 1.0 |
| 356.5 | 1.0 | 348.3 | 1.0 | 343.0 | 1.0 |
| 357.1 | 1.0 | 357.1 | 1.0 | 348.4 | 1.0 |
| 338.4 | 1.0 | 338.7 | 1.0 | 344.3 | 1.0 |
| 352.1 | 1.0 | 336.8 | 1.0 | 352.3 | 1.0 |

| Artificial U2 Medium fine granodiorite | | | | | |
|---|---|---|---|---|---|
| Age | Error | Age | Error | Age | Error |

| (Ma) | (Ma) | (Ma) | (Ma) | (Ma) | (Ma) |
|---|---|---|---|---|---|
| 393.7 | 1.0 | 405.6 | 1.0 | 390.4 | 1.0 |
| 406.4 | 1.0 | 402.0 | 1.0 | 398.9 | 1.0 |
| 403.5 | 1.0 | 390.7 | 1.0 | 410.2 | 1.0 |
| 401.6 | 1.0 | 398.2 | 1.0 | 401.1 | 1.0 |
| 406.6 | 1.0 | 399.0 | 1.0 | 403.2 | 1.0 |
| 389.8 | 1.0 | 405.3 | 1.0 | 397.3 | 1.0 |
| 398.8 | 1.0 | 405.5 | 1.0 | 399.2 | 1.0 |
| 393.9 | 1.0 | 398.9 | 1.0 | 408.3 | 1.0 |
| 395.7 | 1.0 | 394.6 | 1.0 | 394.4 | 1.0 |
| 391.8 | 1.0 | 404.5 | 1.0 | 405.8 | 1.0 |
| 395.2 | 1.0 | 404.1 | 1.0 | 401.7 | 1.0 |
| 385.8 | 1.0 | 395.2 | 1.0 | 401.7 | 1.0 |
| 396.6 | 1.0 | 392.2 | 1.0 | 384.5 | 1.0 |
| 401.0 | 1.0 | 406.5 | 1.0 | 400.8 | 1.0 |
| 393.4 | 1.0 | 396.7 | 1.0 | 406.2 | 1.0 |
| 404.3 | 1.0 | 393.8 | 1.0 | 394.9 | 1.0 |
| 399.8 | 1.0 | 393.8 | 1.0 | 391.0 | 1.0 |
| 389.0 | 1.0 | 413.4 | 1.0 | 397.7 | 1.0 |
| 402.7 | 1.0 | 399.9 | 1.0 | 397.2 | 1.0 |
| 409.2 | 1.0 | 403.2 | 1.0 | 396.4 | 1.0 |
| 398.6 | 1.0 | 398.7 | 1.0 | 394.3 | 1.0 |
| 406.5 | 1.0 | 396.2 | 1.0 | 392.2 | 1.0 |
| 397.8 | 1.0 | 402.6 | 1.0 | 403.8 | 1.0 |
| 397.5 | 1.0 | 399.2 | 1.0 | 398.1 | 1.0 |
| 389.8 | 1.0 | 403.8 | 1.0 | 403.1 | 1.0 |
| 397.9 | 1.0 | 391.6 | 1.0 | 401.2 | 1.0 |
| 398.4 | 1.0 | 390.3 | 1.0 | 398.4 | 1.0 |
| 403.0 | 1.0 | 405.9 | 1.0 | 403.5 | 1.0 |
| 405.8 | 1.0 | 404.6 | 1.0 | 398.5 | 1.0 |
| 405.7 | 1.0 | 395.2 | 1.0 | 391.4 | 1.0 |
| 394.6 | 1.0 | 408.5 | 1.0 | 390.0 | 1.0 |
| 392.0 | 1.0 | 389.0 | 1.0 | 400.0 | 1.0 |
| 396.6 | 1.0 | 400.1 | 1.0 | 407.3 | 1.0 |
| 402.5 | 1.0 | 396.9 | 1.0 | 395.5 | 1.0 |
| 393.2 | 1.0 | 410.3 | 1.0 | 408.1 | 1.0 |
| 401.7 | 1.0 | 392.1 | 1.0 | 393.0 | 1.0 |
| 395.7 | 1.0 | 404.3 | 1.0 | 403.0 | 1.0 |
| 386.3 | 1.0 | 397.4 | 1.0 | 398.9 | 1.0 |
| 395.6 | 1.0 | 393.3 | 1.0 | 404.2 | 1.0 |

| Artificial U1 Mesocratic granite | | | | | |
|---|---|---|---|---|---|
| Age (Ma) | Error (Ma) | Age (Ma) | Error (Ma) | Age (Ma) | Error (Ma) |

| | | | | | |
|---|---|---|---|---|---|
| 451.3 | 1.0 | 455.9 | 1.0 | 449.7 | 1.0 |
| 450.2 | 1.0 | 450.9 | 1.0 | 450.2 | 1.0 |
| 445.1 | 1.0 | 452.2 | 1.0 | 455.0 | 1.0 |
| 451.4 | 1.0 | 447.1 | 1.0 | 454.1 | 1.0 |
| 456.4 | 1.0 | 444.0 | 1.0 | 453.6 | 1.0 |
| 453.0 | 1.0 | 453.8 | 1.0 | 442.7 | 1.0 |
| 448.1 | 1.0 | 451.0 | 1.0 | 453.1 | 1.0 |
| 441.0 | 1.0 | 455.7 | 1.0 | 442.7 | 1.0 |
| 447.7 | 1.0 | 441.5 | 1.0 | 446.3 | 1.0 |
| 442.4 | 1.0 | 448.1 | 1.0 | 446.0 | 1.0 |
| 447.8 | 1.0 | 452.5 | 1.0 | 446.7 | 1.0 |
| 440.3 | 1.0 | 451.7 | 1.0 | 456.3 | 1.0 |
| 451.0 | 1.0 | 447.8 | 1.0 | 446.9 | 1.0 |
| 442.9 | 1.0 | 447.9 | 1.0 | 436.4 | 1.0 |
| 447.6 | 1.0 | 458.8 | 1.0 | 443.5 | 1.0 |
| 456.1 | 1.0 | 452.2 | 1.0 | 456.1 | 1.0 |
| 455.7 | 1.0 | 455.1 | 1.0 | 453.7 | 1.0 |
| 441.0 | 1.0 | 451.9 | 1.0 | 448.6 | 1.0 |
| 454.0 | 1.0 | 452.4 | 1.0 | 457.5 | 1.0 |
| 445.9 | 1.0 | 456.9 | 1.0 | 452.6 | 1.0 |
| 451.5 | 1.0 | 448.6 | 1.0 | 453.8 | 1.0 |
| 447.8 | 1.0 | 457.6 | 1.0 | 457.6 | 1.0 |
| 447.2 | 1.0 | 453.1 | 1.0 | 453.8 | 1.0 |
| 450.9 | 1.0 | 450.4 | 1.0 | 449.7 | 1.0 |
| 449.9 | 1.0 | 451.6 | 1.0 | 451.7 | 1.0 |
| 445.9 | 1.0 | 436.2 | 1.0 | 437.1 | 1.0 |
| 462.4 | 1.0 | 452.0 | 1.0 | 462.8 | 1.0 |
| 448.6 | 1.0 | 451.7 | 1.0 | 452.7 | 1.0 |
| 437.6 | 1.0 | 449.6 | 1.0 | 456.0 | 1.0 |
| 451.8 | 1.0 | 443.2 | 1.0 | 453.9 | 1.0 |
| 456.3 | 1.0 | 441.5 | 1.0 | 451.5 | 1.0 |
| 453.2 | 1.0 | 457.5 | 1.0 | 452.3 | 1.0 |
| 457.7 | 1.0 | 447.1 | 1.0 | 463.9 | 1.0 |
| 451.6 | 1.0 | 449.8 | 1.0 | 460.4 | 1.0 |
| 457.7 | 1.0 | 441.2 | 1.0 | 452.9 | 1.0 |
| 445.4 | 1.0 | 449.2 | 1.0 | 451.7 | 1.0 |
| 447.0 | 1.0 | 446.2 | 1.0 | 450.4 | 1.0 |
| 454.0 | 1.0 | 450.4 | 1.0 | 455.6 | 1.0 |
| 456.3 | 1.0 | 446.6 | 1.0 | 454.3 | 1.0 |

| Artificial Sample A | | | | | |
|---|---|---|---|---|---|
| Age (Ma) | Error (Ma) | Age (Ma) | Error (Ma) | Age (Ma) | Error (Ma) |

| | | | | | |
|---|---|---|---|---|---|
| 301.6 | 1.0 | 301.3 | 1.0 | 302.2 | 1.0 |
| 299.8 | 1.0 | 294.0 | 1.0 | 303.5 | 1.0 |
| 305.1 | 1.0 | 309.5 | 1.0 | 305.3 | 1.0 |
| 298.9 | 1.0 | 291.2 | 1.0 | 300.2 | 1.0 |
| 300.4 | 1.0 | 302.2 | 1.0 | 296.7 | 1.0 |
| 312.4 | 1.0 | 303.9 | 1.0 | 292.8 | 1.0 |
| 304.3 | 1.0 | 303.5 | 1.0 | 306.1 | 1.0 |
| 299.8 | 1.0 | 294.5 | 1.0 | 308.5 | 1.0 |
| 293.7 | 1.0 | 303.9 | 1.0 | 306.2 | 1.0 |
| 308.3 | 1.0 | 305.4 | 1.0 | 292.9 | 1.0 |
| 286.0 | 1.0 | 305.1 | 1.0 | 302.1 | 1.0 |
| 304.4 | 1.0 | 299.0 | 1.0 | 306.0 | 1.0 |
| 302.4 | 1.0 | 289.0 | 1.0 | 300.6 | 1.0 |
| 304.0 | 1.0 | 299.8 | 1.0 | 296.9 | 1.0 |
| 297.6 | 1.0 | 300.6 | 1.0 | 297.4 | 1.0 |
| 308.5 | 1.0 | 298.8 | 1.0 | 301.9 | 1.0 |
| 301.6 | 1.0 | 289.3 | 1.0 | 297.0 | 1.0 |
| 302.8 | 1.0 | 304.2 | 1.0 | 301.1 | 1.0 |
| 297.8 | 1.0 | 291.7 | 1.0 | 289.9 | 1.0 |
| 299.1 | 1.0 | 298.3 | 1.0 | 301.6 | 1.0 |
| 310.7 | 1.0 | 300.5 | 1.0 | 296.4 | 1.0 |
| 313.4 | 1.0 | 294.9 | 1.0 | 303.4 | 1.0 |
| 299.8 | 1.0 | 309.4 | 1.0 | 300.9 | 1.0 |
| 294.1 | 1.0 | 300.7 | 1.0 | 300.5 | 1.0 |
| 309.8 | 1.0 | 303.8 | 1.0 | 297.2 | 1.0 |
| 295.7 | 1.0 | 301.4 | 1.0 | 296.6 | 1.0 |
| 303.8 | 1.0 | 307.0 | 1.0 | 295.3 | 1.0 |
| 296.3 | 1.0 | 304.7 | 1.0 | 291.9 | 1.0 |
| 303.0 | 1.0 | 297.9 | 1.0 | 302.5 | 1.0 |
| 297.1 | 1.0 | 297.2 | 1.0 | 302.1 | 1.0 |
| 290.8 | 1.0 | 301.7 | 1.0 | 293.9 | 1.0 |
| 291.4 | 1.0 | 304.7 | 1.0 | 299.8 | 1.0 |
| 301.6 | 1.0 | 307.2 | 1.0 | 297.5 | 1.0 |
| 301.1 | 1.0 | 300.8 | 1.0 | 301.3 | 1.0 |
| 306.6 | 1.0 | 303.3 | 1.0 | 305.8 | 1.0 |
| 310.5 | 1.0 | 294.5 | 1.0 | 289.9 | 1.0 |
| 285.6 | 1.0 | 301.4 | 1.0 | 299.7 | 1.0 |
| 291.3 | 1.0 | 294.3 | 1.0 | 299.7 | 1.0 |
| 304.3 | 1.0 | 299.2 | 1.0 | 303.3 | 1.0 |
| 303.6 | 1.0 | 312.3 | 1.0 | 305.3 | 1.0 |
| 299.7 | 1.0 | 304.9 | 1.0 | 297.0 | 1.0 |
| 297.9 | 1.0 | 313.5 | 1.0 | 304.0 | 1.0 |
| 296.5 | 1.0 | 298.7 | 1.0 | 308.5 | 1.0 |
| 293.9 | 1.0 | 300.3 | 1.0 | 300.5 | 1.0 |

| | | | | | |
|---|---|---|---|---|---|
| 305.3 | 1.0 | 298.5 | 1.0 | 301.6 | 1.0 |
| 292.8 | 1.0 | 301.7 | 1.0 | 300.2 | 1.0 |
| 306.2 | 1.0 | 290.0 | 1.0 | 299.7 | 1.0 |
| 294.4 | 1.0 | 295.0 | 1.0 | 309.3 | 1.0 |
| 292.4 | 1.0 | 300.1 | 1.0 | 307.6 | 1.0 |
| 297.6 | 1.0 | 306.7 | 1.0 | 312.6 | 1.0 |
| 295.6 | 1.0 | 293.5 | 1.0 | 301.9 | 1.0 |
| 299.9 | 1.0 | 309.8 | 1.0 | 301.7 | 1.0 |
| 295.0 | 1.0 | 288.8 | 1.0 | 293.9 | 1.0 |
| 307.1 | 1.0 | 291.4 | 1.0 | 300.9 | 1.0 |
| 298.7 | 1.0 | 300.8 | 1.0 | 303.1 | 1.0 |
| 305.7 | 1.0 | 300.8 | 1.0 | 303.2 | 1.0 |
| 301.6 | 1.0 | 295.2 | 1.0 | 298.0 | 1.0 |
| 308.8 | 1.0 | 293.2 | 1.0 | 288.1 | 1.0 |
| 297.6 | 1.0 | 306.1 | 1.0 | 302.4 | 1.0 |
| 300.2 | 1.0 | 302.6 | 1.0 | 295.7 | 1.0 |
| 305.1 | 1.0 | 305.9 | 1.0 | 291.6 | 1.0 |
| 297.7 | 1.0 | 309.0 | 1.0 | 296.7 | 1.0 |
| 296.5 | 1.0 | 297.9 | 1.0 | 295.3 | 1.0 |
| 306.2 | 1.0 | 304.1 | 1.0 | 310.4 | 1.0 |
| 296.5 | 1.0 | 298.0 | 1.0 | 307.2 | 1.0 |
| 288.4 | 1.0 | 303.8 | 1.0 | 298.2 | 1.0 |
| 292.5 | 1.0 | 300.5 | 1.0 | 296.2 | 1.0 |
| 305.4 | 1.0 | 302.3 | 1.0 | 310.8 | 1.0 |
| 301.6 | 1.0 | 299.7 | 1.0 | 304.1 | 1.0 |
| 298.5 | 1.0 | 303.5 | 1.0 | 297.2 | 1.0 |
| 294.1 | 1.0 | 303.6 | 1.0 | 306.9 | 1.0 |
| 307.8 | 1.0 | 299.7 | 1.0 | 288.0 | 1.0 |
| 304.0 | 1.0 | 295.3 | 1.0 | 304.2 | 1.0 |
| 308.2 | 1.0 | 306.6 | 1.0 | 309.7 | 1.0 |
| 300.3 | 1.0 | 296.8 | 1.0 | 299.1 | 1.0 |
| 300.3 | 1.0 | 300.1 | 1.0 | 294.6 | 1.0 |
| 298.7 | 1.0 | 317.9 | 1.0 | 300.9 | 1.0 |
| 307.5 | 1.0 | 298.4 | 1.0 | 305.5 | 1.0 |
| 301.9 | 1.0 | 294.0 | 1.0 | 292.7 | 1.0 |
| 306.6 | 1.0 | 304.6 | 1.0 | 306.9 | 1.0 |
| 306.4 | 1.0 | 297.3 | 1.0 | 295.7 | 1.0 |
| 298.0 | 1.0 | 303.2 | 1.0 | 296.8 | 1.0 |
| 288.6 | 1.0 | 292.7 | 1.0 | 307.6 | 1.0 |
| 296.6 | 1.0 | 301.7 | 1.0 | 296.3 | 1.0 |
| 301.9 | 1.0 | 289.7 | 1.0 | 294.1 | 1.0 |
| 303.0 | 1.0 | 300.9 | 1.0 | 300.8 | 1.0 |
| 298.6 | 1.0 | 296.8 | 1.0 | 293.2 | 1.0 |
| 298.6 | 1.0 | 311.2 | 1.0 | 298.3 | 1.0 |

| | | | | | |
|---|---|---|---|---|---|
| 295.3 | 1.0 | 300.2 | 1.0 | 314.0 | 1.0 |
| 305.8 | 1.0 | 312.1 | 1.0 | 301.9 | 1.0 |
| 309.7 | 1.0 | 298.3 | 1.0 | 291.8 | 1.0 |
| 294.0 | 1.0 | 351.3 | 1.0 | 296.4 | 1.0 |
| 289.5 | 1.0 | 354.1 | 1.0 | 300.4 | 1.0 |
| 303.1 | 1.0 | 340.7 | 1.0 | 297.9 | 1.0 |
| 309.7 | 1.0 | 340.4 | 1.0 | 299.7 | 1.0 |
| 308.8 | 1.0 | 345.4 | 1.0 | 302.8 | 1.0 |
| 296.0 | 1.0 | 352.0 | 1.0 | 299.3 | 1.0 |
| 304.9 | 1.0 | 347.2 | 1.0 | 297.8 | 1.0 |
| 293.5 | 1.0 | 342.1 | 1.0 | 299.1 | 1.0 |
| 296.4 | 1.0 | 351.9 | 1.0 | 302.2 | 1.0 |
| 302.8 | 1.0 | 343.2 | 1.0 | 300.2 | 1.0 |
| 304.7 | 1.0 | 346.0 | 1.0 | 298.4 | 1.0 |
| 309.5 | 1.0 | 352.1 | 1.0 | 294.8 | 1.0 |
| 304.9 | 1.0 | 348.4 | 1.0 | 303.7 | 1.0 |
| 303.0 | 1.0 | 348.8 | 1.0 | 297.6 | 1.0 |
| 304.1 | 1.0 | 353.7 | 1.0 | 307.8 | 1.0 |
| 296.5 | 1.0 | 347.6 | 1.0 | 313.6 | 1.0 |
| 294.2 | 1.0 | 352.7 | 1.0 | 301.5 | 1.0 |
| 303.3 | 1.0 | 351.4 | 1.0 | 401.1 | 1.0 |
| 305.1 | 1.0 | 344.4 | 1.0 | 399.5 | 1.0 |
| 304.4 | 1.0 | 362.0 | 1.0 | 397.1 | 1.0 |
| 293.7 | 1.0 | 354.3 | 1.0 | 400.8 | 1.0 |
| 298.5 | 1.0 | 355.4 | 1.0 | 399.8 | 1.0 |
| 303.1 | 1.0 | 352.5 | 1.0 | 404.9 | 1.0 |
| 302.8 | 1.0 | 350.3 | 1.0 | 403.7 | 1.0 |
| 302.7 | 1.0 | 336.6 | 1.0 | 401.9 | 1.0 |
| 300.5 | 1.0 | 345.4 | 1.0 | 396.0 | 1.0 |
| 297.4 | 1.0 | 353.7 | 1.0 | 408.2 | 1.0 |
| 307.7 | 1.0 | 349.7 | 1.0 | 402.5 | 1.0 |
| 306.2 | 1.0 | 335.4 | 1.0 | 395.5 | 1.0 |
| 303.6 | 1.0 | 343.5 | 1.0 | 393.9 | 1.0 |
| 296.5 | 1.0 | 351.0 | 1.0 | 389.2 | 1.0 |
| 305.2 | 1.0 | 349.9 | 1.0 | 394.2 | 1.0 |
| 304.7 | 1.0 | 350.0 | 1.0 | 407.3 | 1.0 |
| 291.2 | 1.0 | 349.8 | 1.0 | 400.0 | 1.0 |
| 310.5 | 1.0 | 361.2 | 1.0 | 403.2 | 1.0 |
| 303.9 | 1.0 | 352.0 | 1.0 | 401.9 | 1.0 |
| 302.9 | 1.0 | 356.2 | 1.0 | 403.1 | 1.0 |
| 299.5 | 1.0 | 351.6 | 1.0 | 395.8 | 1.0 |
| 300.8 | 1.0 | 359.1 | 1.0 | 411.2 | 1.0 |
| 307.8 | 1.0 | 363.1 | 1.0 | 398.8 | 1.0 |
| 307.9 | 1.0 | 360.4 | 1.0 | 406.6 | 1.0 |

| | | | | | |
|---|---|---|---|---|---|
| 295.5 | 1.0 | 347.4 | 1.0 | 402.8 | 1.0 |
| 300.1 | 1.0 | 356.1 | 1.0 | 395.1 | 1.0 |
| 298.3 | 1.0 | 341.3 | 1.0 | 396.8 | 1.0 |
| 296.1 | 1.0 | 339.1 | 1.0 | 405.9 | 1.0 |
| 310.4 | 1.0 | 347.9 | 1.0 | 397.2 | 1.0 |
| 315.9 | 1.0 | 358.7 | 1.0 | 407.9 | 1.0 |
| 299.8 | 1.0 | 341.0 | 1.0 | 395.4 | 1.0 |
| 299.6 | 1.0 | 350.4 | 1.0 | 402.7 | 1.0 |
| 295.5 | 1.0 | 353.9 | 1.0 | 401.2 | 1.0 |
| 296.7 | 1.0 | 347.8 | 1.0 | 398.0 | 1.0 |
| 299.3 | 1.0 | 397.8 | 1.0 | 397.8 | 1.0 |
| 306.4 | 1.0 | 409.1 | 1.0 | 398.0 | 1.0 |
| 290.8 | 1.0 | 397.4 | 1.0 | 401.6 | 1.0 |
| 291.0 | 1.0 | 386.6 | 1.0 | 403.6 | 1.0 |
| 306.5 | 1.0 | 400.6 | 1.0 | 389.7 | 1.0 |
| 294.4 | 1.0 | 402.8 | 1.0 | 400.0 | 1.0 |
| 300.3 | 1.0 | 403.4 | 1.0 | 400.0 | 1.0 |
| 300.4 | 1.0 | 395.6 | 1.0 | 407.8 | 1.0 |
| 308.3 | 1.0 | 410.1 | 1.0 | 461.7 | 1.0 |
| 300.4 | 1.0 | 399.0 | 1.0 | 447.7 | 1.0 |
| 452.8 | 1.0 | 442.0 | 1.0 | 437.0 | 1.0 |
| 448.9 | 1.0 | 442.0 | 1.0 | 451.9 | 1.0 |
| 444.5 | 1.0 | 433.7 | 1.0 | 445.6 | 1.0 |
| 441.9 | 1.0 | 453.5 | 1.0 | | |

Table S5: Artificial U–Pb created for the scenario A3.

| Artificial U2 leucomonzogranite | | | | | |
|---|---|---|---|---|---|
| Age (Ma) | Error (Ma) | Age (Ma) | Error (Ma) | Age (Ma) | Error (Ma) |
| 305.2 | 1.0 | 309.9 | 1.0 | 294.1 | 1.0 |
| 303.1 | 1.0 | 301.0 | 1.0 | 303.0 | 1.0 |
| 298.9 | 1.0 | 290.8 | 1.0 | 303.2 | 1.0 |
| 302.2 | 1.0 | 305.8 | 1.0 | 297.2 | 1.0 |
| 302.9 | 1.0 | 304.9 | 1.0 | 307.6 | 1.0 |
| 301.0 | 1.0 | 307.6 | 1.0 | 301.0 | 1.0 |
| 285.4 | 1.0 | 298.3 | 1.0 | 303.9 | 1.0 |
| 290.4 | 1.0 | 292.5 | 1.0 | 301.2 | 1.0 |
| 303.2 | 1.0 | 304.8 | 1.0 | 304.3 | 1.0 |
| 304.7 | 1.0 | 296.8 | 1.0 | 300.4 | 1.0 |
| 291.5 | 1.0 | 301.0 | 1.0 | 296.8 | 1.0 |
| 303.8 | 1.0 | 306.5 | 1.0 | 306.5 | 1.0 |
| 293.0 | 1.0 | 300.4 | 1.0 | 296.5 | 1.0 |
| 296.3 | 1.0 | 301.6 | 1.0 | 301.1 | 1.0 |
| 302.0 | 1.0 | 304.4 | 1.0 | 295.5 | 1.0 |

| | | | | | |
|---|---|---|---|---|---|
| 306.7 | 1.0 | 291.0 | 1.0 | 283.9 | 1.0 |
| 289.9 | 1.0 | 318.7 | 1.0 | 296.2 | 1.0 |
| 288.6 | 1.0 | 299.0 | 1.0 | 301.6 | 1.0 |
| 301.1 | 1.0 | 299.9 | 1.0 | 305.0 | 1.0 |
| 300.6 | 1.0 | 297.9 | 1.0 | 302.2 | 1.0 |
| 308.2 | 1.0 | 305.1 | 1.0 | 298.2 | 1.0 |
| 302.2 | 1.0 | 284.1 | 1.0 | 295.8 | 1.0 |
| 303.1 | 1.0 | 309.1 | 1.0 | 308.1 | 1.0 |
| 294.6 | 1.0 | 296.2 | 1.0 | 293.4 | 1.0 |
| 305.1 | 1.0 | 298.5 | 1.0 | 296.0 | 1.0 |
| 291.5 | 1.0 | 311.7 | 1.0 | 301.8 | 1.0 |
| 286.1 | 1.0 | 290.3 | 1.0 | 304.2 | 1.0 |
| 294.5 | 1.0 | 307.1 | 1.0 | 304.5 | 1.0 |
| 299.8 | 1.0 | 293.8 | 1.0 | 303.2 | 1.0 |
| 300.2 | 1.0 | 297.8 | 1.0 | 304.5 | 1.0 |
| 304.0 | 1.0 | 314.5 | 1.0 | 297.0 | 1.0 |
| 304.4 | 1.0 | 300.4 | 1.0 | 300.0 | 1.0 |
| 299.1 | 1.0 | 298.8 | 1.0 | 297.5 | 1.0 |
| 298.6 | 1.0 | 299.2 | 1.0 | 307.7 | 1.0 |
| 302.6 | 1.0 | 304.6 | 1.0 | 312.1 | 1.0 |
| 289.9 | 1.0 | 306.3 | 1.0 | 297.0 | 1.0 |
| 300.3 | 1.0 | 301.4 | 1.0 | 305.7 | 1.0 |
| 294.8 | 1.0 | 292.4 | 1.0 | 309.5 | 1.0 |
| 302.4 | 1.0 | 299.7 | 1.0 | 298.8 | 1.0 |

| Artificial U2 fine grain granodiorite | | | | | |
|---|---|---|---|---|---|
| Age (Ma) | Error (Ma) | Age (Ma) | Error (Ma) | Age (Ma) | Error (Ma) |
| 324.1 | 1.0 | 324.2 | 1.0 | 329.3 | 1.0 |
| 319.6 | 1.0 | 330.8 | 1.0 | 322.5 | 1.0 |
| 310.4 | 1.0 | 319.1 | 1.0 | 325.9 | 1.0 |
| 322.6 | 1.0 | 324.8 | 1.0 | 329.5 | 1.0 |
| 322.5 | 1.0 | 331.7 | 1.0 | 323.5 | 1.0 |
| 322.3 | 1.0 | 332.4 | 1.0 | 318.3 | 1.0 |
| 323.3 | 1.0 | 330.6 | 1.0 | 326.0 | 1.0 |
| 320.4 | 1.0 | 329.0 | 1.0 | 334.8 | 1.0 |
| 332.7 | 1.0 | 328.7 | 1.0 | 324.6 | 1.0 |
| 328.1 | 1.0 | 308.1 | 1.0 | 331.0 | 1.0 |
| 320.8 | 1.0 | 332.1 | 1.0 | 325.8 | 1.0 |
| 317.6 | 1.0 | 328.7 | 1.0 | 328.0 | 1.0 |
| 318.8 | 1.0 | 327.1 | 1.0 | 317.0 | 1.0 |
| 307.2 | 1.0 | 320.4 | 1.0 | 316.3 | 1.0 |
| 316.2 | 1.0 | 339.0 | 1.0 | 318.6 | 1.0 |
| 328.6 | 1.0 | 320.4 | 1.0 | 326.6 | 1.0 |

| | | | | | |
|---|---|---|---|---|---|
| 334.7 | 1.0 | 323.0 | 1.0 | 337.0 | 1.0 |
| 325.1 | 1.0 | 327.3 | 1.0 | 316.6 | 1.0 |
| 316.2 | 1.0 | 320.2 | 1.0 | 336.8 | 1.0 |
| 333.3 | 1.0 | 324.5 | 1.0 | 332.6 | 1.0 |
| 323.1 | 1.0 | 321.5 | 1.0 | 318.2 | 1.0 |
| 334.3 | 1.0 | 311.7 | 1.0 | 330.2 | 1.0 |
| 313.1 | 1.0 | 324.1 | 1.0 | 326.1 | 1.0 |
| 318.3 | 1.0 | 323.2 | 1.0 | 326.1 | 1.0 |
| 325.1 | 1.0 | 322.2 | 1.0 | 323.8 | 1.0 |
| 323.7 | 1.0 | 317.4 | 1.0 | 322.0 | 1.0 |
| 326.8 | 1.0 | 319.0 | 1.0 | 318.3 | 1.0 |
| 327.4 | 1.0 | 323.3 | 1.0 | 323.6 | 1.0 |
| 327.1 | 1.0 | 321.7 | 1.0 | 328.6 | 1.0 |
| 318.6 | 1.0 | 314.7 | 1.0 | 335.9 | 1.0 |
| 331.1 | 1.0 | 328.3 | 1.0 | 316.9 | 1.0 |
| 321.4 | 1.0 | 326.7 | 1.0 | 325.2 | 1.0 |
| 324.4 | 1.0 | 318.4 | 1.0 | 331.0 | 1.0 |
| 330.9 | 1.0 | 317.8 | 1.0 | 329.2 | 1.0 |
| 321.1 | 1.0 | 326.9 | 1.0 | 323.0 | 1.0 |
| 323.9 | 1.0 | 317.4 | 1.0 | 318.6 | 1.0 |
| 325.4 | 1.0 | 334.5 | 1.0 | 327.6 | 1.0 |
| 315.9 | 1.0 | 326.7 | 1.0 | 331.0 | 1.0 |
| 329.2 | 1.0 | 325.2 | 1.0 | 322.3 | 1.0 |

| Artificial U2 medium grain monzogranite | | | | | |
|---|---|---|---|---|---|
| Age (Ma) | Error (Ma) | Age (Ma) | Error (Ma) | Age (Ma) | Error (Ma) |
| 344.9 | 1.0 | 344.4 | 1.0 | 349.2 | 1.0 |
| 340.5 | 1.0 | 347.3 | 1.0 | 358.3 | 1.0 |
| 345.9 | 1.0 | 355.2 | 1.0 | 349.9 | 1.0 |
| 342.2 | 1.0 | 348.6 | 1.0 | 344.3 | 1.0 |
| 348.5 | 1.0 | 343.2 | 1.0 | 347.9 | 1.0 |
| 359.1 | 1.0 | 347.8 | 1.0 | 360.4 | 1.0 |
| 347.9 | 1.0 | 346.5 | 1.0 | 350.2 | 1.0 |
| 345.3 | 1.0 | 350.7 | 1.0 | 350.7 | 1.0 |
| 339.8 | 1.0 | 352.8 | 1.0 | 357.2 | 1.0 |
| 346.0 | 1.0 | 356.0 | 1.0 | 345.0 | 1.0 |
| 347.4 | 1.0 | 348.5 | 1.0 | 350.4 | 1.0 |
| 351.8 | 1.0 | 351.0 | 1.0 | 345.6 | 1.0 |
| 354.8 | 1.0 | 357.6 | 1.0 | 360.2 | 1.0 |
| 340.9 | 1.0 | 343.4 | 1.0 | 360.1 | 1.0 |
| 341.7 | 1.0 | 342.7 | 1.0 | 346.4 | 1.0 |
| 351.0 | 1.0 | 355.3 | 1.0 | 353.9 | 1.0 |
| 349.9 | 1.0 | 356.7 | 1.0 | 339.5 | 1.0 |

| | | | | | |
|---|---|---|---|---|---|
| 349.0 | 1.0 | 340.6 | 1.0 | 352.1 | 1.0 |
| 351.5 | 1.0 | 337.4 | 1.0 | 348.7 | 1.0 |
| 355.4 | 1.0 | 358.1 | 1.0 | 347.4 | 1.0 |
| 340.3 | 1.0 | 344.0 | 1.0 | 363.3 | 1.0 |
| 347.3 | 1.0 | 358.2 | 1.0 | 344.9 | 1.0 |
| 347.0 | 1.0 | 344.3 | 1.0 | 356.4 | 1.0 |
| 348.9 | 1.0 | 351.7 | 1.0 | 343.6 | 1.0 |
| 344.0 | 1.0 | 351.2 | 1.0 | 337.2 | 1.0 |
| 351.0 | 1.0 | 337.7 | 1.0 | 355.9 | 1.0 |
| 340.0 | 1.0 | 340.5 | 1.0 | 343.5 | 1.0 |
| 348.8 | 1.0 | 347.8 | 1.0 | 346.9 | 1.0 |
| 349.6 | 1.0 | 344.4 | 1.0 | 349.5 | 1.0 |
| 351.2 | 1.0 | 341.6 | 1.0 | 343.9 | 1.0 |
| 353.8 | 1.0 | 347.6 | 1.0 | 357.4 | 1.0 |
| 349.0 | 1.0 | 363.2 | 1.0 | 341.3 | 1.0 |
| 343.7 | 1.0 | 337.9 | 1.0 | 351.7 | 1.0 |
| 348.8 | 1.0 | 348.3 | 1.0 | 354.9 | 1.0 |
| 344.5 | 1.0 | 343.1 | 1.0 | 354.1 | 1.0 |
| 348.2 | 1.0 | 346.5 | 1.0 | 351.6 | 1.0 |
| 351.8 | 1.0 | 341.4 | 1.0 | 345.9 | 1.0 |
| 352.0 | 1.0 | 352.9 | 1.0 | 349.1 | 1.0 |
| 350.3 | 1.0 | 348.4 | 1.0 | 354.7 | 1.0 |

| Artificial Sample A | | | | | |
|---|---|---|---|---|---|
| Age (Ma) | Error (Ma) | Age (Ma) | Error (Ma) | Age (Ma) | Error (Ma) |
| 299.1 | 1.0 | 303.4 | 1.0 | 292.7 | 1.0 |
| 297.8 | 1.0 | 287.3 | 1.0 | 299.6 | 1.0 |
| 294.1 | 1.0 | 302.0 | 1.0 | 301.5 | 1.0 |
| 303.9 | 1.0 | 312.2 | 1.0 | 296.0 | 1.0 |
| 300.0 | 1.0 | 302.1 | 1.0 | 309.3 | 1.0 |
| 299.0 | 1.0 | 294.6 | 1.0 | 306.7 | 1.0 |
| 305.3 | 1.0 | 296.1 | 1.0 | 307.0 | 1.0 |
| 292.3 | 1.0 | 302.8 | 1.0 | 303.6 | 1.0 |
| 291.5 | 1.0 | 295.6 | 1.0 | 307.9 | 1.0 |
| 306.7 | 1.0 | 301.7 | 1.0 | 296.9 | 1.0 |
| 300.2 | 1.0 | 303.8 | 1.0 | 301.3 | 1.0 |
| 306.1 | 1.0 | 287.6 | 1.0 | 296.0 | 1.0 |
| 306.4 | 1.0 | 299.3 | 1.0 | 293.5 | 1.0 |
| 296.6 | 1.0 | 292.4 | 1.0 | 300.9 | 1.0 |
| 291.9 | 1.0 | 296.4 | 1.0 | 310.5 | 1.0 |
| 299.3 | 1.0 | 297.3 | 1.0 | 302.4 | 1.0 |
| 291.7 | 1.0 | 282.1 | 1.0 | 287.4 | 1.0 |
| 308.4 | 1.0 | 298.7 | 1.0 | 294.4 | 1.0 |

| | | | | | |
|---|---|---|---|---|---|
| 296.6 | 1.0 | 300.2 | 1.0 | 291.7 | 1.0 |
| 299.1 | 1.0 | 294.1 | 1.0 | 303.3 | 1.0 |
| 297.4 | 1.0 | 298.7 | 1.0 | 293.9 | 1.0 |
| 298.3 | 1.0 | 301.2 | 1.0 | 292.2 | 1.0 |
| 290.9 | 1.0 | 300.9 | 1.0 | 305.6 | 1.0 |
| 305.4 | 1.0 | 289.7 | 1.0 | 297.2 | 1.0 |
| 287.5 | 1.0 | 295.5 | 1.0 | 288.9 | 1.0 |
| 293.2 | 1.0 | 295.8 | 1.0 | 315.5 | 1.0 |
| 297.3 | 1.0 | 300.8 | 1.0 | 306.9 | 1.0 |
| 291.7 | 1.0 | 304.9 | 1.0 | 304.8 | 1.0 |
| 296.2 | 1.0 | 303.2 | 1.0 | 305.8 | 1.0 |
| 300.4 | 1.0 | 303.2 | 1.0 | 303.5 | 1.0 |
| 289.6 | 1.0 | 304.4 | 1.0 | 309.5 | 1.0 |
| 296.6 | 1.0 | 312.1 | 1.0 | 288.6 | 1.0 |
| 299.7 | 1.0 | 304.1 | 1.0 | 307.9 | 1.0 |
| 294.9 | 1.0 | 292.7 | 1.0 | 306.1 | 1.0 |
| 287.4 | 1.0 | 295.2 | 1.0 | 299.0 | 1.0 |
| 297.4 | 1.0 | 297.8 | 1.0 | 294.4 | 1.0 |
| 301.8 | 1.0 | 301.6 | 1.0 | 296.3 | 1.0 |
| 305.6 | 1.0 | 304.1 | 1.0 | 309.3 | 1.0 |
| 303.7 | 1.0 | 300.8 | 1.0 | 299.7 | 1.0 |
| 304.8 | 1.0 | 302.0 | 1.0 | 308.9 | 1.0 |
| 301.8 | 1.0 | 294.5 | 1.0 | 287.9 | 1.0 |
| 302.3 | 1.0 | 301.8 | 1.0 | 304.8 | 1.0 |
| 301.6 | 1.0 | 297.3 | 1.0 | 296.4 | 1.0 |
| 301.7 | 1.0 | 303.3 | 1.0 | 293.6 | 1.0 |
| 292.6 | 1.0 | 309.5 | 1.0 | 315.5 | 1.0 |
| 299.2 | 1.0 | 306.3 | 1.0 | 300.0 | 1.0 |
| 309.0 | 1.0 | 309.4 | 1.0 | 297.2 | 1.0 |
| 306.8 | 1.0 | 290.6 | 1.0 | 284.3 | 1.0 |
| 294.5 | 1.0 | 291.7 | 1.0 | 303.4 | 1.0 |
| 293.4 | 1.0 | 283.0 | 1.0 | 302.2 | 1.0 |
| 303.9 | 1.0 | 297.9 | 1.0 | 293.6 | 1.0 |
| 286.6 | 1.0 | 294.6 | 1.0 | 295.4 | 1.0 |
| 294.5 | 1.0 | 312.6 | 1.0 | 300.1 | 1.0 |
| 292.4 | 1.0 | 308.4 | 1.0 | 300.3 | 1.0 |
| 292.0 | 1.0 | 295.5 | 1.0 | 300.7 | 1.0 |
| 292.8 | 1.0 | 300.7 | 1.0 | 311.3 | 1.0 |
| 309.4 | 1.0 | 306.8 | 1.0 | 297.7 | 1.0 |
| 288.0 | 1.0 | 311.5 | 1.0 | 296.1 | 1.0 |
| 306.2 | 1.0 | 296.4 | 1.0 | 290.2 | 1.0 |
| 310.7 | 1.0 | 304.1 | 1.0 | 295.1 | 1.0 |
| 301.1 | 1.0 | 301.8 | 1.0 | 280.0 | 1.0 |
| 292.7 | 1.0 | 308.5 | 1.0 | 293.5 | 1.0 |

| | | | | | |
|---|---|---|---|---|---|
| 302.1 | 1.0 | 309.2 | 1.0 | 302.4 | 1.0 |
| 304.9 | 1.0 | 303.2 | 1.0 | 295.0 | 1.0 |
| 299.7 | 1.0 | 301.4 | 1.0 | 301.5 | 1.0 |
| 302.7 | 1.0 | 299.3 | 1.0 | 292.9 | 1.0 |
| 296.6 | 1.0 | 297.7 | 1.0 | 291.7 | 1.0 |
| 295.2 | 1.0 | 306.3 | 1.0 | 299.0 | 1.0 |
| 309.0 | 1.0 | 301.0 | 1.0 | 309.5 | 1.0 |
| 299.5 | 1.0 | 301.1 | 1.0 | 298.8 | 1.0 |
| 303.4 | 1.0 | 295.6 | 1.0 | 300.7 | 1.0 |
| 303.7 | 1.0 | 300.9 | 1.0 | 303.4 | 1.0 |
| 301.8 | 1.0 | 305.9 | 1.0 | 297.3 | 1.0 |
| 302.4 | 1.0 | 304.6 | 1.0 | 294.5 | 1.0 |
| 283.9 | 1.0 | 298.1 | 1.0 | 304.2 | 1.0 |
| 296.0 | 1.0 | 290.0 | 1.0 | 288.3 | 1.0 |
| 302.5 | 1.0 | 300.1 | 1.0 | 298.8 | 1.0 |
| 297.0 | 1.0 | 293.3 | 1.0 | 303.6 | 1.0 |
| 306.3 | 1.0 | 296.8 | 1.0 | 310.8 | 1.0 |
| 313.9 | 1.0 | 304.1 | 1.0 | 300.9 | 1.0 |
| 297.8 | 1.0 | 311.8 | 1.0 | 311.3 | 1.0 |
| 293.8 | 1.0 | 303.5 | 1.0 | 294.9 | 1.0 |
| 299.8 | 1.0 | 299.8 | 1.0 | 305.4 | 1.0 |
| 306.0 | 1.0 | 302.3 | 1.0 | 303.1 | 1.0 |
| 302.2 | 1.0 | 305.7 | 1.0 | 308.8 | 1.0 |
| 303.3 | 1.0 | 295.1 | 1.0 | 293.0 | 1.0 |
| 298.9 | 1.0 | 312.4 | 1.0 | 302.0 | 1.0 |
| 306.4 | 1.0 | 292.1 | 1.0 | 300.8 | 1.0 |
| 296.6 | 1.0 | 296.4 | 1.0 | 299.4 | 1.0 |
| 298.3 | 1.0 | 311.0 | 1.0 | 300.8 | 1.0 |
| 303.2 | 1.0 | 294.4 | 1.0 | 287.9 | 1.0 |
| 297.2 | 1.0 | 298.4 | 1.0 | 290.9 | 1.0 |
| 303.1 | 1.0 | 303.0 | 1.0 | 299.5 | 1.0 |
| 294.1 | 1.0 | 304.9 | 1.0 | 312.7 | 1.0 |
| 289.9 | 1.0 | 299.0 | 1.0 | 302.6 | 1.0 |
| 306.1 | 1.0 | 293.0 | 1.0 | 303.7 | 1.0 |
| 298.5 | 1.0 | 298.1 | 1.0 | 302.1 | 1.0 |
| 304.7 | 1.0 | 294.0 | 1.0 | 305.7 | 1.0 |
| 310.1 | 1.0 | 283.9 | 1.0 | 299.6 | 1.0 |
| 303.2 | 1.0 | 308.0 | 1.0 | 298.8 | 1.0 |
| 298.8 | 1.0 | 312.8 | 1.0 | 293.5 | 1.0 |
| 309.1 | 1.0 | 292.4 | 1.0 | 292.6 | 1.0 |
| 295.2 | 1.0 | 300.7 | 1.0 | 304.5 | 1.0 |
| 295.9 | 1.0 | 301.3 | 1.0 | 300.9 | 1.0 |
| 300.5 | 1.0 | 298.1 | 1.0 | 307.5 | 1.0 |
| 295.0 | 1.0 | 301.9 | 1.0 | 296.5 | 1.0 |

| | | | | | |
|---|---|---|---|---|---|
| 295.5 | 1.0 | 360.0 | 1.0 | 324.8 | 1.0 |
| 307.4 | 1.0 | 344.7 | 1.0 | 320.7 | 1.0 |
| 308.1 | 1.0 | 344.5 | 1.0 | 313.9 | 1.0 |
| 308.0 | 1.0 | 350.1 | 1.0 | 314.5 | 1.0 |
| 300.8 | 1.0 | 340.3 | 1.0 | 323.2 | 1.0 |
| 302.0 | 1.0 | 356.7 | 1.0 | 320.3 | 1.0 |
| 301.0 | 1.0 | 350.0 | 1.0 | 328.5 | 1.0 |
| 303.0 | 1.0 | 343.0 | 1.0 | 321.6 | 1.0 |
| 297.9 | 1.0 | 345.1 | 1.0 | 322.2 | 1.0 |
| 297.5 | 1.0 | 338.3 | 1.0 | 320.5 | 1.0 |
| 306.5 | 1.0 | 351.0 | 1.0 | 326.5 | 1.0 |
| 297.5 | 1.0 | 351.8 | 1.0 | 322.9 | 1.0 |
| 299.0 | 1.0 | 343.3 | 1.0 | 328.6 | 1.0 |
| 296.5 | 1.0 | 348.7 | 1.0 | 323.0 | 1.0 |
| 295.0 | 1.0 | 351.1 | 1.0 | 321.7 | 1.0 |
| 306.9 | 1.0 | 346.9 | 1.0 | 333.8 | 1.0 |
| 296.3 | 1.0 | 355.4 | 1.0 | 311.0 | 1.0 |
| 299.3 | 1.0 | 356.8 | 1.0 | 322.2 | 1.0 |
| 294.9 | 1.0 | 349.1 | 1.0 | 328.6 | 1.0 |
| 301.2 | 1.0 | 358.8 | 1.0 | 329.1 | 1.0 |
| 302.7 | 1.0 | 340.6 | 1.0 | 336.6 | 1.0 |
| 294.8 | 1.0 | 346.6 | 1.0 | 316.2 | 1.0 |
| 297.8 | 1.0 | 353.2 | 1.0 | 318.5 | 1.0 |
| 299.2 | 1.0 | 352.8 | 1.0 | 330.1 | 1.0 |
| 292.6 | 1.0 | 338.7 | 1.0 | 330.4 | 1.0 |
| 299.9 | 1.0 | 349.4 | 1.0 | 331.8 | 1.0 |
| 303.0 | 1.0 | 400.1 | 1.0 | 322.8 | 1.0 |
| 299.4 | 1.0 | 396.9 | 1.0 | 326.7 | 1.0 |
| 296.2 | 1.0 | 392.5 | 1.0 | 326.3 | 1.0 |
| 290.2 | 1.0 | 387.5 | 1.0 | 322.5 | 1.0 |
| 305.1 | 1.0 | 400.2 | 1.0 | 328.7 | 1.0 |
| 302.0 | 1.0 | 387.6 | 1.0 | 322.1 | 1.0 |
| 306.7 | 1.0 | 398.0 | 1.0 | 317.7 | 1.0 |
| 309.3 | 1.0 | 399.0 | 1.0 | 331.0 | 1.0 |
| 325.1 | 1.0 | 413.5 | 1.0 | 319.2 | 1.0 |
| 321.1 | 1.0 | 396.1 | 1.0 | 317.9 | 1.0 |
| 331.4 | 1.0 | 396.7 | 1.0 | 319.6 | 1.0 |
| 326.0 | 1.0 | 387.8 | 1.0 | 330.3 | 1.0 |
| 361.7 | 1.0 | 349.0 | 1.0 | 320.4 | 1.0 |
| 348.6 | 1.0 | 354.1 | 1.0 | 336.3 | 1.0 |
| 351.6 | 1.0 | 357.3 | 1.0 | 318.7 | 1.0 |
| 345.1 | 1.0 | 337.7 | 1.0 | 327.7 | 1.0 |
| 349.7 | 1.0 | 347.2 | 1.0 | 336.5 | 1.0 |
| 354.8 | 1.0 | 350.7 | 1.0 | 331.9 | 1.0 |

| | | | | | |
|---|---|---|---|---|---|
| 349.3 | 1.0 | 356.1 | 1.0 | 327.0 | 1.0 |
| 354.9 | 1.0 | 359.5 | 1.0 | 326.4 | 1.0 |
| 348.1 | 1.0 | 346.0 | 1.0 | 321.9 | 1.0 |
| 354.3 | 1.0 | 351.4 | 1.0 | 340.6 | 1.0 |
| 356.0 | 1.0 | 356.4 | 1.0 | 358.4 | 1.0 |
| 344.2 | 1.0 | 348.3 | 1.0 | | |

Table S6: Artificial U–Pb created for the scenario A4.

| Artificial U2 leucomonzogranite | | | | | |
|---|---|---|---|---|---|
| Age (Ma) | Error (Ma) | Age (Ma) | Error (Ma) | Age (Ma) | Error (Ma) |
| 296.1 | 1.0 | 297.9 | 1.0 | 310.9 | 1.0 |
| 293.3 | 1.0 | 300.9 | 1.0 | 300.4 | 1.0 |
| 299.7 | 1.0 | 308.1 | 1.0 | 295.6 | 1.0 |
| 317.0 | 1.0 | 311.2 | 1.0 | 302.4 | 1.0 |
| 295.1 | 1.0 | 298.3 | 1.0 | 300.1 | 1.0 |
| 288.6 | 1.0 | 290.3 | 1.0 | 300.8 | 1.0 |
| 294.5 | 1.0 | 298.5 | 1.0 | 297.9 | 1.0 |
| 293.7 | 1.0 | 304.0 | 1.0 | 295.5 | 1.0 |
| 293.7 | 1.0 | 302.7 | 1.0 | 300.6 | 1.0 |
| 302.7 | 1.0 | 304.8 | 1.0 | 307.3 | 1.0 |
| 304.6 | 1.0 | 304.6 | 1.0 | 302.5 | 1.0 |
| 305.8 | 1.0 | 298.2 | 1.0 | 305.8 | 1.0 |
| 306.2 | 1.0 | 308.6 | 1.0 | 301.7 | 1.0 |
| 294.9 | 1.0 | 298.5 | 1.0 | 294.3 | 1.0 |
| 297.3 | 1.0 | 300.2 | 1.0 | 303.0 | 1.0 |
| 304.1 | 1.0 | 292.3 | 1.0 | 305.9 | 1.0 |
| 309.9 | 1.0 | 295.4 | 1.0 | 297.8 | 1.0 |
| 300.0 | 1.0 | 303.9 | 1.0 | 293.5 | 1.0 |
| 304.9 | 1.0 | 302.8 | 1.0 | 300.0 | 1.0 |
| 298.3 | 1.0 | 289.2 | 1.0 | 298.7 | 1.0 |
| 300.8 | 1.0 | 311.7 | 1.0 | 291.4 | 1.0 |
| 302.1 | 1.0 | 292.5 | 1.0 | 301.5 | 1.0 |
| 302.6 | 1.0 | 305.2 | 1.0 | 297.2 | 1.0 |
| 296.8 | 1.0 | 292.3 | 1.0 | 302.4 | 1.0 |
| 292.0 | 1.0 | 305.6 | 1.0 | 309.0 | 1.0 |
| 297.5 | 1.0 | 300.4 | 1.0 | 298.8 | 1.0 |
| 288.8 | 1.0 | 311.5 | 1.0 | 304.4 | 1.0 |
| 300.4 | 1.0 | 307.1 | 1.0 | 298.9 | 1.0 |
| 294.4 | 1.0 | 304.5 | 1.0 | 303.4 | 1.0 |
| 318.7 | 1.0 | 304.7 | 1.0 | 297.4 | 1.0 |
| 304.7 | 1.0 | 290.4 | 1.0 | 288.1 | 1.0 |
| 299.8 | 1.0 | 297.0 | 1.0 | 293.1 | 1.0 |
| 299.1 | 1.0 | 301.2 | 1.0 | 294.1 | 1.0 |

| | | | | | |
|---|---|---|---|---|---|
| 297.1 | 1.0 | 293.3 | 1.0 | 307.1 | 1.0 |
| 300.1 | 1.0 | 294.2 | 1.0 | 304.3 | 1.0 |
| 298.0 | 1.0 | 303.4 | 1.0 | 299.4 | 1.0 |
| 303.6 | 1.0 | 296.9 | 1.0 | 295.6 | 1.0 |
| 309.6 | 1.0 | 299.4 | 1.0 | 305.1 | 1.0 |
| 296.1 | 1.0 | 303.3 | 1.0 | 301.5 | 1.0 |

| Artificial U2 fine grain monzogranite | | | | | |
|---|---|---|---|---|---|
| Age (Ma) | Error (Ma) | Age (Ma) | Error (Ma) | Age (Ma) | Error (Ma) |
| 311.1 | 1.0 | 318.6 | 1.0 | 320.8 | 1.0 |
| 305.7 | 1.0 | 310.4 | 1.0 | 306.8 | 1.0 |
| 324.8 | 1.0 | 307.7 | 1.0 | 314.6 | 1.0 |
| 303.0 | 1.0 | 315.9 | 1.0 | 307.8 | 1.0 |
| 314.6 | 1.0 | 306.1 | 1.0 | 324.7 | 1.0 |
| 312.6 | 1.0 | 304.2 | 1.0 | 305.4 | 1.0 |
| 322.5 | 1.0 | 313.2 | 1.0 | 307.4 | 1.0 |
| 313.2 | 1.0 | 299.9 | 1.0 | 308.6 | 1.0 |
| 312.0 | 1.0 | 314.0 | 1.0 | 304.3 | 1.0 |
| 317.2 | 1.0 | 308.4 | 1.0 | 318.1 | 1.0 |
| 309.2 | 1.0 | 301.6 | 1.0 | 304.5 | 1.0 |
| 306.0 | 1.0 | 310.5 | 1.0 | 313.0 | 1.0 |
| 314.7 | 1.0 | 305.8 | 1.0 | 319.5 | 1.0 |
| 324.1 | 1.0 | 306.2 | 1.0 | 312.7 | 1.0 |
| 307.4 | 1.0 | 300.7 | 1.0 | 297.5 | 1.0 |
| 300.2 | 1.0 | 299.2 | 1.0 | 305.9 | 1.0 |
| 303.4 | 1.0 | 307.3 | 1.0 | 316.3 | 1.0 |
| 297.4 | 1.0 | 312.3 | 1.0 | 311.8 | 1.0 |
| 308.6 | 1.0 | 319.3 | 1.0 | 319.8 | 1.0 |
| 318.7 | 1.0 | 307.7 | 1.0 | 310.4 | 1.0 |
| 315.5 | 1.0 | 315.9 | 1.0 | 310.0 | 1.0 |
| 310.5 | 1.0 | 316.7 | 1.0 | 311.0 | 1.0 |
| 310.4 | 1.0 | 317.2 | 1.0 | 308.6 | 1.0 |
| 311.4 | 1.0 | 307.3 | 1.0 | 307.5 | 1.0 |
| 307.0 | 1.0 | 311.1 | 1.0 | 313.6 | 1.0 |
| 312.9 | 1.0 | 318.5 | 1.0 | 310.6 | 1.0 |
| 317.7 | 1.0 | 314.6 | 1.0 | 309.2 | 1.0 |
| 311.2 | 1.0 | 310.2 | 1.0 | 318.8 | 1.0 |
| 314.0 | 1.0 | 313.8 | 1.0 | 307.1 | 1.0 |
| 300.4 | 1.0 | 311.4 | 1.0 | 311.3 | 1.0 |
| 311.8 | 1.0 | 310.6 | 1.0 | 323.2 | 1.0 |
| 312.5 | 1.0 | 305.4 | 1.0 | 305.0 | 1.0 |
| 316.3 | 1.0 | 313.9 | 1.0 | 300.5 | 1.0 |
| 316.1 | 1.0 | 316.1 | 1.0 | 304.5 | 1.0 |

| | | | | | |
|---|---|---|---|---|---|
| 309.0 | 1.0 | 311.1 | 1.0 | 309.1 | 1.0 |
| 297.9 | 1.0 | 308.6 | 1.0 | 310.2 | 1.0 |
| 303.5 | 1.0 | 310.1 | 1.0 | 318.8 | 1.0 |
| 297.9 | 1.0 | 309.6 | 1.0 | 305.1 | 1.0 |
| 315.3 | 1.0 | 315.6 | 1.0 | 295.9 | 1.0 |

| Artificial U2 Medium grain monzonogranite | | | | | |
|---|---|---|---|---|---|
| Age (Ma) | Error (Ma) | Age (Ma) | Error (Ma) | Age (Ma) | Error (Ma) |
| 327.6 | 1.0 | 312.8 | 1.0 | 302.6 | 1.0 |
| 318.8 | 1.0 | 310.4 | 1.0 | 313.1 | 1.0 |
| 313.4 | 1.0 | 315.3 | 1.0 | 327.0 | 1.0 |
| 317.6 | 1.0 | 320.1 | 1.0 | 322.4 | 1.0 |
| 329.1 | 1.0 | 322.2 | 1.0 | 316.2 | 1.0 |
| 311.9 | 1.0 | 321.5 | 1.0 | 311.7 | 1.0 |
| 322.4 | 1.0 | 318.0 | 1.0 | 322.9 | 1.0 |
| 326.9 | 1.0 | 318.6 | 1.0 | 306.4 | 1.0 |
| 319.8 | 1.0 | 319.2 | 1.0 | 324.1 | 1.0 |
| 315.2 | 1.0 | 315.3 | 1.0 | 320.1 | 1.0 |
| 315.6 | 1.0 | 321.0 | 1.0 | 322.3 | 1.0 |
| 317.4 | 1.0 | 316.1 | 1.0 | 319.5 | 1.0 |
| 313.7 | 1.0 | 321.0 | 1.0 | 318.2 | 1.0 |
| 318.4 | 1.0 | 315.8 | 1.0 | 308.3 | 1.0 |
| 312.1 | 1.0 | 325.0 | 1.0 | 311.0 | 1.0 |
| 320.6 | 1.0 | 315.0 | 1.0 | 323.6 | 1.0 |
| 329.1 | 1.0 | 323.2 | 1.0 | 316.0 | 1.0 |
| 322.6 | 1.0 | 309.2 | 1.0 | 325.1 | 1.0 |
| 320.7 | 1.0 | 305.8 | 1.0 | 304.9 | 1.0 |
| 327.6 | 1.0 | 309.9 | 1.0 | 316.9 | 1.0 |
| 328.5 | 1.0 | 317.5 | 1.0 | 312.4 | 1.0 |
| 310.3 | 1.0 | 322.6 | 1.0 | 321.9 | 1.0 |
| 320.7 | 1.0 | 324.5 | 1.0 | 322.5 | 1.0 |
| 312.0 | 1.0 | 319.8 | 1.0 | 325.5 | 1.0 |
| 318.2 | 1.0 | 319.0 | 1.0 | 327.3 | 1.0 |
| 320.8 | 1.0 | 325.9 | 1.0 | 318.6 | 1.0 |
| 309.2 | 1.0 | 312.7 | 1.0 | 313.3 | 1.0 |
| 329.2 | 1.0 | 327.0 | 1.0 | 324.9 | 1.0 |
| 329.7 | 1.0 | 326.8 | 1.0 | 319.7 | 1.0 |
| 321.4 | 1.0 | 322.9 | 1.0 | 326.6 | 1.0 |
| 314.2 | 1.0 | 325.4 | 1.0 | 312.8 | 1.0 |
| 322.7 | 1.0 | 318.5 | 1.0 | 316.4 | 1.0 |
| 310.4 | 1.0 | 306.5 | 1.0 | 318.4 | 1.0 |
| 320.9 | 1.0 | 315.4 | 1.0 | 312.1 | 1.0 |
| 326.9 | 1.0 | 317.3 | 1.0 | 323.3 | 1.0 |

| | | | | | |
|---|---|---|---|---|---|
| 313.0 | 1.0 | 320.9 | 1.0 | 321.6 | 1.0 |
| 324.7 | 1.0 | 318.9 | 1.0 | 321.5 | 1.0 |
| 308.8 | 1.0 | 319.2 | 1.0 | 330.7 | 1.0 |
| 314.7 | 1.0 | 320.0 | 1.0 | 317.1 | 1.0 |

| U1 Mesocratic granite | | | | | |
|---|---|---|---|---|---|
| Age (Ma) | Error (Ma) | Age (Ma) | Error (Ma) | Age (Ma) | Error (Ma) |
| 339.0 | 1.0 | 345.7 | 1.0 | 328.4 | 1.0 |
| 336.1 | 1.0 | 331.2 | 1.0 | 323.1 | 1.0 |
| 333.2 | 1.0 | 328.7 | 1.0 | 324.9 | 1.0 |
| 322.2 | 1.0 | 323.3 | 1.0 | 326.7 | 1.0 |
| 334.3 | 1.0 | 325.0 | 1.0 | 329.7 | 1.0 |
| 328.2 | 1.0 | 331.0 | 1.0 | 327.8 | 1.0 |
| 340.0 | 1.0 | 328.3 | 1.0 | 323.6 | 1.0 |
| 327.8 | 1.0 | 328.8 | 1.0 | 338.8 | 1.0 |
| 334.8 | 1.0 | 340.4 | 1.0 | 332.9 | 1.0 |
| 330.1 | 1.0 | 319.6 | 1.0 | 337.1 | 1.0 |
| 339.0 | 1.0 | 333.2 | 1.0 | 341.0 | 1.0 |
| 312.9 | 1.0 | 329.2 | 1.0 | 327.3 | 1.0 |
| 336.2 | 1.0 | 327.7 | 1.0 | 327.8 | 1.0 |
| 324.1 | 1.0 | 339.4 | 1.0 | 327.1 | 1.0 |
| 337.8 | 1.0 | 324.5 | 1.0 | 340.6 | 1.0 |
| 336.5 | 1.0 | 330.7 | 1.0 | 335.3 | 1.0 |
| 336.5 | 1.0 | 335.7 | 1.0 | 333.4 | 1.0 |
| 329.1 | 1.0 | 331.2 | 1.0 | 329.4 | 1.0 |
| 330.8 | 1.0 | 330.3 | 1.0 | 339.2 | 1.0 |
| 338.4 | 1.0 | 334.5 | 1.0 | 325.7 | 1.0 |
| 328.4 | 1.0 | 325.9 | 1.0 | 334.3 | 1.0 |
| 332.1 | 1.0 | 334.4 | 1.0 | 320.8 | 1.0 |
| 335.4 | 1.0 | 326.8 | 1.0 | 332.9 | 1.0 |
| 327.9 | 1.0 | 332.2 | 1.0 | 333.7 | 1.0 |
| 326.0 | 1.0 | 331.6 | 1.0 | 332.3 | 1.0 |
| 327.5 | 1.0 | 331.7 | 1.0 | 335.9 | 1.0 |
| 317.8 | 1.0 | 325.1 | 1.0 | 335.9 | 1.0 |
| 335.4 | 1.0 | 338.6 | 1.0 | 329.9 | 1.0 |
| 323.6 | 1.0 | 329.6 | 1.0 | 326.8 | 1.0 |
| 339.7 | 1.0 | 335.0 | 1.0 | 323.3 | 1.0 |
| 333.8 | 1.0 | 324.4 | 1.0 | 333.7 | 1.0 |
| 340.5 | 1.0 | 335.7 | 1.0 | 338.3 | 1.0 |
| 326.9 | 1.0 | 324.4 | 1.0 | 323.8 | 1.0 |
| 331.0 | 1.0 | 332.5 | 1.0 | 332.1 | 1.0 |
| 334.2 | 1.0 | 325.3 | 1.0 | 327.9 | 1.0 |
| 331.5 | 1.0 | 331.0 | 1.0 | 327.5 | 1.0 |

| | | | | | |
|---|---|---|---|---|---|
| 343.0 | 1.0 | 326.0 | 1.0 | 334.1 | 1.0 |
| 332.3 | 1.0 | 330.8 | 1.0 | 337.6 | 1.0 |
| 330.9 | 1.0 | 328.9 | 1.0 | 321.0 | 1.0 |

| Artificial Sample A | | | | | |
|---|---|---|---|---|---|
| Age (Ma) | Error (Ma) | Age (Ma) | Error (Ma) | Age (Ma) | Error (Ma) |
| 297.9 | 1.0 | 294.8 | 1.0 | 291.7 | 1.0 |
| 287.6 | 1.0 | 299.2 | 1.0 | 285.6 | 1.0 |
| 297.8 | 1.0 | 303.6 | 1.0 | 294.7 | 1.0 |
| 298.4 | 1.0 | 290.2 | 1.0 | 299.0 | 1.0 |
| 299.8 | 1.0 | 305.8 | 1.0 | 302.9 | 1.0 |
| 306.0 | 1.0 | 309.6 | 1.0 | 301.1 | 1.0 |
| 289.9 | 1.0 | 293.1 | 1.0 | 298.6 | 1.0 |
| 299.4 | 1.0 | 313.5 | 1.0 | 301.2 | 1.0 |
| 296.5 | 1.0 | 298.6 | 1.0 | 294.4 | 1.0 |
| 294.6 | 1.0 | 296.9 | 1.0 | 298.7 | 1.0 |
| 296.9 | 1.0 | 300.0 | 1.0 | 303.1 | 1.0 |
| 303.7 | 1.0 | 301.1 | 1.0 | 294.6 | 1.0 |
| 301.6 | 1.0 | 299.4 | 1.0 | 296.7 | 1.0 |
| 307.4 | 1.0 | 299.1 | 1.0 | 302.7 | 1.0 |
| 295.0 | 1.0 | 306.9 | 1.0 | 290.8 | 1.0 |
| 295.6 | 1.0 | 302.9 | 1.0 | 298.1 | 1.0 |
| 303.5 | 1.0 | 295.5 | 1.0 | 302.0 | 1.0 |
| 304.6 | 1.0 | 300.7 | 1.0 | 301.3 | 1.0 |
| 302.4 | 1.0 | 304.5 | 1.0 | 300.1 | 1.0 |
| 307.9 | 1.0 | 309.4 | 1.0 | 300.7 | 1.0 |
| 310.5 | 1.0 | 303.9 | 1.0 | 297.0 | 1.0 |
| 293.0 | 1.0 | 316.1 | 1.0 | 304.2 | 1.0 |
| 307.6 | 1.0 | 301.2 | 1.0 | 305.2 | 1.0 |
| 296.6 | 1.0 | 308.4 | 1.0 | 307.9 | 1.0 |
| 305.0 | 1.0 | 294.0 | 1.0 | 312.8 | 1.0 |
| 305.9 | 1.0 | 309.2 | 1.0 | 302.8 | 1.0 |
| 308.6 | 1.0 | 303.4 | 1.0 | 307.3 | 1.0 |
| 305.4 | 1.0 | 300.0 | 1.0 | 315.8 | 1.0 |
| 295.1 | 1.0 | 290.7 | 1.0 | 297.5 | 1.0 |
| 312.5 | 1.0 | 295.6 | 1.0 | 298.4 | 1.0 |
| 314.3 | 1.0 | 291.6 | 1.0 | 282.8 | 1.0 |
| 298.8 | 1.0 | 301.4 | 1.0 | 281.2 | 1.0 |
| 303.7 | 1.0 | 299.7 | 1.0 | 290.0 | 1.0 |
| 305.3 | 1.0 | 296.9 | 1.0 | 304.1 | 1.0 |
| 308.6 | 1.0 | 302.4 | 1.0 | 299.4 | 1.0 |
| 306.9 | 1.0 | 303.5 | 1.0 | 300.7 | 1.0 |
| 290.7 | 1.0 | 299.6 | 1.0 | 301.3 | 1.0 |

| | | | | | |
|---|---|---|---|---|---|
| 294.2 | 1.0 | 299.1 | 1.0 | 290.0 | 1.0 |
| 297.7 | 1.0 | 298.1 | 1.0 | 296.5 | 1.0 |
| 291.5 | 1.0 | 304.0 | 1.0 | 300.8 | 1.0 |
| 299.5 | 1.0 | 294.5 | 1.0 | 293.9 | 1.0 |
| 299.4 | 1.0 | 297.6 | 1.0 | 294.6 | 1.0 |
| 307.5 | 1.0 | 298.7 | 1.0 | 298.1 | 1.0 |
| 297.3 | 1.0 | 305.9 | 1.0 | 305.9 | 1.0 |
| 296.8 | 1.0 | 295.9 | 1.0 | 297.3 | 1.0 |
| 307.9 | 1.0 | 308.7 | 1.0 | 302.6 | 1.0 |
| 303.6 | 1.0 | 305.5 | 1.0 | 305.4 | 1.0 |
| 299.7 | 1.0 | 296.7 | 1.0 | 302.4 | 1.0 |
| 304.1 | 1.0 | 307.5 | 1.0 | 294.7 | 1.0 |
| 297.0 | 1.0 | 298.4 | 1.0 | 305.4 | 1.0 |
| 294.7 | 1.0 | 300.0 | 1.0 | 297.8 | 1.0 |
| 294.0 | 1.0 | 307.0 | 1.0 | 314.0 | 1.0 |
| 297.2 | 1.0 | 293.1 | 1.0 | 300.0 | 1.0 |
| 309.9 | 1.0 | 300.7 | 1.0 | 298.2 | 1.0 |
| 303.6 | 1.0 | 300.3 | 1.0 | 293.0 | 1.0 |
| 303.1 | 1.0 | 298.9 | 1.0 | 296.6 | 1.0 |
| 296.7 | 1.0 | 301.5 | 1.0 | 297.2 | 1.0 |
| 307.6 | 1.0 | 288.5 | 1.0 | 294.3 | 1.0 |
| 313.1 | 1.0 | 296.4 | 1.0 | 306.7 | 1.0 |
| 312.9 | 1.0 | 308.0 | 1.0 | 303.8 | 1.0 |
| 290.9 | 1.0 | 301.8 | 1.0 | 302.7 | 1.0 |
| 303.7 | 1.0 | 307.2 | 1.0 | 296.6 | 1.0 |
| 310.7 | 1.0 | 303.2 | 1.0 | 300.8 | 1.0 |
| 292.6 | 1.0 | 311.1 | 1.0 | 289.4 | 1.0 |
| 296.4 | 1.0 | 302.5 | 1.0 | 298.6 | 1.0 |
| 302.7 | 1.0 | 295.6 | 1.0 | 313.7 | 1.0 |
| 293.2 | 1.0 | 292.9 | 1.0 | 297.1 | 1.0 |
| 292.4 | 1.0 | 301.0 | 1.0 | 302.9 | 1.0 |
| 302.1 | 1.0 | 290.1 | 1.0 | 290.2 | 1.0 |
| 300.8 | 1.0 | 307.7 | 1.0 | 298.1 | 1.0 |
| 308.0 | 1.0 | 302.6 | 1.0 | 307.4 | 1.0 |
| 293.9 | 1.0 | 298.6 | 1.0 | 297.2 | 1.0 |
| 299.0 | 1.0 | 298.9 | 1.0 | 303.3 | 1.0 |
| 307.1 | 1.0 | 290.2 | 1.0 | 293.5 | 1.0 |
| 302.9 | 1.0 | 299.8 | 1.0 | 298.8 | 1.0 |
| 300.6 | 1.0 | 293.5 | 1.0 | 298.5 | 1.0 |
| 294.3 | 1.0 | 303.8 | 1.0 | 292.0 | 1.0 |
| 306.3 | 1.0 | 308.4 | 1.0 | 292.4 | 1.0 |
| 299.2 | 1.0 | 297.2 | 1.0 | 308.5 | 1.0 |
| 298.1 | 1.0 | 293.6 | 1.0 | 308.8 | 1.0 |
| 302.6 | 1.0 | 297.8 | 1.0 | 304.8 | 1.0 |

| | | | | | |
|---|---|---|---|---|---|
| 293.9 | 1.0 | 296.8 | 1.0 | 295.9 | 1.0 |
| 300.2 | 1.0 | 316.0 | 1.0 | 292.3 | 1.0 |
| 299.6 | 1.0 | 304.0 | 1.0 | 298.7 | 1.0 |
| 312.0 | 1.0 | 303.1 | 1.0 | 308.2 | 1.0 |
| 294.5 | 1.0 | 305.0 | 1.0 | 291.9 | 1.0 |
| 296.1 | 1.0 | 299.1 | 1.0 | 296.9 | 1.0 |
| 298.2 | 1.0 | 303.3 | 1.0 | 299.7 | 1.0 |
| 313.0 | 1.0 | 296.8 | 1.0 | 302.3 | 1.0 |
| 307.7 | 1.0 | 305.0 | 1.0 | 293.4 | 1.0 |
| 302.3 | 1.0 | 297.7 | 1.0 | 300.4 | 1.0 |
| 291.6 | 1.0 | 297.5 | 1.0 | 297.0 | 1.0 |
| 293.3 | 1.0 | 298.5 | 1.0 | 304.7 | 1.0 |
| 300.0 | 1.0 | 295.5 | 1.0 | 293.9 | 1.0 |
| 294.1 | 1.0 | 299.6 | 1.0 | 305.4 | 1.0 |
| 300.6 | 1.0 | 295.8 | 1.0 | 303.8 | 1.0 |
| 299.0 | 1.0 | 292.0 | 1.0 | 301.7 | 1.0 |
| 303.0 | 1.0 | 303.5 | 1.0 | 305.3 | 1.0 |
| 309.1 | 1.0 | 284.0 | 1.0 | 305.8 | 1.0 |
| 294.6 | 1.0 | 291.7 | 1.0 | 296.1 | 1.0 |
| 301.0 | 1.0 | 297.3 | 1.0 | 309.6 | 1.0 |
| 309.8 | 1.0 | 303.7 | 1.0 | 300.0 | 1.0 |
| 306.8 | 1.0 | 292.7 | 1.0 | 302.8 | 1.0 |
| 301.6 | 1.0 | 297.3 | 1.0 | 292.7 | 1.0 |
| 295.5 | 1.0 | 307.4 | 1.0 | 301.8 | 1.0 |
| 287.7 | 1.0 | 298.6 | 1.0 | 302.9 | 1.0 |
| 298.7 | 1.0 | 288.3 | 1.0 | 293.5 | 1.0 |
| 299.7 | 1.0 | 293.0 | 1.0 | 290.2 | 1.0 |
| 302.5 | 1.0 | 300.5 | 1.0 | 293.2 | 1.0 |
| 287.1 | 1.0 | 289.5 | 1.0 | 304.5 | 1.0 |
| 293.9 | 1.0 | 298.9 | 1.0 | 294.1 | 1.0 |
| 281.6 | 1.0 | 297.5 | 1.0 | 299.1 | 1.0 |
| 297.5 | 1.0 | 295.1 | 1.0 | 304.1 | 1.0 |
| 307.1 | 1.0 | 303.3 | 1.0 | 289.2 | 1.0 |
| 300.8 | 1.0 | 302.2 | 1.0 | 294.0 | 1.0 |
| 301.1 | 1.0 | 300.2 | 1.0 | 301.4 | 1.0 |
| 296.7 | 1.0 | 304.3 | 1.0 | 303.0 | 1.0 |
| 313.4 | 1.0 | 303.7 | 1.0 | 309.4 | 1.0 |
| 307.7 | 1.0 | 307.0 | 1.0 | 306.0 | 1.0 |
| 314.3 | 1.0 | 313.9 | 1.0 | 307.2 | 1.0 |
| 308.5 | 1.0 | 311.0 | 1.0 | 321.5 | 1.0 |
| 305.5 | 1.0 | 304.7 | 1.0 | 316.3 | 1.0 |
| 319.4 | 1.0 | 310.4 | 1.0 | 310.9 | 1.0 |
| 312.8 | 1.0 | 306.3 | 1.0 | 308.9 | 1.0 |
| 305.7 | 1.0 | 311.7 | 1.0 | 328.2 | 1.0 |

| | | | | | |
|---|---|---|---|---|---|
| 321.0 | 1.0 | 318.8 | 1.0 | 313.1 | 1.0 |
| 313.0 | 1.0 | 309.4 | 1.0 | 310.9 | 1.0 |
| 308.0 | 1.0 | 305.3 | 1.0 | 324.3 | 1.0 |
| 307.3 | 1.0 | 311.9 | 1.0 | 322.7 | 1.0 |
| 304.0 | 1.0 | 318.9 | 1.0 | 323.5 | 1.0 |
| 313.3 | 1.0 | 321.0 | 1.0 | 320.1 | 1.0 |
| 311.3 | 1.0 | 326.8 | 1.0 | 311.5 | 1.0 |
| 303.0 | 1.0 | 318.3 | 1.0 | 324.0 | 1.0 |
| 318.3 | 1.0 | 304.5 | 1.0 | 324.2 | 1.0 |
| 309.2 | 1.0 | 326.6 | 1.0 | 316.6 | 1.0 |
| 300.6 | 1.0 | 319.8 | 1.0 | 328.9 | 1.0 |
| 311.9 | 1.0 | 317.8 | 1.0 | 319.6 | 1.0 |
| 323.0 | 1.0 | 321.4 | 1.0 | 321.1 | 1.0 |
| 302.5 | 1.0 | 319.4 | 1.0 | 312.5 | 1.0 |
| 314.0 | 1.0 | 318.9 | 1.0 | 323.2 | 1.0 |
| 310.5 | 1.0 | 324.0 | 1.0 | 310.2 | 1.0 |
| 326.8 | 1.0 | 315.6 | 1.0 | 320.9 | 1.0 |
| 317.3 | 1.0 | 320.8 | 1.0 | 328.4 | 1.0 |
| 308.3 | 1.0 | 322.2 | 1.0 | 322.1 | 1.0 |
| 310.6 | 1.0 | 316.6 | 1.0 | 315.6 | 1.0 |
| 306.0 | 1.0 | 329.0 | 1.0 | 318.7 | 1.0 |
| 313.8 | 1.0 | 317.4 | 1.0 | 310.5 | 1.0 |
| 319.9 | 1.0 | 329.4 | 1.0 | 308.8 | 1.0 |
| 304.0 | 1.0 | 316.6 | 1.0 | 314.2 | 1.0 |
| 328.3 | 1.0 | 318.9 | 1.0 | 325.2 | 1.0 |
| 326.8 | 1.0 | 320.3 | 1.0 | 318.8 | 1.0 |
| 328.7 | 1.0 | 313.5 | 1.0 | 315.5 | 1.0 |
| 322.1 | 1.0 | 326.4 | 1.0 | 335.9 | 1.0 |
| 339.9 | 1.0 | 332.5 | 1.0 | 331.6 | 1.0 |
| 331.9 | 1.0 | 331.9 | 1.0 | 344.2 | 1.0 |
| 325.0 | 1.0 | 331.0 | 1.0 | | |

Table S7: Artificial U–Pb created for the scenario A5.

| Artificial U2 leucomonzogranite | | | | | |
|---|---|---|---|---|---|
| Age (Ma) | Error (Ma) | Age (Ma) | Error (Ma) | Age (Ma) | Error (Ma) |
| 309.2 | 1.0 | 295.4 | 1.0 | 301.3 | 1.0 |
| 300.8 | 1.0 | 301.0 | 1.0 | 304.2 | 1.0 |
| 303.2 | 1.0 | 301.7 | 1.0 | 297.1 | 1.0 |
| 305.8 | 1.0 | 310.1 | 1.0 | 291.3 | 1.0 |
| 296.8 | 1.0 | 309.5 | 1.0 | 298.7 | 1.0 |
| 296.7 | 1.0 | 305.1 | 1.0 | 287.5 | 1.0 |
| 301.8 | 1.0 | 298.1 | 1.0 | 291.2 | 1.0 |
| 293.2 | 1.0 | 312.4 | 1.0 | 293.7 | 1.0 |

| | | | | | |
|---|---|---|---|---|---|
| 289.6 | 1.0 | 285.2 | 1.0 | 303.8 | 1.0 |
| 311.4 | 1.0 | 298.7 | 1.0 | 309.6 | 1.0 |
| 303.1 | 1.0 | 292.3 | 1.0 | 293.5 | 1.0 |
| 303.1 | 1.0 | 294.2 | 1.0 | 305.7 | 1.0 |
| 295.1 | 1.0 | 300.9 | 1.0 | 307.1 | 1.0 |
| 303.5 | 1.0 | 304.5 | 1.0 | 306.0 | 1.0 |
| 293.9 | 1.0 | 304.0 | 1.0 | 300.2 | 1.0 |
| 300.1 | 1.0 | 296.1 | 1.0 | 301.8 | 1.0 |
| 301.6 | 1.0 | 305.8 | 1.0 | 298.9 | 1.0 |
| 303.0 | 1.0 | 304.1 | 1.0 | 293.2 | 1.0 |
| 302.8 | 1.0 | 292.4 | 1.0 | 302.7 | 1.0 |
| 296.8 | 1.0 | 292.4 | 1.0 | 292.3 | 1.0 |
| 297.0 | 1.0 | 299.0 | 1.0 | 299.0 | 1.0 |
| 296.0 | 1.0 | 302.5 | 1.0 | 300.5 | 1.0 |
| 290.5 | 1.0 | 301.4 | 1.0 | 290.2 | 1.0 |
| 299.3 | 1.0 | 308.2 | 1.0 | 307.9 | 1.0 |
| 298.6 | 1.0 | 295.1 | 1.0 | 306.5 | 1.0 |
| 298.0 | 1.0 | 297.9 | 1.0 | 303.6 | 1.0 |
| 289.4 | 1.0 | 298.0 | 1.0 | 301.4 | 1.0 |
| 297.8 | 1.0 | 300.4 | 1.0 | 317.3 | 1.0 |
| 301.0 | 1.0 | 290.1 | 1.0 | 303.1 | 1.0 |
| 297.1 | 1.0 | 305.5 | 1.0 | 303.6 | 1.0 |
| 295.4 | 1.0 | 302.5 | 1.0 | 299.4 | 1.0 |
| 288.0 | 1.0 | 300.1 | 1.0 | 294.3 | 1.0 |
| 297.7 | 1.0 | 292.9 | 1.0 | 298.1 | 1.0 |
| 315.3 | 1.0 | 296.7 | 1.0 | 305.5 | 1.0 |
| 291.7 | 1.0 | 291.7 | 1.0 | 301.5 | 1.0 |
| 287.6 | 1.0 | 312.2 | 1.0 | 296.8 | 1.0 |
| 304.2 | 1.0 | 297.2 | 1.0 | 300.0 | 1.0 |
| 298.6 | 1.0 | 292.8 | 1.0 | 296.3 | 1.0 |
| 301.8 | 1.0 | 300.0 | 1.0 | 292.8 | 1.0 |

| Artificial U2 fine grain granodiorite | | | | | |
|---|---|---|---|---|---|
| Age (Ma) | Error (Ma) | Age (Ma) | Error (Ma) | Age (Ma) | Error (Ma) |
| 300.4 | 1.0 | 288.0 | 1.0 | 292.9 | 1.0 |
| 304.7 | 1.0 | 293.2 | 1.0 | 299.0 | 1.0 |
| 301.2 | 1.0 | 297.8 | 1.0 | 298.1 | 1.0 |
| 314.2 | 1.0 | 304.4 | 1.0 | 301.5 | 1.0 |
| 292.3 | 1.0 | 300.0 | 1.0 | 307.2 | 1.0 |
| 297.0 | 1.0 | 300.1 | 1.0 | 303.8 | 1.0 |
| 300.5 | 1.0 | 297.6 | 1.0 | 303.6 | 1.0 |
| 292.6 | 1.0 | 296.7 | 1.0 | 299.7 | 1.0 |
| 305.5 | 1.0 | 290.9 | 1.0 | 292.9 | 1.0 |

| | | | | | |
|---|---|---|---|---|---|
| 296.1 | 1.0 | 305.8 | 1.0 | 302.6 | 1.0 |
| 298.6 | 1.0 | 285.3 | 1.0 | 303.3 | 1.0 |
| 301.3 | 1.0 | 315.3 | 1.0 | 306.0 | 1.0 |
| 289.2 | 1.0 | 297.6 | 1.0 | 300.8 | 1.0 |
| 308.9 | 1.0 | 297.5 | 1.0 | 308.1 | 1.0 |
| 297.1 | 1.0 | 306.5 | 1.0 | 290.0 | 1.0 |
| 301.3 | 1.0 | 304.9 | 1.0 | 296.2 | 1.0 |
| 291.1 | 1.0 | 301.6 | 1.0 | 296.0 | 1.0 |
| 296.1 | 1.0 | 288.4 | 1.0 | 296.4 | 1.0 |
| 297.1 | 1.0 | 300.1 | 1.0 | 294.6 | 1.0 |
| 298.5 | 1.0 | 295.6 | 1.0 | 301.4 | 1.0 |
| 312.6 | 1.0 | 316.3 | 1.0 | 304.9 | 1.0 |
| 298.6 | 1.0 | 311.1 | 1.0 | 288.5 | 1.0 |
| 293.6 | 1.0 | 307.5 | 1.0 | 305.2 | 1.0 |
| 288.0 | 1.0 | 297.4 | 1.0 | 291.6 | 1.0 |
| 297.3 | 1.0 | 309.5 | 1.0 | 306.3 | 1.0 |
| 290.1 | 1.0 | 293.0 | 1.0 | 299.3 | 1.0 |
| 292.6 | 1.0 | 300.5 | 1.0 | 296.2 | 1.0 |
| 303.0 | 1.0 | 310.2 | 1.0 | 305.7 | 1.0 |
| 313.9 | 1.0 | 302.0 | 1.0 | 293.8 | 1.0 |
| 298.1 | 1.0 | 294.4 | 1.0 | 307.2 | 1.0 |
| 295.8 | 1.0 | 306.3 | 1.0 | 302.0 | 1.0 |
| 303.8 | 1.0 | 303.8 | 1.0 | 300.0 | 1.0 |
| 288.5 | 1.0 | 284.6 | 1.0 | 301.5 | 1.0 |
| 311.1 | 1.0 | 303.3 | 1.0 | 305.2 | 1.0 |
| 298.1 | 1.0 | 296.2 | 1.0 | 298.7 | 1.0 |
| 295.0 | 1.0 | 305.4 | 1.0 | 309.3 | 1.0 |
| 299.8 | 1.0 | 296.5 | 1.0 | 299.0 | 1.0 |
| 298.6 | 1.0 | 304.1 | 1.0 | 303.9 | 1.0 |
| 297.1 | 1.0 | 304.6 | 1.0 | 296.4 | 1.0 |

| Artificial U2 medium grain mozonogranite | | | | | |
|---|---|---|---|---|---|
| Age (Ma) | Error (Ma) | Age (Ma) | Error (Ma) | Age (Ma) | Error (Ma) |
| 303.7 | 1.0 | 303.7 | 1.0 | 300.2 | 1.0 |
| 304.4 | 1.0 | 303.1 | 1.0 | 295.7 | 1.0 |
| 295.3 | 1.0 | 294.3 | 1.0 | 291.0 | 1.0 |
| 301.3 | 1.0 | 309.4 | 1.0 | 301.0 | 1.0 |
| 308.8 | 1.0 | 294.8 | 1.0 | 310.0 | 1.0 |
| 297.5 | 1.0 | 304.7 | 1.0 | 302.0 | 1.0 |
| 298.5 | 1.0 | 294.6 | 1.0 | 295.6 | 1.0 |
| 301.9 | 1.0 | 299.9 | 1.0 | 308.0 | 1.0 |
| 300.8 | 1.0 | 301.9 | 1.0 | 288.4 | 1.0 |
| 309.7 | 1.0 | 296.5 | 1.0 | 301.8 | 1.0 |

| | | | | | |
|---|---|---|---|---|---|
| 295.0 | 1.0 | 295.0 | 1.0 | 297.1 | 1.0 |
| 306.4 | 1.0 | 308.2 | 1.0 | 299.9 | 1.0 |
| 297.6 | 1.0 | 290.0 | 1.0 | 292.7 | 1.0 |
| 300.4 | 1.0 | 303.0 | 1.0 | 311.5 | 1.0 |
| 301.0 | 1.0 | 304.8 | 1.0 | 298.1 | 1.0 |
| 304.1 | 1.0 | 300.4 | 1.0 | 291.2 | 1.0 |
| 299.0 | 1.0 | 299.1 | 1.0 | 294.7 | 1.0 |
| 301.0 | 1.0 | 300.8 | 1.0 | 308.0 | 1.0 |
| 293.4 | 1.0 | 292.7 | 1.0 | 293.4 | 1.0 |
| 297.7 | 1.0 | 302.8 | 1.0 | 301.7 | 1.0 |
| 298.1 | 1.0 | 298.7 | 1.0 | 311.6 | 1.0 |
| 308.4 | 1.0 | 287.5 | 1.0 | 300.6 | 1.0 |
| 296.5 | 1.0 | 308.3 | 1.0 | 304.1 | 1.0 |
| 288.2 | 1.0 | 300.2 | 1.0 | 300.5 | 1.0 |
| 307.8 | 1.0 | 284.0 | 1.0 | 307.2 | 1.0 |
| 310.9 | 1.0 | 303.3 | 1.0 | 299.9 | 1.0 |
| 296.2 | 1.0 | 295.6 | 1.0 | 303.6 | 1.0 |
| 296.8 | 1.0 | 300.4 | 1.0 | 299.5 | 1.0 |
| 302.3 | 1.0 | 298.1 | 1.0 | 304.8 | 1.0 |
| 296.6 | 1.0 | 293.6 | 1.0 | 299.7 | 1.0 |
| 300.4 | 1.0 | 304.5 | 1.0 | 300.6 | 1.0 |
| 291.4 | 1.0 | 295.9 | 1.0 | 302.4 | 1.0 |
| 307.0 | 1.0 | 295.7 | 1.0 | 303.7 | 1.0 |
| 303.3 | 1.0 | 305.4 | 1.0 | 299.9 | 1.0 |
| 294.6 | 1.0 | 303.3 | 1.0 | 313.9 | 1.0 |
| 293.3 | 1.0 | 294.4 | 1.0 | 305.4 | 1.0 |
| 310.4 | 1.0 | 305.2 | 1.0 | 296.0 | 1.0 |
| 301.9 | 1.0 | 298.6 | 1.0 | 301.3 | 1.0 |
| 306.9 | 1.0 | 292.5 | 1.0 | 305.1 | 1.0 |

| Artificial U1 mesocratic granite | | | | | |
|---|---|---|---|---|---|
| Age (Ma) | Error (Ma) | Age (Ma) | Error (Ma) | Age (Ma) | Error (Ma) |
| 309.3 | 1.0 | 303.5 | 1.0 | 314.0 | 1.0 |
| 310.3 | 1.0 | 290.0 | 1.0 | 308.5 | 1.0 |
| 301.3 | 1.0 | 307.0 | 1.0 | 298.9 | 1.0 |
| 298.8 | 1.0 | 311.8 | 1.0 | 307.2 | 1.0 |
| 305.7 | 1.0 | 291.4 | 1.0 | 297.2 | 1.0 |
| 299.7 | 1.0 | 297.8 | 1.0 | 299.7 | 1.0 |
| 299.5 | 1.0 | 299.3 | 1.0 | 300.3 | 1.0 |
| 294.0 | 1.0 | 302.9 | 1.0 | 293.6 | 1.0 |
| 290.9 | 1.0 | 303.4 | 1.0 | 294.6 | 1.0 |
| 307.4 | 1.0 | 294.8 | 1.0 | 299.4 | 1.0 |
| 296.3 | 1.0 | 308.7 | 1.0 | 300.5 | 1.0 |

| | | | | | |
|---|---|---|---|---|---|
| 306.7 | 1.0 | 300.5 | 1.0 | 302.4 | 1.0 |
| 292.4 | 1.0 | 299.6 | 1.0 | 314.1 | 1.0 |
| 309.6 | 1.0 | 302.6 | 1.0 | 302.2 | 1.0 |
| 296.2 | 1.0 | 298.9 | 1.0 | 295.3 | 1.0 |
| 297.4 | 1.0 | 301.4 | 1.0 | 301.3 | 1.0 |
| 311.9 | 1.0 | 312.8 | 1.0 | 296.9 | 1.0 |
| 295.7 | 1.0 | 294.9 | 1.0 | 293.3 | 1.0 |
| 290.1 | 1.0 | 298.3 | 1.0 | 300.2 | 1.0 |
| 293.5 | 1.0 | 298.2 | 1.0 | 297.7 | 1.0 |
| 295.6 | 1.0 | 287.1 | 1.0 | 297.3 | 1.0 |
| 294.6 | 1.0 | 305.7 | 1.0 | 297.7 | 1.0 |
| 291.4 | 1.0 | 308.6 | 1.0 | 293.0 | 1.0 |
| 302.1 | 1.0 | 299.3 | 1.0 | 287.0 | 1.0 |
| 299.0 | 1.0 | 295.8 | 1.0 | 296.4 | 1.0 |
| 306.6 | 1.0 | 298.8 | 1.0 | 304.3 | 1.0 |
| 307.0 | 1.0 | 302.9 | 1.0 | 291.6 | 1.0 |
| 307.0 | 1.0 | 309.4 | 1.0 | 301.8 | 1.0 |
| 300.4 | 1.0 | 304.4 | 1.0 | 292.9 | 1.0 |
| 306.0 | 1.0 | 300.4 | 1.0 | 310.6 | 1.0 |
| 298.0 | 1.0 | 294.8 | 1.0 | 309.1 | 1.0 |
| 298.3 | 1.0 | 302.9 | 1.0 | 301.9 | 1.0 |
| 296.1 | 1.0 | 309.4 | 1.0 | 299.1 | 1.0 |
| 299.7 | 1.0 | 307.4 | 1.0 | 299.9 | 1.0 |
| 304.6 | 1.0 | 294.8 | 1.0 | 304.3 | 1.0 |
| 301.3 | 1.0 | 296.2 | 1.0 | 302.1 | 1.0 |
| 290.6 | 1.0 | 302.3 | 1.0 | 298.0 | 1.0 |
| 286.5 | 1.0 | 298.8 | 1.0 | 301.5 | 1.0 |
| 293.4 | 1.0 | 304.5 | 1.0 | 301.9 | 1.0 |

| Artificial Sample A | | | | | |
|---|---|---|---|---|---|
| Age (Ma) | Error (Ma) | Age (Ma) | Error (Ma) | Age (Ma) | Error (Ma) |
| 292.0 | 1.0 | 293.9 | 1.0 | 297.5 | 1.0 |
| 301.1 | 1.0 | 297.1 | 1.0 | 290.8 | 1.0 |
| 298.5 | 1.0 | 308.4 | 1.0 | 304.2 | 1.0 |
| 308.6 | 1.0 | 298.7 | 1.0 | 296.1 | 1.0 |
| 300.1 | 1.0 | 299.8 | 1.0 | 297.0 | 1.0 |
| 308.9 | 1.0 | 299.9 | 1.0 | 305.7 | 1.0 |
| 304.4 | 1.0 | 305.6 | 1.0 | 300.4 | 1.0 |
| 297.3 | 1.0 | 297.4 | 1.0 | 298.5 | 1.0 |
| 303.3 | 1.0 | 300.3 | 1.0 | 292.4 | 1.0 |
| 303.6 | 1.0 | 287.3 | 1.0 | 294.5 | 1.0 |
| 294.1 | 1.0 | 304.3 | 1.0 | 305.4 | 1.0 |
| 299.7 | 1.0 | 300.8 | 1.0 | 305.9 | 1.0 |

| | | | | | |
|---|---|---|---|---|---|
| 300.4 | 1.0 | 308.0 | 1.0 | 293.4 | 1.0 |
| 296.7 | 1.0 | 297.8 | 1.0 | 301.0 | 1.0 |
| 299.4 | 1.0 | 306.3 | 1.0 | 306.2 | 1.0 |
| 297.0 | 1.0 | 305.8 | 1.0 | 300.0 | 1.0 |
| 305.9 | 1.0 | 301.4 | 1.0 | 304.4 | 1.0 |
| 303.5 | 1.0 | 297.9 | 1.0 | 301.5 | 1.0 |
| 300.6 | 1.0 | 297.3 | 1.0 | 296.7 | 1.0 |
| 300.6 | 1.0 | 300.3 | 1.0 | 303.6 | 1.0 |
| 298.1 | 1.0 | 307.1 | 1.0 | 297.4 | 1.0 |
| 306.7 | 1.0 | 302.1 | 1.0 | 293.0 | 1.0 |
| 300.1 | 1.0 | 298.8 | 1.0 | 298.3 | 1.0 |
| 295.7 | 1.0 | 293.3 | 1.0 | 302.9 | 1.0 |
| 298.5 | 1.0 | 297.9 | 1.0 | 305.0 | 1.0 |
| 302.9 | 1.0 | 297.0 | 1.0 | 300.2 | 1.0 |
| 304.8 | 1.0 | 299.2 | 1.0 | 304.7 | 1.0 |
| 300.4 | 1.0 | 291.6 | 1.0 | 294.1 | 1.0 |
| 306.7 | 1.0 | 305.9 | 1.0 | 301.4 | 1.0 |
| 304.1 | 1.0 | 303.6 | 1.0 | 303.4 | 1.0 |
| 302.4 | 1.0 | 296.6 | 1.0 | 291.7 | 1.0 |
| 305.1 | 1.0 | 306.1 | 1.0 | 304.5 | 1.0 |
| 298.5 | 1.0 | 300.9 | 1.0 | 295.9 | 1.0 |
| 303.9 | 1.0 | 294.9 | 1.0 | 305.7 | 1.0 |
| 298.2 | 1.0 | 301.0 | 1.0 | 303.8 | 1.0 |
| 306.3 | 1.0 | 291.3 | 1.0 | 312.4 | 1.0 |
| 293.3 | 1.0 | 299.6 | 1.0 | 304.9 | 1.0 |
| 299.7 | 1.0 | 298.8 | 1.0 | 307.9 | 1.0 |
| 294.6 | 1.0 | 305.6 | 1.0 | 297.0 | 1.0 |
| 293.2 | 1.0 | 278.7 | 1.0 | 292.7 | 1.0 |
| 299.2 | 1.0 | 300.1 | 1.0 | 311.7 | 1.0 |
| 306.1 | 1.0 | 291.6 | 1.0 | 304.9 | 1.0 |
| 300.6 | 1.0 | 297.9 | 1.0 | 295.1 | 1.0 |
| 300.4 | 1.0 | 303.8 | 1.0 | 290.6 | 1.0 |
| 309.1 | 1.0 | 298.4 | 1.0 | 293.9 | 1.0 |
| 297.4 | 1.0 | 301.3 | 1.0 | 309.0 | 1.0 |
| 304.2 | 1.0 | 300.3 | 1.0 | 300.7 | 1.0 |
| 302.4 | 1.0 | 301.7 | 1.0 | 302.4 | 1.0 |
| 293.4 | 1.0 | 300.1 | 1.0 | 287.4 | 1.0 |
| 311.0 | 1.0 | 312.2 | 1.0 | 295.5 | 1.0 |
| 314.1 | 1.0 | 294.4 | 1.0 | 308.9 | 1.0 |
| 295.7 | 1.0 | 303.4 | 1.0 | 298.8 | 1.0 |
| 307.6 | 1.0 | 298.2 | 1.0 | 293.2 | 1.0 |
| 296.7 | 1.0 | 291.6 | 1.0 | 294.8 | 1.0 |
| 293.6 | 1.0 | 292.5 | 1.0 | 313.1 | 1.0 |
| 307.5 | 1.0 | 297.5 | 1.0 | 301.5 | 1.0 |

| | | | | | |
|---|---|---|---|---|---|
| 293.4 | 1.0 | 303.3 | 1.0 | 290.8 | 1.0 |
| 293.0 | 1.0 | 298.5 | 1.0 | 304.4 | 1.0 |
| 290.2 | 1.0 | 305.9 | 1.0 | 306.3 | 1.0 |
| 310.5 | 1.0 | 297.8 | 1.0 | 297.5 | 1.0 |
| 301.2 | 1.0 | 294.1 | 1.0 | 296.9 | 1.0 |
| 304.9 | 1.0 | 307.2 | 1.0 | 304.7 | 1.0 |
| 298.4 | 1.0 | 298.4 | 1.0 | 304.0 | 1.0 |
| 297.0 | 1.0 | 289.8 | 1.0 | 302.7 | 1.0 |
| 301.4 | 1.0 | 297.3 | 1.0 | 300.0 | 1.0 |
| 297.8 | 1.0 | 293.9 | 1.0 | 304.1 | 1.0 |
| 317.5 | 1.0 | 294.5 | 1.0 | 304.7 | 1.0 |
| 300.8 | 1.0 | 293.9 | 1.0 | 297.3 | 1.0 |
| 297.6 | 1.0 | 297.1 | 1.0 | 296.7 | 1.0 |
| 290.9 | 1.0 | 294.9 | 1.0 | 304.6 | 1.0 |
| 310.6 | 1.0 | 300.9 | 1.0 | 304.4 | 1.0 |
| 312.7 | 1.0 | 289.5 | 1.0 | 305.1 | 1.0 |
| 304.5 | 1.0 | 299.0 | 1.0 | 300.2 | 1.0 |
| 304.8 | 1.0 | 298.7 | 1.0 | 299.8 | 1.0 |
| 296.0 | 1.0 | 309.0 | 1.0 | 302.5 | 1.0 |
| 299.3 | 1.0 | 305.6 | 1.0 | 305.6 | 1.0 |
| 303.6 | 1.0 | 302.2 | 1.0 | 296.3 | 1.0 |
| 296.2 | 1.0 | 315.9 | 1.0 | 305.6 | 1.0 |
| 296.4 | 1.0 | 297.9 | 1.0 | 304.5 | 1.0 |
| 301.6 | 1.0 | 302.8 | 1.0 | 296.5 | 1.0 |
| 308.5 | 1.0 | 314.1 | 1.0 | 298.9 | 1.0 |
| 301.0 | 1.0 | 297.4 | 1.0 | 295.8 | 1.0 |
| 304.7 | 1.0 | 299.5 | 1.0 | 300.7 | 1.0 |
| 297.0 | 1.0 | 305.5 | 1.0 | 297.1 | 1.0 |
| 288.8 | 1.0 | 300.2 | 1.0 | 304.9 | 1.0 |
| 297.1 | 1.0 | 304.7 | 1.0 | 292.4 | 1.0 |
| 287.4 | 1.0 | 299.9 | 1.0 | 305.5 | 1.0 |
| 300.0 | 1.0 | 301.3 | 1.0 | 295.0 | 1.0 |
| 303.5 | 1.0 | 308.0 | 1.0 | 297.2 | 1.0 |
| 303.1 | 1.0 | 297.7 | 1.0 | 292.8 | 1.0 |
| 296.3 | 1.0 | 306.9 | 1.0 | 301.1 | 1.0 |
| 302.2 | 1.0 | 301.8 | 1.0 | 300.1 | 1.0 |
| 294.8 | 1.0 | 307.4 | 1.0 | 300.7 | 1.0 |
| 302.1 | 1.0 | 304.0 | 1.0 | 294.1 | 1.0 |
| 305.1 | 1.0 | 308.3 | 1.0 | 295.7 | 1.0 |
| 304.9 | 1.0 | 303.2 | 1.0 | 299.5 | 1.0 |
| 293.6 | 1.0 | 301.1 | 1.0 | 293.4 | 1.0 |
| 300.4 | 1.0 | 294.9 | 1.0 | 292.3 | 1.0 |
| 297.6 | 1.0 | 303.2 | 1.0 | 299.4 | 1.0 |
| 293.5 | 1.0 | 291.9 | 1.0 | 309.7 | 1.0 |

| | | | | | |
|---|---|---|---|---|---|
| 298.7 | 1.0 | 292.8 | 1.0 | 297.2 | 1.0 |
| 298.8 | 1.0 | 292.6 | 1.0 | 300.0 | 1.0 |
| 302.3 | 1.0 | 292.3 | 1.0 | 292.1 | 1.0 |
| 300.0 | 1.0 | 310.1 | 1.0 | 303.9 | 1.0 |
| 294.2 | 1.0 | 287.5 | 1.0 | 301.5 | 1.0 |
| 302.1 | 1.0 | 303.5 | 1.0 | 309.8 | 1.0 |
| 298.7 | 1.0 | 307.9 | 1.0 | 289.9 | 1.0 |
| 304.1 | 1.0 | 299.2 | 1.0 | 305.2 | 1.0 |
| 294.4 | 1.0 | 294.0 | 1.0 | 308.2 | 1.0 |
| 295.1 | 1.0 | 294.2 | 1.0 | 296.7 | 1.0 |
| 296.6 | 1.0 | 299.0 | 1.0 | 300.1 | 1.0 |
| 308.0 | 1.0 | 296.2 | 1.0 | 302.3 | 1.0 |
| 298.1 | 1.0 | 295.1 | 1.0 | 300.9 | 1.0 |
| 292.1 | 1.0 | 295.2 | 1.0 | 294.5 | 1.0 |
| 304.9 | 1.0 | 290.4 | 1.0 | 306.6 | 1.0 |
| 301.0 | 1.0 | 299.2 | 1.0 | 300.2 | 1.0 |
| 298.3 | 1.0 | 310.0 | 1.0 | 298.5 | 1.0 |
| 287.4 | 1.0 | 297.3 | 1.0 | 297.0 | 1.0 |
| 290.7 | 1.0 | 297.5 | 1.0 | 307.1 | 1.0 |
| 291.7 | 1.0 | 304.9 | 1.0 | 291.3 | 1.0 |
| 300.1 | 1.0 | 306.8 | 1.0 | 297.8 | 1.0 |
| 302.4 | 1.0 | 298.5 | 1.0 | 300.3 | 1.0 |
| 289.7 | 1.0 | 284.9 | 1.0 | 310.2 | 1.0 |
| 300.7 | 1.0 | 293.0 | 1.0 | 306.1 | 1.0 |
| 294.9 | 1.0 | 303.7 | 1.0 | 299.6 | 1.0 |
| 296.0 | 1.0 | 292.8 | 1.0 | 308.7 | 1.0 |
| 301.2 | 1.0 | 300.7 | 1.0 | 294.0 | 1.0 |
| 291.8 | 1.0 | 298.8 | 1.0 | 304.1 | 1.0 |
| 302.7 | 1.0 | 296.9 | 1.0 | 309.9 | 1.0 |
| 298.7 | 1.0 | 301.9 | 1.0 | 292.2 | 1.0 |
| 298.1 | 1.0 | 304.8 | 1.0 | 303.2 | 1.0 |
| 300.2 | 1.0 | 296.7 | 1.0 | 293.8 | 1.0 |
| 293.2 | 1.0 | 299.9 | 1.0 | 304.7 | 1.0 |
| 290.7 | 1.0 | 306.0 | 1.0 | 297.6 | 1.0 |
| 303.7 | 1.0 | 294.3 | 1.0 | 306.6 | 1.0 |
| 301.8 | 1.0 | 291.3 | 1.0 | 295.4 | 1.0 |
| 312.3 | 1.0 | 290.0 | 1.0 | 292.8 | 1.0 |
| 302.8 | 1.0 | 297.7 | 1.0 | 299.6 | 1.0 |
| 294.5 | 1.0 | 291.5 | 1.0 | 308.8 | 1.0 |
| 300.1 | 1.0 | 303.3 | 1.0 | 299.8 | 1.0 |
| 295.0 | 1.0 | 290.0 | 1.0 | 302.8 | 1.0 |
| 302.3 | 1.0 | 295.3 | 1.0 | 299.0 | 1.0 |
| 310.4 | 1.0 | 300.6 | 1.0 | 298.6 | 1.0 |
| 304.2 | 1.0 | 296.0 | 1.0 | 312.1 | 1.0 |

| | | | | | |
|---|---|---|---|---|---|
| 300.6 | 1.0 | 304.8 | 1.0 | 301.5 | 1.0 |
| 302.2 | 1.0 | 299.1 | 1.0 | 293.2 | 1.0 |
| 306.2 | 1.0 | 297.2 | 1.0 | 298.2 | 1.0 |
| 304.1 | 1.0 | 296.1 | 1.0 | 301.7 | 1.0 |
| 309.2 | 1.0 | 302.0 | 1.0 | 306.2 | 1.0 |
| 301.3 | 1.0 | 290.9 | 1.0 | 299.0 | 1.0 |
| 300.8 | 1.0 | 302.9 | 1.0 | 298.6 | 1.0 |
| 300.1 | 1.0 | 305.2 | 1.0 | 301.5 | 1.0 |
| 287.9 | 1.0 | 304.6 | 1.0 | 295.7 | 1.0 |
| 291.3 | 1.0 | 302.5 | 1.0 | 298.3 | 1.0 |
| 317.3 | 1.0 | 304.7 | 1.0 | 304.4 | 1.0 |
| 311.9 | 1.0 | 308.0 | 1.0 | | |

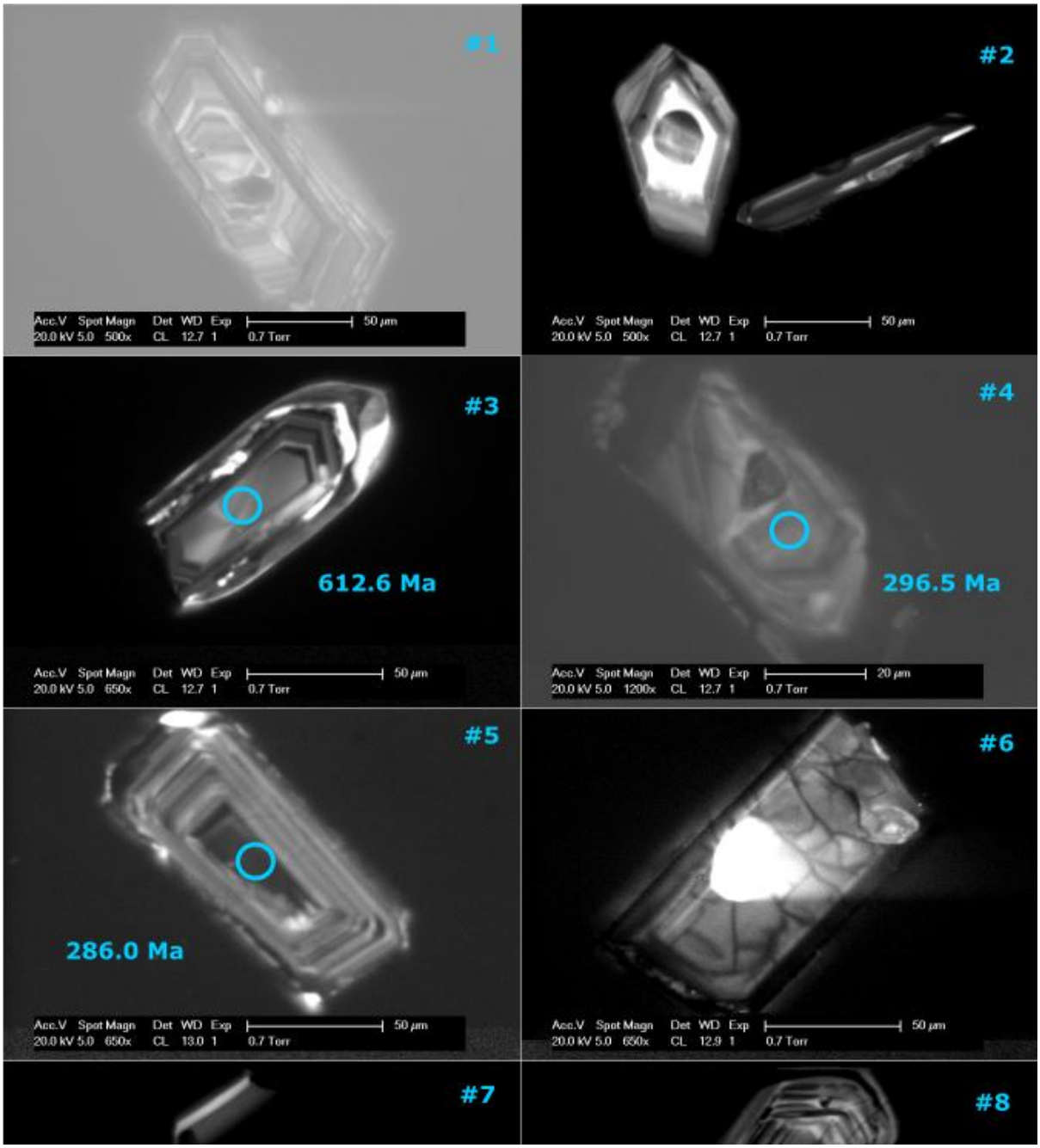
#1
Acc.V Spot Magn Det WD Exp 50 µm
20.0 kV 5.0 500x CL 12.7 1 0.7 Torr
#2
Acc.V Spot Magn Det WD Exp 50 µm
20.0 kV 5.0 500x CL 12.7 1 0.7 Torr
#3
612.6 Ma
Acc.V Spot Magn Det WD Exp 50 µm
20.0 kV 5.0 650x CL 12.7 1 0.7 Torr
#4
296.5 Ma
Acc.V Spot Magn Det WD Exp 20 µm
20.0 kV 5.0 1200x CL 12.7 1 0.7 Torr
#5
286.0 Ma
Acc.V Spot Magn Det WD Exp 50 µm
20.0 kV 5.0 650x CL 13.0 1 0.7 Torr
#6
Acc.V Spot Magn Det WD Exp 50 µm
20.0 kV 5.0 650x CL 12.9 1 0.7 Torr
#7
#8

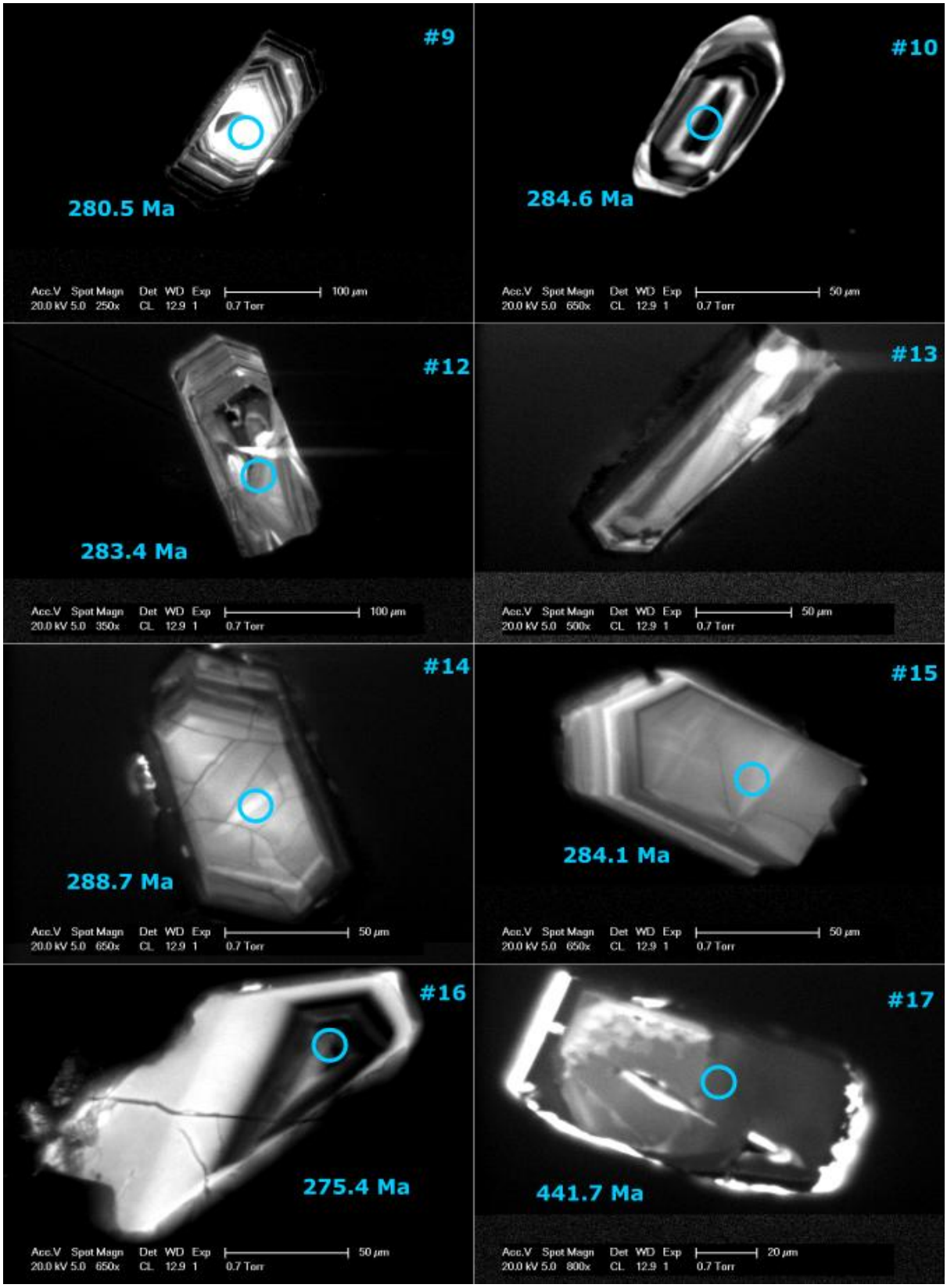
#9
280.5 Ma
Acc.V Spot Magn Det WD Exp 100 µm
20.0 kV 5.0 250x CL 12.9 1 0.7 Torr
#10
284.6 Ma
Acc.V Spot Magn Det WD Exp 50 µm
20.0 kV 5.0 650x CL 12.9 1 0.7 Torr
#12
283.4 Ma
Acc.V Spot Magn Det WD Exp 100 µm
20.0 kV 5.0 350x CL 12.9 1 0.7 Torr
#13
Acc.V Spot Magn Det WD Exp 50 µm
20.0 kV 5.0 500x CL 12.9 1 0.7 Torr
#14
288.7 Ma
Acc.V Spot Magn Det WD Exp 50 µm
20.0 kV 5.0 650x CL 12.9 1 0.7 Torr
#15
284.1 Ma
Acc.V Spot Magn Det WD Exp 50 µm
20.0 kV 5.0 650x CL 12.9 1 0.7 Torr
#16
275.4 Ma
Acc.V Spot Magn Det WD Exp 50 µm
20.0 kV 5.0 650x CL 12.9 1 0.7 Torr
#17
441.7 Ma
Acc.V Spot Magn Det WD Exp 20 µm
20.0 kV 5.0 800x CL 12.9 1 0.7 Torr

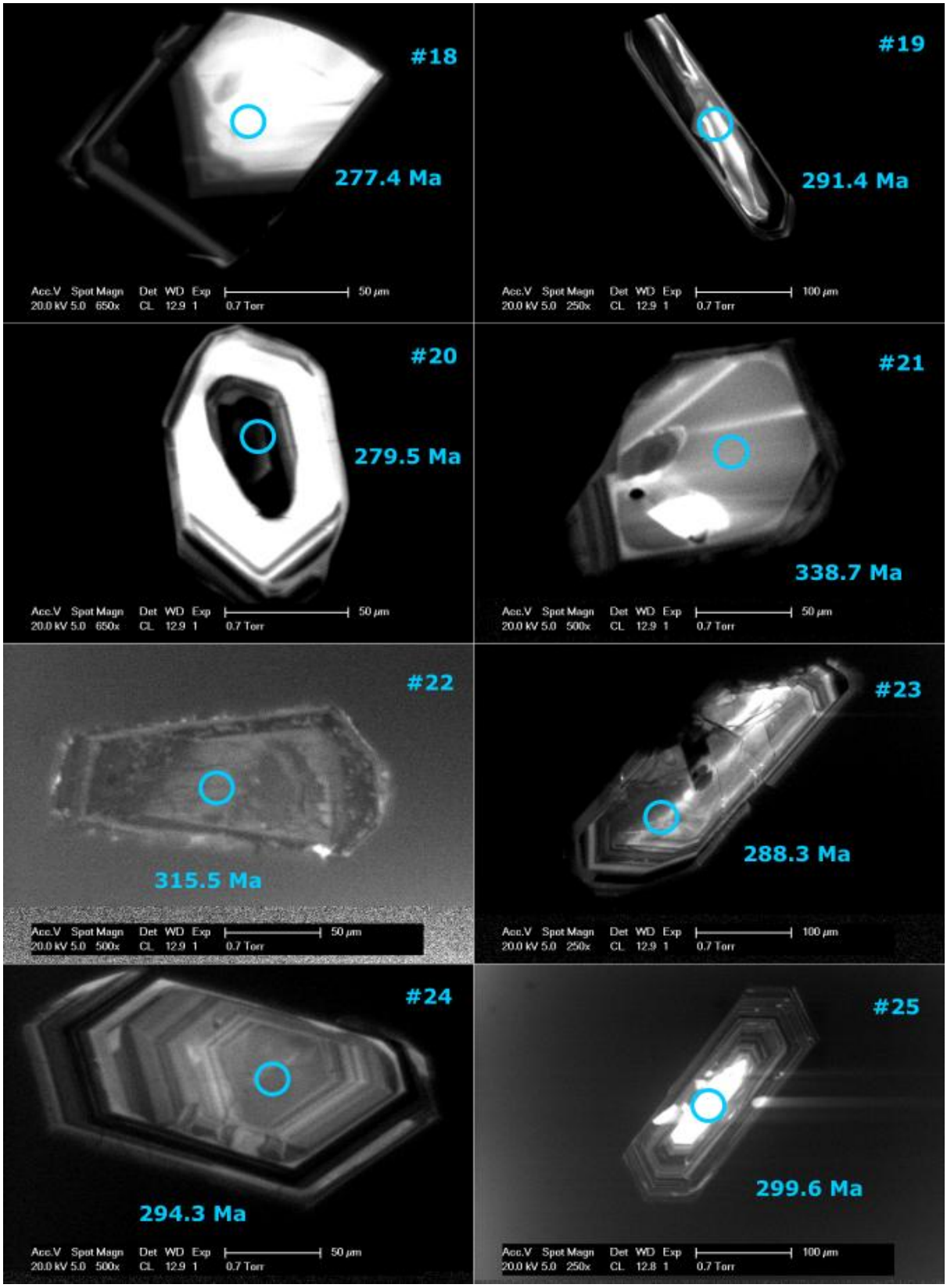
#18
277.4 Ma
Acc.V Spot Magn Det WD Exp 50 µm
20.0 kV 5.0 650x CL 12.9 1 0.7 Torr
#19
291.4 Ma
Acc.V Spot Magn Det WD Exp 100 µm
20.0 kV 5.0 250x CL 12.9 1 0.7 Torr
#20
279.5 Ma
Acc.V Spot Magn Det WD Exp 50 µm
20.0 kV 5.0 650x CL 12.9 1 0.7 Torr
#21
338.7 Ma
Acc.V Spot Magn Det WD Exp 50 µm
20.0 kV 5.0 500x CL 12.9 1 0.7 Torr
#22
315.5 Ma
Acc.V Spot Magn Det WD Exp 50 µm
20.0 kV 5.0 500x CL 12.9 1 0.7 Torr
#23
288.3 Ma
Acc.V Spot Magn Det WD Exp 100 µm
20.0 kV 5.0 250x CL 12.9 1 0.7 Torr
#24
294.3 Ma
Acc.V Spot Magn Det WD Exp 50 µm
20.0 kV 5.0 500x CL 12.9 1 0.7 Torr
#25
299.6 Ma
Acc.V Spot Magn Det WD Exp 100 µm
20.0 kV 5.0 250x CL 12.8 1 0.7 Torr

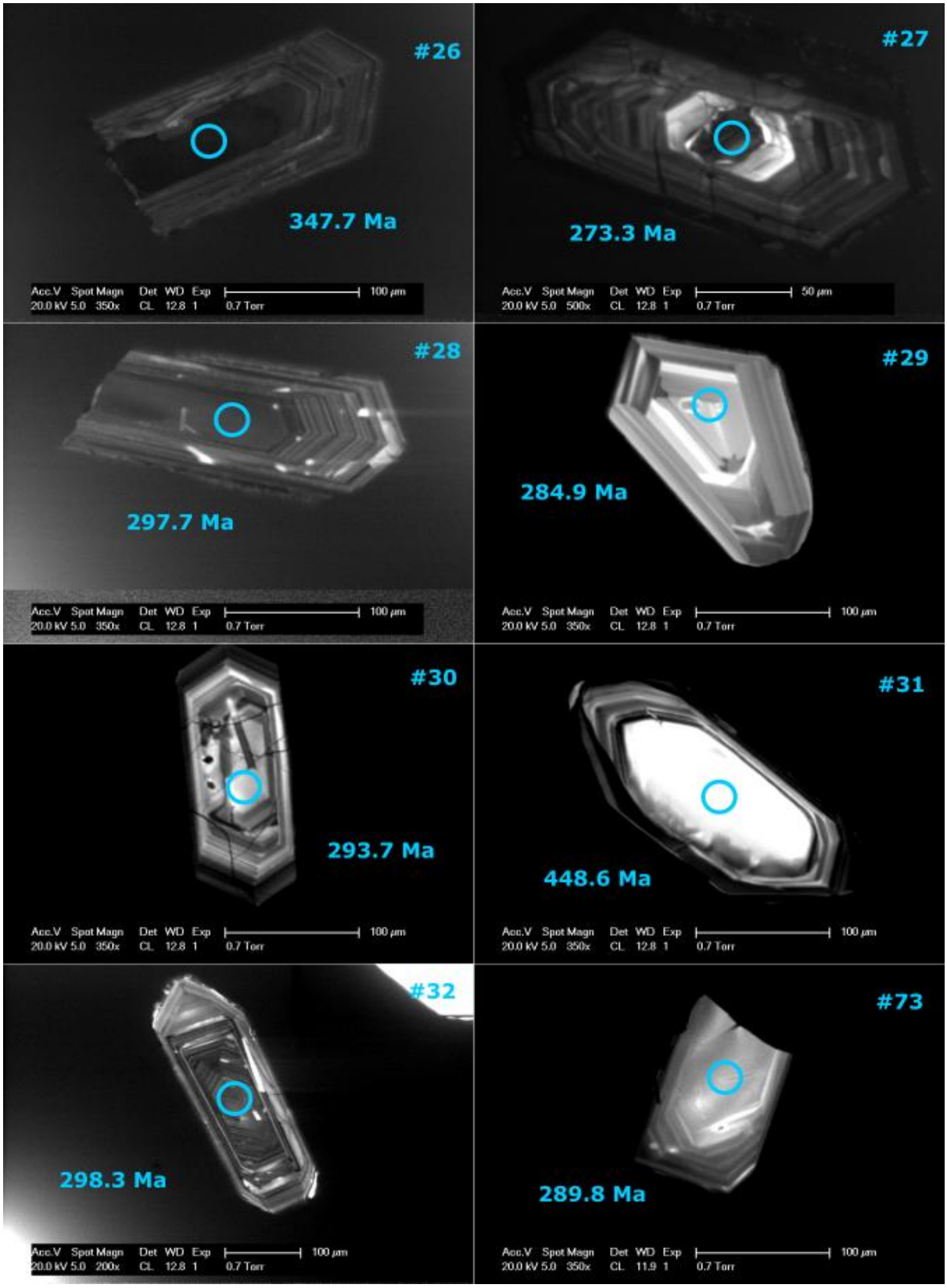
#26
347.7 Ma
Acc.V Spot Magn Det WD Exp 100 µm
20.0 kV 5.0 350x CL 12.8 1 0.7 Torr
#27
273.3 Ma
Acc.V Spot Magn Det WD Exp 50 µm
20.0 kV 5.0 500x CL 12.8 1 0.7 Torr
#28
297.7 Ma
Acc.V Spot Magn Det WD Exp 100 µm
20.0 kV 5.0 350x CL 12.8 1 0.7 Torr
#29
284.9 Ma
Acc.V Spot Magn Det WD Exp 100 µm
20.0 kV 5.0 350x CL 12.8 1 0.7 Torr
#30
293.7 Ma
Acc.V Spot Magn Det WD Exp 100 µm
20.0 kV 5.0 350x CL 12.8 1 0.7 Torr
#31
448.6 Ma
Acc.V Spot Magn Det WD Exp 100 µm
20.0 kV 5.0 350x CL 12.8 1 0.7 Torr
#32
298.3 Ma
Acc.V Spot Magn Det WD Exp 100 µm
20.0 kV 5.0 200x CL 12.8 1 0.7 Torr
#73
289.8 Ma
Acc.V Spot Magn Det WD Exp 100 µm
20.0 kV 5.0 350x CL 11.9 1 0.7 Torr

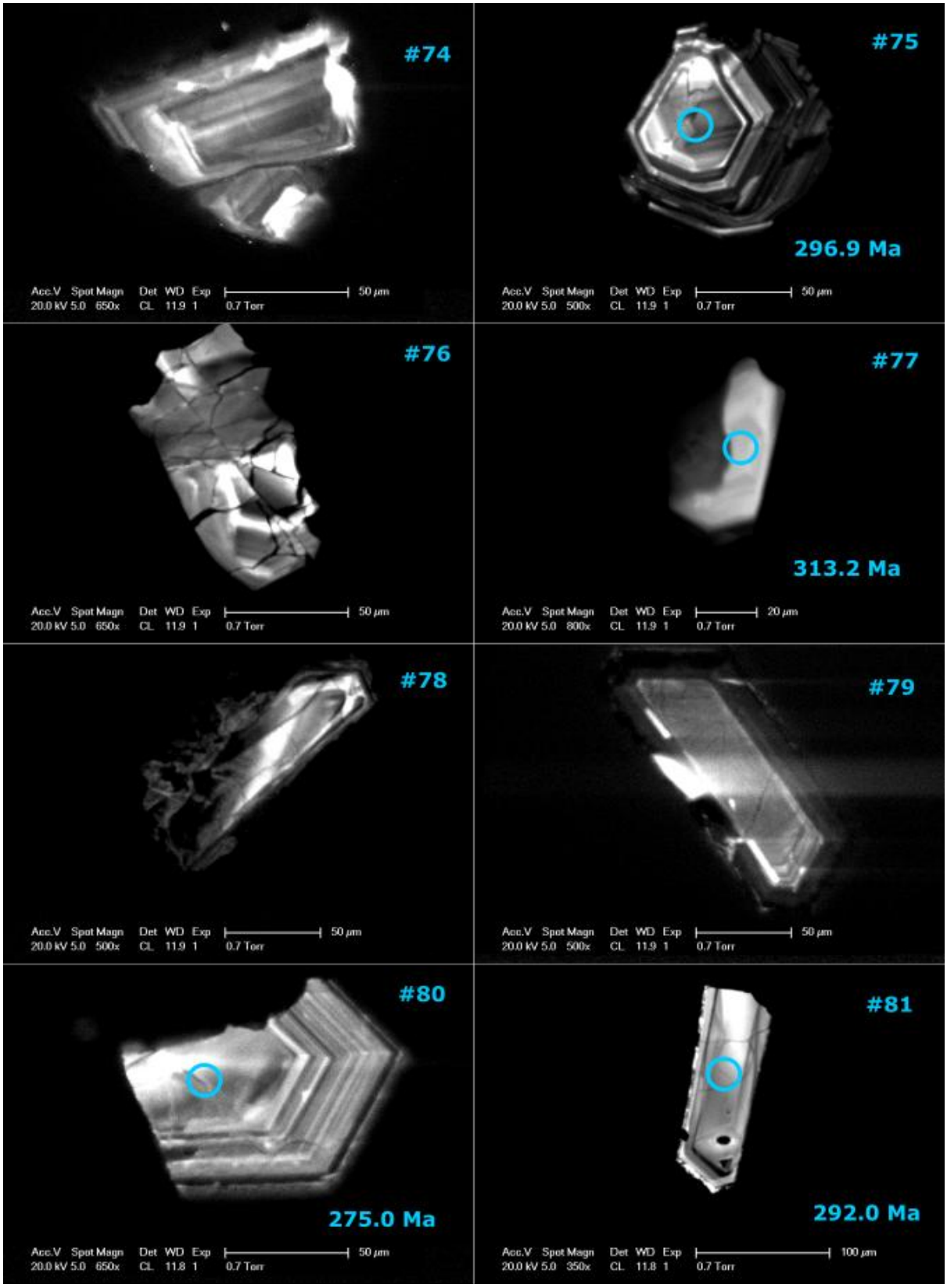
#74
Acc.V Spot Magn Det WD Exp 50 µm
20.0 kV 5.0 650x CL 11.9 1 0.7 Torr
#75
296.9 Ma
Acc.V Spot Magn Det WD Exp 50 µm
20.0 kV 5.0 500x CL 11.9 1 0.7 Torr
#76
Acc.V Spot Magn Det WD Exp 50 µm
20.0 kV 5.0 650x CL 11.9 1 0.7 Torr
#77
313.2 Ma
Acc.V Spot Magn Det WD Exp 20 µm
20.0 kV 5.0 800x CL 11.9 1 0.7 Torr
#78
Acc.V Spot Magn Det WD Exp 50 µm
20.0 kV 5.0 500x CL 11.9 1 0.7 Torr
#79
Acc.V Spot Magn Det WD Exp 50 µm
20.0 kV 5.0 500x CL 11.9 1 0.7 Torr
#80
275.0 Ma
Acc.V Spot Magn Det WD Exp 50 µm
20.0 kV 5.0 650x CL 11.8 1 0.7 Torr
#81
292.0 Ma
Acc.V Spot Magn Det WD Exp 100 µm
20.0 kV 5.0 350x CL 11.8 1 0.7 Torr

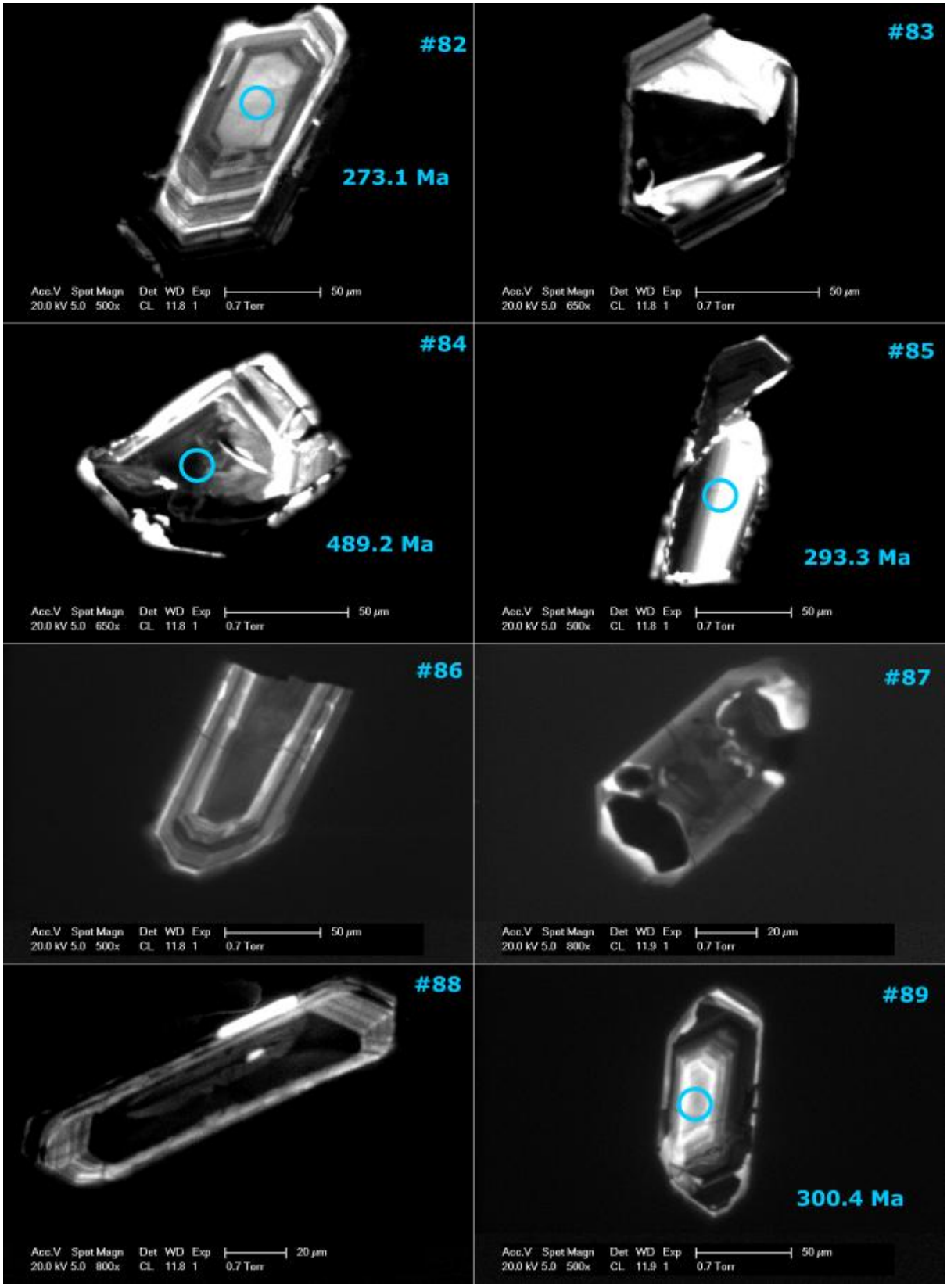
#82
273.1 Ma
Acc.V Spot Magn Det WD Exp 50 µm
20.0 kV 5.0 500x CL 11.8 1 0.7 Torr
#83
Acc.V Spot Magn Det WD Exp 50 µm
20.0 kV 5.0 650x CL 11.8 1 0.7 Torr
#84
489.2 Ma
Acc.V Spot Magn Det WD Exp 50 µm
20.0 kV 5.0 650x CL 11.8 1 0.7 Torr
#85
293.3 Ma
Acc.V Spot Magn Det WD Exp 50 µm
20.0 kV 5.0 500x CL 11.8 1 0.7 Torr
#86
Acc.V Spot Magn Det WD Exp 50 µm
20.0 kV 5.0 500x CL 11.8 1 0.7 Torr
#87
Acc.V Spot Magn Det WD Exp 20 µm
20.0 kV 5.0 800x CL 11.9 1 0.7 Torr
#88
Acc.V Spot Magn Det WD Exp 20 µm
20.0 kV 5.0 800x CL 11.8 1 0.7 Torr
#89
300.4 Ma
Acc.V Spot Magn Det WD Exp 50 µm
20.0 kV 5.0 500x CL 11.9 1 0.7 Torr

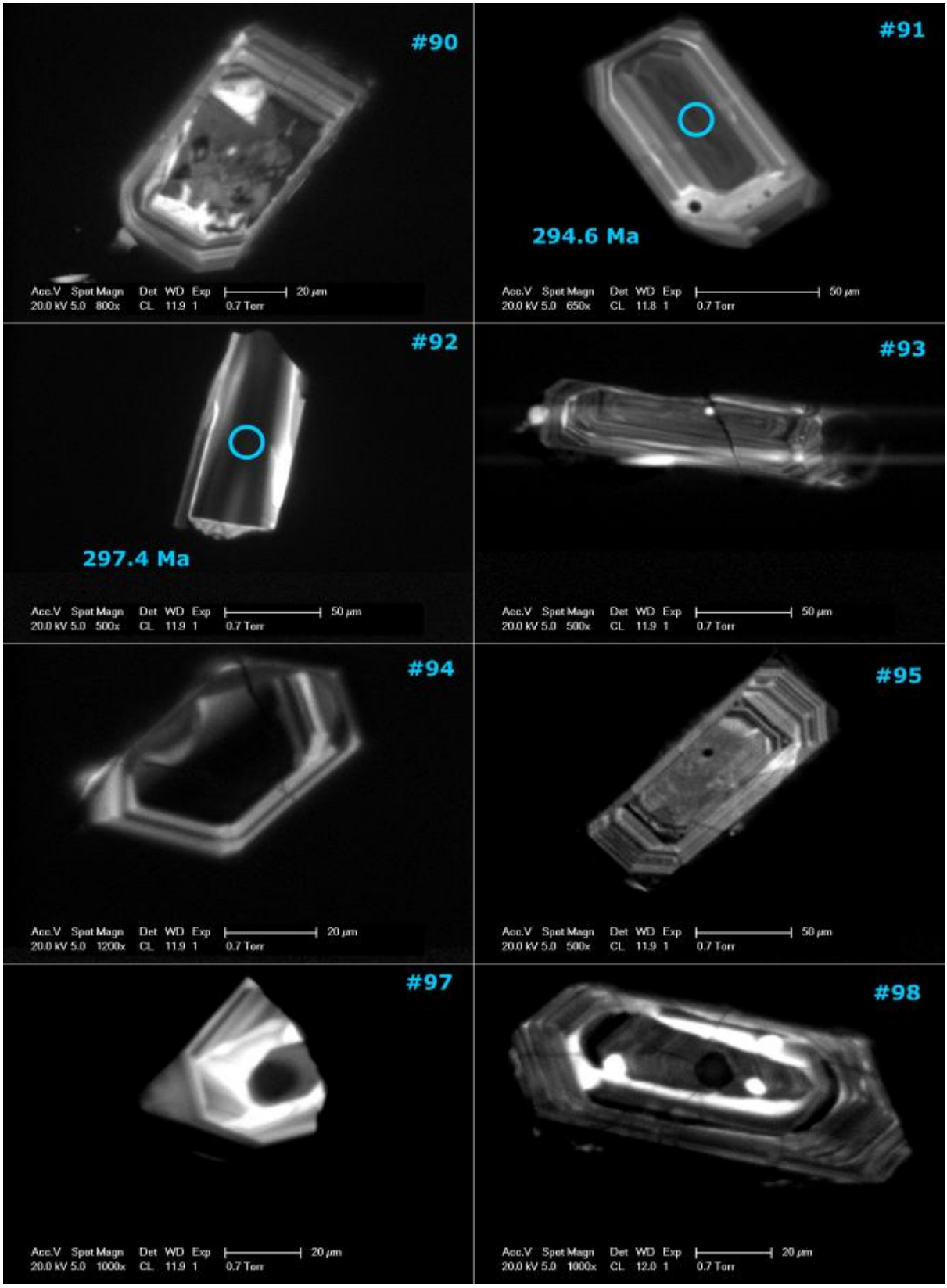
#90
Acc.V Spot Magn Det WD Exp 20 µm
20.0 kV 5.0 800x CL 11.9 1 0.7 Torr
#91
294.6 Ma
Acc.V Spot Magn Det WD Exp 50 µm
20.0 kV 5.0 650x CL 11.8 1 0.7 Torr
#92
297.4 Ma
Acc.V Spot Magn Det WD Exp 50 µm
20.0 kV 5.0 500x CL 11.9 1 0.7 Torr
#93
Acc.V Spot Magn Det WD Exp 50 µm
20.0 kV 5.0 500x CL 11.9 1 0.7 Torr
#94
Acc.V Spot Magn Det WD Exp 20 µm
20.0 kV 5.0 1200x CL 11.9 1 0.7 Torr
#95
Acc.V Spot Magn Det WD Exp 50 µm
20.0 kV 5.0 500x CL 11.9 1 0.7 Torr
#97
Acc.V Spot Magn Det WD Exp 20 µm
20.0 kV 5.0 1000x CL 11.9 1 0.7 Torr
#98
Acc.V Spot Magn Det WD Exp 20 µm
20.0 kV 5.0 1000x CL 12.0 1 0.7 Torr


#99
Acc.V Spot Magn Det WD Exp 50 µm
20.0 kV 5.0 650x CL 12.0 1 0.7 Torr
#100
Acc.V Spot Magn Det WD Exp 50 µm
20.0 kV 5.0 650x CL 11.9 1 0.7 Torr
#101
Acc.V Spot Magn Det WD Exp 50 µm
20.0 kV 5.0 650x CL 11.9 1 0.7 Torr
#102
Acc.V Spot Magn Det WD Exp 20 µm
20.0 kV 5.0 800x CL 11.9 1 0.7 Torr
#103
Acc.V Spot Magn Det WD Exp 50 µm
20.0 kV 5.0 500x CL 11.9 1 0.7 Torr
#104
657.6 Ma
Acc.V Spot Magn Det WD Exp 50 µm
20.0 kV 5.0 650x CL 11.9 1 0.7 Torr
#105
252.2 Ma
Acc.V Spot Magn Det WD Exp 20 µm
20.0 kV 5.0 800x CL 12.0 1 0.7 Torr
#106
Acc.V Spot Magn Det WD Exp 50 µm
20.0 kV 5.0 500x CL 11.9 1 0.7 Torr

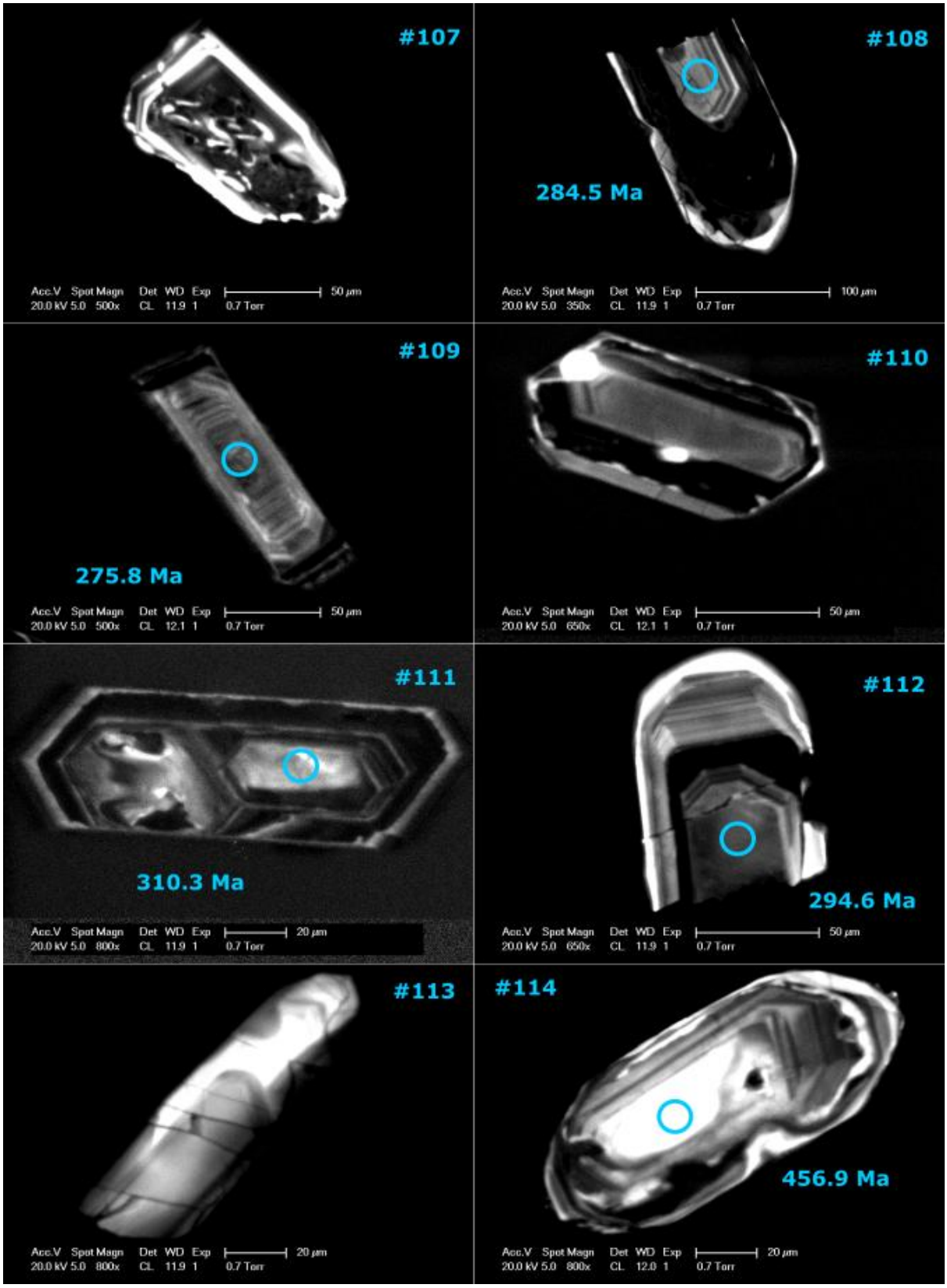
#107
Acc.V Spot Magn Det WD Exp 50 µm
20.0 kV 5.0 500x CL 11.9 1 0.7 Torr
#108
284.5 Ma
Acc.V Spot Magn Det WD Exp 100 µm
20.0 kV 5.0 350x CL 11.9 1 0.7 Torr
#109
275.8 Ma
Acc.V Spot Magn Det WD Exp 50 µm
20.0 kV 5.0 500x CL 12.1 1 0.7 Torr
#110
Acc.V Spot Magn Det WD Exp 50 µm
20.0 kV 5.0 650x CL 12.1 1 0.7 Torr
#111
310.3 Ma
Acc.V Spot Magn Det WD Exp 20 µm
20.0 kV 5.0 800x CL 11.9 1 0.7 Torr
#112
294.6 Ma
Acc.V Spot Magn Det WD Exp 50 µm
20.0 kV 5.0 650x CL 11.9 1 0.7 Torr
#113
Acc.V Spot Magn Det WD Exp 20 µm
20.0 kV 5.0 800x CL 11.9 1 0.7 Torr
#114
456.9 Ma
Acc.V Spot Magn Det WD Exp 20 µm
20.0 kV 5.0 800x CL 12.0 1 0.7 Torr

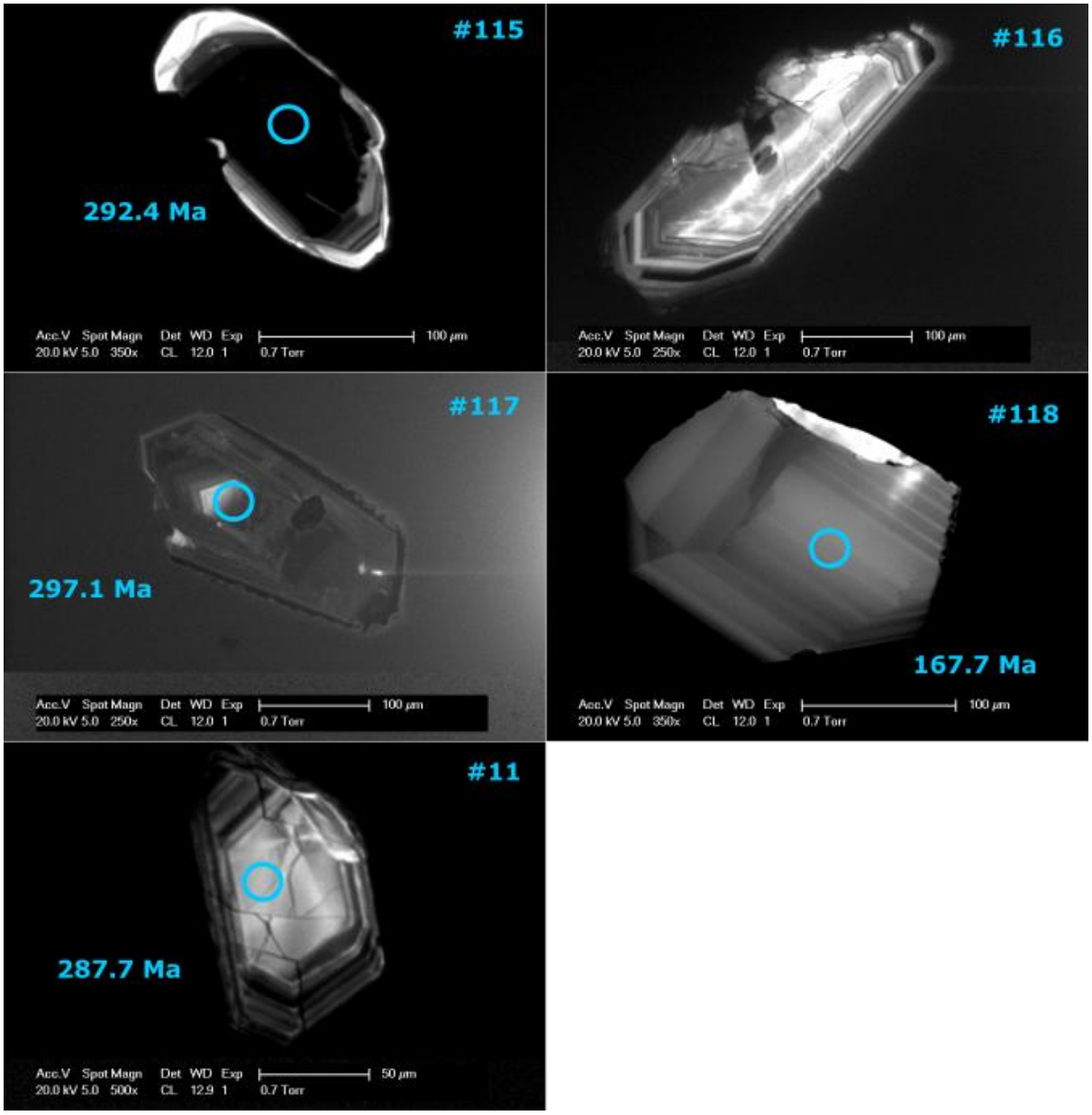
#115
292.4 Ma
Acc.V Spot Magn Det WD Exp 100 µm
20.0 kV 5.0 350x CL 12.0 1 0.7 Torr
#116
Acc.V Spot Magn Det WD Exp 100 µm
20.0 kV 5.0 250x CL 12.0 1 0.7 Torr
#117
297.1 Ma
Acc.V Spot Magn Det WD Exp 100 µm
20.0 kV 5.0 250x CL 12.0 1 0.7 Torr
#118
167.7 Ma
Acc.V Spot Magn Det WD Exp 100 µm
20.0 kV 5.0 350x CL 12.0 1 0.7 Torr
#11
287.7 Ma
Acc.V Spot Magn Det WD Exp 50 µm
20.0 kV 5.0 500x CL 12.9 1 0.7 Torr

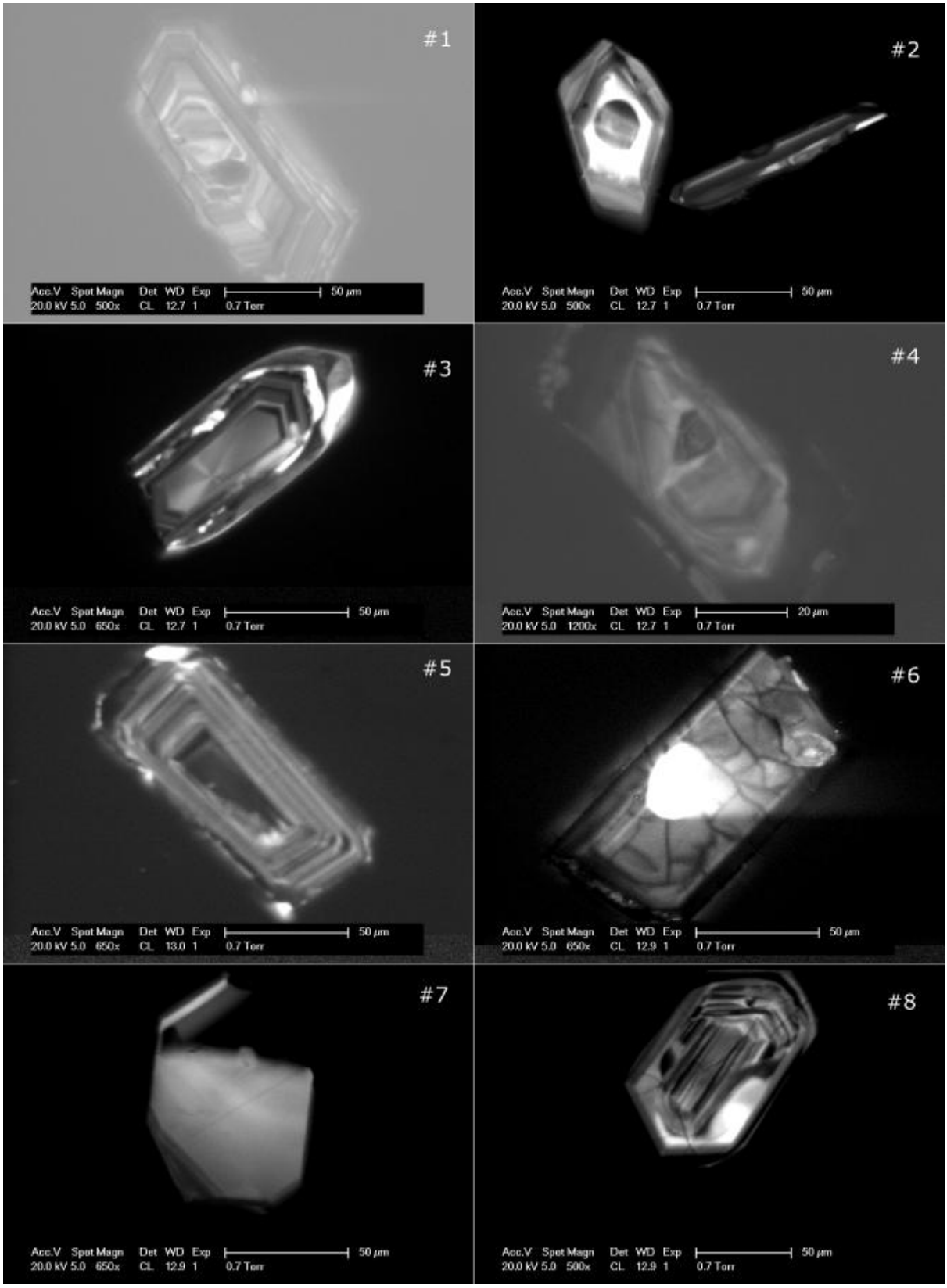
#1
Acc.V Spot Magn Det WD Exp 50 µm
20.0 kV 5.0 500x CL 12.7 1 0.7 Torr
#2
Acc.V Spot Magn Det WD Exp 50 µm
20.0 kV 5.0 500x CL 12.7 1 0.7 Torr
#3
Acc.V Spot Magn Det WD Exp 50 µm
20.0 kV 5.0 650x CL 12.7 1 0.7 Torr
#4
Acc.V Spot Magn Det WD Exp 20 µm
20.0 kV 5.0 1200x CL 12.7 1 0.7 Torr
#5
Acc.V Spot Magn Det WD Exp 50 µm
20.0 kV 5.0 650x CL 13.0 1 0.7 Torr
#6
Acc.V Spot Magn Det WD Exp 50 µm
20.0 kV 5.0 650x CL 12.9 1 0.7 Torr
#7
Acc.V Spot Magn Det WD Exp 50 µm
20.0 kV 5.0 650x CL 12.9 1 0.7 Torr
#8
Acc.V Spot Magn Det WD Exp 50 µm
20.0 kV 5.0 500x CL 12.9 1 0.7 Torr

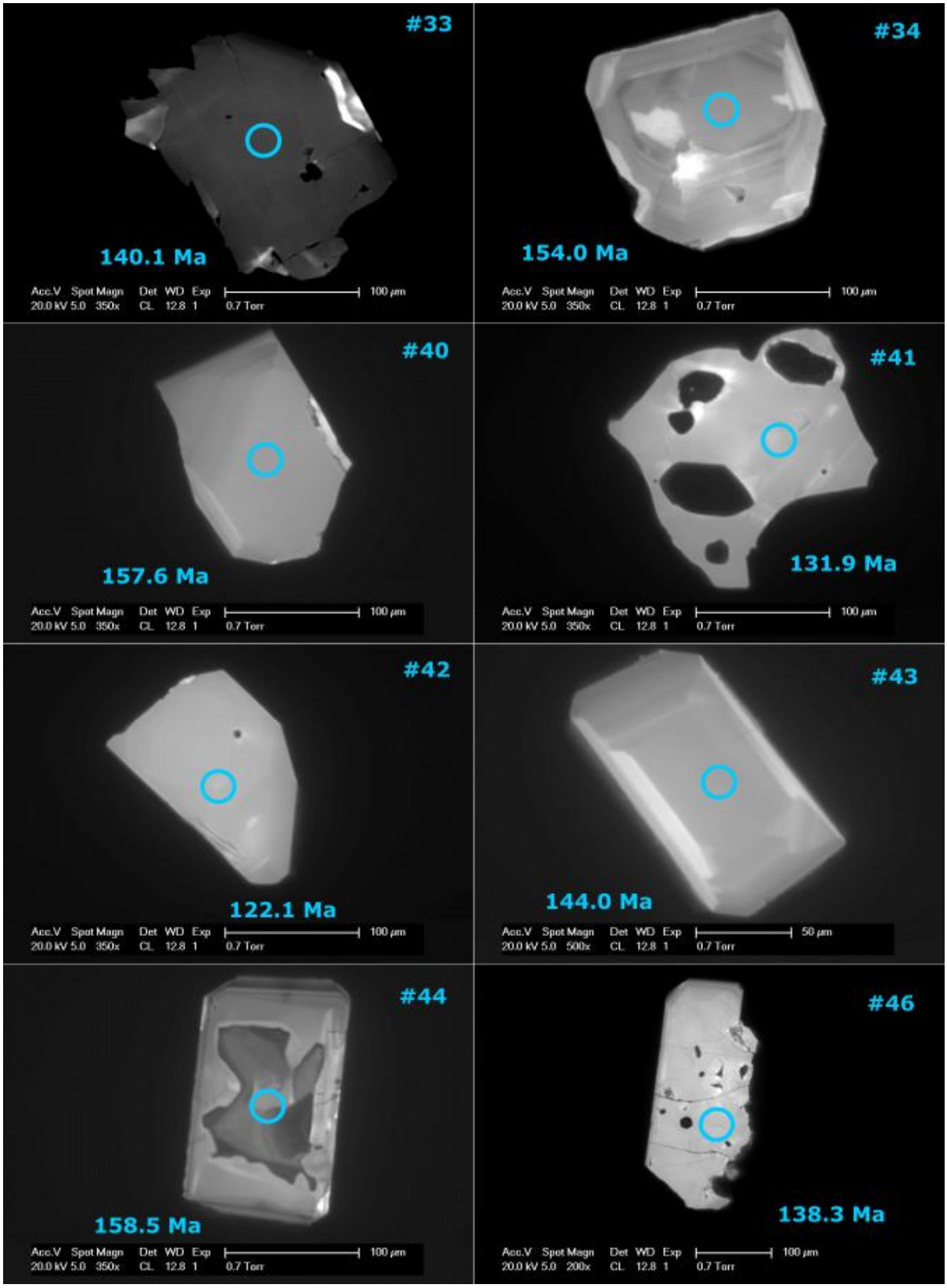
#33
140.1 Ma
Acc.V Spot Magn Det WD Exp 100 µm
20.0 kV 5.0 350x CL 12.8 1 0.7 Torr
#34
154.0 Ma
Acc.V Spot Magn Det WD Exp 100 µm
20.0 kV 5.0 350x CL 12.8 1 0.7 Torr
#40
157.6 Ma
Acc.V Spot Magn Det WD Exp 100 µm
20.0 kV 5.0 350x CL 12.8 1 0.7 Torr
#41
131.9 Ma
Acc.V Spot Magn Det WD Exp 100 µm
20.0 kV 5.0 350x CL 12.8 1 0.7 Torr
#42
122.1 Ma
Acc.V Spot Magn Det WD Exp 100 µm
20.0 kV 5.0 350x CL 12.8 1 0.7 Torr
#43
144.0 Ma
Acc.V Spot Magn Det WD Exp 50 µm
20.0 kV 5.0 500x CL 12.8 1 0.7 Torr
#44
158.5 Ma
Acc.V Spot Magn Det WD Exp 100 µm
20.0 kV 5.0 350x CL 12.8 1 0.7 Torr
#46
138.3 Ma
Acc.V Spot Magn Det WD Exp 100 µm
20.0 kV 5.0 200x CL 12.8 1 0.7 Torr

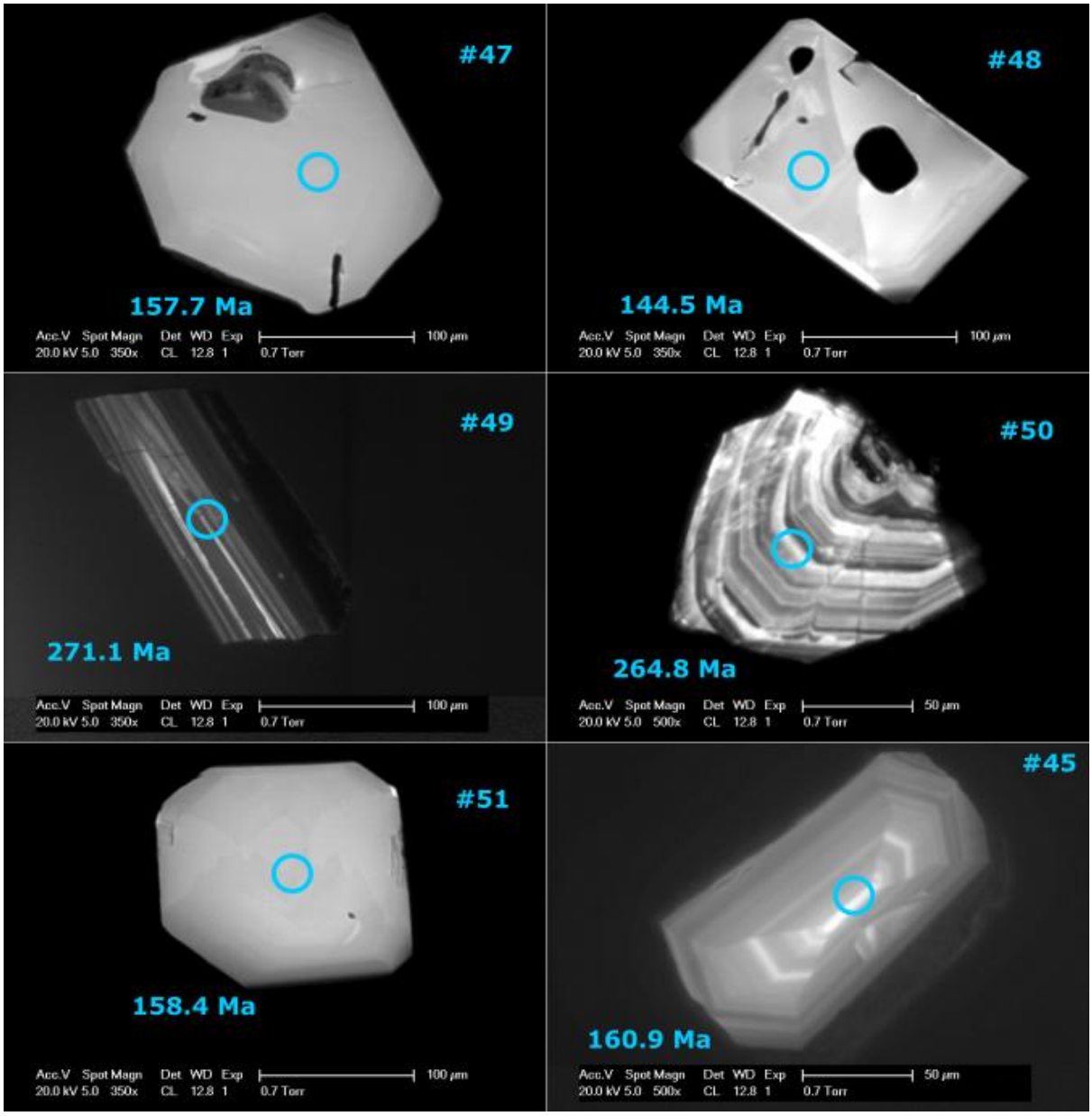
#47
157.7 Ma
Acc.V Spot Magn Det WD Exp 100 µm
20.0 kV 5.0 350x CL 12.8 1 0.7 Torr
#48
144.5 Ma
Acc.V Spot Magn Det WD Exp 100 µm
20.0 kV 5.0 350x CL 12.8 1 0.7 Torr
#49
271.1 Ma
Acc.V Spot Magn Det WD Exp 100 µm
20.0 kV 5.0 350x CL 12.8 1 0.7 Torr
#50
264.8 Ma
Acc.V Spot Magn Det WD Exp 50 µm
20.0 kV 5.0 500x CL 12.8 1 0.7 Torr
#51
158.4 Ma
Acc.V Spot Magn Det WD Exp 100 µm
20.0 kV 5.0 350x CL 12.8 1 0.7 Torr
#45
160.9 Ma
Acc.V Spot Magn Det WD Exp 50 µm
20.0 kV 5.0 500x CL 12.8 1 0.7 Torr

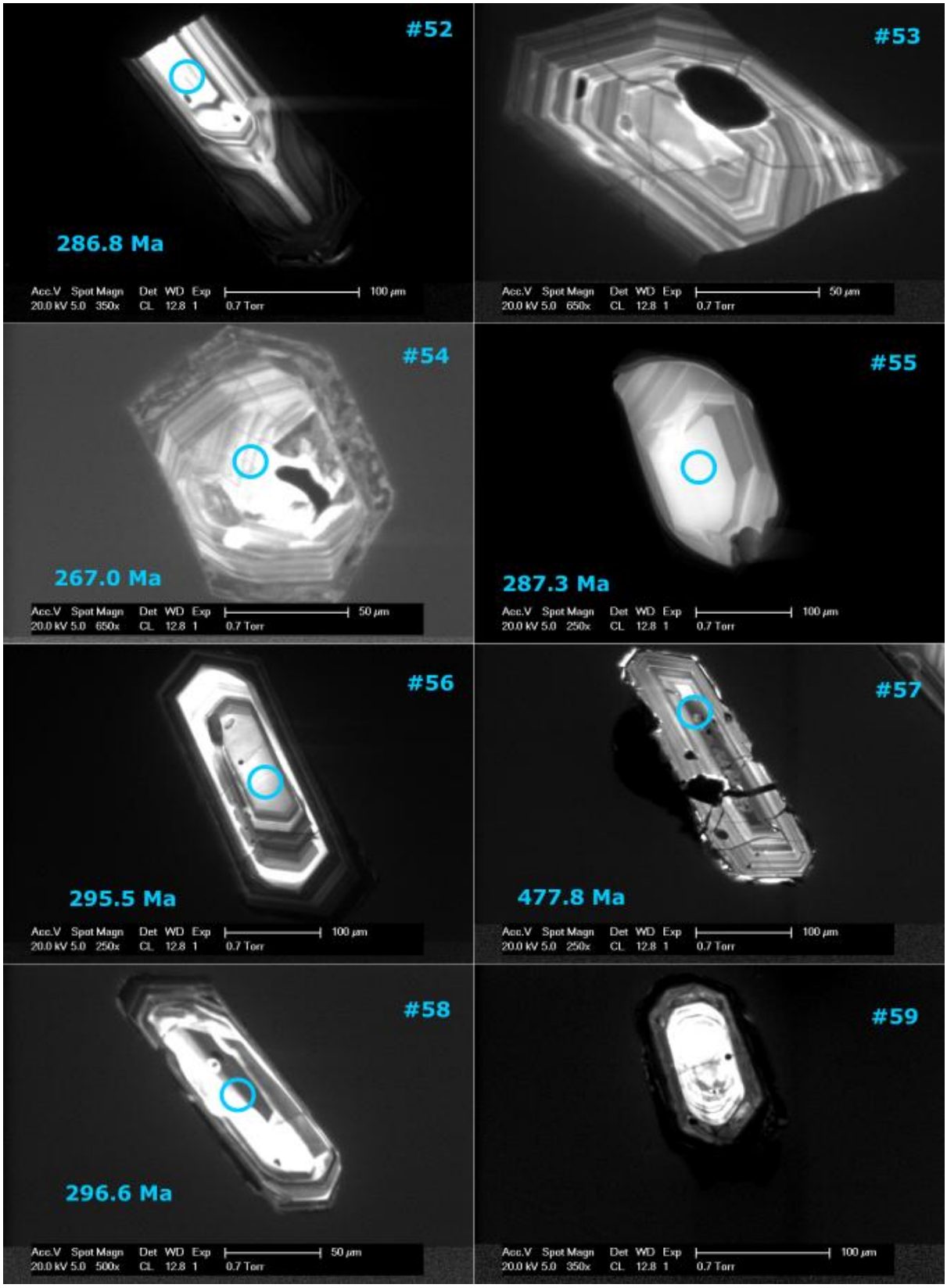
#52
286.8 Ma
Acc.V Spot Magn Det WD Exp 100 µm
20.0 kV 5.0 350x CL 12.8 1 0.7 Torr
#53
Acc.V Spot Magn Det WD Exp 50 µm
20.0 kV 5.0 650x CL 12.8 1 0.7 Torr
#54
267.0 Ma
Acc.V Spot Magn Det WD Exp 50 µm
20.0 kV 5.0 650x CL 12.8 1 0.7 Torr
#55
287.3 Ma
Acc.V Spot Magn Det WD Exp 100 µm
20.0 kV 5.0 250x CL 12.8 1 0.7 Torr
#56
295.5 Ma
Acc.V Spot Magn Det WD Exp 100 µm
20.0 kV 5.0 250x CL 12.8 1 0.7 Torr
#57
477.8 Ma
Acc.V Spot Magn Det WD Exp 100 µm
20.0 kV 5.0 250x CL 12.8 1 0.7 Torr
#58
296.6 Ma
Acc.V Spot Magn Det WD Exp 50 µm
20.0 kV 5.0 500x CL 12.8 1 0.7 Torr
#59
Acc.V Spot Magn Det WD Exp 100 µm
20.0 kV 5.0 350x CL 12.8 1 0.7 Torr

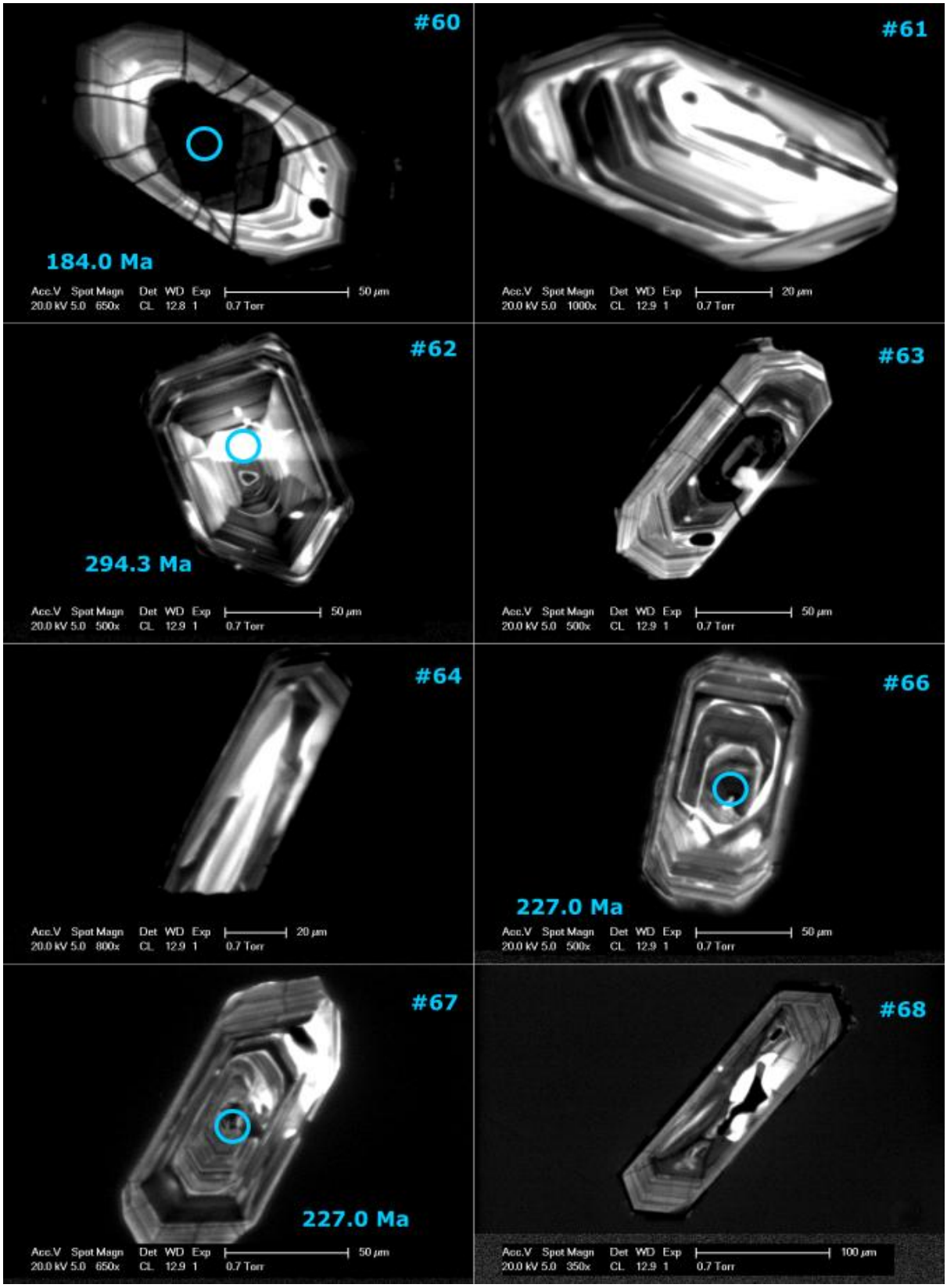
#60
184.0 Ma
Acc.V Spot Magn Det WD Exp 50 µm
20.0 kV 5.0 650x CL 12.8 1 0.7 Torr
#61
Acc.V Spot Magn Det WD Exp 20 µm
20.0 kV 5.0 1000x CL 12.9 1 0.7 Torr
#62
294.3 Ma
Acc.V Spot Magn Det WD Exp 50 µm
20.0 kV 5.0 500x CL 12.9 1 0.7 Torr
#63
Acc.V Spot Magn Det WD Exp 50 µm
20.0 kV 5.0 500x CL 12.9 1 0.7 Torr
#64
Acc.V Spot Magn Det WD Exp 20 µm
20.0 kV 5.0 800x CL 12.9 1 0.7 Torr
#66
227.0 Ma
Acc.V Spot Magn Det WD Exp 50 µm
20.0 kV 5.0 500x CL 12.9 1 0.7 Torr
#67
227.0 Ma
Acc.V Spot Magn Det WD Exp 50 µm
20.0 kV 5.0 650x CL 12.9 1 0.7 Torr
#68
Acc.V Spot Magn Det WD Exp 100 µm
20.0 kV 5.0 350x CL 12.9 1 0.7 Torr


#69
286.6 Ma
Acc.V Spot Magn Det WD Exp 50 µm
20.0 kV 5.0 650x CL 12.9 1 0.7 Torr
#70
286.6 Ma
Acc.V Spot Magn Det WD Exp 50 µm
20.0 kV 5.0 650x CL 12.9 1 0.7 Torr
#71
272.4 Ma
Acc.V Spot Magn Det WD Exp 50 µm
20.0 kV 5.0 650x CL 12.9 1 0.7 Torr
#72
Acc.V Spot Magn Det WD Exp 50 µm
20.0 kV 5.0 650x CL 12.9 1 0.7 Torr
#119
Acc.V Spot Magn Det WD Exp 100 µm
20.0 kV 5.0 350x CL 12.0 1 0.7 Torr
#120
Acc.V Spot Magn Det WD Exp 100 µm
20.0 kV 5.0 350x CL 12.0 1 0.7 Torr
#121
Acc.V Spot Magn Det WD Exp 20 µm
20.0 kV 5.0 800x CL 12.0 1 0.7 Torr
#122
291.2 Ma
Acc.V Spot Magn Det WD Exp 100 µm
20.0 kV 5.0 350x CL 12.0 1 0.7 Torr

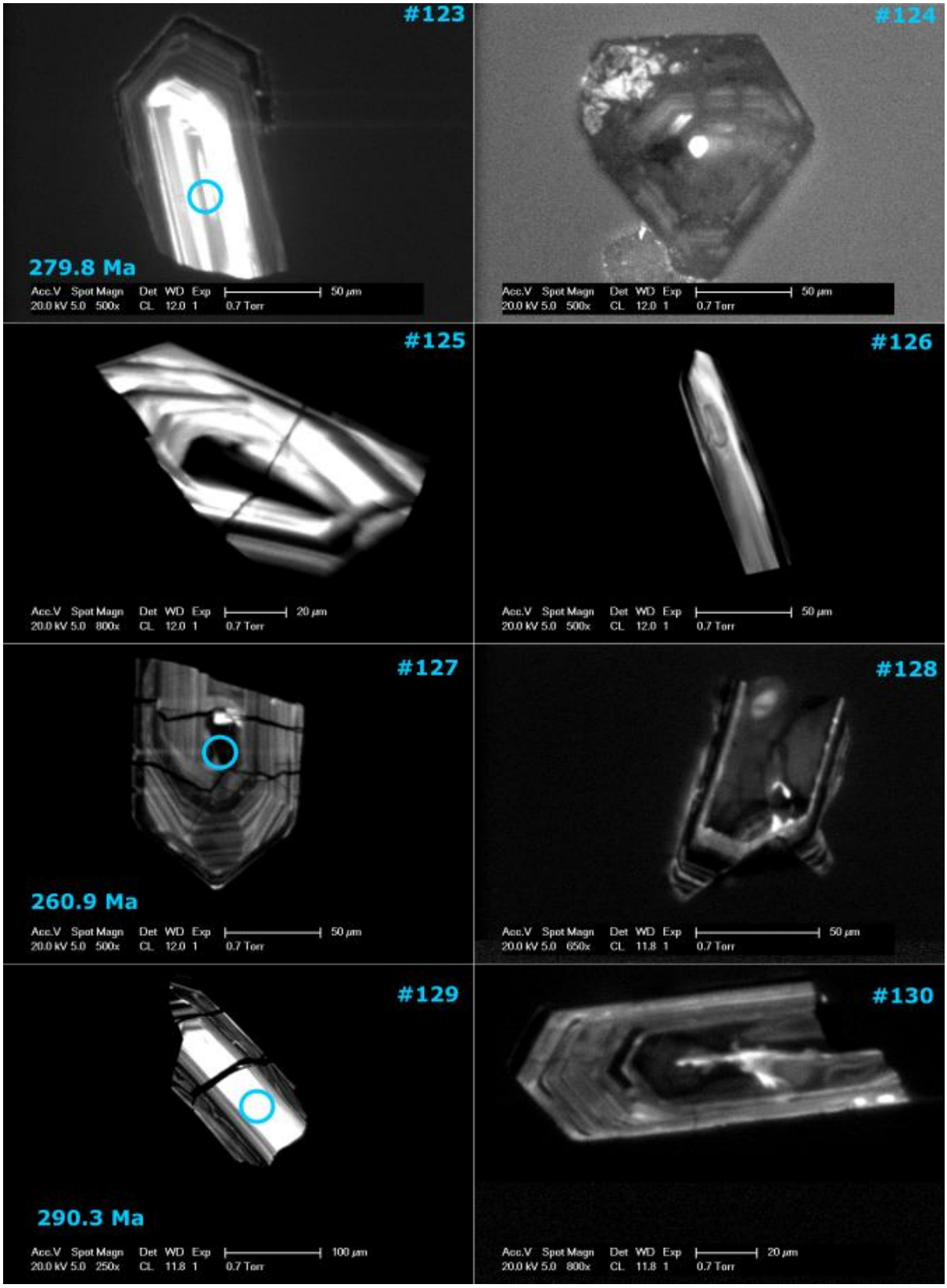
#123
279.8 Ma
Acc.V Spot Magn Det WD Exp 50 µm
20.0 kV 5.0 500x CL 12.0 1 0.7 Torr
#124
Acc.V Spot Magn Det WD Exp 50 µm
20.0 kV 5.0 500x CL 12.0 1 0.7 Torr
#125
Acc.V Spot Magn Det WD Exp 20 µm
20.0 kV 5.0 800x CL 12.0 1 0.7 Torr
#126
Acc.V Spot Magn Det WD Exp 50 µm
20.0 kV 5.0 500x CL 12.0 1 0.7 Torr
#127
260.9 Ma
Acc.V Spot Magn Det WD Exp 50 µm
20.0 kV 5.0 500x CL 12.0 1 0.7 Torr
#128
Acc.V Spot Magn Det WD Exp 50 µm
20.0 kV 5.0 650x CL 11.8 1 0.7 Torr
#129
290.3 Ma
Acc.V Spot Magn Det WD Exp 100 µm
20.0 kV 5.0 250x CL 11.8 1 0.7 Torr
#130
Acc.V Spot Magn Det WD Exp 20 µm
20.0 kV 5.0 800x CL 11.8 1 0.7 Torr

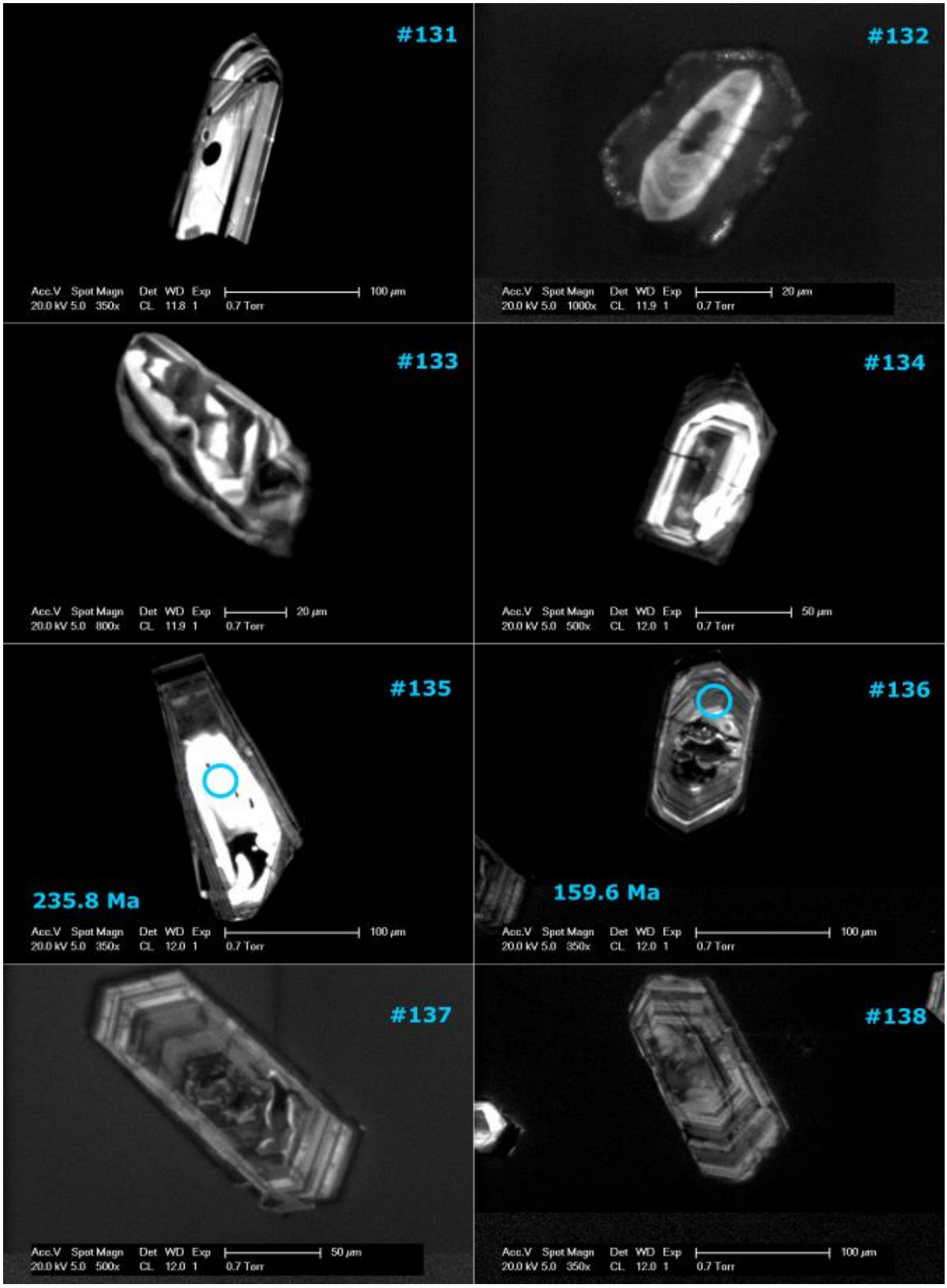
#131
Acc.V Spot Magn Det WD Exp 100 µm
20.0 kV 5.0 350x CL 11.8 1 0.7 Torr
#132
Acc.V Spot Magn Det WD Exp 20 µm
20.0 kV 5.0 1000x CL 11.9 1 0.7 Torr
#133
Acc.V Spot Magn Det WD Exp 20 µm
20.0 kV 5.0 800x CL 11.9 1 0.7 Torr
#134
Acc.V Spot Magn Det WD Exp 50 µm
20.0 kV 5.0 500x CL 12.0 1 0.7 Torr
#135
235.8 Ma
Acc.V Spot Magn Det WD Exp 100 µm
20.0 kV 5.0 350x CL 12.0 1 0.7 Torr
#136
159.6 Ma
Acc.V Spot Magn Det WD Exp 100 µm
20.0 kV 5.0 350x CL 12.0 1 0.7 Torr
#137
Acc.V Spot Magn Det WD Exp 50 µm
20.0 kV 5.0 500x CL 12.0 1 0.7 Torr
#138
Acc.V Spot Magn Det WD Exp 100 µm
20.0 kV 5.0 350x CL 12.0 1 0.7 Torr

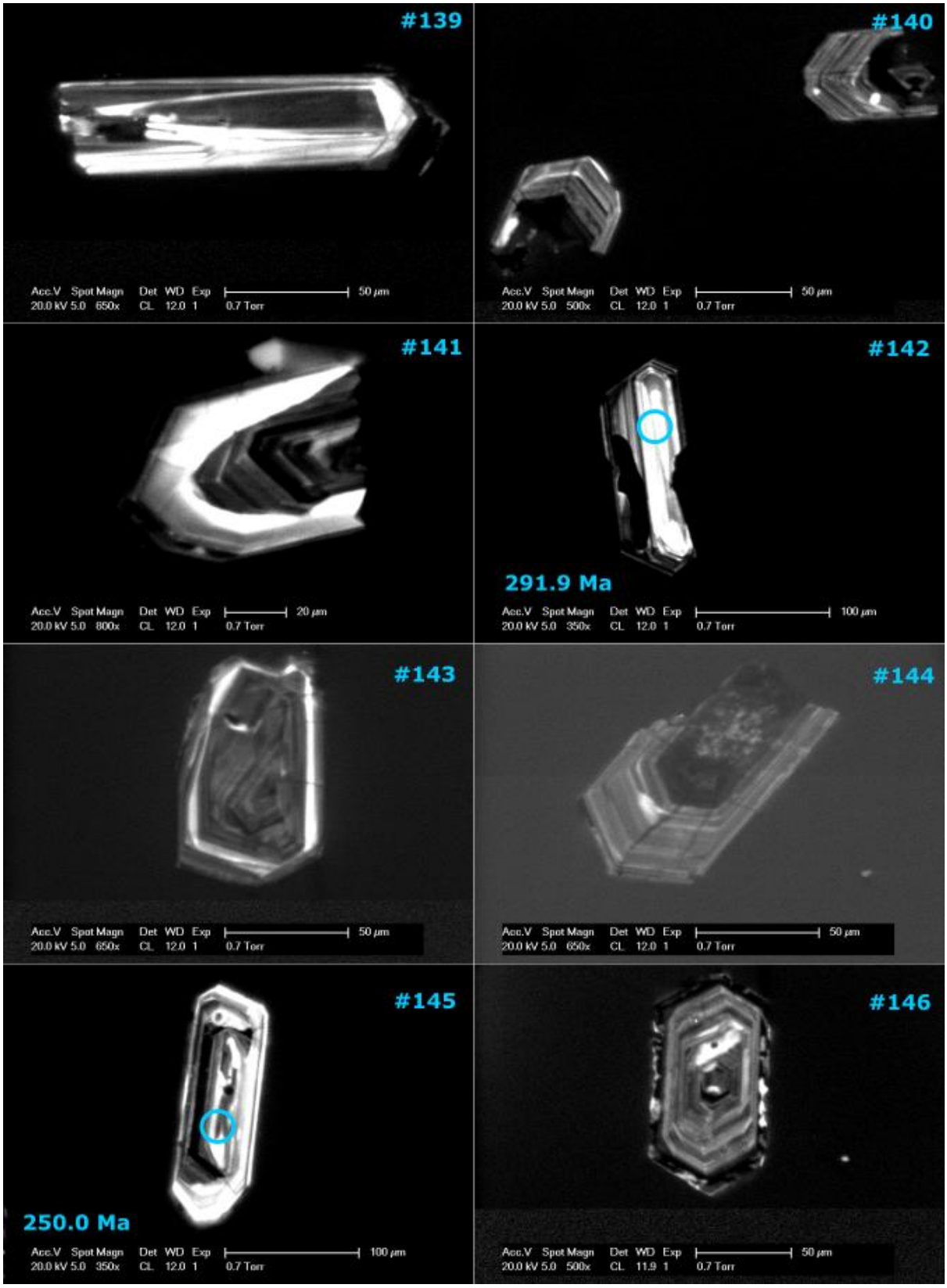
#139
Acc.V Spot Magn Det WD Exp 50 µm
20.0 kV 5.0 650x CL 12.0 1 0.7 Torr
#140
Acc.V Spot Magn Det WD Exp 50 µm
20.0 kV 5.0 500x CL 12.0 1 0.7 Torr
#141
Acc.V Spot Magn Det WD Exp 20 µm
20.0 kV 5.0 800x CL 12.0 1 0.7 Torr
#142
291.9 Ma
Acc.V Spot Magn Det WD Exp 100 µm
20.0 kV 5.0 350x CL 12.0 1 0.7 Torr
#143
Acc.V Spot Magn Det WD Exp 50 µm
20.0 kV 5.0 650x CL 12.0 1 0.7 Torr
#144
Acc.V Spot Magn Det WD Exp 50 µm
20.0 kV 5.0 650x CL 12.0 1 0.7 Torr
#145
250.0 Ma
Acc.V Spot Magn Det WD Exp 100 µm
20.0 kV 5.0 350x CL 12.0 1 0.7 Torr
#146
Acc.V Spot Magn Det WD Exp 50 µm
20.0 kV 5.0 500x CL 11.9 1 0.7 Torr

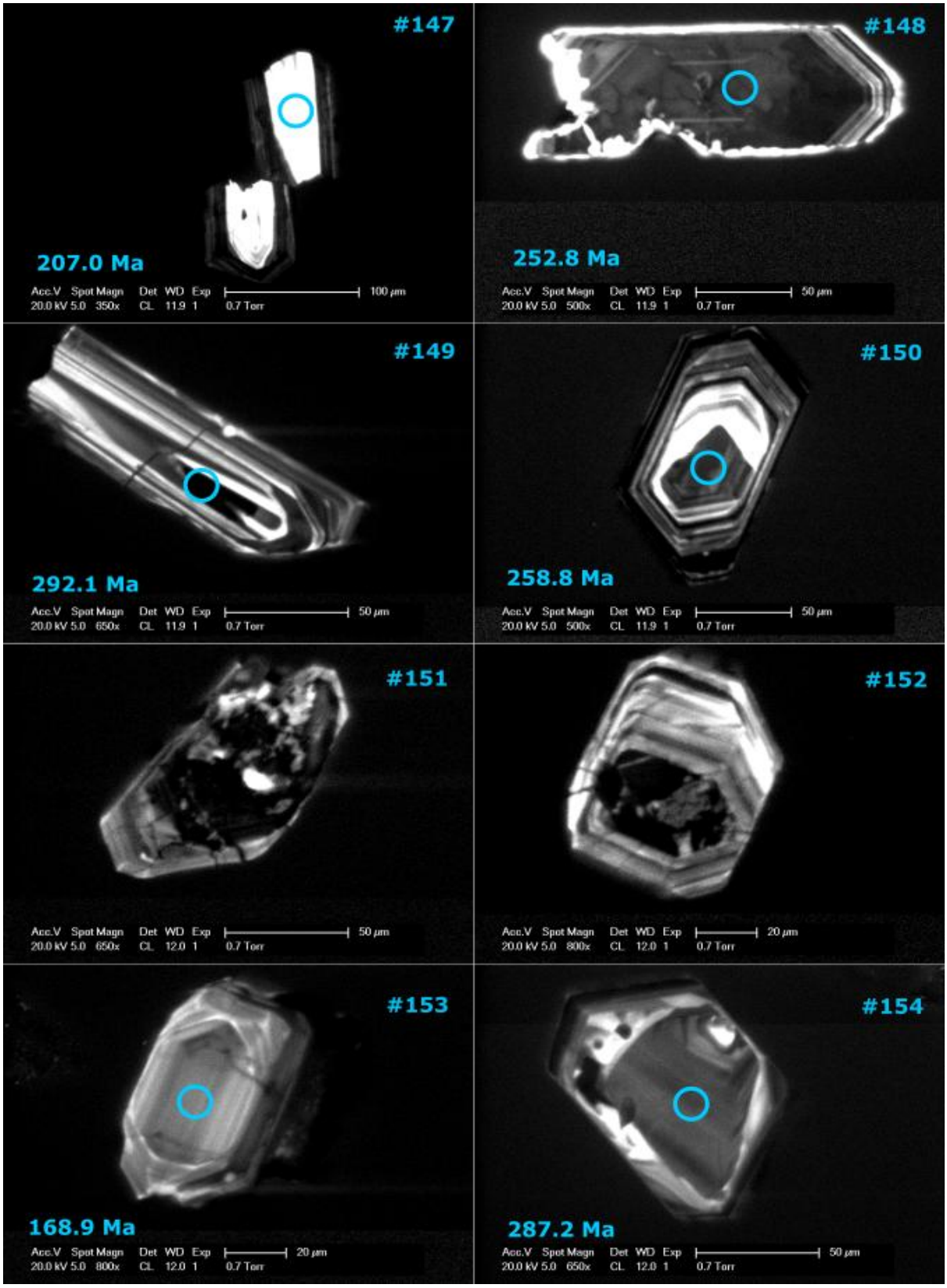
#147
207.0 Ma
Acc.V Spot Magn Det WD Exp 100 µm
20.0 kV 5.0 350x CL 11.9 1 0.7 Torr
#148
252.8 Ma
Acc.V Spot Magn Det WD Exp 50 µm
20.0 kV 5.0 500x CL 11.9 1 0.7 Torr
#149
292.1 Ma
Acc.V Spot Magn Det WD Exp 50 µm
20.0 kV 5.0 650x CL 11.9 1 0.7 Torr
#150
258.8 Ma
Acc.V Spot Magn Det WD Exp 50 µm
20.0 kV 5.0 500x CL 11.9 1 0.7 Torr
#151
Acc.V Spot Magn Det WD Exp 50 µm
20.0 kV 5.0 650x CL 12.0 1 0.7 Torr
#152
Acc.V Spot Magn Det WD Exp 20 µm
20.0 kV 5.0 800x CL 12.0 1 0.7 Torr
#153
168.9 Ma
Acc.V Spot Magn Det WD Exp 20 µm
20.0 kV 5.0 800x CL 12.0 1 0.7 Torr
#154
287.2 Ma
Acc.V Spot Magn Det WD Exp 50 µm
20.0 kV 5.0 650x CL 12.0 1 0.7 Torr


#155
Acc.V Spot Magn Det WD Exp 20 µm
20.0 kV 5.0 800x CL 12.0 1 0.7 Torr
#156
263.9 Ma
Acc.V Spot Magn Det WD Exp 50 µm
20.0 kV 5.0 650x CL 12.0 1 0.7 Torr
#157
Acc.V Spot Magn Det WD Exp 50 µm
20.0 kV 5.0 650x CL 12.0 1 0.7 Torr
#158
312.5 Ma
Acc.V Spot Magn Det WD Exp 50 µm
20.0 kV 5.0 500x CL 11.9 1 0.7 Torr
#159
Acc.V Spot Magn Det WD Exp 50 µm
20.0 kV 5.0 500x CL 11.9 1 0.7 Torr
#160
243.9 Ma
Acc.V Spot Magn Det WD Exp 50 µm
20.0 kV 5.0 650x CL 11.9 1 0.7 Torr
#161
243.6 Ma
Acc.V Spot Magn Det WD Exp 50 µm
20.0 kV 5.0 500x CL 11.9 1 0.7 Torr
#162
166.1 Ma
Acc.V Spot Magn Det WD Exp 50 µm
20.0 kV 5.0 500x CL 11.9 1 0.7 Torr

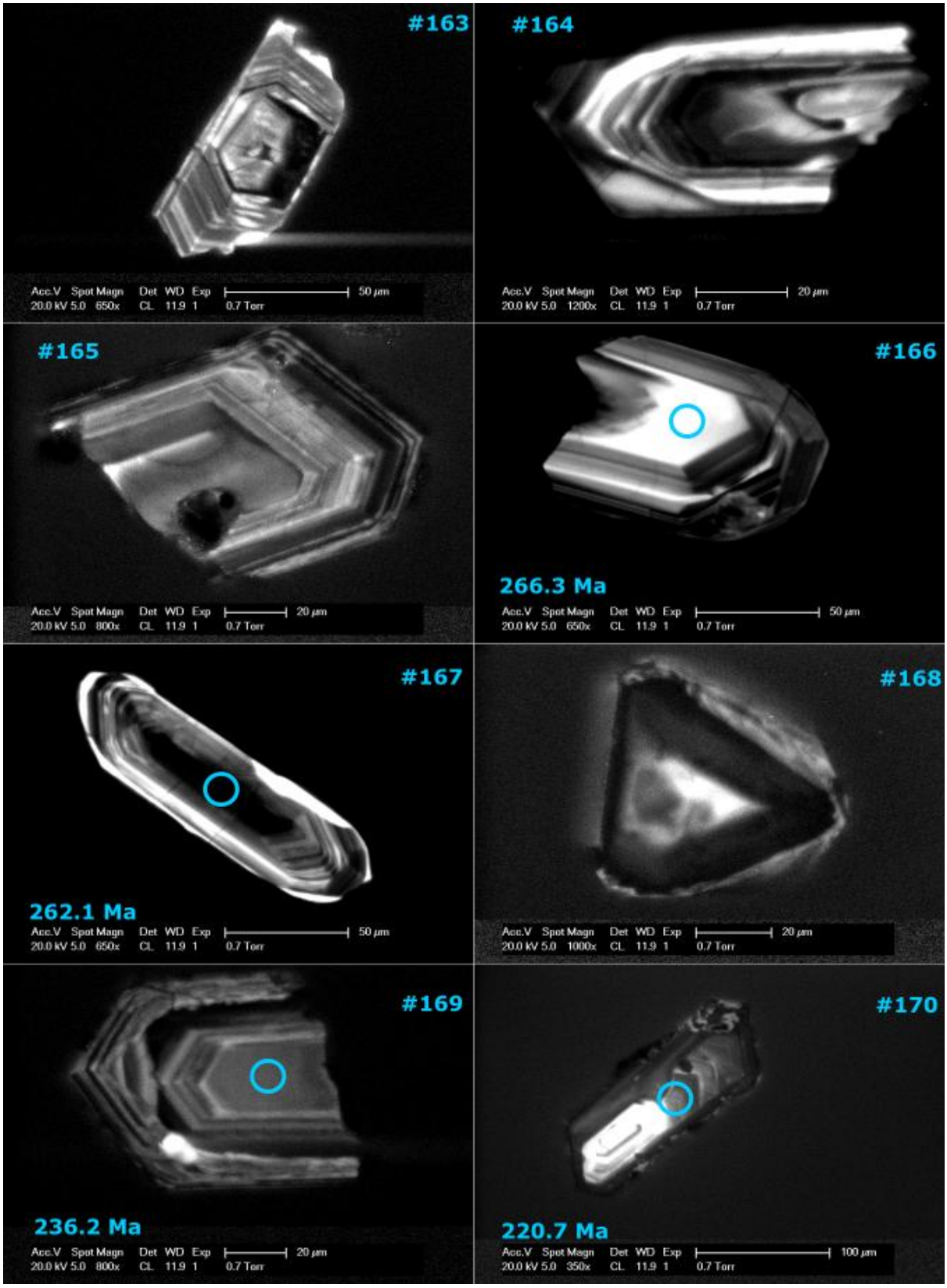
#163
Acc.V Spot Magn Det WD Exp 50 µm
20.0 kV 5.0 650x CL 11.9 1 0.7 Torr
#164
Acc.V Spot Magn Det WD Exp 20 µm
20.0 kV 5.0 1200x CL 11.9 1 0.7 Torr
#165
Acc.V Spot Magn Det WD Exp 20 µm
20.0 kV 5.0 800x CL 11.9 1 0.7 Torr
#166
266.3 Ma
Acc.V Spot Magn Det WD Exp 50 µm
20.0 kV 5.0 650x CL 11.9 1 0.7 Torr
#167
262.1 Ma
Acc.V Spot Magn Det WD Exp 50 µm
20.0 kV 5.0 650x CL 11.9 1 0.7 Torr
#168
Acc.V Spot Magn Det WD Exp 20 µm
20.0 kV 5.0 1000x CL 11.9 1 0.7 Torr
#169
236.2 Ma
Acc.V Spot Magn Det WD Exp 20 µm
20.0 kV 5.0 800x CL 11.9 1 0.7 Torr
#170
220.7 Ma
Acc.V Spot Magn Det WD Exp 100 µm
20.0 kV 5.0 350x CL 11.9 1 0.7 Torr

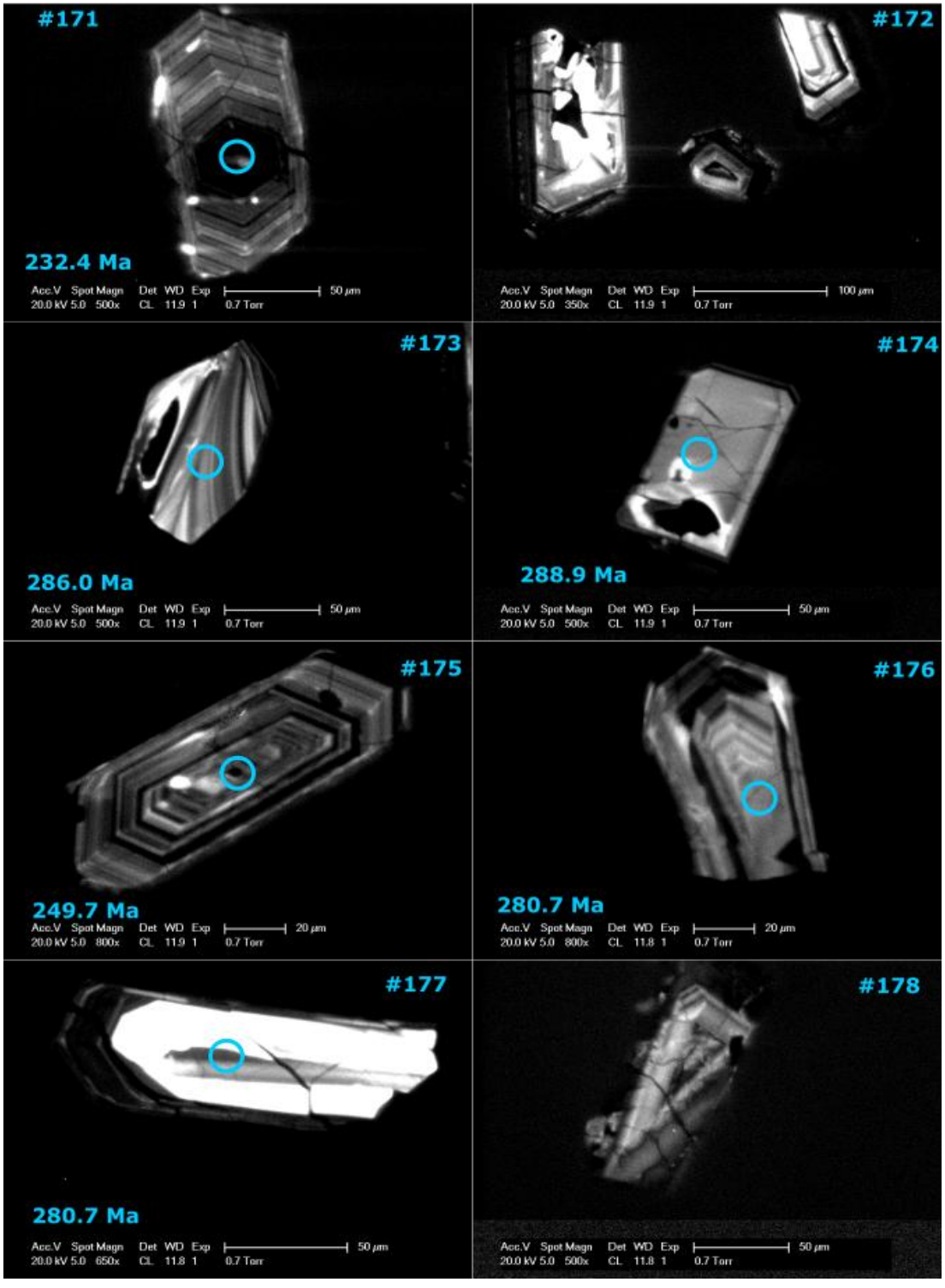
#171
232.4 Ma
Acc.V Spot Magn Det WD Exp 50 µm
20.0 kV 5.0 500x CL 11.9 1 0.7 Torr
#172
Acc.V Spot Magn Det WD Exp 100 µm
20.0 kV 5.0 350x CL 11.9 1 0.7 Torr
#173
286.0 Ma
Acc.V Spot Magn Det WD Exp 50 µm
20.0 kV 5.0 500x CL 11.9 1 0.7 Torr
#174
288.9 Ma
Acc.V Spot Magn Det WD Exp 50 µm
20.0 kV 5.0 500x CL 11.9 1 0.7 Torr
#175
249.7 Ma
Acc.V Spot Magn Det WD Exp 20 µm
20.0 kV 5.0 800x CL 11.9 1 0.7 Torr
#176
280.7 Ma
Acc.V Spot Magn Det WD Exp 20 µm
20.0 kV 5.0 800x CL 11.8 1 0.7 Torr
#177
280.7 Ma
Acc.V Spot Magn Det WD Exp 50 µm
20.0 kV 5.0 650x CL 11.8 1 0.7 Torr
#178
Acc.V Spot Magn Det WD Exp 50 µm
20.0 kV 5.0 500x CL 11.8 1 0.7 Torr

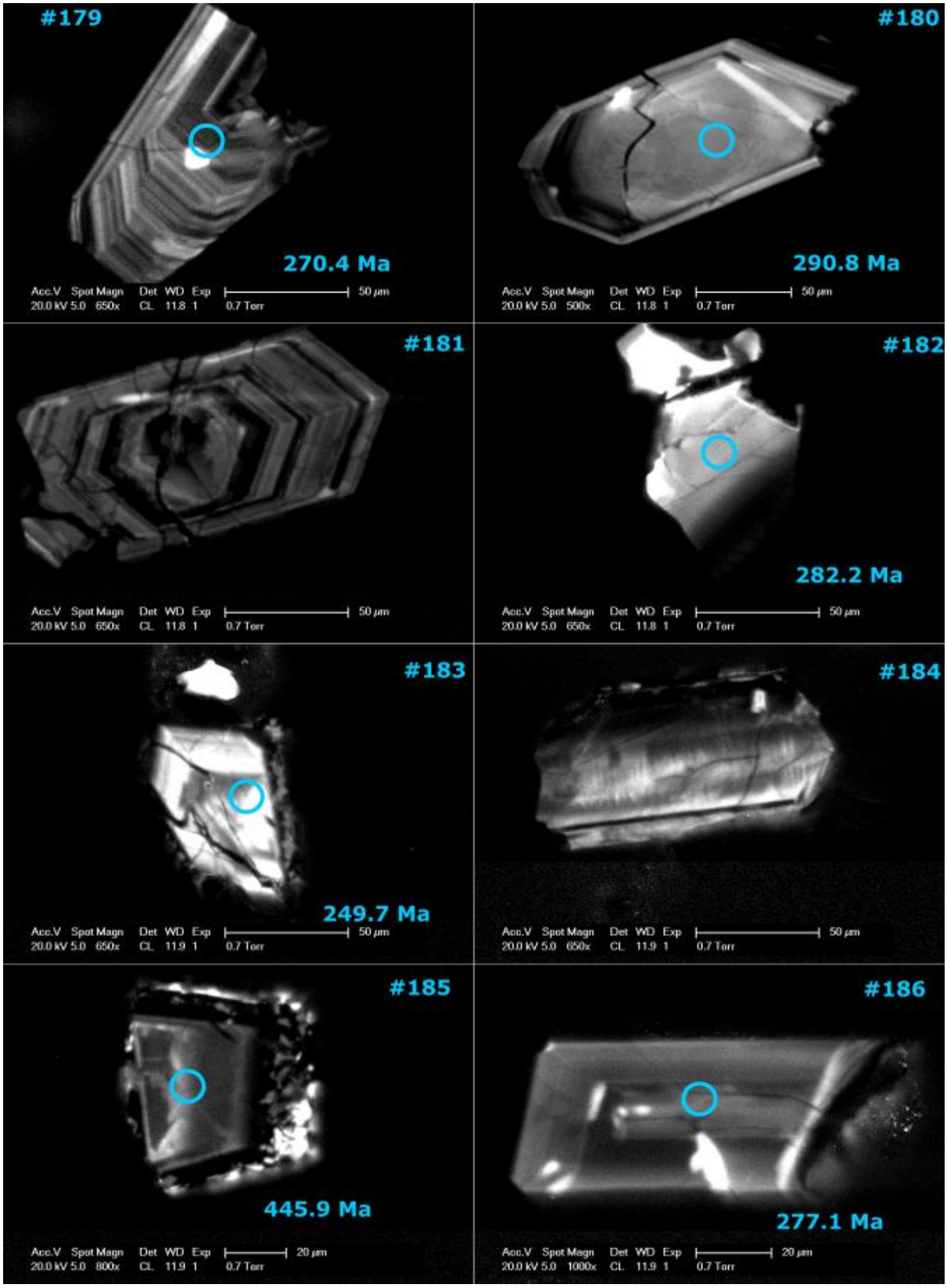
#179
270.4 Ma
Acc.V Spot Magn Det WD Exp 50 µm
20.0 kV 5.0 650x CL 11.8 1 0.7 Torr
#180
290.8 Ma
Acc.V Spot Magn Det WD Exp 50 µm
20.0 kV 5.0 500x CL 11.8 1 0.7 Torr
#181
Acc.V Spot Magn Det WD Exp 50 µm
20.0 kV 5.0 650x CL 11.8 1 0.7 Torr
#182
282.2 Ma
Acc.V Spot Magn Det WD Exp 50 µm
20.0 kV 5.0 650x CL 11.8 1 0.7 Torr
#183
249.7 Ma
Acc.V Spot Magn Det WD Exp 50 µm
20.0 kV 5.0 650x CL 11.9 1 0.7 Torr
#184
Acc.V Spot Magn Det WD Exp 50 µm
20.0 kV 5.0 650x CL 11.9 1 0.7 Torr
#185
445.9 Ma
Acc.V Spot Magn Det WD Exp 20 µm
20.0 kV 5.0 800x CL 11.9 1 0.7 Torr
#186
277.1 Ma
Acc.V Spot Magn Det WD Exp 20 µm
20.0 kV 5.0 1000x CL 11.9 1 0.7 Torr


Fig. S1: Zircon grains analysed in this work. The circles represent the places where the SIMS excavated the grain to estimate the U–Pb ages. The bottom number in the figures represent the U–Pb ages deconvolved from the grains. The numbers in the top right corner represent the grain number used in the laboratory.